ELUCIDATION OF CHEMICAL REACTIONS BY TWO-DIMENSIONAL RESONANCE RAMAN SPECTROSCOPY

Brian Paul Molesky

A dissertation submitted to the faculty of the University of North Carolina at Chapel Hill in partial fulfillment of the requirements for the degree of Doctor of Philosophy in the Department of Chemistry in the College of Arts and Sciences

Chapel Hill
2016

Approved by:

Yosuke Kanai

Andrew Moran

James Cahoon

Joanna Atkin

Scott Warren

ABSTRACT

Brian Paul Molesky: Elucidation of Chemical Reactions by Two-Dimensional Resonance Raman Spectroscopy
(Under the direction of Andrew Moran)

It has been shown for many systems, including photosynthetic complexes, molecule-semiconductor interfaces, and bulk heterojunctions, that interaction between electronic and nuclear dynamics may heavily influence chemical mechanisms. Four-wave-mixing spectroscopies (i.e. transient absorption, two-dimensional spectroscopy) provide some insight into such non-equilibrium processes but are limited by the single "population time" available in these types of experiments. In this dissertation, two-dimensional resonance Raman spectroscopy (2DRR) is developed to obtain new information regarding chemical reactions that possess time coincident electronic and nuclear evolution. These new insights can only be acquired through higher-order techniques possessing two "population times". Specifically, the coherent reaction mechanism in triiodide photodissociation and structural heterogeneity in myoglobin are investigated.

All multidimensional spectroscopies have roots in the off-resonant multidimensional Raman techniques developed from the late 1980's to the early 2000's. Throughout their development these experiments were plagued with technical challenges that eventually halted further use. In this dissertation it is shown through rigorous experimental tests that the technical challenges of the past are obviated for 2DRR, which is done under electronically resonant conditions. The key is that under electronic resonance the harmonic character of vibrational

modes contributes to the signal. Under off-resonant conditions signal generation depends on much weaker effects.

Upon absorption of light ranging from ~250 to ~500 nm triiodide photodissociates into diiodide and radical iodine on the same time scale as the period of triiodide's symmetric stretch, impulsively initiating coherence in the stretching coordinate of diiodide. In this dissertation, the sensitivity of 2DRR to coherent reaction mechanisms is shown by directly measuring, for the first time, how the nonequilibrium geometry of triiodide at the moment of photodissociation determines the stretching frequency of diiodide.

The functions of heme proteins involve ligand binding and dissociation events, which are facilitated by the fast exchange of energy between the heme and aqueous solvent. It is known that the heme's propionic acid side chains act as an effective "gateway" for this fast energy exchange. In this dissertation it is shown that the propionic chains within myoglobin posses significant structural heterogeneity, suggesting that this may be an important factor in facilitating the functions of heme proteins.

To my parents, Phil and Linda Molesky; my grandparents; my great-grandparents; and so on...

ACKNOWLEDGEMENTS

I would like to first thank my advisor, Dr. Andrew Moran, for his guidance and support throughout my doctoral studies. None of the work presented in this dissertation would have been possible without him. I would also like to thank past colleagues in the Moran group, including Dr. Brant West, Dr. Jordan Womick, and Dr. Stephen Miller, for training me when I first began here at UNC. Of course I also thank my current colleagues, Zhenkun Guo, Dr. Paul Giokas, Thomas Cheshire, Olivia Williams, and Andrew "Android" Ross, for their contributions to the work. I thank my undergraduate academic/research advisor at the University of South Carolina, Dr. Donna A. Chen, for initially directing me along the path of physical chemistry and for her unwavering dedication to my academic and professional success. I also thank my high school chemistry teacher, Mrs. Mary Jo Laslo, for first opening my eyes to the wonders of chemistry. Additionally I express gratitude to Kathy Wood and the rest of the IME for their support over the past five years. Finally, I owe a great deal of thanks to all of my family and friends, without whom I would not have made it through this doctoral program or even gotten here in the first place.

TABLE OF CONTENTS

LIST OF TABLES

LIST OF FIGURES

LIST OF ABBREVIATIONS AND SYMBOLS

1D	one-dimensional
2D	two-dimensional
2DFT	two-dimensional Fourier transform
2DIR	two-dimensional infrared spectroscopy
2DRR	two-dimensional resonance Raman spectroscopy
2DUV	two-dimensional ultraviolet spectroscopy
3DIR	three-dimensional infrared spectroscopy
4WM	four-wave-mixing
6WM	six-wave-mixing
a	hollow core fiber bore radius
A	amplitude
Å	angstrom
$A(\omega,T)$	absorption as a function of frequency and time
AP	actinic pump
Ar	argon
atm	atmosphere
α_{nm}	hollow core fiber attenuation constant for mode EH_{nm}
B_m	Boltzmann population of level m
BBO	β-barium borate
β_{nm}	hollow core fiber phase constant for mode EH_{nm}
c	speed of light
c	collective bath coordinate
C	concentration

$C(T)$	correlation function
CCD	charge coupled device
cm	centimeter
cm^{-1}	wavenumber
CMOS	complimentary metal-oxide semiconductor
CS_2	carbon disulfide
CSRS	coherent Stokes Raman scattering
$\chi^{(5)}$	fifth-order susceptibility
d	distance or dimensionless displacement
DO	diffractive optic
Δ	energy gap fluctuation amplitude or temporal width of laser pulse
ΔA	transient absorption
$\Delta\Delta A$	transient pump-repump-probe absorption
$\delta\omega_{ab}(t)$	time dependent energy gap fluctuations
e	electron charge
e	excited state index
E	energy
E	electric field amplitude
$E^{(3)}$	direct third order signal field
$E^{(5)}$	direct fifth order signal field
$E(t)$	electric field
E_{BB}	broadband response electric field
E_{cas}	cascaded electric field

E_{FSRS}	FSRS response electric field
EH_{nm}	hollow core fiber hybrid laser beam mode, nm
eV	electron volt
ESA	excited state absorption
ESE	excited state emission
ε	extinction coefficient
η_a	deviation of the harmonic mode frequency, a, from its mean value
η_{nm}	hollow core fiber coupling efficiency for mode EH_{nm}
Fe	iron
FROG	frequency resolved optical gating
fs	femtosecond
FSRS	femtosecond stimulated Raman spectroscopy
FT	Fourier Transform
FWHM	full width at half maximum
g	ground state index
g/mm	grooves per millimeter
$g(t)$	line broadening function
GDD	group delay dispersion
GSB	ground state bleach
GVD	group velocity dispersion
GVM	group velocity mismatch
GW	jiga Watt ;)
γ_{nm}	propagation constant for mode, nm
Γ	exponential damping function or absorbance line width

h	Planck's constant
$\hbar$	reduced Planck's constant ($=h/2\pi$)
H	Hamiltonian operator
$H^{(0)}$	time-independent Hamiltonian
H'	time-dependent Hamiltonian
HCF	hollow core fiber
His	histidine
HWHM	half width half max
Hz	Hertz
I_2^-	diiodide ion
I_3^-	triiodide ion
$I\bullet$	radical iodine
I	laser intensity
I_{AP}	actinic pump intensity
I_{RP}	Raman pump intensity
I_{St}	Stokes intensity
$I_{cascade}$	intensity of cascade response
$I_{direct}^{(3)}$	intensity of direct third-order response
$I_{direct}^{(5)}$	intensity of direct fifth-order response
IR	infrared
$J_{gu,gm}(\omega_2)$	describes vibrational wavepacket motion in ω_2
Δk	wavevector mismatch
k_B	Boltzmann factor

k_n	wavevector of pulse “n”
kHz	kilohertz
KI	potassium iodide
ℓ	hollow core fiber length
l	pathlength
LEPS	London-Eyring-Polanyi-Sato
LO	local oscillator
λ	reorganization energy or wavelength or perturbative factor
Λ	bath fluctuation relaxation rate
Λ^{-1}	bath fluctuation relaxation time
m	mass
m_e	electron mass
MbO_2	oxymyoglobin (oxygen-ligated myoglobin)
MD	molecular dynamics
MEM	maximum entropy method
metMb	metmyoglobin (water-ligated myoglobin)
mL	milliliter
mm	millimeter
mM	millimolar
mOD	milli optical density
μm	micrometer
μ	transition dipole
$\hat{\mu}(t)$	dipole operator
μ_{eg}	electronic transition dipole

μJ	micro Joule
N	number density or order
n	total refractive index
n_0	linear refractive index
n_2	nonlinear refractive index
$n_e(I)$	intensity dependent electron concentration
Ne	neon
nm	nanometer
nJ	nano Joule
ω	frequency in wavenumbers (cm^{-1})
ω_0	carrier frequency
ϖ_a	mean value of the harmonic mode frequency, a
ω_{ab}	energy gap between states a and b
$\omega_{ab}(t)$	time dependent energy gap between states
$\bar{\omega}_{ab}$	average energy gap between states
ω_{AP}	actinic pump frequency
ω_L	laser carrier frequency
ω_p	plasma frequency
ω_{pr}	probe frequency
ω_{pu}	pump frequency
ω_{RP}	Raman pump frequency
ω_{vib}	vibrational frequency

p	product ground state index or gas pressure
$p*$	product excited state index
P	power
$P^{(n)}$	polarization at nth order
P_{cr}	critical power for self-focusing
PES	potential energy surface
pm	picometers
PORS	polarizability response spectroscopy
PP	pump-probe
PRP	pump-repump-probe
ps	picoseconds
ϕ	phase or phase shift
Φ	dihedral angle
$\psi(t)$	wavefunction
r	reactant ground state index
$r*$	reactant excited state index
R	relaxed (protein state)
R_{ab}	bond length
$R^{(n)}(t)$	response function term at nth order
RAPTORS	resonant pump third-order Raman spectroscopy
RISRS	resonant impulsive stimulated Raman scattering
RP	Raman pump
ρ	intermode correlation parameters
$\hat{\rho}(t)$	time dependent density operator

$S^{(n)}(t)$	response function at nth order
$S^{(3)}(\tau)$	transient grating signal field
$S(\omega_2, \omega_t)$	correlation spectrum
$S(\omega_1, \omega_2)$	2DRR spectrum
$S(\tau_1, \omega_2)$	FSRS like signal
$S_{CAS}(\tau_1, \omega_t)$	cascade response
$S_{SRS}(\omega_t)$	SRS response
$S_{TG}(\tau_1, \omega_t)$	transient grating response
SCF	solid core fiber
SPM	self-phase modulation
SRS	stimulated Raman scattering
ss	symmetric stretch
St	Stokes
σ	cross section or Gaussian width parameter
σ_a	inhomogeneous line width of mode a
$\sigma_{abs}(\omega)$	absorption line shape
$\sigma_{fl}(\omega)$	fluorescence line shape
T	tense (protein state)
T	time interval or temperature
τ	time delay or interval or standard deviation of temporal Gaussian
t	time point or interval
TA	transient absorption

TEM_{nm}	Gaussian laser beam mode, nm
TG	transient grating
Ti	titanium
Ti:S	titanium sapphire
TOD	third order dispersion
Tr	trace
θ	angle
$\theta(\tau)$	Heaviside step function or temporal phase
U	cubic expansion coefficients
u_{nm}	hollow core fiber modal constant
UV	ultraviolet
V	volume, potential, or coupling
V_{ge}	dipole operator
VIS	visible
ν	frequency or ratio of external and internal media refractive indices
$\xi(t)$	Gaussian envelope function
ξ_L	laser electric field amplitude

CHAPTER 1: INTRODUCTION

1.1. Uncovering Ultrafast Chemistry in Condensed Phases

Perturbative models that assume an equilibrium initial condition before the nonradiative transition of interest (i.e. Marcus equation, Forester energy transfer)[1-3] are poor when applied to photoinduced electronic relaxation mechanisms that occur on the same time scale as nuclear motions of the system and surroundings. It has been shown for many systems, including polymer-fullerene blends, photosynthetic complexes, and semiconductor interfaces, that time-coincident electronic and nuclear evolution may result in non-trivial quantum effects such as bursts of population flow in charge transfer processes.[4-8] These processes can involve coherent reaction mechanisms in which nuclear motions of the reactant and product are correlated.

The interaction between electronic and nuclear dynamics that occurs on fast timescales may also play a significant role in important sub-picosecond energy transfer processes.[9-15] In heme proteins fast energy exchange between the heme and the surroundings is vital to functions that reorganize the heme, like ligand binding and dissociation. Heme reorganization translates into structural changes of the protein matrix affecting conformation and further activity.[16-21] Line broadening mechanisms of the vibrational modes involved in the exchange of energy are of particular interest because they reflect fluctuations in the geometry of moieties within the heme that are relevant to this process.

In this dissertation, two-dimensional resonance Raman spectroscopy (2DRR) is developed to investigate coherent reaction mechanisms and line broadening mechanisms in

ultrafast condensed phase chemistry. Specifically, the coherence transfer from reactant to product in the photodissociation of triiodide and structural heterogeneity in myoglobin are studied. The viability of 2DRR is proven for gaining valuable new insights into important chemistry involving time coincident electronic and nuclear evolution. The work presented herein has been featured as Editor's Choice in the *Journal of Chemical Physics* for the years 2014 and 2015.[22,23]

The key contributions of this dissertation are as follows:

- Developed 2DRR for studies of fast chemical reactions.
- Showed that 2DRR reveals correlations between nuclear motions of the reactant and product in triiodide photodissociation.
- Utilized 2DRR to measure structural heterogeneity in vibrational coordinates of myoglobin responsible for energy exchange with the surrounding environment.
- Generated deep UV laser pulses by cofilamentation of near IR and visible pulses in high pressure Ne.

1.2. Development of Multidimensional Resonance Raman Spectroscopy

Over the past 20 years multidimentional spectroscopies have become fairly widespread with applications in physics, chemistry, and biology.[24-33] The most common multidimensional technique, known as '2D spectroscopy', takes advantage of a photon echo-like pulse sequence to eliminate the trade-off between time and frequency resolution inherent to traditional one-dimensional (i.e. pump-probe) experiments.[28-30,34,35] Currently, 2D spectroscopy is implemented throughout the light spectrum and has generated new insights into dynamics ranging from energy transfer in photosynthesis to chemical equilibrium exchange in liquids.[36-46]

The development of all multidimensional spectroscopies originated from picosecond coherent Raman studies in the late 1970's and early 1980's. At the time researchers claimed it was possible to distinguish homogeneous and inhomogeneous line broadening mechanisms using one-dimensional coherent Raman techniques.[47-52] Theory work in 1985 proved this to be impossible.[53] In fact higher-order, multidimensional techniques would be required to gain such information.[53-55] However, implementation of the theorized experiments was met with substantial technical challenges.[55-65] Although success was finally achieved in 2002[62], further development of multidimensional Raman essentially ceased due to the challenges involved.

It is important to note that the experiments attempted up to that point were done under conditions where the sample was transparent to the perturbing laser pulses. In 2DRR, where all laser pulses are electronically resonant with the sample, the difference in selection rules obviates the technical challenges of the past. The key is that Franck-Condon activity promotes signal generation from both harmonic and anharmonic modes under conditions of electronic resonance. Under off-resonant conditions the signal depends solely on anharmonic modes or other relatively weak effects like nonlinear coordinate-dependence of the polarizability.[55,59,65] The difference is illustrated in Figure 1.1. As evidence of this critical distinction, detailed analyses rooted in both theory and experiment are presented in Chapters 4 and 6 for triiodide and myoglobin, respectively. The findings of these analyses are supported by a previous discussion by Hamm and coworkers.[66]

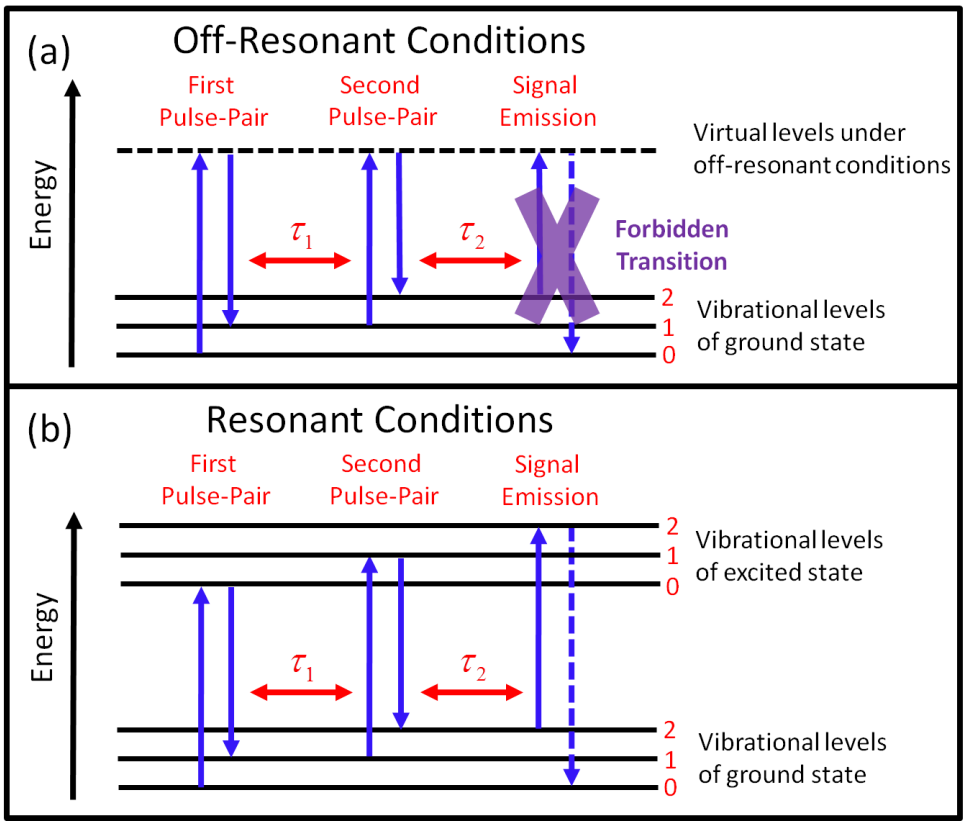

Figure 1.1. In a two-dimensional Raman experiment a pair of time-coincident laser pulses excites the sample before a delay period, τ_1. Another pair of time-coincident pulses then reexcites the sample. After a second delay period, τ_2, a final laser pulse induces signal emission. (a) Under off-resonant conditions, where the sample is transparent to the laser excitation and is thus promoted to virtual levels, selection rules dictate that harmonic modes cannot contribute to the signal intensity. Generation of the desired signal depends on weak effects like anharmonicity or nonlinear coordinate-dependence of the polarizability. This is the origin of the technical challenges experienced in multidimensional coherent Raman experiments conducted under off-resonant conditions. (b) Under resonant conditions, where the sample absorbs the laser light and is promoted to real excited states, both harmonic modes and anharmonic modes contribute to the signal generation mechanism, obviating the aforementioned challenges.

The development of 2DRR in this dissertation is motivated by the use of related methods for studies of molecular photochemistry[67-78] and experimental advances that have stimulated growth in the field of coherent multi-dimensional spectroscopy.[24,25,36,79-82] The primary purposes

of 2DRR are to understand coherent reaction mechanisms and uncover structural heterogeneity that accompanies fast photochemistry.

1.3. Coherent Photodissociation of Triiodide

The observation of coherent vibrational motion concomitant with electronic processes has been reported for a multitude of interesting systems including proteins, photosynthetic complexes, quantum dots, semi-conductor interfaces, aggregates, and photovoltaics.[4-15,40,83-102] However, the origin and function of this phenomenon is still under debate.[5,6,13,93,103-106] To discern the role of coherent nuclear motion in important processes like electron transfer and energy transfer, a detailed understanding of coherent reaction mechanisms must be obtained. Direct measurement of correlations between reactant and product motions are necessary for full comprehension of the relationship between structure and function.[107]

It is impossible to directly measure correlations between a reactant and product with four-wave-mixing (4WM) spectroscopies, including pump-probe techniques and 2D spectroscopy, because there is only one 'population time' in which nuclear evolution takes place. Additionally, in 4WM spectroscopies the photochemistry is always initiated from the equilibrium geometry of the reactant. Two population times are necessary to prepare a nonequilibrium reactant state before the photochemical reaction is induced. By measuring the reactant in the first period of evolution and the product in the second period, correlations between the nonequilibrium geometry of the reactant and the vibrational motion of the product can be determined. Each experimentally controlled period of evolution is a dimension of the experiment.

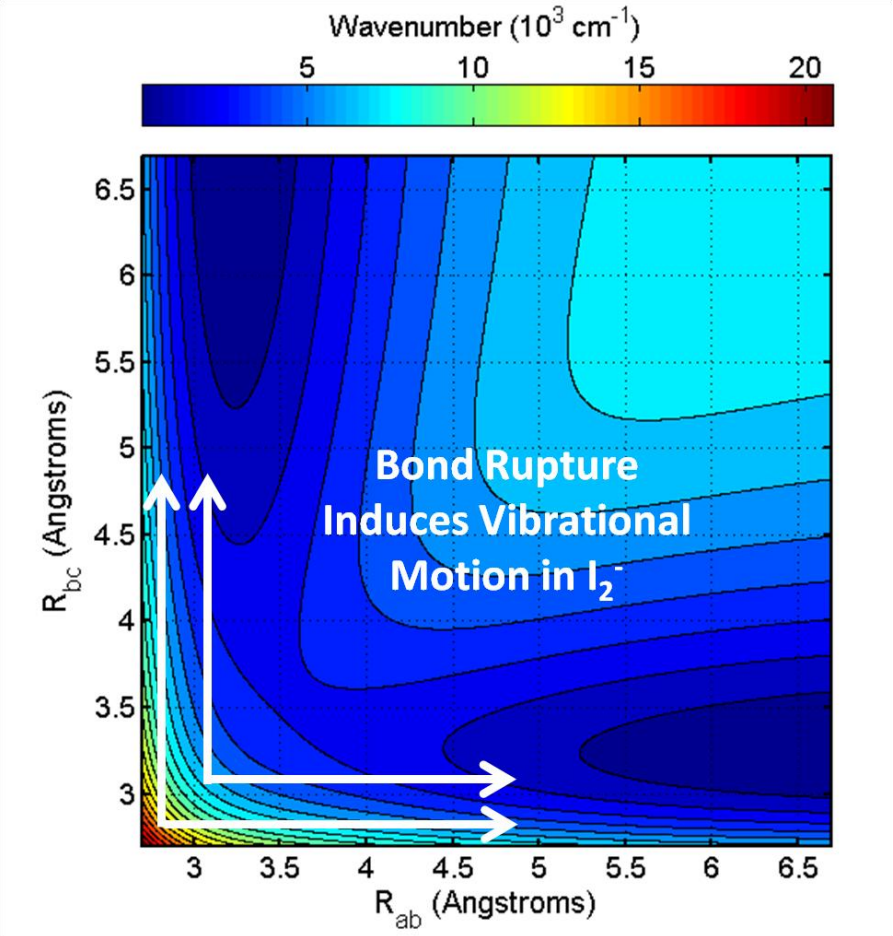

Figure 1.2. Potential energy surface (PES) for the photodissociation of triiodide. [108,109] Here R_{ab} and R_{bc} are the bond lengths between adjacent iodine atoms. A ground state wavepacket at equilibrium is promoted to the excited electronic state, where force is accumulated due to the steep gradient of the PES. A finite displacement in the asymmetric stretch induces photodissociation of triiodide into diiodide ions and iodine radicals. This entire process occurs in approximately 300 fs, the period of triiodide's symmetric stretch. As such the reaction is impulsive and the wavepacket transitions from reactant to product without loss of coherence. 2DRR studies determine how the nonequilibrium geometry of triiodide at the time of photodissociation directly determines the distribution of vibrational quanta in diiodide.

In this dissertation the sensitivity of 2DRR to coherent reaction mechanisms is demonstrated with measurements of the photodissociation of triiodide in solution. Triiodide photodissociation was studied at length using one-dimensional stimulated and resonance Raman spectroscopies in the 1990's.[109-119] The investigation in this dissertation is motivated by

knowledge of this extraordinary reaction mechanism. Upon the absorption of light ranging from ~250 to ~500nm triiodide is electronically excited and motion is activated along the symmetric stretch vibrational coordinate. Due to the steep gradient of the anharmonic potential energy surface (PES), illustrated in Figure 1.2, the ensemble 'wavepacket' quickly traverses the PES along the symmetric stretch until a finite displacement along the asymmetric stretch induces dissociation into atomic iodine and vibrationally hot diiodide ions.[114-116,120] The chemical equation is given in Equation 1.1. The diiodide ions, produced directly in the electronic ground state, possess near 20 vibrational quanta of energy and dump most it into the solvent within 3-4 ps.[110,115,119,120]

$$I_3^- + h\nu \rightarrow I_2^- + I\bullet \tag{1.1}$$

The photodissociation of triiodide occurs on a time scale shorter than[110,120], or comparable to[116,121], the vibrational period of its symmetric stretch (i.e. ≤ 300fs), such that coherence is impulsively initiated in the stretching coordinate of diiodide. This key feature of the chemical reaction allows for a 'coherence transfer transition' from reactant to product in which the nonequilibrium geometry of triiodide at the time of photodissociation directly determines the vibrational frequency of the diiodide symmetric stretch (i.e. the distribution of vibrational quanta in diiodide ions). In other words, the vibrational wavepacket transitions between reactant and product states without loss of coherence. In Chapter 5 2DRR experiments selectively detect vibrational motions of the reactant and product in separate periods of nuclear evolution (i.e. 'dimensions') to directly measure this correlation for the first time. Along with triiodide photodissociation, 2DRR is sensitive to other photochemical processes where the chemistry occurs on the same time scale as the system's vibrational period(s), such as ligand dissociation in heme proteins.[122]

1.4. Structural Heterogeneity and Vibrational Energy Exchange in Myoglobin

The biological functions of many heme proteins, including the transfer and storage of molecular oxygen, catalysis, electron transfer, and signaling, intimately involve ligand binding and dissociation events.[123] These events transfer vibrational energy to the heme, initiating correlated structural changes with large amplitudes.[19] Fast exchange of energy with the aqueous surroundings is critical for mediating operations of heme proteins because reorganization of the heme directly affects the protein's tertiary and quaternary structure. The structure of the protein backbone then determines its activity.[16-21] Perhaps the most commonly known example of this is the transition of hemoglobin between R (relaxed) and T (tense) states upon binding and dissociation of oxygen molecules to and from the Fe atoms within its heme groups. These conformational changes form a feedback loop controlling hemoglobin's affinity for oxygen. Modulation of its oxygen affinity enables the uptake, transport, and delivery of oxygen, as well as the disposal of carbon dioxide.[19-21]

To mediate these processes, vibrational energy is quickly funneled to the solvent through the heme's propionic acid side chains that extend from the protein's hydrophobic pocket. The propionic acid chains are hydrogen bound to water molecules in the external environment, facilitating this fast energy exchange.[124-129] The protein matrix is less effective than the solvent for this purpose despite having approximately 90 van der Waals contacts with the heme.[19] The mechanism of energy transfer from heme to solvent via the propionic acid chains was first proposed by Hochstrasser and coworkers in 1994.[124] Molecular dynamics simulations in subsequenct years by Straub and coworkers supported this proposal.[125,126] Finally in 2006 experimental work on native and mutant myoglobin variants by Kitagawa and coworkers and Mizuntani and coworkers confirmed that indeed the fast exchange of heat between the heme and

aqueous solvent was made possible by the 'funneling' of vibrational energy through the propionic acid chains.[127,128]

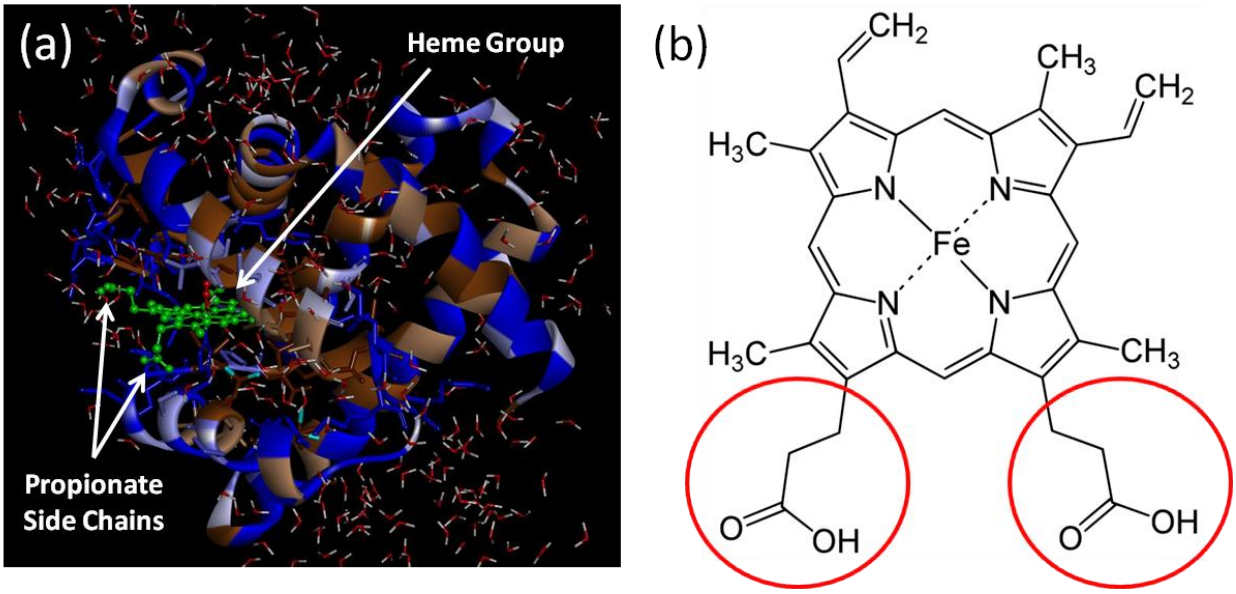

Figure 1.3. (a) A single molecule of myoglobin in an aqueous bath. The heme group, colored in green, is tucked in the protein's hydrophobic pocket except for the propionic acid side chains which extend into the surrounding environment and are hydrogen bound to water molecules. (b) The structure of the heme group possessed by myoglobin. The propionic acid side chains are circled in red. 2DRR studies suggest that structural heterogeneity of the propionic acid chains may play an important role in the fast rate of energy exchange between the heme and aqueous solvent.

Containing only one active site, myoglobin is an excellent model system for studies of vibrational energy exchange in heme proteins.[16,17,21,123] Figure 1.3(a) shows one molecule of myoglobin in aqueous solution. The heme group and propionic acid side chains are clearly marked in Figure 1.3(a) and shown separately in Figure 1.3(b). Myoglobin's primary biological function is to store and release molecular oxygen in muscle tissue.[21] Following photodissociation of the ligand many vibrational modes of the heme are activated including in-plane porphyrin modes, out-of-plane modes such as the Fe-His stretch, and bending and wagging

of the side chains.[83,84,130] By concerted action of these modes, vibrational energy is redistributed into the surroundings in about 4-6 ps, primarily through the propionic acid side chains.[46,123-129,131-134]

In this dissertation 2DRR is used to study structural heterogeneity involved with this process. The ability to distinguish homogeneous and inhomogeneous line broadening mechanisms in myoglobin is motivated by the goals of the earliest multidimensional Raman experiments,[53,135] as well as the many experimental and theoretical studies of this system and other heme proteins.[16,18,19,46,83,84,98,123-129,131-133] Figure 1.4 illustrates the spectroscopic signatures of these mechanisms, which are much like those established in 2DIR experiments.[24,28,34,38] Inhomogeneous broadening indicates correlation between vibrational frequencies in each of the two experimental dimensions (i.e. periods of nuclear evolution), revealing structural heterogeneity in the system.[136,137] This information cannot be obtained from one-dimensional Raman spectroscopies.[53-55]

In Chapter 7 it is shown that the greatest amount of structural heterogeneity in the heme group of myoglobin is associated with a vibrational mode localized on the propionic acid side chains, suggesting that the propionic acid chains posses significant geometric variation at equilibrium, which may play an important role in the fast rate of energy exchange between the heme and aqueous solvent. It is also shown that the amount of inhomgeneous broadening in the Fe-His stretch reflects variation of the Fe-His bond length, influenced by the geometry of the protein around the active site. The work demonstrates the usefulness of 2DRR for obtaining new insights into the role of line broadening mechanisms in important ultrafast chemistry of heme proteins and other complex systems with many active vibrational coordinates.

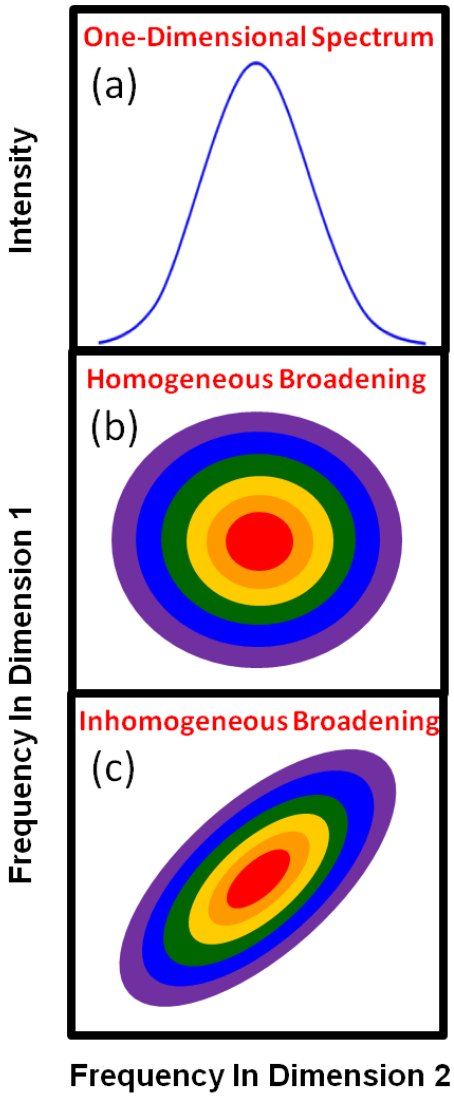

Figure 1.4. Signatures of homoegeneous and inhomogeneous line broadening in 2DRR. (b) In the limit of pure homogeneous broadening the 2D line shape of a peak associated with some vibrational mode will appear entirely circular, indicating that the frequencies detected in the experiment's two time periods of evolution (i.e. the experiment's two 'dimensions') are not correlated. (c) Inhomogeneous broadening will cause elongation of the 2D peak about the diagonal revealing correlation between vibrational motions detected in separate dimensions. Correlated 2DRR line shapes imply that geometric fluctuations are slow compared to vibrational dephasing, indicating that the molecular structures involved possess geometric sub-ensembles at equilibrium (i.e. structural heterogeneity). (a) By integrating over dimension 1 a spectrum is obtained where the intensity in either (b) or (c), equivalently, is plotted against one frequency dimension. This is the type of spectrum gathered in 1D techniques (i.e. pump-probe). Information regarding inhomogeneous broadening, and thus structural heterogeneity, is not obtainable with 1D spectroscopies.

1.5. Dissertation Contents

The introductory chapter has provided background and context for the work contained in this dissertation. To aid in navigation, brief descriptions of the content of remaining chapter are now presented. Chapter 2 describes the theoretical framework behind spectroscopic models and methods that are commonly employed in condensed phase studies, underpinning the more complex developments in later chapters. Chapter 3 discusses the nontraditional methods of femtosecond pulse generation and the four- and six-wave mixing spectroscopies that are developed and/or utilized in this work.

The next two chapters are focused on the photodissociation of triiodide. Chapter 4 contains the initial development and implementation of 2DRR. Ground-state vibrations of triiodide are probed with deep UV laser pulses generated by filamentation in high pressure Ne. A model is developed to understand the signals, allowing for comparison between experiment and theory. This comparison, along with a battery of rigorous tests, proves that 2DRR measurements of triiodide are insusceptible to the technical challenges that had previously plagued nonresonant multidimensional Raman experiments.

In Chapter 5 2DRR is used to expose correlations between coherent nuclear motions of the reactant and product in the photodissociation of triiodide. A theoretical model is developed in which the chemical reaction is treated as a ‘coherence transfer transition’ from triiodide to diiodide. Predictions of this model match the experimental results. It is shown how the nonequilibrium geometry of the reactant directly determines the vibrational frequency of the product.

Chapters 6 and 7 involve studies of myoglobin. In Chapter 6 versions of 2DRR are developed in which the second dimension of the experiment is obtained directly in the frequency domain, akin to a femtosecond stimulated Raman spectroscopy (FSRS) experiment but with total elimination, or significant reduction, of the unwanted background. The pronounced improvement in sensitivity and data acquisition rate is utilized in a study of water ligated myoglobin. Theoretical modeling and rigorous experimental tests confirm that 2DRR measurements of heme proteins are free from the technical challenges of nonresonant multidimensional Raman.

In Chapter 7 the power of 2DRR is leveraged to investigate line broadening mechanisms in both oxygen- and water- ligated myoglobin. Signatures of inhomogeneous broadening are established with model calculations, and it is shown that the greatest amount of structural heterogeneity is associated with the heme's propionic acid side chains. Molecular dynamics simulations suggest that this reflects fluctuations in their geometries. Knowledge of these fluctuations may be useful for understanding functional mechanisms of heme proteins because the side chains act as a gateway for thermal energy exchange between the heme and aqueous solvent.[124-129]

Finally, Chapter 8 provides some concluding remarks on the prior chapters. In addition, the future direction of this work is discussed by presenting an ongoing investigation of deoxygenated myoglobin and carbonmonoxide ligated myoglobin. It is suggested that the structural heterogeneity in the propionic acid side chains of the heme translates into heterogeneity in the rate of thermal energy transfer to the solvent.

1.6. REFERENCES

(1) Mukamel, S. *Principles of Nonlinear Optical Spectroscopy*; Oxford University Press: New York, 1995.

(2) Nitzan, A. *Chemical Dynamics in Condensed Phases: Relaxation, Transfer, and Reactions in Condensed Molecular Systems*; Oxford University Press: New York, 2006.

(3) Valkunas, L.; Abramavicius, D.; Mančal, T. *Molecular Excitation Dynamics and Relaxation: Quantum Theory and Spectroscopy*; Wiley-VCH: Weinheim, 2013.

(4) *Quantum Effects in Biology*; Cambridge University Press: Cambridge, 2014.

(5) Fuller, F. D.; Pan, J.; Gelzinis, A.; Butkus, V.; Senlik, S. S.; Wilcox, D. E.; Yocum, C. F.; Valkunas, L.; Abramavicius, D.; Ogilvie, J. P. *Nat. Chem.* **2014**, *6*, 706.

(6) Song, Y.; Clafton, S. N.; Pensack, R. D.; Kee, T. W.; Scholes, G. D. *Nat. Commun.* **2014**, *5*, 4933.

(7) Tisdale, W. A.; Williams, K. J.; Timp, B. A.; Norris, D. J.; Aydil, E. S.; Zhu, X.-Y. *Science* **2010**, *328*, 1543.

(8) Zimmermann, C.; Willig, F.; Ramakrishna, S.; Burfeindt, B.; Pettinger, B.; Eichberger, R.; Storck, W. *J. Phys. Chem. B* **2001**, *105*, 9245.

(9) Chin, A. W.; Prior, J.; Rosenbach, R.; Caycedo-Soler, F.; Huelga, S. F.; Plenio, M. B. *Nat. Phys.* **2013**, *9*, 113.

(10) Christensson, N.; Kauffmann, H. F.; Pullerits, T.; Mančal, T. *J. Phys. Chem. B* **2012**, *116*, 7449.

(11) Fujihashi, Y.; Fleming, G. R.; Ishizaki, A. *J. Chem. Phys.* **2015**, *142*, 212403.

(12) Jun, S.; Yang, C.; Isaji, M.; Tamiaki, H.; Kim, J.; Ihee, H. *J. Phys. Chem. Lett.* **2014**, *5*, 1386.

(13) Kolli, A.; O'Reilly, E. J.; Scholes, G. D.; Olaya-Castro, A. *J. Chem. Phys.* **2012**, *137*, 174109.

(14) Perlík, V.; Seibt, J.; Cranston, L. J.; Cogdell, R. J.; Lincoln, C. N.; Savolainen, J.; Šanda, F.; Mančal, T.; Hauer, J. *J. Chem. Phys.* **2015**, *142*, 212434.

(15) Womick, J. M.; Moran, A. M. *J. Phys. Chem. B* **2011**, *115*, 1347.

(16) Austin, R. H.; Beeson, K. W.; Eisenstein, L.; Frauenfelder, H.; Gunsalus, I. C. *Biochemistry* **1975**, *14*, 5355.

(17) Debrunner, P. G.; Frauenfelder, H. *Annu. Rev. Phys. Chem.* **1982**, *33*, 283.

(18) Elber, R.; Karplus, M. *J. Am. Chem. Soc.* **1990**, *112*, 9161.

(19) Miller, R. J. D. *Annu. Rev. Phys. Chem.* **1991**, *42*, 581.

(20) Perutz, M. F. *Nature* **1970**, *228*, 726.

(21) Perutz, M. F.; Fermi, G.; Luisi, B. *Acc. Chem. Res.* **1987**, *20*, 309.

(22) Molesky, B. P.; Giokas, P. G.; Guo, Z.; Moran, A. M. *J. Chem. Phys.* **2014**, *141*, 114202.

(23) Molesky, B. P.; Guo, Z.; Moran, A. M. *J. Chem. Phys.* **2015**, *142*, 212405.

(24) Asplund, M. C.; Zanni, M. T.; Hochstrasser, R. M. *Proc. Natl. Acad. Sci. U.S.A.* **2000**, *97*, 8219.

(25) Brixner, T.; Mančal, T.; Stiopkin, I. V.; Fleming, G. R. *J. Chem. Phys.* **2004**, *121*, 4221.

(26) Cowen, M. L.; Ogilvie, J. P.; Miller, R. J. D. *Chem. Phys. Lett.* **2004**, *386*, 184.

(27) Golonzka, O.; Khalil, M.; Demirdöven, N.; Tokmakoff, A. *Phys. Rev. Lett.* **2001**, *86*, 2154.

(28) Hamm, P.; Zanni, M. T. *Concepts and Methods of 2D Infrared Spectroscopy*; Cambridge University Press: Cambridge, 2011.

(29) Jonas, D. M. *Annu. Rev. Phys. Chem.* **2003**, *54*, 425.

(30) Ogilvie, J. P.; Kubarych, K. J. *Adv. At. Mol. Opt. Phys.* **2009**, *57*, 249.

(31) Pakoulev, A. V.; Block, S. B.; Yurs, L. A.; Mathew, N. A.; Kornau, K. M.; Wright, J. C. *Phys. Chem. Lett.* **2010**, *1*, 822.

(32) Slenkamp, K. M.; Lynch, M. S.; Kuiken, B. E. V.; Brookes, J. F.; Bannan, C. C.; Daifuku, S. L.; Khalil, M. *J. Chem. Phys.* **2014**, *140*, 084505.

(33) Wright, J. C. *Annu. Rev. Phys. Chem.* **2011**, *62*, 209.

(34) Cho, M. *Chem. Rev.* **2008**, *108*, 1331.

(35) Cundiff, S. T.; Mukamel, S. *Phys. Today* **2013**, *66*, 44.

(36) Khalil, M.; Demirdöven, N.; Tokmakoff, A. *J. Phys. Chem. A* **2003**, *107*, 5258.

(37) Kim, Y. S.; Hochstrasser, R. M. *Proc. Natl. Acad. Sci. U.S.A.* **2005**, *102*, 11185.

(38) Fayer, M. D. *Annu. Rev. Phys. Chem.* **2009**, *60*, 21.

(39) Anna, J. M.; Ross, M. R.; Kubarych, K. J. *J. Phys. Chem. A* **2009**, *113*, 6544.

(40) Collini, E.; Wong, C. Y.; Wilk, K. E.; Curmi, P. M. G.; Brumer, P.; Scholes, G. D. *Nature* **2010**, *463*, 644.

(41) Schlau-Cohen, G. S.; Ishizaki, A.; Fleming, G. R. *Chem. Phys.* **2011**, *386*, 1.

(42) Bixner, O.; Lukeš, V.; Mančal, T.; Hauer, J.; Milota, F.; Fischer, M.; Pugliesi, I.; Bradler, M.; Schmid, W.; Riedle, E.; Kauffmann, H. F.; Christensson, N. *J. Chem. Phys.* **2012**, *136*, 204503.

(43) Lynch, M. S.; Slenkamp, K. M.; Khalil, M. *J. Chem. Phys.* **2012**, *136*, 241101.

(44) Lewis, K. L. M.; Ogilvie, J. P. *J. Phys. Chem. Lett.* **2012**, *3*, 503.

(45) West, B. A.; Molesky, B. P.; Giokas, P. G.; Moran, A. M. *Chem. Phys.* **2013**, *423*, 92.

(46) Consani, C.; Auböck, G.; Mourik, F. V.; Chergui, M. *Science* **2013**, *339*, 1586.

(47) Laubereau, A.; Kaiser, W. *Rev. Mod. Phys.* **1978**, *50*, 607.

(48) Schosser, C. L.; Dlott, D. D. *J. Chem. Phys.* **1984**, *80*, 1394.

(49) Laubereau, A.; Wochner, G.; Kaiser, W. *Phys. Rev. A* **1976**, *13*, 2212.

(50) George, S. M.; Harris, A. L.; Berg, M.; Harris, C. B. *J. Chem. Phys.* **1984**, *80*, 83.

(51) George, S. M.; Auweter, H.; Harris, C. B. *J. Chem. Phys.* **1980**, *73*, 5573.

(52) Zinth, W.; Nuss, M. C.; Kaiser, W. *Phys. Rev. A* **1984**, *30*, 1139.

(53) Loring, R. F.; Mukamel, S. *J. Chem. Phys.* **1985**, *83*, 2116.

(54) Tanimura, Y.; Mukamel, S. *J. Chem. Phys.* **1993**, *99*, 9496.

(55) Jansen, T. I. C.; Snijders, J. G.; Duppen, K. *J. Chem. Phys.* **2001**, *114*, 10910.

(56) Ivanecky, J. E.; Wright, J. C. *Chem. Phys. Lett.* **1993**, *206*, 437.

(57) Tominaga, K.; Yoshihara, K. *J. Chem. Phys.* **1996**, *104*, 4419.

(58) Steffen, T.; Duppen, K. *J. Chem. Phys.* **1997**, *106*, 3854.

(59) Tokmakoff, A.; Lang, M. J.; Larsen, D. S.; Fleming, G. R.; Chernyak, V.; Mukamel, S. *Phys. Rev. Lett.* **1997**, *79*, 2702.

(60) Blank, D. A.; Kaufman, L. J.; Fleming, G. R. *J. Chem. Phys.* **1999**, *111*, 3105.

(61) Ulness, D. J.; Kirkwood, J. C.; Albrecht, A. C. *J. Chem. Phys.* **1998**, *108*, 3897.

(62) Kubarych, K. J.; Milne, C. J.; Lin, S.; Astinov, V.; Miller, R. J. D. *J. Chem. Phys.* **2002**, *116*, 2016.

(63) Wilson, K. C.; Lyons, B.; Mehlenbacher, R.; Sabatini, R.; McCamant, D. W. *J. Chem. Phys.* **2009**, *131*, 214502.

(64) Kaufman, L. J.; Heo, J.; Ziegler, L. D.; Fleming, G. R. *Phys. Rev. Lett.* **2002**, *88*, 207402.

(65) Mehlenbacher, R. D.; Lyons, B.; Wilson, K. C.; Du, Y.; McCamant, D. W. *J. Chem. Phys.* **2009**, *131*, 244512.

(66) Garrett-Roe, S.; Hamm, P. *J. Chem. Phys.* **2009**, *130*, 164510.

(67) Fujiyoshi, S.; Takeuchi, S.; Tahara, T. *J. Phys. Chem. A* **2003**, *107*, 494.

(68) McCamant, D. W.; Kukura, P.; Yoon, S.; Mathies, R. A. *Rev. Sci. Instrum.* **2004**, *75*, 4971.

(69) Underwood, D. F.; Blank, D. A. *J. Phys. Chem. A* **2005**, *109*, 3295.

(70) Kukura, P.; McCamant, D. W.; Mathies, R. A. *Annu. Rev. Phys. Chem.* **2007**, *58*, 461.

(71) Moran, A. M.; Nome, R. A.; Scherer, R. F. *J. Chem. Phys.* **2007**, *127*, 184505.

(72) Marek, M. S.; Buckup, T.; Motzkus, M. *J. Phys. Chem. B* **2011**, *115*, 8328.

(73) Kraack, J. P.; Wand, A.; Buckup, T.; Motzkus, M.; Ruhman, S. *Phys. Chem. Chem. Phys.* **2013**, *15*, 14487.

(74) Weigel, A.; Dobryakov, A.; Klaumünzer, B.; Sajadi, M.; Saalfrank, P.; Ernsting, N. P. *J. Phys. Chem. B* **2011**, *115*, 3656.

(75) Yu, W.; Zhou, J.; Bragg, A. E. *J. Phys. Chem. Lett.* **2012**, *3*, 1321.

(76) Park, S.; Kim, J.; Scherer, N. F. *Phys. Chem. Chem. Phys.* **2012**, *14*, 8116.

(77) Grumstrup, E. M.; Chen, Z.; Vary, R. P.; Moran, A. M.; Schanze, K. S.; Papanikolas, J. M. *J. Phys. Chem. B* **2013**, *117*.

(78) Silva, W. R.; Frontiera, R. R. *Phys. Chem. Chem. Phys.* **2016**, DOI: 10.1039/c5cp06195d.

(79) Goodno, G. D.; Dadusc, G.; Miller, R. J. D. *J. Opt. Soc. Am. B* **1998**, *15*, 1791.

(80) Hybl, J. D.; Ferro, A. A.; Jonas, D. M. *J. Chem. Phys.* **2001**, *115*, 6606.

(81) Tekavec, P. F.; Lott, G. A.; Marcus, A. H. *J. Chem. Phys.* **2007**, *127*, 214307.

(82) Shim, S.-H.; Zanni, M. T. *Phys. Chem. Chem. Phys.* **2009**, *11*, 748.

(83) Rosca, F.; Kumar, A. T. N.; Ye, X.; Sjodin, T.; Demidov, A. A.; Champion, P. M. *J. Phys. Chem. A* **2000**, *104*, 4280.

(84) Zhu, L.; Wang, W.; Sage, J. T.; Champion, P. M. *J. Raman Spectrosc.* **1995**, *26*, 527.

(85) Vos, M. H.; Jones, M. R.; Hunter, C. N.; Breton, J.; Martin, J.-L. *Proc. Natl. Acad. Sci. U.S.A.* **1994**, *91*, 12701.

(86) Vos, M. H.; Rappaport, F.; Lambry, J.-C.; Breton, J.; Martin, J.-L. *Nature* **1993**, *363*, 320.

(87) Halpin, A.; Johnson, P. J. M.; Tempelaar, R.; Murphy, R. S.; Knoester, J.; Jansen, T. L. C.; Miller, R. J. D. *Nat. Chem.* **2014**, *6*, 196.

(88) Milota, F.; Prokhorenko, V. J.; Mančal, T.; Berlepsch, H. V.; Bixner, O.; Kauffmann, H. F.; Hauer, J. *J. Phys. Chem. A* **2013**, *117*, 6007.

(89) Schlau-Cohen, G. S.; Calhoun, T. R.; Ginsberg, N. S.; Read, E. L.; Ballottari, M.; Bassi, R.; Grondelle, R. V.; Fleming, G. R. *J. Phys. Chem. B* **2009**, *113*, 15352.

(90) Read, E. L.; Engel, G. S.; Calhoun, T. R.; Mančal, T.; Ahn, T. K.; Blankenship, R. E. *Proc. Natl. Acad. Sci. U.S.A.* **2007**, *104*, 14203.

(91) Scholes, G. D.; Fleming, G. R.; Olaya-Castro, A.; Grondelle, R. V. *Nat. Chem.* **2011**, *3*, 763.

(92) Lee, H.; Cheng, Y.-C.; Fleming, G. R. *Science* **2007**, *316*, 1462.

(93) Romero, E.; Augulis, R.; Novoderezhkin, V. L.; Ferretti, M.; Thieme, J.; Zigmantas, D.; Grondelle, R. V. *Nat. Phys.* **2014**, *10*, 676.

(94) Westenhoff, S.; Paleček, D.; Edlund, P.; Smith, P.; Zigmantas, D. *J. Am. Chem. Soc.* **2012**, *134*, 16484.

(95) Ryu, I. S.; Dong, H.; Fleming, G. R. *J. Phys. Chem. B* **2014**, *118*, 1381.

(96) Collini, E.; Scholes, G. D. *Science* **2009**, *323*, 369.

(97) Vos, M. H.; Lambry, J.-C.; Robles, S. J.; Youvan, D. C.; Breton, L.; Martin, J.-L. *Proc. Natl. Acad. Sci. U.S.A.* **1991**, *88*, 8885.

(98) Zhu, L.; Sage, T.; Champion, P. M. *Science* **1994**, *266*, 629.

(99) Dexheimer, S. L.; Wang, Q.; Peteanu, L. A.; Pollard, W. T.; Mathies, R. A.; Shank, C. V. *Chem. Phys. Lett.* **1992**, *188*, 62.

(100) Pollard, W. T.; Dexheimer, S. L.; Wang, Q.; Peteanu, L. A.; Shank, C. V.; Mathies, R. A. *J. Phys. Chem.* **1992**, *96*, 6147.

(101) Peteanu, L. A.; Schoenlein, R. W.; Wang, Q.; Mathies, R. A.; Shank, C. V. *Proc. Natl. Acad. Sci. U.S.A.* **1993**, *90*, 11762.

(102) Wang, Q.; Schoenlein, R. W.; Peteanu, L. A.; Mathies, R. A.; Shank, C. V. *Science* **1994**, *266*, 422.

(103) Tiwari, V.; Peters, W. K.; Jonas, D. M. *Proc. Natl. Acad. Sci. U.S.A.* **2013**, *110*, 1203.

(104) Chenu, A.; Christensson, N.; Kauffmann, H. F.; Mančal, T. *Sci. Rep.* **2013**, *3*, 1.

(105) Huelga, S. F.; Plenio, M. B. *Contemp. Phys.* **2013**, *54*, 181.

(106) Falke, S. M.; Rozzi, C. A.; Brida, D.; Maiuri, M.; Amato, M.; Sommer, E.; Sio, A. D.; Rubio, A.; Cerullo, G.; Molinari, E.; Lienau, C. *Science* **2014**, *344*, 1001.

(107) Senlik, S. S.; Policht, V. R.; Ogilvie, J. P. *J. Phys. Chem. Lett.* **2015**, *6*, 2413.

(108) Banin, U.; Kosloff, R.; Ruhman, S. *Chem. Phys.* **1994**, *183*, 289.

(109) Johnson, A. E.; Myers, A. B. *J. Chem. Phys.* **1995**, *102*, 3519.

(110) Banin, U.; Kosloff, R.; Ruhman, S. *Isr. J. Chem.* **1993**, *33*, 141.

(111) Benjamin, I.; Banin, U.; Ruhman, S. *J. Chem. Phys.* **1993**, *98*, 8337.

(112) Johnson, A. E.; Myers, A. B. *J. Phys. Chem.* **1996**, *100*, 7778.

(113) Johnson, A. E.; Myers, A. B. *J. Chem. Phys.* **1996**, *104*, 2497.

(114) Gershgoren, E.; Gordon, E.; Ruhman, S. *J. Chem. Phys.* **1997**, *106*, 4806.

(115) Kühne, T.; Küster, R.; Vöhringer, P. *Chem. Phys.* **1998**, *233*, 161.

(116) Hess, S.; Bürsing, H.; Vöhringer, P. *J. Chem. Phys.* **1999**, *111*, 5461.

(117) Banin, U.; Ruhman, S. *J. Chem. Phys.* **1993**, *98*, 4391.

(118) Banin, U.; Ruhman, S. *J. Chem. Phys.* **1993**, *99*, 9318.

(119) Banin, U.; Waldman, A.; Ruhman, S. *J. Chem. Phys.* **1992**, *96*, 2416.

(120) Kühne, T.; Vöhringer, P. *J. Chem. Phys.* **1996**, *105*, 10788.

(121) Nishiyama, Y.; Terazima, M.; Kimura, Y. *J. Phys. Chem. B* **2012**, *116*, 9023.

(122) Molesky, B. P.; Guo, Z.; Cheshire, T.; Moran, A. M. *(Manuscript in Preparation)* **2016**.

(123) Vos, M. H. *Biochim. Biophys. Acta* **2008**, *1777*, 15.

(124) Lian, T.; Locke, B.; Kholodenko, Y.; Hochstrasser, R. M. *J. Phys. Chem.* **1994**, *98*, 11648.

(125) Sagnella, D. E.; Straub, J. E. *J. Phys. Chem. B* **2001**, *105*, 7057.

(126) Bu, L.; Straub, J. E. *J. Phys. Chem. B* **2003**, *107*, 10634.

(127) Gao, Y.; Koyama, M.; El-Mashtoly, S. F.; Hayashi, T.; Harada, K.; Mizutani, Y.; Kitagawa, T. *Chem. Phys. Lett.* **2006**, *429*, 239.

(128) Koyama, M.; Neya, S.; Mizutani, Y. *Chem. Phys. Lett.* **2006**, *430*, 404.

(129) Zhang, Y.; Fujisaki, H.; Straub, J. E. *J. Phys. Chem. B* **2007**, *111*, 3243.

(130) Hu, S.; Smith, K. M.; Spiro, T. G. *J. Am. Chem. Soc.* **1996**, *118*, 12638.

(131) Li, P.; Sage, J. T.; Champion, P. M. *J. Chem. Phys.* **1992**, *97*, 3214.

(132) Lim, M.; Jackson, T. A.; Anfinrud, P. A. *J. Phys. Chem.* **1996**, *100*, 12043.

(133) Ye, X.; Demidov, A.; Rosca, F.; Wang, W.; Kumar, A.; Ionaseu, D.; Zhu, L.; Barrick, D.; Wharton, D.; Champion, P. M. *J. Phys. Chem. A* **2003**, *107*, 8156.

(134) Martin, J.-L.; Vos, M. H. *Annu. Rev. Biophys. Biomol. Struct.* **1992**, *21*, 199.

(135) Berg, M.; Bout, D. A. V. *Acc. chem. Res.* **1997**, *30*, 65.

(136) Demirdöven, N.; Khalil, M.; Golonzka, O.; Tokmakoff, A. *J. Phys. Chem. A* **2001**, *105*, 8025.

(137) Venkatramani, R.; Mukamel, S. *J. Chem. Phys.* **2002**, *117*, 11089.

CHAPTER 2: SPECTROSCOPY AND DYNAMICS IN CONDENSED PHASES

2.1. Introduction

Unlike spectroscopic measurements in the gas phase, it is not feasible to describe condensed phase spectra in terms of sum over states formulas such as Fermi's Golden Rule.[1-3] Although the interesting part of a condensed phase sample (e.g. some particular solute species) may have a relatively small number of degrees of freedom, the number of degrees of freedom in the environment (e.g. the solvent) is enormous, preventing such a purely explicit description. As such, a reduced description of spectroscopy is necessary to properly describe condensed phase measurements. In a reduced description only a few interesting states of the system are considered explicitly while all other states of the system and environment are relegated to the "bath".[4-7] These bath states enter the description as collision induced random fluctuations of the energy gap(s) between the explicitly treated states. Since each member of an ensemble exists in a slightly different environment, the energy gap(s) for each member is (are) also slightly different. This leads to the appearance of broad features in condensed phase spectra, contrasting with the numerous sharp features observed in the gas phase.[5] Generally, condensed phase systems obey the ergodic hypothesis, and thus the time averaged behavior of an ensemble member is equivalent to the ensemble average itself.[7,8] This principal allows consideration of the stochastic fluctuation of the bath and its effect on the system in terms of time correlation functions. The cumulant expansion is a powerful tool for solving time correlation functions, allowing for the generation of a useful 'line broadening function' that accurately captures the

time scale and amplitude of the fluctuations induced by the bath.[7,9] The line broadening function makes it possible to model the time trajectory of the dipole operator in order to build spectroscopic response functions by describing the dephasing of correlated motions in the system that originate from perturbative electric field(s).[4,7] Convolution of the response function with the electric field(s) gives the material polarization; this is the observable measured in optical spectroscopies. This approach applies to response functions of all orders which are most clearly represented in a graphical way using Feynman diagrams that map particular paths through the density matrix.[10,11]

The rest of this chapter lays a theoretical foundation that will be used throughout the remaining chapters and appendices to build spectroscopic response functions that describe the fifth order signals measured via two-dimensional resonance Raman spectroscopy (2DRR) and, for comparative purposes, unwanted cascades of third order processes. The comparison between experiment and theory, of which the basis is described in this chapter, will prove that direct fifth order resonance Raman signals are measured while contributions from unwanted cascades are suppressed.

In Section 2.2 time dependent perturbation theory for the density operator is used to build an expression for the material polarization containing time correlation functions of the dipole operator.[2,5,12,13] The perturbations are field matter interactions between an external electric field and the material of interest. In Section 2.3 a physically appropriate line broadening function is obtained using the cumulant expansion and knowledge of Gaussian statistics.[4,5,7,9,14] This function is used to generate absorption and fluorescence spectra.[7,14] In Section 2.4 Feynman diagrams are introduced to construct spectroscopic response functions, clarifying how these useful diagrammatic representations translate into rigorous mathematical models.[5,10-12]

2.2. Time Dependent Perturbation Theory for the Density Operator

In optical spectroscopies it is more convenient to describe the time evolution of quantum systems with the density operator than with the wavefunction. Expectation values are more readily calculated using the density operator formalism, and this approach most naturally portrays the time-ordering of interactions between a material and an external electric field (the perturbation in optical spectroscopies).[5,12] The definition of the density operator is given in Equation 2.1 as the outer product of the wavefunction and its complex conjugate.

$$\hat{\rho}(t) = |\psi(t)\rangle\langle\psi(t)| \tag{2.1}$$

It can equivalently be thought of as a matrix. Diagonal elements, called populations, describe the probability of occupying a particular state. Off-diagonal elements, called coherences, give the probability that the system is in a superposition of states. Although there are significant advantages to using the density operator, consistency with the Schrodinger equation and equivalence to the wavefunction are exemplified in Equation 2.2.

$$\begin{aligned}\frac{\partial\hat{\rho}}{\partial t} &= \frac{\partial|\psi(t)\rangle\langle\psi(t)|}{\partial t} = \left|\frac{\partial\psi(t)}{\partial t}\right\rangle\langle\psi(t)| + |\psi(t)\rangle\left\langle\frac{\partial\psi(t)}{\partial t}\right| \\ &= \left(\frac{-iH}{\hbar}\right)|\psi(t)\rangle\langle\psi(t)| + |\psi(t)\rangle\langle\psi(t)|\left(\frac{iH}{\hbar}\right) \\ &= \frac{-i}{\hbar}\left[H, |\psi(t)\rangle\langle\psi(t)|\right] = \frac{-i}{\hbar}[H,\rho]\end{aligned} \tag{2.2}$$

After a simple algebraic reorganization Equation 2.2 becomes Equation 2.3, the quantum Liouville equation, analogous to the Schrodinger equation.

$$i\hbar\frac{\partial\hat{\rho}}{\partial t} = [H,\rho] \tag{2.3}$$

To consider the time evolution of a weakly perturbed system the Hamiltonian is partitioned into a time-independent material related term, $H^{(0)}$, and a time-dependent perturbative term, $\lambda H'(t)$, where λ interpolates between the unperturbed ($\lambda = 0$) and fully perturbed ($\lambda = 1$) system.

$$H = H^{(0)} + \lambda H'(t) \tag{2.4}$$

The density operator is expressed as a perturbative expansion to N[th] order, indicating the number of interactions between the material and perturbation.

$$\rho(t) = \rho^{(0)}(t) + \lambda\rho^{(1)}(t) + \lambda^2\rho^{(2)}(t) + \cdots + \lambda^N\rho^{(N)}(t) \tag{2.5}$$

Substitution of Equations 2.5 and 2.4 into Equation 2.3 gives a differential equation that when solved generates the following expression for the density operator at N[th] order.

$$\rho^{(N)}(t) = -\frac{i}{\hbar}\int_{-\infty}^{t}\left[H'(t_N), \rho^{(N-1)}\right]dt_N \tag{2.6}$$

Here t_N is the point in time of the N[th] interaction between the material and perturbation, and t is the time of observation. For convenience the time point arguments in Equation 2.6 are expressed in terms of time intervals, $\tau_N = t - t_N$.

$$\rho^{(N)}(t) = -\frac{i}{\hbar}\int_{0}^{\infty}\left[H'(t-\tau_N), \rho^{(N-1)}\right]d\tau_N \tag{2.7}$$

Equation 2.7 contains N nested commutators, possessing 2^N terms at N[th] order. Only the highest order commutator is shown explicitly. In Equations 2.6 and 2.7 the lower limits of integration, 0 and $-\infty$, are used equally to indicate the equilibrium system, which is appropriate because both

initial times yield the same result. The material polarization at N[th] order is the expectation value of the dipole operator or, equivalently, the trace of the dipole operator acting on the N[th] order density matrix.[5,12]

$$P^{(N)}(t) = \left\langle \hat{\mu}(t) \right\rangle = Tr\left[\hat{\mu}(t) \rho^{(N)}(t) \right] \tag{2.8}$$

Equation 2.9 is presented to stress the convenience of this formulation over that of the wavefunction approach.

$$\begin{aligned} P^{(1)}(t) &= \left\langle \psi^{(1)}(t) \middle| \mu \middle| \psi^{(0)}(t) \right\rangle + \left\langle \psi^{(0)}(t) \middle| \mu \middle| \psi^{(1)}(t) \right\rangle \\ P^{(2)}(t) &= \left\langle \psi^{(2)}(t) \middle| \mu \middle| \psi^{(0)}(t) \right\rangle + \left\langle \psi^{(1)}(t) \middle| \mu \middle| \psi^{(1)}(t) \right\rangle + \left\langle \psi^{(0)}(t) \middle| \mu \middle| \psi^{(2)}(t) \right\rangle \\ P^{(2)}(t) &= \left\langle \psi^{(3)}(t) \middle| \mu \middle| \psi^{(0)}(t) \right\rangle + \left\langle \psi^{(2)}(t) \middle| \mu \middle| \psi^{(1)}(t) \right\rangle + \left\langle \psi^{(1)}(t) \middle| \mu \middle| \psi^{(2)}(t) \right\rangle + \left\langle \psi^{(0)}(t) \middle| \mu \middle| \psi^{(3)}(t) \right\rangle \end{aligned} \tag{2.9}$$

In the wavefunction approach one must solve for every expectation value of the dipole operator in which the orders of the bra and ket sum to N. Clearly the density operator approach is superior and more physically motivated. The perturbative part of the Hamiltonian is defined as the dot product of the material dipole operator and the external electric field. To simplify the derivation, the dipole operator and electric field are considered to be scalar quantities.

$$H'(t-\tau_N) = -\hat{\mu}(\tau_N) \cdot E(t-\tau_N) \tag{2.10}$$

Substitution of Equation 2.10 into Equation 2.7 gives Equation 2.11.

$$\rho^{(N)}(t) = \frac{i}{\hbar} \int_0^\infty \left[\hat{\mu}(\tau_N) \cdot E(t-\tau_N), \rho^{(N-1)} \right] d\tau_N \tag{2.11}$$

For simplicity's sake only the first order polarization is considered explicitly.

$$
\begin{aligned}
P^{(1)}(t) &= Tr\left[\hat{\mu}(t)\rho^{(1)}(t)\right] \\
&= Tr\left[\hat{\mu}(t)\frac{i}{\hbar}\int_0^\infty\left[\hat{\mu}(\tau_1),\rho^{(0)}(-\infty)\right]E(t-\tau_1)d\tau_1\right] \\
&= \frac{i}{\hbar}\int_0^\infty Tr\left[\hat{\mu}(t)\left[\hat{\mu}(\tau_1),\rho^{(0)}(-\infty)\right]\right]E(t-\tau_1)d\tau_1 \\
&= \frac{i}{\hbar}\int_0^\infty Tr\left[\left[\hat{\mu}(\tau_1),\hat{\mu}(0)\right]\rho^{(0)}(-\infty)\right]E(t-\tau_1)d\tau_1
\end{aligned}
\tag{2.12}
$$

The last line of Equation 2.11 utilizes the identity $Tr\left[A\left[B,C\right]\right]=Tr\left[\left[A,B\right]C\right]$ and the previously used relationship, $\tau_N = t - t_N$. Finally, Equation 2.12 can be expressed using time correlation functions because condensed phase systems obey the ergodic hypothesis.[1,5,7,8,12]

$$
P^{(1)}(t) = \frac{i}{\hbar}\theta(\tau_1)\int_0^\infty\left(\left\langle\hat{\mu}(\tau_1)\hat{\mu}(0)\right\rangle - \left\langle\hat{\mu}(0)\hat{\mu}(\tau_1)\right\rangle\right)E(t-\tau_1)d\tau_1 \tag{2.13}
$$

The equilibrium density operator, $\rho^{(0)}(-\infty)$, is implicit to the time correlation functions in Equation 2.13. The Heaviside step function, $\theta(\tau)$, is introduced to enforce causality. Time correlation functions encode information about how the system loses memory of the initial state prepared by the perturbative electric field.[5,12] This behavior is illustrated in Figure 2.1 where the dephasing of correlated motions in the system is governed by the line broadening function obtained in the next section.

In this section an expression has been built for the first order material polarization that is based on time correlation functions of the dipole operator. Time correlation functions characterize how the system is affected by thermally induced collisions with the environment. These interactions are the origin of the broad spectral features observed in the condensed phase (see Figure 2.3).

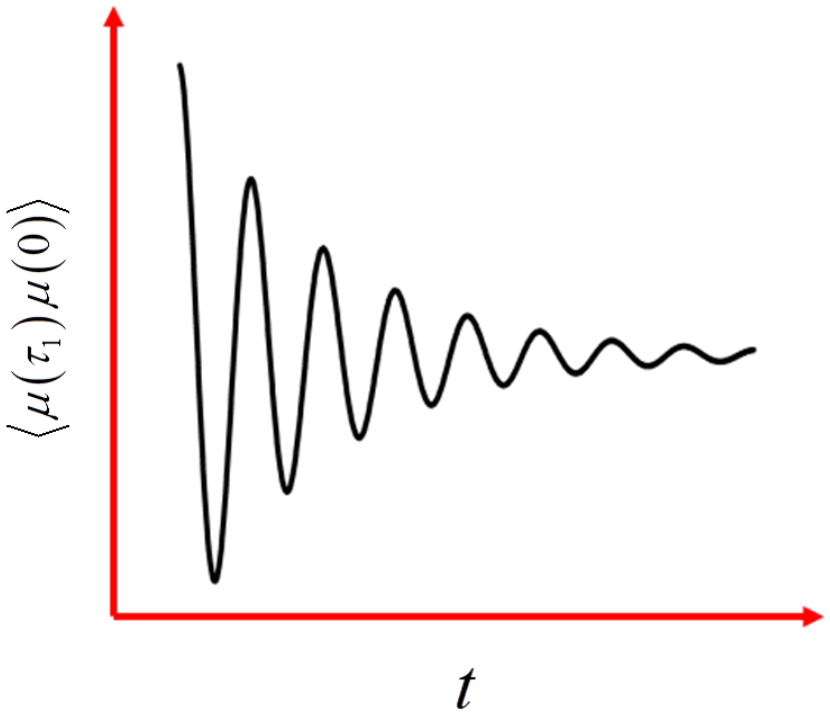

Figure 2.1. The line broadening function, $g(t)$, governs the damping of oscillations in the dipole operator correlation function due to random thermally driven collisions between the system and environment. After some time the oscillations dephase entirely as the system loses memory of the state initially prepared by the perturbative electric field.

2.3. Obtaining the Line Broadening Function

The massive number of degrees of freedom that characterize quantum processes in the condensed phase prevents the explicit treatment of the system's total Hamiltonian; it is generally impossible to know all the states. Instead a reduced description is used where only a few 'interesting' states are considered explicitly.[6] These states comprise the 'system', and all other states are assigned to the 'bath'.[4] To account for the bath states, the system states are allowed to fluctuate. Generally these bath induced fluctuations are modeled by coupling the system to a very large number of harmonic oscillators possessing many, many degrees of freedom.[5,12] As such the central limit theorem indicates that fluctuations due to the bath should behave according

to Gaussian statistics. In this section, knowledge of Gaussian statistics and the power of the cumulant expansion are utilized to generate a useful line broadening function parameterized by characteristic properties of these fluctuations.[7,9] The final form of the function is applied to generate absorption and fluorescence spectra.[14] This approach generalizes to all orders of perturbation and all processes, obviates explicit knowledge of the bath states, and draws connections to the broad Gaussian line shapes observed in the condensed phase.

Consider a two-state system where the frequency reflecting the energy gap between states experiences random fluctuations at equilibrium.[4,5,7,12]

$$\omega_{ab}(t) = \bar{\omega}_{ab} + \delta\omega_{ab}(t) \tag{2.14}$$

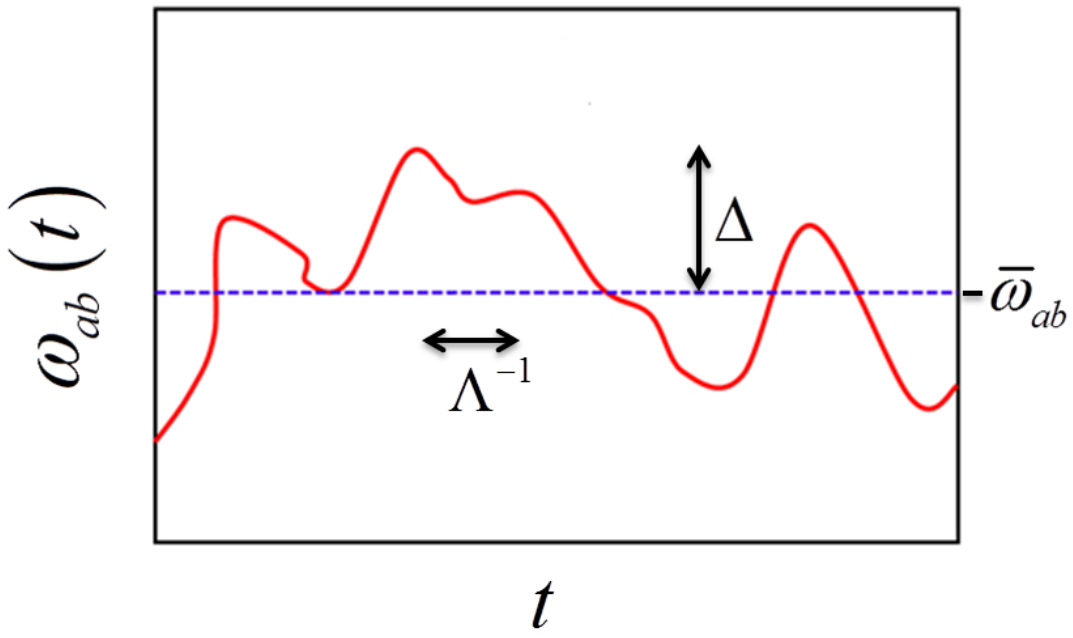

Figure 2.2. The energy gap between states of a two level system fluctuates about the mean due to random thermal motions of the environment. The fluctuations are characterized by their amplitude, Δ, and relaxation time, Λ^{-1} (see Equation 2.24).

Here $\bar{\omega}_{ab}$ is the mean frequency and $\delta\omega_{ab}(t)$ represents the stochastic fluctuations. The equation of motion for this system is given in Equation 2.15.[5]

$$\frac{d}{dt}\hat{H}'_{ba}(t) = -i\omega_{ab}(t)\hat{H}'_{ba}(t) \tag{2.15}$$

Integration generates the matrix element of the perturbative Hamiltonian associated with a transition from state a to state b.[5]

$$\hat{H}'_{ba}(t) = \hat{H}'_{ba}\exp\left[-i\int_0^t dt'\omega_{ab}(t')\right] \tag{2.16}$$

Now consider the two-point time correlation function

$$\left\langle \hat{H}'_{ba}(t)\hat{H}'_{ab}(0)\right\rangle = \left|\hat{H}'_{ba}\right|^2 \exp\left[-i\int_0^t dt'\omega_{ab}(t')\right]. \tag{2.17}$$

By expanding $\omega_{ab}(t')$ according to Equation 2.14 and removing the mean frequency from the integral, Equation 2.17 becomes Equation 2.18.

$$\left\langle \hat{H}'_{ba}(t)\hat{H}'_{ab}(0)\right\rangle = \left|\hat{H}'_{ba}\right|^2 \exp(-i\bar{\omega}_{ab}t)\exp\left[-i\int_0^t dt'\delta\omega_{ab}(t')\right] \tag{2.18}$$

A cumulant expansion is conducted on the integrand.[5,7]

$$\left\langle \hat{H}'_{ba}(t)\hat{H}'_{ab}(0)\right\rangle = \left|\hat{H}'_{ba}\right|^2 \exp(-i\bar{\omega}_{ab}t)\exp\left[-i\int_0^t dt_1\left\langle\delta\omega_{ab}(t_1)\right\rangle - \frac{1}{2}\int_0^t dt_1\int_0^t dt_2\left\langle\delta\omega_{ab}(t_2)\delta\omega_{ab}(t_1)\right\rangle\right] \tag{2.19}$$

The expansion has been truncated at the second term because Gaussian distributions are fully characterized by the first two cumulants. However, the first order cumulant is equal to zero (i.e.

$\left\langle \delta\omega_{ab}(t_1) \right\rangle = 0$) for equilibrium systems whose fluctuations are normally distributed about the mean.[7,9] The second term in the expansion is the key and is denoted by $g(t)$. Equation 2.19 becomes Equation 2.20.

$$\begin{aligned} \left\langle \hat{H}'_{ba}(t)\hat{H}'_{ab}(0) \right\rangle &= \left|\hat{H}'_{ba}\right|^2 \exp\left[-i\bar{\omega}_{ab}t - \frac{1}{2}\int_0^t dt_1 \int_0^t dt_2 \left\langle \delta\omega_{ab}(t_2)\delta\omega_{ab}(t_1) \right\rangle \right] \\ &= \hat{H}'^2_{ba} \exp\left[-i\bar{\omega}_{ab}t - g(t) \right] \end{aligned} \tag{2.20}$$

For convenience the double integral in $g(t)$ can be converted to a single integral in Equation 2.22 due to the time symmetry of the correlation function, $\left\langle \delta\omega_{ab}(t_2)\delta\omega_{ab}(t_1) \right\rangle$, at equilibrium.[5]

$$\left\langle \delta\omega_{ab}(t_2)\delta\omega_{ab}(t_1) \right\rangle = \left\langle \delta\omega_{ab}(t_2 - t_1)\delta\omega_{ab}(0) \right\rangle = \left\langle \delta\omega_{ab}(t_1 - t_2)\delta\omega_{ab}(0) \right\rangle \tag{2.21}$$

$$\begin{aligned} g(t) &= \frac{1}{2}\int_0^t dt_1 \int_0^t dt_2 \left\langle \delta\omega_{ab}(t_1 - t_2)\delta\omega_{ab}(0) \right\rangle = \int_0^t dt_1 \int_0^{t_1} dt_2 \left\langle \delta\omega(t_1 - t_2)\delta\omega(0) \right\rangle \\ &= \int_0^t dT\,(t - T)\left\langle \delta\omega(T)\delta\omega(0) \right\rangle \end{aligned} \tag{2.22}$$

Here $T = t_1 - t_2$. Note that this function depends on a time interval rather than points in time. To solve for $g(t)$ a practical form must be chosen for $\left\langle \delta\omega(T)\delta\omega(0) \right\rangle$. An exponentially decaying function, known as Kubo's function, is useful for this purpose.[5,9]

$$\left\langle \delta\omega(T)\delta\omega(0) \right\rangle = \Delta^2 \exp(-\Lambda T) \tag{2.23}$$

Through substitution of Equation 2.23 into Equation 2.22 a line broadening function is obtained, parameterized by the fluctuation amplitude, Δ, and the rate at which these fluctuations relax, Λ.

$$g(t) = \Delta^2 \int_0^t dT\,(t-T)\exp(-\Lambda T) = \frac{\Delta^2}{\Lambda^2}\left[\exp(-\Lambda t) + \Lambda t - 1\right] \tag{2.24}$$

For the vast majority of condensed phase systems the fluctuation amplitude is much greater than the relaxation rate, such that $\Lambda/\Delta \ll 1$.[7] In this inhomogeneous or slow modulation limit the line broadening function takes the form given in Equation 2.25.[5]

$$g(t) = \frac{1}{2}\Delta^2 t^2, \qquad \Lambda/\Delta << 1 \tag{2.25}$$

Equation 2.25 indicates that condensed phase systems have Gaussian line shapes because they are coupled strongly to the bath and possess slowly relaxing fluctuations. Now the time correlation function of the two-level system can be expressed in a physical way where the line broadening function encodes the loss of correlation due to fluctuations induced by the bath.[7]

$$\left\langle \hat{H}'_{ba}(t)\hat{H}'_{ab}(0)\right\rangle = \left|\hat{H}'_{ba}\right|^2 \exp\left[-i\bar{\omega}_{ab}t - g(t)\right] = \left|\hat{H}'_{ba}\right|^2 \exp\left[-i\bar{\omega}_{ab}t - \frac{1}{2}\Delta^2 t^2\right] \tag{2.26}$$

To illustrate the Gaussian line shapes seen in condensed phase spectra the perturbative Hamiltonian is defined assuming a monochromatic field with an amplitude of 1. As in Section 2.2 the dipole operator and electric field are considered to be scalar quantities.

$$\hat{H}'(t) = -\mu E(t) = -\mu|E|\exp(i\omega t) = -\mu\exp(i\omega t) \tag{2.27}$$

The absorbance and fluorescence line shapes are then calculated by integration of Equation 2.26 after defining the reference frequency, $\bar{\omega}_{eg}$, as the isobestic point and substitution of Equation 2.27.[5,7,14] The indices are expressed as g and e to represent a ground state and an excited state.

$$\sigma_{abs}(\omega) = \left|\mu_{eg}\right|^2 \int_{-\infty}^{\infty} \exp\left[i\left(\omega - \bar{\omega}_{eg} - \lambda\right)t - \frac{1}{2}\Delta^2 t^2 \right] dt$$
$$= \frac{\left|\mu_{eg}\right|^2}{\sqrt{2\pi\Delta^2}} \exp\left[\frac{-\left(\omega - \bar{\omega}_{eg} - \lambda\right)^2}{2\Delta^2} \right] \quad (2.28)$$

$$\sigma_{fl}(\omega) = \left|\mu_{eg}\right|^2 \int_{-\infty}^{\infty} \exp\left[i\left(\omega - \bar{\omega}_{eg} + \lambda\right)t - \frac{1}{2}\Delta^2 t^2 \right] dt$$
$$= \frac{\left|\mu_{eg}\right|^2}{\sqrt{2\pi\Delta^2}} \exp\left[\frac{-\left(\omega - \bar{\omega}_{eg} + \lambda\right)^2}{2\Delta^2} \right] \quad (2.29)$$

Here λ is the nuclear reorganization energy of the system.[15]

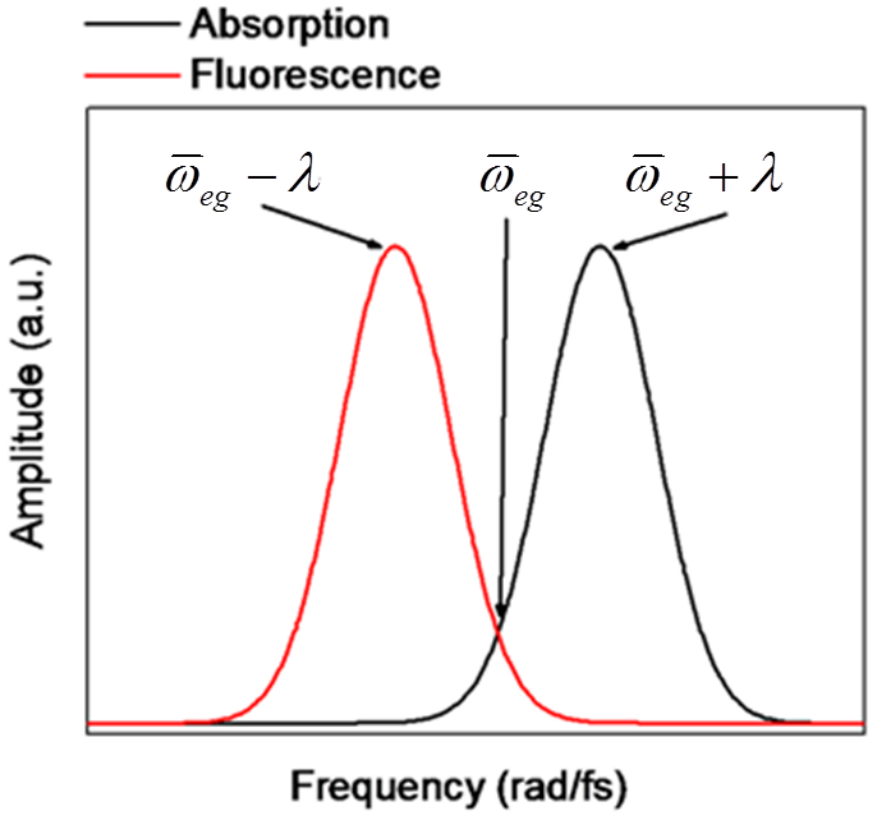

Figure 2.3. In the homogenous limit of line broadening, absorption and fluorescence spectra possess Gaussian line shapes as described in Equations 2.28 and 2.29.

In this section a physically meaningful line broadening function was obtained that is based on characteristic properties of the bath induced energy gap fluctuations. This function governs dephasing of correlated motions that originate from external electric fields (see Figure 2.1) and accurately accounts for the Gaussian line shapes observed in condensed phase measurements (see Figure 2.3). The approach detailed here was applied to a two-level system at first order in perturbation but is applicable to any number of levels and all orders. It does not require knowledge of the bath states.

2.4. Feynman Diagrams and Response Functions

The first order polarization in Equation 2.13 can be considered as a response function, $S^{(1)}(\tau_1)$, convoluted with an external electric field.[5,12]

$$P^{(1)}(t) = \int_0^\infty S^{(1)}(\tau_1) E(t-\tau_1)\, d\tau_1 \tag{2.30}$$

At first order the response function for a two-level system is relatively simple and is the sum of only two terms

$$S^{(1)}(\tau_1) = \left(\frac{i}{\hbar}\right)^1 \theta(\tau_1)\left[R_1(\tau_1) + R_2(\tau_1)\right] \tag{2.31}$$

where $R_2(\tau_1) = \left[R_1(\tau_1)\right]^*$. The Heaviside step function, $\theta(\tau_1)$ enforces causality. At Nth order there are 2^N terms in the response function, corresponding to the number of terms in the density operator.[3,14] Half of the terms are unique and the other half are their complex conjugates. Each term maps a different path through the density matrix and is related to a sum of wavevectors

corresponding to the N perturbative electric fields, which are modeled classically according to Equation 2.32.

$$E(r,t) = \xi(t)\exp\left[i(kr - \omega t)\right] \tag{2.32}$$

Here $\xi(t)$ is a slowly varying envelope function, ω is the frequency, and k is the wavevector. Dominant terms in the response function are selected experimentally through conservation of momentum by controlling the wavevectors of the incident fields.[16] Regardless, the number of relevant terms becomes very large at higher order, and the response function can be difficult to consider in an experimental context.[17-19] Feynman diagrams are used to alleviate this problem by graphical representation.[10,11,20] Listed below are a series of rules that facilitate interpretation of Feynman diagrams and their translation into terms of the response function.[5]

1. Two vertical lines represent the density operator where time runs from bottom to top.
2. The diagram must start and end in a population.
3. Arrows on the left (right) of the diagram indicate interactions with the ket (bra).
4. Incoming (outgoing) arrows change the state of the system as to raise (lower) the energy.
5. Each diagram possesses N+1 arrows (i.e. interactions) pertaining to N interactions with external electric fields followed by a signal emission event. Signal emission is always represented by an outgoing dashed arrow on the side of the ket (i.e. the left).
6. A transition dipole matrix element is written for each interaction including signal emission.
7. For each period between interactions where the system exists in a coherence a propagation function is written containing the frequency associated with the energy gap

of the bra and ket states and a damping function. For the purposes of this chapter homogeneous damping functions are used.

8. Arrows pointing to the right (left) are associated with positive (negative) wavevectors and frequencies.
9. The wavevector (frequency) of the signal is determined by the sum of the incident field wavevectors (frequencies)
10. Diagrams possessing an odd (even) number of interactions with the bra correspond to negative (positive) terms in the response function.

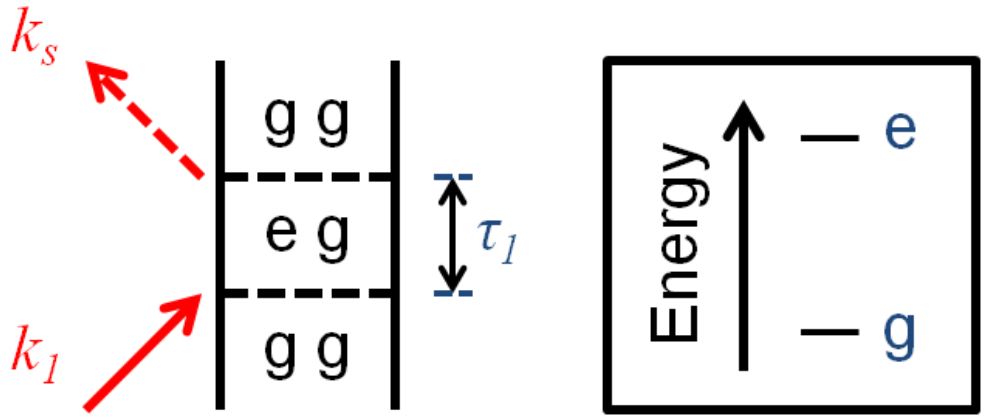

Figure 2.4. Feynman diagram for linear absorption of a two level system. Electric fields are denoted by their wavevectors. τ_1 represents the time period of evolution between interaction with the incident field and signal emission. The term in the response function where k_1 is negative is irrelevant because the signal is measured in the direction of the incident field.

As the simplest case consider the Feynman diagram for linear absorption of a two level system presented in Figure 2.4. The electric fields are denoted by their wavevectors to connect the diagram to the experiment. Note that the term in the response function where k_1 is negative is not represented because the signal is measured in the direction of the incident field.[16] By employing the rules given above, the Feynman diagram translates into Equation 2.33.

$$R(\tau_1) = |\mu_{eg}|^2 \exp\left[-i\omega_{eg}\tau_1 - \Gamma_{eg}\tau_1\right] \tag{2.33}$$

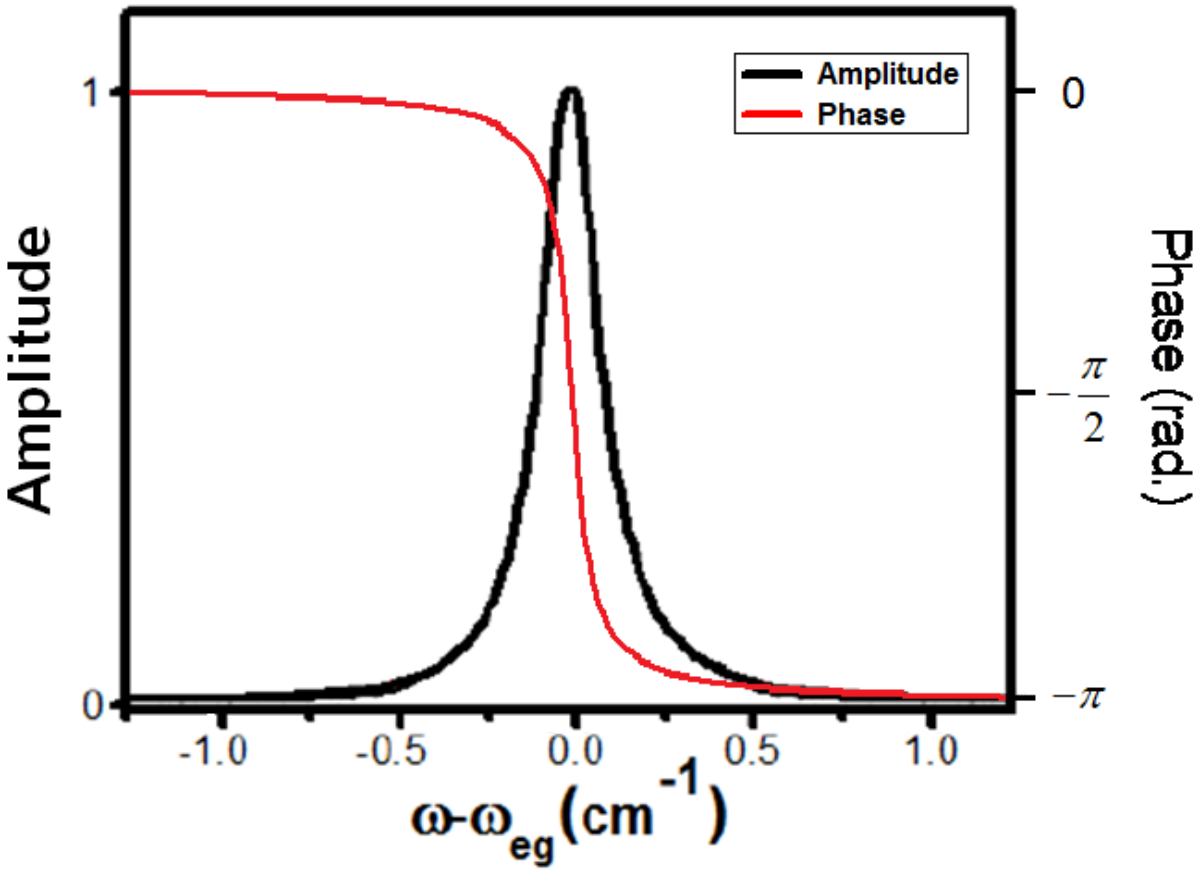

Figure 2.5. Convolution of a quasi monochromatic electric field with the term in the first order response function for linear absorption gives a Lorentzian line shape when a homogeneous damping function is employed. A phase shift of $-\frac{\pi}{2}$ is observed when the frequency of the incident field is equivalent to the electronic energy gap of the system. Amplitude is quickly eliminated as the field is detuned from resonance.

According to Mukamel's "snapshot limit" a quasi monochromatic electric field is assumed such that the duration is long compared to electronic dephasing.[14] The field is treated as a scalar quantity for convenience. Integration of the response function convolved with the electric field gives the term in the first order polarization corresponding to linear absorption. This term

possesses a Lorentzian line shape (see Figure 2.5) because a homogeneous (i.e. exponential) damping function, Γ_{eg}, is employed.

$$P^{(1)}(\omega) = \int_0^\infty R(\tau_1)\xi(\tau_1)\exp(i\omega\tau_1)\,d\tau_1 = |\mu_{eg}|^2 \int_0^\infty \xi(\tau_1)\exp\left[i\omega\tau_1 - i\omega_{eg}\tau_1 - \Gamma_{eg}\tau_1\right]d\tau_1$$
$$= \xi(\omega)|\mu_{eg}|^2 \frac{(\omega - \omega_{eg} + i\Gamma_{eg})}{(\omega - \omega_{eg})^2 + \Gamma_{eg}^2} \tag{2.34}$$

The phase of the polarization in Equation 2.34 is given according to Equation 2.35.[5]

$$\Phi(\omega) = -\arctan\left\{\frac{\mathrm{Im}\left[P^{(1)}(\omega)\right]}{\mathrm{Re}\left[P^{(1)}(\omega)\right]}\right\} \tag{2.35}$$

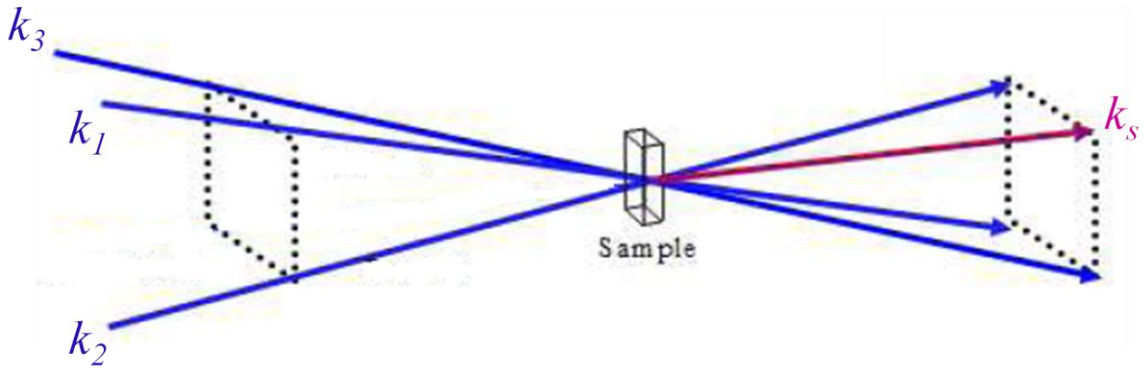

Figure 2.6. Experimental geometry for the incident fields in a third order spectroscopy known as transient grating. k_1 and k_2 arrive simultaneously, there is a delay, and then k_3 induces signal emission in the direction $k_s = -k_1 + k_2 + k_3$. In a traditional pump-probe experiment (transient absorption) the same phase matching condition applies; however the first two field matter interactions occur with a single field (the pump) such that $k_1 = k_2$, and thus the signal is irradiated in the direction of the probe ($k_s = k_3$).

Now consider the Feynman diagrams given in Figure 2.7 for third order spectroscopies with the phase matching condition $k_s = -k_1 + k_2 + k_3$. This condition is standard for third order

spectroscopies and is enforced by the experimental geometry of the incident fields.[21,22] In the type of experiment considered here the field(s) with wavevectors $-k_1$ and k_2 arrive simultaneously such that either interaction can be considered to occur first. These interactions are 'pump' interactions and may occur with one field (transient absorption) or two separate fields (transient grating) depending on the experiment. There is a time delay and the final interaction occurs with the 'probe' (k_3). The signal is emitted in the direction $k_s = -k_1 + k_2 + k_3$.[21,22]

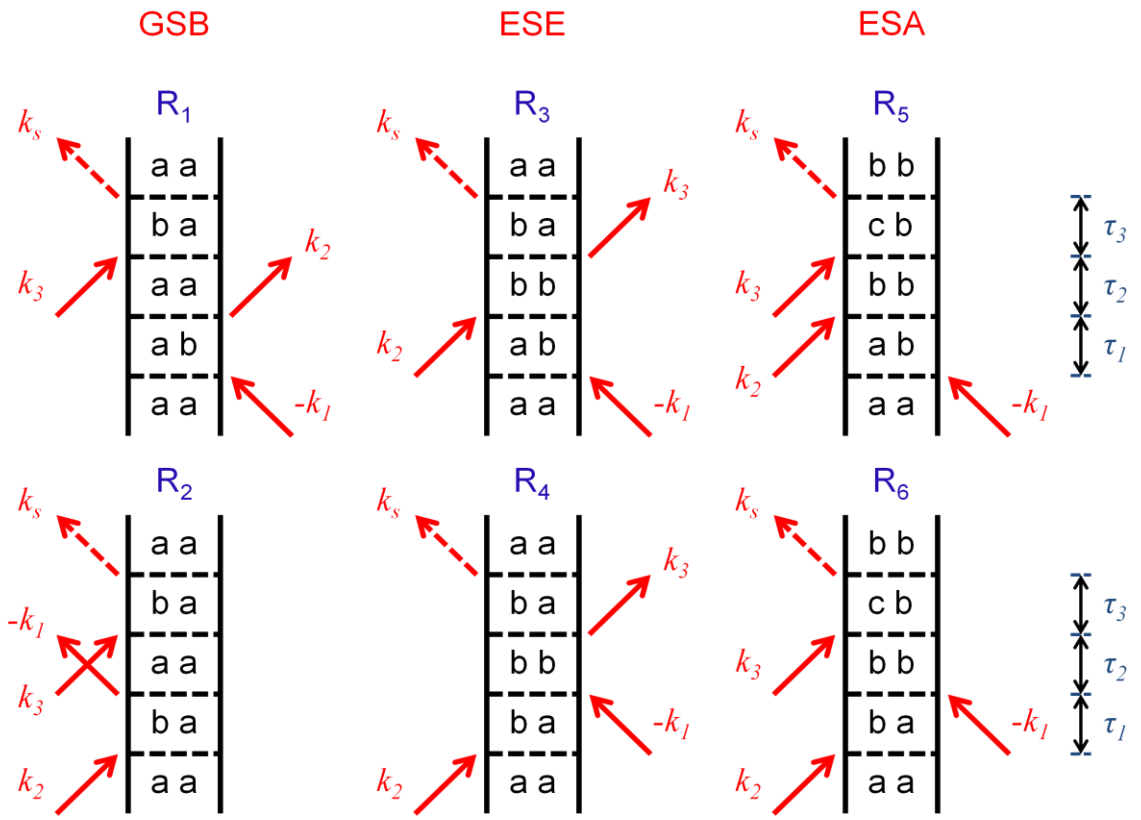

Figure 2.7. Feynman diagrams for third order spectroscopies with the phase matching condition $k_s = -k_1 + k_2 + k_3$ applied to a three level system where $E_a < E_b < E_c$. Note that the system considered here does not undergo population relaxation. Electric fields are denoted by their wavevectors and τ values represent periods of evolution between field matter interactions. Each diagram represents a term in the response function. GSB and ESE terms have a positive sign and correspond to a decrease in absorption relative to the ground state. ESA terms have a negative sign and correspond to an increase in absorption relative to the ground state.

There are six terms in the response function relevant to these experimental conditions. Three varieties of terms exist, ground state bleach (GSB) terms, excited state emission (ESE) terms, and excited state absorption (ESA) terms. GSB terms are those where the sample evolves in a ground state population during τ_2. If the sample evolves in an excited state population during τ_2 the related term is either an ESE or ESA. ESE terms are those that end in a ground state population. ESA terms end in an excited state population. GSB and ESE terms correspond to a decrease in absorption relative to the ground state and possess a positive sign. ESA terms possess a negative sign and correspond to an increase in absorption relative to the ground state. To illustrate each of these classes of terms a three level system is considered where $E_a < E_b < E_c$. Note that the system considered here does not undergo population relaxation. By application of the rules given earlier, the diagrams in Figure 2.7 are translated into their corresponding terms in the response function, shown in Equation 2.36.

$$\begin{aligned}
R_1(\tau_1,\tau_2,\tau_3) &= |\mu_{ba}|^4 \exp(-i\omega_{ab}\tau_1 - i\omega_{ba}\tau_3 - \Gamma_{ab}\tau_1 - \Gamma_{ba}\tau_3) \\
R_2(\tau_1,\tau_2,\tau_3) &= |\mu_{ba}|^4 \exp(-i\omega_{ba}\tau_1 - i\omega_{ba}\tau_3 - \Gamma_{ba}\tau_1 - \Gamma_{ba}\tau_3) \\
R_3(\tau_1,\tau_2,\tau_3) &= |\mu_{ba}|^4 \exp(-i\omega_{ab}\tau_1 - i\omega_{ba}\tau_3 - \Gamma_{ab}\tau_1 - \Gamma_{ba}\tau_3) \\
R_4(\tau_1,\tau_2,\tau_3) &= |\mu_{ba}|^4 \exp(-i\omega_{ba}\tau_1 - i\omega_{ba}\tau_3 - \Gamma_{ba}\tau_1 - \Gamma_{ba}\tau_3) \\
R_5(\tau_1,\tau_2,\tau_3) &= -|\mu_{ba}|^2 |\mu_{cb}|^2 \exp(-i\omega_{ab}\tau_1 - i\omega_{cb}\tau_3 - \Gamma_{ab}\tau_1 - \Gamma_{cb}\tau_3) \\
R_6(\tau_1,\tau_2,\tau_3) &= -|\mu_{ba}|^2 |\mu_{cb}|^2 \exp(-i\omega_{ba}\tau_1 - i\omega_{cb}\tau_3 - \Gamma_{ba}\tau_1 - \Gamma_{cb}\tau_3)
\end{aligned} \tag{2.36}$$

To clarify the location of the resonances related to the terms in Equation 2.36 these terms are convolved with the pump ($-k_1$ and k_2) and probe (k_3) fields and Fourier transformed into the frequency domain. The pump fields are considered to be identical. The resulting terms in the third order polarization are given in Equation 2.37 where N is the number density.[5]

$$
\begin{aligned}
P_1^{(3)}(\omega) &= \frac{N}{\hbar^3}\frac{\xi_{pu}^2\xi_{pr}\left|\mu_{ba}\right|^4}{\left(-\omega_{pu}-\omega_{ab}+i\Gamma_{ab}\right)\left(\omega_{pr}-\omega_{ba}+i\Gamma_{ba}\right)} \\
P_2^{(3)}(\omega) &= \frac{N}{\hbar^3}\frac{\xi_{pu}^2\xi_{pr}\left|\mu_{ba}\right|^4}{\left(\omega_{pu}-\omega_{ba}+i\Gamma_{ba}\right)\left(\omega_{pr}-\omega_{ba}+i\Gamma_{ba}\right)} \\
P_3^{(3)}(\omega) &= \frac{N}{\hbar^3}\frac{\xi_{pu}^2\xi_{pr}\left|\mu_{ba}\right|^4}{\left(-\omega_{pu}-\omega_{ab}+i\Gamma_{ab}\right)\left(\omega_{pr}-\omega_{ba}+i\Gamma_{ba}\right)} \\
P_4^{(3)}(\omega) &= \frac{N}{\hbar^3}\frac{\xi_{pu}^2\xi_{pr}\left|\mu_{ba}\right|^4}{\left(\omega_{pu}-\omega_{ba}+i\Gamma_{ba}\right)\left(\omega_{pr}-\omega_{ba}+i\Gamma_{ba}\right)} \\
P_5^{(3)}(\omega) &= -\frac{N}{\hbar^3}\frac{\xi_{pu}^2\xi_{pr}\left|\mu_{ba}\right|^2\left|\mu_{cb}\right|^2}{\left(-\omega_{pu}-\omega_{ab}+i\Gamma_{ab}\right)\left(\omega_{pr}-\omega_{cb}+i\Gamma_{cb}\right)} \\
P_6^{(3)}(\omega) &= -\frac{N}{\hbar^3}\frac{\xi_{pu}^2\xi_{pr}\left|\mu_{ba}\right|^2\left|\mu_{cb}\right|^2}{\left(\omega_{pu}-\omega_{ba}+i\Gamma_{ba}\right)\left(\omega_{pr}-\omega_{cb}+i\Gamma_{cb}\right)}
\end{aligned}
\tag{2.37}
$$

The locations of the resonances for each term are illustrated in Figure 2.8. The terms in Equation 2.37 measure the upper two quadrants. Again, GSB and ESE terms have a positive sign while ESA terms have a negative sign. Equation 2.37 describes Lorentzian line shapes because homogeneous damping functions are employed. Terms in the polarization possess significant amplitude only when the pump and probe fields are resonant with the corresponding energy gaps of the system.[5]

In this section the usefulness of Feynman diagrams for representing terms in the response function has been exemplified at both first and third order in perturbation. Connections have been drawn between such diagrams and the relevant experimental schemes. The rules stated in this section can be used to accomplish the translation between diagram and function at any order and for any experiment. Terms in the response function can be convolved with electric fields to produce terms in the polarization.

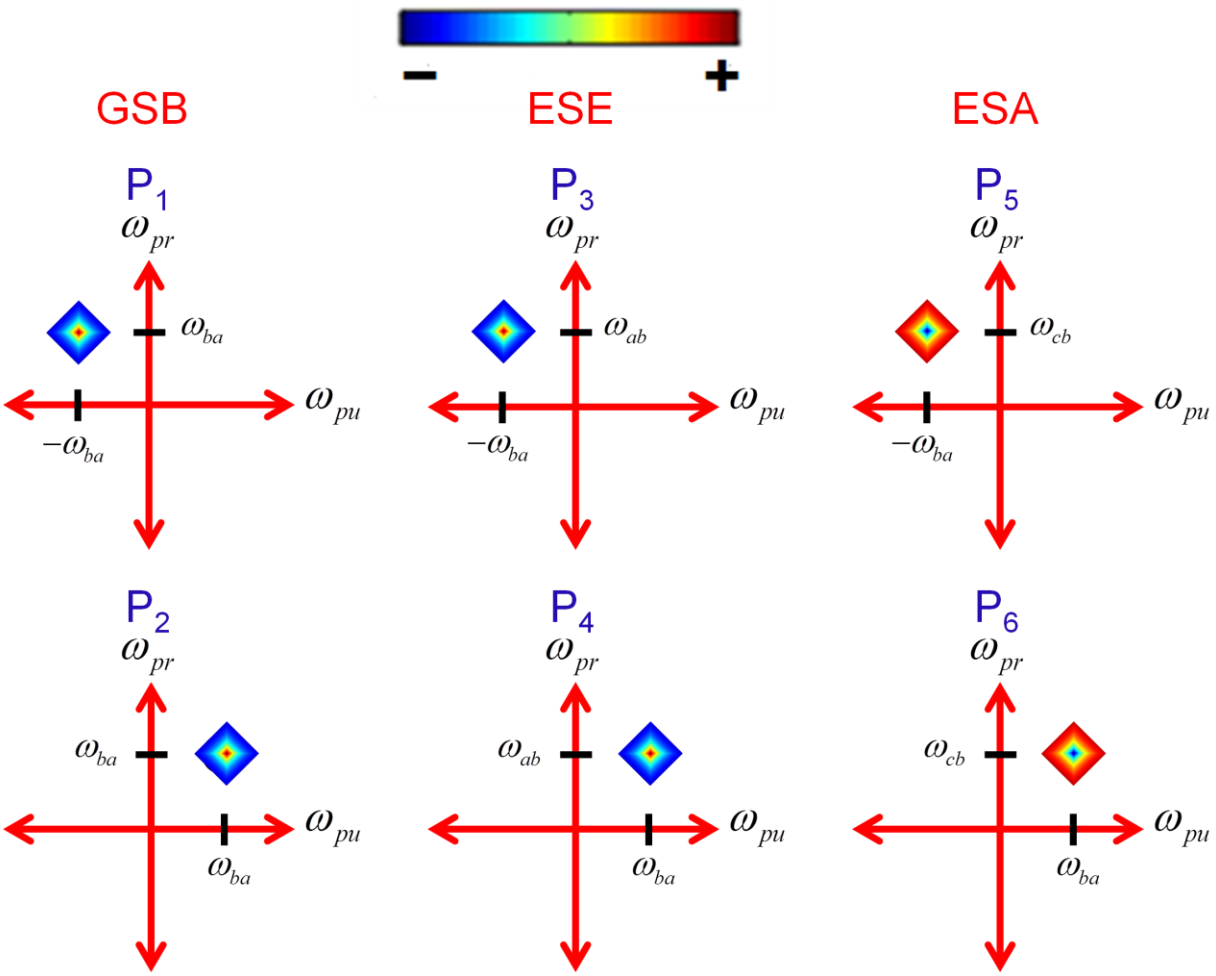

Figure 2.8. Locations of the resonances measured by each of the six terms in the third order polarization given in Equation 2.37. The terms considered here measure the upper two quadrants. GSB and ESE (ESA) terms are positive (negative) two-dimensional Lorentzians that decay to 0 as the pump and/or probe are detuned from resonance. Terms in the polarization possess significant amplitude only when both the pump and probe fields are resonant with the corresponding electronic energy gaps of the system.

2.5. Summary

In this chapter time dependent perturbation theory was used for the density operator to build an expression for the first order polarization containing time correlation functions of the dipole operator that decay as the system loses memory of the initial state prepared by the

perturbative electric field(s). A physically relevant line broadening function was obtained by the cumulant expansion and knowledge of Gaussian statistics. It was shown how this line broadening function describes the observation of Gaussian line shapes in condensed phases due to bath induced fluctuations of the system. Rules were presented enabling the conversion of Feynman diagrams into terms in the response function. The rules were employed for linear absorption and pump-probe spectroscopies but are universal to all orders of perturbation and all experiments. Terms obtained by application of the rules were convolved with electric fields to produce terms in the first and third order polarizations. The theoretical framework laid out in this chapter will be applied in future chapters to model the higher order two-dimensional resonance Raman signals measured in this dissertation and, for comparative purposes, cascades of third order processes. Comparison between experiment and theory will prove the validity of the measured signals and the usefulness of the technique developed herein.

2.6. REFERENCES

(1) Yang, M.; Fleming, G. R. *Chem. Phys.* **2002**, *282*, 163.

(2) Atkins, P.; Friedman, R. *Molecular Quantum Mechanics*, 4th ed.; Oxford University Press: Oxford, 2005.

(3) Boyd, R. W. *Nonlinear Optics*, 3rd ed.; Academic Press: Burlington, 2008.

(4) Cho, M. *Chem. Rev.* **2008**, *108*, 1331.

(5) Moran, A. M. *Chemistry 488: Molecular Spectroscopy*; Class Notes, 2013.

(6) Valkunas, L.; Abramavicius, D.; Mančal, T. *Molecular Excitation Dynamics and Relaxation: Quantum Theory and Spectroscopy*; Wiley-VCH: Weinheim, 2013.

(7) Nitzan, A. *Chemical Dynamics in Condensed Phases: Relaxation, Transfer, and Reactions in Condensed Molecular Systems*; Oxford University Press: New York, 2006.

(8) Parson, W. W. *Modern Optical Spectroscopy with Examples from Biophysics and Biochemistry*; Springer-Verlag: New York, 2007.

(9) Kubo, R. *J. Phys. Soc. Jpn.* **1962**, *17*, 1100.

(10) Druet, S. A. J.; Taran, J. P. E. *Prog. Quant. Electr* **1981**, *7*, 1.

(11) Yee, T. K.; Gustafson, T. K. *Phys. Rev. A* **1978**, *18*, 1597.

(12) Tokmakoff, A. Nonlinear Spectroscopy; MIT Department of Chemistry: Cambridge, 2009; Vol. 2016.

(13) Levine, I. N. *Quantum Chemistry*, 6th ed.; Pearson Prentice Hall: Upper Saddle River, 2009.

(14) Mukamel, S. *Principles of Nonlinear Optical Spectroscopy*; Oxford University Press: New York, 1995.

(15) Memming, R. *Semiconductor Electrochemistry*; Wiley-VCH: Weinheim, 2001.

(16) Abramavicius, D.; Mukamel, S. *Chem. Rev.* **2004**, *104*, 2073.

(17) Guo, Z.; Molesky, B. P.; Cheshire, T. P.; Moran, A. M. *J. Chem. Phys.* **2015**, *143*, 124202.

(18) Molesky, B. P.; Giokas, P. G.; Guo, Z.; Moran, A. M. *J. Chem. Phys.* **2014**, *141*, 114202.

(19) Molesky, B. P.; Guo, Z.; Moran, A. M. *J. Chem. Phys.* **2015**, *142*, 212405.

(20) Boyd, R. W.; Mukamel, S. *Phys. Rev. A* **1984**, *29*, 1973.

(21) Lepetit, L.; Chériaux, G.; Joffre, M. *J. Opt. Soc. Am. B.* **1995**, *12*, 2467.

(22) Gallagher, S. M.; Albrecht, A. W.; Hybl, J. D.; Landin, B. L.; Rajaram, B.; Jonas, D. M. *J. Opt. Soc. Am. B.* **1998**, *15*, 2338.

CHAPTER 3: METHODS OF FEMTOSECOND PULSE GENERATION AND RELEVANT ULTRAFAST TECHNIQUES

3.1. Introduction

The research contained in this dissertation is motivated by ultrafast chemistry where nuclear motions of the system occur on the same time scale as the electronic process. Primarily photodissociation reactions are studied.[1-3] However, electron transfer and energy transfer processes may also involve such dynamics.[4,5] To enable direct investigation of the correlated nuclear motions in these mechanisms, two dimensional resonance Raman spectroscopies (2DRR) are developed and implemented. One-dimensional techniques are also utilized to gain a preliminary, broader view of the chemistry before executing the more complicated 2D experiments.

For each and all of the experiments contained in this dissertation, ultrashort laser pulses of varying color and bandwidth are required to achieve the necessary temporal resolution for the dynamics of each system. This chapter will review the methods for generating laser pulses relevant to this work and will detail the techniques in which they are used. Section 3.2 will discuss spectral broadening in hollow-core fibers. Section 3.3 reviews third-harmonic generation in filaments. Section 3.4 details transient absorption spectroscopy which also prepares the reader for a discussion of pump-repump-probe in section 3.6. Section 3.5 explains transient grating spectrosocopy which frames the discussion of the remaining 2DRR techniques discussed in sections 3.6 and 3.7.

3.2. Spectral Broadening of Femtosecond Pulses Using Hollowcore Fibers

In this dissertation hollow core fiber (HCF) waveguides are used to prepare ~25fs visible laser pulses for studies of myoglobin and triiodide.[1-3] The fiber cladding is made of fused silica to enclose the incident light, and the interior is pressurized with Ar to provide a transparent medium for significant self-phase modulation (SPM). For transmission of high intensity laser pulses HCFs are superior to solid core fibers (SCFs)[6] because gaseous media have much greater breakdown thresholds and weaker optical nonlinearities than solid media.[7-9] Although as a result greater interactions lengths are needed. Beneficially, however, the strength of these nonlinearities is easily tuned by changing the type and/or pressure of the gas.[6] HCFs support hybrid modes which are beyond the scope of this discussion except to say that EH_{11} is the lowest order mode and has a spatial profile similar to the TEM_{00} mode for Gaussian beams.[10] The electric field of a laser pulse coupled to the EH_{nm} mode, propagating along the fiber axis z, is given according to Equation 3.1.

$$E_{nm}(z,t) == E_{0nm}\exp\left(-\frac{t^2}{2\tau^2}\right)\exp\left[-i\left(\omega_0 t-\gamma_{nm}z\right)\right] \tag{3.1}$$

Here E_{0nm} is the maximum amplitude of the field, τ is the standard deviation of the temporal Gaussian, ω_0 is the carrier frequency, and γ_{nm} is a term known as the 'propagation constant'.[11]

$$\gamma_{nm} = \beta_{nm} + i\alpha_{nm} \tag{3.2}$$

The real component of the propagation constant, given in Equation 3.3, is called the 'phase constant'. The imaginary component, shown in Equation 3.4, is the 'attenuation constant'.[6,9,10,12]

$$\beta_{nm} = \frac{2\pi n\left(\lambda, p, I\left(t\right)\right)}{\lambda}\left[1-\frac{1}{2}\left(\frac{u_{nm}\lambda}{2\pi a}\right)^2\right] \tag{3.3}$$
$$n\left(\lambda, p, I\left(t\right)\right) = n_0\left(\lambda, p\right) + n_2\left(\lambda, p\right) I\left(t\right)$$

$$\alpha_{nm} = \left(\frac{u_{nm}}{2\pi}\right)^2 \frac{\lambda^2}{a^3} \frac{\nu^2+1}{\sqrt{\nu^2-1}} \tag{3.4}$$

Here λ is the wavelength of light, a is the fiber bore radius, p is the gas pressure, I is the laser intensity, n_0 is the linear refractive index, n_2 is the nonlinear refractive index, n is the total refractive index, ν is the ratio between the refractive indices of the external (fused silica) and internal (Ar) materials, and u_{nm} is a modal constant that increases in magnitude with the mode order.[6] Using Equation 3.1 as the definition of the field, the intensity is given in Equation 3.5.

$$I\left(t\right) = E_{nm}^{*} E_{nm} = I_0 \exp\left(-\frac{t^2}{\tau^2}\right) \tag{3.5}$$

As the pulse passes some point in space the intensity rises, peaks, and decays. This time dependent intensity creates a varying index of refraction due to the nonlinear component (see Equation 3.3). As a result there is a phase shift and the pulse spectrum broadens. This is the process of SPM. The time derivative of the phase constant represents the time dependent frequency shift per unit length of the fiber. The sign is negative according to Equations 3.1 and 3.2.

$$\begin{aligned}\Delta\omega(t) &= -\frac{d\beta_{nm}(t)}{dt} = -\frac{2\pi n_2(\lambda,p)}{\lambda}\left[1-\frac{1}{2}\left(\frac{u_{nm}\lambda}{2\pi a}\right)^2\right]\frac{dI(t)}{dt} \\ &= -\frac{2\pi n_2(\lambda,p)}{\lambda}\left[1-\frac{1}{2}\left(\frac{u_{nm}\lambda}{2\pi a}\right)^2\right]\left[\frac{-t}{\tau^2}I_0\exp\left(-\frac{t^2}{2\tau^2}\right)\right] \\ &= \rho t I_0 \exp\left(-\frac{t^2}{2\tau^2}\right)\end{aligned} \tag{3.6}$$

Here ρ is used to represent the constant factor which is positive when $n_2(\lambda,p)$ is positive (this is the case for most materials other than plasmas).

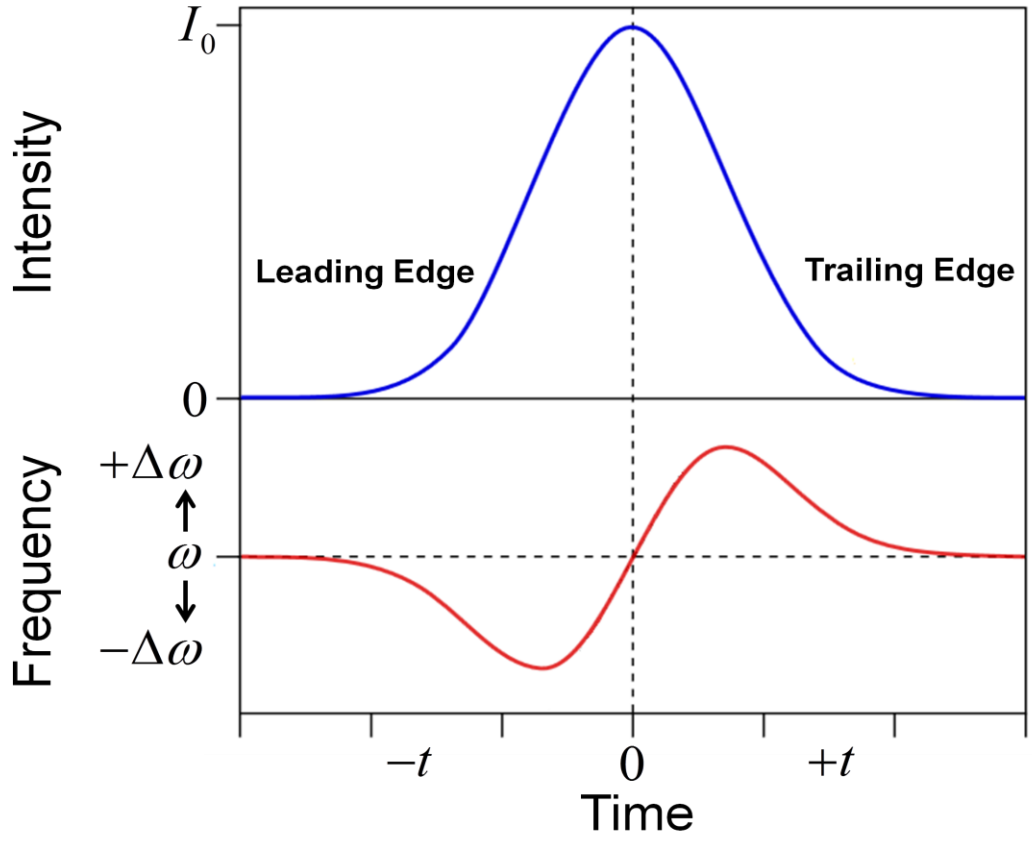

Figure 3.1. A Gaussian pulse propagating through a hollow-core fiber experiences self-phase modulation due to the intensity dependent refractive index of the gaseous medium. The frequency of the pulse experiences a red shift at the leading edge (i.e. $t<0$) and a blue shift at the trailing edge (i.e. $t>0$). At the peak ($t=0$), where the intensity possesses no slope, the phase shift is 0 and there is no change in frequency.

Figure 3.1 and Equation 3.6 show that the pulse red shifts at the leading edge (i.e. $t < 0$) and blue shifts at the trailing edge (i.e. $t > 0$). At the peak, where the intensity possesses no slope ($t = 0$), the phase shift is 0 and there is no change in frequency. Multiplication of Equation 3.6 by the length of fiber gives the total effect of SPM.

Propagation through HCFs can be thought of as a series of grazing angle Fresnel reflections off the fiber's inner surface.[6,10] Due to partial transmission at the walls of the capillary HCFs are very lossy[9,12], unlike SCFs which take advantage of total internal reflection.[12] The attenuation constant shows how this loss depends on the fiber mode, the wavelength of light λ, the bore radius of the fiber a, and the refractive indices of the cladding and gas. Since the magnitude increases with the mode order, HCFs tend to discriminate against higher order modes.[6,10] Attenuation of all modes becomes more significant as the wavelength of light increases or the fiber bore radius decreases. Equation 3.7 gives the transmitted power for the EH_{nm} mode through a fiber of length ℓ, where η_{nm} is the coupling efficiency.[13]

$$P_{nm} = \eta_{nm} \exp\left(-2\alpha_{nm}\ell\right) \tag{3.7}$$

The coupling efficiency is unique for each mode but is related to the ratio of the $1/e^2$ beam waist radius and the fiber bore radius. When this ratio is greater than 0.64 essentially no light is coupled to modes higher than that of lowest order.[13] This assumes perfect alignment along the path of the fiber.[14] Of course the beam can be intentionally misaligned to populate higher order modes for purposes of cross modal phase matching in third harmonic generation.[15] As the spot size becomes larger than the fiber bore diameter light is clipped on the aperture and the overall coupling efficiency is diminished.[13] The attenuation of all modes increases with the length of the

fiber but is more detrimental to higher order modes due to the factor u_{nm} which increases with the mode order.[6,9,10,13,14]

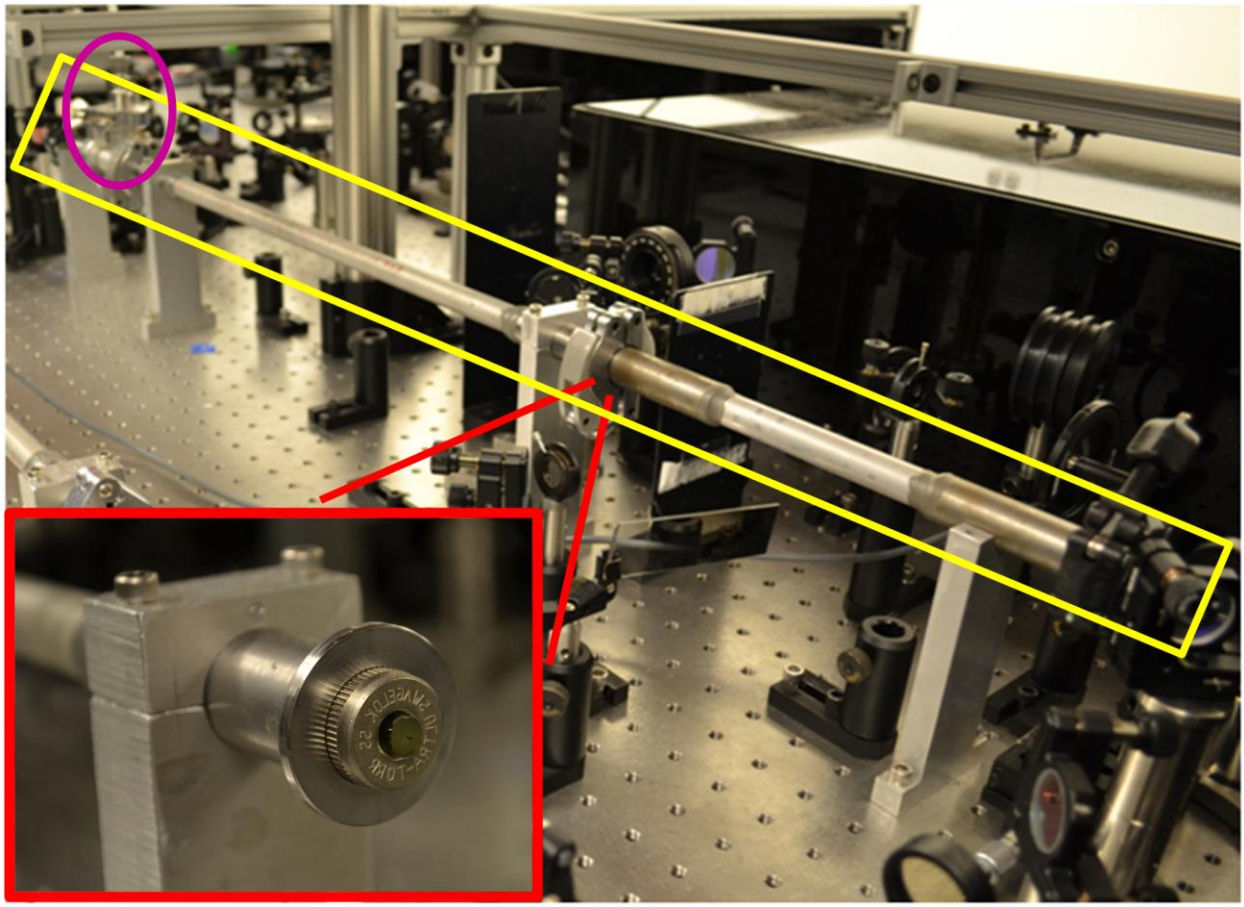

Figure 3.2. The mounting system and air tight housing for a hollow-core fiber, specially designed to ensure perfect alignment to the path of the beam. The fiber is contained within a glass rod positioned within the central part of the housing. The rod is held in place by Swagelok Ultra-Torr fittings located where pairs of vacuum components are clamped together. The entire custom housing is highlighted in yellow, supported by four custom mounts. The image in red shows the fiber inside of the glass rod cradled by an Ultra-Torr fitting where the vacuum components have been disjoined to provide a better look. The gas inlet/outlet is circled in magenta.

In this work HCFs are pressurized with Ar by mounting of the fiber in an air-tight housing specially designed to ensure perfect alignment of the fiber to the direction of the beam.

Photos of the setup are shown in Figure 3.2. Fiber diameters as well as alignment and focusing conditions are chosen to prevent significant coupling into higher order modes. Fiber lengths are selected to balance between a sufficient interaction distance and acceptable field attenuation. The Ar pressure is set to maximize spectral broadening while ensuring stability of the outgoing beam. Specific parameters can be found in Chapters 5 and #. The mounting system and fiber housing used in this work represent an upgrade to a previous design utilized in the Moran group[15-17] which was in turn based on a system engineered by the Bradforth group.[18]

3.3. Third Harmonic Generation by Filamentation of Femtosecond Pulses

Cofilamentation of 800nm and 400nm light in a gaseous medium is an effective way of generating pulses at the third and fourth harmonic of a Ti:S laser system via four-wave mixing (4WM) processes that take place within the filament.[19,20] The dominant processes are shown in Equation 3.8.

$$\begin{aligned} 2\omega + 2\omega - \omega &\rightarrow 3\omega \\ 3\omega + 2\omega - \omega &\rightarrow 4\omega \end{aligned} \tag{3.8}$$

Here ω is the fundamental frequency of the Ti:S laser. Although both processes occur to a significant degree, this section focuses on production of the third harmonic. Figure 3.3 illustrates the mechanism of filament generation. Laser pulses are focused into the gas such that the power density becomes greater than the critical power for self-focusing defined in Equation 3.9.[21-24]

$$P_{cr} = \frac{\lambda^2}{2\pi n_0 n_2} \tag{3.9}$$

Here λ is the wavelength of light, n_0 is the linear refractive index, and n_2 is the nonlinear refractive index. Self-focusing is a result of the optical Kerr effect and further increases the

power density, ionizing the gas to form a plasma. The negative refractive index of the plasma defocuses the beam until the power density is below the threshold for ionization but still greater than the critical power for self-focusing.[25,26] The change in refractive index due to the plasma is given in Equation 3.10.[24,27,28]

$$\Delta n = -\frac{\omega_p^2}{2\omega^2} = -\frac{4\pi e^2 n_e(I)}{2\omega^2 m_e} \tag{3.10}$$

Here ω_p is the plasma frequency, ω is the optical frequency, e and m_e are the charge and mass of the electron, and $n_e(I)$ is the intensity dependent electron concentration.

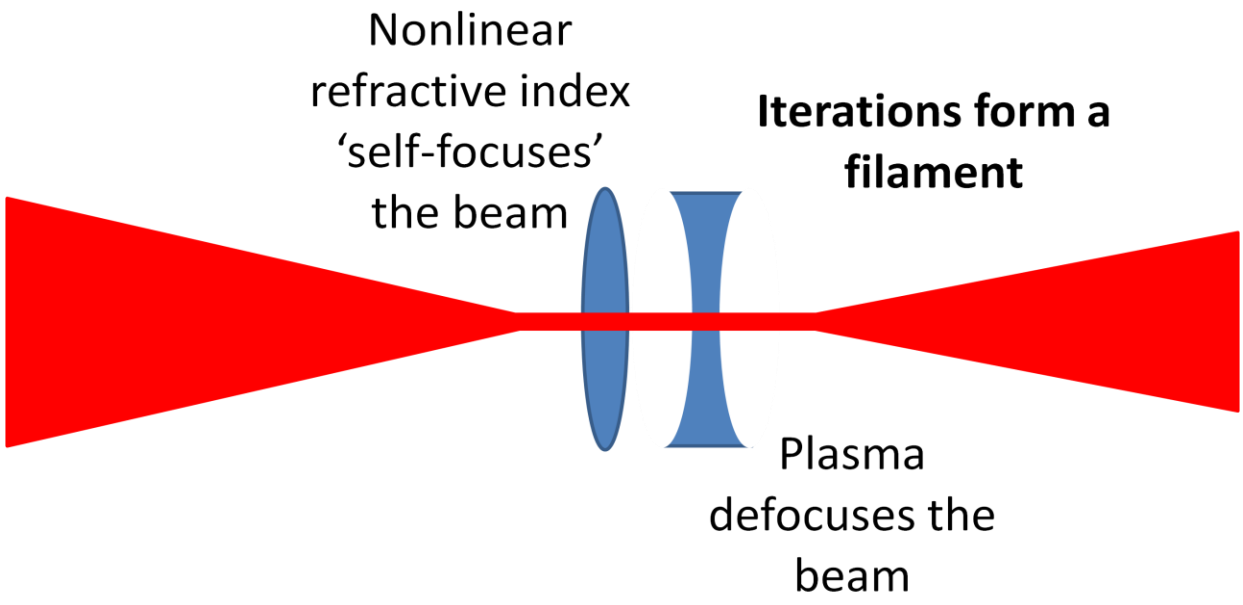

Figure 3.3. The process of filament generation. A high-energy laser beam is focused into a gas by a lens or mirror until the power density is great enough to cause Kerr effect induced self-focusing of the beam. The gaseous medium is ionized to form a plasma which defocuses the light. These processes iterate, forming a filament, until enough energy is lost through ionization of the gas to destabilize the balance between self-focusing from the Kerr-effect and defocusing from the plasma. Depending on the pulse duration and intensity as well as the type of gas and pressure, filaments can be as short as a centimeter or as long as meters. The filaments generated in this work are on the length scale of centimeters.

The balance between self-focusing and plasma induced defocusing causes the formation of a filament in which the beam waist is 'clamped' until enough energy is lost through gas ionization to disrupt the balance.[22,24,29,30] To moderate the density of the plasma and maximize the length of the filament, noble gases are chosen as the nonlinear media because of their relatively high ionization potentials compared to other gases. This ensures that energy is lost as slowly as possible and provides longer interaction lengths[27] for self-phase modulation and the FWM processes that result in UV light.

Although hollow-core fiber (HCF) waveguides have also been shown to be effective tools for the production of ultrashort UV pulses[12,31-33], filamentation holds many advantages for this purpose over HCFs. In HCFs cross modal phase matching of the incident 400nm and 800nm light can product sub-20fs laser pulses at the third harmonic through careful alignment of the incoming beams.[15] In filaments attention to phase matching becomes much less critical because 'intensity clamping' ensures that all fields remain strongly coupled to one another.[20] Alignment is easily achieved because it is only necessary that the 400nm and 800nm beams are collinear in free space. There are no 10's to 100's of micron apertures to which the incident light must be tediously coupled.[19,20,29] Additionally filaments are capable of supporting much greater incident pulse powers because there is no damageable waveguide.[22] They are much less lossy because there are no Fresnel reflections off a fused silica cladding, and the only major source of loss is multiphoton ionization of the gaseous medium.[24] It is clear that the physics for pulse propagation through a filament are significantly different than those for propagation through HCFs. As such the equations given in the previous section do not properly describe the spectral broadening and general behavior of the laser pulse in a filament.[20] For this purpose Equation

3.11 shows a description of a Gaussian temporal envelope propagating through a cofilament based on the slowly varying wave approximation modified to include ionization effects.[20,27,34]

$$\begin{aligned}\frac{\partial A_j(z,r,t)}{\partial z} &= \frac{i}{2k(\omega_j)}\left(\frac{\partial^2}{\partial r^2}+\frac{1}{r}\frac{\partial}{\partial r}\right)A_j(z,r,t)-\frac{1}{GVM_{1j}}\frac{\partial}{\partial t}A_j(z,r,t)\\ &-i\frac{\beta_j}{2}\frac{\partial^2}{\partial t^2}A_j(z,r,t)+i\frac{\omega_j n_2 I_j}{c}\left(1+\frac{i}{\omega_j}\frac{\partial}{\partial t}\right)\left|A_j(z,r,t)\right|^2 A_j(z,r,t) \qquad (3.11)\\ &-i\frac{1}{2\omega_j c}\left(1+\frac{i}{\omega_j}\frac{\partial}{\partial t}\right)^{-1}\omega_p^2(z,r,t)A_j(z,r,t)+P_j^{NL}(t)\end{aligned}$$

Here $A_j(z,r,t)$ is the envelope, $k(\omega_j)$ is the frequency profile of the wavenumber, GVM_{1j} is the group velocity mismatch with the fundamental, β_j is a phase constant, ω_j is the central optical frequency, c is the speed of light, $\omega_p(z,r,t)$ is the plasma frequency, and $P_j^{NL}(t)$ is time-domain nonlinear polarization related to the atomic nonlinear susceptibilities of the medium. The subscript j distinguishes between the fundamental, second harmonic, and third harmonic beams. The model includes spatiotemporal Kerr-effect induced self-action of the laser pulse, dispersion from the gas and plasma, beam diffraction, and ionization effects including loss and related nonlinear phenomenon. The terms related to conventional SPM can be isolated by neglecting those involving the plasma (i.e. $n_e = 0$, $\omega_p = 0$, and $\left(\frac{1}{\omega_0}\right)\left(\frac{d}{dt}\right) = 0$). It is not possible to isolate the terms associated with ionization induced spectral broadening without losing the balance between self-focusing and defocusing which would negate these factors.[27]

Traditionally the method of filamentation for UV production is implemented using top of the line commercial laser systems that support sub-30fs, >2mJ fundamental pulses enabling the generation of a filament under loose focusing conditions to keep the beam divergence low.[19,20,22]

Large beam divergence can destabilize the filament and cause degradation of the output beam's spatiotemporal profile, affecting the compressibility of the pulse.[19,20] These negative impacts can be mediated by careful choice of noble gas and gas pressure.[22] A technical hallmark of the work in Chapter 4 is the use of high pressure Ne to accomplish the generation of third harmonic pulses suitable for the triiodide studies in this dissertation using a less advanced, partially homebuilt laser system. The relatively high ionization potential and low nonlinear refractive index in comparison to Ar make Ne capable of withstanding the experimental conditions in Chapter 4 (see the Chapter 4 and Appendix A for the experimental conditions, illustration of the gas cell, and details of the Ne/Ar comparison).[35]

3.4. Transient Absorption Spectroscopy

Transient absorption (TA) is third order in perturbation and can be considered as measuring the dynamic absorption spectrum of a nonequilibrium species as it relaxes. First, an electronically resonant 'pump' beam excites a fraction of the system from equilibrium within the spot size of the laser. This fraction depends on the extinction coefficient of the sample at the pump wavelength and the intensity of the pump.[36] It is kept fairly small, typically <10%, to ensure perturbative conditions. The excitation itself can be thought of in either a classical or quantum sense. In a quantum consideration one photon is absorbed by the sample. In a classical consideration there are two interactions with the electric field of the pump beam. Both of these interpretations are equivalent and accurate according to the particle-wave duality of light. After the sample is excited there is a delay period, T, and a probe beam passes through the excited volume. Transmitted probe light is dispersed by frequency on a suitable detector producing a spectrum of intensity vs. detection frequency at a particular time along relaxation of the system. By varying the delay and acquiring spectra at predetermined intervals between the pump and

probe, evolution of the transient species is measured over an amount of time appropriate for the dynamics of interest. If the purpose of the measurement is to record oscillations in the spectrum, the step size is carefully chosen to enforce the appropriate Fourier window. At each delay time the probe transmission is measured under both pump-on and pump-off conditions to acquire the difference in absorption between the equilibrium and nonequilibrium system. The transient spectrum is then determined as a function of time and frequency, illustrated by Equation 3.12.

$$\Delta A(\omega,T) = A_{pump-on}(\omega,T) - A_{pump-off}(\omega,T) = A_{noneq}(\omega,T) - A_{eq}(\omega,T) \qquad (3.12)$$

This works because the signal wavevector is equivalent to the probe wavevector according to the phase matching condition in TA, $k_s = -k_1 + k_2 + k_3$ [37,38] where $k_1 = k_2$.

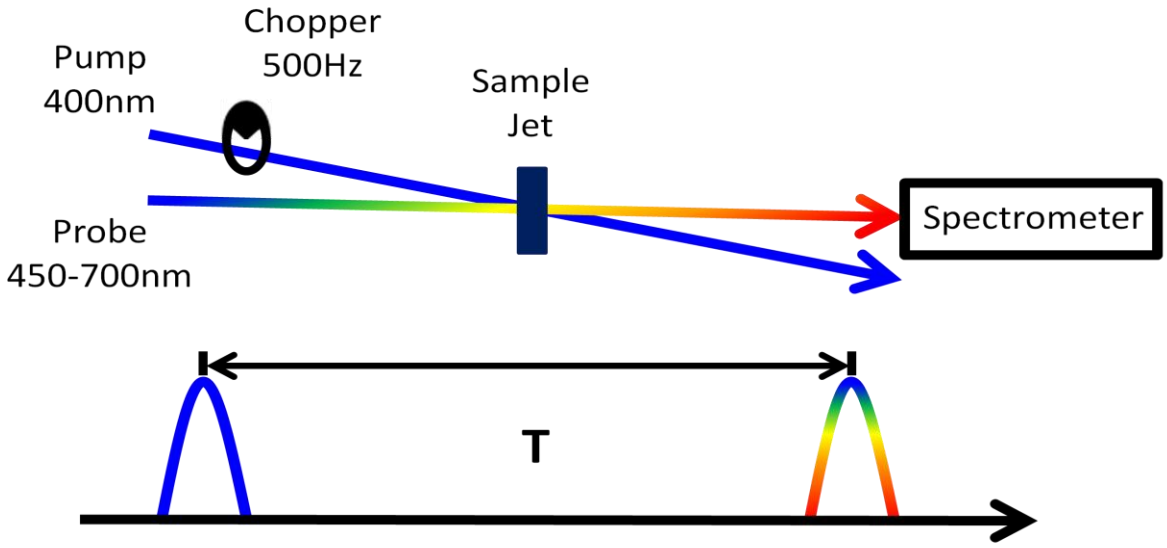

Figure 3.4. Experimental design of the transient absorption experiments completed in this dissertation. A 400nm pump beam excites the sample from equilibrium. After a delay, T, the probe arrives and passes through the excited volume. Transmitted probe light is then dispersed by frequency on a suitable detector. A chopper in the path of the pump spinning at 500Hz, half the rep rate of the laser, alternates between pump-on, pump-off conditions with each laser shot to measure the signal according to Equation 3.12. The signal is measured over a delay range appropriate for the sample and dynamics of interest.

The experimental conditions for the TA measurements conducted in this dissertation are identical to those for the pump-repump-probe experiment detailed in Chapter 5, except that only one pump beam is utilized and the chopper wheel is operated at 500Hz to alternate between pump-on, pump-off with each laser shot. A diagram depicting this simpler design is given in Figure 3.4.

For a two level system TA measures two classes of terms in the response function, ground state bleach (GSB) terms and excited state emission (ESE) terms. As discussed in Section 4 of Chapter 2 spectral components originating from either GSB or ESE have a negative sign and show a decrease in absorption after the sample is excited. This decrease in absorption corresponds to an increase in probe transmission through the transient species relative to the equilibrium system. For GSB signal contributions this increase in probe transmission is due to the decrease in ground state population after a fraction of the sample has been promoted to the excited state. For ESE signal contributions it is due to emission of light from the excited state population, stimulated by the probe. At long delay times GSB and ESE are distinguished by the Stokes shift of the ESE due to nuclear relaxation of the system. At short delay times ESE and GSB contributions overlap and are indistinguishable.[39,40] For systems possessing more than two levels, excited state absorption (ESA) terms can also be measured. As discussed in Section 4 of Chapter 2 spectral components originating from ESA have a positive sign and show an increase in absorption for the transient species. This corresponds to a decrease in probe transmission, attributable to resonance of the probe light with an energy gap between the excited state prepared by the pump and a higher lying excited state.

3.5. Transient Grating Spectroscopy

Like TA, transient grating (TG) is a third order, pump-probe technique utilizing the phase matching condition, $k_s = -k_1 + k_2 + k_3$.[37,38] TG measures the same classes of terms in the response function as TA, but possesses some key beneficial differences. Unlike TA which employs only one pump beam that interacts with the sample twice, TG utilizes two time coincident pump beams in a noncollinear geometry causing emission of the signal in a background free direction (see Figure 2.6). Although now there are two pump beams rather than just one, the excitation can still be considered as either a quantum or classical process. The quantum interpretation is analogous to a double-slit experiment.[41] The material absorbs only one photon but in a superposition of the photon originating from either beam. The classical interpretation is identical to that for TA, except that the two pump interactions occur with separate, noncollinear fields.

Since the pump beams do not have identical wavevectors they interfere creating spatially periodic areas of constructive and destructive interference. In areas of constructive interference the sample is excited. In areas of destructive interference the sample is left at equilibrium forming a population grating. The population grating can be thought of as a series of 'fringes'.[42-44] After a delay, T, the probe beam arrives and is scattered off the grating in the signal direction, i.e. the sum of the wavevectors of incident fields. The efficiency of this scattering process depends on the number of fringes encountered by the probe and determines the sharpness with which the signal direction is defined. The number of fringes the probe sees is related to the fringe density defined by the spot size at the sample and the distance between fringes. This distance, typically on the order of 10 microns, is given according to Bragg's law (i.e. $d = \frac{\lambda}{2\sin\theta}$

) and thus depends on the angle between interfering pump beams, θ.[42-44] The time evolution of the population grating is determined by the response function of the sample and encodes the experimental observable. Figure 3.5 illustrates the concept of grating formation and shows an example population grating produced in a TG measurement. The parameters used to calculate this grating correspond to the experimental conditions in Chapter 4. The angle between the 266nm pump beams is 6.1 degrees resulting in the presence of 17 fringes within the 120 micron FWHM laser spot.

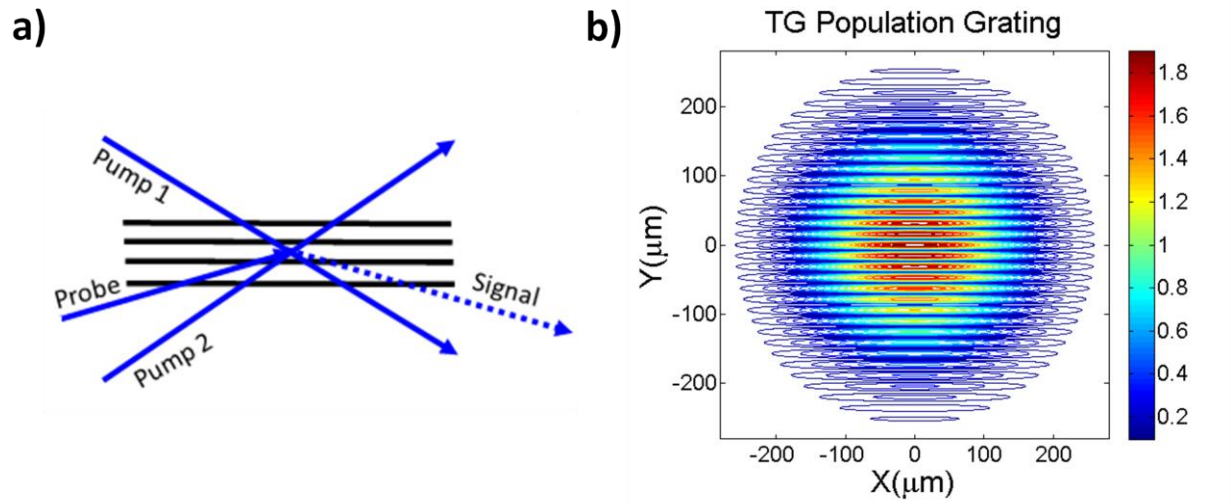

Figure 3.5. (a) The concept of grating formation in transient grating measurements. Two time-coincident noncollinear pump beams overlap in the sample interfering to form a population grating. After a delay the probe arrives and is scattered off the grating in the signal direction $k_s = -k_1 + k_2 + k_3$ where k_1 and k_2 are the pump beams and k_3 is the probe. (b) An example population grating produced in a TG measurement viewed along the propagation direction. The parameters used to calculate this grating correspond to experimental conditions in Chapter 4. X and Y are dimensions in the laboratory frame.

Since signal intensities are typically 1000x weaker than the probe, background free detection in TG is an enormous advantage regarding signal to noise, allowing for the use of lower laser fluences and the measurement of signals much weaker than what is possible in TA.

It is only necessary that the signal intensity is greater than the noise of the detector. Better still the background free signal can be detected interferometrically by overlap with a weak reference field, further enhancing the signal to noise ratio and enabling resolution of the absorptive and dispersive components.[45-50] The expression for this heterodyne signal is given in Equation 3.13.[51,52]

$$I = \left|E_{ref}\right|^2 + \left|E_S(t)\right|^2 + 2\left|E_{ref}E_S(t)\right|\cos\left(\phi_{ref} - \phi_S\right) \tag{3.13}$$

By considering that the reference field is much stronger than the signal field (i.e. $\left|E_{ref}\right| \gg \left|E_S(t)\right|$) $\left|E_S(t)\right|^2$ can be eliminated from Equation 3.2. Also since the reference field is experimentally delayed, $\left|E_{ref}\right|^2$ can be removed from Equation 3.2 through numerical processing. The measured interferogram is Fourier transformed into the time domain where a Gaussian apodization function is applied to isolate the third term. Inverse Fourier transform yields Equation 3.14.

$$I = 2\left|E_{ref}E_S(t)\right|\cos\left(\phi_{ref} - \phi_S\right) \tag{3.14}$$

While the homodyne signal intensity depends quadratically on the signal field and contains no phase information (i.e. $I = \left|E_S(t)\right|^2$), the heterodyne signal retains all information necessary for obtaining the phase, scales linearly with the signal field, and is in fact amplified by a factor of $2\left|E_{ref} / E_S(t)\right|$ in relation to the homodyne signal.[49,51] The real component corresponds to the transient absorption of the sample equivalent to the information given by TA.[53,54] The imaginary component corresponds to transient dispersion which can be sensitive to the solvent and/or a thermal grating formed by fast recovery of the ground state.[45-47] The phase of the signal also enables determination of the signs of its components.

As evidenced by Equation 3.14 the difficulty in achieving interferometric detection is maintaining a constant phase relationship between the reference and signal fields. Equation 3.15 illustrates this difficulty in terms of the incident fields.[51]

$$\Delta\phi = \phi_{ref} - \phi_S = \frac{\pi}{2} + \phi_\chi + \left(\phi_{pump1} - \phi_{pump2}\right) - \left(\phi_{ref} - \phi_{probe}\right) \tag{3.15}$$

Here $\frac{\pi}{2}$ is the phase shift between the polarization and field emitted by the material, and ϕ_χ is the phase shift originating from the complex nonlinear susceptibility. Air currents, humidity issues, temperature fluctuations, and vibrations of optics are all factors that easily disrupt this delicate relationship by inducing changes in the relative pathlengths of incident beams. For visible laser pulses just a 16nm difference in pathlength induces a 10° phase shift. One way of mediating these disruptive factors is by sheer brute force control over the mechanical stability and experimental environment.[55] Another is by continuous monitoring of phase fluctuations and reactive compensation via a feedback loop and piezoelectric transducers.[56-59] Both are tedious, expensive, and extremely complex. In this dissertation passive phase stabilization is achieved through utilizing a diffractive optic (DO) based interferometer. In such a device one DO splits two beams into their +1 and -1 diffraction orders creating two identical pump beams and a probe and reference beam that are also identical. All four beams are incident on common optics negating phase fluctuations due to mechanical vibrations. Furthermore the close proximity of all four beams ensures the sampling of identical temperature and humidity conditions resulting in self canceling of all other fluctuations.[49-52,60-64] A schematic of the DO interferometer as it is used for TG measurements in Chapter 4 is given in Figure 3.6.

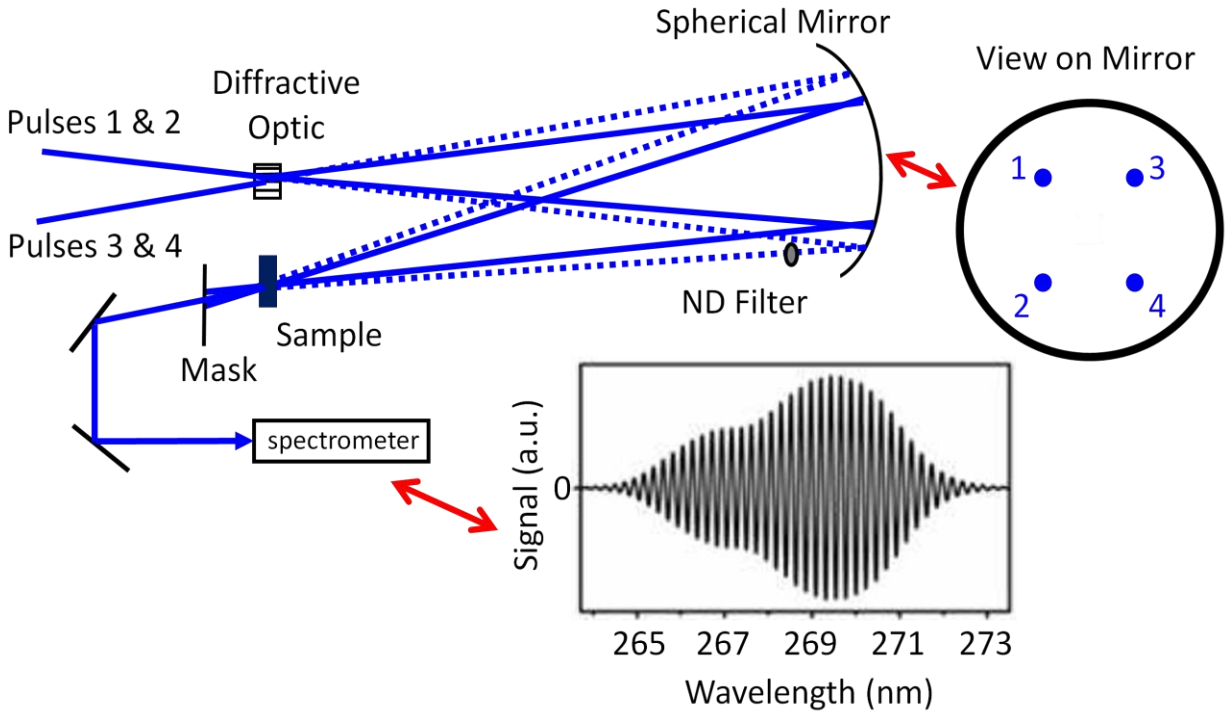

Figure 3.6. The diffractive optic (DO) based interferometer used for TG measurements in this dissertation. Two beams enter the setup with an experimentally controlled delay between them. Both are focused onto the DO splitting each into its +1 and -1 diffraction orders. These four beams are incident on a spherical mirror which focuses them onto the sample. Beams 1-3 induce the polarization response and the signal is emitted collinearly with beam 4, an attenuated reference field for interferometric detection. A typical interferogram is shown.

3.6. Six-Wave Mixing Spectrocopies

Six-wave mixing (6WM) techniques are fifth order in perturbation. The simplest 6WM spectroscopy executed in this dissertation is 'pump-repump-probe' (PRP). The experimental conditions and technical details for this experiment are given in Chapter 5. Figure 3.7 is based off Figure 5.5 and depicts the experimental setup for the purpose of local illustration. PRP can be thought of as TA spectroscopy with an additional pump step before the probe step. Like in TA the equilibrium system interacts twice with a pump beam and is promoted to a nonequilibrium state. After a delay a second pump beam interacts twice with the nonequilibrium

system at a specific point along the decay defined by the time between pump beams. After a second delay the probe arrives inducing signal emission. In this way it is possible to measure chemical processes beginning from nonequilibrium nuclear geometries. Lower order spectroscopies can only measure chemistry beginning from equilibrium. This principle of inducing chemistry from nonequilibrium reactant states and then probing components of the system extends to all six-wave mixing spectroscopies, allowing measurement of nuclear coherences between the photochemical reactant and product.

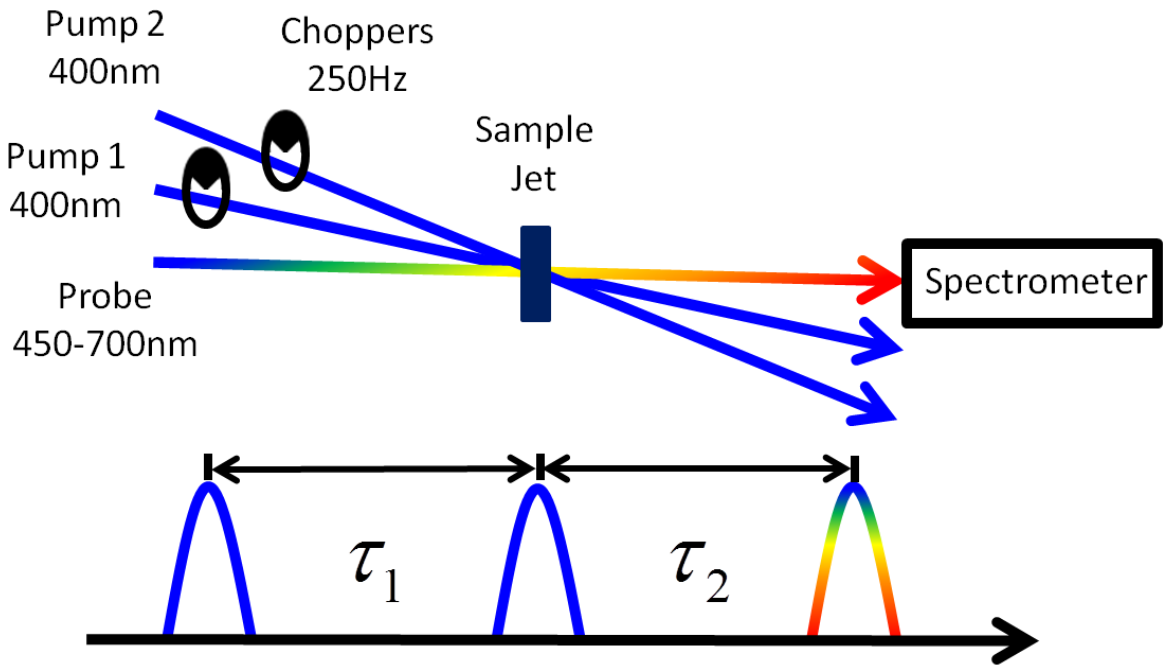

Figure 3.7. Experimental design of the pump-repump-probe experiments completed in this dissertation. A 400nm pump beam excites the sample from equilibrium. After a delay, τ_1, another identical pump beam reexcites the system from a nonequilibrium state. There is another delay, τ_2, and the probe arrives passing through the excited volume. Transmitted probe light is then dispersed by frequency on a suitable detector. Choppers in the paths of both pump beams spinning at 250Hz, a quarter of the laser's rep rate, alternate between the four conditions needed to measure the signal according to Equation 3.16. Appropriate delay ranges are chosen based on the sample and dynamics of interest.

The PRP spectrum is generated by varying the delay between pump beams as well as the delay between the second pump and probe. For each combination of delays, measurements are taken under four conditions: pumps-on, pump1-on pump2-off, pump1-off pump2-on, and pumps-off. As such the PRP spectrum is determined according to Equation 3.16.[65-67]

$$\begin{aligned}
\Delta\Delta A(\omega,\tau_1,\tau_2) &= \Delta A_{pumps-on}(\omega,\tau_1,\tau_2) - \Delta A_{\substack{pump1-on \\ pump2-off}}(\omega,\tau_1,\tau_2) - \Delta A_{\substack{pump1-off \\ pump2-on}}(\omega,\tau_1,\tau_2) \\
\Delta A_{pumps-on}(\omega,\tau_1,\tau_2) &= A_{pumps-on}(\omega,\tau_1,\tau_2) - A_{pumps-off}(\omega,\tau_1,\tau_2) \\
\Delta A_{\substack{pump1-on \\ pump2-off}}(\omega,\tau_1,\tau_2) &= A_{\substack{pump1-on \\ pump2-off}}(\omega,\tau_1,\tau_2) - A_{pumps-off}(\omega,\tau_1,\tau_2) \\
\Delta A_{\substack{pump1-off \\ pump2-on}}(\omega,\tau_1,\tau_2) &= A_{\substack{pump1-off \\ pump2-on}}(\omega,\tau_1,\tau_2) - A_{pumps-off}(\omega,\tau_1,\tau_2)
\end{aligned} \tag{3.16}$$

This is necessary because all three signals (i.e. ΔA terms in Equation 3.#) are collinear with the probe (k_5) according to the phase matching condition $k_s = -k_1 + k_2 - k_3 + k_4 + k_5$ where $k_1 = k_2$ and $k_3 = k_4$.

To increase sensitivity, reduce data acquisition time, and achieve resolution of the dispersive and absorptive signal components, a greater number of beams can be used to obtain information at the same order in perturbation. In this dissertation four-beam and five-beam geometries are utilized. The experimental conditions and technical details can be found in Chapters 4 and 5. Figures 3.8 and 3.9 show the DO interferometers used for the four and five-beam experiments. These figures are based off Figures 5.4 and 4.4 and are shown here for local illustration. Four-beam geometry six-wave mixing experiments can be thought of as an initial TA style pump step followed by the steps of a TG measurement. First, two interactions with a pump beam prepare a nonequilibrium system. After a delay a pair of noncollinear time coincident pump beams reexcites the system and creates a population grating in the sample similar to that illustrated in Figure 3.5.[42-44] There is a final delay and the probe arrives scattering off the grating

according to the phase matching condition $k_s = k_1 - k_2 + k_3 - k_4 + k_5$ [61] where $k_1 = k_2$. If the reactant is resonant with the 'TG beams', as is the case for experimental tests in Chapter 6, then the fifth-order signal is collinear with a third-order signal and the initial pump beam must be chopped to isolate the higher order signal. Spectra are obtained under pump1-on and pump1-off conditions. If the reactant is not resonant with the 'TG beams', as is the case in Chapter 5, then the higher order signal is background free and can be measured directly without chopping any beams. Interferometric detection is readily achieved because of a reference field that is automatically collinear with the signal as in TG.

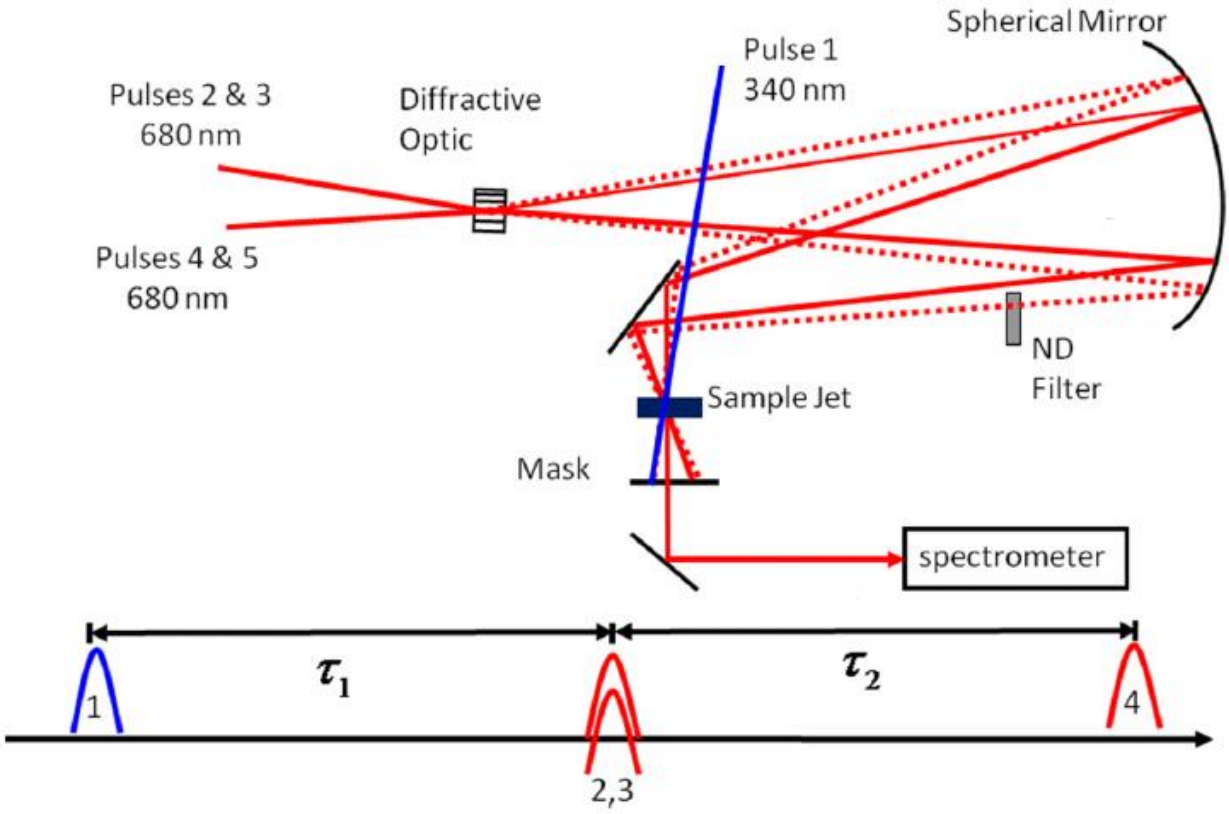

Figure 3.8. The diffractive optic (DO) based interferometer used for 4-beam six wave mixing experiments in Chapter 5. This setup operates much like the TG interferometer shown in Figure 3.6 but with a preliminary pump step (340nm pulse 1) such that there are two delay periods and four beams induce the polarization response of the sample. Again the signal is emitted collinearly with an attenuated reference field for interferometric detection.

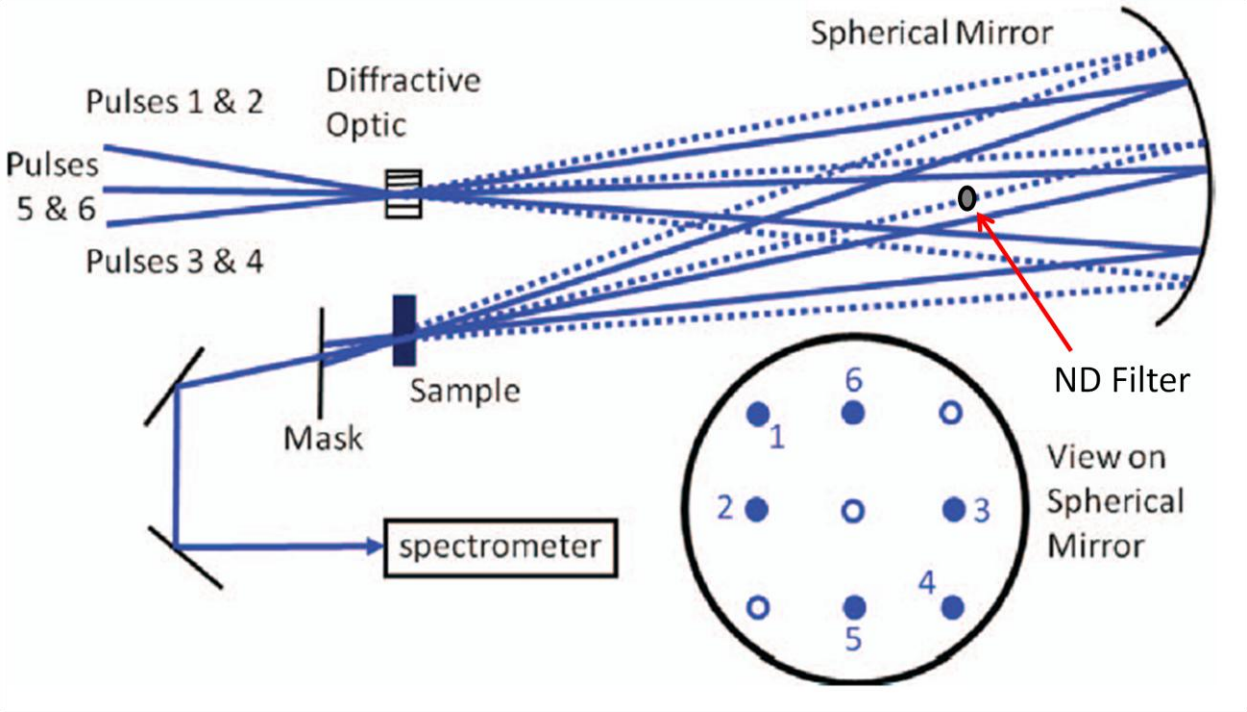

Figure 3.9. The diffractive optic (DO) based interferometer used for 5-beam six wave mixing experiments in Chapter 4. Each of the three incoming beams is split into -1, 0, and +1 diffraction orders with equal intensities producing the portrayed view on the spherical mirror. Beams represented by open circles are blocked by a mask. Beams 1 and 2 arrive first exciting the sample and producing a population grating. After a delay beams 3 and 4 arrive reexciting the sample from a nonequilibrium state. Beam 5 induces signal emission collinearly with an attenuated reference field, beam 6, for interferometric detection.

For five-beam geometries the phase matching condition is the same as for the four-beam geometry (i.e. $k_s = k_1 - k_2 + k_3 - k_4 + k_5$[61]) but $k_1 \neq k_2$ such that the higher order signal is always background free.[61] In this geometry all beams are generated in a DO by splitting three incoming beams into their +1, 0, and -1 orders. Initially a pair of time coincident noncollinear pump beams creates a population grating in the sample. After a delay another pair of pump beams interferes with the initial grating creating a more complicated pattern from which the probe is scattered after a second delay. Here the angle between the pump beams in each pair is half of what it is in the four-beam geometry and TG experiments (i.e. for 266nm beams the angle is

6.1°/2=3.05°). This reduction in the separation angle increases the spacing between fringes and reduces the fringe density[42-44] such that there are 9 fringes within the 120 micron FWHM laser spot rather than 17. Regardless, when the probe arrives the desired signal is scattered sharply in the phase matched direction, collinear with a weak reference field for interferometric detection. Examples of the initial grating and the total grating produced in the five-beam 6WM experiments detailed in Chapter 4 are illustrated in Figure 3.10.

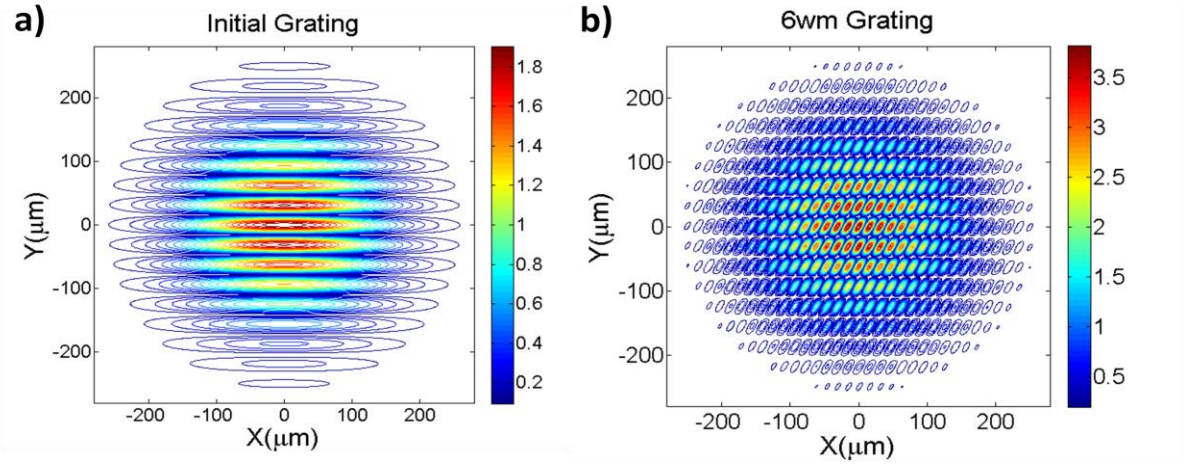

Figure 3.10. (a) An example population grating produced by the first pair of time coincident noncollinear pump beams in the 5-beam 6WM experiment. The number of fringes within the 120 micron FWHM spot size is reduced from 17 to 9 in comparison to TG experiments conducted under similar conditions. This reduction in fringe density originates in the lesser angular separation between pump beams. (b) The final 6WM grating from which the probe is scattered. The pattern is more complicated because two pairs of time coincident noncollinear pump beams interfere to generate this grating. The parameters used to calculate both gratings correspond to experimental conditions in Chapter 4. Both gratings are viewed along the propagation direction. X and Y are dimensions in the laboratory frame.

3.7. Femtosecond Stimulated Raman Spectroscopy by Six-Wave Mixing

In this dissertation Femtosecond Stimulated Raman Spectroscopy (FSRS) by six-wave mixing (6WM) is developed and conducted in both four-beam and five-beam geometries. The

benefits over traditional three-beam FSRS[68], the experimental conditions, and the technical details are given in Chapters 6 and 7. Figured 3.11 is based off of Figures 6.1 and 6.3 and is shown here to illustrate the beam geometries and pulse arrival scheme for the purpose of understanding the gratings formed in each experiment. Figure 3.11d shows the five-beam experiment but equally represents the four-beam technique if the number of actinic pump beams is reduced to one. In the five-beam geometry an electronic process is activated by a pair of identical actinic pump beams which form a static grating in the sample.[42-44] They are beams 1 and 2 in Figure 3.11b. The pattern of this grating is similar to the initial grating formed in the 6WM experiments considered in the last section. An example is shown in Figure 3.12a. After a variable delay, time coincident Raman pump and Stokes beams arrive and stimulate a coherent Raman response. They are beams 4 and 5 in Figure 3.11b. They also produce a grating however it is more complex than those previously considered. Due to the relative orientation of the Stokes beam and Raman pump the resulting grating is tilted diagonally as shown in Figure 3.12b. Also since these beams are not the same frequency the grating pattern is mobile and the fringes move quickly, diagonally down to the right. In fact, because of the broadband nature of the Stokes beam (i.e. its bandwidth contains many frequencies) the grating consists of different components moving at different rates. The final FSRS grating, shown in Figure 3.12c, is the convolution of the coherent Raman grating and the grating formed by the actinic pump beams. Its inference pattern moves diagonally down to the left. After a fixed delay the final Raman pump, beam 3 in Figure 3.11b, is scattered off this dynamic grating in the signal direction $k_s = k_1 - k_2 + k_3 - k_4 + k_5$ [61], experiencing a 'Doppler' shift to the red. The magnitude of the shift depends on the frequency differences between bandwidth components of the Stokes beam and the Raman pump that created the nonstatic grating. When a frequency difference matches a

vibrational frequency of the sample the signal is resonantly enhanced at the corresponding wavelength.

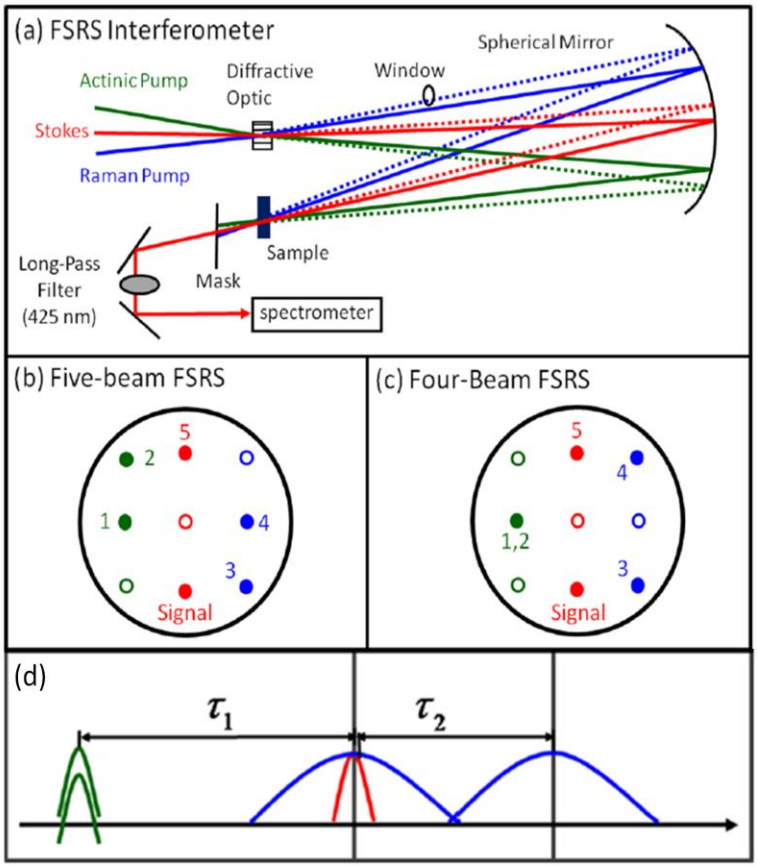

Figure 3.11. (a) The interferometer used for FSRS by 6WM experiments in this dissertation. This design is much like the interferometer shown in Figure 3.9. However each of the three incoming beams is a different color. Therefore each exits the DO at a different angle preventing collinearity with a reference field. (b) The five-beam FSRS geometry. (c) The four-beam FSRS geometry. (d) The pulse arrival scheme. Actinic pump(s) arrive(s) first activating some electronic process. After a variable delay, τ_1, the first Raman pump (beam 4) and the Stokes beam (beam 5) arrive. The window shown in (a) enforces another delay, τ_2, and the final Raman pump (beam 3) is scattered off the FSRS grating.

In the four beam geometry a single actinic pump (beam 1,2 in Figure 3.11c) is used so there is no initial static grating. Additionally the fringe density in the dynamic coherent Raman grating is lesser due to the smaller angle between the time coincident Raman pump and Stokes

beams (beams 4 and 5 in Figure 3.11c). The diagonal tilt is less pronounced as well. In the four beam geometry there is a lower order signal collinear with the higher order signal that must be eliminated in a manner similar to the method used in the four beam experiment discussed in the previous section. In both the four and five beam geometries a broadband pump-repump-probe signal is separated from the fifth order Raman signal by numerical processing for which details are given in Chapter 6.

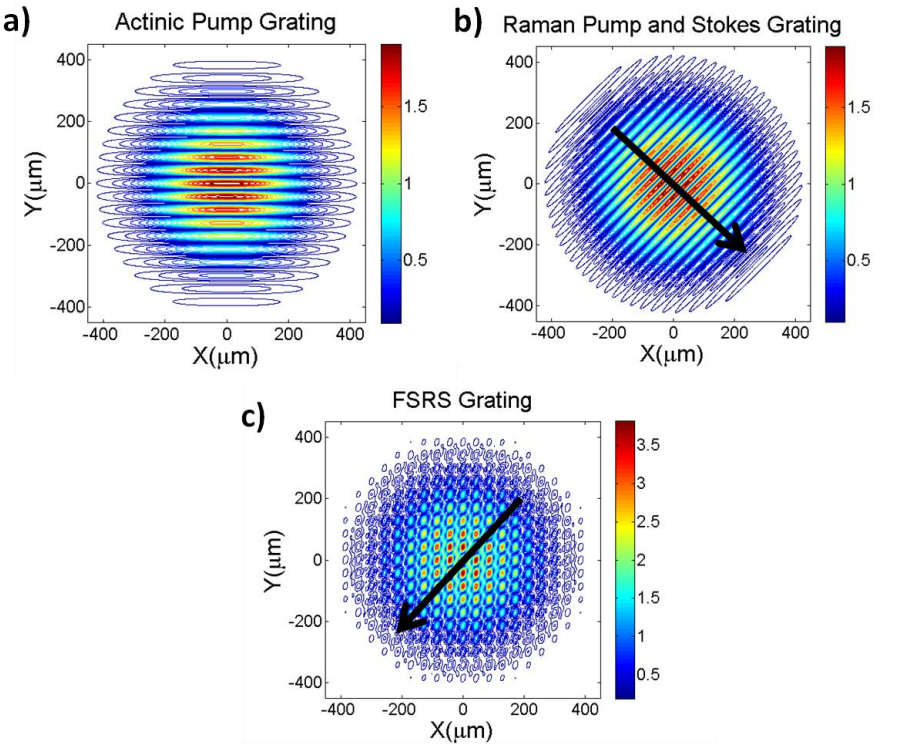

Figure 3.12. (a) The static grating formed by the time coincident noncollinear actinic pump beams in the 5-beam geometry experiment. In the 4-beam experiment a singular actinic pump is used and this grating is not formed (b) In both the 4 and 5-beam experiments the Raman pump and Stokes beams create a dynamic population grating in the sample because the beams have different frequencies. The fringes move down to the right. (c) In the 5-beam experiment the gratings in (a) and (b) interfere forming a more complicated dynamic grating whose fringes move down to the left. In both the 4 and 5-beam experiments the final Raman pump is scattered off the respective dynamic grating, experiencing a 'Doppler' shift based on the fringe velocities. When that velocity matches a resonance frequency in the sample the signal is resonantly enhanced at the corresponding wavelength.

3.8. Summary

In Chapter 3 methods of femtosecond pulse generation relevant to this work were discussed, specifically spectral broadening in hollow-core fibers and third harmonic generation in filaments. The techniques in which these pulses are applied were also detailed, including transient absorption and transient grating spectroscopies, pump-repump-probe, a newly developed 2D six-wave mixing form of transient grating, and the newly development FSRS by six-wave mixing. The methods of pulse generation and the experimental techniques, both one-dimensional and two-dimensional, that were discussed in this chapter will be critical for the investigations in the remaining chapters of this dissertation.

3.9. REFERENCES

(1) Guo, Z.; Molesky, B. P.; Cheshire, T. P.; Moran, A. M. *J. Chem. Phys.* **2015**, *143*, 124202.

(2) Molesky, B. P.; Giokas, P. G.; Guo, Z.; Moran, A. M. *J. Chem. Phys.* **2014**, *141*, 114202.

(3) Molesky, B. P.; Guo, Z.; Moran, A. M. *J. Chem. Phys.* **2015**, *142*, 212405.

(4) Chenu, A.; Scholes, G. D. *Annu. Rev. Phys. Chem.* **2015**, *66*, 69.

(5) Consani, C.; Auböck, G.; Mourik, F. V.; Chergui, M. *Science* **2013**, *339*, 1586.

(6) Nisoli, M.; DeSilvestri, S.; Svelto, O. *Appl. Phys. Lett.* **1996**, *68*, 2793.

(7) Stolen, R. H.; Lin, C. *Phys. Rev. A* **1978**, *17*, 1448.

(8) Nurhuda, M.; Suda, A.; Kaku, M.; Midorikawa, K. *Appl. Phys. B* **2007**, *89*, 209.

(9) Kolevatova, O. A.; Naumov, A. N.; Zheltikov, A. M. *Opt. Commun.* **2003**, *217*, 169.

(10) Nisoli, M.; Stagira, S.; DeSilvestri, S.; Svelto, O.; Sartania, S.; Cheng, Z.; Lenzner, M.; Spielmann, C.; Krausz, F. *Appl. Phys. B* **1997**, *65*, 189.

(11) Novotny, L.; Hafner, C. *Phys. Rev. E* **1994**, *50*, 4094.

(12) Durfee, C. G.; Misoguti, L.; Backus, S.; Kapteyn, H. C.; Murnane, M. M. *J. Opt. Soc. Am. B* **2002**, *19*, 822.

(13) Nubling, R. K.; Harrington, J. A. *Opt. Eng.* **1998**, *37*, 2454.

(14) Saito, M.; Sato, S.; Miyagi, M. *J. Opt. Soc. Am. A* **1993**, *10*, 277.

(15) West, B. A.; Moran, A. M. *J. Phys. Chem. Lett.* **2012**, *3*, 2575.

(16) West, B. A.; Womick, J. M.; Moran, A. M. *J. Chem. Phys.* **2011**, *135*, 114505.

(17) West, B. A.; Womick, J. M.; Moran, A. M. *J. Phys. Chem. A* **2011**, *115*, 8630.

(18) Jailaubekov, A. E.; Bradforth, S. E. *Appl. Phys. Lett.* **2005**, *87*, 021107.

(19) Fuji, T.; Horio, T.; Suzuki, T. *Opt. Lett.* **2007**, *32*, 2481.

(20) Fuji, T.; Suzuki, T.; Serebryannikov, E. E.; Zheltikov, A. M. *Phys. Rev. A* **2009**, *80*, 063822.

(21) Hauri, C. P.; Kornelis, W.; Helbing, F. W.; Heinrich, A.; Couairon, A.; Mysyrowicz, A.; Biegert, J.; Keller, U. *Appl. Phys. B* **2004**, *79*, 673.

(22) Stibenz, G.; Zhavoronkov, N.; Steinmeyer, G. *Opt. Lett.* **2006**, *31*, 274.

(23) Champeaux, S.; Bergé, L. *Phys. Rev. E* **2003**, *68*, 066603.

(24) Braun, A.; Korn, G.; Liu, X.; Du, D.; Squier, J.; Mourou, G. *Opt. Lett.* **1995**, *20*, 73.

(25) Bergé, L.; Skupin, S.; Nuter, R.; Kasparian, J.; Wolf, J. P. *Rep. Prog. Phys.* **2007**, *70*, 1633.

(26) Couairon, A.; Mysyrowicz, A. *Phys. Rep.* **2007**, *441*, 47.

(27) Serebryannikov, E. E.; Goulielmakis, E.; Zheltikov, A. M. *New J. Phys.* **2008**, *10*, 093001.

(28) Wagner, N. L.; Gibson, E. A.; Popmintchev, T.; Christov, I. P.; Murnane, M. M.; Kapteyn, H. C. *Phys. Rev. Lett.* **2004**, *93*, 173902.

(29) Couairon, A.; Franco, M.; Mysyrowicz, A.; Biegert, J.; Keller, U. *Opt. Lett.* **2005**, *30*, 2657.

(30) Berg⌜, L.; Couairon, A. *Phys. Rev. Lett.* **2000**, *86*, 1003.

(31) Durfee, C. G.; Backus, S.; Murnane, M. M.; Kapteyn, H. C. *Opt. Lett.* **1997**, *22*, 1565.

(32) Durfee, C. G.; Backus, S.; Kapteyn, H. C.; Murnane, M. M. *Opt. Lett.* **1999**, *24*, 697.

(33) Misoguti, L.; Backus, S.; Durfee, C. G.; Bartels, R.; Murnane, M. M.; Kapteyn, H. C. *Phys. Rev. Lett.* **2001**, *87*, 013601.

(34) Goulielmakis, E.; Koehler, S.; Reiter, B.; Schultze, M.; Verhoef, A. J.; Serebryannikov, E. E.; Zheltikov, A. M.; Krausz, F. *Opt. Lett.* **2008**, *33*, 1407.

(35) Wang, D.; Leng, Y.; Xu, Z. *Appl. Phys. B* **2013**, *111*, 447.

(36) Berera, R.; Grondelle, R. V.; Kennis, J. T. M. *Photosynth. Res.* **2009**, *101*, 105.

(37) Lepetit, L.; Chériaux, G.; Joffre, M. *J. Opt. Soc. Am. B* **1995**, *12*, 2467.

(38) Gallagher, S. M.; Albrecht, A. W.; Hybl, J. D.; Landin, B. L.; Rajaram, B.; Jonas, D. M. *J. Opt. Soc. Am. B* **1998**, *15*, 2338.

(39) Kovalenko, S. A.; Ruthmann, J.; Ernsting, N. P. *Chem. Phys. Lett.* **1997**, *271*, 40.

(40) Vos, M. H.; Jones, M. R.; Hunter, C. N.; Breton, J.; Lambry, J. C.; Martin, J. L. *Biochem.* **1994**, *33*, 6750.

(41) Rahav, S.; Mukamel, S. *PNAS* **2010**, *107*, 4825.

(42) Eichler, H. J.; Gunter, P.; Pohl, D. W. *Laser Induced Dynamic Gratings*; Springer-Verlag: New York, 1986; Vol. 50.

(43) Brown, E. J.; Zhang, Q.; Dantus, M. *J. Chem. Phys.* **1999**, *110*, 5772.

(44) Fayer, M. D. *Annu. Rev. Phys. Chem.* **1982**, *33*, 63.

(45) Terazima, M.; Hara, T.; Hirota, N. *Chem. Phys. Lett.* **1995**, *246*, 577.

(46) Vöhringer, P.; Scherer, N. F. *J. Phys. Chem.* **1995**, *99*, 2684.

(47) Nelson, K. A.; Casalegno, R.; Miller, R. J. D.; Fayer, M. D. *J. Chem. Phys.* **1982**, *77*, 1144.

(48) Hara, T.; Hirota, N.; Terazima, M. *J. Phys. Chem.* **1996**, *100*, 10194.

(49) Maznev, A. A.; Nelson, K. A.; Rogers, J. A. *Opt. Lett.* **1998**, *23*, 1319.

(50) Cowan, M. L.; Ogilvie, J. P.; Miller, R. J. D. *Chem. Phys. Lett.* **2004**, *386*, 184.

(51) Goodno, G. D.; Dadusc, G.; Miller, R. J. D. *J. Opt. Soc. Am. B* **1998**, *15*, 1791.

(52) Brixner, T.; Mančal, T.; Stiopkin, I. V.; Fleming, G. R. *J. Chem. Phys.* **2004**, *121*, 4221.

(53) Jonas, D. M. *Annu. Rev. Phys. Chem.* **2003**, *54*, 425.

(54) Mukamel, S. *Principles of Nonlinear Optical Spectroscopy*; Oxford University Press: New York, 1995.

(55) Strauss, J.; Hundhausen, M.; Ley, L. *Appl. Phys. Lett.* **1996**, *69*, 875.

(56) Zhang, T.; Borca, C. N.; Li, X.; Cundiff, S. T. *Opt. Express* **2005**, *13*, 7432.

(57) Volkov, V.; Schanz, R.; Hamm, P. *Opt. Lett.* **2005**, *30*, 2010.

(58) Scherer, N. F.; Carlson, R. J.; Matro, A.; Du, M.; Ruggiero, A. J.; Romero-Rochin, V.; Cina, J. A.; Fleming, G. R.; Rice, S. A. *J. Chem. Phys.* **1991**, *95*, 1487.

(59) Matsuo, S.; Tahara, T. *Chem. Phys. Lett.* **1997**, *264*, 636.

(60) Underwood, D. F.; Blank, D. A. *J. Phys. Chem. A* **2003**, *107*, 956.

(61) Khurmi, C.; Berg, M. A. *J. Phys. Chem. A* **2008**, *112*, 3364.

(62) Gundogdu, K.; Stone, K. W.; Turner, D. B.; Nelson, K. A. *Chem. Phys.* **2007**, *341*, 89.

(63) Kim, J.; Wong, C. Y.; Nair, P. S.; Fritz, K. P.; Kumar, S.; Scholes, G. D. *J. Phys. Chem.* **2006**, *110*, 25371.

(64) Moran, A. M.; Maddox, J. B.; Hong, J. W.; Kim, J.; Nome, R. A.; Bazan, G. C.; Mukamel, S.; Scherer, N. F. *J. Chem. Phys.* **2006**, *124*, 194904.

(65) Pique, J. P.; Engel, Y. M.; Levine, R. D.; Chen, Y.; Field, R. W.; Kinsey, J. L. *J. Chem. Phys.* **1988**, *88*, 5972.

(66) Ishikawa, H.; Nagao, C.; Mikami, N. *J. Chem. Phys.* **1997**, *106*, 2980.

(67) Busby, E.; Carroll, E. C.; Chinn, E. M.; Chang, L.; Moulé, A. J.; Larsen, D. S. *J. Phys. Chem. Lett.* **2011**, *2*, 2764.

(68) Kukura, P.; Yoon, S.; Mathies, R. A. *Anal. Chem.* **2006**, *78*, 5952.

CHAPTER 4: MULTIDIMENSIONAL RESONANCE RAMAN SPECTROSCOPY BY SIX-WAVE MIXING IN THE DEEP UV[1]

4.1. Introduction

Recent experimental advances have motivated tremendous growth in the field of coherent multi-dimensional spectroscopy.[1-7] The most widespread technique, two-dimensional (2D) spectroscopy, employs a photon echo-like pulse sequence to overcome the tradeoff between time and frequency resolution made in traditional transient absorption experiments.[8-12] The power of 2D spectroscopy has been leveraged to obtain new insights into dynamics ranging from energy transfer in photosynthesis to chemical equilibrium exchange in liquids.[4,13-22] In contrast, multi-dimensional Raman techniques are not yet widely applied because of technical challenges involved in implementation.[23-25] Nonetheless, optical pump-Raman probe experiments have been used to interrogate the structural dynamics that accompany a variety of photoinduced relaxation processes (e.g. internal conversion, electron transfer). Time and frequency domain versions of Femtosecond Stimulated Raman Spectroscopy (FSRS) are capable of probing vibrational resonances in solvated chromophores throughout the entire "fingerprint" range.[26-39] A second class of techniques developed by the research groups of Scherer and Blank, referred to here as Polarizability Response Spectroscopy (PORS), is designed to detect the low-frequency ($<300 cm^{-1}$) Raman response of the solvent that surrounds a solute.[40-44]

[1] This chapter previously appeared as an article in the Journal of Chemical Physics. The original citation is as follows: Molesky, B. P.; Giokas, P. G.; Guo, Z.; Moran, A. M. *J. Chem. Phys.* **2014**, *141*, 114202.

The basic information conveyed by the technique employed in this work is described in Figure 4.1. A fifth-order polarization is induced with a sequence of five electronically resonant laser pulses. The first pair of time-coincident laser pulses initiates coherent vibrational motions in τ_1 by way of a stimulated Raman process. Interactions with the second pulse-pair similarly induce vibrational coherences in the experimentally controlled delay, τ_2. The experiment is motivated by knowledge of correlated nuclear motions in τ_1 and τ_2. For example, depending on the value of τ_1, the wavepacket in τ_2 can be initiated at the equilibrium position or (either) turning point in a particular vibrational coordinate. In addition, the signal field may carry signatures of the wavepacket's location at the time the signal is radiated, because the resonance frequency is generally coordinate-dependent for a Franck-Condon active mode. Figure 4.1 illustrates three potential applications of the present technique. Inhomogeneous broadening (i.e. structural heterogeneity) can be uncovered as in earlier work on intermoleculear motions in off-resonant systems.[24,25] The technique can also be used to study photochemical dynamics if beams with different frequencies are incorporated.[26,37,39,45] Finally, the experiment is sensitive to anharmonicity in the potential energy surfaces for Franck-Condon active modes.[45]

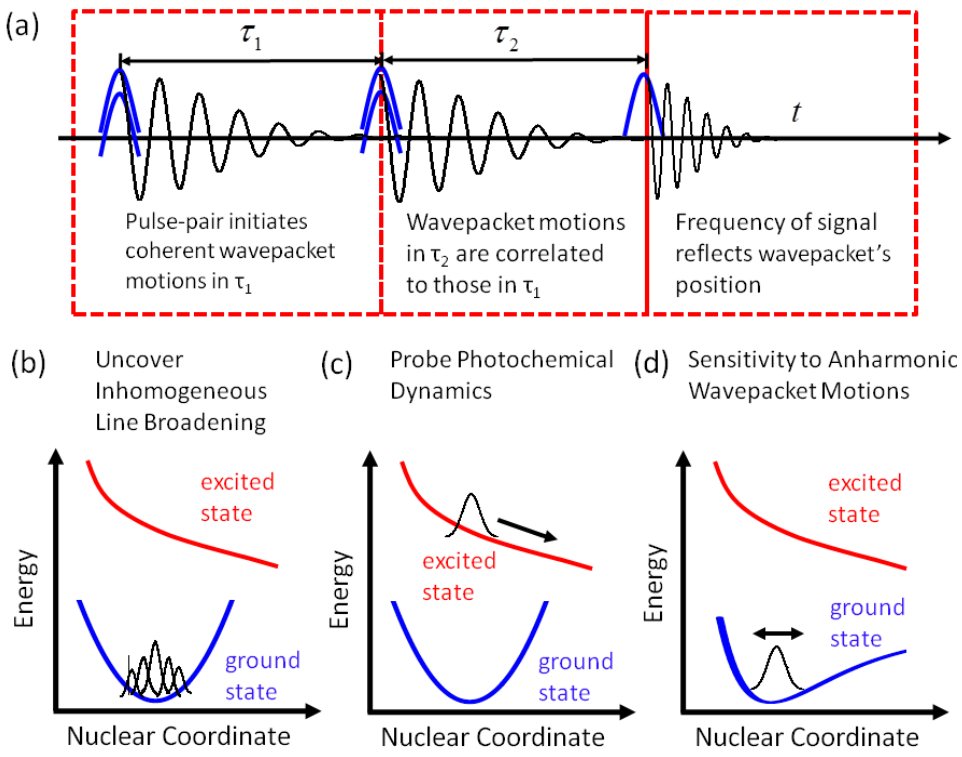

Figure 4.1. (a) The present experiment involves a sequence of five electronically resonant pulses and two experimentally controlled delay times. Coherent wavepacket motions are resolved in τ_1 and τ_2, whereas the signal frequency reflects the position and/or phase of the wavepacket. Fifth-order resonance Raman experiments can be used to investigate (b) line broadening mechanisms, (c) photochemical dynamics, and (d) shapes of potential energy surfaces.

In this article, we implement the six-wave mixing experiment described in Figure 4.1 in the deep UV spectral range. The capabilities of the experimental setup are demonstrated with application to a model system, triiodide (I_3^-), which was studied at length using stimulated and resonance Raman spectroscopies in the 1990's.[46-53] I_3^- is an ideal model system with which to develop the present technique, because ground state wavepacket motion in the symmetric stretching coordinate dominates the response in the deep UV.[46,50] We describe technical aspects of the experiment in addition to exploring the information provided by various representations of

the signal. In one representation, correlations between vibrational coherences in the two experimentally controlled delay times, τ_1 and τ_2, are exposed through a straightforward Fourier transformation of the wavelength-integrated signal (i.e. a 2D Raman spectrum). We also show that additional insights can be derived by dispersing the signal pulse in a spectrometer, because the signal spectrum encodes information regarding the wavepacket's position by way of the (time-evolving) emission frequency. Experimental signals are compared to model calculations in which a cumulant expansion is used to avoid a computationally expensive sum-over-states.

Undesired third-order signal cascades significantly challenge off-resonant Raman spectroscopies conducted on pure liquids and concentrated mixtures.[24,25,54-57] Third-order cascades involve a sequence in which the third-order polarization on one molecule radiates a field that induces a third-order polarization in a second molecule. The second molecule may then radiate a signal pulse in the same direction as the fifth-order signal of interest. Such third-order cascades are negligible in the present experiments because (i) the electronically resonant response does not possesses "forbidden" vibronic transitions (i.e. overtones are "allowed") and (ii) I_3^- exhibits extremely large-amplitude ground state wavepacket motions in the deep UV.[46,50] With respect to cascades, our analysis suggests that Franck-Condon activity is the key distinction between signal generation mechanisms on and off of electronic resonance. Franck-Condon activity promotes signal intensity for both harmonic and anharmonic modes on resonance, whereas the off-resonant signal generation mechanism relies on potentially weak effects such as anharmonicty or nonlinear coordinate-dependence of the polarizability.[55,57,58]

Applications of 2D electronic spectroscopies in the deep UV (2DUV) have progressed steadily in recent years.[21,22,59-63] The development of such experiments is primarily motivated by biological systems (e.g. DNA, proteins) and elementary organic photochemistries (e.g.

electrocyclic ring-opening).[21,64,65] Experimental work carried out to date suggests that 2DUV experiments must overcome several significant technical challenges including dispersion management, suppression of sample photo-ionization, and the large off-resonant response of the solvent near time-zero.[60,66-68] We see the present 2D Raman experiment as an alternate multi-dimensional spectroscopy that, with further development, can be routinely applied in the deep UV. The key issue is that molecular vibrations typically dephase on a time scale that is much longer than the width of the coherence spike that plagues 2DUV methods. Of course, six-wave mixing signal strengths are weaker than those associated with 2DUV measurements because of the higher-order of the nonlinearity. The approach taken here achieves the required sensitivity and data acquisition rate by combining a background-free (six-pulse) laser beam geometry with interferometric signal detection.

4.2. Experimental Methods

4.2.1. Third-Harmonic Generation via Filamentation in High-Pressure Ne

This study employs a newly-developed source of femtosecond laser pulses at the third- and fourth-harmonics of a Ti:Sapphire laser, wherein filamentation in noble gases is used instead of nonlinear optical crystals.[21,61,69,70] Development of this setup was initially motivated by applications involving 200-nm laser pulses. Here, we make use of the 267-nm laser pulses that are also produced in the filament. The bandwidths of these third-harmonic pulses are not as large as those generated in hollow-core fibers;[71-73] however, we find that the present filamentation-based approach yields larger pulse energies, requires much less maintenance, and does not compromise the stability of the UV beam (<5% root-mean-square fluctuations). Moreover, the pulse durations are sufficient for detection of vibrational coherences in I_3^-,

because the symmetric stretching mode has a period of 300 fs. Below, we describe the conditions under which suitable third-harmonic laser pulses are obtained.

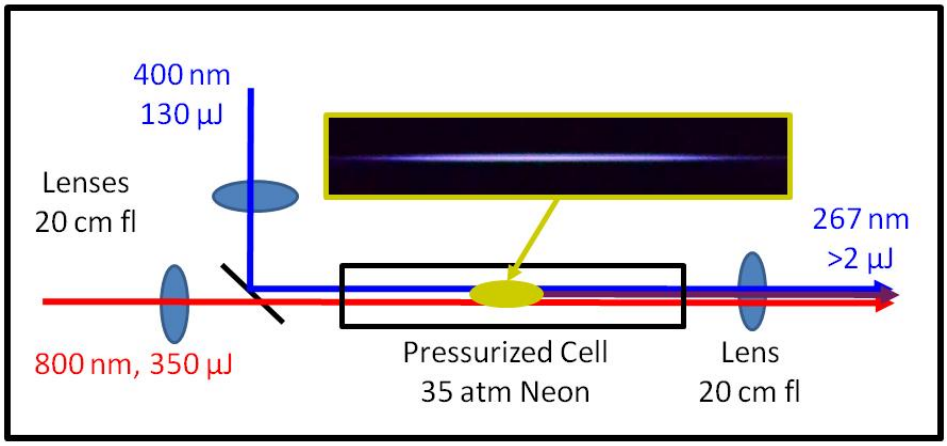

Figure 4.2. Setup used to generate third-harmonic laser pulses. Spectral widths of the 800-nm and 400-nm pulses are 350 cm^{-1} and 200 cm^{-1}, respectively. Third-harmonic pulses with spectral widths greater than 300 cm^{-1} are obtained at 35 atm in neon gas.

The experimental setup used to generate third-harmonic pulses is depicted in Figure 4.2. The pulses are generated by overlapping the filaments associated with 800-nm and 400-nm laser beams inside a pressurized cell filled with neon gas. Third-harmonic generation is dominated by the nonlinearity, $k_3 = 2k_2 - k_1$ (subscripts are orders of the harmonics); direct third-harmonic generation via the fundamental, $k_3 = 3k_1$, is 50-100 times less efficient because of greater phase mismatch.[21,61,69] The spectral widths of the fundamental and second-harmonic pulses are 350 cm^{-1} and 200 cm^{-1}, respectively. The spectral width of the second-harmonic is much narrower than that of the fundamental, because it is produced using a 0.75-mm-thick BBO crystal; this is not problematic as the desired bandwidth (>300 cm^{-1}) is still obtained at the third-harmonic. This apparatus differs from that used in earlier work in that we have upgraded the cell to accommodate higher pressures.[21,61] The components of the cell are described in Appendix A.

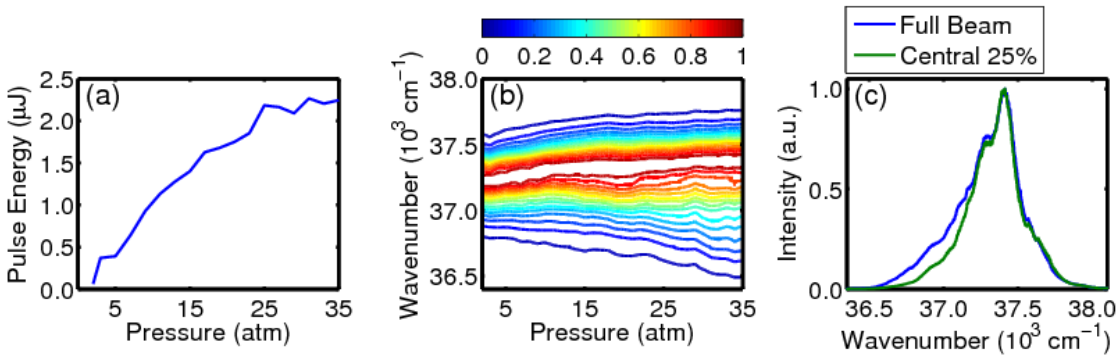

Figure 4.3. (a) Pulse energy measured as a function of neon pressure. (b) Intensity-normalized spectra of third-harmonic pulses measured as a function of neon pressure. (c) In neon, the spectral width measured for the full beam differs little from that of the central 25% (i.e. 25% of the intensity). Neon is superior to argon as a nonlinear medium in this respect (see Appendix A).

In order to conduct the experiments, laser pulses that are short compared to the 300-fs vibrational period of the symmetric stretching mode in I_3^- must be employed. We generate pulses with spectral widths slightly greater than 300 cm^{-1} (i.e. 55 fs at the Fourier transform limit). This amount of bandwidth represents a reasonable compromise between time resolution and experimental difficulties (e.g. stability, dispersion management). Figure 4.3 shows that the pulse energy and the spectral width of the third-harmonic increases with pressure up to 35 atm. Caution should be taken in using laser pulses with spectra that are broadened by self- and cross-phase modulation, because the propensity for spectral broadening is largest in the center of the Gaussian beam, where the field is most intense.[74] We find that the spectrum is quite uniform across the spatial profile of the third-harmonic when neon gas is used as the nonlinear medium. In contrast, a significant amount of spectral heterogeneity in the beam profile is observed when argon is substituted for neon (see Appendix A).

The pulses are compressed to durations of 60-65 fs using a pair of fused silica prisms separated by 15 cm. The prism compressor compensates for the second-order dispersion

accumulated in several transmissive optics (e.g. exit window of the pressurized cell, a lens, beam splitters, diffractive optic). Third-order dispersion accumulated in the prism compressor does not have a significant impact on the pulse duration because of the modest spectral width. Thus, we do not compensate for residual third-order dispersion using a (lossy) grating compressor.[75]

4.2.2 Six-Wave Mixing Interferometer

Fifth-order nonlinear spectroscopies have been conducted using a variety of laser beam geometries. For example, PORS employs a four-beam geometry in which a third-order signal is radiated in the same direction as the desired nonlinearity.[41,43] Thus, the signal of interest must be isolated through modulation of at least one of the incoming beams. In contrast, 2D off-resonant Raman spectroscopies of pure liquids employed six-pulse, background-free geometries.[24,25] Similarly, the key to the success of the present experiment is the ingenious laser beam geometry developed by Mark Berg.[76-78] In Berg's experiments, standard transmission gratings are used to produce a beam pattern in which passive interferometric signal detection is accomplished by way of a reference field that is automatically collinear with the signal after the sample. Here, this approach is combined with spectral interferometry to achieve the data acquisition rate and sensitivity required for our application.

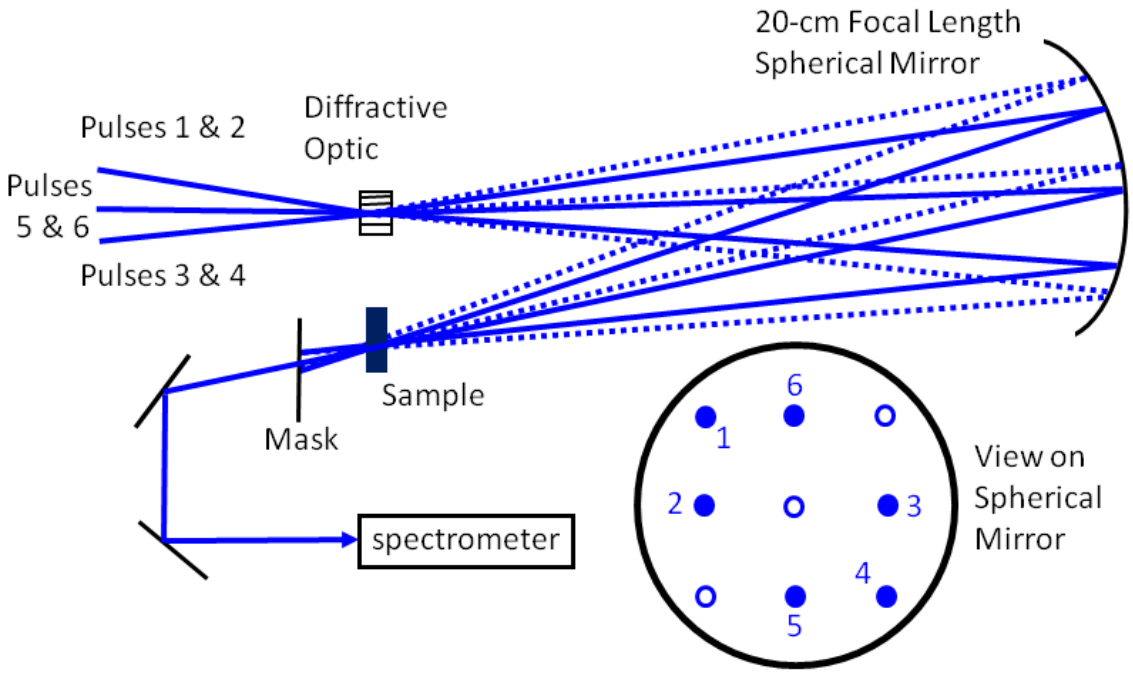

Figure 4.4. Diffractive optic-based interferometer used for six-wave mixing experiments. Each of the three incoming beams is split into 0, -1, and +1 diffraction orders with equal intensities (the diffraction orders are vertically displaced). Beams represented with open circles are blocked with a mask before the sample. The fifth-order signal is radiated in the direction $k_1 - k_2 + k_3 - k_4 + k_5$, and is collinear with the reference field (pulse 6) used for interferometric signal detection after the sample.

Figure 4.4 depicts the interferometer used in the present experiments. Three non-collinear beams are focused onto a diffractive optic (DO, Holoeye) with a 20-cm focal length spherical mirror. At 267 nm, the 0 and +/-1 diffraction orders produced by the DO possess equal intensities (this DO was originally fabricated for operation near 200 nm). The angle between the +/-1 diffraction orders is 6.1º at 267 nm, where the diffraction orders are separated vertically. The desired grid of nine laser beams is generated by aligning the three incoming beams such that the outermost beams cross at 6.1º in the DO and are bisected by the third beam. The beams must be

carefully aligned initially; however, the alignment is easy to maintain because the incoming beams are never color-tuned.

Any delay between the 0 and +/-1 diffraction orders originating from a single beam must be small compared to the pulse duration. To minimize such delays, the DO is oriented with the grating etched on the side of the optic from which the beams exit. Thus, to a good approximation, the various diffraction orders do not travel different distances through the DO. Cross-correlations of the pulses suggest that the +/-1 diffraction orders arrive simultaneously, whereas the zeroeth-order pulse is delayed by 5 fs. This small delay of the zeroeth-order pulse is not compensated for with transmissive optics in order to minimize dispersion and keep the setup simple to operate.

The spherical mirror is tilted off-axis by a small amount (approximately 5°) to horizontally displace the incoming and reflected beams, and the diffractive optic is oriented such that the 0 and +/-1 diffraction orders are separated vertically. The 1-mm depth of focus of the laser beams is large compared to the 0.07 mm difference in focal lengths caused by spherical aberration (a comparison of beams 1 and 2 in Figure 4.4). Several previous diffractive optic-based four-wave mixing experiments have made use of a similar configuration.[1,5,60] The spherical mirror is positioned 40 cm from the diffractive optic, so that the laser pulses possess the same spatiotemporal properties at the sample and diffractive optic. Spectra of the laser pulses transmitted through a 100-μm pinhole at the sample position are insensitive to vertical and horizontal displacement of the pinhole. The signals (both four-wave and six-wave mixing) are also insensitive to small adjustments in the alignments of the incoming beams, and we have proven that features of the signals can be reproduced with slightly different alignments on different days (see Appendix A). Thus, the influence of spatial chirp of the laser beams before

the sample appears to be negligible. A general concern for diffractive-optic based experiments is that both the signal and reference field (pulse 6) possess spatial chirp after the sample.[1] Such spatial chirp after the sample is minimal in the present work because of the fairly narrow spectral widths of the UV laser pulses (< 3 nm).

The FWHM-spot size of each beam at the sample is 120 μm, and each of the incoming pulses is 10 nJ. The peak power of each laser pulse is kept below 5 GW/cm^2 to suppress undesired ionization of the solute and solvent.[68,79,80] The sample is flowed through a wire-guided jet with a thickness of 300 μm, where the volume of the reservoir is 50 mL.[81] We find that the amount of scattered light produced by the jet is significantly smaller that observed with a cuvette. Typically, we acquire 60 points (with step sizes of 33-60 fs) in each dimension, τ_1 and τ_2, and average the signals over 10-20 scans of the delay lines. Linear absorbance spectra of the solutions are measured before and after the experiments to confirm the absence of degradation.

Spectral interferometry is used for signal detection in order to boost sensitivity and facilitate rapid data acquisition.[82,83] In all experiments, signals are detected using a back-illuminated CCD array (Princeton Instruments PIXIS 100B) mounted on a 0.3 meter spectrograph with a 3600 g/mm grating. Under the conditions summarized above, the signal generates roughly 300 counts on the detector with an integration time of 150 ms. The sensitivity afforded by interferometic signal detection is essential to the success of the experiment because of the small signal intensity and low efficiency of the detector in the deep UV.

4.2.3. Sample Preparation

As described in previous literature,[48] triiodide solutions are prepared by mixing solid I_2 (Aldrich) with 5-fold molar excess of KI (Aldrich) in ethanol (Decon Labs, 200 proof). The

solution was stirred for one hour to fully dissolve the solid. The absorbance of the solutions is equal to 0.4 at 270 nm in 300 μm path length, which corresponds to a concentration of 1 mM.

4.3. Model Calculations

4.3.1. Hamiltonian

The reduced description developed in this section partitions the Hamiltonian into system and bath components.[84-86] The system consists of two electronic energy levels, whereas all nuclear coordinates are included in the bath. Thus, we avoid a costly sum-over-states in optical response functions that would be found if the intramolecular modes were treated explicitly as part of the system. The three components of the Hamiltonian, $H = H_{sys} + H_{bath} + H_{sys-bath}$, are given by

$$H_{sys} = \hbar\omega_g |g\rangle\langle g| + \hbar\omega_e |e\rangle\langle e|, \tag{4.1}$$

$$H_{bath} = \frac{1}{2}\sum_i \left[\frac{p_i^2}{m_i} + m_i\omega_i^2 q_i^2 \right] \left[|g\rangle\langle g| + |e\rangle\langle e| \right], \tag{4.2}$$

and

$$H_{sys-bath} = |g\rangle \left[Q_{g,c} + Q_{g,ss} \right] \langle g| + |e\rangle \left[Q_{e,c} + Q_{e,ss} \right] \langle e| \tag{4.3}$$

State g is the ground state and e represents the excited state that is in resonance with the laser pulse. The bath consists of displaced harmonic oscillators for which the associated variables are written in lower case (m_i, ω_i, and q_i). The primary oscillator coordinates in $H_{sys-bath}$ are related to the displaced harmonic modes in H_{bath} by $Q_{\alpha,c} = \sum_{i \neq ss} m_i\omega_i^2 d_{\alpha,i} q_i$ and $Q_{\alpha,ss} = m_{ss}\omega_{ss}^2 d_{\alpha,ss} q_{ss}$,

where $d_{\alpha,i}$ is the displacement of mode i in state α (i.e. the coupling strength). The subscript c denotes a collective bath coordinate, and ss represents the symmetric stretching vibration of I_3^-.

4.3.2. Nonlinear Response Functions

Six-wave mixing experiments correspond to fifth-order in time-dependent perturbation theory. A single field-matter interaction occurs with each of the incoming laser beams, and the sixth interaction radiates the signal field that is measured. The fifth-order polarization is given by[85]

$$P^{(5)}(t) = N\int_0^\infty dt_5\int_0^\infty dt_4\int_0^\infty dt_3\int_0^\infty dt_2\int_0^\infty dt_1 S^{(5)}\left(t_5,t_4,t_3,t_2,t_1\right)E_5(t-t_5)E_4(t-t_5-t_4) \\ E_3(t-t_5-t_4-t_3)E_2(t-t_5-t_4-t_3-t_2)E_1(t-t_5-t_4-t_3-t_2-t_1) \tag{4.4}$$

where $S^{(5)}\left(t_5,t_4,t_3,t_2,t_1\right)$ is the material response function, N is the number density of molecules in the sample, and t_i are intervals between field-matter interactions. In our calculations, the form of the electric field for laser pulse j is given by

$$E_j(t) = \xi_j \exp\left(-t^2/2\Delta_j^2\right)\cos\left(\omega_j t\right) \tag{4.5}$$

where ξ_j is the electric-field amplitude, Δ_j is the temporal width, and ω_j is the carrier frequency of the laser pulse. The frequencies, durations, and intensities of all five pulses (j =1-5) are identical. Under perfect phase-matching conditions, the signal field is related to the fifth-order polarization by

$$E^{(5)}\left(t\right) = \frac{i2\pi l\omega_t}{n\left(\omega_t\right)c}P^{(5)}\left(t\right) \tag{4.6}$$

where $n(\omega_t)$ is the sample's refractive index and c is the speed of light.

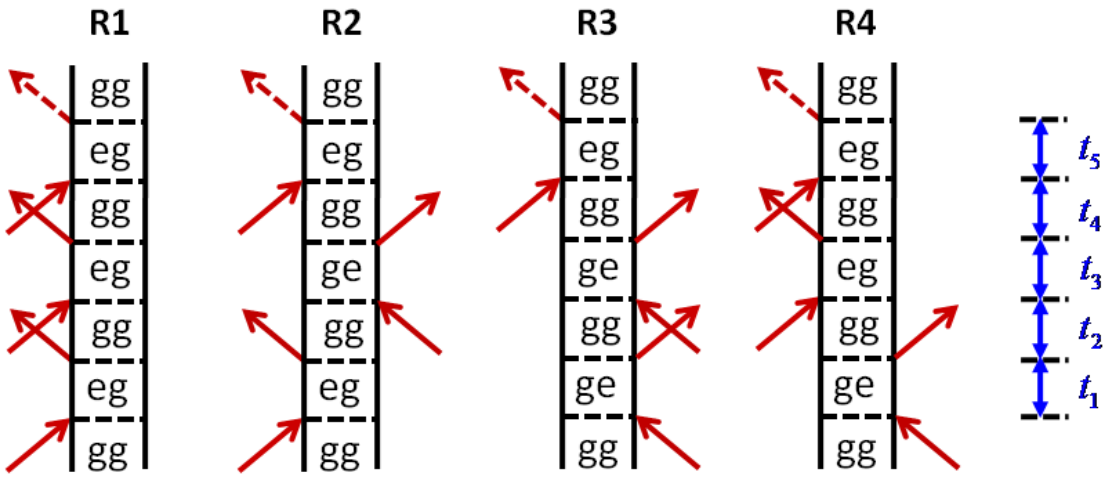

Figure 4.5. Double-sided Feynman diagrams for the four dominant terms in the fifth-order response function. The indices g and e represent the ground state and the second-to-lowest energy excited state in I_3^-, respectively. Contributions from terms that evolve in excited state populations in t_2 and t_4 are negligible under our experimental conditions because of ultrafast solvation, internal conversion, and photodissociation processes.[46,49]

The second-to-lowest energy excited state of I_3^- is photoexcited on the higher-energy side of the resonance in the present experiments. As a result, solvation, internal conversion, and photodissociation ensure that excited state dynamics contribute to the signal only at delay times that are short compared to vibrational dephasing. Therefore, our model treats only ground state wavepacket motions induced by field-matter interactions with a single electronic resonance. This aspect of the deep-UV optical response of I_3^- was recognized in earlier Raman studies (see Section 4.3.4).[46,50] The diagrams shown in Figure 4.5 represent the four dominant terms in the response function

$$S^{(5)}\left(t_5,t_4,t_3,t_2,t_1\right)=\left(\frac{i}{\hbar}\right)^5\sum_{j=1}^{4}\left[R_j\left(t_5,t_4,t_3,t_2,t_1\right)-R_j^*\left(t_5,t_4,t_3,t_2,t_1\right)\right] \tag{4.7}$$

where each of the time intervals, t_j, is greater than or equal to zero. In each of these terms, wavepacket motions in the ground electronic state occur during t_2 and t_4; to an approximation, these intervals correspond to the two experimentally controlled delay times, τ_1 and τ_2. Sophisticated nonlinear response functions have been developed for related experiments in recent literature.[34-36] In this work, we utilize a simple and computationally tractable form of the response function in order to capture the basic physics.

The correlation function for the energy gap between electronic states can be viewed as the key quantity that governs the optical response.[85] Dynamics in this gap are often modeled in terms of interactions with a bath of harmonic oscillators.[84-86] If motions of the two primary coordinates in $H_{sys-bath}$ are uncorrelated, then the correlation function for the energy gap can be written as

$$C\left(t\right)=\frac{1}{\hbar^2}\left[\left\langle U_c\left(t\right)U_c\left(0\right)\right\rangle+\left\langle U_{ss}\left(t\right)U_{ss}\left(0\right)\right\rangle\right] \tag{4.8}$$

where $U_c\left(t\right)=Q_{e,c}\left(t\right)-Q_{g,c}\left(t\right)$ and $U_{ss}\left(t\right)=Q_{e,ss}\left(t\right)-Q_{g,ss}\left(t\right)$. We employ correlation functions corresponding to overdamped and underdamped modes[85]

$$\left\langle U_c\left(t\right)U_c\left(0\right)\right\rangle=\left[2\lambda k_BT-i\lambda\Lambda\right]\exp\left(-\Lambda t\right) \tag{4.9}$$

and

$$\left\langle U_{ss}(t)U_{ss}(0)\right\rangle = \frac{d_{ss}^2\omega_{ss}^2}{2}\left[\coth\left(\frac{\hbar\omega_{ss}}{2k_BT}\right)\cos(\omega_{ss}t) - i\sin(\omega_{ss}t)\right] \tag{4.10}$$

where λ is the reorganization energy for the collective coordinate, Λ is the rate of relaxation in the collective coordinate, and d_{ss} is the dimensionless displacement for the symmetric stretch of I_3^-. The high-temperature limit, $k_BT >> \hbar\Lambda$, has been assumed in the above correlation function for the collective coordinate.

With the correlation functions in hand, the four dominant terms in the response function are readily obtained using a cumulant expansion approach for which details are given in Appendix A. The terms in the response function can be written as

$$\begin{aligned} R_1(t_5,t_4,t_3,t_2,t_1) = \left|\mu_{eg}\right|^6 \exp\left[-i\omega_{eg}(t_1+t_3+t_5)\right]\exp\Big[&-g\ (t_5)+g\ (t_4+t_5)-g\ (t_3+t_4+t_5)\\ &+g\ (t_2+t_3+t_4+t_5)-g\ (t_1+t_2+t_3+t_4+t_5)-g\ (t_4)+g\ (t_3+t_4)\\ &-g\ (t_2+t_3+t_4)+g\ (t_1+t_2+t_3+t_4)-g\ (t_3)+g\ (t_2+t_3)\\ &-g\ (t_1+t_2+t_3)-g\ (t_2)+g\ (t_1+t_2)-g\ (t_1)\Big] \end{aligned} \tag{4.11}$$

$$\begin{aligned} R_2(t_5,t_4,t_3,t_2,t_1) = \left|\mu_{eg}\right|^6 \exp\left[-i\omega_{eg}(t_1-t_3+t_5)\right]\exp\Big[&-g^*(t_3)+g^*(t_3+t_4+t_5)\\ &-g^*(t_3+t_4)+g\ (t_2)-g\ (t_1+t_2)-g^*(t_4+t_5)+g^*(t_4)-g\ (t_2+t_3)\\ &+g\ (t_1+t_2+t_3)-g\ (t_5)+g\ (t_2+t_3+t_4+t_5)-g\ (t_1+t_2+t_3+t_4+t_5)\\ &-g\ (t_2+t_3+t_4)+g\ (t_1+t_2+t_3+t_4)-g\ (t_1)\Big] \end{aligned} \tag{4.12}$$

$$\begin{aligned} R_3(t_5,t_4,t_3,t_2,t_1) = \left|\mu_{eg}\right|^6 \exp\left[-i\omega_{eg}(-t_1-t_3+t_5)\right]\exp\Big[&-g^*(t_1)+g^*(t_1+t_2)\\ &-g^*(t_1+t_2+t_3)+g^*(t_1+t_2+t_3+t_4+t_5)-g^*(t_1+t_2+t_3+t_4)\\ &-g^*(t_2)+g^*(t_2+t_3)-g^*(t_2+t_3+t_4+t_5)+g^*(t_2+t_3+t_4)-g^*(t_3)\\ &+g^*(t_3+t_4+t_5)-g^*(t_3+t_4)-g^*(t_4+t_5)+g^*(t_4)-g\ (t_5)\Big] \end{aligned} \tag{4.13}$$

and

$$
\begin{aligned}
R_4(t_5,t_4,t_3,t_2,t_1) = \left|\mu_{eg}\right|^6 \exp\left[-i\omega_{eg}\left(-t_1+t_3+t_5\right)\right]\exp\Big[&-g^*(t_1)+g^*(t_1+t_2+t_3+t_4+t_5)\\
&-g^*(t_1+t_2+t_3+t_4)+g^*(t_1+t_2+t_3)-g^*(t_1+t_2)-g^*(t_2+t_3+t_4+t_5)\\
&+g^*(t_2+t_3+t_4)-g^*(t_2+t_3)+g^*(t_2)-g\ (t_5)+g\ (t_4+t_5)\\
&-g\ (t_3+t_4+t_5)-g\ (t_4)+g\ (t_3+t_4)-g\ (t_3)\Big].
\end{aligned}
\tag{4.14}
$$

The line shape function is given by $g(t) = g_c(t) + g_{ss}(t)$, where the component associated with primary oscillator j can be obtained from the corresponding correlation functions in the energy gap using

$$
g_j(t) = \frac{1}{\hbar^2}\int_0^t d\tau_2 \int_0^{\tau_2} d\tau_1 \left\langle U_j(\tau_1) U_j(0)\right\rangle. \tag{4.15}
$$

The line shape functions for the two primary coordinates are[85]

$$
g_c(t) = \left(\frac{2\lambda k_B T}{\Lambda^2} - i\frac{\lambda}{\Lambda}\right)\left[\exp(-\Lambda t) + \Lambda t - 1\right] \tag{4.16}
$$

and

$$
g_{ss}(t) = \frac{d_{ss}^2\omega_{ss}^2}{2}\left\{\coth\left(\frac{\hbar\omega_{ss}}{2k_B T}\right)\left[1-\cos(\omega_{ss}t)\right] + i\left[\sin(\omega_{ss}t) - \omega_{ss}t\right]\right\}. \tag{4.17}
$$

Depending on the experimental conditions, twelve additional terms can make significant contributions to the fifth-order response function of a two-level system. Formulas for these additional terms are given in Appendix A.

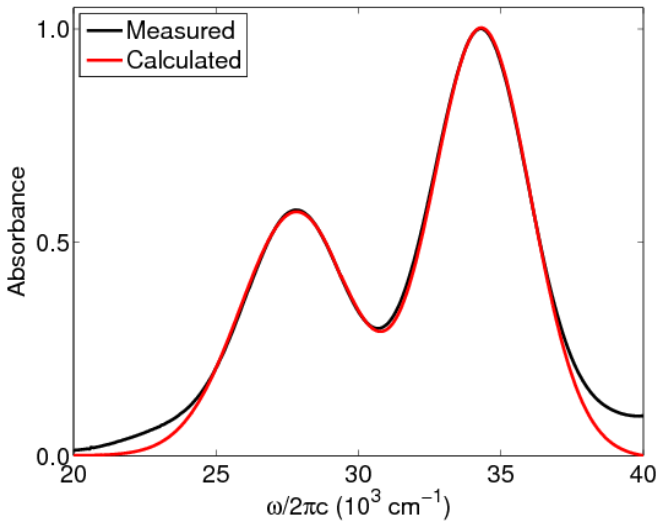

Figure 4.6. Measured and calculated absorbance spectra for I_3^- in ethanol are overlaid. The line shape of the second-to-lowest energy resonance is simulated using Equation 4.18. Parameters are given in Table 4.1. The lower energy resonance is approximated with a Gaussian function with a peak of 0.57, center of 27830 cm^{-1}, and standard deviation of 1975 cm^{-1} in order to estimate its contribution to the low-energy side of the resonance of interest.

In summary, the above model requires three key parameters to describe nuclear motions in the solute-solvent complex. (i) The dimensionless displacement, d_{ss}, partly governs the amplitude of wavepacket motion in the symmetric stretching coordinate. (ii) The reorganization energy, λ, induces electronic dephasing in odd-ordered time-intervals (t_1, t_3, and t_5) and also influences the amplitude of wavepacket motion in even-order time-intervals (t_2 and t_4). That is, the amount of force imparted to the wavepacket (in t_2 and t_4) increases as the electronic dephasing rate (in t_1, t_3, and t_5) decreases, because the ground-state wavepacket is then initiated on the ground state potential energy surface with a greater displacement from its equilibrium position. For similar reasons, resonance Raman cross sections generally decrease as the homogeneous line width increases.[87,88] (iii) The effect of the time scale of the bath, Λ^{-1}, is not

obvious *a priori*, although a line-narrowing effect should be anticipated if Λ becomes (unreasonably) large.[85] The high-temperature limit assumed above ($\hbar\Lambda << k_B T$) should apply to I_3^-, because the absorbance line shape is essentially Gaussian.

4.3.3. Parameterization of Spectroscopic Model for Triiodide

Anharmonic excited state potential energy surfaces were treated in earlier studies of I_3^- in order to obtain insight into the photo-dissociation mechanism.[47-53] Detailed knowledge of the excited state potential energy surface is not required to simulate the present experiments, because the ground state wavepacket motions are determined primarily by the gradient on the excited state potential energy surface at the Franck-Condon geometry. The key is that the period of the vibration (300 fs) is much longer than the dephasing time (<20 fs).[87] Moreover, the harmonic approximation made for the ground electronic state is justified by the progression of (to a good approximation) equally spaced transitions observed in resonance Raman spectra.[48] In this section, we obtain a set of parameters for the present harmonic model that is consistent with the more detailed models employed in earlier work.

The absorbance spectrum imposes valuable constraints on the model parameters. To start, we consider the contribution of all coordinates except the symmetric stretch to the line width. In earlier resonance Raman studies, Johnson and Myers showed that a low-frequency intermolecular mode (between the solute and solvent) near 13 cm^{-1} dominates electronic dephasing and also broadens resonance Raman transitions through unresolved combination bands.[49,50] The reorganization energy of the intermolecular mode in their model was roughly 3440 cm^{-1}. Thus, the parameter, λ, should be larger than 3440 cm^{-1} because the bath implicitly includes additional coordinates. In Figure 4.6, we compute the absorbance spectrum of I_3^- using

$$\sigma(\omega) = \left|\mu_{eg}\right|^2 \int_0^\infty dt \exp\left[i\left(\omega - \omega_{eg}\right)t - g(t)\right] \tag{4.18}$$

where the parameters are defined in the previous section. The time scale of the bath Λ^{-1} is set equal to 1 ps to produce a Gaussian line shape (the line shape changes negligibly if Λ^{-1} increases further). We find that the line width is recovered when d_{ss}=7.0 and λ / hc=4400 cm^{-1}. Johnson and Myers carried out simulations using a related harmonic model in which the dimensionless displacement for the symmetric stretch was set equal to 7.0.[48] Thus, we consider this a reasonable estimate for use in simulations.

4.3.4. Basis for Approximations in Response Function

The response function developed above employs equilibrium correlation functions and involves only terms that evolve as ground state wavepackets during the two experimentally controlled delay times. This section addresses three points that motivate these approximations:

(i) Earlier studies of I_3^- have shown that the UV wavelength range is dominated by ground state wavepacket motions.[46,50] Excited state emission does not contribute significantly because excited state solvation, internal conversion to the lower energy excited state, and photodissociation are much faster than the 300-fs vibrational period of I_3^-.[46,50] This separation in time scales was the key to the comparison between resonance Raman and resonant impulsive stimulated Raman expermients carried out by Johnson and Myers.[50] Photodissociation may initiate vibrational coherence in the I_2 photoproduct, but such nonlinearities are dominant only in the visible spectral range.[46,51-53]

(ii) In a related (fifth-order) optical pump-Raman probe experiment, Vöhringer and co-workers detected coherent Raman spectra subsequent to photodissociation of I_3^- in the visible spectral range, where the I_2^- photoproduct dominates the response.[53] As shown below, the

reaction-induced vibrational dynamics of the photoproduct observed in this study are markedly different than the signals we observe in the deep UV. Rapid sub-picosecond evolution in the vibrational spectrum was observed in Vöhringer's study, whereas the Raman spectrum acquired in τ_2 is insensitive to the τ_1 delay time in our experiments (i.e. intensity oscillates but the resonance frequencies do not shift). Vöhringer also observed an intense transient resonance near 70 cm^{-1} at delay times less than 1 picosecond, while we observe only the resonance associated with the symmetric stretch at all delay times, τ_1 .

(iii) The terms in Figure 4.5 are obtained under essentially the same assumptions made by Johnson and Myers in their comparison of resonance Raman and RISRS signals for I_3^- in the deep UV (i.e. the optical response is dominated by ground state wavepacket motions in the deep UV).[46,50] In I_3^-, the key issue is that the wavepacket dynamics in t_1 , t_3 , and t_5 are governed by the excited state potential energy gradient at the Franck-Condon geometry, because the vibrational period of the symmetric stretch (300 fs) is long compare to electronic dephasing (<20 fs).[87] Because of this separation in time scales, a harmonic model may be employed even though the excited state is reactive because the wavepacket does not return to the Franck-Condon geometry before the coherence between the ground and excited state dephases. Equilibrium (harmonic) correlation functions have similarly been utilized in spontaneous resonance Raman studies of systems that undergo photoinduced electron transfer and internal conversion processes.[88,89]

Terms in which I_3^- evolves in excited state populations during t_2 and/or t_4 will become prominent in coherent Raman experiments carried out with visible laser pulses. We acknowledge that such terms should not be modeled with equilibrium correlation functions, because they lead to internal conversion and photodissociation processes. These non-radiative

relaxation mechanisms should be explicitly accounted for in experiments that probe the system in the visible spectral range where the I_2 photoproduct dominates the optical response.[47,51-53,90] Of course, the shape of the excited state potential energy surface in regions displaced from the Franck-Condon geometry must be accurately described to capture spectroscopic signatures of such photodissociation dynamics.

Table 4.1. Parameters of Spectroscopic Model Based on Cumulant Expansion

[(a)]Parameter	Value
$\omega_{eg}/2\pi c$	34400 cm^{-1}
λ/hc	4400 cm^{-1}
Λ^{-1}	1 ps
$\omega_{ss}/2\pi c$	112 cm^{-1}
d_{ss}	7.0
$\omega_L/2\pi c$	37210 cm^{-1}
Δ	32 fs
[(b)] μ_{eg}	8.8 D

[(a)]Parameters of $\sigma(\omega)$ in Equation 4.18 and fifth-order response functions in Equations 4.11-4.14.

4.4. Results and Discussion

This section investigates the coherent Raman response of I_3^- from a variety of perspectives. Traditional transient grating spectroscopy is first used to establish basic aspects of the Raman response of I_3^- under our experimental conditions. Six-wave mixing signals are then

examined with two different representations. In one representation, correlations between the vibrational resonances in the two experimentally controlled delay times, τ_1 and τ_2, are exposed through a straightforward 2D Fourier transform (2DFT). Signals are additionally displayed in three dimensions (τ_1, ω_2, and ω_t) for a more alternate perspective on the wavepacket dynamics.

4.4.1. Four-Wave Mixing Spectroscopy

Femtosecond transient absorption spectroscopies were used to probe the coherent Raman response of I_3^- in several earlier works.[46,51-53] Here, we present stimulated Raman spectra obtained under our particular experimental conditions to facilitate discussion of the six-wave mixing measurements presented below. Transient grating signals acquired with laser pulses generated in the two-color filament (see Section 4.2.1) are presented in Figure 4.7a. This four-wave mixing experiment is conducted with the interferometer shown in Figure 4.4 by (i) entirely blocking one of the incoming pump beams and (ii) blocking only the zeroeth-order beam associated with the second pump beam (the signal and local oscillator beams are the same).[1,91] Oscillations in the signal intensity with a period near 300 fs, which is characteristic of ground state wavepacket motion in I_3^-,[46,50] are clearly evident in the contour plot in Figure 4.7a. The phases of the recurrences are essentially independent of the detection wavenumber. Of course, this behavior is not surprising, because the bandwidth of the laser pulse is narrow compared to the absorbance line width.

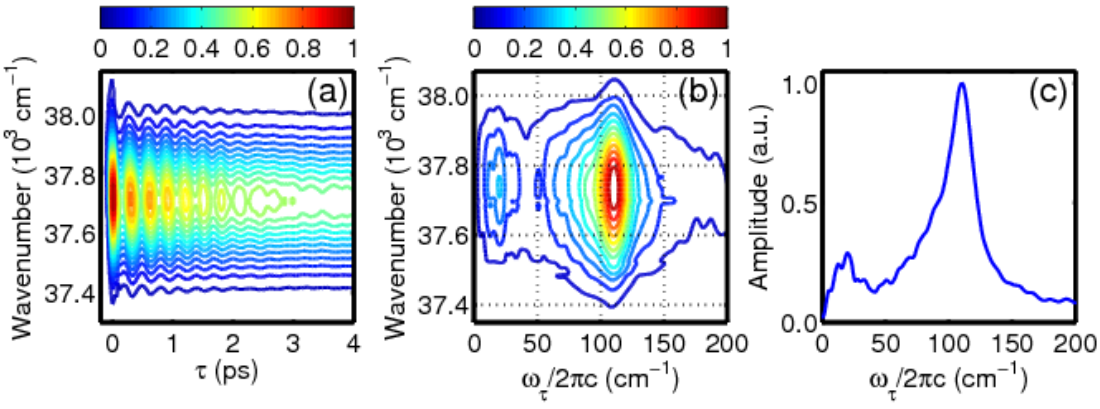

Figure 4.7. (a) Absolute value of the transient grating signal field for I_3^- in ethanol. The delay, τ, separates photo-excitation and detection. (b) Fourier transform of oscillations in the transient grating signals obtained at various detection wavenumbers. (c) Absolute value of stimulated Raman spectrum found by integrating over the detection wavenumber in panel (b). The symmetric stretch is located at 112 cm^{-1}, whereas the lower energy resonance near 20 cm^{-1} corresponds to a (solute-solvent) intermolecular mode.

In Figure 4.7b, the oscillatory component of the response at each detection wavenumber is isolated by subtracting an exponential function and a constant offset from the absolute value of the transient grating signal shown in panel (a). Parameters of this "baseline" are found (for each pixel on CCD array) using a least-squares fitting routine implemented in Matlab. The analysis is carried out from τ =0.1 ps to 4.0 ps in order to eliminate contributions from the non-resonant "coherence" spike that dominates when all three pulses are overlapped in the sample.[66,67] The contour plot in Figure 4.7b reveals two resonances. The symmetric stretching resonance is located near 112 cm^{-1}, whereas the (solute-solvent) intermolecular mode discussed in Section 4.3.3 contributes near 20 cm^{-1}. The anti-symmetric stretching mode, which is located near 145 cm^{-1}, is known to possess some (broken symmetry-induced) Franck-Condon activity in ethanol.[48] It is possible that the anti-symmetric stretch gives rise to a "shoulder" of the intense resonance near 145 cm^{-1} in the detection wavenumber-integrated Raman spectrum (see Figure 4.7c). The

symmetric stretch is of primary interest in this work, because this resonance dominates the six-wave mixing response. That is, compared to the measurements in Figure 4.7, the relative contributions of the intermolecular mode and anti-symmetric stretch will be even smaller in six-wave mixing because of the higher-order of the nonlinearity.

4.4.2. Two-Dimensional Fourier Transform Resonance Raman Spectra

A 2DFT Raman spectrum in which the signal is integrated over the detection wavenumber is a convenient representation for analysis of the six-wave mixing data.[92] Figure 4.8 displays the oscillatory parts of the real and imaginary components of the complex signal field in addition to their respective Fourier transforms. Fourier transformation is carried out by generalizing the algorithm used to process the data in Figure 4.7 to two dimensions; an exponential function and a constant are subtracted from each one-dimensional slice of the signal (in both τ_1 and τ_2) to isolate the oscillatory part of the response. In previous work, we were able to separate absorptive and dispersive signal components using the thermal grating produced by systems that undergo fast non-radiative relaxation (e.g. DNA nucleobases, ring-opening systems).[93] We do not observe such a thermal grating in I_3^- when the delay is scanned out to 0.5 ns and therefore do not yet have a systematic way to set the phase of the six-wave mixing signal. Nonetheless, it is still preferable to work with the complex signal rather than the absolute value, because the quality of the Raman spectrum is sensitive to the phase angle.

In Figure 4.8, the two parts of the signal are separated based on (i) dominance of vibrational oscillations in the real signal component (consistent with the absorptive response) and (ii) dominance of an undesired four-wave mixing signal in the imaginary signal component (consistent with the dispersive response). Notably, the choice of which part of the signal is real

and imaginary is somewhat arbitrary without an all-optical phasing method, because the two components can be reversed along with their associated information content (i.e. a shift in the signal phase of +/-π/2 is arbitrary). However, the finding of different behaviors at orthogonal phase angles is robust using our procedure (additional data are provided in the Appendix A). As shown in Figure 4.8, the real signal component yields higher-quality Raman spectra because of prominent vibrational oscillations. In contrast, the imaginary signal component possesses oscillations with smaller amplitudes and also carries small contributions from a *direct* four-wave mixing signal with a wavevector given by $k_2 + k_3 - k_5$ when all laser pulses are overlapped in the sample (see Appendix A). For these reasons, we focus our attention on the real signal component and discard data acquired during the region of pulse overlap. We remark that this phasing procedure is implemented only to enhance the signal-to-noise ratio of the 2D Raman spectrum (no conclusion reached in this section hinges on precise knowledge of the absolute signal phase). Third-order cascades, which are negligible in the Raman component of the signal (see Section 4.5), are 180º out-of-phase with the direct fifth-order resonance Raman response.[94] The signal phase was leveraged to suppress third-order cascades in off-resonant experiments (where the desired and undesired fields are 90º out-of-phase),[24,25] but this is not possible under resonant conditions.

The 2D Raman spectrum corresponding to the real signal component is dominated by resonances in the upper-right and lower-left quadrants (at $\omega_1 = \omega_2$ =112 cm^{-1}). This pair of quadrants carries redundant information (when pulse-pair 1&2 and pulses 3&4 are time-coincident), as does the upper-left and lower-right quadrants. These resonances represent terms in the response function that evolve as coherences between vibrational levels that differ by 1 quantum level in both τ_1 and τ_2. Coherences involving several pairs of levels may contribute to

each peak, because the small anharmonicity of the ground state potential energy surface prevents spectral resolution of these nonlinearities.

Interestingly, resonances are not detected in the upper-left and lower-right quadrants. Calculations are useful for confirming that this aspect of the signal is consistent with the nonlinear response function described in Section 4.3. In Figure 4.9, we present signals obtained by evaluating $P^{(5)}(t)$ numerically with the parameters given in Table 4.1. The calculated signal field is then fed into the same Matlab software used to process the experimental data to facilitate a direct comparison. Apodization functions are applied before Fourier transformation, because vibrational dephasing is not included in the line broadening function for the symmetric stretching coordinate. This does not impact physical insights because the electronic dephasing time is dominant in t_1, t_3, and t_5 (i.e. explicit inclusion of damping in $g_{ss}(t)$ would produce indistinguishable results). The calculations capture the essential aspects of the measured signals. Resonances in the upper-right and lower-left quadrants dominate the 2DFT spectrum. In addition, the calculations reveal much weaker resonances in the two additional quadrants. These weaker resonances represent nonlinearities in which the vibrational coherences in τ_1 have opposite signs to those in τ_2.

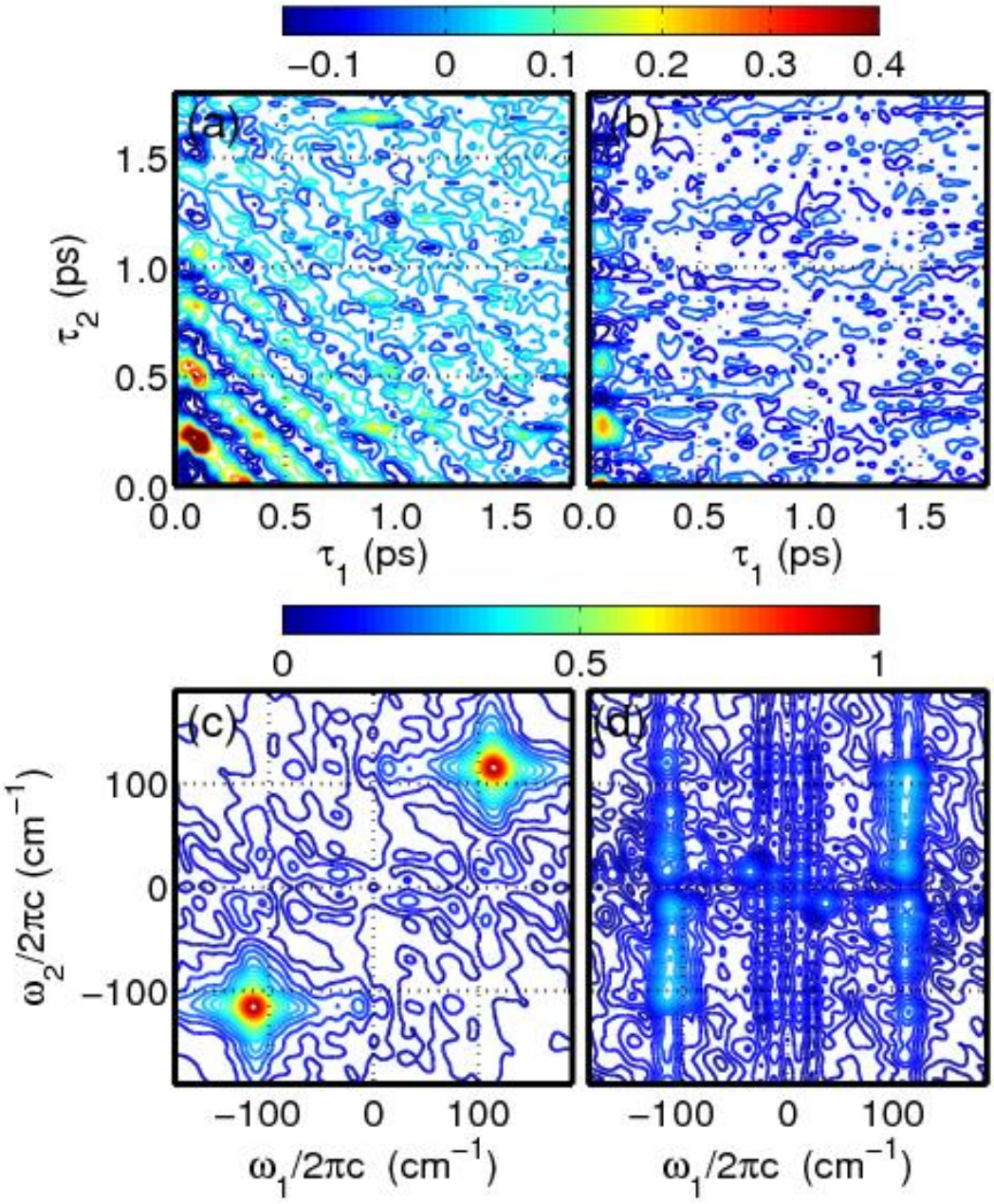

Figure 4.8. The (a) real and (b) imaginary parts of the six-wave mixing signal field of I_3^- in ethanol. Absorptive and dispersive responses dominate the real and imaginary signal components, respectively. Vibrational recurrences with large amplitudes are found in the real signal component shown in panel (a). Absolute values of 2D resonance Raman spectra for the (c) real and (d) imaginary signal components are shown below the respective time-domain signals. A higher-quality Raman spectrum is obtained with the real signal component. The non-oscillatory part of the signal has been subtracted from panels (a) and (b), so that the Raman response can be more clearly visualized.

In order to understand the pattern of resonances in the 2DFT spectrum, it is useful to consider each term in the response function as possessing two classes of line broadening functions, $g(t)$: (i) functions in which both t_2 and t_4 appear in the argument represent correlated dynamics; (ii) functions in which either t_2 or t_4 appear in the argument (not both time intervals) represent uncorrelated time evolution. Terms analogous to type (i) notably give rise to photon echoes in third-order spectroscopy by imposing correlations between t_1 and t_3. Inspection of the response functions shows that R_2 and R_4 must make the dominant contributions to the resonances in the upper-left and lower-right quadrants, because the type (ii) line broadening functions evolve as complex conjugates in either t_2 or t_4 (but not both). This phase relationship is understood by considering that the first and second pair of field-matter interactions do not occur on the same side of the Feynman diagrams in Figure 4.5 for R_2 and R_4. For example, in R_2, the complex conjugate is taken for every type (ii) line shape function with t_4 in the argument (e.g. $g^*(t_3+t_4+t_5)$), whereas complex conjugates are not taken for type (ii) functions with t_2 in the argument (e.g. $g(t_2+t_3)$).

If the R_2 and R_4 response functions contained only the type (ii) line broadening terms, then resonances in the upper-left and lower-right quadrants would dominate. However, these terms must compete with type (i) functions, such as $g(t_1+t_2+t_3)$ in R_2, that give rise to resonances in the upper-right and lower-left quadrants. The type (i) terms outcompete the type (ii) terms in R_2 and R_4, because the time intervals t_1, t_3, and t_5 also appear in the arguments of these functions. Mathematically speaking, the phase accumulated in each of these time intervals lifts cancellations between the sums of line broadening functions in Equations 4.11-4.14. From a

physical perspective, dephasing of the electronic coherences in t_1, t_3, and t_5 is accompanied by relaxation in the symmetric stretching mode; the amount of motion in the symmetric stretch must be small, because the electronic dephasing time (<20 fs) is much shorter than the vibrational period (<300 fs). Still, these dynamics are crucial for the stimulated Raman process. The amplitudes of the vibrational coherences in t_2 and t_4 generally decrease as the electronic dephasing times become shorter. In R_1-R_4, all line broadening functions involving t_2 and t_4 will cancel each other if $t_1 = t_3 = t_5 = 0$ (i.e. if electronic dephasing is instantaneous). This understanding of the fifth-order response invokes physical insights that were originally recognized at third-order in perturbation theory.[87,88]

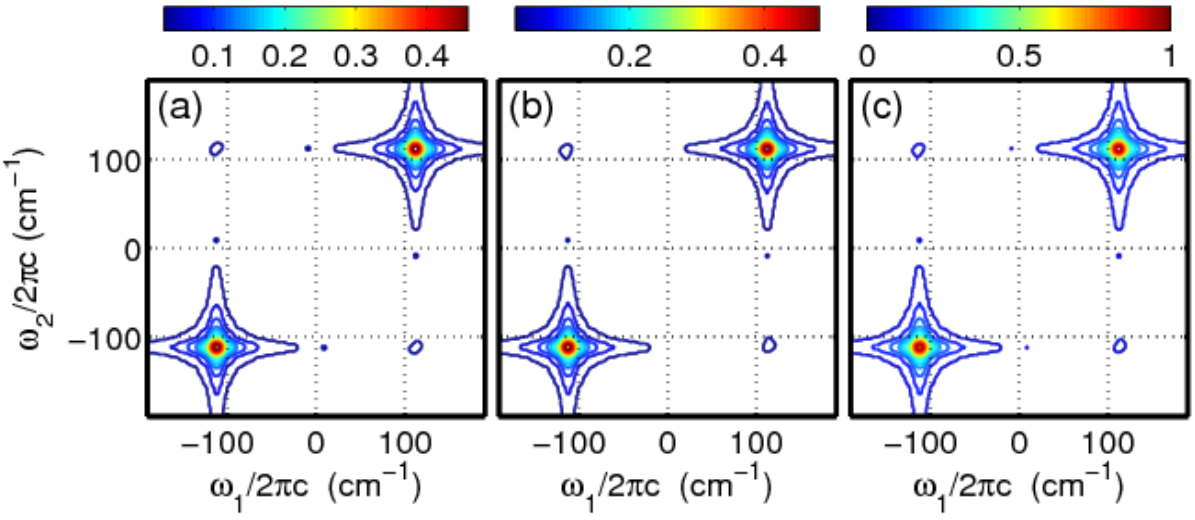

Figure 4.9. 2D resonance Raman spectra computed with: (a) terms R_1 and R_3; (b) terms R_2 and R_4; (c) all terms, R_1-R_4. As in the experimental measurements, dominant resonances are found in the upper-right and lower-left quadrants.

4.4.3. Analyzing Wavepacket Dynamics in Three Dimensions

The 2D resonance Raman spectra presented in Section 4.4.2 do not take full advantage of the experimental implementation, because the signal is integrated over the detection frequency. This third dimension distinguishes the information content of the present experiment from that of FSRS, where the vibrational resonances are directly imprinted on the spectrum of the signal field.[27,34,35,37,39] This section explores a representation of the data that takes into account the detection frequency, ω_t, in addition to the two experimentally controlled delay times. It is envisioned that this perspective on wavepacket motion will be particularly useful for studies of reactive system such as I_3^- and/or systems with highly anharmonic potentials.

The present experiment can be viewed as a sequence in which the first pulse-pair initiates a wavepacket that is probed with the final three pulses.[40-42] Knowledge of the maxima and minima in the signal intensity shown in Figure 4.7a does not give unambiguous information about the wavepacket's position, because the sign of the gradient on the excited state potential energy surface is undetermined. Dynamics in the signal spectrum must be examined to determine the phase of wavepacket motion. To access this information, we employ a representation, where the signal is Fourier transformed with respect to τ_2 (but not τ_1) in Figure 4.10a. As in the data presented above, a baseline is subtracted from the signal in τ_2 before Fourier transformation in order to isolate the oscillatory part of the response. Therefore, the (time-evolving) Raman spectrum of the system appears in the conjugate domain, ω_2 (i.e. incoherent relaxation does not contribute). In addition to ω_2, the signal is displayed with respect to the detection frequency, ω_t. This two-dimensional representation of the signal in ω_2 and ω_t

will hereafter be referred to as a "correlation spectrum" and will be denoted as $S(\omega_2, \omega_t)$. The correlation spectra analyzed in this work focus only on the region of the Raman spectrum associated with the symmetric stretch, because the low-frequency intermolecular mode (near 20 cm^{-1}) observed in the transient grating signals (see Figure 4.7) is below the detection threshold of the six-wave mixing experiment.

The isosurface in Figure 4.10b displays recurrences in the magnitude of the correlation spectrum as a function of τ_1. Mean vibrational and emission frequencies are computed at each delay time, τ_1, using the formula

$$\langle \omega_j \rangle = \frac{\int_{-\infty}^{\infty} d\omega_t \int d\omega_2 S(\omega_2, \omega_t) \omega_j}{\int_{-\infty}^{\infty} d\omega_t \int d\omega_2 S(\omega_2, \omega_t)} \tag{4.19}$$

where ω_j represents either ω_2 or ω_t (i.e. motions are characterized in both dimensions). The dynamics in the emission and vibrational frequencies are presented in Figure 4.10c and 4.10d, respectively. The data are fit to a damped sinusoidal function

$$F(t) = A_0 + A_1 \sin(\omega t + \phi) \exp(-\Gamma t) \tag{4.20}$$

for which the parameters are given in Table 4.2.

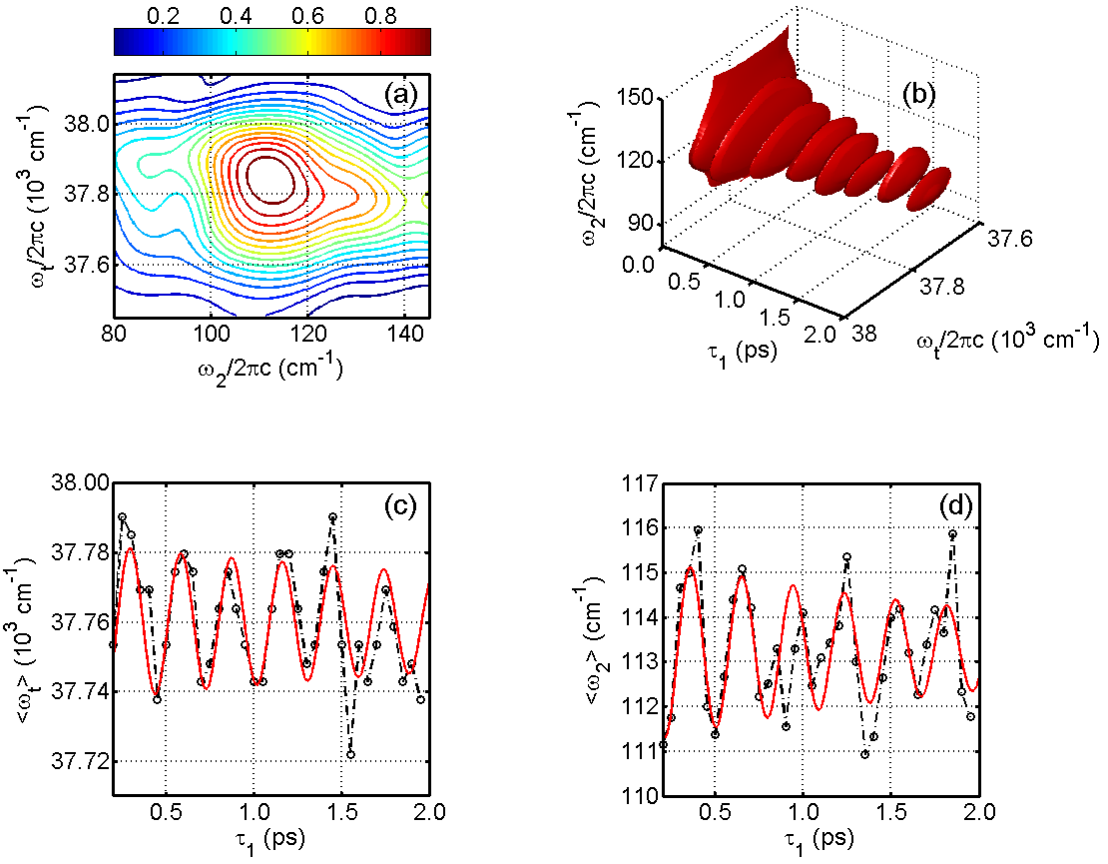

Figure 4.10. (a) Correlation spectrum, $S(\omega_2, \omega_t)$, measured at τ_1=100 fs. (b) Isosurface of signal is drawn at 40% of the maximum intensity. (c) Mean detection frequency, $\langle \omega_t \rangle$, and fit to Equation 4.20. (d) Mean vibrational frequency, $\langle \omega_2 \rangle$, and fit to Equation 4.20. Noise associated with $\langle \omega_t \rangle$ and $\langle \omega_2 \rangle$ increases with τ_1, because the signal magnitude decreases. Fitting parameters are given in Table 4.2.

Recurrences in the mean emission frequency, $\langle \omega_t \rangle$, are readily observed in all data sets. In analogy with related third-order experiments, we suggest that such oscillations reflect the energy gap between electronic states at the position of the wavepacket, which is dynamic in τ_1. Transient absorption studies of several systems have demonstrated that recurrences with 180°-phase-shifts may be observed at high and low detection frequencies when the spectral width of a

probe pulse is comparable to the total absorbance line width.[90,95] Under these conditions, high and low detection frequencies correspond to opposite turning points on the potential energy surface. Such phase-shifted oscillations in $\langle \omega_t \rangle$ are not very pronounced in the current data, because the spectral width of the laser pulse is narrower than the total absorption line width. Nonetheless, as shown in Figure 4.10c, we detect a beat in $\langle \omega_t \rangle$ with an amplitude near 20 cm^{-1}. Figure 4.11 presents calculated signals, which are treated using the same data-processing software used to handle the experimental data shown in Figure 4.10. The calculations confirm that it is indeed reasonable to observe recurrences in $\langle \omega_t \rangle$ under our experimental conditions. Moreover, the calculated amplitude of the recurrence (15 cm^{-1}) is similar to that observed experimentally (20 cm^{-1}).

Oscillations in the mean vibrational frequency, $\langle \omega_2 \rangle$, are also observed, although the amplitude marginally exceeds the detection threshold. With inspiration provided by related techniques,[45] we hypothesize that recurrences in $\langle \omega_2 \rangle$ with small amplitudes should be anticipated in systems, such as I_3^-, with weak ground-state anharmonicities. That is, the amplitude of $\langle \omega_2 \rangle$ reflects variation in the curvature of the potential energy surface at nonequilibrium geometries traversed by the wavepacket in the delay time, τ_1. For example, the second derivative of a one-dimensional potential energy function varies linearly in the mode displacement if a cubic expansion is considered. Consistent with this interpretation, calculations based on a purely harmonic model presented in Figure 4.11d predict an oscillation amplitude in $\langle \omega_2 \rangle$ that is roughly two times smaller than that observed experimentally (see Table 4.2). Key differences between the experiment and model are further illustrated in Figure 4.13, where

(correlated) dynamics in $\langle \omega_2 \rangle$ and $\langle \omega_t \rangle$ are plotted in three dimensions. The "spiral" shape associated with the measurement is broader in the $\langle \omega_2 \rangle$ dimension than that predicted with the harmonic model. Therefore, we tentatively attribute the larger amplitude of $\langle \omega_2 \rangle$ found in the experimental data to a small amount of anharmonicity of the ground state potential.

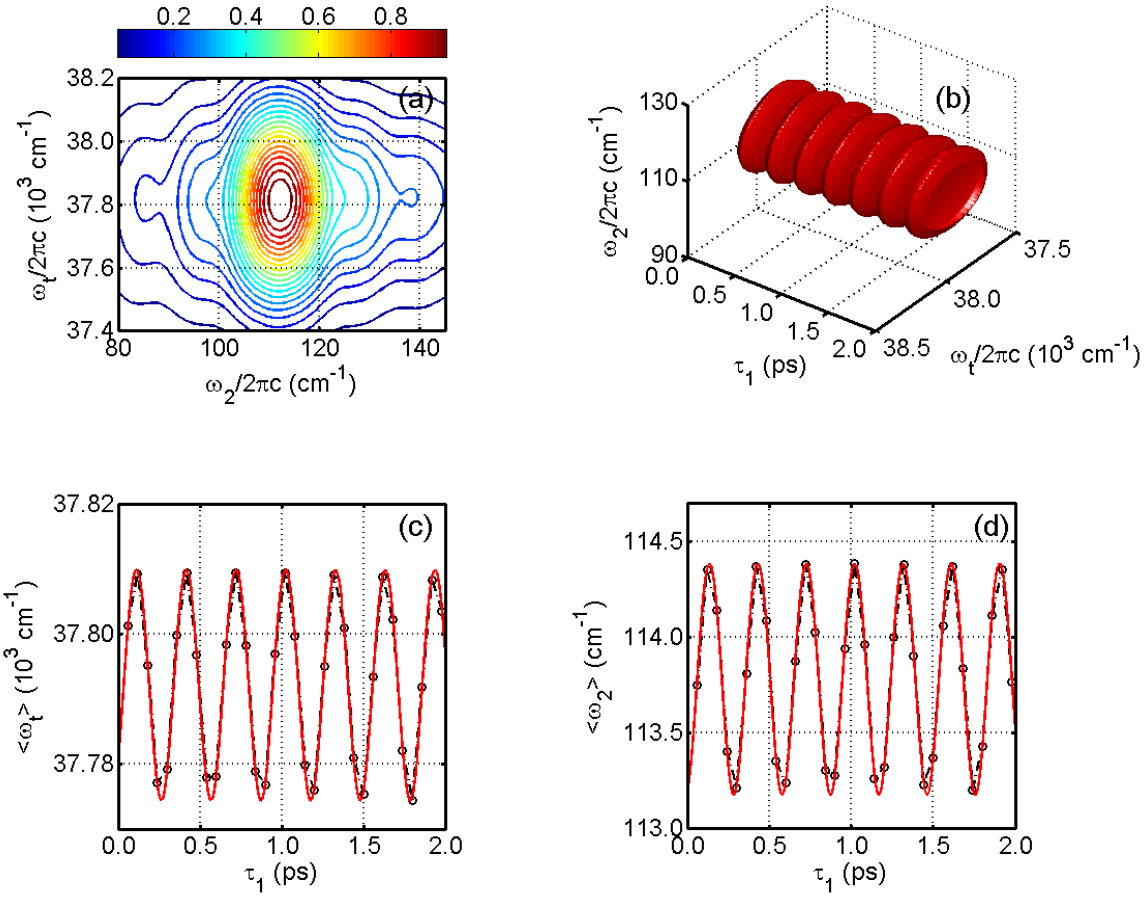

Figure 4.11. (a) Correlation spectrum, $S(\omega_2, \omega_t)$, calculated at τ_1=100 fs. (b) Isosurface of signal is drawn at 60% of the maximum intensity. (c) Mean detection frequency, $\langle \omega_t \rangle$, and fit to Equation 4.20. (d) Mean vibrational frequency, $\langle \omega_2 \rangle$, and fit to Equation 4.20. Signals are calculated using the parameters given in Table 4.1. Fitting parameters are given in Table 4.2.

Correlations in $\langle\omega_2\rangle$ and $\langle\omega_t\rangle$ are illustrated using the representation shown in Figure 4.12. Anharmonicity contributes in a straightforward way to amplitude in $\langle\omega_2\rangle$. However, as in traditional third-order experiments,[90,95] oscillatory amplitude in $\langle\omega_t\rangle$ depends on the magnitude of the mode displacement, the inhomogeneous line width, and the pulse duration. The interplay between these three factors is fairly well-understood. Amplitude in $\langle\omega_t\rangle$ increases with both the mode displacement and heterogeneity in the absorbance line shape. Short (impulsive) laser pulses are required to observe oscillations; however, coherent dynamics must also vanish in the impulsive limit, so an intermediate pulse width is most desirable for this type of technique. Although the present experiment is not sensitive to such effects, we anticipate that more complex (and informative) trajectories in $\langle\omega_2\rangle$ and $\langle\omega_t\rangle$ can be derived from two-color measurements conducted on reactive systems.

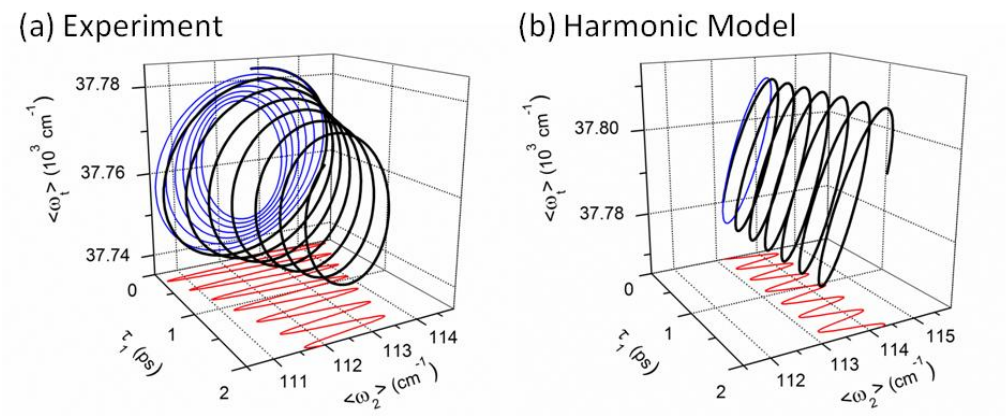

Figure 4.12. Dynamics in mean vibrational and emission frequencies, $\langle\omega_2\rangle$ and $\langle\omega_t\rangle$, adapted from the fits shown in Figures 4.10 and 4.11. The average values of the two variables are shifted by small amounts between (a) experimental and (b) theory. The shapes of the spirals can still be directly compared because the magnitudes of the ranges are identical in the two panels. It is predicted that anharmonicity, which is absent in the model, causes the spiral to expand in the $\langle\omega_2\rangle$ dimension.

Table 4.2. Dynamics in Correlation Spectra

[a]Parameter	Measured $\langle\omega_t\rangle$	Measured $\langle\omega_2\rangle$	Calculated $\langle\omega_t\rangle$	Calculated $\langle\omega_2\rangle$
[b] A_0	37759±2 cm^{-1}	113.3±0.5	37795±1 cm^{-1}	113.7±0.3
[b] A_1	26±7 cm^{-1}	2.1±0.3	15±1 cm^{-1}	1.2±0.3
Ω	114±3 cm^{-1}	114±5 cm^{-1}	113±1 cm^{-1}	113±1 cm^{-1}
ϕ	1.5±0.3 rad.	0.2±0.4 rad.	-3.9±0.1 rad.	-4.5±0.1 rad.
t	4.3±1.0 ps	2.3±1.0 ps	∞	∞

[a] Parameters of Equation 4.20.
[b]The signal amplitude has arbitrary units.

4.5. Relative Magnitudes of Cascaded Third-Order and Direct Fifth-Order Signals in 2D Resonance Raman Spectroscopies

4.5.1. Background

In this section, we consider a potential experimental complication, third-order cascades, that is known to challenge electronically off-resonant 2D Raman spectroscopies.[54-56,96] Cascaded third-order nonlinearities are processes in which light radiated by the third-order polarization of one molecule contributes to the third-order polarization of a second molecule (i.e. molecules A and B in Figure 4.13). The second molecule may then radiate a signal field in the same direction as the fifth-order nonlinearity of interest. The signal cascade does not carry information beyond

that associated with the third-order response; however, its spectroscopic signatures can be quite difficult to distinguish from the desired fifth-order signal. Cascaded third-order nonlinearities exhibit the same intensity dependence as the direct fifth-order signal and may also possess vibrational resonances at the same frequencies.

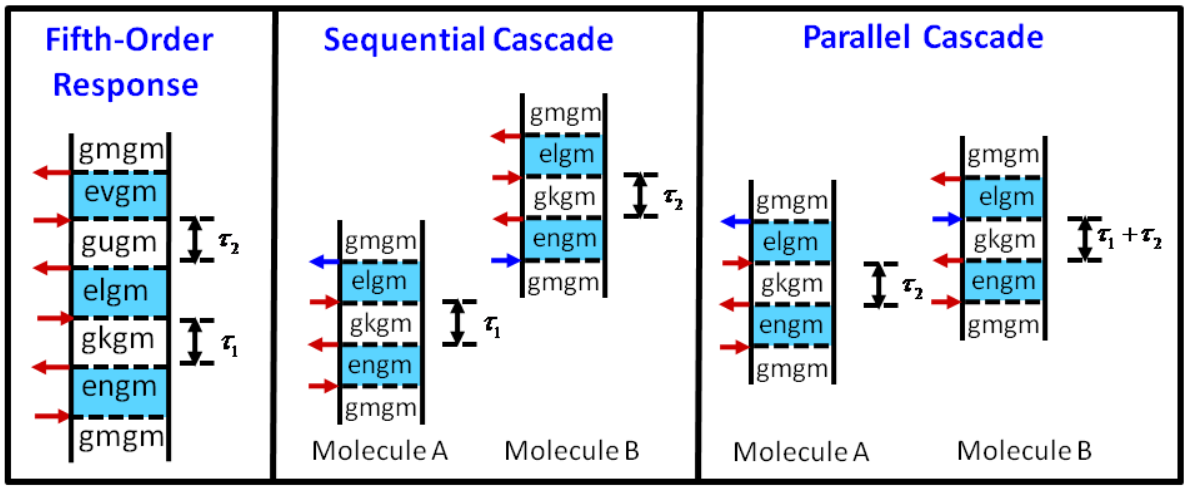

Figure 4.13. Examples of Feynman diagrams associated with a direct fifth-order nonlinearity, a sequential third-order cascade ($k_1 - k_2 + k_3$), and a parallel third-order cascade ($k_3 - k_4 + k_5$). The indices, g and e, represent electronic states, whereas dummy indices denote the vibrational energy levels of the ground (m, k, u) and excited electronic states (n, l, v). In the cascaded third-order diagrams, interactions associated with blue arrows correspond to emission and/or absorption of the field radiated at the intermediate step in the process. Direct fifth-order nonlinearities and third-order cascades involve three and four electronic coherences (shaded blue intervals) between the ground and excited states, respectively. As a consequence, contributions from third-order cascades decrease as the electronic dephasing rate increases.

In off-resonant 2D Raman spectroscopies, a key issue is that the direct fifth-order Raman response is (weakly) allowed by one of two mechanisms: vibrational anharmonicity and/or nonlinear coordinate dependence of the polarizability.[58,97] This makes the experiment a potentially powerful tool for investigating anharmonic couplings in liquids. Unfortunately, cascaded third-order nonlinearities typically outcompete the relatively low intensities of the

anharmonicity-induced fifth-order signals under off-resonant conditions.[54,56,96] Below, we show that the dominance of cascaded third-order signal intensities encountered in off-resonant fifth-order Raman spectroscopies does not generalize to experiments conducted under resonant conditions, because electronic dephasing and Franck-Condon activity (for harmonic and/or anharmonic modes) suppress contributions from third-order cascades.

4.5.2. Model Calculations

We compute the ratio of cascaded third-order and direct fifth-order signals in this section using an analytical, sum-over-states description to avoid complications associated with comparing the magnitudes of two quantities obtained through numerical integration (e.g. the cumulant expansion approach described in Section 4.3). The model is developed in Appendix A using the "snapshot limit", where it is assumed that the laser pulse durations are long compared to electronic dephasing but short compared to the vibrational period.[85] Both of these assumptions are reasonable for the present application to I_3^-. We also treat the subset of terms that evolve in ground state populations (see Section 4.3.4) because ground-state wavepacket motions dominate the response in the UV.[46,50] The model is well-suited for comparing direct and cascaded signal strengths, but may miss subtler aspects of the fifth-order line shapes such as the relative magnitudes of peaks in different quadrants.

The key quantity under consideration is the ratio in the cascaded third-order and direct fifth-order signal field

$$\frac{E_{cas}(t)}{E^{(5)}(t)} = \left(\frac{7}{25}\right)\frac{E_{par}(t)+E_{seq}(t)}{E^{(5)}(t)} \tag{4.21}$$

where the factor of 7/25 represents the isotropic orientational average with all-parallel electric field polarizations.[98] The direct fifth-order signal is denoted $E^{(5)}(t)$, whereas the cascades are divided into parallel and sequential components, $E_{par}(t)$ and $E_{seq}(t)$. Here, we consider the four classes of cascaded nonlinearities (two parallel and two sequential) known to challenge off-resonant 2D Raman spectroscopies.[24,54] The intermediate phase-matching conditions corresponding to the two sequential cascades are $k_1 - k_2 + k_3$ and $-k_1 + k_2 + k_4$, whereas those associated with the two parallel cascades are $k_3 - k_4 + k_5$ and $k_1 - k_2 + k_5$. For example, Figure 4.13 displays Feynman diagrams associated with sequential and parallel third-order cascades for the intermediate phase-matching conditions, $k_1 - k_2 + k_3$ and $k_3 - k_4 + k_5$, respectively. Feynman diagrams and response functions associated with all cascaded third-order signal components are given in Appendix A.

The ratio in the cascaded third-order and direct fifth-order signal strengths can be written as[98,99]

$$\frac{E_{cas}(t)}{E^{(5)}(t)} = \left(\frac{7}{25}\right)\frac{lN\omega_t\left|\mu_{eg}\right|^2}{2n(\omega_t)\varepsilon_0\hbar c}\frac{\eta^{(3)}_{par}(\tau_1,\tau_2)+\eta^{(3)}_{seq}(\tau_1,\tau_2)}{\eta^{(5)}_{direct}(\tau_1,\tau_2)} \tag{4.22}$$

where l is the path length, N is the number density, ω_t is the signal frequency, $n(\omega_t)$ is the refractive index, and the auxiliary functions are defined in Appendix A. Equation 4.22 makes clear that experiments involving dilute solutions carry advantages compared to those conducted on pure liquids because the ratio, $E_{cas}(t)/E^{(5)}(t)$, is linear in the number density. For example, the number density employed in the present experiment is roughly 15,000 times lower than that associated with pure CS_2, which is known to generate intense cascaded third-order signals under

off-resonant conditions.[24,54] Of course, the number density is only one important consideration, because the signal generation mechanisms are quite different on and off resonance. As indicated in Figure 4.13, one key difference is that the ratio, $E_{cas}(t)/E^{(5)}(t)$, scales as the inverse of the absorbance line width, Γ_{eg}, because of the different numbers of electronic coherences associated with the cascaded third-order and direct fifth-order signal ($\phi_1^{(3)}(\tau)\,\phi_1^{(3)}(\tau)/\phi_1^{(5)}(\tau) \propto \Gamma_{eg}^{-1}$).

Perhaps the most important distinction between resonant and off-resonant conditions is that signal generation is allowed for (harmonic and/or anharmonic) Franck-Condon active modes on resonance. From a mathematical perspective, the primary issue is that $E_{cas}(t)$ and $E^{(5)}(t)$ involve sums of products of 8 and 6 vibrational overlap integrals, respectively. In order to illustrate the effect of Franck-Condon activity, we have evaluated the ratio, $E_{cas}(t)\ /E^{(5)}(t)$, with respect to the dimensionless potential energy displacement, d, in Figure 4.14. This calculation employs a harmonic ground state surface (with frequency of 112 cm^{-1}) and the anharmonic excited state potential energy surface determined by Myers (see Appendix A).[48] Here, we have Fourier transformed the signal fields, $E_{cas}(t)$ and $E^{(5)}(t)$, with respect to τ_1 and τ_2

$$\frac{E_{cas}(\omega_1,\omega_2)}{E^{(5)}(\omega_1,\omega_2)} = \frac{\int_{-\infty}^{\infty} d\tau_1 \int_{-\infty}^{\infty} d\tau_2 E_{cas} E^{(5)}(\tau_1,\tau_2)\exp(i\omega_1\tau_1 + i\omega_2\tau_2)}{\int_{-\infty}^{\infty} d\tau_1 \int_{-\infty}^{\infty} d\tau_2 E^{(5)}(\tau_1,\tau_2)\exp(i\omega_1\tau_1 + i\omega_2\tau_2)} \tag{4.23}$$

to obtain the ratios at $\omega_1 = \omega_2 = \pm$ 112 cm^{-1} (i.e. on the diagonal of the 2D spectrum). Thus, the calculation in Figure 4.14 represents the ratio of peak magnitudes measured in the upper-right/lower-left quadrants in Figure 4.8c (i.e. this analysis does not apply to the vibrationally

incoherent component of the signal). The key finding is that the ratio, $|E_{cas}|/|E^{(5)}|$, is 10^{-7}-10^{-3} in the range of the dimensionless displacement, d, relevant to I_3^-. Empirical estimates for d range from 7.0-8.8 (see Appendix A).[48] The large difference in the order of magnitude is important, because it suggests that the prediction is robust. That is, expressions for the signals can be developed in different ways (e.g. Gaussian line shapes instead of Lorentzian), but such details are unlikely to account for several orders of magnitude.

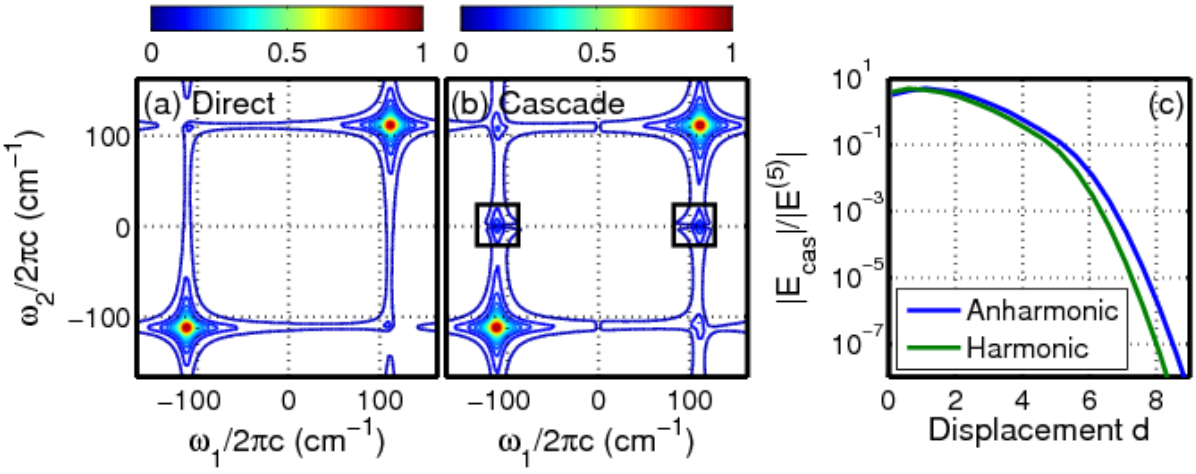

Figure 4.14. Absolute values of the (a) direct fifth-order and (b) cascaded third-order signal magnitudes at $\omega_1 = \omega_2 = \pm 112$ cm^{-1} are shown for a dimensionless potential energy displacement of 7.0, where an empirical anharmonic excited state potential energy surface is employed (see Appendix A). The ratio, $|E_{cas}(\omega_1,\omega_2)|/|E^{(5)}(\omega_1,\omega_2)|$, is computed using (blue) an empirical anharmonic model and (green) a harmonic model with equal ground and excited state frequencies (112 cm^{-1}). The calculations suggest that third-order cascades in the Raman response are at least three orders-of-magnitude weaker than the direct fifth-order signal in I_3^- based on previous estimates for the displacement (7.0 and 8.8 for harmonic and anharmonic models, see Appendix A).[48] The features at ω_2 =0 cm^{-1} (enclosed in boxes) in the cascaded signal spectrum represent imperfect subtraction of the non-oscillatory component of the signal (this is not a vibrational resonance).

Physical insight in the behavior illustrated in Figure 4.14 is challenged by the numerous terms contained in the response functions (i.e. ~6^4 and ~6^6 terms at third and fifth-orders). Thus, it is useful to consider the basic aspects of the subset of terms that contribute to the (diagonal) resonances at $\omega_1 = \omega_2 = \pm 112$ cm^{-1}. Because the dominant parallel cascade scales as the product of two third-order polarizations, $E_{cas}(t) \propto P^{(3)}(\tau_1 + \tau_2, t) P^{(3)}(\tau_2, t)$, the key terms in the response function involve products of complex exponential functions with the following forms,

$$\exp\left[ia\omega_{vib}(\tau_1 + \tau_2)\right]\exp\left[ib\omega_{vib}\tau_2\right] = \exp\left[ia\omega_{vib}\tau_1 + i\omega_{vib}\tau_2(a-b)\right] \qquad (4.24)$$

where a and b represent the differences in quantum numbers. Terms may contribute to the peak at $\omega_1 = \omega_2 = \omega_{vib} = \pm 112$ cm^{-1} if $a = \pm 1$ and b =0. Thus, the third-order polarization of one of the molecules involved in the parallel cascade must evolve in a vibrational population (instead of a vibrational coherence) during the delay, τ_2. For this reason, significant contribution of the parallel cascade at $\omega_1 = \omega_2 = \pm 112$ cm^{-1} requires large overlap integrals for vibrational states that possess the same quantum number. This explains why the ratio, $|E_{cas}| / |E^{(5)}|$, in Figure 4.14 is largest when the displacement, d, is small (e.g. $\langle 0|1\rangle / \langle 0|0\rangle = d/\sqrt{2}$).

Physical insight into the ratio, $|E_{cas}| / |E^{(5)}|$, can also be derived by inspection of the (third-order) experimental transient grating signal for I_3^- shown in Figure 4.7. The key issue is that the vibrational amplitude is roughly 50% of the total signal intensity. In the context of Equation 4.24, this means that signal components in which b =0 have small magnitudes. The incoherent part of the signal is the cascade's most important ingredient at $\omega_1 = \omega_2 = \pm 112$ cm^{-1}; oscillatory behavior feeds both E_{cas} and $E^{(5)}$, whereas contributions of the incoherent signal

component are unique to E_{cas}. Thus, it will generally be found that the parallel cascade for the diagonal peak at the fundamental frequency is negligible if the incoherent part of the third-order response does not dominate the signal (i.e. if the mode displacement is extremely large). We remark that the point illustrated in Figure 4.15 applies only to parallel cascades (not sequential cascades) in which the ground state wavepacket motions dominate the response. As discussed in Section 4.3.4, I_3^- has long been recognized as an excellent model for ground state wavepacket motions when photoexcited and probed in the UV.[46,50]

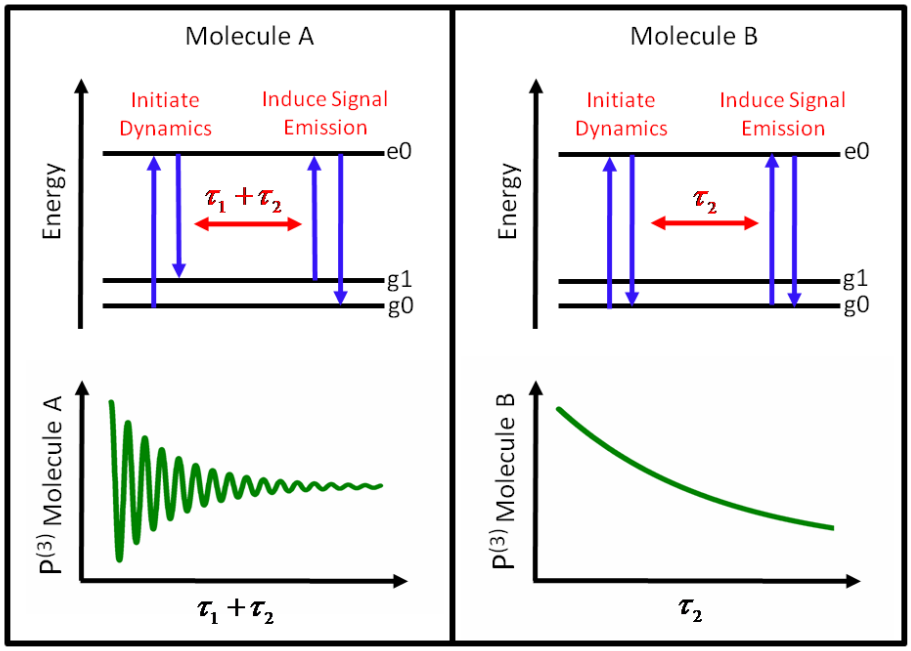

Figure 4.15. Parallel cascades that produce peaks at $\omega_1 = \omega_2 = \pm 112$ cm^{-1} combine an oscillatory component of the response at one molecule (molecule A) with an incoherent component of the response at a second molecule (molecule B). The vibrational quantum number is changed by the first pulse-pair on molecule A, whereas a vibrational coherence is not produced in τ_2 on molecule B (see Equation 4.24). The 2D line shape becomes asymmetric (i.e. broader in ω_2) if the magnitude of the polarization on molecule B relaxes (e.g. due to solvation) on the same time scale as vibrational dephasing. Parallel cascades at $\omega_1 = \omega_2 = \pm 112$ cm^{-1} are much weaker than the direct fifth-order signal in I_3^-, because the oscillatory part of the third-order response is near 50% of the total third-order signal magnitude.

The insights derived from our model echo the discussion of Hamm and co-workers who suggested that the challenges encountered in off-resonant Raman experiments partly originate in the forbidden nature of the response for harmonic modes.[94] Here, we have shown that Franck-Condon activity under resonant conditions changes the signal generation mechanism entirely. The present model calculations suggest that cascades are, at worst, on the same order of magnitude as the direct fifth-order signal in electronically resonant experiments carried out with similar optical densities. Importantly, our calculations indicate that a large mode displacement is required for the direct fifth-order signal to outcompete the cascade in a system with a single mode. For this reason, it is not clear if the present experimental approach can be successfully adapted to molecules with modest mode displacements.

4.5.3. Signatures of Direct and Cascaded Nonlinearities in Spectroscopic Line Shapes

In some cases, contributions from third-order cascades can be identified by comparing their spectroscopic signatures to the measured signals.[54,56,57] As discussed above, the cascaded third-order response should be dominated by a parallel cascade in this laser beam geometry. Sequential cascades are predicted to be relatively inefficient and, unlike the measured signals, possess essentially identical signal intensities in all four quadrants of the 2D spectrum (see Figure A.33 in Appendix A). For these reasons, we conclude that contributions from sequential cascades are negligible and focus on spectroscopic signatures of the parallel cascade in this section.

In Figure 4.16, an experimental 2D spectrum (average of five experiments) is compared to a 2D spectrum associated with a parallel cascade that is calculated using an experimental transient grating signal field, $S^{(3)}(\tau)$. The 2D spectrum corresponding to the parallel cascade is

generated by two-dimensional Fourier transformation of the product, $S^{(3)}(\tau_2)\, S^{(3)}(\tau_1+\tau_2)$. As in off-resonant 2D Raman spectra,[54] this calculation reveals that the parallel cascade decays faster in τ_2 than it does in τ_1. This difference in decay times manifests as a 30% broader line width in the ω_2 dimension for the 2D spectrum of the cascade in Figure 4.16. Figure 4.15 illustrates how the decay of the incoherent signal component induces asymmetry in the 2D line shape of the parallel cascade. In our experiments, I_3^- is excited on the high-frequency side of the absorbance spectrum, where the incoherent part of the response decays because of solvation of the ground-state "hole" wavepacket (see Figure 13.7 in Reference [85]). Thus, the key to the asymmetry in the line shape is that solvation and vibrational dephasing occur on the same time scale (i.e. the cascaded 2D spectrum would appear symmetric if solvation was slow compared to vibrational dephasing). In contrast, the measured 2D spectrum has indistinguishable line widths in ω_1 and ω_2. This symmetric shape is consistent with the theoretical prediction for the direct fifth-order process (see Figure 4.9).

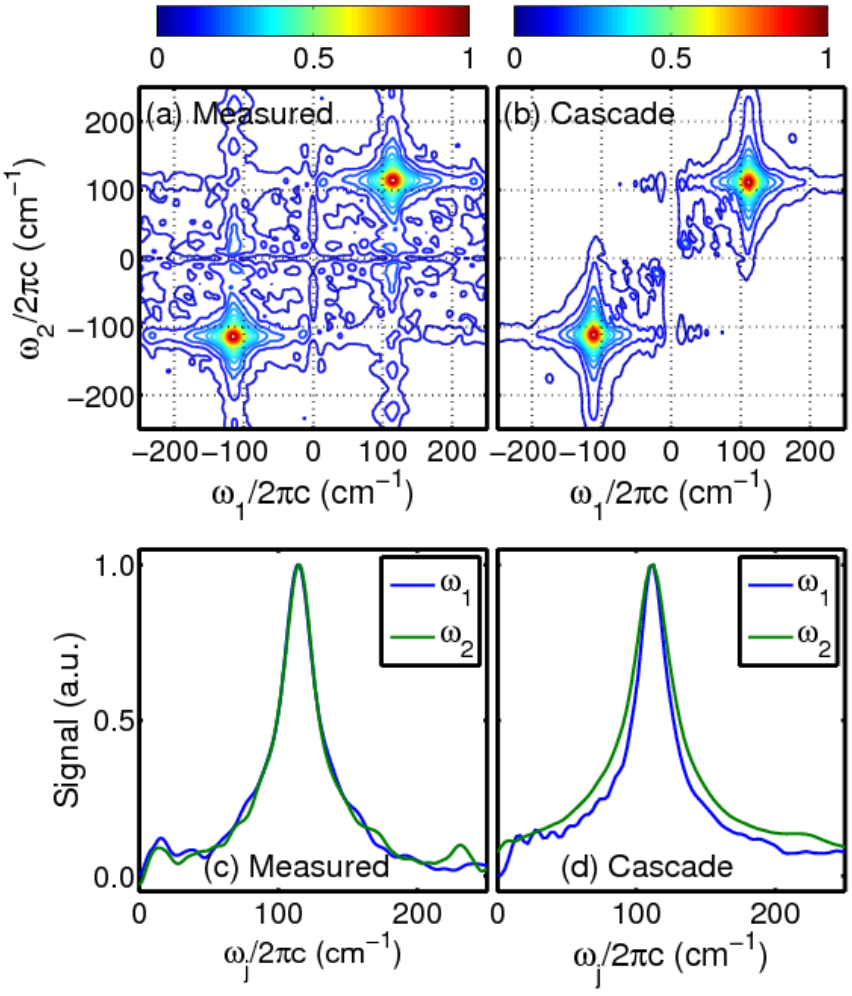

Figure 4.16. Absolute values of two-dimensional Raman spectra (a) measured by six-wave mixing and (b) the parallel cascade computed using an experimental third-order transient grating measurement. Slices of the two-dimensional Raman spectra are displayed at ω_1 =112 cm^{-1} (blue) and ω_2 =112 cm^{-1} (green) for the **(c)** experimental measurement and the (d) simulated parallel cascade. The line width of the parallel cascade is 30% larger in ω_2 than it is in ω_1 because of incoherent solvation dynamics in the ground electronic state.

4.5.4. Distinguishing Direct and Cascaded Nonlinearities Based on Signal Phases

Under electronically resonant conditions, 90º phase-shifts are accumulated in each time interval shaded in blue in Figure 4.13. The additional electronic coherence involved in the

cascaded nonlinearity imposes a phase-difference of 90º between the two processes. Phase-shifts of 90º and 180º are also accumulated by the direct and cascaded nonlinearities when the numbers of emission events are taken into account, respectively. Thus, the total phase-difference between the absorptive components of the direct fifth-order and cascaded third-order signal fields is 180º under resonant conditions.[94] This section presents control experiments based on this difference in sign.

Knowledge of the absolute signal phase requires a well-defined reference. To this end, we establish the phase-angle of the fifth-order signal field by comparing it to the phase-angle of the direct third-order signal field, which differs from the fifth-order signal by 180º (i.e. the sign of the polarization changes for every two levels in perturbation theory).[85] It follows that the direct third-order signal and cascaded nonlinearity possess the same sign under resonant conditions. Here, we employ four-beam geometries to facilitate comparison of the third and fifth-order signal phases. The key advantage associated with four-beam geometries is that the direct third and fifth-order responses possess the same amount of phase-mismatch, thereby allowing a direct comparison between these two signal phases. Cascaded nonlinearities do not possess the same amount of phase mismatch as the direct processes, which can be problematic if the shift in the cascaded signal phase accumulated in the sample changes the signal sign.[24] In order to rule out such undesired propagation effects, we have compared signals phases in three different four-beam geometries and a range of sample thicknesses.

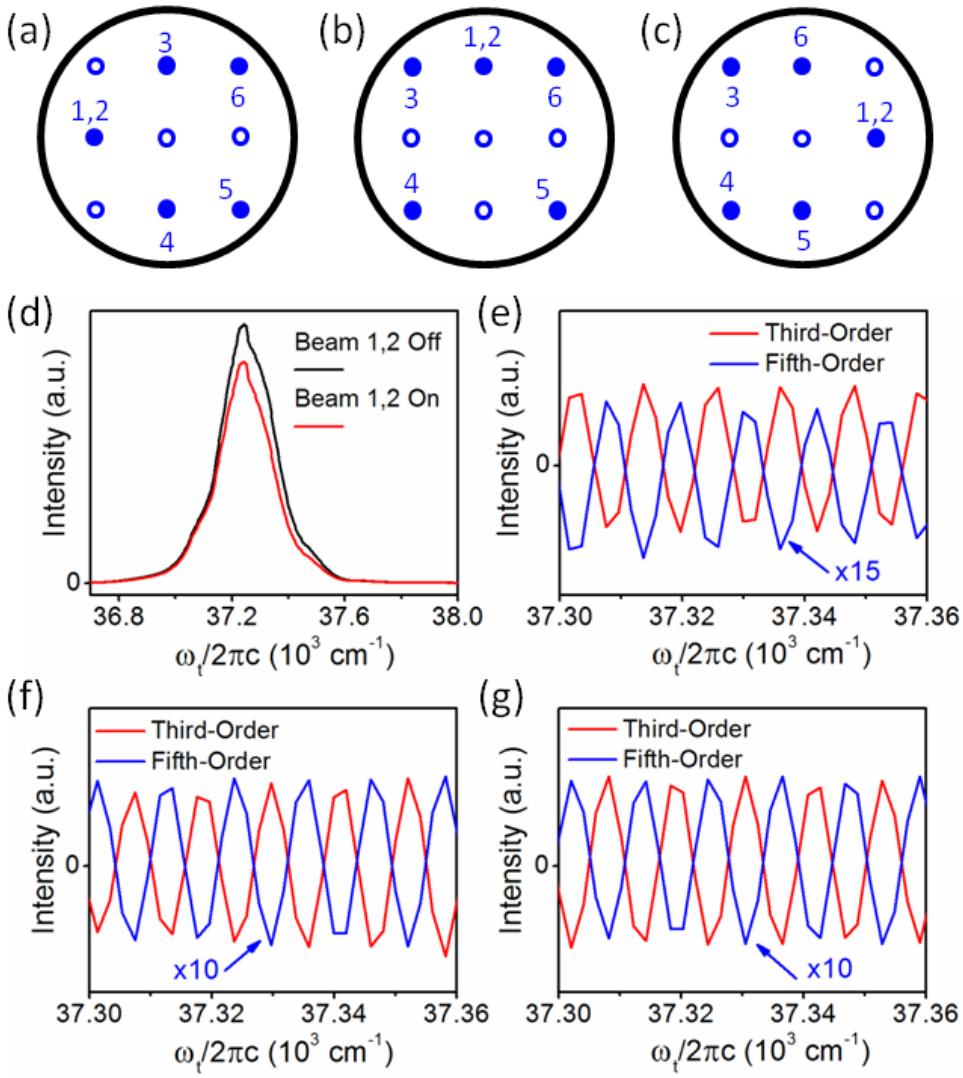

Figure 4.17. (a)-(c) Three laser beam geometries are used to establish the relative phase-angles of third and fifth-order signals. Both signal fields are radiated in the direction, $k_3 - k_4 + k_5$, because the first two field-matter interactions occur with the same beam (beam 1,2) in the fifth-order experiment. (d) The homodyne-detected signal intensity is measured with and without beam 1,2 using geometry (a). The reduction in signal intensity caused by beam 1,2 confirms that the nonlinearity interferes destructively with the third-order signal. Portions of interferograms are measured for the direct third-order (beam 1,2 blocked) and the direct fifth-order signals (obtained as the difference, beam 1,2 on – beam 1,2 off) at τ_1=0.3 ps and τ_2=0.3 ps. The interference fringes show that the third and fifth-order signal phases differ by approximately 180° (this behavior has been confirmed for delay times up to 3 ps). The measurement in panel (e) corresponds to geometry (a); the measurement in panel (f) corresponds to geometry (b); the measurement in panel (g) corresponds to geometry (c).

Table 4.3. Parameters of Model Used to Compute Magnitudes of Direct Fifth-Order and Cascaded Third-Order Signals

[a]Parameter	Value
$\left(\omega_L - \omega_{eg}\right)/2\pi c$	2810 cm^{-1}
d	varied
Γ_{vib}/c	10 cm^{-1}
Γ_{eg}	2010 cm^{-1}
μ_{eg}	8.8 D
N	1.2×10^{24} m^{-3}
$\omega_t/2\pi c$	37200 cm^{-1}
$n\left(\omega_t\right)$	1.4
l	0.3 mm

[a] Calculations employ a harmonic ground-state potential energy surface with a frequency of 112 cm^{-1} and the anharmonic excited state potential energy surface determined by Myers.[48] Details are given in the Appendix A.

Figure 4.17 presents three four-beam geometries that facilitate analysis of the signal phase (i.e. these geometries are obtained by changing the mask in the six-wave mixing interferometer). The indices in this figure carry the same meaning as those in Figure 4.4. The first two field-matter interactions, which are derived from a single laser beam (labeled beam 1,2 in Figure 4.17), initiate dynamics in τ_1, whereas τ_2 corresponds to the delay between the pulse-pair 3,4 and pulse 5. Both the third and fifth-order signals are radiated in the direction $k_3 - k_4 + k_5$, because the wavevectors associated with the first two interactions cancel in the fifth-order process (i.e. $k_1 - k_2 + k_3 - k_4 + k_5 = k_3 - k_4 + k_5$). As mentioned above, the direct third and

fifth-order processes accumulate identical amounts of phase mismatch in each geometry. In contrast, the amount of phase mismatch associated with each of the four types of cascades may vary. Therefore, the relative signs of the third and fifth-order signals must be independent of the geometry and sample thickness if the direct fifth-order response is generally dominant.

In order to establish the relative phase of the fifth-order signal, we begin with a simple and easily interpreted experimental test. In Figure 4.17d, homodyne-detected signals are displayed with and without beam 1,2 in the geometry shown in panel (a). The decrease in the measured signal intensity found with beam 1,2 blocked indicates that the nonlinearity induced by beam 1,2 interferes destructively with the third-order signal (the interferograms shown in Figure 4.17e follow from this result). These observations can be interpreted by considering the components of the total signal intensity under perfect phase-matching conditions

$$\left|E^{(3)}+E^{(5)}+E_{cas}\right|^2 \approx \left|E^{(3)}\right|^2 + 2\left|E^{(3)}\right|\left|E^{(5)}\right|\cos\left(180^\circ\right) + 2\left|E^{(3)}\right|\left|E_{cas}\right|\cos\left(0^\circ\right) \qquad (4.25)$$

where it is assumed that the direct third order signal field, $E^{(3)}$, is large compared to the direct fifth-order and cascaded responses, $E^{(5)}$ and E_{cas}. The second and third terms on the right side of Equation 4.25 have negative and positive signs, respectively. Thus, a beam 1,2-induced decrease in signal intensity is predicted if $\left|E^{(5)}\right| >> \left|E_{cas}\right|$, whereas an increase in signal intensity is predicted if $\left|E_{cas}\right| >> \left|E^{(5)}\right|$. The sign of the second term is always negative in these four-beam geometries, whereas the sign of the third term depends on both the geometry and sample thickness.

We have confirmed that indistinguishable results are obtained in all three geometries shown in Figure 4.17 with sample thickness of 200, 300, and 500 μm; beam 1,2 always induces a

decrease in the total signal intensity for delay times up to 3 ps (i.e. the delay range relevant to the present study). Reproducibility of the signal sign in various geometries, which are subject to different phase-matching conditions, suggests that the direct fifth-order signal is generally larger than the cascaded third-order signal under resonant conditions in I_3^-. These results may also be understood in terms of the ground-state depletion induced by beam 1,2 (i.e. as in a pump-repump-probe experiment).[100] For example, a 10% reduction in the homodyne-detected signal intensity suggests that approximately 5% of the molecules in the focal volume are photoexcited. Such an understanding of ground-state depletion is relevant only to the direct fifth-order process, because each molecule involved in a third-order cascade possesses independent ground and excited state populations.

The test described in Figure 4.17 establishes that the sign of the measured signal field is generally opposite to the four-wave mixing signal. Slightly more than 50% of signal corresponds to the Raman response, whereas the remainder is incoherent (i.e. a pump-repump-probe signal). It is therefore desirable to take this test one step further and isolate the Raman component of the signal. In Figure 4.18, we present a more challenging measurement in which vibrational coherences in the third and fifth-order signals are compared to establish their phase-relationship. The absorptive component of the third-order signal is found using the all-optical phasing method demonstrated by Scholes and co-workers.[101] The same phase setting is then applied to the fifth-order signal obtained by measuring differences with beam 1,2 blocked and unblocked.[40,43]

In Figure 4.18b, the vibrational coherence associated with the six-wave mixing response is obtained by setting the delay between pulses 1,2 and pulse-pair 3,4, τ_1, equal to 350 fs, which corresponds to the first maximum in the third-order vibrational coherence. The delay between

pulse-pair 3,4 and pulse 5 , τ_2 , is then scanned to obtain the fifth-order vibrational coherence. The delay between pulse-pair 3,4 and pulse 5 is scanned a total of 70 times, where scans with beam 1,2 blocked and unblocked are interleaved (i.e. 35 of each). Attainment of a single 1D slice with signal-to-noise comparable to that shown in Figure 4.18b requires approximately 60 minutes of signal averaging (the intensity of beam 1,2 is not increased above 5GW/cm^2 because of the potential for photoionization-induced artifacts).[60,68]

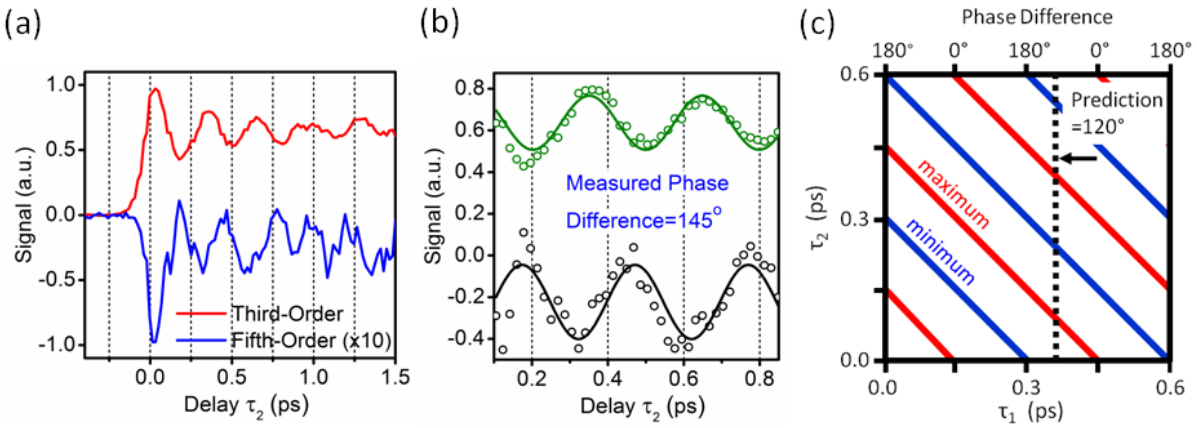

Figure 4.18. (a) Absorptive parts of the wavelength-integrated third and fifth-order signal fields are measured using the geometry shown in Figure 4.17a. The delay axis, τ_2 , corresponds to the delay between the pulse-pair 3,4 and pulse 5 (τ_1 =350 fs and τ_2 is scanned). (b) Absorptive parts of vibrational coherences are fit with sinusoidal functions to quantify the phase difference. (c) The delay axis, τ_1 , is translated in the phase-difference associated with the absorptive components of third and (direct) fifth-order vibrational coherences. The response is measured at a delay time predicted to yield an approximate 120° phase difference (at the dashed line). This control experiment suggests that the direct fifth-order Raman response is much larger than the cascaded nonlinearity.

Figure 4.18c explains how to convert the delay, τ_1, into the predicted phase-difference between third and fifth-order signal fields. A phase-difference of exactly 120º is predicted based on the delay, τ_1=350 fs, and the 300-fs period of the vibrational mode (i.e. 50 fs is 17% of the

300-fs period of the vibration). The measured phase difference of 145° differs from the value predicted for the direct fifth-order signal by 25°. It should also be noted that the phase of the vibrational coherence in the six-wave mixing signal shifts towards negative time (to the left in Figure 4.18a), because the value of τ_1 is not an integer-multiple of the 300-fs vibrational period. It may be instructive to consider that the nodes in the wave, $\cos\left[\omega_{vib}\left(\tau_1+\tau_2\right)\right]$, shift toward lesser values of τ_2 as the amount of phase accumulated in τ_1, $\omega_{vib}\left(\tau_1\right)$, increases.

While useful for establishing generality of the signal phase, the interpretation of signals acquired in the four-beam geometries is somewhat complicated by variability in the phase-matching efficiencies for cascaded nonlinearities (e.g. see tables of phase-matching efficiencies in Appendix A). For this reason, we also compare signs of third and fifth-order signal phases using a three-beam geometry in which both direct and cascaded nonlinearities are well phase-matched. The three laser pulses are derived from the zeroeth-order beams in our experimental setup (see Figure 4.4). In this geometry, the efficiencies of the direct fifth-order and parallel cascaded responses are equal, whereas the sequential cascades are roughly 90% less efficient. The signals are detected using a CMOS array mounted on a miniature spectrometer. The resolution of the spectrometer is comparable to the width of the laser spectrum, so we simply integrate over the few pixels on which the probe light is incident. The two pump beams are chopped at 250 Hz using synchronized chopper wheels. Thus, pump-probe and pump-repump-signals are acquired for every four shots of the laser system. The delay lines are scanned 20 times over a total of 50 points, and 500 spectra are acquired at each point per scan.

Pump-probe and pump-repump-probe signals measured in the three-beam gometry are displayed in Figure 4.19. As in Figure 4.18, the two signals have opposite signs, and the signal

magnitudes differ by roughly a factor of 10. As in the four-beam geometries, the observation of signals with opposite signs indicates that the magnitude of the direct fifth-order nonlinearity is larger than that of the cascaded response. The relative magnitudes of the pump-probe and pump-repump-probe signals are also consistent with dominance of the direct response; cascades would interfere destructively with the direct fifth-order response, thereby reducing the overall signal magnitude. The signal-to-noise ratio of the pump-repump-probe signal is not sufficient for detecting vibrational coherences (noise level is 0.1 mOD). Nonetheless, as mentioned above, the Raman response is greater than 50% of the total signal magnitude in I_3^-. It should also be noted that the six-wave mixing geometry employed in this work is superior to the three-beam geometry in terms of cascade suppression (see Table 4.4) .

In summary, we have confirmed that the signs of the third and fifth-order signals are opposite and that this behavior is independent of the laser beam geometry and sample thickness. Tests were conducted in both four-beam geometries and a conventional three-beam (pump-repump-probe) geometry. We have also shown that the third and fifth-order vibrational phases shown in Figure 4.18 deviate by approximately 25º and 155º from (the simplest) theoretical prediction, respectively. It is not clear if the 25º deviation reflects an experimental issue (e.g. uncertainty in phase calibration, uncertainties in time-zeroes) or some aspect of the system that has not been accounted for. For example, higher-energy electronic resonances in I_3^- may influence the dispersive part of the signal even though the laser pulse is resonant with a single excited state (i.e. dispersive line shape have long tails). The blue-shift of the laser from the peak of the absorbance spectrum may also be a factor. In any case, the main conclusion to be drawn from the measurements described in this section is that the magnitude of the direct fifth-order response of I_3^- is generally larger than that associated with third-order cascades. Extraordinary

engineering solutions, such as those employed in off-resonance studies,[24] are therefore not required to suppress cascades in I_3^-.

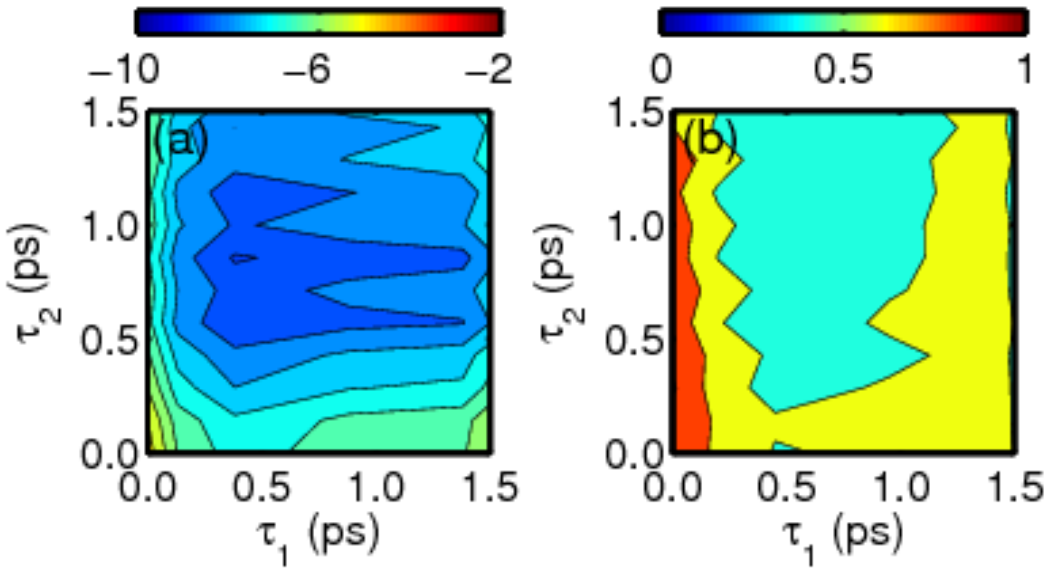

Figure 4.19. (a) Pump-probe (ΔA) and (b) pump-repump-probe (ΔΔA) signals are measured simultaneously in a jet with a 300-μm path length using the three zeroeth-order laser beams in interferometer (signals are represented in mOD). The observation of signals with opposite signs in (a) and (b) indicates that the direct fifth-order response is greater than that associated with third-order cascades. The three-beam geometry is useful for establishing the intrinsic relative magnitudes of the direct and cascaded responses, because both nonlinearities are well-phase matched.

4.5.5 Concentration Dependence of the Six-Wave Mixing Signal Field

In this section, we present six-wave mixing signal intensities acquired at a series of concentrations to distinguish contributions from direct and cascaded nonlinearities. Recent 3D-IR studies have similarly ruled out contributions from third-order cascades based on the concentration dependence at small optical densities.[94,99] Attenuation of the incoming beams and absorption of the signal must be treated to interpret data acquired at optical densities greater than

~0.1, which are typically required in resonance Raman experiments. As shown in Appendix A, such effects are fairly straightforward to account for with a simple model. Here, signals are examined at fixed delay times (rather than obtaining 2D spectra at a series of concentrations), because attainment of adequate statistics is not possible with the 2-hour data acquisition time required for a 2D spectrum. Nonetheless, signals obtained at fixed delay times should still be sensitive to cascaded nonlinearities in I_3^-, because the Raman response is more than 50% of the total signal strength.

Six-wave mixing signal intensities measured at a series of concentrations are presented in Figure 4.20. The points in these plots represent the wavelength-integrated, homodyne-detected signal intensity. We analyze the homodyne-detected signal intensity (rather than the heterodyne-detected signal intensity) to simplify the analysis; attenuation of the local oscillator beam would have to be measured and incorporated in the model if heterodyne detection was utilized. The sample is contained in a 200-μm path length cuvette that is held in a rotating mount. The sample moves approximately 120 μm/ms (i.e. a point on the circle traced by the laser beam), so each shot of the laser is incident on a fresh portion of the solution. The concentrations are scanned two times (with fresh solutions), and a total of 60 spectra are acquired at each point (each point in plot represents a total of 6000 laser shots). Dependences of the direct and cascaded signal intensities on the absorbance are also calculated using the model presented in Appendix A. The simulated signal intensities shown in Figure 4.20 are multiplied by constants in order to overlay them with the data.

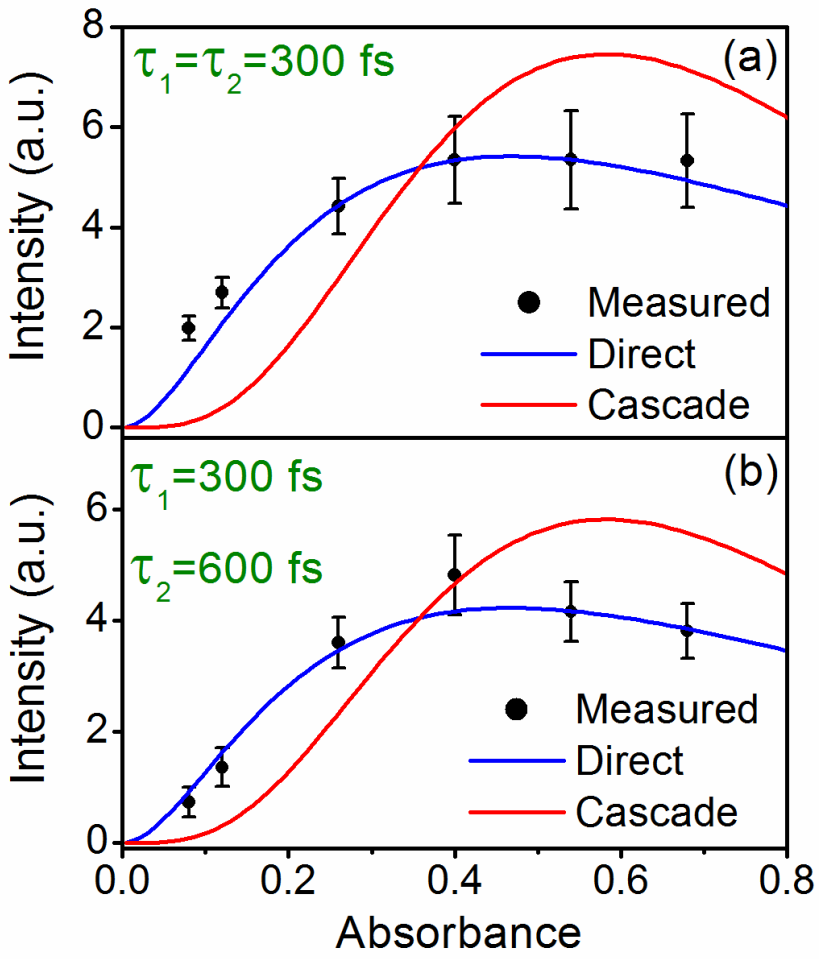

Figure 4.20. Six-wave mixing signal intensities measured at (a) $\tau_1 = \tau_2$ =300 fs and (b) τ_1=300 fs, τ_2 =600 fs. Dependences of the direct (blue) and cascaded (red) signal intensities on the absorbance are simulated using the model described in Appendix A (the simulated intensities are multiplied by constants in order to overlay them with the data). The concentration dependences of the direct and cascaded processes differ, because the cascade is induced by the primary four-wave mixing response accumulated in the sample (see Appendix A). These data are consistent with dominance of the direct fifth-order signal field.

The two delay times shown in Figure 4.20 are chosen to test whether or not the concentration dependence of the signal differs on or off of the diagonal, $\tau_1 = \tau_2$. Notably, the signals plotted in Figures 4.20a and 4.20b correspond to maxima and minima in the vibrational amplitude, respectively. Agreement between the experiments and simulations for the direct

response suggests that the signal field is dominated by the direct fifth-order nonlinearity in the range of concentrations employed in the experiments. For reference, the 2D data shown in Figure 4.8 were acquired at the concentration that produces an absorbance of 0.3 in the 200-μm path length employed in Figure 4.20.

4.5.6. Comment on the Relative Magnitudes of Third and Fifth-Order Signals Fields

The relative magnitudes of the third and fifth-order signals shown in Figures 4.17-4.19 underscore the key distinction between resonant and off-resonant conditions – that all vibronic transitions are allowed for Franck-Condon active modes on resonance. These measurements show that the amplitude of the third-order signal field is 10-20 times larger than that of the fifth-order signal field. As in a pump-repump-probe experiment,[100] this difference in signal magnitudes should be anticipated under resonant conditions in which 5-10% of the molecules in the focal volume are photoexcited. In contrast, forbidden steps in the fifth-order process under off-resonant conditions inflate the ratio between third and fifth-order signal magnitudes significantly. For example, Wright obtained an estimate of $E^{(3)} / E^{(5)} \approx 18{,}000$ for intramolecular vibrations in liquid toluene using the CHORES technique ($E^{(3)} / E_{cas} \approx \sqrt{50,000}$ and $E_{cas} / E^{(5)} \approx \sqrt{6500}$).[96]

The large magnitude of $E^{(3)} / E^{(5)}$ associated with off-resonant experiments is problematic, because it directly impacts the ratio between the cascaded third-order and direct fifth-order signal fields, $E_{cas} / E^{(5)}$.[99] The four-wave mixing response must be suppressed by roughly three orders of magnitude (without attenuating the direct fifth-order signal) to achieve success under off-resonant conditions. It has been shown that such suppression can be achieved

through a combination of heterodyne detection and laser beam geometries that impose large phase-mismatch for cascades.[24] The geometries employed in these earlier works may also be useful for cascade suppression under resonant conditions; however, heterodyne detection cannot be leveraged for contrast because of the 180° phase-difference between the direct and cascaded responses.

Table 4.4. Calculated Wavevector Mismatches for Direct and Cascaded Nonlinearities in Geometry Shown in Figure 4.4

Wavevector of Intermediate Nonlinearity	Δk_A (cm^{-1})	Δk_B (cm^{-1})	[(a),(b)] $f_j\left(\Delta k_j l\right)$
$k_1 - k_2 + k_3 - k_4 + k_5$ (Direct 5th-Order Signal)	-235	----------	-0.01
$k_1 - k_2 + k_3$ (Sequential Cascade #1)	-470	-235	7.0×10^{-4}
$k_2 - k_1 + k_4$ (Sequential Cascade #2)	-235	700	-2.7×10^{-3}
$k_1 - k_2 + k_5$ (Parallel Cascade #1)	-470	235	7.0×10^{-4}
$k_3 - k_4 + k_5$ (Parallel Cascade #2)	0	-235	-0.09

[(a)]The path length is 300 μm.

[(b)] Direct and cascaded signal generation efficiencies are computed using $\mathrm{sinc}\left(\Delta k_A l/2\right)$ and $\mathrm{sinc}\left(\Delta k_A l/2\right)\mathrm{sinc}\left(\Delta k_B l/2\right)$, respectively.

Contributions from cascades in our data are difficult to quantify based on the above experimental tests, because the cascaded nonlinearity is always superposed with an intense direct

fifth-order response. It should be emphasized that the model calculations presented in Figure 4.14 pertain only to the component of the signal that oscillates at the fundamental frequency in τ_1 and τ_2 (i.e. the signal component of interest). This argument does not apply to the incoherent part of the signal. It is our understanding that the mode displacement controls the distribution of cascaded signal intensity between coherent and incoherent signal components. Considering the signal-to-noise ratios present in our experimental tests, cascaded nonlinearities could easily be 10% of the total signal magnitude (i.e. slightly above the noise floor). Of course, such small contributions do not preclude analysis of the direct fifth-order signal field, particularly if they are concentrated in the (vibrationally) incoherent part of the response.

4.6. Conclusions

In summary, we have conducted six-wave mixing experiments with I_3^- using deep UV laser pulses generated in a two-color filament. The experiments demonstrate that high-quality signals are readily obtained with the data acquisition rate and sensitivity afforded by combining a background-free laser beam geometry with spectral interferometry. Signals were examined in two different representations. One representation simply carried out a 2D Fourier transform with respect to the two experimentally controlled delay times using the wavelength-integrated signal field. The pattern of resonances in the 2D spectrum is well-described with response functions based on a cumulant expansion. The second representation involves three dimensions: the first experimentally controlled delay time, τ_1; the Fourier transform of the second delay time, ω_2; the detection frequency, ω_t. Correlation spectra associated with ω_2 and ω_t reveal that both the detection frequency and signal magnitude oscillate in τ_1 due to wavepacket motions in the symmetric stretching coordinate. These oscillations encode information about anharmonic

motions in the ground state (which are weak in I_3^-), and the dynamic energy gap between electronic states. It will be interesting to examine systems with multiple Franck-Condon active modes using this technique. Pulses with broader bandwidths may also enhance sensitivity by increasing the oscillation amplitude in $\langle \omega_t \rangle$.

The analysis presented in Section 4.5 suggests that cascaded third-order nonlinearities, which significantly challenged fifth-order off-resonant Raman spectroscopies,[24,25,54-57] do not dominate the fifth-order resonance Raman response of I_3^-. This interpretation of the response is supported by four aspects of the measured signals: the line shapes, the signal phase, concentration dependence, and the relative magnitudes of third and fifth-order signals. Consistency between these fairly unrelated aspects of the signals constitutes strong evidence that the direct fifth-order signal field is much larger than the cascaded signal field. The model calculations presented in Section 4.5.2 suggest that the cascaded signal contribution to the peak at $\omega_1 = \omega_2 = \pm 112$ cm^{-1} is more than three orders of magnitude smaller than that associated with the direct fifth-order response. It should be emphasized that this analysis pertains only to the signal component that oscillates at the fundamental mode frequency in both dimensions. In other words, the mode displacement controls how the cascaded signal intensity is distributed between (vibrationally) coherent and incoherent signal components (see Section 4.5.6). For this reason, it is presently unclear if this method can be successfully applied to larger molecules, which generally possess smaller mode displacements (i.e. I_3^- has an extraordinarily large mode displacement). Alternate laser beam geometries may be considered for such cases.[24]

Applications of 2D electronic spectroscopy in the deep UV are challenged by dispersion management and the large off-resonant response of the sample medium near time-zero.[21,22,59-

[63,66-68] The present work shows that multi-dimensional resonance Raman experiments are largely immune to these technical limitations. Most importantly, vibrational dephasing is much slower than electronic dephasing, so the coherence spike associated with the region of laser pulse overlap is not as problematic. Regarding dispersion management, low-frequency (<1000 cm^{-1}) vibrational resonances are readily probed with manageable laser bandwidths. For example, the (functionally important) modes localized to disulphide bridges in proteins are found below 500 cm^{-1} and may be excellent targets for six-wave mixing experiments that employ 200-nm laser pulses.[102] Higher-frequency vibrational resonances (>1000 cm^{-1}) may be probed without extraordinary resources by incorporating pairs of laser pulses with spectra shifted by amounts equal to the mode frequencies of interest. Such a two-color approach would circumvent the need for sub-20-fs pulses.

4.7. REFERENCES

(1) Goodno, G. D.; Dadusc, G.; Miller, R. J. D. *J. Opt. Soc. Am. B* **1998**, *15*, 1791.

(2) Asplund, M. C.; Zanni, M. T.; Hochstrasser, R. M. *Proc. Natl. Acad. Sci.* **2000**, *97*, 8219.

(3) Hybl, J. D.; Albrecht Ferro, A.; Jonas, D. M. *J. Chem. Phys.* **2001**, *115*, 6606.

(4) Khalil, M.; Demirdöven, N.; Tokmakoff, A. *J. Phys. Chem. A* **2003**, *107*, 5258.

(5) Brixner, T.; Mancal, T.; Stiopkin, I. V.; Fleming, G. R. *J. Chem. Phys.* **2004**, *121*, 4221.

(6) Tekavec, P. F.; Lott, G. A.; Marcus, A. H. *J. Chem. Phys.* **2007**, *127*, 214307/1.

(7) Shim, S.-H.; Zanni, M. T. *Phys. Chem. Chem. Phys.* **2009**, *11*, 748.

(8) Jonas, D. M. *Annu. Rev. Phys. Chem.* **2003**, *54*, 425.

(9) Ogilvie, J. P.; Kubarych, K. J. *Adv. At. Mol. Opt. Phys.* **2009**, *57*, 249.

(10) Hamm, P.; Zanni, M. T. *Concepts and Methods of 2D Infrared Spectroscopy*; Cambridge University Press: Cambridge, 2011.

(11) Cundiff, S. T.; Mukamel, S. *Physics Today* **2013**, *66*, 45.

(12) Cho, M. *Chem. Rev.* **2008**, *108*, 1331.

(13) Kim, Y. S.; Hochstrasser, R. M. *Proc. Natl. Acad. Sci.* **2005**, *102*, 11185.

(14) Fayer, M. D. *Annu. Rev. Phys. Chem.* **2009**, *60*, 21.

(15) Anna, J. M.; Ross, M. R.; Kubarych, K. J. *J. Phys. Chem. A* **2009**, *113*, 6544.

(16) Collini, E.; Wong, C. Y.; Wilk, K. E.; Curmi, P. M. G.; Brumer, P.; Scholes, G. D. *Nature* **2010**, *463*, 644.

(17) Schlau-Cohen, G. S.; Ishizaki, A.; Fleming, G. R. *Chem. Phys.* **2011**, *386*, 1.

(18) Bixner, O.; Lukes, V.; Mancal, T.; Hauer, J.; Milota, F.; Fischer, M.; Pugliesi, I.; Bradler, M.; Schmid, W.; Riedle, E.; Kauffmann, H. F.; Christensson, N. *J. Chem. Phys.* **2012**, *136*, 204503/1.

(19) Lynch, M. S.; Slenkamp, K. M.; Khalil, M. *J. Chem. Phys.* **2012**, *136*, 241101.

(20) Lewis, K. L. M.; Ogilvie, J. P. *J. Phys. Chem. Lett.* **2012**, *3*, 503.

(21) West, B. A.; Molesky, B. P.; Giokas, P. G.; Moran, A. M. *Chem. Phys.* **2013**, *423*, 92.

(22) Consani, C.; Auböck, G.; van Mourik, F.; Chergui, M. *Science* **2013**, *339*, 1586.

(23) Berg, M.; Vanden Bout, D. A. *Acc. Chem. Res.* **1997**, *30*, 65.

(24) Kubarych, K. J.; Milne, C. J.; Lin, S.; Astinov, V.; Miller, R. J. D. *J. Chem. Phys.* **2002**, *116*, 2016.

(25) Kaufman, L. J.; Heo, J.; Ziegler, L. D.; Fleming, G. R. *Phys. Rev. Lett.* **2002**, *88*, 207402:1.

(26) Fujiyoshi, S.; Takeuchi, S.; Tahara, T. *J. Phys. Chem. A* **2003**, *107*, 494.

(27) Kukura, P.; McCamant, D. W.; Mathies, R. A. *Annu. Rev. Phys. Chem.* **2007**, *58*, 461.

(28) Weigel, A.; Dobryakov, A.; Klaumünzer, B.; Sajadi, M.; Saalfrank, P.; Ernsting, N. P. *J. Phys. Chem. B* **2011**, *115*, 3656.

(29) Rhinehart, J. M.; Challa, J. R.; McCamant, D. W. *J. Phys. Chem. B* **2012**, *116*, 10522.

(30) Yu, W.; Zhou, J.; Bragg, A. E. *J. Phys. Chem. Lett.* **2012**, *3*, 1321.

(31) Grumstrup, E. M.; Chen, Z.; Vary, R. P.; Moran, A. M.; Schanze, K. S.; Papanikolas, J. P. *J. Phys. Chem. B* **2013**, *117*, 8245.

(32) Lee, J.; Challa, J. R.; McCamant, D. W. *J. Raman Spectrosc.* **2013**, *44*, 1263.

(33) Pontecorvo, E.; Ferrante, C.; Elles, C. G.; Scopigno, T. *Opt. Express* **2013**, *21*, 6866.

(34) Cina, J. A.; Kovac, P. A. *J. Phys. Chem. A* **2013**, *117*, 6084.

(35) Dorfman, K. E.; Fingerhut, B. P.; Mukamel, S. *J. Chem. Phys.* **2013**, *139*, 124113.

(36) Harbola, U.; Umapathy, S.; Mukamel, S. *Phys. Rev. A* **2013**, *88*, 011801.

(37) Kraack, J. P.; Wand, A.; Buckup, T.; Motzkus, M.; Ruhman, S. *Phys. Chem. Chem. Phys.* **2013**, *15*, 14487.

(38) Liebers, J.; Scaria, A.; Materny, A.; Kleinekathöfer, U. *Phys. Chem. Chem. Phys.* **2010**, *12*, 1351.

(39) Marek, M. S.; Buckup, T.; Motzkus, M. *J. Phys. Chem. B* **2011**, *115*, 8328.

(40) Underwood, D. F.; Blank, D. A. *J. Phys. Chem. A* **2005**, *109*, 3295.

(41) Moran, A. M.; Nome, R. A.; Scherer, N. F. *J. Chem. Phys.* **2007**, *127*, 184505:1.

(42) Sun, X.; Stratt, R. M. *Phys. Chem. Chem. Phys.* **2012**, *14*, 6320.

(43) Park, S.; Kim, J.; Scherer, N. F. *Phys. Chem. Chem. Phys.* **2012**, *14*, 8116.

(44) Schmidtke, S. J.; Underwood, D. F.; Blank, D. A. *J. Phys. Chem. A* **2005**, *109*, 7033.

(45) Takeuchi, S.; Ruhman, S.; Tsuneda, T.; Chiba, M.; Taketsugu, T.; Tahara, T. *Science* **2008**, *322*, 1073.

(46) Banin, U.; Kosloff, R.; Ruhman, S. *Isr. J. Chem.* **1993**, *33*, 141.

(47) Benjamin, I.; Banin, U.; Ruhman, S. *J. Chem. Phys.* **1993**, *98*, 8337.

(48) Johnson, A. E.; Myers, A. B. *J. Chem. Phys.* **1995**, *104*, 3519.

(49) Johnson, A. E.; Myers, A. B. *J. Phys. Chem.* **1996**, *100*, 7778.

(50) Johnson, A. E.; Myers, A. B. *J. Chem. Phys.* **1996**, *104*, 2497.

(51) Gershgoren, E.; Gordon, E.; Ruhman, S. *J. Chem. Phys.* **1997**, *106*, 4806.

(52) Kühne, T.; Küster, R.; Vöhringer, P. *Chem. Phys.* **1998**, *233*, 161.

(53) Hess, S.; Bürsing, H.; Vöhringer, P. *J. Chem. Phys.* **1999**, *111*, 5461.

(54) Blank, D. A.; Kaufman, L. J.; Fleming, G. R. *J. Chem. Phys.* **1999**, *111*, 3105.

(55) Jansen, T. I. C.; Snijders, J. G.; Duppen, K. *J. Chem. Phys.* **2001**, *114*, 109210.

(56) Wilson, K. C.; Lyons, B.; Mehlenbacher, R.; Sabatini, R.; McCamant, D. W. *J. Chem. Phys.* **2009**, *131*, 214502.

(57) Mehlenbacher, R.; Lyons, B.; Wilson, K. C.; Du, Y.; McCamant, D. W. *J. Chem. Phys.* **2009**, *131*, 244512.

(58) Tokmakoff, A.; Lang, M. J.; Larsen, D. S.; Fleming, G. R.; Chernyak, V.; Mukamel, S. *Phys. Rev. Lett.* **1997**, *79*, 2702.

(59) Tseng, C.-H.; Sándor, P.; Kotur, M.; Weinacht, T. C.; Matsika, S. *J. Phys. Chem. A* **2012**, *116*, 2654.

(60) West, B. A.; Moran, A. M. *J. Phys. Chem. Lett.* **2012**, *3*, 2575.

(61) West, B. A.; Giokas, P. G.; Molesky, B. P.; Ross, A. D.; Moran, A. M. *Opt. Express* **2013**, *21*, 2118.

(62) Krebs, N.; Pugliesi, I.; Hauer, J.; Riedle, E. *New. J. Phys.* **2013**, *15*, 085016.

(63) Widom, J. R.; Johnson, N. P.; von Hippel, P. H.; Marcus, A. H. *New. J. Phys.* **2013**, *15*, 025028.

(64) Rahav, S.; Mukamel, S. *Angew. Chem. In. Ed.* **2010**, *49*, 9666.

(65) Rivalta, I.; Nenov, A.; Cerullo, G.; Mukamel, S.; Garavelli, M. *Int. J. Quantum Chem.* **2014**, *114*, 85.

(66) Zimdars, D.; Francis, R. S.; Ferrante, C.; Fayer, M. D. *J. Chem. Phys.* **1997**, *106*, 7498.

(67) Ajdarzadeh Oskouei, A.; Bräm, O.; Cannizzo, A.; van Mourik, F.; Tortschanoff, A.; Chergui, M. *J. Mol. Liq.* **2008**, *141*, 118.

(68) West, B. A.; Womick, J. M.; Moran, A. M. *J. Phys. Chem. A* **2011**, *115*, 8630.

(69) Fuji, T.; Suzuki, T.; Serebryannikov, E. E.; Zheltikov, A. *Phys. Rev. A* **2009**, *80*, 063822.

(70) Ghotbi, M.; Beutler, M.; Noack, F. *Opt. Lett.* **2010**, *35*, 3492.

(71) Durfee, C. G.; Backus, S.; Kapteyn, H. C.; Murnane, M. M. *Opt. Lett.* **1999**, *24*, 697.

(72) Jailaubekov, A. E.; Bradforth, S. E. *Appl. Phys. Lett.* **2005**, *87*, 021107:1.

(73) West, B. A.; Molesky, B. P.; Montoni, N. P.; Moran, A. M. *New. J. Phys.* **2013**, *15*, 025007.

(74) Aközbek, N.; Becker, A.; Chin, S. L. *Laser Phys.* **2005**, *15*, 607.

(75) Fork, R. L.; Cruz, C. H. B.; Becker, P. C.; Shank, C. V. *Opt. Lett.* **1987**, *12*, 483.

(76) van Veldhoven, E.; Khurmi, C.; Zhang, X.; Berg, M. A. *ChemPhysChem* **2007**, *8*, 1761.

(77) Kern, S. J.; Kalyanasis, S.; Berg, M. A. *Nano. Lett.* **2011**, *11*, 3493.

(78) Berg, M. A. *Adv. Chem. Phys.* **2012**, *150*, 1.

(79) Pecourt, J.-M.; Peon, J.; Kohler, B. *J. Am. Chem. Soc.* **2001**, *123*, 10370.

(80) Reuther, A.; Iglev, H.; Laenan, R.; Laubereau, A. *Chem. Phys. Lett.* **2000**, *325*, 360.

(81) Tauber, M. J.; Mathies, R. A.; Chen, X.; Bradforth, S. E. *Rev. Sci. Instrum.* **2003**, *74*, 4958.

(82) Lepetit, L.; Chériaux, G.; Joffre, M. *J. Opt. Soc. Am. B* **1995**, *12*, 2467.

(83) Gallagher, S. M.; Albrecht, A. W.; Hybl, J. D.; Landin, B. L.; B~Rajaram; Jonas, D. M. *J. Opt. Soc. Am. B* **1998**, *15*, 2338.

(84) Nitzan, A. *Chemical Dynamics in Condensed Phases*; Oxford University Press: Oxford, 2006.

(85) Mukamel, S. *Principles of Nonlinear Optical Spectroscopy*; Oxford University Press: New York, 1995.

(86) Valkunas, L.; Abramavicius, D.; Mančal, T. *Molecular Excitation Dynamics and Relaxation: Quantum Theory and Spectroscopy* Wiley-VCH: Weinheim, 2013.

(87) Myers, A. B. Excited Electronic State Properties From Ground-State Resonance Raman Intensities. In *Laser Techniques in Chemistry*; Myers, A. B., Rizzo, T. R., Eds.; John Wiley & Sons: New York, 1995; Vol. 23; pp 325.

(88) Moran, A. M.; Kelley, A. M. *J. Chem. Phys.* **2001**, *115*, 912.

(89) Kelley, A. M. *J. Phys. Chem. A* **1999**, *103*, 6891.

(90) Yang, T.-S.; Chang, M.-S.; Hayashi, M.; Lin, S. H.; Vöhringer, P.; Dietz, W.; Scherer, N. F. *J. Chem. Phys.* **1999**, *110*, 12070.

(91) Moran, A. M.; Maddox, J. B.; Hong, J. W.; Kim, J.; Nome, R. A.; Bazan, G. C.; Mukamel, S.; Scherer, N. F. *J. Chem. Phys.* **2006**, *124*, 194904:1.

(92) Ren, H.; Lai, Z.; Biggs, J. D.; Wang, J.; Mukamel, S. *Phys. Chem. Chem. Phys.* **2013**, *15*, 19457.

(93) West, B. A.; Womick, J. M.; Moran, A. M. *J. Phys. Chem. A* **2013**, *117*, 5865.

(94) Garret-Roe, S.; Hamm, P. *J. Chem. Phys.* **2009**, *130*, 164510.

(95) Zhang, J.; Wang, Z.; Kobayashi, T. *Phys. Rev. B* **2008**, *77*, 153202:1.

(96) Ivanecky III, J. E.; Wright, J. C. *Chem. Phys. Lett.* **1993**, *206*, 437.

(97) Okumara, K.; Tanimura, Y. *J. Chem. Phys.* **1997**, *107*, 2267.

(98) Ding, F.; Fulmer, E. C.; Zanni, M. T. *J. Chem. Phys.* **2005**, *123*, 094502.

(99) Fulmer, E. C.; Ding, F.; Zanni, M. T. *J. Chem. Phys.* **2005**, *122*, 034302.

(100) Busby, E.; Carroll, E. C.; Chinn, E. M.; Chang, L.; Moulé, A. J.; Larsen, D. S. *J. Phys. Chem. Lett.* **2011**, *2*, 2764.

(101) Turner, D. B.; Wilk, K. E.; Curmi, P. M. G.; Scholes, G. D. *J. Phys. Chem. Lett.* **2011**, *2*, 1904.

(102) Van Wart, H. E.; Lewis, A.; Scheraga, H. A.; Saeva, F. D. *Proc. Natl. Acad. Sci.* **1973**, *70*, 2619.

CHAPTER 5: ELUCIDATION OF REACTIVE WAVEPACKETS BY TWO-DIMENSIONAL RESONANCE RAMAN SPECTROSCOPY[1]

5.1. Introduction

Models used to describe photoinduced electronic relaxation mechanisms in condensed phases are often based on perturbative descriptions at the level of Fermi's Golden Rule (e.g. Marcus equation, Forster energy transfer).[1-3] Such second-order rate theories typically assume an equilibrium initial condition in the photoexcited state of the system prior to the non-radiative transition of interest. This assumption is generally poor when applied to processes that occur on a time scale faster than solvation and/or vibrational dephasing. Recent studies show that non-trivial quantum effects may emerge when electronic and nuclear relaxation processes become time-coincident.[4] For example, in charge transfer processes that are time-coincident with vibrational dephasing, bursts of population flow have been observed in polymer-fullerene blends,[5] photosynthetic complexes,[6] and at interfaces of semiconductors.[7,8] Transient coupling between electronic and vibrational degrees of freedom has also been implicated in sub-picosecond energy transfer transitions.[9-15] The two-dimensional resonance Raman (2DRR) techniques developed in this work are motivated by new insights into these types of non-equilibrium dynamics.

In this paper, the sensitivity of 2DRR spectroscopy to coherent reaction mechanisms is demonstrated with measurements conducted on the photodissociation process of triiodide. Two-

[1] This chapter previously appeared as an article in the Journal of Chemical Physics. The original citation is as follows: Guo, Z.; Molesky, B. M.; Cheshire, T. P.; Moran, A. M. *J. Chem. Phys.* **2015**, *143*, 124202.

color laser pulse configurations are used to selectively detect vibrational motions of the triiodide reactant and/or diiodide photoproduct in the two dimensions of the 2DRR spectrum. The unique power of the technique is ultimately realized using a pulse sequence, where vibrational resonances of triiodide and diiodide appear in separate dimensions. These "cross peaks" represent events in which a nuclear wavepacket transitions between reactant and product states without loss of coherence. Below we explore how 2DRR spectroscopy can be used to expose non-trivial correlations between the nonequilibrium geometry of the reactant and vibrational coherence frequency of the product. Such information cannot be derived from four-wave mixing spectroscopies, which possess only one "population time" in which nuclear wavepacket motions take place.

Ultrafast spectroscopic investigations of the photodissociation process in solvated triiodide are motivated by knowledge of the extraordinary reaction mechanism in this well-defined system.[16-23] Light absorption by triiodide in the ultraviolet spectral range induces photodissociation on a time-scale that is shorter than[16,19] or comparable to[22,24] the vibrational period of diiodide. Photodissociation of triiodide acts as an impulse that initiates vibrational coherence in the bond stretching coordinate of diiodide. Information about the geometry changes that transform the reactant to the photoproduct can be derived from oscillatory components of transient absorption signals. For example, earlier work has shown that the oscillatory amplitude reflects symmetry breaking in the excited state,[20] whereas the "chirp" in the waveform of the vibrational coherence represents time evolution of the bond strength during the reaction.[22] It has also been demonstrated that photodissociation yields distinct populations of free solvated diiodide and a contact fragment pair (diiodide and iodine).[25] Of relevance to the present 2DRR study, recent work suggests that the vibrational mode in free solvated diiodide

dephases on a time scale that is longer than the 300-fs vibrational period, whereas overdamped vibrational motion tends to take place in the contact radical pair.[24]

We recently measured 2DRR spectra of triiodide using deep UV laser pulses.[26] This approach was sensitive to ground state wavepacket motions in the triiodide molecule, but did not convey detailed information about the photodissociation mechanism. Examination of this simple nonlinearity was motivated by the ability to compare experimental 2DRR spectra with those simulated using the Hamiltonian of triiodide determined in earlier spontaneous resonance Raman studies.[27-29] Together with a battery of control experiments, these simulations were essential for ruling out cascades of four-wave mixing signal fields, which are known to significantly challenge 2D Raman experiments conducted under off-resonant conditions.[30-34] We concluded that the desired 2DRR response will generally be dominant in systems with large excited state potential energy surface displacements. In effect, Franck-Condon activity obviates the selection rules that favor cascaded signal intensity under off-resonant conditions.

5.2. 2DRR Spectra Simulated for a Reactive Model System

As implemented in this work, 2DRR spectroscopy is a fifth-order technique in which vibrational coherences are detected in two delay times between laser pulses. In contrast, vibrational coherences may be investigated during only one pulse delay time in a traditional third-order pump-probe spectroscopy. The goal of the model presented in this section is to establish spectroscopic signatures corresponding to particular classes of terms in the 2DRR response function. It is important to carry out such an analysis, because the 2DRR nonlinearity is more complicated than that associated with a traditional pump-probe experiment.[1]

Vibrational motions in the ground electronic state of triiodide were detected in our earlier all-UV 2DRR experiments.[26] Here, sensitivity to the diiodide photoproduct is derived by applying laser pulses in a spectral range that is electronically off-resonant with triiodide at equilibrium.[16-23] The patterns of 2DRR resonances associated with such two-color pulse sequences are explored with model calculations below.

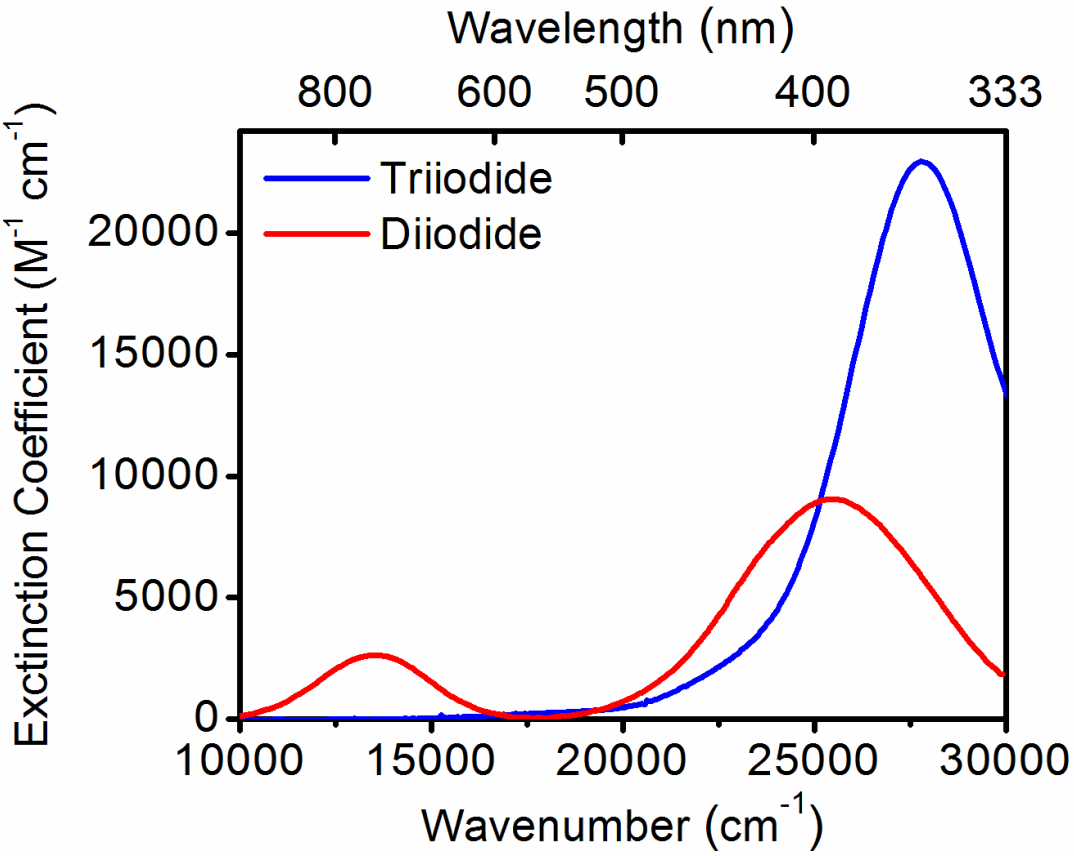

Figure 5.1. Linear absorbance spectra of triiodide and diiodide in ethanol. The absorbance spectrum of triiodide is directly measured, whereas that of diiodide is derived from Reference [35] because it is not stable in solution. Diiodide is probed on the picosecond time scale in the present work. The electronic resonance frequencies associated with this nonequilibrium state of diiodide are likely red-shifted from those displayed above.

5.2.1. Model Hamiltonians

The electronic resonances relevant to the experiments conducted in this work are displayed in Figure 5.1. The resonance of triiodide centered near 27,800 cm^{-1} is excited in all experiments. In a single experiment, either the lower (13,300 cm^{-1}) or higher-frequency (25,400 cm^{-1}) electronic resonance of diiodide is probed (i.e. the 2DRR experiments presented below are two-color rather than three-color). Therefore, the nonlinear optical response associated with all measurements presented below may be simulated using a Hamiltonian in which each molecule, triiodide and diiodide, is treated as an effective two-level electronic system. Explicit inclusion of additional off-resonant electronic states will have a negligible impact on these signals. The effective Hamiltonian for triiodide can be written as

$$H_{triiodide} = |r\rangle\langle r|\sum_{m=0}^{\infty}|m\rangle\langle m|\left[E_r + E_m\right] + |r*\rangle\langle r*|\sum_{n=0}^{\infty}|n\rangle\langle n|\left[E_{r*} + E_n\right] \tag{5.1}$$

whereas that of diiodide is given by

$$H_{diiodide} = |p\rangle\langle p|\sum_{m=0}^{\infty}|m\rangle\langle m|\left[E_p + E_m\right] + |p*\rangle\langle p*|\sum_{n=0}^{\infty}|n\rangle\langle n|\left[E_{p*} + E_n\right]. \tag{5.2}$$

Here, r and p represent the ground electronic states of triiodide and diiodide, whereas an asterisk is used to denote the excited electronic state. The energies, E_r and E_r^* (E_p and E_p^*), correspond to the ground and excited states, respectively. The dummy indices, m and n, represent vibrational levels belonging to the ground and excited electronic states.

The transition energies of each system, $E_{r*} - E_r$ and $E_{p*} - E_p$, are readily derived from the absorbance spectra presented in Figure 5.1. The two potential energy surfaces that belong to

each molecule must also be described in order to generate the vibrational energy levels, E_m and E_n. The ground state potential energy surfaces must be modeled with a far greater level of detail than the excited state potential energy surfaces in order for the model to generate realistic spectroscopic signals. Insensitivity to the global excited state potential energy surfaces is taken into account when writing the summations over quantized vibrational levels for the dissociative excited states in $H_{triiodide}$ and $H_{diiodide}$. We next discuss the approximations made in the descriptions of the potential energy surfaces in a qualitative way. Further technical details about the parameterization of the potential energy surfaces are given in Appendix B.

The summations over quantized levels for the ground states in $H_{triiodide}$ and $H_{diiodide}$ are clearly motivated. Previous literature can be used to guide decisions about parameters.[16,19,27] The vibrational motions of triiodide and diiodide detected in this work are known to occur in the electronic ground states, because the excited states of both systems are dissociative.[16,19] Vibrational resonances in the ground electronic state of triiodide have been detected in both spontaneous and stimulated Raman experiments carried out with deep and near ultraviolet laser beams.[16,27] In this work, signals will be simulated using a harmonic ground-state potential for triiodide, because only the lowest-energy vibrational states contribute to the signals. Resonance Raman experiments suggest that the harmonic approximation is indeed reasonable for these energy levels.[27] In two-color transient absorption experiments (ultraviolet pump with visible and near-infrared probes), the relationship between the vibrational phase and detection wavelength was used to assign wavepacket motions to the electronic ground state in diiodide.[16,19] The ground state potential energy surface of diiodide is modeled using a cubic potential in this work, because higher-energy vibrational levels (near 12 quanta) are known to contribute to the response following photodissociation.[19] Introduction of the cubic potential is required to obtain

agreement between theoretical and experimental vibrational frequencies, but does not impact the patterns of peaks in the 2DRR spectra.

The shapes of the excited state potentials require far less detail than those of the ground states, because the experiments presented here are sensitive only to the potential energy gradient near the Franck-Condon geometry.[36] This aspect of the response is made clear by the absence of vibronic progressions in the absorbance spectra shown in Figure 5.1. In the semiclassical perspective, this means that the wavepacket initiated on the excited state potential energy surface does not return to the Franck-Condon geometry before electronic dephasing is complete (i.e. electronic dephasing is on the order of 10-20 fs).[37] The excited state potential energy gradient near the Franck-Condon geometry primarily governs the amplitude of the wavepacket stimulated in the ground electronic state. Here, we use the cubic fitting parameters for the London-Eyring-Polanyi-Sato (LEPS) excited state potential energy surface of triiodide in ethanol.[18,27] Johnson and Myers used a similar displaced oscillator model for triiodide to achieve reasonable agreement with spontaneous Raman spectra.[27] The gradient of the excited state potential energy surface of diiodide at the Franck-Condon geometry is approximated by displacing a replica of the cubic ground state potential energy surface. We have chosen a set of parameters that produces a gradient which is consistent with models used in other work (see Appendix B).[24,25]

5.2.2. Response Functions

We consider three types of 2DRR nonlinearities: (i) both dimensions correspond to the triiodide reactant; (ii) both dimensions correspond to the diiodide photoproduct; (iii) the vibrational resonances of triiodide and diiodide appear in separate dimensions. As in Section 5.2.1, we use a notation where the indices r and $r*$ represent the ground and lowest-energy

excited electronic states of the triiodide reactant. Likewise, p and $p*$ correspond to the ground and lowest-energy excited states of the diiodide photoproduct. Vibrational levels associated with these electronic states are specified by dummy indices (m, n, j, k, l, u, v, w). The Feynman diagrams presented in Figure 5.2 show that the vibrational coherences detected in 2DRR spectra evolve in the two time intervals with even indices (t_2 and t_4). Electronic (or vibronic) coherences, which dephase in 10's of fs for solvated triiodide, evolve in the time intervals that correspond to odd indices (t_1, t_3, and t_5). It is useful to consider that the experimentally controlled pulse delay times, τ_1 and τ_2, are good approximations to the time intervals between field-matter interactions, t_2 and t_4.

The first class of nonlinearities shown in Figure 5.2 (i.e. terms 1-4) involves vibrational motions of only the triiodide reactant.[26] In contrast to terms 1-4, the Feynman diagrams associated with the other two classes of response functions incorporate the photodissociation process as a transfer of vibronic coherence from triiodide to diiodide either before (terms 5-8) or after (terms 9-12) evolution of the vibrational coherence in t_2 (i.e. the delay time, τ_1). In the present model, we assume that the reaction is faster than the 300-fs period of the symmetric stretching coordinate in triiodide. This separation in time scales is consistent with the finding of vibrational coherence in diiodide (i.e. vibrational motions in the ensemble can dephase if the reaction is not impulsive). It was understood in earlier studies that photodissociation is faster than the 300-fs vibrational period.[16,19] However, some later work suggests that the reaction takes place on nearly the same time scale as the vibrational period (i.e. a few hundred femtoseconds).[22,24] In any case, we consider the impulsive approximation to be reasonable here, because it does not impact the pattern of peaks in the 2DRR spectra.

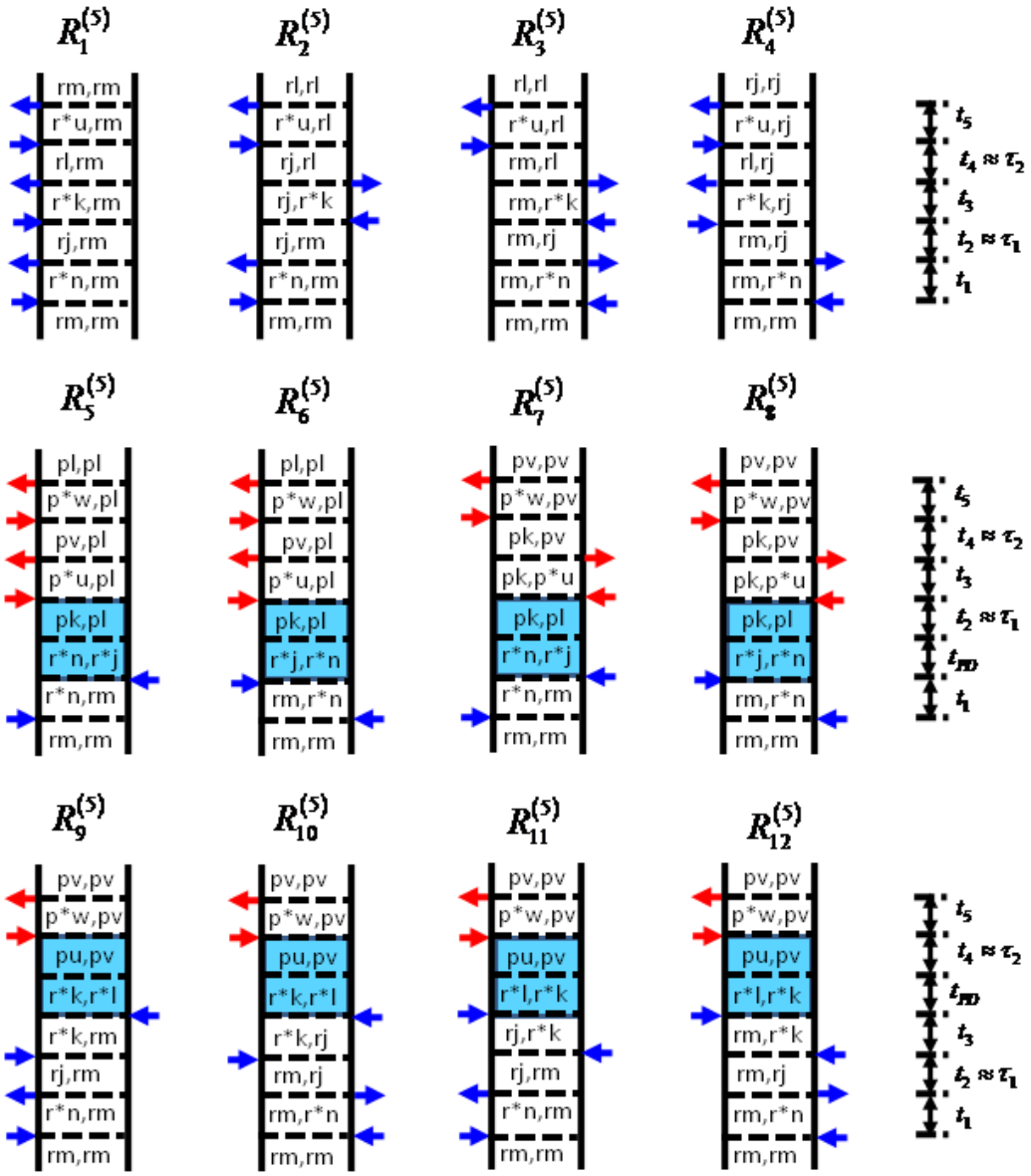

Figure 5.2. Feynman diagrams associated with dominant 2DRR nonlinearities. Blue and red arrows represent pulses resonant with triiodide and diiodide, respectively. The indices r and $r*$ represent the ground and excited electronic states of the triiodide reactant, whereas p and $p*$ correspond to the diiodide photoproduct. Vibrational levels associated with these electronic states are specified by dummy indices (m, n, j, k, l, u, v, w). Each row represents a different class of terms: (i) both dimensions correspond to triiodide in terms 1-4; (ii) both dimensions correspond to diiodide in terms 5-8; (iii) vibrational resonances of triiodide and diiodide appear in separate dimensions in terms 9-12. The intervals shaded in blue represent a non-radiative transfer of vibronic coherence from triiodide to diiodide.

As in Reference [26], response functions are written in the "snapshot" limit, where the laser pulses are short compared to the vibrational period but long compared to electronic dephasing.[1] Both approximations are appropriate for the experiments described below. We additionally take the finite bandwidths of the laser pulses into account in the expressions for the nuclear wavepackets. Under these approximations, the polarization components consist of products of Lorentzian functions (see Appendix B for derivation). For example, the first term is given by

$$P_1^{(5)}(\omega_1,\omega_2) = -\frac{N\xi_{UV}^5 \left|\mu_{r^*r}\right|^6}{\hbar^5} \sum_{mnjklu} B_m \langle n|m\rangle\langle n|j\rangle\langle k|j\rangle\langle k|l\rangle\langle u|l\rangle\langle u|m\rangle \times L_{r^*n,rm}(\omega_{UV}) D_{rj,rm}(\omega_1) L_{r^*k,rm}(\omega_{UV}) D_{rl,rm}(\omega_2) L_{r^*u,rm}(\omega_t) \tag{5.3}$$

where

$$L_{r^*n,rm}(\omega) = \frac{1}{\omega - \omega_{r^*r} - \omega_{nm} + i\Gamma_{r^*r}} \tag{5.4}$$

and

$$D_{rk,rm}(\omega) = \frac{2\Gamma_{vib} + 4\Lambda_{UV}}{\omega_{km}^2 + \left(\Gamma_{vib} + 2\Lambda_{UV}\right)^2}\left(\frac{1}{\omega - \omega_{km} + i\Gamma_{vib}}\right). \tag{5.5}$$

Here, $\langle n|m\rangle$ is a vibrational overlap integral, where the index on the left represents the vibrational level of the excited electronic state (i.e. the same notation is used in Reference [38]). The subscript of the electric field, *UV*, denotes an interaction with the lowest-energy electronic resonance of triiodide (VIS denotes an interaction with either electronic resonance of diiodide). The remaining 11 response functions are given in Appendix B.

The parameters given in Table 5.1 are chosen to approximate the properties of triiodide and diiodide. The electronic and vibrational resonance frequencies of both systems have been determined in earlier studies.[16-23,26] We take the potential energy surface of the ground state of triiodide to be harmonic in agreement with spontaneous resonance Raman experiments.[27] The excited state potential energy surface of triiodide and both the ground and excited state potential energy surfaces of diiodide are expanded to the cubic term.[26] Cubic expansion coefficients of -1 cm^{-1} (see Equation B.2 in Appendix B) approximate the LEPS surface of triiodide[17] and capture the 100-cm^{-1} gap between successive energy levels in diiodide near 20 vibrational quanta.[19] Evaluation of the vibrational overlap integrals in the response function is accomplished by assuming a dimensionless displacement of 7.0 for both triiodide and diiodide. This value of the displacement is consistent with spontaneous Raman measurements[27] and our previous 2DRR study of triiodide.[26] A displacement of 7.0 also produces an excited state potential energy gradient in diiodide (225 eV/pm) that is identical to that associated with a commonly employed exponential surface at a displacement of only 9 pm from the Franck-Condon geometry.[24,25] As discussed in Section 5.2.1, this gradient is the key quantity that must be reproduced by the present model, because electronic dephasing is fast compared to the vibrational period.

Table 5.1. Parameters of Model Used to Compute 2DRR Spectra

[a]Parameter	Value
$\omega_{r^*r} / 2\pi c$	27,800 cm^{-1}
[b] $\omega_{p^*p} / 2\pi c$	13,300 cm^{-1} & 25,400 cm^{-1}
[c] $\omega_{r,vib} / 2\pi c = \omega_{r^*,vib} / 2\pi c$	111 cm^{-1}
[c] $\omega_{p,vib} / 2\pi c = \omega_{p^*,vib} / 2\pi c$	114 cm^{-1}
[c] $U_{3,r} / hc$	0 cm^{-1}
[c] $U_{3,r^*} / hc = U_{3,p} / hc = U_{3,p^*} / hc$	-1 cm^{-1}
$\Gamma_{r,vib} / c = \Gamma_{r^*,vib} / c = \Gamma_{p,vib} / c = \Gamma_{p^*,vib} / c$	10 cm^{-1}
$\Gamma_{r^*r} / c = \Gamma_{p^*p} / c$	2000 cm^{-1}
[d] μ_{r^*r}	2.3 D
[d] μ_{p^*p}	1.0 D
[e] $\omega_{UV} / 2\pi c$	29,400 & 25,000 cm^{-1}
[f] $\omega_{VIS} / 2\pi c$	14,705 & 18,900 cm^{-1}
$\omega_t / 2\pi c$	$\omega_{VIS} / 2\pi c$
$\Lambda_{UV} / c = \Lambda_{VIS} / c$	500 cm^{-1}

[a] The indices r and p represent triiodide and diiodide, respectively. Asterisks indicate the lowest-energy excited electronic states of the molecules.
[b] The electronic resonance of diiodide that is probed depends on the particular experiment (see Section 5.3). In terms 1-4 and 9-12, the resonance is located at 25,400 cm^{-1}, whereas in terms 5-8 it is equal to 13,300 cm^{-1}.
[c] Parameters of Equation B.1 in Appendix B.
[d] Magnitudes of transition dipoles do not impact line shapes of simulated 2DRR spectra.
[e] In Figure 5.3, "pump" wavenumbers are: 25,000 cm^{-1} for terms 1-4; 29,400 cm^{-1} for terms 5-8; 25,000 cm^{-1} for terms 9-12.
[f] In Figure 5.3, "probe" wavenumbers are 14,705 cm^{-1} in terms 5-8 and 20,000 cm^{-1} in terms 9-12, respectively.

5.2.3 Calculated 2DRR Spectra

Figure 5.3 presents signals that are simulated for the three types of nonlinearities. Terms 1-4 yield resonances in only the upper right and lower left quadrants of Figure 5.3a because of interferences between components of the response function.[26] For terms 5-8 in Figure 5.3b, suppression of signal intensity in the upper left and lower right quadrants originates in the same types of interferences found in terms 1-4. In terms 1-8, evolution of the system in the time intervals, t_2 and t_4, is always described by a pair of coherences in which only one of the vibrational indices is modified by the third and fourth field-matter interactions (e.g. rj in terms 2 and 4 or pl in terms 5 and 6). In contrast, calculations based on terms 9-12 yield peaks with equal intensities in all four quadrants in Figure 5.3c. *The unique pattern of resonances found in terms 9-12 reflects independence of the vibrational coherences that evolve during* t_2 and t_4. The key issue is that the photodissociaton process takes place *between* the t_2 and t_4 time intervals in terms 9-12 (see Figure 5.2). Therefore, the vibrational coherence in the time interval t_4 involves a sets of indices that are fully independent from those in t_2. In contrast, photodissociation occurs before vibrational coherences evolve in t_2 in terms 5-8, thereby placing constraints on the vibrational coherences that evolve in t_2 and t_4.

In summary, the model calculations presented in this section demonstrate that cross peaks between triiodide and diiodide appear in all four quadrants of the 2DRR spectrum. These 2DRR cross peaks may be induced with a pulse configuration in which UV pulses are employed before the τ_2 delay time, and a visible pulse is applied afterwards (see terms 9-12). This particular signature of cross peaks will generalize to other systems in which vibrational coherences of the reactant and product evolve in the ground electronic states. For such systems, only cross peaks

between the reactant and product will yield resonances in the upper left and lower right quadrants. The key issue is that the third and fourth field-matter interactions must take place with either the ket or bra in terms 1-8, thereby allowing a difference in only one of the indices that describes the coherences in τ_1 and τ_2 (see Figure 5.2).

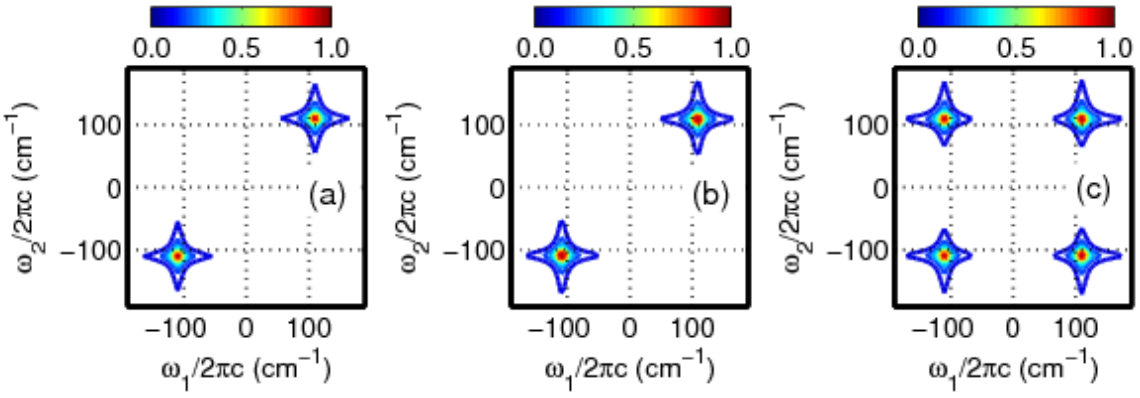

Figure 5.3. Absolute values of 2DRR spectra computed using (a) the sum of terms 1-4 in Equation B.16, (b) the sum of terms 5-8 in Equation B.17, and (c) the sum of terms 9-12 in Equation B.18 (Equations B.16-B18 are in Appendix B). The frequency dimensions, ω_1 and ω_2, are conjugate to the delay times, τ_1 and τ_2 (see Figure 5.2). Signal components of the type shown in panel (a) are generally detected in one-color experiments. Two-color 2DRR approaches are used to detect nonlinearities that correspond to panels (b) and (c) in this work. The peaks displayed in Figure 5.3c are unique in that resonances of the reactant and product are found in ω_1 and ω_2, respectively.

5.3. Experimental Methods

The 2DRR experiments conducted in this work utilize either five or three laser beams to obtain the fifth-order response. Measurements conducted in these geometries must contend with a background of residual laser light and/or lower-order nonlinearities, because fewer than six laser beams are employed.[26] In this section, we describe the two experimental setups and discuss how sources of background are dealt with.

5.3.1. Conducting 2DRR Spectroscopy with a Five-Beam Geometry

Detection of signal components described by terms 5-8 in Figure 5.2 is accomplished with a geometry of five laser beams. In Figure 5.4, it is shown that a 340 nm laser beam is simply added to an existing diffractive optic-based transient grating setup operational at 680 nm.[39] A slightly modified version of this interferometer has been described elsewhere.[40,41] Briefly, the 680 nm beams are focused on the diffractive optic with a 20-cm focal length spherical mirror and cross at 5.4º. The angle between the +1 and -1 diffraction orders is also 5.4º. Thus, a square pattern of 680 nm beams appears on the 20 cm focal length spherical mirror. The spherical mirror is tilted off-axis by approximately 5º (i.e. the minimum amount) in order to image the spot from the diffractive optic onto the sample. Focusing conditions of the 340 nm beam are optimized to match the 200 μm FWHM spot sizes of the 680 nm beams.

The 340 nm and 680 nm laser beams are produced by focusing a 0.8 mJ, 60 fs laser beam at 800 nm into a 43 cm long hollow core fiber with a 250 μm inner diameter. The continuum produced in the fiber spans the full visible spectral range. A 4 uJ, 40 nm wide portion of the continuum centered at 680 nm is filtered in a fused silica prism compressor. Most of the 680 nm beam (65%) is used to generate 340 nm light in a 100 micron thick, Type I Beta Barium Borate (BBO) crystal. In order to minimize lossy reflections, the 340 nm beam is directly imaged from the BBO onto the sample using a 15 cm focal length spherical mirror placed 30 cm from the BBO. Residual 680 nm light is filtered using a 1 mm thick fused silica polarizer. A lossy second compression step is not required for the 340 nm beam because of precompensation for dispersion in the aforementioned prism compressor; the polarizer used to filter residual 680 nm light compensates for negative chirp in the 340 nm pulse.

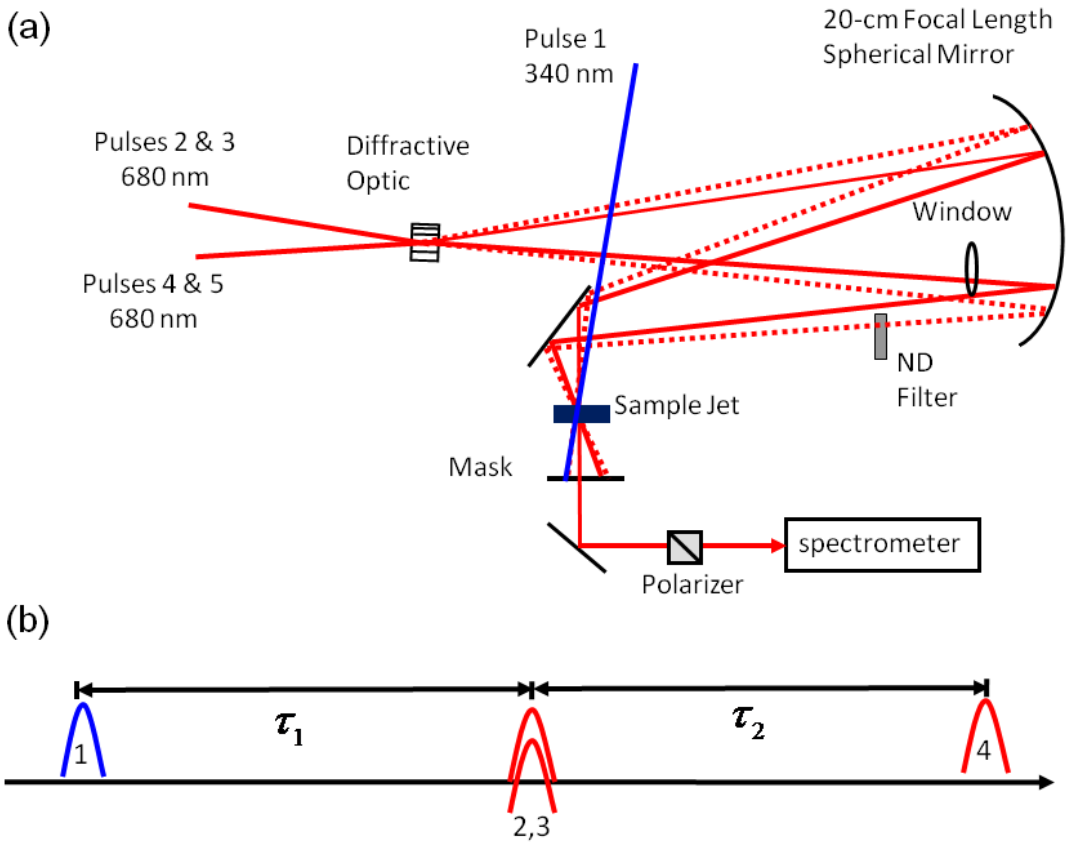

Figure 5.4. (a) Diffractive optic-based interferometer used to detect signal components described by terms 5-8 in Figure 5.2. Each of the two 680 nm beams is split into -1 and +1 diffraction orders with equal intensities at the diffractive optic. The signal is collinear with the reference field (pulse 5) used for interferometric signal detection. (b) The 340 nm pulse induces photodissociation and vibrational coherence in the diiodide photoproduct during the delay, τ_1. The time-coincident 680 nm pulses, 2 and 3, reinitiate the vibrational coherence in diiodide during the delay, τ_2.

In this pulse sequence, the 40 fs, 340 nm pulse (pulse 1 in Figure 5.4) induces a photodissociation process that leaves the diiodide photoproduct in a vibrational coherence as suggested by terms 5-8 in Figure 5.2. A time-coincident pair of 25 fs, 680 nm laser pulses (pulses 2 and 3 in Figure 5.4) reinitiates the vibrational coherence in diiodide during the delay, τ_2. The fourth pulse (also at 680 nm) induces signal emission. The fifth pulse, which is

attenuated by a factor of 1000 before the sample, is used for heterodyne detection by spectral interferometry.[42,43] The signal phase can be determined using the method devised by Turner and Scholes in this beam geometry,[44] because the 340 nm pulse does not factor into the phase calibration. Scherer and Blank have employed similar laser beam geometries and phasing schemes in related fifth-order experiments.[45-47]

An undesired four-wave mixing response may be radiated by the solvent in the same direction as the fifth-order signal in this geometry. However, because the sample is transparent at 680 nm, this four-wave mixing signal is approximately 50 times smaller than that associated with the solute at delay times greater than 80 fs. Moreover, the desired signal radiated by the solute exhibits a vibrational coherence with a period of 300 fs. Insensitivity of this setup to intramolecular vibrations of the solvent was confirmed by scanning the delay, τ_2, with the 340 nm beam blocked. Thus, the assignment of the experimentally observed 112-cm^{-1} vibrational resonance to the solute is unambiguous.[26] The 2DRR experiment may be conducted without chopping the 340 nm beam, because the desired fifth-order nonlinearity dominates the total response of the solution. Conducting the experiment without chopping the 340 nm beam greatly speeds up data acquisition and facilitates signal averaging.

Signals are detected using a back-illuminated CCD array (Princeton Instruments PIXIS 100B) mounted on a 0.3 meter spectrograph with a 600 g/mm grating. The signal generates roughly 80 counts/ms on the detector with 150 nJ, 340 nm pulses and 200 nJ, 680 nm pulses. All beams possess the same electric field polarization and are focused to 200 μm at the sample position. The two delay lines are scanned 20 times and averaged. The step sizes are 40 fs in both dimensions.

5.3.2. Conducting 2DRR Spectroscopy with a Three-Beam Geometry

Signal components of the type described by terms 9-12 are detected using a three-pulse geometry (i.e. a standard pump-repump-probe experiment).[48] As shown in Figure 5.5, the first two pulses that arrive at the sample are 25 fs, 400 nm pulses produced by self-phase modulation in a hollow core fiber,[49] whereas the third pulse is a visible continuum produced in a 3 mm thick sapphire plate. The 400 nm beams are focused onto the sample with a 30 cm focal length spherical mirror, whereas the continuum is relayed from the sapphire plate onto the sample using a single 5 cm focal length mirror (the continuum focuses 35 cm from the spherical mirror). The FWHM spot sizes of the 400 nm beams are 600 μm, whereas that of the continuum is 400 μm. Angles between the adjacent beams are 5°. Pulse energies of the 400 nm beams range from 150-300 nJ in various experiments, and we observe no differences in the vibrational lineshapes obtained within this range of pulse energies. The phases of the two chopper wheels, which are both operated at 250 Hz, are shifted by 90° to acquire signals under the four conditions needed to produce a pump-repump-probe signal ($\Delta\Delta A$).[48] Signal detection is accomplished with a CMOS array detector that is synchronized to the 1-kHz repetition rate of the laser system. The noise level of a pump-repump-probe signal is approximately 0.1 mOD in this setup. The delay lines are scanned 10 times with step sizes of 40 fs and averaged.

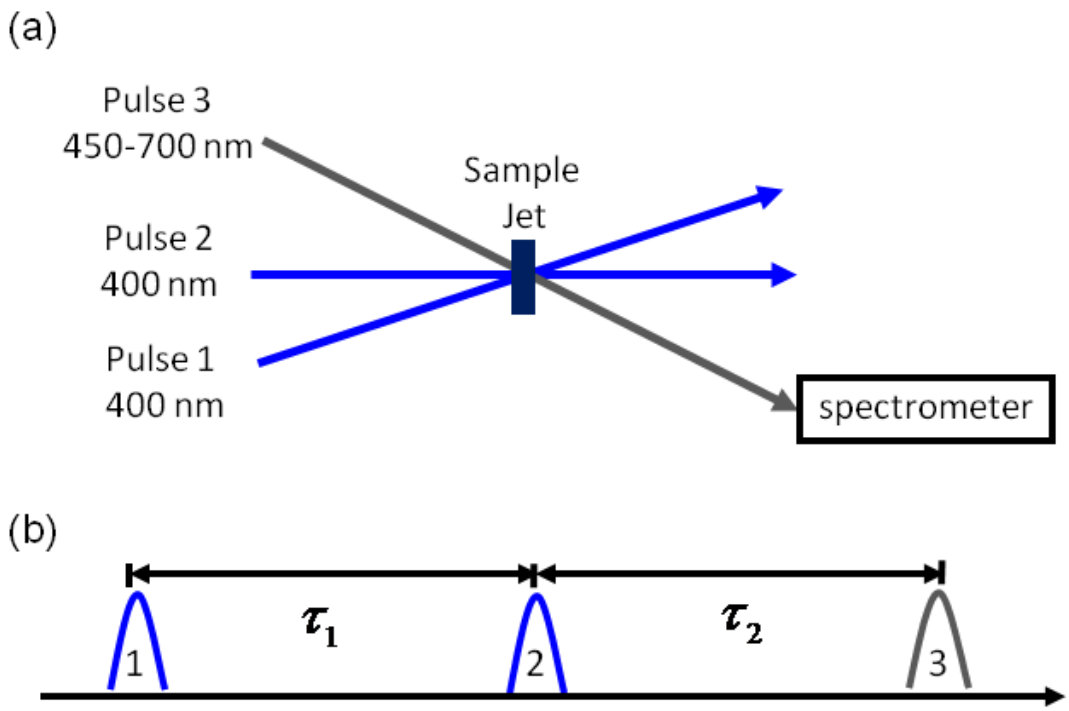

Figure 5.5. (a) Pump-repump-probe beam geometry used to detect signal components described by terms 9-12 in Figure 5.2. (b) The first 400 nm pulse promotes a stimulated Raman response in the ground electronic state of the triiodide reactant during the delay, τ_1. The second pulse induces photodissociation of the non-equilibrium reactant, thereby giving rise to vibrational coherence in the diiodide photoproduct during the delay, τ_2. Sensitivity to diiodide is enhanced by signal detection in the visible spectral range.

Two field-matter interactions with triiodide occur with each of the 400 nm pump pulses in this experiment. The first pulse stimulates wavepacket motion in the ground electronic state of triiodide as indicated in terms 9-12. The application of a second 400 nm pulse ensures that the signals are primarily sensitive to vibrational coherences of triiodide during τ_1 (i.e. signal contributions from diiodide are negligible during τ_1). The key issue is that the transient electronic resonance of triiodide is dominant at 400 nm (i.e. the bleach of the ground state). The second 400 nm pulse induces photodissociation of triiodide and leaves the diiodide photoproduct

in a vibrational coherence in τ_2. Signal detection in the visible spectral range enhances sensitivity to the diiodide product in the delay, τ_2.

5.3.3. Sample Preparation and Handling

Triiodide solutions are prepared by mixing solid I_2 (Aldrich) with 5-fold molar excess of KI (Aldrich) in ethanol (Decon Labs, 200 proof). The solutions are stirred for one hour to fully dissolve the solid. The absorbance of the solutions is equal to 0.5 at 400 nm in a 300 μm path length. The sample is flowed through a wire-guided jet with a thickness of 300 μm, where the volume of the reservoir is 50 mL.

5.4. Experimental Results

In this section, we present 2DRR signals obtained for triiodide using two-color pulse sequences. We begin by reviewing properties of the third-order pump-probe response to facilitate the subsequent discussion of 2DRR spectra.

5.4.1. Third-Order Stimulated Raman Response

The pump-probe signals shown in Figure 5.6 illustrate several aspects of the stimulated Raman response of triiodide. Vibrational coherences are observed throughout the visible spectral range as in earlier work on this system.[16-23] The modulation depth of the oscillations is greatest in the range, 18,000-21,000 cm^{-1} (475-555 nm). Coherences at detection wavenumbers below 20,000 cm^{-1} (500 nm) are dominated by diiodide, whereas signals acquired at detection wavenumbers above 20,000 cm^{-1} possess significant contributions from ground state wavepacket motions of triiodide. The vibrational coherences detected below 20,000 cm^{-1} are similarly

assigned to the ground electronic state of diiodide, because the excited state potential energy surface is dissociative.[50]

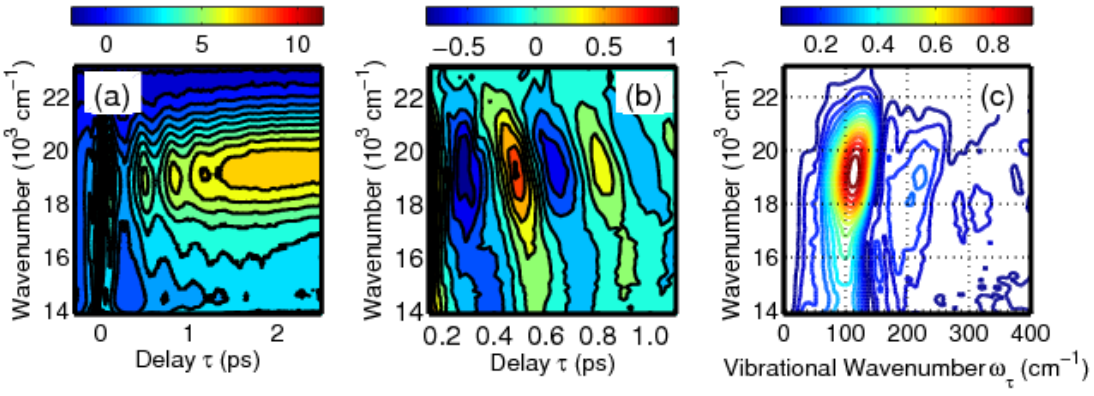

Figure 5.6. (a) Transient absorption signals (in mOD) obtained for triiodide with a 400 nm pump pulse and continuum probe pulse. (b) The coherent component of the signal is isolated by subtracting sums of 2 exponentials from the total signal presented in panel (a). (c) Fourier transformation of the signal between delay times of 0.1 and 2.5 ps shows that the vibrational frequency decreases as the detection wavenumber decreases. Dispersion in the vibrational frequency reflects sensitivity to high-energy quantum states in the anharmonic potential of diiodide.[19]

The photodissociation process is known to cause the period of vibrational motion to evolve as the delay increases.[22] In Figure 5.6b, such "chirped" wavepacket dynamics are evidenced by time evolution in the orientations of the nodal contour lines of the signal. It has been established that the strength of the chemical bond weakens as the symmetry of triiodide breaks immediately following light absorption.[16-23] The reactive wavepacket departs from the Franck-Condon geometry as one of the bonds ruptures, thereby giving rise to the time dependence of the vibrational frequency observed in Figure 5.6b. The dependence of the vibrational period on the detection wavenumber reflects sensitivity to highly excited states in the

anharmonic potential of the diiodide product. Kühne and Vöhringer determined that experiments with visible probe pulses are sensitive to states with 10-30 vibrational quanta.[19]

5.4.2. 2DRR Response of the Diiodide Photoproduct

The 2DRR response of the diiodide photoproduct is detected using the two-color approach described in Figure 5.4. The signals shown in Figure 5.7 are Fourier transformed to reveal peaks in the upper right and lower left quadrants of the 2DRR spectrum. The resonances appear near 100 cm^{-1} in both dimensions, which indicates that the experiment is sensitive to states of diiodide that possess roughly 20 vibrational quanta.[19] Vibrational resonances are not detected in the other two quadrants of the 2DRR spectrum as in our earlier study of ground state wavepacket motions in triiodide.[26] The locations of the peaks in the experimental 2DRR spectrum agree with the prediction made for terms 5-8 in Figure 5.3 (i.e. the terms this pulse sequence is designed to detect).

The data shown in Figure 5.7b indicate that the vibrational dephasing rate is slightly faster in τ_1 than it is in τ_2 (i.e. the line width is slightly larger in ω_1 than it is in ω_2). We attribute this difference in line widths to intramolecular relaxation and inertial solvation processes that occur following photodissociation in τ_1. The photoproduct is likely far from equilibrium when the vibration fully damps near 2 ps; however, a significant amount of solute-to-solvent vibrational energy transfer may still take place on this time scale.[17] This view of the information carried by each dimension of the 2DRR signal is consistent with interpretations of related optical pump/Raman probe experiments.[45-47,51-53] That is, the relaxation processes detected in the first delay time, τ_1, are related to those investigated with traditional pump-probe

experiments (e.g. vibrational cooling).[16-23] Scanning the second delay time, τ_2, essentially yields a snapshot of the vibrational spectrum as the system relaxes in τ_1.[18]

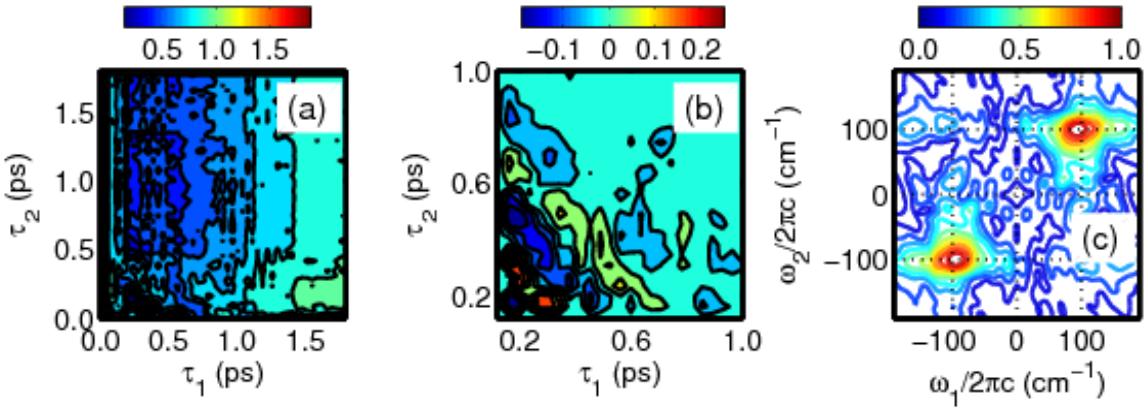

Figure 5.7. 2DRR signals associated with terms 5-8 are obtained using the two-color approach described in Figure 5.4. (a) The total signal possesses both coherent and incoherent components. (b) The coherent (Raman) component of the signal is isolated by subtracting sums of two exponentials from the total signal presented in panel (a). (c) The two-dimensional Fourier transformation of the signal in panel (b) in delay ranges, τ_1 and τ_2, between 0.15 and 2.0 ps reveals resonances in the upper right and lower left quadrants. This pattern of 2DRR resonances is consistent with calculations based on terms 5-8 (see Figure 5.3), which this experiment is designed to detect.

5.4.3. 2DRR Cross Peaks Between Triiodide and Diiodide

The 2DRR spectra theoretically predicted in Figure 5.3 are consistent with the experimental measurements shown in Figure 5.7 (terms 5-8) and our earlier all-UV 2DRR spectra (terms 1-4).[26] In both cases, peaks are found in only the upper right and lower left quadrants because of interferences between numerous terms in the response function. In this section, we test the prediction that signal components corresponding to terms 9-12 will give rise to resonances in all four quadrants of the 2DRR spectrum (see Figure 5.3c). This unique pattern

of resonances signifies a process in which a vibrational wavepacket transitions between reactant and product states without loss of coherence.

The 2DRR data presented in Figure 5.8 are obtained using the experimental setup described in Figure 5.5. The pump-repump-probe signals exhibit oscillations in both dimensions, which may be Fourier transformed to produce 2DRR spectra. Signals acquired at several detection wavenumbers are displayed to illustrate a transition between regimes in which motions of triiodide or diiodide dominate the second dimension, ω_2. At a detection wavenumber of 22,500 cm^{-1} (444 nm), where absorption of triiodide is dominant, the pattern of resonances is consistent with terms 1-4 (see Figure 5.3a). However, intensities of the vibrational resonances in the upper left and lower right quadrants of the 2DRR spectrum increase as the detection wavenumber is detuned from the absorption spectrum of triiodide. At detection wavenumbers less than 19,500 cm^{-1} (513 nm), we observe peaks with equal intensities in all four quadrants, which is consistent with the prediction made for terms 9-12 in Figure 5.3c.

The detection of peaks with equal intensities in all four quadrants is consistent with nonlinearities of the type shown in terms 9-12. The peak positions are also consistent with this assignment. The 112-cm^{-1} vibrational resonance in ω_1 is notably independent of the detection wavenumber (as it should be for the reactant). In contrast, the frequency of the vibrational resonance in ω_2 decreases as the detection wavenumber decreases. For example, we observe resonances in ω_2 at 110 cm^{-1} and 100 cm^{-1} for detection wavenumbers of 22,500 cm^{-1} (444 nm) and 18,000 cm^{-1} (555 nm), respectively.

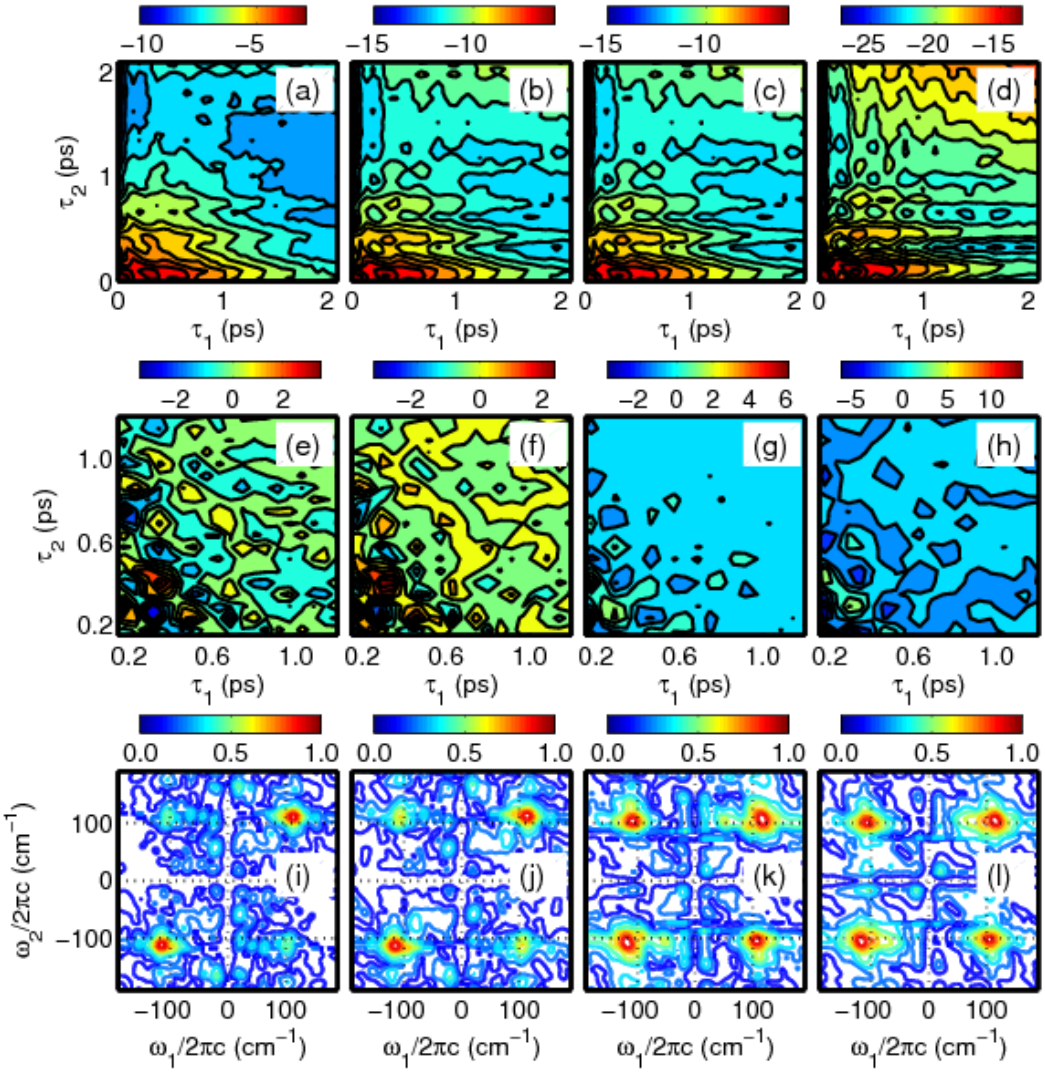

Figure 5.8. 2DRR data are obtained using the two-color approach described in Figure 5.5. Each column corresponds to a different detection wavenumber: 22,500 cm^{-1} (444 nm) in column 1; 21,000 cm^{-1} (476 nm) in column 2; 19,500 cm^{-1} (513 nm) in column 3; 18,000 cm^{-1} (555 nm) in column 4. (a)-(d) Total pump-repump-probe signal in mOD. (e)-(h) Coherent parts of the pump-repump-probe signals displayed in the first row. (i)-(l) 2DRR spectra are generated by Fourier transforming the signals shown in the second row in delay ranges, τ_1 and τ_2, between 0.15 and 2.0 ps. The data show that peaks in the upper left and lower right quadrants emerge as the detection wavenumber becomes off-resonant with triiodide. Signals acquired at detection wavenumbers above 21,000 cm^{-1} (476 nm) are dominated by stimulated Raman processes in the ground electronic state of triiodide (terms 1-4). In contrast, signals acquired at detection wavenumbers below 19,500 cm^{-1} (513 nm) are consistent with terms 9-12, where vibrational resonances in ω_1 and ω_2 correspond to triiodide and diiodide, respectively.

As discussed in Section 5.4.1, correlation between the vibrational frequency and detection wavenumber is a signature that diiodide contributes to the signal (i.e. the origin of the response transitions from terms 1-4 to terms 9-12 as the detection frequency decreases).[50] At present, 2DRR spectra cannot be measured at detection wavenumbers below 18,000 cm^{-1} (555 nm) in this setup, because of the substantial background that must be removed by chopping the pump and repump laser beams. Nonetheless, the transition between the two aforementioned regimes (i.e. terms 1-4 versus terms 9-12) is made sufficiently clear in the range of detection frequencies where adequate signal strength is obtained.

Cascades of four-wave mixing signal fields challenge the application of 2D Raman spectroscopy under off-resonant conditions. Cascades were ruled out in our previous all-UV 2DRR study of triiodide using control experiments based on the signal phase, concentration dependence of the signal intensity, and the relative phases of the vibrations detected in four and six-wave mixing signals.[26] The direct 2DRR response should be even more dominant in the present study, because lower-frequency laser beams are employed. Moreover, the direct response is favored in the present experiments for the same reasons discussed at length in Reference [26]. In Appendix B, we demonstrate that the sign of the 2DRR response is consistent with the direct fifth-order nonlinearity rather than a cascade.

5.4.4. Summary of 2DRR Signal Components

In this section, we summarize our attainment of 2DRR spectra associated with the three types of signal components. Figure 5.9 displays the present results alongside the 2DRR spectrum for ground state wavepacket motions of triiodide obtained in earlier work.[26] As shown in Figure 5.9a, the application of all-UV pulses yields a 2DRR spectrum in which the vibrational

resonances of triiodide appear in both dimensions (i.e. terms 1-4 in Figure 5.2). Similarly, vibrational motions of diiodide dominate both dimensions in Figure 5.9b , because only the first pulse is resonant with equilibrium triiodide (i.e. terms 5-8 in Figure 5.2). Finally, vibrational motions of triiodide and diiodide are detected in separate dimensions in Figure 5.9c. Here, only the final pulse to arrive at the sample is electronically off-resonant with triiodide (i.e. terms 9-12 in Figure 5.2). This type of nonlinearity is unique in that it gives rise to 2DRR spectra in which peaks with equal intensities appear in all four quadrants. The terms in the response function responsible for these peaks reflect a sequence in which a wavepacket in the symmetric stretching coordinate of triiodide transforms into a wavepacket in the bond stretching mode of diiodide without loss of coherence. 2DRR spectroscopy is specially equipped for investigations of such coherent dynamics, because it possesses two electronic "population times". In contrast, traditional third-order pump-probe experiments only have one population time.

The signature of cross peaks demonstrated in Figure 5.9 will not necessarily generalize to all systems. In the photodissociation process of triiodide, the key is that the wavepacket motions take place on the ground state potential energy surfaces of both the reactant and product. For signal components associated with terms 1-8, this means that both the third and fourth field-matter interactions occur with either the ket or bra (see Figure 5.2). In contrast, the constraints that suppress intensity in the upper left and lower right quadrants in Figures 5.9a and 5.9b may be lifted in systems with bound excited states, thereby yielding peaks in all four quadrants. Nonetheless, it is likely that strategies such as three-color pulse sequences can be used in systems with bound excited states to isolate the desired signal components.

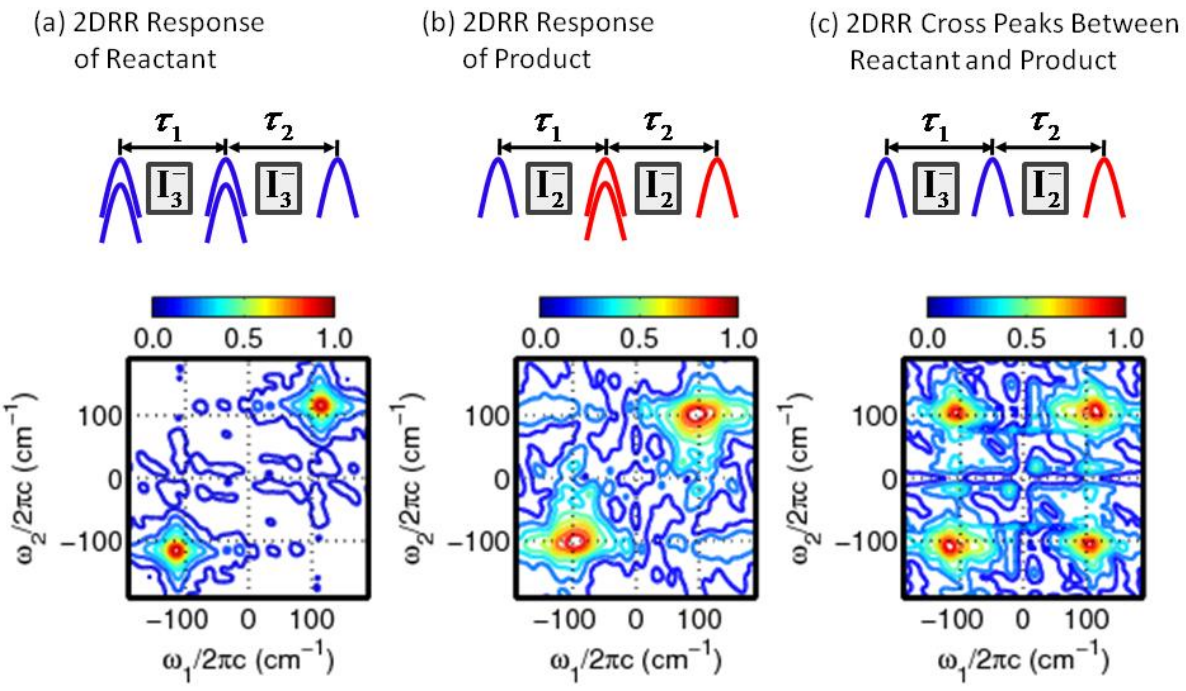

Figure 5.9. Summary of 2DRR experiments conducted on triiodide: (a) the response of triiodide was detected in both dimensions in Reference [26]; (b) the response of the diiodide photoproduct is detected in both dimensions (see Figure 5.7); (c) the response of triiodide and diiodide are detected in separate dimensions (see Figure 5.8). Blue and red laser pulses represent wavelengths that are electronically resonant with triiodide and diiodide, respectively.

5.5. Nonequilibrium Correlation Between Reactants and Products

We have focused to this point on establishing signatures of cross peaks between triiodide and diiodide in 2DRR spectra (see Figure 5.9c). Of course, the vibrational resonance frequencies of both species can be determined by lower-order pump-probe experiments.[16,19-21] The information unique to 2DRR spectroscopy pertains to the correlated vibrational motions of the reactant and product. In this section, we explore a time-frequency representation of the signal that is well-suited for physical insight into the photodissociation process of triiodide.

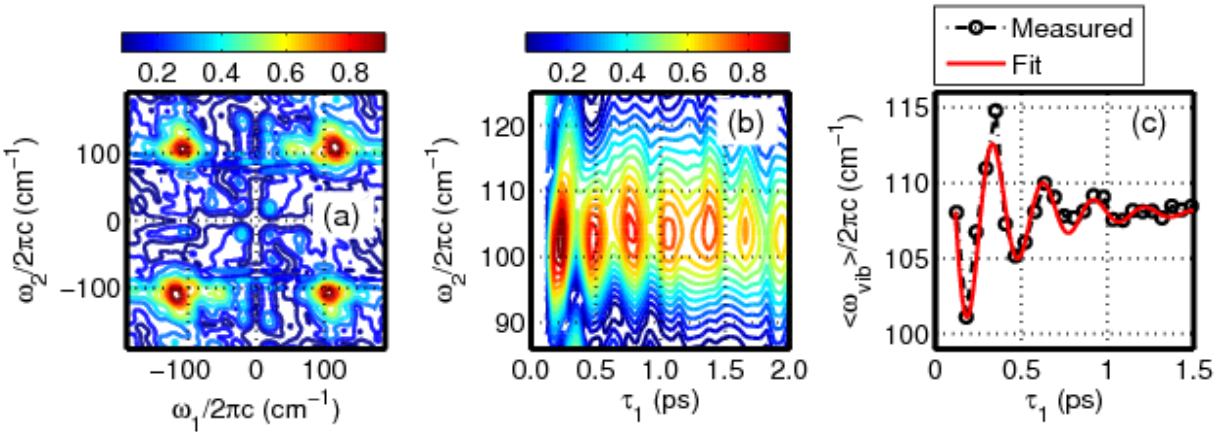

Figure 5.10. 2DRR response of triiodide in ethanol with a detection wavenumber of 19,500 cm^{-1} (513 nm). (a) Resonances in all four quadrants of the 2DRR spectrum signify cross peaks between triiodide (in ω_1) and diiodide (in ω_2). (b) Quantum beats in the Raman spectrum of diiodide are observed when the 2DRR spectrum in panel (a) is inverse Fourier transformed with respect to ω_1. (c) Oscillations in the mean vibrational frequency are analyzed using Equation 5.6. Such oscillatory behavior suggests that the vibrational coherence frequency of diiodide is sensitive to vibrational motions of triiodide in the delay time, τ_1.

For the present system, it is our view that the frequency-domain representation of the 2DRR signal is primarily useful for confirming that the reactant and product dominate separate dimensions (see Figure 5.9). Once this is established, we suggest that the physical insight into the dissociation process is most clearly derived by leaving the first dimension in the time domain as displayed in Figure 5.10b. Here, the τ_1 dimension represents wavepacket motion of triiodide in its ground electronic state, whereas the vibrational spectrum of diiodide is displayed in the ω_2 dimension. The mean vibrational frequency shown in Figure 5.10c is generated using the weighted average

$$\left\langle \omega_{vib}(\tau_1) \right\rangle = \frac{\int d\omega_2 S(\tau_1, \omega_2)\omega_2}{\int d\omega_2 S(\tau_1, \omega_2)} \tag{5.6}$$

where $S(\tau_1, \omega_2)$ denotes the signal displayed in Figure 5.10b. The oscillations in $\langle \omega_{vib}(\tau_1) \rangle$ indicate that the vibrational coherence frequency of diiodide depends on the time-evolving nonequilibrium geometry of triiodide in the delay time, τ_1. The fit shown in Figure 5.10c reveals extrema in $\langle \omega_{vib}(\tau_1) \rangle$ of 99 and 111 cm^{-1} near the turning points of the wavepacket at delay times of 170 and 325 fs, respectively.

The LEPS potential energy surface of triiodide in ethanol shown in Figure 5.11 facilitates a discussion of the signal generation mechanism in terms of a microscopic picture.[17,27] As suggested by Figure 5.11a, the first pulse induces an electronic coherence and initiates a wavepacket in the symmetric stretching mode on the ground state potential (i.e. a stimulated Raman process). The turning points of the wavepacket can be estimated using the 300 fs period of the vibration and approximate 0.6 Å bond length displacement between the ground and excited state potential energy minima (i.e. 0.6 Å is the projection of the symmetric stretching coordinate onto the individual bond lengths).[27] We estimate that the wavepacket is stimulated in the ground state at bond lengths, R_{ab}=R_{bc}, near 3.06 Å by assuming a 20 fs electronic dephasing time. Here, the turning point is computed by adding 20/75*0.6 Å to the equilibrium bond length of 2.9 Å (75 fs is 1/4 of the vibrational period and 20 fs is the electronic dephasing time).[18] In other words, we estimate that the wavepacket moves approximately 0.16 Å from the equilibrium position of 2.9 Å during the electronic coherence induced by the first laser pulse before undergoing oscillations on the ground state potential energy surface in τ_1. Notably, small changes in the numbers chosen for this analysis do not impact the physical interpretation of the experiment.

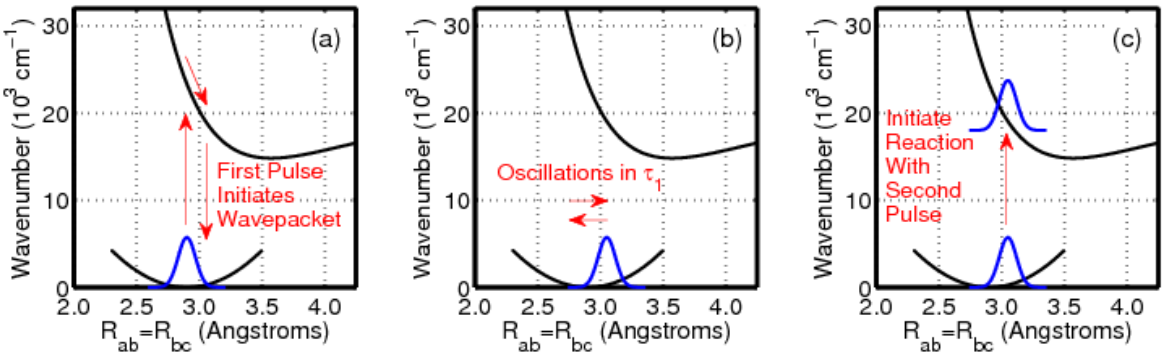

Figure 5.11. The sequence of events associated with the 2DRR signals shown in Figure 5.10. R_{ab} and R_{bc} denote the two bond lengths in triiodide. (a) The first pulse initiates a ground state wavepacket in the symmetric stretching coordinate. Force is accumulated when both bond lengths increase during the electronic coherence induced by the first laser pulse. (b) Wavepacket motion on the ground state potential energy surface is detected in the delay between the pump and repump laser pulses, τ_1. (c) Photodissociation of triioide is initiated from a nonequilibrium geometry by the repump laser pulse. The Raman spectrum of diiodide may then be detected by scanning the delay of a probe pulse, τ_2.

Following ground state wavepacket initiation by the pump pulse, the application of a repump laser pulse promotes the vibrational wavepacket in triiodide to the excited state potential energy surface, where asymmetric motion induces dissociation of the molecule (see Figures 5.11b and 5.11c). The 20 fs pump and repump laser pulses are much shorter than the 300 fs vibrational period, and the wavepacket moves very little along the symmetric stretching coordinate before photodissociation.[20] For these reasons, the geometry of triiodide from which the reaction commences is sensitive to the delay time, τ_1. By contrast, in a traditional (third-order) transient absorption spectroscopy, the reactive wavepacket must always be promoted onto the excited state potential energy surface from the equilibrium geometry (i.e. bond lengths of approximately 2.9 Å).

Correlation between the wavepacket in the symmetric stretching coordinate of triiodide and the vibrational coherence frequency of diiodide can be visualized by converting the delay time, τ_1, into the position of the wavepacket in the symmetric stretching coordinate (i.e. the bond lengths in triiodide, R_{ab}=R_{bc}). In Figure 5.12, the inner and outer turning points of the wavepacket are taken to correspond to the minima and maxima in $\langle \omega_{vib}(\tau_1) \rangle$ shown in Figure 5.10c. Translation between the delay, τ_1, and the bond lengths is achieved by applying the model described above to $\langle \omega_{vib}(\tau_1) \rangle$. That is, we estimate that the wavepacket is located at 2.74 and 3.06 Å at delay times, τ_1, of 170 and 325 fs, respectively. Each revolution of the spiral in Figure 5.12 represents one period of vibrational motion in τ_1. The spiral focuses inward towards the equilibrium bond length because of damping in $\langle \omega_{vib}(\tau_1) \rangle$. The orientation of the spiral during the first cycle of the wavepacket suggests that bond length displacements of approximately 0.1 Å in triiodide produce a 6.8-cm^{-1} shift in the vibrational coherence frequency of diiodide.

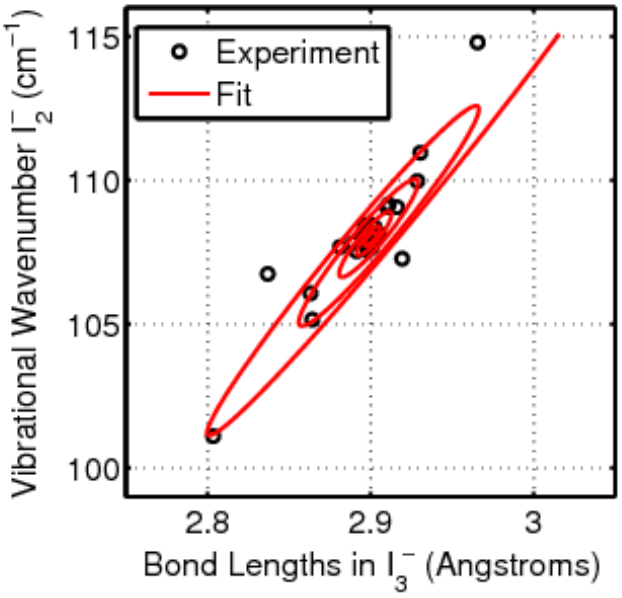

Figure 5.12. Correlation between the vibrational wavenumber of the diiodide photoproduct and the pair of bond lengths in the triiodide reactant, R_{ab}=R_{bc}, is illustrated by analyzing the dynamics in the mean vibrational coherence frequency, $\langle \omega_{vib}(\tau_1) \rangle$, shown in Figure 5.10c. The delay time, τ_1, is converted into the position of the wavepacket in the symmetric stretching coordinate using the model presented in Figure 5.11. Each revolution of the spiral corresponds to 300 fs. The wavepacket oscillates around the equilibrium bond length until vibrational dephasing is complete. The diagonal slant in the spiral suggests that a bond length displacement of 0.1 Å in triiodide induces a shift of 6.8 cm^{-1} in the vibrational coherence frequency of diiodide.

The primary goal of the analysis presented in this section is to demonstrate the type of information that 2DRR spectroscopy can provide about nonequilibrium dynamics. Although our data suggests correlation between triiodide and diiodide, further theoretical work will be needed to draw firm conclusions about the relationship established in Figure 5.12. We have considered two possibilities. First, the geometry of the triiodide from which the reaction is initiated may influence the distribution of vibrational quanta in diiodide through a straightforward Franck-Condon mechanism as discussed in earlier work on triiodide in the gas phase.[54] Indeed, a

second-order perturbative theory for photodissociation processes suggests that the populations of the vibrational states in a product may be weighted by overlap integrals involving the nuclear coordinates of the reactant.[55] Of course, the vibrational coherence frequency of diiodide is known to be sensitive to the distribution of vibrational quanta because of anharmonicity.[19] A second possibility is that the correlation displayed in Figure 5.12 reflects interactions between dissociated fragments. Small inter-fragment distances have been suggested to influence vibrational coherence frequencies in solution on short time scales (i.e. fragment recoil).[19] Ruhman and co-workers have also recently discovered the presence of contact fragment pairs in solution (i.e. fragments in close proximity).[25] It is not yet clear if contributions from distinct relaxation channels are relevant to the present observations. Nishiyama et al. found evidence that vibrational dephasing may be faster than or comparable to the vibrational period in contact ion pairs, which suggests that 2DRR spectroscopy may be insensitive to these species.[24]

5.6. Concluding Remarks

In summary, we have demonstrated that 2DRR spectra carry unique signatures of vibronic coherence transfer in triiodide. The patterns of resonances associated with three different types of nonlinearities are summarized in Figure 5.9. The unique pattern of resonances associated with cross peaks between triiodide and diiodide facilitates insights into the reaction mechanism. Moreover, cross peaks between triiodide and diiodide provide information about nonequilibrium behavior that cannot be derived from traditional pump-probe experiments, where reactants are always photo-initiated from the equilibrium geometry of the ground state. The present experiments suggest positive correlation between the bond lengths of the triiodide reactant and the vibrational coherence frequency of the diiodide photoproduct (see Figure 5.12).

We suggest that correlation between these variables can be explained by Franck-Condon activity and/or by sensitivity to interfragment interactions.[24,25,55]

2DRR spectroscopy may reveal coherent reaction dynamics in any system where a light-activated non-radiative transition is fast compared to the period of vibrational motion. A non-radiative transition, rather than the direct action of laser pulses, serves as an impulse that initiates vibrational coherence in such systems. Triiodide has long been recognized as a well-defined model system for reaction-induced wavepacket motions; however, these types of dynamics may also be detected in larger systems that possess numerous Franck-Condon active coordinates. For example, the photodissociation process of myoglobin is known to exhibit reaction-induced vibrational coherences in both the doming and iron-histidine stretching coordinates.[56] Champion and co-workers uncovered these dynamics with a sophisticated modulation scheme in third-order stimulated Raman experiments.[57] New physical insights can be derived at fifth-order, because the photodissociation reaction can be initiated from a well-defined nonequilibrium geometry of the heme moiety. Fast non-radiative transitions also initiate vibrational coherences in bulk-heterojunction systems,[5] photosynthetic complexes,[9-13,58] and molecule-semiconductor interfaces.[7,8] These systems may also be well-suited to 2DRR investigations.

5.7. REFERENCES

(1) Mukamel, S. *Principles of Nonlinear Optical Spectroscopy*; Oxford University Press: New York, 1995.

(2) Nitzan, A. *Chemical Dynamics in Condensed Phases*; Oxford University Press: Oxford, 2006.

(3) Valkunas, L.; Abramavicius, D.; Mančal, T. *Molecular Excitation Dynamics and Relaxation: Quantum Theory and Spectroscopy* Wiley-VCH: Weinheim, 2013.

(4) *Quantum Effects in Biology*; Mohseni, M.; Omar, Y.; Engel, G. S.; Plenio, M. B., Eds.; Cambridge University Press: Cambridge, 2014.

(5) Song, Y.; Clafton, S. N.; Pensack, R. D.; Kee, T. W.; Scholes, G. D. *Nat. Commun.* **2014**, *5*, 4933.

(6) Fuller, F. D.; Pan, J.; Gelzinis, A.; Butkus, V.; Senlik, S. S.; Wilcox, D. E.; Yocum, C. F.; Valkunas, L.; Abramavicius, D.; Ogilvie, J. P. *Nature Chemistry* **2014**, *6*, 706.

(7) Tisdale, W. A.; Williams, K. J.; Timp, B. A.; Norris, D. J.; Aydil, E. S.; Zhu, X.-Y. *Science* **2010**, *328*, 1543.

(8) Zimmerman, C.; Willig, F.; Ramakrishna, S.; Burfeindt, B.; Pettinger, B.; Eichenberger, R.; Storck, W. *J. Phys. Chem. B* **2001**, *105*, 9245.

(9) Womick, J. M.; Moran, A. M. *J. Phys. Chem. B* **2011**, *115*, 1347.

(10) Christensson, N.; Kauffmann, H. F.; Pullerits, T.; Mančal, T. *J. Phys. Chem. B* **2011**, *116*, 7449.

(11) Kolli, A.; O'Reilly, E. J.; Scholes, G. D.; Olaya-Castro, A. *J. Chem. Phys.* **2012**, *137*, 174109.

(12) Chin, A. W.; Prior, J.; Rosenbach, R.; Caycedo-Soler, F.; Huelga, S. F.; Plenio, M. B. *Nature Phys.* **2013**, *9*, 113.

(13) Fujihashi, Y.; Fleming, G. R.; Ishizaki, A. *J. Chem. Phys.* **2015**, *142*, 212403.

(14) Jun, S.; Yang, C.; Isaji, M.; Tamiaki, H.; Kim, J.; Ihee, H. *J. Phys. Chem. Lett.* **2014**, *5*, 1386.

(15) Perlík, V.; Seibt, J.; Cranston, L. J.; Cogdell, R. J.; Lincoln, C. N.; Savolainen, J.; Šanda, F.; Mančal, T.; Hauer, J. *J. Chem. Phys.* **2015**, *142*, 212434.

(16) Banin, U.; Kosloff, R.; Ruhman, S. *Isr. J. Chem.* **1993**, *33*, 141.

(17) Benjamin, I.; Banin, U.; Ruhman, S. *J. Chem. Phys.* **1993**, *98*, 8337.

(18) Banin, U.; Kosloff, R.; Ruhman, S. *Chem. Phys.* **1994**, *183*, 289.

(19) Kühne, T.; Vöhringer, P. *J. Chem. Phys.* **1996**, *105*, 10788.

(20) Gershgoren, E.; Gordon, E.; Ruhman, S. *J. Chem. Phys.* **1997**, *106*, 4806.

(21) Kühne, T.; Küster, R.; Vöhringer, P. *Chem. Phys.* **1998**, *233*, 161.

(22) Hess, S.; Bürsing, H.; Vöhringer, P. *J. Chem. Phys.* **1999**, *111*, 5461.

(23) Yang, T.-S.; Chang, M.-S.; Hayashi, M.; Lin, S. H.; Vöhringer, P.; Dietz, W.; Scherer, N. F. *J. Chem. Phys.* **1999**, *110*, 12070.

(24) Nishiyama, Y.; Terazima, M.; Kimura, Y. *J. Phys. Chem. B* **2012**, *116*, 9023.

(25) Baratz, A.; Ruhman, S. *Chem. Phys. Lett.* **2008**, *461*, 211.

(26) Molesky, B. P.; Giokas, P. G.; Guo, Z.; Moran, A. M. *J. Chem. Phys.* **2014**, *114*, 114202.

(27) Johnson, A. E.; Myers, A. B. *J. Chem. Phys.* **1995**, *104*, 3519.

(28) Johnson, A. E.; Myers, A. B. *J. Phys. Chem.* **1996**, *100*, 7778.

(29) Johnson, A. E.; Myers, A. B. *J. Chem. Phys.* **1996**, *104*, 2497.

(30) Ivanecky III, J. E.; Wright, J. C. *Chem. Phys. Lett.* **1993**, *206*, 437.

(31) Ulness, D. J.; Kirkwood, J. C.; Albrecht, A. C. *J. Chem. Phys.* **1998**, *108*, 3897.

(32) Blank, D. A.; Kaufman, L. J.; Fleming, G. R. *J. Chem. Phys.* **1999**, *111*, 3105.

(33) Kubarych, K. J.; Milne, C. J.; Lin, S.; Astinov, V.; Miller, R. J. D. *J. Chem. Phys.* **2002**, *116*, 2016.

(34) Wilson, K. C.; Lyons, B.; Mehlenbacher, R.; Sabatini, R.; McCamant, D. W. *J. Chem. Phys.* **2009**, *131*, 214502.

(35) Herrmann, V.; Krebs, P. *J. Phys. Chem.* **1995**, *99*, 6794.

(36) Myers, A. B. Excited Electronic State Properties From Ground-State Resonance Raman Intensities. In *Laser Techniques in Chemistry*; Myers, A. B., Rizzo, T. R., Eds.; John Wiley & Sons: New York, 1995; Vol. 23; pp 325.

(37) Heller, E. J. *Acc. Chem. Res.* **1981**, *14*, 368.

(38) Myers, A. B.; Mathies, R. A.; Tannor, D. J.; Heller, E. J. *J. Chem. Phys.* **1982**, *77*, 3857.

(39) Goodno, G. D.; Dadusc, G.; Miller, R. J. D. *J. Opt. Soc. Am. B* **1998**, *15*, 1791.

(40) West, B. A.; Womick, J. M.; Moran, A. M. *J. Phys. Chem. A* **2011**, *115*, 8630.

(41) West, B. A.; Womick, J. M.; Moran, A. M. *J. Phys. Chem. A* **2013**, *117*, 5865.

(42) Lepetit, L.; Chériaux, G.; Joffre, M. *J. Opt. Soc. Am. B* **1995**, *12*, 2467.

(43) Gallagher, S. M.; Albrecht, A. W.; Hybl, J. D.; Landin, B. L.; Rajaram, B.; Jonas, D. M. *J. Opt. Soc. Am. B* **1998**, *15*, 2338.

(44) Turner, D. B.; Wilk, K. E.; Curmi, P. M. G.; Scholes, G. D. *J. Phys. Chem. Lett.* **2011**, *2*, 1904.

(45) Underwood, D. F.; Blank, D. A. *J. Phys. Chem. A* **2005**, *109*, 3295.

(46) Moran, A. M.; Nome, R. A.; Scherer, N. F. *J. Chem. Phys.* **2007**, *127*, 184505:1.

(47) Park, S.; Kim, J.; Scherer, N. F. *Phys. Chem. Chem. Phys.* **2012**, *14*, 8116.

(48) Busby, E.; Carroll, E. C.; Chinn, E. M.; Chang, L.; Moulé, A. J.; Larsen, D. S. *J. Phys. Chem. Lett.* **2011**, *2*, 2764.

(49) Molesky, B. P.; Guo, Z.; Moran, A. M. *J. Chem. Phys.* **2015**, *142*, 212405.

(50) Chen, E. C. M.; Wentworth, W. E. *J. Phys. Chem.* **1985**, *89*, 4099.

(51) Marek, M. S.; Buckup, T.; Motzkus, M. *J. Phys. Chem. B* **2011**, *115*, 8328.

(52) Valley, D. T.; Hoffman, D. P.; Mathies, R. A. *Phys. Chem. Chem. Phys.* **2015**, *17*, 9231.

(53) Kukura, P.; McCamant, D. W.; Mathies, R. A. *Annu. Rev. Phys. Chem.* **2007**, *58*, 461.

(54) Zanni, M. T.; Greenblatt, J.; Davis, A. V.; Neumark, D. M. *J. Chem. Phys.* **1999**, *111*, 2991.

(55) Band, Y. B.; Freed, K. F. *J. Chem. Phys.* **1977**, *67*, 1462.

(56) Champion, P. M.; Rosca, F.; Ionascu, D.; Cao, W.; Ye, X. *Faraday. Discuss.* **2004**, *127*, 123.

(57) Kumar, A. T. N.; Rosca, F.; Widom, A.; Champion, P. M. *J. Chem. Phys.* **2001**, *114*, 701.

(58) Fuller, F. D.; Pan, J.; Gelzinis, A.; Butkus, V.; Senlik, S. S.; Wilcox, D. E.; Yocum, C. F.; Valkunas, L.; Abramavicius, D.; Ogilvie, J. P. *Nature Chem.* **2014**, *6*, 706.

CHAPTER 6: FEMTOSECOND STIMULATED RAMAN SPECTROSCOPY BY SIX-WAVE MIXING[1]

6.1. Introduction

Femtosecond Stimulated Raman Spectroscopy (FSRS) has emerged as a powerful method for investigating ultrafast structural dynamics in condensed phases.[1-12] Recent applications have revealed new insights into systems ranging from proteins[9,10,12] to organic photovoltaic materials.[4,11] The FSRS technique is essentially a sequence of two events: (i) an electronically resonant (actinic) pump pulse initiates a photochemical process; (ii) a stimulated Raman spectrum is obtained at various delay times using a combination of narrowband and broadband laser pulses. Simultaneous probing of all vibrational resonances in the fingerprint region of the spectrum and sensitivity to dynamics on the 100-fs time scale are the primary selling points for the technique. The key is that the precision in the delay between photoexcitation and initiation of the Raman response is determined by the convolution of femtosecond laser pulses in FSRS (although the vibrational frequencies can notably evolve during the free induction decay).[13-15] In contrast, precision in the delay time and spectral resolution are intrinsically coupled in experiments that employ spontaneous Raman probes, because initiation of the Raman response requires a spontaneous fluctuation of the radiation field.[16]

[1] This chapter previously appeared as an article in the Journal of Chemical Physics. The original citation is as follows: Molesky, B. P.; Zuo, G.; Moran, A. M. *J. Chem. Phys.* **2015**, *142*, 212405.

Foremost among the technical challenges that may be encountered in a three-beam implementation of FSRS is a substantial background associated with residual laser light and third-order processes that are radiated in the same direction as the signal. The third-order nonlinearities include a broadband pump-probe signal and a stimulated Raman scattering response (SRS). Of course, undesired signal components that are generated by subsets of the incoming beams (e.g. pump-probe and SRS) can always be eliminated by chopping the incident beams and/or by modulating the frequency of the narrowband pulse.[17-19] The magnitude of the background depends on the particular properties of the sample and the frequencies of the Raman pump and Stokes pulses. The pulses involved in the Raman probe are often tuned into pre-electronic-resonance with the photoproduct, where the equilibrium system is transparent.[1,17,20] The amount of background may be reduced to a non-problematic level under these conditions. In contrast, the method presented in this work is motivated by a more general situation, wherein all pulses are electronically resonant with the equilibrium system. Lower-order nonlinearities and the pump-repump-probe response may then become dominant, particularly in systems with small normal mode displacements.

In this work, we implement laser beam geometries that either reduce or fully eliminate residual laser light and the background of third-order nonlinearities present in traditional FSRS. Figure 6.1 explains how a five-beam geometry can be used to spatially separate most of the background from the FSRS signal emission. It should be noted that, while Figure 6.1 assumes detection of Stokes shifted emission, the same approach can be employed with anti-Stokes detection. Elimination of these undesired signal components greatly enhances sensitivity and reduces data acquisition times compared to a traditional approach in which three incoming beams are utilized. The broadband pump-repump-probe response of the sample is not spatially

filtered in the present approach, because this undesired nonlinearity is phase-matched in the same direction as the FSRS signal. Nonetheless, the pump-repump-probe response can be suppressed in the five-beam geometry by introducing a delay between the two Raman pump pulses, τ_2. This delay enforces the order of field-matter interactions unique to the FSRS response.

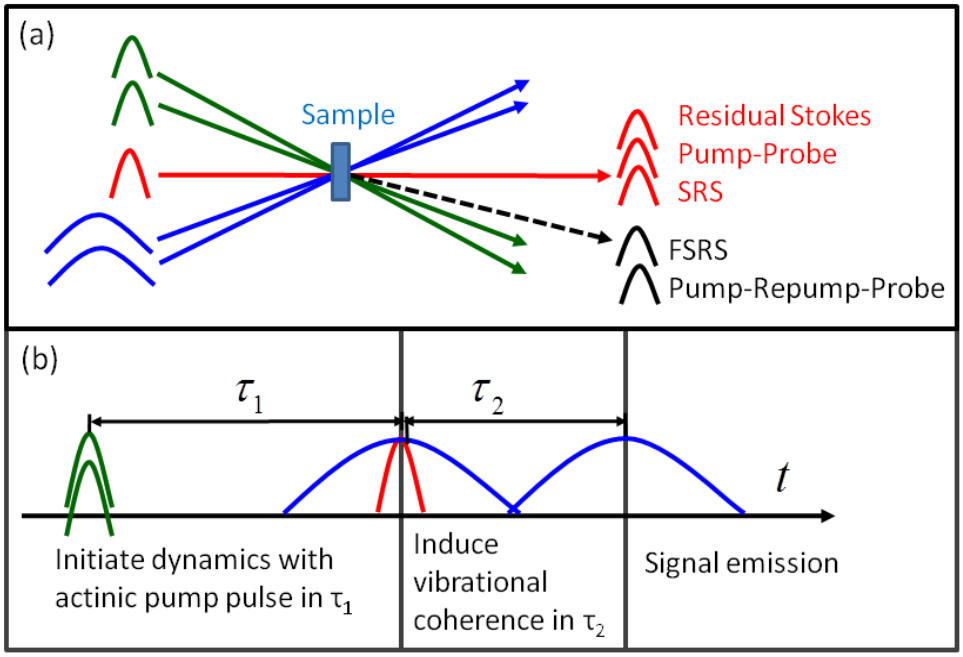

Figure 6.1. (a) A five-beam FSRS geometry is used in this work to eliminate the portion of the background associated with residual Stokes light and third-order nonlinearities. The color code is as follows: the actinic pump is green, the Raman pump is blue, and the Stokes pulse is red. (b) Relaxation dynamics are probed in the delay between the actinic pump and Stokes pulses, τ_1. The fixed time delay, τ_2, is used to suppress a broadband pump-repump-probe response.

The present approach to FSRS is demonstrated with metmyoglobin (metMb), which is the ferric form (Fe^{+3}) of the protein. Photoexcitation induces ground state recovery within several picoseconds (rather than ligand dissociation and recombination) in metMb, because water binds to the distal side of the heme group.[21-25] Upon photoexcitation of the Soret band, the ground electronic state of metMb is repopulated through one of two relaxation mechanisms that

have been delineated in recent work by Chergui and co-workers.[23] The most efficient pathway (57% efficiency) involves sub-picosecond internal conversion from a high-energy charge-transfer state formed immediately after photoexcitation. In the second pathway, the ground state is repopulated within 5 picoseconds following a cascade of transitions through iron spin states. In both processes, excess vibrational energy is dissipated within several picoseconds following ground state recovery. We employ metMb as a model system here in order to establish the validity of the present technique for investigations of heme proteins. Future studies may then focus on understanding photochemical processes in related systems (e.g. photodissociation, electron transfer).

Cascades of third-order signals have been recognized as a serious experimental complication in off-resonant fifth-order Raman experiments conducted on pure liquids and concentrated mixtures.[26-30] Cascades involve a sequence in which the third-order polarization induced on one molecule radiates a signal field that induces a third-order polarization in a second molecule. The second molecule then radiates a signal field in the same direction as the fifth-order signal of interest. The central problem in off-resonant experiments is that direct (desired) and cascaded (undesired) signals are respectively forbidden and allowed by the lowest order terms in the polarization responses (i.e. harmonic potentials with polarizabilities that depend linearly on the vibrational coordinates).[27,31-33] One key to the success of electronically resonant FSRS is that the signal generation mechanism does not rely on such higher-order terms in the expansion of the potential energy.[15,34-36] Unlike off-resonant experiments, resonant FSRS signal generation is allowed for all Franck-Condon active modes (whether they are harmonic or not). Moreover, the solute concentrations employed in resonant FSRS experiments are typically more than 10,000 times smaller than those associated with samples in which cascades are known to

dominate the optical response (e.g. pure CS_2). Nonetheless, we have encountered uncertainties among specialists regarding the potential for cascades in electronically resonant FSRS, which should be dealt with before studies of photochemical mechanisms are pursued. For this reason, significant effort is put forth in this work to rule out contributions from cascades with experimental tests and model calculations.

6.2. Experimental Methods

6.2.1. Laser Pulse Generation

Actinic pump, Raman pump, and Stokes pulses resonant with the Soret band of metMb are employed in the present study (see Figure 6.2). All experiments are based on a Titanium Sapphire laser system that produces 0.8 mJ, 55 fs pulses at 1 kHz. The 410 nm actinic pump pulses are obtained by second harmonic generation of 50 μJ of the fundamental beam in a 0.25 mm thick BBO crystal. Dispersion accumulated in the BBO crystal and several beam splitters, which amounts to roughly 500 fs^2 group delay dispersion (GDD), is pre-compensated for with reflections of the 800-nm pulses on mirrors that impart negative GDD before second harmonic generation. Raman pump pulses are produced by second harmonic generation of the fundamental laser beam in a 1 mm thick BBO crystal. The Raman pump is then sent through a 4F spectral filter consisting of two 2400-g/mm gratings and two 25-cm focal length lenses. Pulses with spectral widths of 50 cm^{-1} are obtained by placing a slit with a 890 μm width at the 2F plane.

The Stokes pulse is produced by doubling the frequency of the fundamental laser beam in a 0.25 mm thick BBO crystal. The resulting 90 μJ, 410 nm second harmonic beam is then focused into a 75 cm long hollow core fiber with a 30 cm focal length lens. The 100 μm inner

diameter of the fiber constitutes a suitable compromise between throughput and spectral broadening. The fiber is housed in a stainless steel cell filled with 1.0 atm of argon gas. The spectrum of the broadened laser pulse that exits the fiber is fairly sensitive to the alignment into the fiber. For this reason, the spectrum of the output is continually monitored with an Ocean Optics spectrometer and laptop computer; adjustments are made after the laser is warmed up to reproduce the spectrum on a daily basis. The Stokes spectrum shown in Figure 6.2 is obtained by spectral filtering of the laser beam in a fused-silica prism compressor with 70-cm prism separation. The instrument response width, which was determined in a 0.25 mm thick fused silica window, is less than 80 fs at Raman shifts ranging from 500-2000 cm^{-1} (i.e. Stokes wavelength range of 415-440 nm).

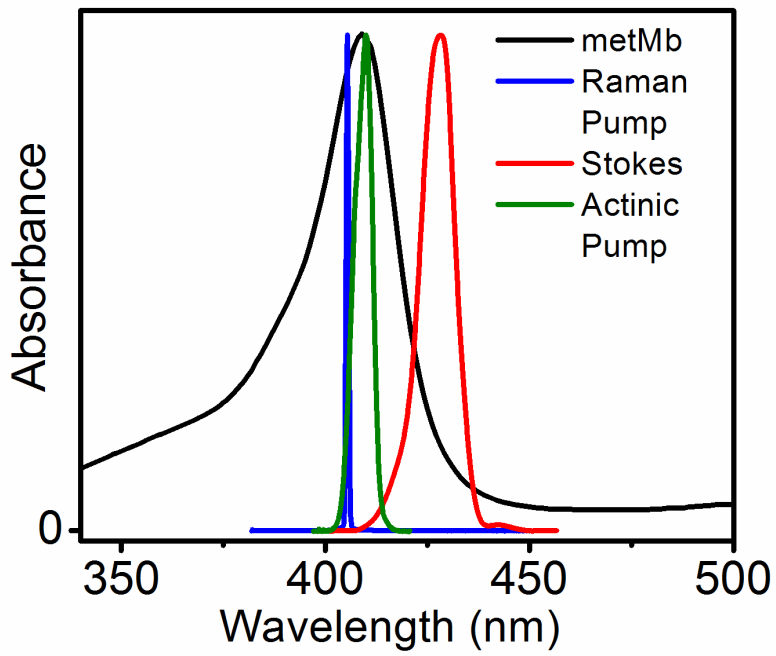

Figure 6.2. Spectra of the actinic pump (green), Raman pump (blue), and Stokes pulses (red) are overlaid on the linear absorbance spectrum of metmyoglobin (black) in aqueous buffer solution at pH=7.0.

6.2.2. Laser Beam Geometries

Experiments are conducted with the diffractive optic-based interferometer shown in Figure 6.3. All beams are focused onto the diffractive optic with a 50 cm focal length spherical mirror. The 20 cm focal length imaging mirror is rotated off-axis by approximately 5º (i.e. the minimum amount). The actinic pump and Raman pump beams cross at approximately 6.9º in the diffractive optic and are bisected by the Stokes beam. The angles between the +1 and -1 diffraction orders of the actinic and Raman pump beams are both 6.9º. The angle between the +1 and -1 diffraction orders of the Stokes beam is 7.2º. Approximately 25% of each incident beam is diffracted into each of the three diffraction orders (0 and +/-1). Subsets of the 9 beams can be selected to conduct a variety of four and six-wave mixing experiments. We utilize the two beam patterns shown in Figures 6.3b and 6.3c in this work.

The laser beam geometry displayed in Figure 6.3b was developed by Mark Berg for studies of multidimensional population dynamics.[37,38] The signal is detected in the direction, $k_1 - k_2 + k_3 - k_4 + k_5$. The key advantage of this geometry is that the signal is free from a background of direct third-order signal fields when the beam diameters are small compared to their separation after the sample. As discussed in our earlier study of triiodide,[35] a direct third-order signal is radiated in the direction $k_1 + k_4 - k_5$ when the actinic pump and Stokes beams overlap. This response vanishes at positive delay times, $\tau_1 > 0$, because pulses 1 and 5 establish the holographic grating in the sample; this can be proven by blocking either beam 2 or 3 at positive delay times. Notably, this undesired signal (near $\tau_1 = 0$) does not possess narrow vibrational resonances due to the 250-cm^{-1} spectral width of the actinic pump pulse. It is therefore removed when the broadband baseline is subtracted in the signal processing algorithm

described in Section 6.3. Beams 2 or 3 may also be chopped if dynamics at sub-100 fs delay times are of interest.

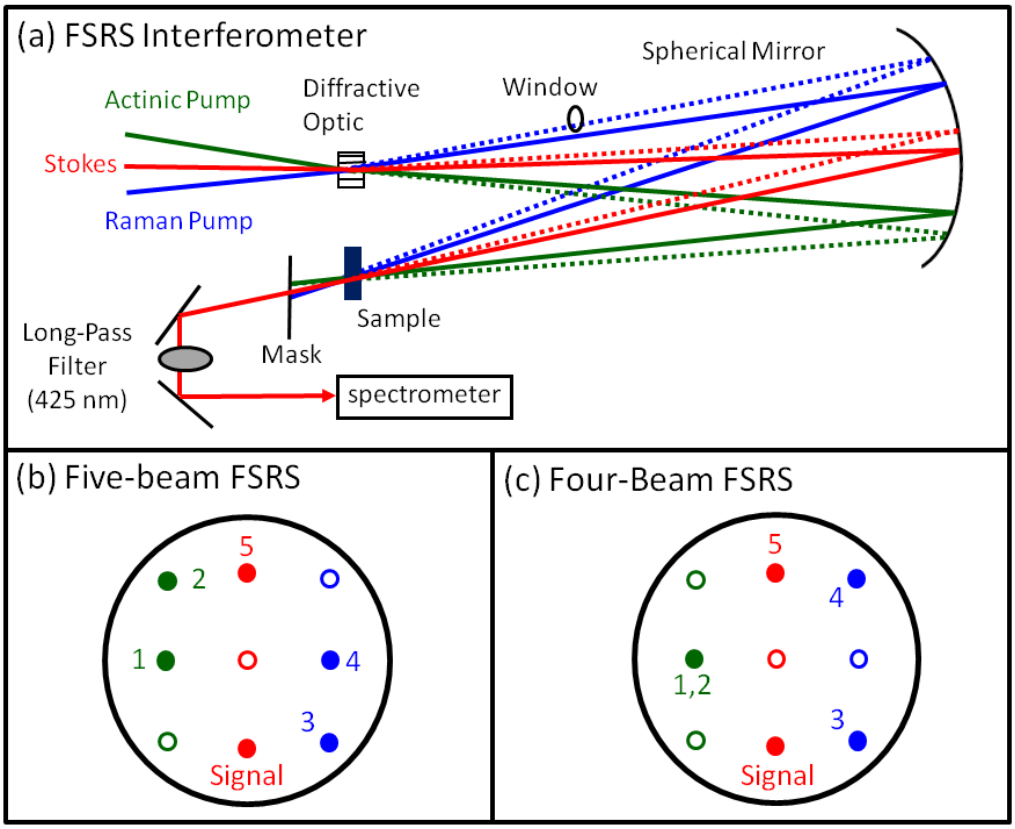

Figure 6.3. (a) Diffractive optic-based interferometer used for FSRS measurements. The transparent fused silica window delays pulse 3 by 290 fs with respect to pulse 4 (delay τ_2 in Figure 6.1). (b) A five-beam geometry is used to detect the FSRS signal in the background-free direction, $k_1 - k_2 + k_3 - k_4 + k_5$. (c) The FSRS signal is also radiated in the direction, $k_1 - k_2 + k_3 - k_4 + k_5$ in the four-beam geometry; however, the wavevectors k_1 and k_2 cancel each other, so the signal is radiated in the same direction as a four-wave mixing signal, $k_3 - k_4 + k_5$. In the four-beam geometry, the FSRS signal corresponds to the difference between signals measured with and without the actinic pump beam (beam 1,2). Beams represented with solid circles reach the sample, whereas those represented with open circles are blocked with a mask. The same color code is applied in all panels (Raman pump is blue, actinic pump is green, Stokes beam is red).

The four-beam geometry shown in Figure 6.3c is obtained simply by changing the mask between the diffractive optic and the sample. The signal is again radiated in the direction, $k_1 - k_2 + k_3 - k_4 + k_5$; however, this direction is collinear with the vector $k_3 - k_4 + k_5$, because a single actinic pump beam is employed. The actinic pump beam (beam 1,2) must be chopped in order to remove contributions of the third-order SRS signal.[39-41] Chopping the actinic pump beam significantly increases the data acquisition time and reduces sensitivity compared to the five-beam geometry. Therefore, we use the four-beam geometry only to determine the relative signs of the third- and fifth-order signals in this work.

In both geometries, the beams are focused onto the diffractive optic with a 50 cm focal length spherical mirror. The depth of focus for each beam is approximately 7 mm given the approximate 6 mm beam diameters at the surface of the spherical mirror. The beams are imaged onto the sample with a 20 cm focal length spherical mirror placed 40 cm from the diffractive optic. In the five-beam geometry, beams 1 and 2 are displaced by 2.4 cm and 3.5 cm from the center of the mirror, respectively. The difference in focal lengths induced by spherical aberration for this pair of beams is 0.2 mm (beams 1 and 2 respectively focus 40.02 and 40.04 cm from the imaging mirror). The effects of spherical aberration are minimal, because the 7 mm depth of focus is large compared to the 0.2 mm displacement in the focal position. Thus, the beams propagate through the 0.22 mm thick sample with a negligible change in diameter.

6.2.3. Signal Detection

In all experiments, signals are detected using a back-illuminated CCD array (Princeton Instruments PIXIS 100B) mounted on a 0.3 meter spectrograph with a 1200 g/mm grating. The signal beam is focused to a spot size of 100 μm at the entrance to the spectrograph to obtain

hardware-limited spectral resolution of approximately 10 cm^{-1}. Ultimately, the resolution of the measurement is limited by the 50 cm^{-1} spectral width of the Raman pump beam. The FWHM spot sizes of all laser beams are 200 μm at the sample position. Pulse energies of the actinic pump and Raman pump pulses are 150 nJ and 200 nJ, respectively. The pulse energy of the Stokes beam is 50 nJ. Under these conditions, the total six-wave mixing signal produces 5000 counts on the detector with an integration time of 100 ms under our experimental conditions. The FSRS response is typically 10-20% of the total signal strength (i.e. the majority of the signal field is a broadband pump-repump-probe response). The noise level in each spectrum is less than 20 counts.

6.2.4. Sample Handling

Myoglobin from horse skeletal muscle is purchased from Sigma-Aldrich. The protein is dissolved in 0.1 M sodium phosphate buffer at a pH of 7.0. The solution is centrifuged at 6000 revolutions per minute for 5 minutes before experiments to optimize the optical quality. In all experiments except for those described in Section 6.4.2, the 0.2 mM sample of metMb is flowed through a wire-guided jet with a thickness of 220 μm, where the reservoir volume is 50 mL. Absorbance spectra are measured before and after experiments to confirm the absence of sample degradation. We do not observe changes in the absorbance spectrum of the solution during experiments that require several hours.

Investigation of the concentration dependence of the signal intensity in Section 6.4.2 requires an approach in which the solutions are quickly exchanged without moving the sample holder. To this end, we mounted an aluminum adaptor plate with a slot for a cuvette on a spinning rotation mount (spins at a rate of 720º per second). This setup allows a cuvette with a

0.5 mm path length to be removed and put back into the same position when the samples are exchanged and/or the cuvette is cleaned. FSRS signals are readily detected in this setup; however, we find that it is more susceptible to scattered light than the jet.

6.3. Signal Processing

6.3.1. Algorithm

Figure 6.4 illustrates the signal processing algorithm used in this work with a six-wave mixing signal acquired in the five-beam geometry. The total signal intensity shown in Figure 6.4a exhibits dispersive line shapes, which is a signature of interference between broadband (pump-repump-probe) and FSRS responses. The origin of the interference can be understood by considering the total signal intensity, $I_{total}(\omega)$, as a sum of three terms

$$I_{total}(\omega) = \left|E_{BB}(\omega) + E_{FSRS}(\omega)\right|^2 = I_{BB}(\omega) + I_{FSRS}(\omega) + 2\,\mathrm{Re}\left\{E_{BB}(\omega)E_{FSRS}(\omega)\right\} \qquad (6.1)$$

where $E_{BB}(\omega)$ and $E_{FSRS}(\omega)$ represent the broadband and FSRS components of the signal field ($I_{BB}(\omega)$ and $I_{FSRS}(\omega)$ are signal intensities). The third term in Equation 6.1 is responsible for the dispersive vibrational line shapes in the signal spectrum. In Figure 6.4a, the broadband baseline, $I_{BB}(\omega)$, is obtained by Fourier transforming the total signal intensity, $I_{total}(\omega)$, into the time domain and filtering the peak at 0 fs (see Figure 6.4b). Subtraction of the baseline isolates the third term in Equation 6.1

$$I_{total}(\omega) - I_{BB}(\omega) \approx 2\left|E_{BB}(\omega)\right|\left|E_{FSRS}(\omega)\right|\cos\left[\varphi_{BB}(\omega) - \varphi_{FSRS}(\omega)\right] \qquad (6.2)$$

where $\varphi_{BB}(\omega)$ and $\varphi_{FSRS}(\omega)$ are the phases of the broadband and FSRS signal components. Here, we have assumed that $I_{BB} >> I_{FSRS}$, which is a good approximation in systems with modest mode displacements such as myoglobin.[42] Dominance of the term on the right side of Equation 6.2 is consistent with the dispersive line shapes observed in the measured signals (I_{FSRS} does not possess a dispersive line shape). In systems with large mode displacements, the term linear in the field component, $E_{FSRS}(\omega)$, can be obtained using an external local oscillator that is delayed with respect to the Stokes pulse. The fringe spacing associated with $E_{FSRS}(\omega)$ will be unique in such an implementation, so it can be isolated with a Fourier filter. Such an interferometric detection scheme has been demonstrated in a previous four-wave mixing experiment.[43]

Dependence of the signal on the phase difference, $\varphi_{BB}(\omega)-\varphi_{FSRS}(\omega)$, can be eliminated by applying a second filter function to the inverse Fourier transform of the baseline-subtracted signal (see Figure 6.4c). The filter in Figure 6.4c is displaced from the origin by 60 fs in order to eliminate the residual broadband response. As shown in Figure 6.4d, Fourier transformation of the signal back to the frequency domain yields a complex signal field in which phase information can be eliminated by taking the absolute value

$$\left|E_{FSRS}(\omega)\right| \propto I_{BB}^{-1/2}(\omega)\left|E_{BB}(\omega)E_{FSRS}(\omega)\exp\left[i\varphi_{BB}(\omega)-i\varphi_{FSRS}(\omega)\right]\right|. \qquad (6.3)$$

In Equation 6.3, the magnitude of the FSRS response, $\left|E_{FSRS}(\omega)\right|$, is obtained by multiplication of $\left|E_{BB}(\omega)E_{FSRS}(\omega)\right|$ and $I_{BB}^{-1/2}$. Equation 6.3 also makes clear one of the tradeoffs associated with the present technique. The phase of the FSRS response, $\varphi_{FSRS}(\omega)$, cannot be obtained without knowledge of $\varphi_{BB}(\omega)$, which is a τ_1-dependent quantity. Traditional FSRS is not

subject to this limitation, because the signal is heterodyne-detected with the residual Stokes pulse.[17]

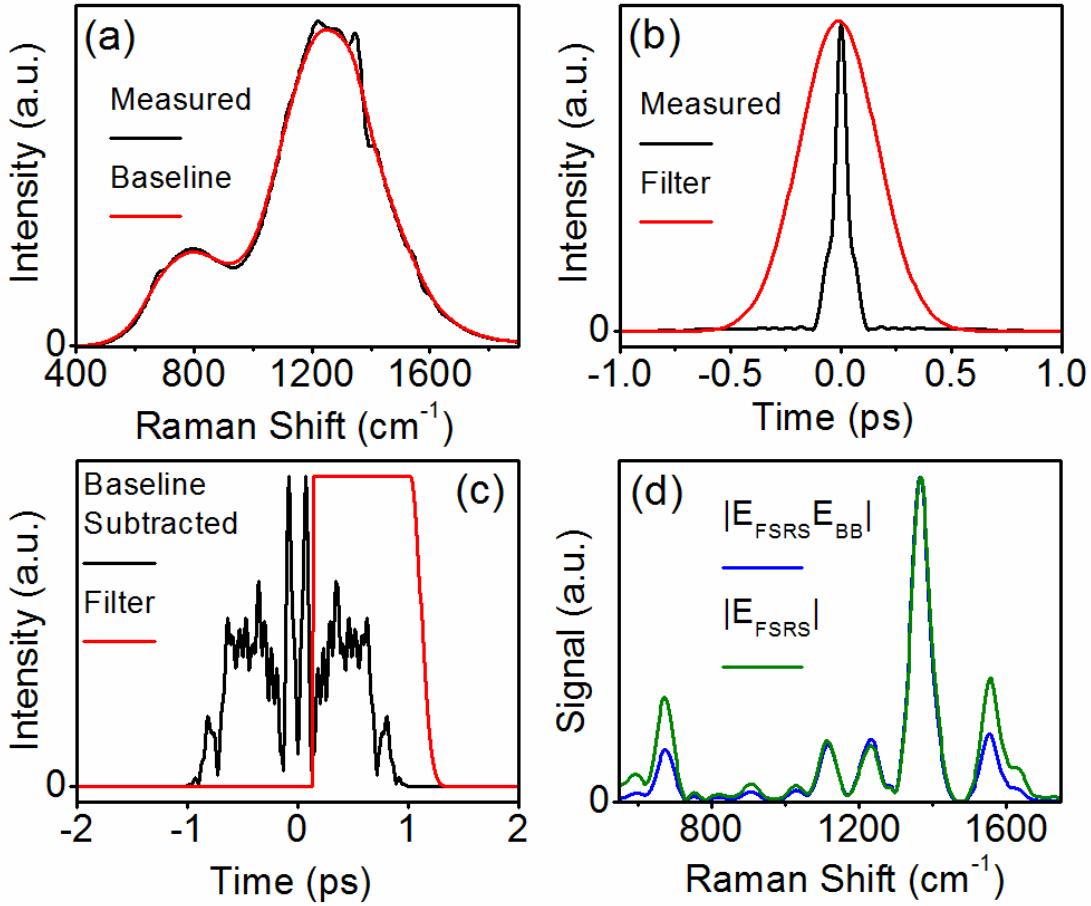

Figure 6.4. (a) This six-wave mixing signal for metMb is obtained in the five-beam FSRS geometry with τ_2 = 290 fs. The broadband baseline is subtracted to isolate the vibrational component of the response. (b) The baseline in panel (a) is obtained by inverse Fourier transforming the measured signal into the time domain, then filtering the broadband part of the response at 0 fs. (c) The baseline-subtracted signal is filtered at positive times after inverse Fourier transformation of the difference between the measured signal and the baseline shown in panel (a). The filter is displaced from the origin by 60 fs to eliminate the residual broadband response, which is dominant at earlier times. (d) The absolute value of the FSRS spectrum is obtained by Fourier transformation of the filtered signal in panel (c).

The Raman spectrum obtained in Figure 6.4d exhibits several known vibrational resonances of metMb.[44] The 670 and 1370-cm^{-1} modes correspond to deformation and bond-stretching motions localized on the tetrapyrrole moiety, respectively. The remaining resonances are primarily localized on the vinyl substituents of the tetrapyrrole group shown in Figure 6.5. Intensities of the resonances in the 1000-1300 cm^{-1} range are enhanced in the present technique, because they coincide with the peak of the Stokes spectrum. In contrast, the peak intensities observed in traditional FSRS are independent of the Stokes intensity.[17]

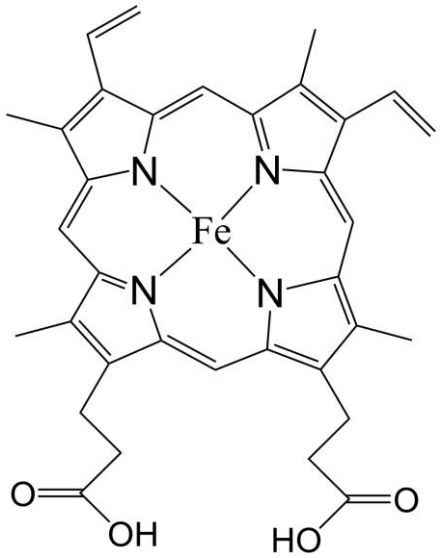

Figure 6.5. Molecular structure of iron protoporphyrin-IX.

In principle, an external (i.e. τ_1-independent) reference field may be used to eliminate $\varphi_{BB}(\omega)$ from consideration.[45] Such an approach is challenged by several technical issues. One problem particular to the present five-beam geometry is that no beam produced by the diffractive optic is perfectly collinear with the signal (there is at least a 0.5º deviation for the beam whose wavevector is most closely matched to that of the signal). Additional cross terms will also appear in Equation 6.1 if an external reference field is introduced, so a different baseline

subtraction algorithm would need to be devised. We are presently working on solutions to these challenges. One key to success may be reduction of the ratio, $|E_{FSRS}(\omega)|/|E_{BB}(\omega)|$, perhaps by using shaped Raman pump pulses.[46]

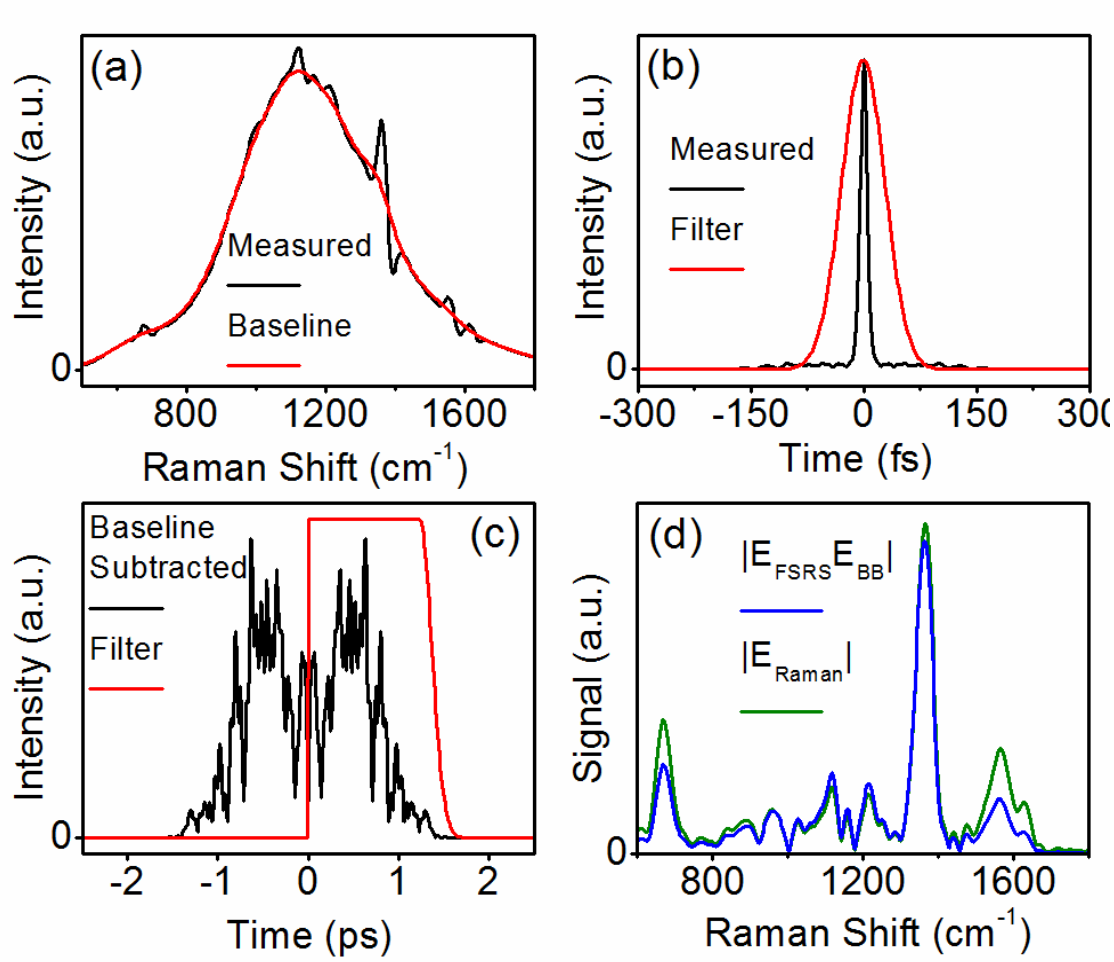

Figure 6.6. This six-wave mixing signal for metMb is obtained in the five-beam FSRS geometry with τ_2 =420 fs. The panels (a)-(d) are defined in the same way as those in Figure 6.4. The vibrational frequencies obtained in this measurement differ by less than 10 cm^{-1} from those found in Figure 6.4. This difference is 5 times less than the bandwidth of the Raman pump pulse (i.e. intrinsic frequency resolution). The vibrational line widths are roughly 25% less than those shown in Figure 6.4. This decrease in the line width with increasing delay, τ_2, is consistent with the theory outlined in Section 6.5.

6.3.2. Adequate Suppression of the Broadband Response

The key to success of the baseline subtraction method is adequate suppression of the broadband pump-repump-probe response. This undesired nonlinearity can be suppressed by increasing the delay between Raman pump pulses, τ_2. An increase in this delay increases the probability that the final field-matter interaction occurs with the final Raman pump pulse to arrive at the sample (see Figure 6.1). This order of field-matter interactions is unique to the FSRS response (see Section 6.5); the last field-matter interaction occurs with the Stokes pulse in the undesired pump-repump-probe response. However, a compromise must be made between signal intensity and background suppression, because the amplitude of the FSRS response increases as τ_2 decreases (the FSRS signal vanishes when τ_2 is longer than the inverse of the vibrational line width).

In Figure 6.6, a FSRS signal acquired with τ_2 = 420 fs is presented. The integration time has been doubled to 200 ms and the signal count rate is roughly 4 times lower than that associated with the measurement in Figure 6.4. The contribution of the FSRS response relative to the total signal is approximately 3-5 times larger than that found with the delay, τ_2 = 290 fs, in Figure 6.4. As such the magnitude of the broadband response near 60 fs in Figure 6.6c is reduced, and there is no need to displace the apodization window from time-zero. The vibrational resonance frequencies displayed in Figures 6.4c and 6.6c are indistinguishable, thereby confirming the theoretically predicted independence of the resonance frequency on the delay, τ_2. Small displacements in the apodization window do not alter the frequencies of the vibrational resonances, because the information is primarily located at times greater than 60 fs.

In the theory outlined in Section 6.5, it is predicted that the line width decreases as the delay, τ_2, increases. Consistent with this prediction, we find that the line widths decrease from approximately 60 cm^{-1} to 45 cm^{-1} when the delay, τ_2, increases from 290 fs to 420 fs. Related line-narrowing effects have been discussed in the context of sum-frequency generation techniques that combine broadband and narrowband laser pulses.[47] We have also examined this issue numerically in a study of short-lived electronic coherences in molecular aggregates.[48] Essentially, the temporal decay of the polarization is determined by the product of the vibrational coherence, which is initiated when the Stokes pulse arrives at the sample, and the envelope of the final Raman pump pulse to arrive at the sample (see Figure 6.1b). Both quantities decay simultaneously when τ_2 = 0 fs, and the measured line width is generally broader than the bandwidth of the Raman pump. However, the envelope of the Raman pump rises as the vibrational coherence decays when τ_2 > 0 fs. This convolution artificially inflates the duration of the polarization, thereby reducing the vibrational line widths.

It is worth noting that suppression of the broadband response in the present implementation is limited by the time-symmetric envelopes of the Raman pump pulses. Overlap between the two Raman pump pulses can be further reduced using etalons. Such an approach has already been successfully demonstrated in the traditional three-beam FSRS geometry.[46]

6.3.3. Summary of Technical Issues Involved in Signal Processing

In summary, FSRS spectra are obtained using the data processing algorithm described above. Key points made in Sections 6.3.1 and 6.3.2 are summarized below.

(i) Success of the approach requires suppression of the broadband pump-repump-probe response using a delay between the two Raman pump pulses. The ratio of the FSRS response to broadband response increases as the delay, τ_2, increases (see Figures 6.4 and 6.6); however, the overall magnitude of the signal intensity decreases as well. Thus, a compromise between signal strength and background suppression must be made.

(ii) The same apodization functions are applied to every spectrum acquired in a particular experiment (all delay times, τ_1). The same apodization functions can be used on different days (and with different samples) provided that the spectra of the laser pulses are maintained.

(iii) An increase in the delay, τ_2, induces a line-narrowing effect. This observation is consistent with theory presented in Section 6.5.

(iv) The vibrational resonance frequencies are unaffected by the delay, τ_2 because vibrational coherences are induced before the final Raman pump pulse arrives at the sample.

(v) In principle, the relative magnitudes of the vibrational resonances may depend on τ_2. The amplitudes of vibrational resonances with the broadest line widths (fastest dephasing times) should decrease the most as τ_2 increases. Notably, the amplitudes of the vibrational resonances reflect the particular spectrum of the Stokes pulse in the four- and five-beam geometries. In contrast, the relative magnitudes of the vibrational resonances are independent of the Stokes spectrum in traditional three-beam FSRS, where the Stokes pulse is used for heterodyne detection.

(vi) Further suppression of the broadband pump-repump-probe response can likely be achieved by reducing the overlap of the Raman pump pulses using etalons. Attenuation of the

broadband response will enable interferometric detection with an external local oscillator.[43] Signs of the vibrational resonances would then be determined.

6.4. Experimental Results

6.4.1. Dependence of FSRS Signal on Incident Pulse Energies

In this section, we examine the dependence of the signal strength on the intensities of the incident laser beams. As in traditional FSRS, the Raman response, $\left|E_{FSRS}(\omega)\right|$, must scale linearly with both I_{AP} and I_{RP}, where I_{AP} and I_{RP} are the intensities of the actinic and Raman pump beams (these intensities represent sums for pulse-pairs 1,2 and 3,4). The broadband response, $\left|E_{BB}(\omega)\right|$, must also scale linearly in both I_{AP} and I_{RP}, because it represents a fifth-order nonlinearity (i.e. a pump-repump-probe signal). Unlike traditional FSRS, $\left|E_{FSRS}(\omega)\right|$ and $\left|E_{BB}(\omega)\right|$ scale as the square root of the Stokes intensity, $I_{St}^{1/2}$, because the signal is not obtained by differential transmission of the Stokes beam.[17]

Figure 6.7 displays both $\left|E_{FSRS}(\omega)E_{BB}(\omega)\right|$ and $\left|E_{FSRS}(\omega)\right|$ obtained for the 1370-cm^{-1} mode, which represents in-plane stretching of the tetrapyrrole moiety,[44] with respect to I_{AP}, I_{RP}, and I_{St}. The pulse energies are cycled within the respective ranges three times and 30 spectra are accumulated at each pulse energy within each cycle (i.e. each point in Figure 6.7 represents a total of 90 spectra or 9000 laser shots). The error bars are determined by computing standard deviations in the signal intensities for the 30 spectra acquired at each pulse energy then propagating the error for each of the three cycles. Experiments conducted on different days yield indistinguishable results. As expected, the measurements in Figure 6.7 suggest that

$\left|E_{FSRS}(\omega)E_{BB}(\omega)\right|$ and $\left|E_{FSRS}(\omega)\right|$, scale as $I_{AP}^2 I_{RP}^2 I_{St}$ and $I_{AP}I_{RP}I_{St}^{1/2}$, respectively. The form of the function used to fit the data is indicated in each panel of Figure 6.7. In all cases, fits conducted with the assumed functions are within the uncertainty ranges of the data. Examination of a larger range of pulse energies could not be accomplished without introducing artifacts caused by sample degradation. We find that the sample degrades during the experiment if the upper limit of each of the pulse energies in Figure 6.7 is doubled.

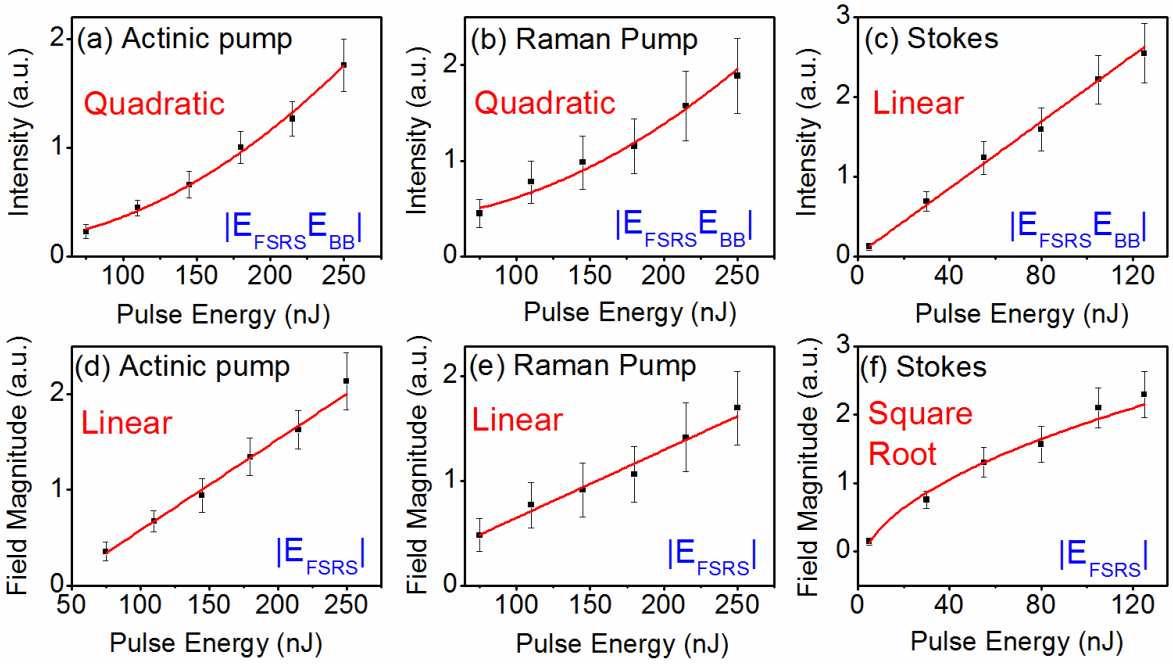

Figure 6.7. Signal intensities corresponding to the vibrational resonance at 1370 cm^{-1} are plotted versus incident pulse energies. In the first row, the signal, $\left|E_{FSRS}(\omega)E_{BB}(\omega)\right|$, is plotted versus energies of the (a) actinic pump, (b) Raman pump, and (c) Stokes beams. In the second row, the signal, $\left|E_{FSRS}(\omega)\right|$, is plotted versus energies of the (d) actinic pump, (e) Raman pump, and (f) Stokes beams. Pulse energies associated with the actinic pump and Raman pump represent sums for the respective pairs of beams at the sample position (i.e. beams 1 and 2 or beams 3 and 4). The functional forms used to fit the data (red lines) are indicated in the respective panels. These data validate the signal processing algorithm described in Section 6.3 and confirm that saturation of the optical response is negligible in these ranges of the pulse energies.

6.4.2. Dependence of FSRS Signal on Sample Concentration

Determination of the dependence of the FSRS signal on solute concentration is one way to rule out contributions from third-order cascades.[49,50] At extremely low optical densities (less than 0.1), the direct (fifth-order) FSRS signal intensity scales as the square of concentration, whereas third-order cascades scale as the fourth power of the concentration. However, saturation effects related to absorption of the incident beams and signal take hold at the optical densities where the experiments are usually conducted (0.7-1.0). Therefore, as in our recent study of triiodide,[35] we develop a simple model in this section to capture the dependence of the signal intensity on concentration. Predictions of the model are then compared to experimental data.

The direct fifth-order signal intensity at position x in the sample is subject to the relation

$$I_{direct}^{(5)}(x,C) \propto C^2 \left|\chi^{(5)}\right|^2 I_{AP}^2(x,C) I_{RP}^2(x,C) I_{St}(x,C) \tag{6.4}$$

where C is concentration and $\chi^{(5)}$ is the fifth-order susceptibility. The laser intensity is given by

$$I_j(x,C) \propto \exp(-\alpha_j C x) \tag{6.5}$$

where α_j is an absorption coefficient (product of $\ln(10)$ and the molar extinction coefficient), and j denotes the type of laser pulse (RP, AP, or St). The signal intensity accumulated at the exit of the sample is obtained by integrating over x

$$I_{direct}^{(5)}(C) \propto C^2 \int_0^a dx I_{AP}^2(x,C) I_{RP}^2(x,C) I_{St}^2(x,C) \exp\left[\alpha_{St} C (x-a)\right] \tag{6.6}$$

where a is the path length and the exponential function represents attenuation of the signal beam as it exits the sample. The susceptibility can be removed from the proportionality in Equation 6.6 because it is independent of x.

Treatment of the cascaded signal field must take into account accumulation of both the primary and secondary third-order signal intensities. For the cascaded process that the five-beam geometry is most susceptible to, the primary four-wave mixing signal intensity scales according to $I_{AP}^2(x,C)I_{St}(x,C)$. The intensity of the secondary four-wave mixing process depends on the product of $I_{RP}^2(x,C)$, which decreases exponentially with x, and the intensity of the primary four-wave mixing signal (denoted as $I_{primary}^{(3)}(x,C)$), which increases in a (slightly) sub-quadratic fashion with x at the optical densities of interest. With consideration of these factors, the cascaded signal intensity may be written as

$$I_{cas}(C) \propto C^2 \int_0^a dx I_{RP}^2(x,C) \exp\left[\alpha_{St} C(x-a)\right] I_{primary}^{(3)}(x,C) \tag{6.7}$$

where the primary four-wave mixing signal intensity at position x is proportional to

$$I_{primary}^{(3)}(C,x) \propto C^2 \int_0^x dx' I_{AP}^2(x',C) I_{St}(x',C) \exp\left[\alpha_{St} C(x'-a)\right]. \tag{6.8}$$

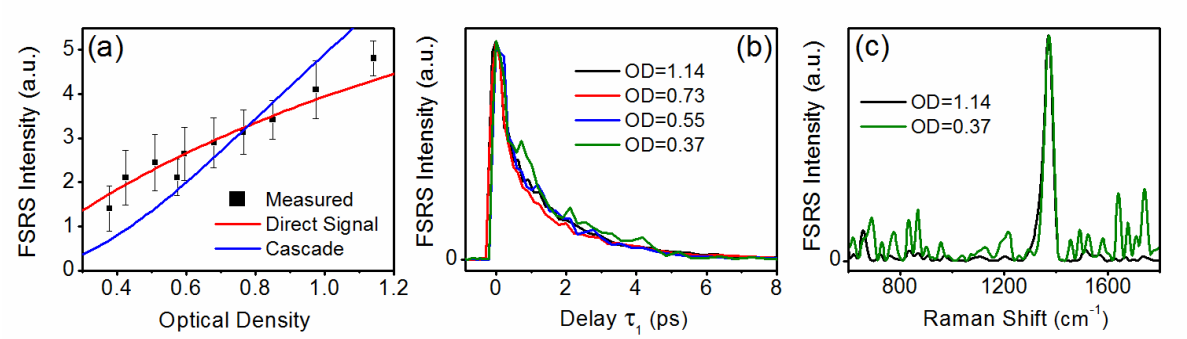

Figure 6.8. (a) FSRS signal intensities associated with the vibrational resonance at 1370 cm^{-1} are plotted versus the optical density of the solution in a 0.5 mm path length. The functions, $I_{direct}^{(5)}(C)$ and $I_{cascade}(C)$, illustrate how the data compare to the concentration dependence predicted for (red) the direct fifth-order signal and (blue) third-order cascades. The functions, $I_{direct}^{(5)}(C)$ and $I_{cascade}(C)$, are multiplied by constants to overlay them with the measured signal intensities. (b) Dynamics in the peak intensity at 1370 cm^{-1} are experimentally indistinguishable at various sample concentrations. (c) Signal intensities are overlaid at the highest and lowest concentrations to illustrate the range in the data quality.

The signal intensity at τ_1=1 ps is plotted versus the optical density of the solution at 410 nm in Figure 6.8. Saturation of the measured signal intensity with increasing optical density is caused by absorption of the incident laser beams. $I_{direct}^{(5)}(C)$ and $I_{cascade}(C)$ are overlaid on the experimental data to illustrate how these functional forms compare to the measurements. The data are more consistent with the model based on the direct fifth-order signal. Figure 6.8b additionally shows that the dynamics are insensitive to the concentration. The features of the signal observed at an optical density of 0.37, which deviate from an exponential decay, are due to noise (not a vibrational coherence). It should also be noted that if the direct and cascaded signals are comparable in magnitude, then signatures of destructive interference between these nonlinearities should be found in the concentration dependence, because direct and cascaded signals have opposite signs.[35] The data show no signs of such interference. FSRS spectra

overlaid at the highest and lowest concentrations demonstrate the range in signal quality in Figure 6.8c. The best signal quality is generally obtained at optical densities near 1.0. In Figure 6.8c the narrow spectral features observed at an optical density of 0.37 are caused by noise. These features are not caused by the shape of the Fourier filter, which is the same for all values of the optical density.

6.4.3. Relative Signs of Third- and Fifth-Order Signals

In this section, we present an experimental test for third-order cascades that takes into account the approximate 180º phase-difference between the direct third- and fifth-order signal fields under resonant conditions.[35,50] This phase-relationship can be understood with simple bookkeeping on the numbers of field-matter interactions and light emission events. Under resonant conditions, a 90º phase-shift is accumulated in each time-interval between field-matter interactions. In a background-free experiment, the number of incoming beams is simply multiplied by 90º (270º and 450º at third- and fifth-order, respectively). Signal field emission adds another 90º such that total phase-shifts of 360º and 540º are, respectively, accumulated in direct third- and fifth-order processes when the signal field emission events are accounted for. Thus, direct third- and fifth-order nonlinearities have opposite signs, because their phases differ by 180º. It is useful to consider that essentially the same idea applies to traditional experiments such as pump probe spectroscopy. For a two-level system, the sign of light transmission changes when a sample is exposed to a pump beam due to ground-state depletion (i.e. a comparison of first and third-order responses). The sign of the signal again changes if a second pump beam is introduced in a pump-repump-probe experiment (i.e. pump-repump-probe signals are absorptive in two-level systems).[51]

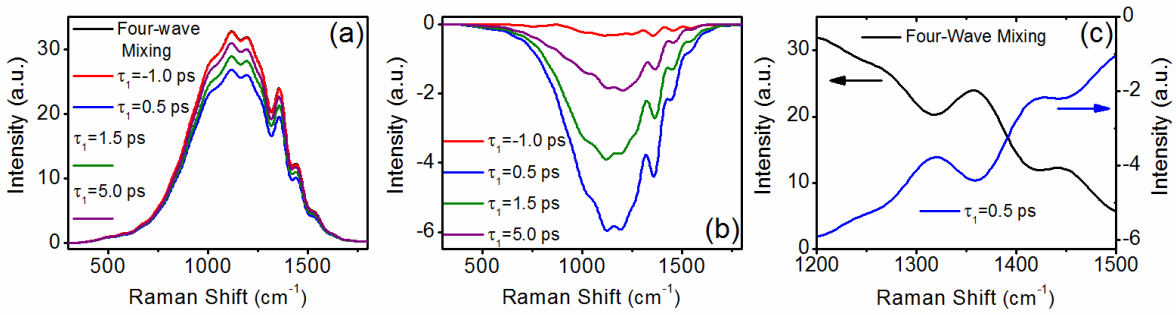

Figure 6.9. (a) Signals acquired in the four-beam geometry at various delay times between the actinic pump and Stokes pulses, τ_1. The signal at τ_1=-0.5 ps is indistinguishable from the four-wave mixing signal measured with the actinic pump pulse blocked. (b) The fifth-order signal is obtained by computing differences between signals acquired with the actinic pump unblocked and blocked (i.e. pump on – pump off). Depletion of the ground state population with the actinic pump pulse is a signature that the direct fifth-order FSRS signal field is measured. In contrast, third-order cascades would induce an increase in the total signal intensity, because such nonlinearities are in-phase with the third-order response. (c) Oscillatory features associated with the vibrational resonances are phase-shifted by approximately 180º in third- and fifth-order measurements (these are magnified views of the data in panels (a) and (b)).

In a cascaded nonlinearity, a phase-shift of approximately 540º is accumulated through the total of 6 (perturbation-theoretic) time-evolution intervals involved in the process. An additional phase-shift of 180º degrees must be added for the two emission events, which results in a total of 720º. Thus, the phase of the absorptive component of the cascaded nonlinearity differs from those associated with the direct third- and fifth-order signals by approximately 0º and 180º, respectively. This is a convenient relationship, because the third-order signal can serve as an "internal standard" for the signal phase.[39-41] The key is to employ a geometry in which the third- and fifth-order signals are equally phase-matched, so that significant phase-shifts are not accumulated through propagation in the medium. The four-beam geometry shown in Figure 6.3b satisfies this criterion, because both interactions with the actinic pump take place with a single

beam. Previous experiments have similarly made use of four-beam geometries in which the signal phase is referenced to that of a background-free third-order signal.[39-41]

Figure 6.9a presents the total signal intensity measured at various delays between the actinic pump and the Stokes pulses, τ_1, in the four-beam geometry. The four-wave mixing signal obtained with the actinic pump beam blocked is also presented as a reference. The four-beam signal is indistinguishable from the four-wave mixing signal at negative delay times, but a decrease in the total signal intensity is observed at positive delay times. Observation of a decrease in signal intensity is expected because of the sign reversal that takes place in the direct third- and fifth-order signals. That is, Figure 6.9a indicates that the direct third- and fifth-order signals interfere destructively. The difference, actinic-pump-on/actinic-pump-off, shown in Figure 6.9b represents the direct fifth-order signal (i.e. the third-order contribution has been removed in the difference). The third- and fifth-order line shapes are additionally overlaid in Figure 6.9c to illustrate the reversal in the signal sign.

We interpret the data shown in Figure 6.9 by considering the following components of the total signal intensity

$$\left|E^{(3)}+E^{(5)}+E_{cas}\right|^2 \approx \left|E^{(3)}\right|^2 + 2\left|E^{(3)}\right|\left|E^{(5)}\right|\cos\left(180^\circ\right) + 2\left|E^{(3)}\right|\left|E_{cas}\right|\cos\left(0^\circ\right) \qquad (6.9)$$

where it is assumed that the direct third-order signal field, $E^{(3)}$, is large compared to the direct fifth-order and cascaded responses, $E^{(5)}$ and E_{cas}. The second and third terms on the right side of Equation 6.9 have negative and positive signs, respectively. An actinic pump-induced decrease in signal intensity is predicted if $\left|E^{(5)}\right| >> \left|E_{cas}\right|$, whereas an increase in signal intensity

is predicted if $|E_{cas}| >> |E^{(5)}|$. The 180º phase-shift associated with the second term on the right side of Equation 6.9 is generally valid, because the direct third- and fifth-order signals have the same amounts of phase mismatch in the four-beam geometry. However, the 0º phase-shift in term 3 is dependent on the sample thickness and amount of phase mismatch for particular cascades. Therefore, we have also confirmed that the same signal sign is measured at path lengths of 0.2, 0.3, and 0.5 mm.

6.4.4. Dynamic Line Shapes of FSRS Signals Obtained by Six-Wave Mixing

In this section, the sensitivity and data acquisition rate of our method are demonstrated by measuring decay profiles of vibrational resonances in metMb. We also compare FSRS signals acquired in the five-beam geometry with cascaded responses simulated using experimental four-wave mixing signals. Simulations of this type were instrumental in identifying signatures of cascades in off-resonant experiments conducted on pure liquids. We also employed a similar approach in a recent multidimensional resonance Raman study of triiodide.[35]

FSRS signals acquired for metMb in the five-beam geometry are presented in Figure 6.10. These data represent the average of two different data sets. In each data set, the τ_1 delay is scanned 30 times in 15 minutes, and 200 points are acquired in each scan. Inspection of the contour plot makes clear that all vibrational resonances fully decay within 10 ps. Figure 6.10b overlays distributions of relaxation times obtained for modes at 670, 1120, 1370, and 1600 cm^{-1} using the maximum entropy method (MEM).[52] Analysis by the MEM is motivated by avoidance of assumptions about the shapes of decay profiles. Although powerful, the MEM is not often used in analysis of femtosecond transients, because it requires exceptionally high signal-to-noise ratios. The 670 and 1370-cm^{-1} resonances represent in-plane modes that are located on the

tetrapyrrole moiety, whereas many of the weaker resonances in the 1000-1300 cm^{-1} and 1400-1650 cm^{-1} wavenumber ranges are localized on the vinyl substituents.[44] Intensities of the resonances in the 1000-1300 cm^{-1} range are enhanced in the present experiments (compared to spontaneous Raman or traditional FSRS), because the intensity of the Stokes pulse maximizes in this range (see Figure 6.2).

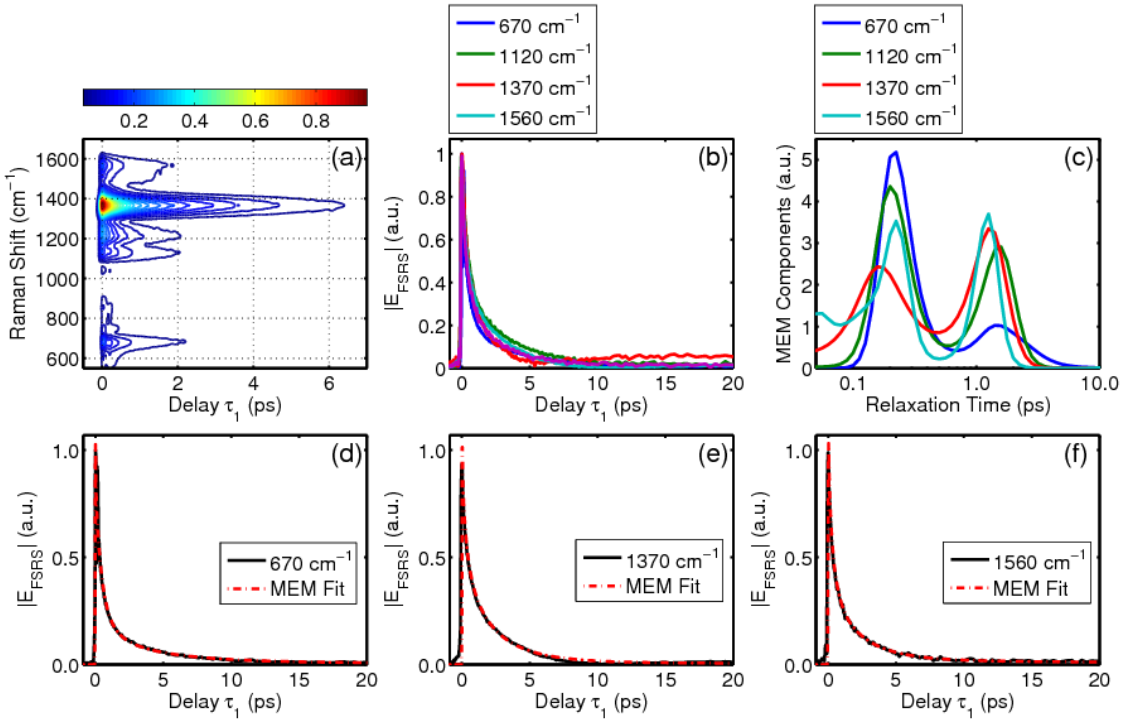

Figure 6.10. (a) Contour plot of the signal field magnitude, $|E_{FSRS}|$, obtained for metMb in the five-beam geometry. (b) Temporal decay profiles for vibrational resonances detected in the FSRS response. (c) Distributions of relaxation times for various resonances are obtained using the maximum entropy method. (d)-(f) FSRS signal field magnitudes are overlaid with fits conducted using the maximum entropy method.

Chergui and co-workers have recently identified two relaxation pathways in metMb that possess nearly equal efficiencies.[23] One pathway repopulates the ground state by way of sub-ps internal conversion from a high-energy charge transfer state, whereas the second pathway

proceeds through a number of intermediate iron spin states. Importantly, transient electronic resonances associated with both pathways overlap with the frequencies of the laser pulses employed in this work (see Figure 6.2). The FSRS experiments described in this section should therefore be sensitive to excited state relaxation even though the nonlinear response near 430 nm possesses significant contributions from the bleach of the Soret band.

The MEM analysis displayed in Figure 6.10c reveals peaks in the kinetic distributions near 0.22 ps and 1.4 ps for all vibrational modes. The peaks in the distributions centered near 0.22 ps encompass the time scales associated with two processes: (i) back-electron transfer between Fe^{2+} and the porphyrin; (ii) ground state recovery via a high-energy charge-separated excited state.[23] The peaks in the MEM distributions centered near 1.4 ps may reflect contributions from the second relaxation pathway, wherein an intermediate iron spin state (with S=1/2) is depopulated with a time constant of 1.1 ps. It is also possible that vibrational cooling dynamics contribute to this second peak in the MEM distribution.[53]

The relative amplitudes of the two peaks in the MEM distributions are fairly similar for the resonances associated with the vinyl substituents (1120 and 1560 cm^{-1}). However, the vibrational modes located on the tetrapyrrole (670 and 1370 cm^{-1}) differ markedly in the relative amplitudes of the two peaks, with the 670 cm^{-1} mode possessing a dominant 0.22-ps component. The signal intensity observed for a particular mode in FSRS reflects the dynamic resonance Raman cross section, which is governed by the difference in nuclear geometries associated with the pair of electronic states that comprise the resonance (i.e. difference in potential energy gradients). It is possible that differences in the relaxation rates observed for various resonances reflect mode-specific details regarding the internal conversion mechanisms in metMb. That is, at short delay times, before a significant amount of vibrational cooling has occurred, the non-

equilibrium distributions of vibrational quanta found in metMb may reflect the propensities for particular coordinates to act as "promoting modes" in the internal conversion processes.

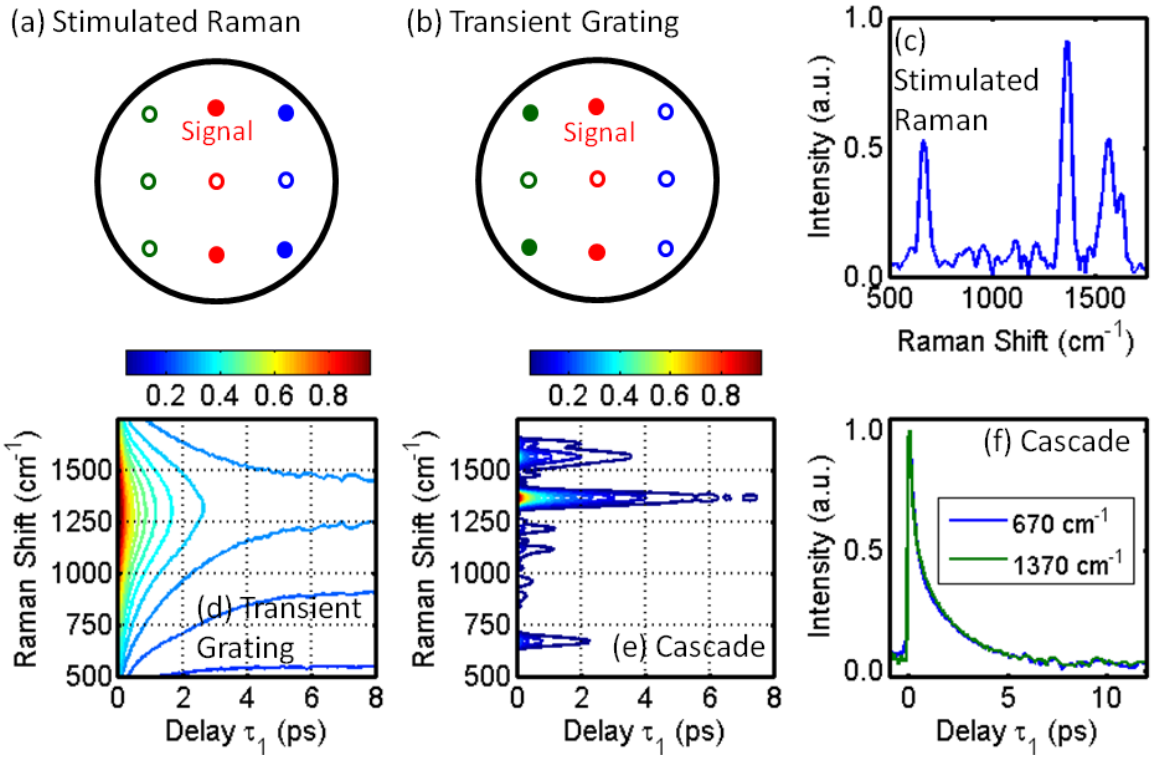

Figure 6.11. Laser beam geometries used to acquire (a) stimulated Raman and (b) transient grating signals shown in (c) and (d), respectively. Beams represented with solid circles reach the sample, whereas those represented with open circles are blocked with a mask. (e) The two four-wave mixing signals are combined to simulate the cascaded response. (f) Unlike the FSRS signals plotted in Figure 6.10, all vibrational resonances decay with indistinguishable temporal profiles in the simulated cascade. Signal magnitudes for the 670 and 1370-cm^{-1} vibrational resonances are shown as examples.

Cascaded signals computed using experimental four-wave mixing responses are displayed in Figure 6.11. This empirical approach does not require knowledge of the form of the optical response function or associated parameters. We assume only that the cascaded process combines a transient grating response (involving the actinic pump and Stokes) with a stimulated Raman response (involving the Raman pump and Stokes). This assumption is consistent with

the phase mismatch factors calculated for the experimental geometry (see below). Both of these four-wave mixing responses, which are denoted here as $S_{TG}(\tau_1, \omega_t)$ and $S_{SRS}(\omega_t)$, are readily measured by blocking the appropriate beams in the interferometer (see Figures 6.11a and 6.11b). The cascaded signal field is then computed by the product, $S_{CAS}(\tau_1, \omega_t) = S_{TG}(\tau_1, \omega_t) S_{SRS}(\omega_t)$.

The two four-wave mixing responses, $S_{TG}(\tau_1, \omega_t)$ and $S_{SRS}(\omega_t)$, and the cascade, $S_{CAS}(\tau_1, \omega_t)$, are shown in Figure 6.11. The four-wave mixing Raman spectrum, $S_{SRS}(\omega_t)$, appears similar to the six-wave mixing FSRS spectrum (at a fixed delay time), which is to be expected because the same Franck-Condon active modes contribute to both nonlinearities. In agreement with recent work on metMb,[23] the signal, $S_{TG}(\tau_1, \omega_t)$, decays within a few picoseconds. The simulated cascade, $S_{CAS}(\tau_1, \omega_t)$, obtained by combining $S_{TG}(\tau_1, \omega_t)$ and $S_{SRS}(\omega_t)$, exhibits negligible changes in the Raman spectrum during the relaxation process (i.e. the overall amplitude changes but the spectrum does not). Such delay time-invariant Raman spectra are inconsistent with the mode-specific transients displayed in Figure 6.10.

In summary, the present analysis suggests that cascades radiated in the 600-1700-cm^{-1} range in metMb will possess Raman spectra that are insensitive to the delay time. In other words, the relative amplitudes of the various peaks will be insensitive to the delay time. Such delay-independent Raman spectra are inconsistent with the measured FSRS signals shown in Figure 6.10. More generally, we anticipate that cascades will be distinguishable from direct processes in related heme proteins, where the relative magnitudes and frequencies of the peaks are known to evolve during the vibrational cooling process.[16]

6.5. Theoretical Analysis of Relative Magnitudes of Resonant FSRS Signals and Cascades

In this section, we use model calculations to compare direct fifth-order and cascaded third-order signal strengths for a model system that approximates metMb. All experimental tests conducted above are consistent with dominance of the direct fifth-order signal. The calculations presented here address the likelihood that this result will generalize to a wider variety of systems and experimental conditions.

6.5.1. Background

Cascades of third-order nonlinearities are generated in all spectroscopies that are fifth-order in the nonlinear polarization (e.g. 2D Raman, pump-repump-probe, visible pump-2DIR probe, etc). Third-order cascades are not unique to experiments that employ five incoming laser beams. In fact, phase-matching conditions for cascades are generally enhanced relative to the direct fifth-order response in geometries that employ few laser beams with small crossing angles.[54] Phase-matching efficiencies become essential design criteria when the intrinsic magnitudes of direct fifth-order signals are small compared to those associated with cascaded third-order processes.[55] Of course, laser beam geometries can be chosen purely as a matter of convenience if the direct signal is known to dominate the response. For example, the proven negligibility of third-order cascades has motivated simplified three-beam approaches in 3D-IR experiments.[56,57]

Cascades are known to significantly challenge off-resonant fifth-order Raman spectroscopies conducted on pure liquids and concentrated mixtures.[30,55,58] High sample concentrations are one reason why cascades are so dominant in these systems. Another reason is that the direct fifth-order signal is forbidden for harmonic systems in which the polarizability

depends linearly on the vibrational coordinate (i.e. lowest-order approximations).[31,33,59] Reliance on higher-order effects for signal generation is particularly problematic, because the cascades are not subject to such restrictions. We have recently discussed why electronically resonant conditions generally make the direct fifth-order response dominant in systems with Franck-Condon active modes.[35] The key is that all displaced modes (harmonic and anharmonic) may contribute to the signal without non-Condon effects in resonant FSRS.[36]

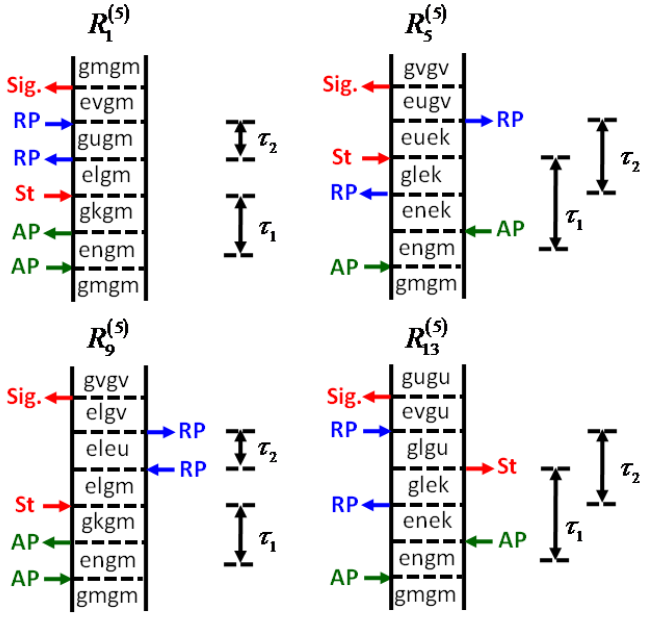

Figure 6.12. Double-sided Feynman diagrams associated with four classes of terms in the FSRS response function. The terms are classified according to whether or not they evolve in ground or excited state populations during the delay times, τ_1 and τ_2. The laser pulses associated with each field-matter interaction are indicated in the figure in the same color-code employed in Figure 6.2.

6.5.2. Response Functions

The FSRS response for a system in which resonance enhancement is dominated by a single pair of electronic states possesses 16 response functions (see Section C.2 in Appendix C).

The response functions can be divided into four classes based on whether or not the system is in the ground or excited state during the two population times (see Figure 6.12 for one member of each class). An earlier theoretical description of FSRS has grouped terms in a related way.[60] In metMb, excited state populations may contribute at sub-picosecond delay times (i.e. before internal conversion is complete), whereas dynamics on the picosecond time scale primarily reflect vibrational cooling in the electronic ground state.[21-25] We consider all terms here as the goal is simply to estimate relative signal strengths for direct and cascaded responses.

It is instructive to consider one of the polarization components in the FSRS response. The polarization component associated with the $R_1^{(5)}$ diagram in Figure 6.12 is given by

$$P_1^{(5)}(\omega_t) = i\frac{N\xi_{AP}^2\xi_{RP}^2\xi_{St}\left|\mu_{eg}\right|^6}{\hbar^5}\sum_{mnkluv} B_m \langle n|m\rangle\langle n|k\rangle\langle l|k\rangle\langle l|u\rangle\langle v|u\rangle\langle v|m\rangle \times L_{en,gm}(\omega_{AP}) D_{gk,gm}(\tau_1) L_{el,gm}(\omega_t) J_{gu,gm}(\omega_t - \omega_{RP}) L_{ev,gm}(\omega_t) \tag{6.10}$$

where ξ_j are the electric field amplitudes associated with the three types of laser pulses (actinic pump, Raman pump, Stokes), N is the number density, μ_{eg} is the electronic transition dipole for the Soret band, B_m is the Boltzmann population of level m, $\langle n|m\rangle$ is a vibrational overlap integral (with excited state index in the bra),[61] and the summation is carried out with respect to dummy indices for vibrational energy levels. The functions, $L_{en,gm}(\omega)$, are Lorentzian line shapes associated with resonances between vibronic levels in electronic states g and e, whereas $D_{gk,gm}(\tau_1)$ describes vibrational wavepacket motion induced by the actinic pump in the delay time, τ_1 (see Section C.2 in Appendix C). The function

$$J_{gu,gm}\left(\omega_t-\omega_{RP}\right)=\frac{\exp\left(-\Lambda_{RP}\tau_2\right)}{\left(\omega_t-\omega_{RP}+\omega_{um}\right)+i\left(\Gamma_{vib}-\Lambda_{RP}\right)} \tag{6.11}$$

provides insight into aspects of the signal that are unique to the present approach. The denominator suggests that the line width of the resonance is reduced by introducing a time delay between Raman pump pulses (i.e. Γ_{vib} and Λ_{RP} have opposite signs). However, the numerator makes clear that such enhancement in spectral resolution comes at the expense of signal intensity; the magnitude of the polarization decreases exponentially with τ_2. These aspects of the model are consistent with the experimental data presented in Section 6.3.

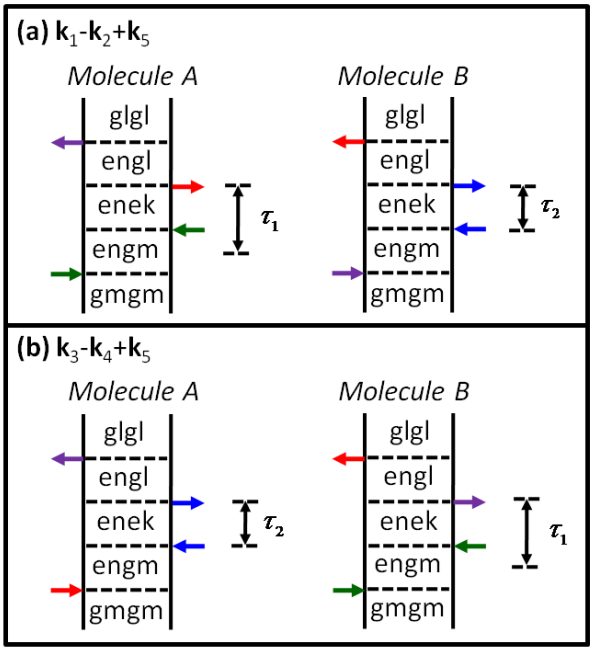

Figure 6.13. Feynman diagrams associated with the nonlinearities on the two molecules involved in third-order cascades with intermediate phase-matching conditions (a) $k_1-k_2+k_5$ and (b) $k_3-k_4+k_5$. Field-matter interactions are color-coded as follows: actinic pump is green; Raman pump is blue; Stokes is red; cascaded signal field is red; the field radiated at the intermediate step in the cascade is purple.

In the present laser beam geometries, we consider third-order cascades with intermediate phase-matching conditions, $k_1 - k_2 + k_5$ and $k_3 - k_4 + k_5$. Additional cascades are possible (e.g. $k_2 - k_1 + k_4$) but possess much smaller phase-matching efficiencies. The polarization components related to the cascaded nonlinearities are summarized in Section C.3 in Appendix C. The two types of cascades essentially permute coherent Stokes Raman scattering (CSRS) and pump-probe (PP) responses on the two molecules involved in the process (see Figure 6.13). For example, third-order polarization components associated with these two types of responses are given by

$$P_{1,PP}^{(3)}(\omega_t) = i\frac{N\xi_{AP}^2\xi_{St}\left|\mu_{eg}\right|^4}{\hbar^3}\sum_{mnkl} B_m \langle n|m\rangle\langle k|m\rangle\langle k|l\rangle\langle n|l\rangle \times L_{en,gm}(\omega_{AP}) D_{en,ek}(\tau_1) L_{en,gl}(\omega_t) \tag{6.12}$$

and

$$P_{1,CSRS}^{(3)}(\omega_t) = -\frac{N\xi_{RP}^2\xi_{St}\left|\mu_{eg}\right|^4}{\hbar^3}\sum_{mnkl} B_m \langle n|m\rangle\langle k|m\rangle\langle k|l\rangle\langle n|l\rangle \times L_{en,gm}(\omega_t) J_{en,ek}(\omega_t - \omega_{RP}) L_{en,gl}(\omega_t) \tag{6.13}$$

where we have derived these expressions under the same assumptions used to describe the direct fifth-order response (see Section C.2 Appendix C). The cascaded signal field is proportional to the product of $P_{1,PP}^{(3)}(\omega_t)$ and $P_{1,CSRS}^{(3)}(\omega_t)$.

The above formulas highlight three key issues that govern relative magnitudes of direct and cascaded responses:

(i) The cascaded signal field scales as the square of the concentration, whereas the field radiated by the fifth-order polarization is linear in concentration. This is one reason why cascades are generally negligible at optical densities employed under resonant conditions in transmissive geometries. For example, the concentration of CS_2, in which cascades are dominant, is roughly 80,000 times larger than the concentration employed here.

(ii) The direct and cascaded responses respectively include 3 and 4 resonant electronic line shape functions, $L_{en,gm}(\omega)$. The direct fifth-order signal field therefore becomes more dominant as the electronic dephasing rate increases.[35] This aspect of the nonlinear response favors the direct fifth-order signal in condensed phases at ambient temperatures, where line widths are generally greater than 1000 cm^{-1}.

(iii) The direct and cascaded polarization components involve sums of products of 8 and 6 vibrational overlap integrals, respectively. The direct fifth-order signal field becomes more dominant as the mode displacement increases because the integrals are all less than 1 and the products of integrals generally decrease as the mode displacement increases. In related work, we found that this effect becomes quite pronounced in systems with extremely large displacements (displacements greater than 3).[35]

6.5.3. Model Calculations

In this section, we evaluate the ratio between the cascaded third-order and direct fifth-order signal magnitudes, $\left|E_{cas}^{(5)}(\omega_t)\right| / \left|E_{direct}(\omega_t)\right|$, which are defined in Sections C.3 and C.2, respectively, in Appendix C. These model calculations are motivated by knowledge of how the relative signal strengths depend on properties of the model system and the frequencies of the

incident pulses. Insights derived from these calculations are not dependent on an optimal parameterization for metMb. Rather, parameters are scanned over wide ranges to explore general effects that apply not only to metMB but also to other heme proteins with similar optical properties. Figure 6.14 presents spectra computed with a displaced 1370-cm^{-1} mode, where the actinic and Raman pump frequencies, ω_{AP} and ω_{RP}, are taken to be equal to the electronic resonance frequency, ω_{eg}. The vibrational resonances appear on a frequency-dependent baseline, which is consistent with the model developed by Ernsting and co-workers.[3] We consider a system with a single harmonic mode to keep the number of parameters manageable. For fundamental transitions, we find that the ratio, $\left|E_{cas}(\omega_t)\right| / \left|E^{(5)}_{direct}(\omega_t)\right|$, is insensitive to the number of vibrational modes in the system.

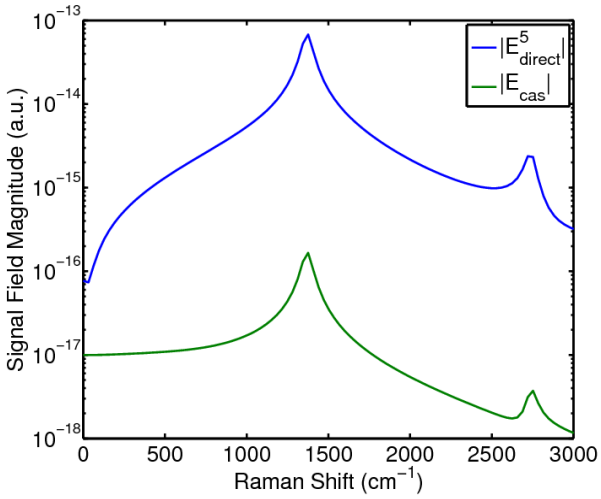

Figure 6.14. Absolute values of signal spectra computed using the models presented in Sections C.2 and C.3 in Appendix C and the parameters in Tables C.1 and C.2. The system possesses a single 1370-cm^{-1} harmonic mode with a displacement of 0.35 (a reasonable estimate for metMb).[42] The frequency of the actinic pump pulse is set equal to the electronic resonance frequency, $\omega_{AP} = \omega_{eg}$. This calculation assumes that the five-beam geometry is employed (cascades are 4 times weaker in the four-beam geometry).

We begin by exploring the parameter space of the mode frequency and displacement in Figure 6.15a. The ratios between $\left|E_{cas}^{(5)}(\omega_t)\right|$ and $\left|E_{direct}(\omega_t)\right|$ are computed at values of the Raman shift, $\omega_{RP}-\omega_t$, equal to the mode frequency (i.e. at the peak of the fundamental transition). The calculations predict extremely small ratios (<0.01) at frequencies near the 1370 cm^{-1} mode. The ratio, $\left|E_{cas}(\omega_t)\right|/\left|E_{direct}^{(5)}(\omega_t)\right|$, increases as the vibrational frequency decreases, but $\left|E_{direct}^{(5)}(\omega_t)\right|$ remains dominant down to the lowest frequency probed in this work (i.e. the 670-cm^{-1} mode). The calculation is carried out over a wide range of mode displacements in order to establish behaviors that will generalize to other systems. Displacements of the 670-cm^{-1} and 1370-cm^{-1} modes are near 0.25 and 0.35, respectively.[53]

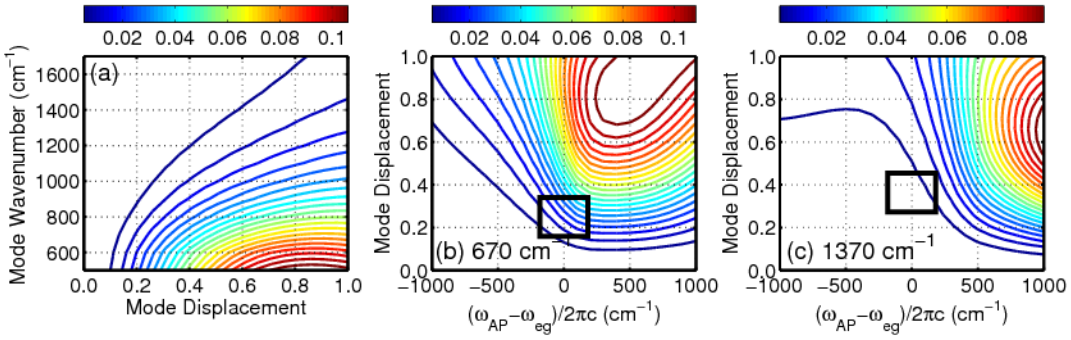

Figure 6.15. (a) The ratio, $\left|E_{cas}(\omega_t)\right|/\left|E_{direct}^{(5)}(\omega_t)\right|$, is computed for a system with a single harmonic mode under electronically resonant conditions, $\omega_{AP}=\omega_{eg}$. The ratio is computed at the value of the Raman Shift equal to the mode frequency (i.e. at the peak of the vibrational resonance). (b) The ratio, $\left|E_{cas}(\omega_t)\right|/\left|E_{direct}^{(5)}(\omega_t)\right|$, is computed for a 670- cm^{-1}mode at various dimensionless displacements and detuning factors, $\omega_{AP}-\omega_{eg}$. (c) The ratio, $\left|E_{cas}(\omega_t)\right|/\left|E_{direct}^{(5)}(\omega_t)\right|$, is computed for a 1370-cm^{-1} mode at various dimensionless mode displacements and detuning factors, $\omega_{AP}-\omega_{eg}$. Boxes are drawn in the regions of the plots relevant to myoglobin in panels (b) and (c).

The laser detuning and mode displacement are varied for the 670 cm^{-1} and 1370-cm^{-1} modes in Figures 6.15b and 6.15c. The calculations suggest greater dominance of $\left|E^{(5)}_{direct}(\omega_t)\right|$ when the actinic and Raman pump beams are tuned to the low-frequency side of the electronic resonance (i.e. $\omega_{AP} < \omega_{eg}$ and $\omega_{RP} < \omega_{eg}$). Notably, the ratio remains small when the beams are within the approximate 1500-cm^{-1} linewidth of the electronic transition ($2\Gamma_{eg}$). Regions of the plots most relevant to the present application to metMb are indicated with boxes. The calculations predict that $\left|E^{(5)}_{direct}(\omega_t)\right|$ remains dominant for displacements between 0 and 1.

The present model system approximates the response of metMb when photoexcited in the region of the Soret band. Inclusion of additional excited states in the model (e.g. higher-energy spin states of iron) is unlikely to affect the ratio because of their relatively small contributions. Increases in $\left|E_{cas}(\omega_t)\right|$ and $\left|E^{(5)}_{direct}(\omega_t)\right|$ are largely offset when new classes of signal components are introduced (e.g. resonances between excited states), because terms with nearly equal weights must then be added to both types of fields. Perhaps the most important issue is that $\left|E^{(5)}_{direct}(\omega_t)\right|$ and $\left|E_{cas}(\omega_t)\right|$ always consist of sums of products of 6 and 8 vibrational overlap integrals, respectively. The terms in $\left|E_{cas}(\omega_t)\right|$ will generally be smaller than those in $\left|E^{(5)}_{direct}(\omega_t)\right|$, because each of the overlap integrals in the product is less than 1. The direct response, $\left|E^{(5)}_{direct}(\omega_t)\right|$, can become many orders of magnitude larger than $\left|E_{cas}(\omega_t)\right|$ in systems with extremely large mode displacements.[35] This, together with the low sample concentrations typically employed in transmissive laser beam geometries, suggests that third-order cascades are unlikely to

outcompete the resonant FSRS response in related systems under similar experimental conditions.

6.6. Concluding Remarks

Four and five-beam implementations of FSRS have been used in this work to significantly reduce the background of residual laser light and lower-order nonlinearities that would be present in the three-beam geometry carried out with the same electronically resonant laser pulses. The background-free nature of the five-beam geometry supports excellent signal-to-noise ratios and short data acquisition times. As with any experimental technique, the present method possesses strengths and limitations that are important to take into account when deciding on an approach. The fast data acquisition rate and sensitivity achieved by the present method come at the expense of nonlinearities that are more complicated than those associated with spontaneous Raman probes. This is one reason why time-resolved spontaneous Raman spectroscopy may be preferred for studies of relaxation dynamics in heme proteins that are slower than 0.7 ps.[16] We envision that the power of the present method may be fully exploited in studies of low-frequency vibrational coherences in τ_1, and their anharmonic couplings to vibrational resonances in τ_2 (i.e. multidimensional analogues of third-order vibrational coherence studies).[53] It may also be possible to implement hybrid FSRS/2D photon echo pulse sequences in a five-beam geometry.

Significant contributions from cascaded nonlinearities have been ruled out with control experiments based on the signal phase, concentration dependence, and spectroscopic line shapes. In addition, we have developed a model to explore how the susceptibility to cascades depends on parameters of the system, the frequencies of the incoming beams, and the laser beam geometry.

Our calculations suggest that third-order cascades are less than 5% of the signal in the entire vibrational frequency range examined in this study. The present work (and our related study of triiodide)[35] suggests that cascades are unlikely to be problematic at the optical densities typically employed in transmissive beam geometries. In such experiments, concentrations are typically tens of thousands of times lower than those associated with the pure liquids and concentrated mixtures in which cascades are known to dominate.[30,55,58] Moreover, Franck-Condon active modes will always dominate the direct fifth-order response under electronically resonant conditions (i.e. the direct response is "allowed" under resonant conditions). Together, the control experiments and model calculations presented here suggest promise for multidimensional resonance Raman investigations of heme proteins.

6.7. REFERENCES

(1) Kukura, P.; McCamant, D. W.; Mathies, R. A. *Annu. Rev. Phys. Chem.* **2007**, *58*, 461.

(2) Frontiera, R. R.; Dasgupta, J.; Mathies, R. A. *J. Am. Chem. Soc.* **2009**, *131*, 15630.

(3) Weigel, A.; Dobryakov, A.; Klaumünzer, B.; Sajadi, M.; Saalfrank, P.; Ernsting, N. P. *J. Phys. Chem. B* **2011**, *115*, 3656.

(4) Yu, W.; Zhou, J.; Bragg, A. E. *J. Phys. Chem. Lett.* **2012**, *3*, 1321.

(5) Kraack, J. P.; Wand, A.; Buckup, T.; Motzkus, M.; Ruhman, S. *Phys. Chem. Chem. Phys.* **2013**, *15*, 14487.

(6) Kraack, J. P.; Buckup, T.; Motzkus, M. *J. Phys. Chem. Lett.* **2013**, *4*, 383.

(7) Pontecorvo, E.; Ferrante, C.; Elles, C. G.; Scopigno, T. *Opt. Express* **2013**, *21*, 6866.

(8) Rhinehart, J. M.; Challa, J. R.; McCamant, D. W. *J. Phys. Chem. B* **2012**, *116*, 10522.

(9) Fang, C.; Frontiera, R. R.; Tran, R.; Mathies, R. A. *Nature* **2009**, *462*, 200.

(10) Oscar, B. G.; Liu, W.; Zhao, Y.; Tang, L.; Wang, Y.; Campbell, R. E.; Fang, C. *Proc. Natl. Acad. Sci.* **2014**, *111*, 10191.

(11) Provencher, F.; Bérubé, N.; Parker, A. W.; Greetham, G. M.; Towrie, M.; Hellmann, C.; Côté, M.; Stingelin, N.; Silva, C.; Hayes, S. C. *Nat. Commun.* **2014**, *5*, 4288.

(12) Wende, T.; Liebel, M.; Schnedermann, C.; Pethick, R. J.; Kukura, P. *J. Phys. Chem. A* **2014**, *118*, 9976.

(13) Mukamel, S.; Biggs, J. D. *J. Chem. Phys.* **2011**, *134*, 161101.

(14) McCamant, D. W. *J. Phys. Chem. B* **2012**, *115*, 9299.

(15) Dorfman, K. E.; Fingerhut, B. P.; Mukamel, S. *J. Chem. Phys.* **2013**, *139*, 124113.

(16) Kruglik, S. G.; Lambry, J.-C.; Martin, J.-L.; Vos, M. H.; Negrerie, M. *J. Raman. Spectrosc.* **2010**, *265-275*.

(17) McCamant, D. W.; Kukura, P.; Yoon, S.; Mathies, R. A. *Rev. Sci. Instrum.* **2004**, *75*, 4971.

(18) Kovalenko, S. A.; Dobryakov, A.; Ernsting, N. P. *Rev. Sci. Instrum.* **2011**, *82*, 063102.

(19) Grumstrup, E. M.; Chen, Z.; Vary, R. P.; Moran, A. M.; Schanze, K. S.; Papanikolas, J. P. *J. Phys. Chem. B* **2013**, *117*, 8245.

(20) McCamant, D. W. Femtosecond Stimulated Raman Spectroscopy of Ultrafast Biophysical Reaction Dynamics, University of California at Berkeley, 2004.

(21) Petrich, J. W.; Poyart, C.; Martin, J.-L. *Biochemistry* **1988**, *27*, 4049.

(22) Ye, X.; Demidov, A.; Rosca, F.; Wang, W.; Kumar, A.; Ionascu, D.; Zhu, L.; Barrick, D.; Wharton, D.; Champion, P. M. *J. Phys. Chem. A* **2003**, *107*, 8156.

(23) Consani, C.; Auböck, G.; Bräm, O.; van Mourik, F.; Chergui, M. *J. Chem. Phys.* **2014**, *140*, 025103.

(24) Martin, J.-L.; Vos, M. H. *Annu. Rev. Biophys. Biomol. Struct.* **2006**, *21*, 199.

(25) Vos, M. H. *Biochim. Biophys. Acta* **2008**, *1777*, 15.

(26) Ivanecky III, J. E.; Wright, J. C. *Chem. Phys. Lett.* **1993**, *206*, 437.

(27) Ulness, D. J.; Kirkwood, J. C.; Albrecht, A. C. *J. Chem. Phys.* **1998**, *108*, 3897.

(28) Blank, D. A.; Kaufman, L. J.; Fleming, G. R. *J. Chem. Phys.* **1999**, *111*, 3105.

(29) Kubarych, K. J.; Milne, C. J.; Lin, S.; Astinov, V.; Miller, R. J. D. *J. Chem. Phys.* **2002**, *116*, 2016.

(30) Wilson, K. C.; Lyons, B.; Mehlenbacher, R.; Sabatini, R.; McCamant, D. W. *J. Chem. Phys.* **2009**, *131*, 214502.

(31) Tokmakoff, A.; Lang, M. J.; Larsen, D. S.; Fleming, G. R.; Chernyak, V.; Mukamel, S. *Phys. Rev. Lett.* **1997**, *79*, 2702.

(32) Jansen, T. I. C.; Snijders, J. G.; Duppen, K. *J. Chem. Phys.* **2001**, *114*, 109210.

(33) Mehlenbacher, R.; Lyons, B.; Wilson, K. C.; Du, Y.; McCamant, D. W. *J. Chem. Phys.* **2009**, *131*, 244512.

(34) Cina, J. A.; Kovac, P. A. *J. Phys. Chem. A* **2013**, *117*, 6084.

(35) Molesky, B. P.; Giokas, P. G.; Guo, Z.; Moran, A. M. *J. Chem. Phys.* **2014**, *141*, 114202.

(36) Tanimura, Y.; Okumura, K. *J. Chem. Phys.* **1996**, *106*, 2078.

(37) van Veldhoven, E.; Khurmi, C.; Zhang, X.; Berg, M. A. *ChemPhysChem* **2007**, *8*, 1761.

(38) Berg, M. A. *Adv. Chem. Phys.* **2012**, *150*, 1.

(39) Underwood, D. F.; Blank, D. A. *J. Phys. Chem. A* **2005**, *109*, 3295.

(40) Moran, A. M.; Nome, R. A.; Scherer, N. F. *J. Chem. Phys.* **2007**, *127*, 184505:1.

(41) Park, S.; Kim, J.; Scherer, N. F. *Phys. Chem. Chem. Phys.* **2012**, *14*, 8116.

(42) Bangcharoenpaurpong, O.; Schomacker, K. T.; Champion, P. M. *J. Am. Chem. Soc.* **1984**, *106*, 5688.

(43) Moran, A. M.; Nome, R. A.; Scherer, N. F. *J. Phys. Chem. A* **2006**, *110*, 10925.

(44) Hu, S.; Smith, K. M.; Spiro, T. G. *J. Am. Chem. Soc.* **1996**, *118*, 12638.

(45) Lepetit, L.; Chériaux, G.; Joffre, M. *J. Opt. Soc. Am. B* **1995**, *12*, 2467.

(46) Hoffman, D. P.; Valley, D.; Ellis, S. R.; Creelman, M.; Mathies, R. A. *Opt. Express* **2013**, *21*, 21685.

(47) Laaser, J. E.; Xiong, W.; Zanni, M. T. *J. Phys. Chem. B* **2011**, *115*, 2536.

(48) Womick, J. M.; Miller, S. A.; Moran, A. M. *J. Phys. Chem. A* **2009**, *113*, 6587.

(49) Ding, F.; Fulmer, E. C.; Zanni, M. T. *J. Chem. Phys.* **2005**, *123*, 094502.

(50) Garret-Roe, S.; Hamm, P. *J. Chem. Phys.* **2009**, *130*, 164510.

(51) Busby, E.; Carroll, E. C.; Chinn, E. M.; Chang, L.; Moulé, A. J.; Larsen, D. S. *J. Phys. Chem. Lett.* **2011**, *2*, 2764.

(52) Kumar, A. T. N.; Zhu, L.; Christian, J. F.; Demidov, A.; Champion, P. M. *J. Phys. Chem. B* **2001**, *105*, 7847.

(53) Rosca, F.; Kumar, A. T. N.; Ye, X.; Sjodin, T.; Demidov, A.; Champion, P. M. *J. Phys. Chem. A* **2000**, *104*, 4280.

(54) Dunlap, B.; Wilson, K. C.; McCamant, D. W. *J. Phys. Chem. A* **2013**, *117*, 6205.

(55) Kubarych, K. J.; Milne, C. J.; Lin, S.; Astinov, V.; Miller, R. J. D. *J. Chem. Phys.* **2002**, *116*, 2016.

(56) Fulmer, E. C.; Ding, F.; Zanni, M. T. *J. Chem. Phys.* **2005**, *122*, 034302.

(57) Mukherjee, S. S.; Skoff, D. R.; Middleton, C. T.; Zanni, M. T. *J. Chem. Phys.* **2013**, *139*, 144205.

(58) Blank, D. A.; Kaufman, L. J.; Fleming, G. R. *J. Chem. Phys.* **1999**, *111*, 3105.

(59) Jansen, T. I. C.; Snijders, J. G.; Duppen, K. *J. Chem. Phys.* **2001**, *114*, 109210.

(60) Sun, Z.; Lu, J.; Zhang, D. H.; Lee, S.-Y. *J. Chem. Phys.* **2008**, *128*, 144114.

(61) Myers, A. B.; Mathies, R. A.; Tannor, D. J.; Heller, E. J. *J. Chem. Phys.* **1982**, *77*, 3857.

CHAPTER 7: TWO-DIMENSIONAL RESONANCE RAMAN SPECTROSCOPY OF WATER- AND OXYGEN- LIGATED MYOGLOBIN

7.1. Introduction

Once the specialization of a small number of experimental groups, multidimensional laser spectroscopies have become fairly widespread in the past 20 years with applications spanning the traditional disciplines of chemistry, biology, and physics.[1-10] The development of multi-dimensional techniques is rooted in the picosecond coherent Raman spectroscopies of the late 1970's and early 1980's.[11-14] At the time, it was unclear whether or not traditional (one-dimensional) coherent Raman measurements could distinguish between homogeneous and inhomogeneous line broadening mechanisms.[15-17] Theoretical work showed that higher-order (multidimensional) methods were indeed required to obtain such information,[18-20] and early success was achieved in Raman echo experiments (i.e. eight-wave mixing).[21] Several experimental groups took up the challenge of conducting six-wave mixing experiments in the mid-1990's but met substantial technical challenges.[22-27] Success in six-wave mixing measurements was achieved after years of exhaustive efforts.[27,28] Difficulties encountered in these pioneering works significantly slowed further development of multidimensional Raman techniques. However, interest in this class of experiments has been reinitiated by related methods that are used to study molecular photochemistries.[29-40]

In this paper, we present two-dimensional resonance Raman (2DRR) measurements that blend different types of higher-order Raman spectroscopies. The multi-beam aspect of the

experiment illustrated in Figure 7.1 is similar in nature to earlier off-resonant 2D Raman work,[27,28] whereas the combination of narrowband and broadband pulses is inspired by Femtosecond Stimulated Raman Spectroscopy (FSRS).[30,32] As depicted in Figure 7.1, the experiment begins when an actinic pump pulse initiates vibrational motion of the system in the variable delay, τ_1. Fourier transformation with respect to τ_1 constitutes the first dimension of the 2DRR spectrum. Vibrational motion is re-initiated by time-coincident Raman pump and Stokes pulses before a second Raman pump pulse induces signal emission. The second dimension of the 2DRR spectrum is obtained by dispersing the signal pulse on an array detector.

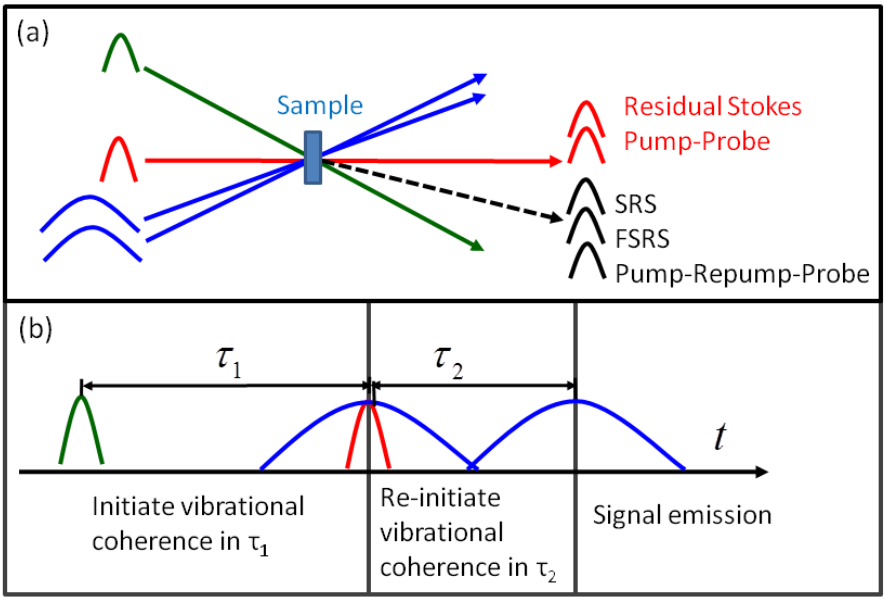

Figure 7.1. (a) A four-beam FSRS geometry is used in this work to eliminate the portion of the background associated with residual Stokes light and a pump-probe response. The color code is as follows: the actinic pump is green, the Raman pump is blue, and the Stokes pulse is red. (b) Vibrational coherences in τ_1 are resolved by numerically Fourier transforming the signal with respect to the delay time. Time-coincident Raman pump and Stokes pulses then initiate a second set of vibrational coherences, which are resolved by dispersing the signal pulse on an array detector. The fixed time delay, τ_2, is used to suppress the broadband pump-repump-probe response of the solution.

The approach is distinct from traditional three-pulse FSRS in that (i) residual laser light does not travel in the same direction as the signal beam and (ii) a fixed delay, τ_2, is used to suppress the intense broadband pump-repump-probe response.[41] The data acquisition rate and sensitivity of our method facilitate detection of the 2DRR response, which is generally less than 5% of the total fifth-order signal. Traditional three-beam FSRS offers other advantages such as automatic heterodyne detection and straightforward implementation of two-color experiments.[30]

Measurements and model calculations are conducted for both metmyoglobin (metMb) and oxymyoglobin (MbO_2) in order to establish signatures of inhomogeneous line broadening and anharmonic coupling in 2DRR spectra. The charge of the iron atom is +3 (ferric) and +2 (ferrous) in metMb and MbO_2, respectively. Of course, the two systems also differ in whether water (metMb) or oxygen (MbO_2) is coordinated on the distal side of the heme group. Sub-100 fs photodissociation of oxygen is induced following photoexcitation in the visible spectral range in MbO_2, whereas metMb relaxes to the ground electronic state by way of non-radiative processes on the picosecond time scale.[42-47] In analogy with other 2D methods, the present 2DRR measurements reveal heterogeneity within the ensembles for the two systems. The 220-cm^{-1} iron-histidine stretching mode is of particular interest because of its prominence in MbO_2, where the heme moiety transitions from a planar to non-planar geometry following photodissociation.[48] In addition, vibrational modes associated with the propionic acid side chains may provide insight into energy exchange between the heme and aqueous solvent.[49-52] Line broadening mechanisms of these modes are intimately connected to such vibrational energy exchange, because they reflect fluctuations in the geometries.

The present work builds upon a variety of experimental approaches that we have developed for conducting 2DRR experiments in recent years.[41,53,54] An earlier report of the

technique employed in this work focused primarily on experimental issues.[41] Control experiments were used to show that the response of metMb exhibits the anticipated (correct) dependence on sample concentration and on the intensities of the incoming beams. The susceptibility of the experiment to cascaded four-wave mixing responses was an issue of primary concern, because these undesired nonlinearities present significant challenges in off-resonant 2D Raman experiments.[26-28,55,56] It was also shown that cascades of four-wave mixing signals are negligible under our experimental conditions. Calculations suggest the selection rules that enhance cascaded signal intensity under electronically off-resonant conditions are obviated when all pulses are electronically resonant with the system. In effect, the direct and cascaded signals compete on the same footing when all laser beams are tuned into electronic resonance. The cascaded signal is weaker than the direct response with optical densities of metMb less than 1.0, because it involves two more field-matter interactions (i.e. it is a higher-order process in this respect). Our analysis suggests that the direct response of myoglobin will also dominate in a conventional three-beam FSRS geometry. That is, it may generally be possible to conduct 2DRR spectroscopy without beam geometries cleverly designed to induce phase mismatch in third-order nonlinearities.

7.2. Experimental Methods

7.2.1. Sample Preparation

Myoglobin from horse skeletal muscle (Sigma-Aldrich) is dissolved in 0.1 M sodium phosphate buffer at a pH of 7.0. The metMb solutions are centrifuged at 6000 revolutions per minute for 15 minutes before each experiment to optimize the optical quality. To convert metMb to MbO_2, 10-fold molar excess of sodium hydrosulfite is added to reduce metMb. Air is then

bubbled through the solution for 15 minutes until it is bright red in color. Attainment of a high quality MbO_2 sample is confirmed by comparison of the sample's linear absorption to the known spectrum of MbO_2. The primary metric is the peak position of the Soret band, which is located at 409 and 418 nm for metMb and MbO_2, respectively.[57] Spontaneous Raman spectra are also used to confirm the position of the most intense in-plane bond stretching vibration (i.e. an oxidation state marker band). The vibrational frequencies of this mode are close to 1373 and 1356 cm^{-1} for metMb and MbO_2 , respectively.[58,59] In all experiments, the 0.2 mM sample of myoglobin is flowed through a wire-guided jet with a thickness of 220 μm, where the reservoir volume is 50 mL.[60] Absorbance spectra are measured before and after experiments to confirm the absence of sample degradation.

7.2.2. Spectroscopic Measurements

In this section, we summarize key aspects of the experimental approach, which is described at length in Reference [41]. As in earlier work, we employ laser pulses which are all resonant with the Soret bands of metMb and MbO_2 (see Figure 7.2). The narrowband Raman pump pulses are generated by sending 70 fs, 410 nm second harmonic pulses through a 4F spectral filter consisting of two 2400 g/mm gratings and two 25 cm focal length lenses. Pulses with spectral widths of 50 cm^{-1} are obtained by placing a slit with a 890 μm width at the 2F plane. Broadband actinic pump and Stokes pulses are produced by focusing a 90 μJ, 410 nm second harmonic beam into a 75 cm long hollow core fiber filled with 1.0 atm of argon gas. The spectrally broadened output of the fiber is compressed using fused-silica prisms separated by 50 cm to achieve an instrument response of 20 fs over the spectral range corresponding to Raman shifts of 200-1500 cm^{-1} (413-437 nm).

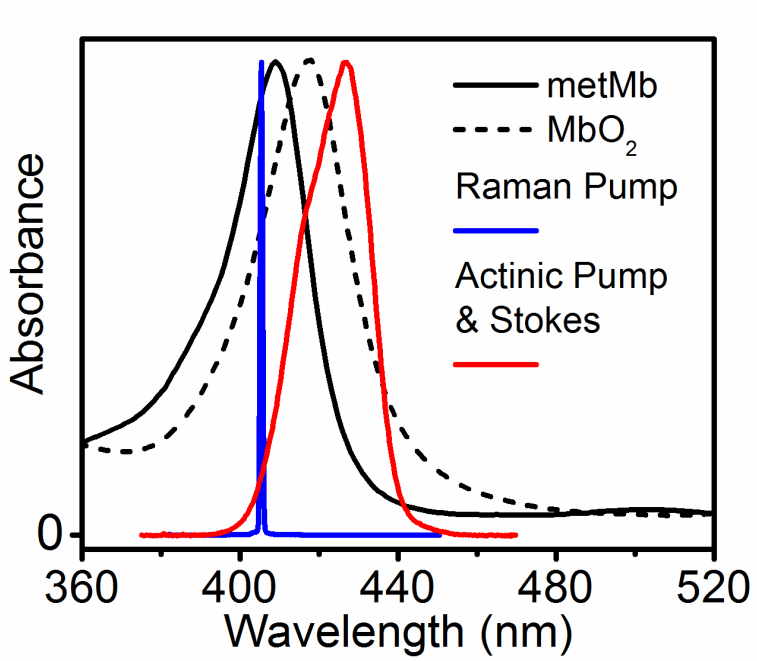

Figure 7.2. Laser spectra are overlaid on the linear absorbance spectra of (a) metMb and (b) MbO_2 in aqueous buffer solution at pH=7.0.

Experiments are conducted with the diffractive optic-based interferometer shown in Figure 7.3. All beams are focused onto the diffractive optic with a 50 cm focal length spherical mirror. Approximately 25% of each incident beam is diffracted into each of the three diffraction orders (0 and +/-1). The 20 cm focal length imaging mirror is rotated off-axis by approximately 5º (i.e. the minimum amount). The actinic pump and Raman pump beams cross at approximately 6.9º in the diffractive optic and are bisected by the Stokes beam. The angle between the +1 and -1 diffraction orders of the Raman pump beams is 6.9º. The angle between +1 and -1 diffraction orders of the actinic pump and Stokes beams is 7.2º; the actinic pump and Stokes pulses have the same spectrum (see Figure 7.2). Pulse energies of the actinic pump and Stokes pulses are 100 nJ each. The pulse energy of each Raman pump pulse is 150 nJ. The FWHM spot sizes of all laser beams are 200 μm at the sample position.

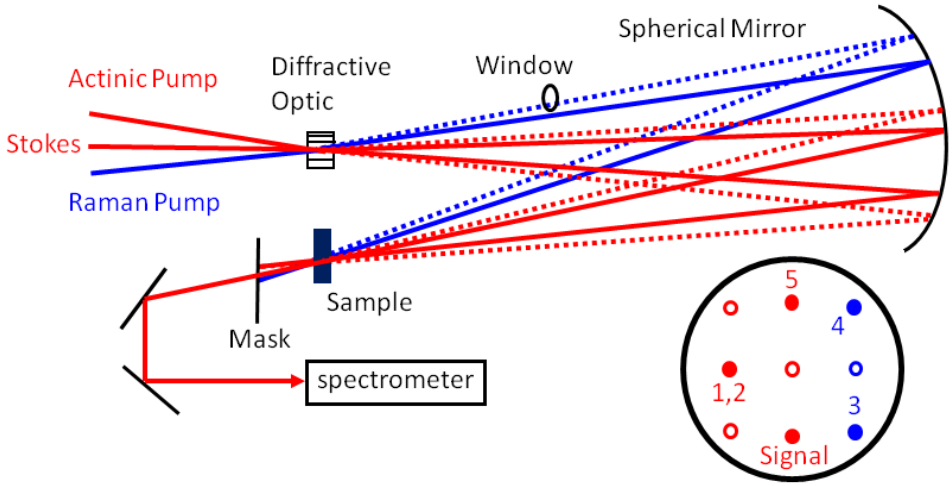

Figure 7.3. Diffractive optic-based interferometer used for 2DRR measurements. The transparent fused silica window delays pulse 3 by 290 fs with respect to pulse 4 (delay τ_2 in Figure 7.1). A four-beam geometry is used to detect the signal radiated in the direction, $k_1 - k_2 + k_3 - k_4 + k_5$; the wavevectors k_1 and k_2 cancel each other. The 2DRR signal is obtained by measuring differences with and without the actinic pump (beam 1,2). Beams represented with solid circles reach the sample, whereas those represented with open circles are blocked with a mask.

We employ a four-beam geometry in which the signal is associated with the difference produced by the actinic pump beam.[41] The four-wave mixing "background" generated by the Raman pump and Stokes pulses is not difficult to subtract, because it is only 10-20 times larger than the desired fifth-order response. We find that the background is most effectively removed by subtracting spectra acquired at negative delay times (far from the rise of the FSRS signal near τ_1 = -10 ps). An alternate approach in which the actinic pump beam is chopped at every delay point results in poor signal quality because of the longer data acquisition time. Despite its smaller background, we opt not to use the five-beam geometry described in Reference [41], because it is more difficult to maintain alignment day-to-day. In addition, color tunable actinic

pump beams may be employed in the four-beam geometry, and such experiments are presently being pursued with the same experimental setup.[54]

Signals are detected using a back-illuminated CCD array (Princeton Instruments PIXIS 100B) mounted on a 0.3 meter spectrograph with a 1200 g/mm grating. The signal beam is focused to a spot size of 100 μm at the entrance to the spectrograph to obtain hardware-limited spectral resolution of approximately 10 cm^{-1}. Ultimately, the resolution of the measurement is limited by the 50 cm^{-1} spectral width of the Raman pump beam. The total FSRS response produces roughly 1000 counts on the detector at each delay point with an integration time of 100 ms. The vibrational coherences associated with the 2DRR component of the response are all less than 5% of the total signal. The delay, τ_1, of the actinic pump is scanned 100 times, and the signal is averaged to optimize the data quality.

7.3. Simulations of 2DRR Spectra

The development of 2DRR spectroscopy is still at an early stage despite a long history of off-resonant 2D Raman work. As mentioned above, signal generation is allowed and forbidden for harmonic systems in resonant and off-resonant experiments, respectively. The implications of this difference in selection rules have not yet been established for information content of the signals. To this end, we begin this section by examining signatures of inhomogeneous broadening and anharmonicity in 2DRR spectra for a pair of vibrational modes. The 2DRR spectrum of myoglobin is then simulated using parameters derived from earlier spontaneous resonance Raman experiments. Insights gained from these calculations will be used to interpret experimental signals in Section 6.4.

7.3.1 Signatures of Inhomogeneous Broadening in 2DRR Spectra

The ability to distinguish inhomogeneous and homogeneous line broadening mechanisms motivated the first multidimensional Raman experiments conducted in the late 1980's and early 1990's.[18,21] The spectroscopic signatures are much like those associated with 2D photon echo experiments, where heterogeneity gives rise to a difference between the diagonal and anti-diagonal widths.[1,8,61,62] Inhomogeneous line broadening is a signature of correlation between the resonance frequencies detected in the two frequency dimensions.[63,64] Unlike Raman echo experiments,[21] the present (fifth-order) 2DRR experiments do not yield the time scale at which correlation decays, because an intermediate "waiting time" cannot be scanned.[18] Rather, we are able to detect the amount of correlation present in the system on the time-scale of the inverse of the vibrational line width.

Spectroscopic signatures are most easily established with calculations based on two vibrational modes and a single electronic resonance. The model developed in Reference [41] can be adapted for this purpose (see Appendix D). We take the mode frequencies to be 400 cm^{-1} and 1100 cm^{-1} in order to produce well-resolved vibrational resonances. Resolution of the various 2DRR peaks also requires that the two mode frequencies and their overtones are well-separated. For example, the overtone of the 400-cm^{-1} mode at 800 cm^{-1} must be well-separated from the fundamental mode frequency at 1100 cm^{-1}. The dimensionless displacement of each mode is set equal to 0.75 so that all key resonances can be observed on the same linear scale for the signal magnitude.

Heterogeneity is introduced by convoluting the signal field defined in Appendix D with a Gaussian function

$$S(\omega_1,\omega_2)=\int_{-\infty}^{\infty}\int_{-\infty}^{\infty}G(\eta_a,\eta_b)E_{2DRR}^{(5)}(\omega_1,\omega_2)d\eta_a d\eta_b \tag{7.1}$$

where

$$G(\eta_a,\eta_b)=\frac{1}{2\pi\sigma_a\sigma_b\sqrt{1-\rho^2}} \times\exp\left\{-\frac{1}{2(1-\rho^2)}\left[\frac{(\varpi_a+\eta_a)^2}{\sigma_a^2}-2\rho\frac{(\varpi_a+\eta_a)(\varpi_b+\eta_b)}{\sigma_a\sigma_b}+\frac{(\varpi_b+\eta_b)^2}{\sigma_b^2}\right]\right\}. \tag{7.2}$$

Here, η_a is the deviation of the harmonic mode frequency, a ,from its mean value, ϖ_a (in cm^{-1}), whereas σ_a is the width of the inhomogeneous distribution. The inter-mode correlation parameter, ρ, ranges from the fully anti-correlated (-1) to fully correlated (+1) limits.[63,64] The signal field depends on ϖ_a and ϖ_b through the vibrational Hamiltonian of the system (see Appendix D).

The calculations in Figure 7.4 are conducted in the anti-correlated (ρ=-0.75), uncorrelated (ρ=0), and correlated (ρ=+0.75) regimes. Of course, the diagonal peaks exhibit correlated line shapes for all cases, because the inhomogeneous widths, σ_a and σ_b, are nonzero. Notably, this signature of inhomogeneous line broadening cannot be derived from one-dimensional Raman spectroscopy (e.g. third-order stimulated Raman and spontaneous Raman measurements). For diagonal 2DRR peaks, the anti-diagonal width is related to homogeneous broadening, whereas the diagonal width represents the combination of homogeneous and inhomogeneous broadening. Unlike the diagonal peaks, the orientations and relative intensities of the cross peaks depend on the correlation parameter, ρ; the cross peaks possess an anti-diagonal and diagonal slant when the correlation parameter is negative and positive, respectively.

The cross peaks exhibit a fairly "round" line shape for the uncorrelated limit in Figure 7.4b. These spectroscopic signatures are much like those established in 2D infrared experiments.[1,8,61,62] The relative intensities of the cross peaks are largest when ρ is positive because of cancellations between terms with opposite signs in $G(\eta_a, \eta_b)$.

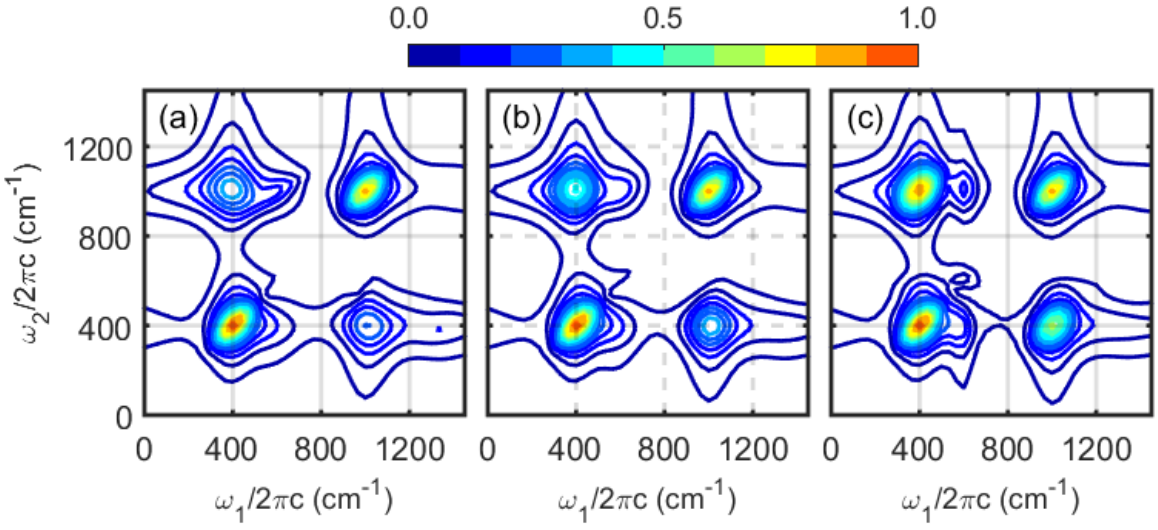

Figure 7.4. 2DRR spectra computed for a pair of harmonic oscillators with inhomogeneous line broadening. The spectra are computed by combining Equations 7.1 and D.20 in Appendix D with the parameters given in Table 7.1. The correlation parameter, ρ, is set equal to (a) -0.75, (b) 0.0, and (c) 0.75. The diagonal peaks always exhibit correlated line shapes, whereas the orientations and intensities of the off-diagonal peaks depend on the correlation parameter, ρ.

7.3.2. Signatures of Anharmonicity in 2DRR Spectra

Signal generation is allowed in off-resonant 2D Raman experiments only if the modes are anharmonic or the polarizability scales nonlinearly with the vibrational coordinates.[19,20] Thus, success in detecting the signal constitutes unambiguous evidence of a non-trivial behavior. Of course, this aspect of the off-resonant nonlinearity also means that the signal will generally be small and that artifacts such as cascades can readily contaminate the signals.[27,28] As noted in our

previous work, 2DRR spectroscopy is "easier" to conduct than off-resonant 2D Raman experiments, because signal generation is allowed for harmonic modes. Unfortunately, this also means that any pair of harmonic Franck-Condon active modes will generate a 2DRR cross peak, thereby complicating signal interpretation. We investigate signatures of anharmonicity in 2DRR spectra in this section. As in Section 6.3.1, calculations are conducted for a pair of vibrational modes and a single electronic resonance. However, we treat only homogeneous line broadening here in order to focus on the effects of anharmonicity. Cubic force constants are added to a harmonic vibrational Hamiltonian as described in Appendix D. The two normal modes mix through cubic force constants that depend on two coordinates. These "off-diagonal" cubic expansion coefficients are denoted as U_{122}, U_{212}, U_{221}, U_{211}, U_{121}, and U_{112}. In contrast, the "diagonal" cubic expansion coefficients, U_{111} and U_{222}, primarily shift the resonances to lower frequencies.

In Figure 7.5, the off-diagonal expansion coefficients are all set equal to three values (-5, 0, and 5 cm^{-1}) to illustrate the effects that these terms have on 2DRR spectra. New resonances are not generated; however, the peak intensities are affected by an intensity borrowing effect that originates in the transformation of Franck-Condon overlap integrals from the harmonic to anharmonic basis sets (see Equation D.23 in Appendix D). Calculations are also carried out for three values of the diagonal expansion coefficients (-5, 0, and 5 cm^{-1}). In general, the cross peak intensities above the diagonal increase relative to those below the diagonal for the anharmonic systems (see Figures 7.5a, 7.5d, 7.5g, and 7.5i). In general, differences between 2DRR spectra for the anharmonic and harmonic (see Figure 7.5e) systems are fairly subtle, which suggests limited potential of the 2DRR technique to reveal anharmonic couplings in the present quasi-degenerate (one-color) configuration.

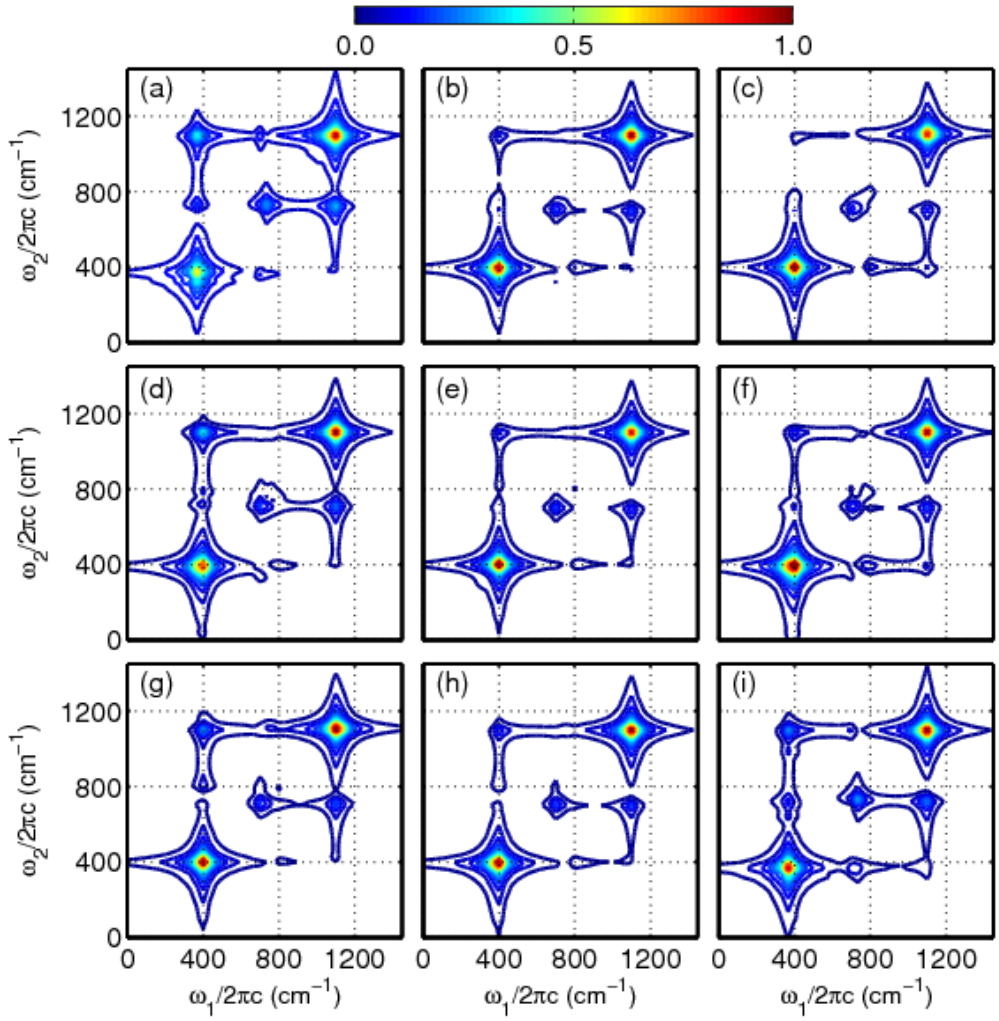

Figure 7.5. 2DRR spectra computed with the anharmonic vibrational Hamiltonian described in Appendix D and the parameters in Table 7.1. The diagonal cubic expansion coefficients are set equal to -5 (first row), 0 (second row), and 5 cm^{-1} (third row). The off-diagonal expansion coefficients are set equal to -5 (first column), 0 (second column), and 5 cm^{-1} (third column). The response of a harmonic system is shown in panel (e). These calculations suggest that anharmonic coupling promotes intensity borrowing effects via the transformation of Franck-Condon overlap integrals from the harmonic to anharmonic basis set (see Equation D.23 in Appendix D). For many of the parameter sets, anharmonicity causes the intensity of the cross peak above the diagonal to increase relative to that of the cross peak below the diagonal. This effect is most pronounced in the left column.

Table 7.1. Parameters of Theoretical Model for System with Two Vibrational Modes

[a]Parameter	Value
$\omega_{eg} / 2\pi c$	23250 cm^{-1}
ω_{AP} & ω_{RP}	set equal to ω_{eg}
[b] ϖ_a	400 cm^{-1}
[b] ϖ_b	1100 cm^{-1}
[c] d_a	0.75
[c] d_b	0.75
Γ_{vib} / c	10 cm^{-1}
Γ_{eg} / c	750 cm^{-1}
μ_{eg}	8.8 D
[d] σ_a & σ_b	35 cm^{-1}

[a] The number density (N), refractive index ($n(\omega_t)$), and path length (l) do not affect these results because normalized intensities are displayed (see Equation D.20 in Appendix D).
[b] The parameter, ϖ_j, is the wavenumber for mode j, $\varpi_j = \omega_j / 2\pi c$.
[c] The parameter, d_j, is the dimensionless potential energy minimum displacement for mode j.
[d] Inhomogeneous line broadening is included only for the calculations shown in Figure 7.5 (see Equations 7.1 and 7.2).

For FSRS signals represented in the traditional way (τ_1 and ω_2 in our notation), it has been shown that anharmonic coupling between modes may cause the vibrational resonance frequencies in ω_2 to oscillate with respect to τ_1 in ring-opening[65] and proton photodissociation[66] reactions. The present model does not predict such dynamics, because the non-oscillatory component of the signal dominates the response under one-color conditions. In previous 2DRR

studies of the photodissociation reaction of triiodide, we observed anharmonicity-induced oscillations in the vibrational resonance frequencies under two-color conditions.[53,54] Although signatures of anharmonicity are more readily derived from two-color 2DRR experiments, it will still be true that cross peaks are generated for all pairs of Franck-Condon active modes (whether they are harmonic or not). Simulated 2DRR spectra will be useful for identifying genuine evidence of anharmonicity.

7.3.3. Predicted 2DRR Spectrum of Myoglobin

Calculations presented in Sections 6.3.1 and 6.3.2 provide basic insights into 2DRR signal interpretation. The simulations suggest that signatures of inhomogeneous line broadening will be fairly obvious, whereas unambiguous evidence of anharmonicity will be difficult to derive from experimental data (particularly in one-color experiments). It will be useful to "estimate" how the 2DRR spectrum of myoglobin should be expected to appear based on earlier work. To this end, the parameters needed to simulate the 2DRR spectrum for a one-color experiment can be obtained from earlier fits to the spontaneous Raman excitation profiles for the Soret band.[67] Notably, these fits are carried out in a basis of harmonic modes.

In Figure 7.6, we present a 2DRR spectrum computed in the homogeneous limit of line broadening using the parameters given in Table 7.2. The four most dominant vibrational modes are included in the model. A peak associated with each mode appears on the diagonal. The most intense cross peak is found at $\omega_1 / 2\pi c$ =220 cm^{-1} (iron-histidine stretch) and $\omega_2 / 2\pi c$ =1356 cm^{-1} (in-plane stretch of heme); the cross peak intensity above the diagonal is greater than that found for the corresponding cross peak below the diagonal. The model additionally suggests that the intensity of the cross peak above the diagonal increases with respect to the peak below the

diagonal as the dimensionless displacements increase. The spectrum in Figure 7.6 exhibits weak off-diagonal peaks that are shifted down the ω_2 axis from the 674-cm^{-1} and 1356-cm^{-1} diagonal peaks by 220 cm^{-1}. These off-diagonal peaks represent sequences in which the system evolves in a coherence at the fundamental 674 cm^{-1} or 1356 cm^{-1} frequency in τ_1 and an inter-mode coherence in τ_2. Finally, we remark that the calculations presented in Figure 7.6, which employ large mode displacements, exhibit a peak associated with an inter-mode vibrational coherence on the diagonal (at $\omega_1 / 2\pi c = \omega_2 / 2\pi c$ =454 cm^{-1}). Detection of this type of resonance requires two modes with significant displacements.

Overall, the calculations presented in Figures 7.4-7.6 suggest that line broadening mechanisms will be the primary information to be derived from 2DRR spectra for myoglobin. Signatures of anharmonicity are likely to be ambiguous in the present quasi-degenerate (one-color) experiments, because the response is allowed for harmonic modes. Moreover, the fairly small potential energy surface displacements found in myoglobin should make most cross peaks difficult to detect.[67]

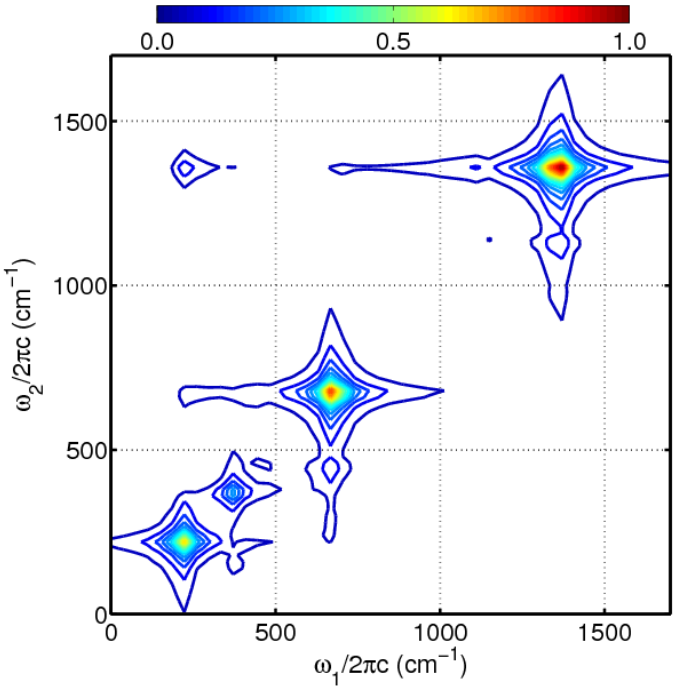

Figure 7.6. 2DRR spectrum of myoglobin computed using parameters obtained by fitting spontaneous resonance Raman excitation profiles.[67] The spectrum is dominated by resonances on the diagonal. The most dominant cross peak is associated with the iron-histidine stretch ($\omega_1 / 2\pi c$ =220 cm^{-1}) and in-plane stretching mode ($\omega_2 / 2\pi c$ =1356 cm^{-1}). The spectra are computed by combining Equation D.20 in Appendix D with the parameters in Table 7.2.

7.4. Results and Discussion

7.4.1. Isolation of 2DRR Signal Components

In this section, we show how the 2DRR response is extracted from the total signal. To begin, the procedure used to obtain the FSRS-like representation of the signal at various delay times, τ_1, was described at length in earlier work.[41] Examples of such FSRS-like signals are shown in Figures 7.7a and 7.7d. The novel aspect of this study is that we carry out a Fourier transformation with respect to τ_1 to generate a 2DRR spectrum. The main challenge in doing so is that the coherent signal component, the component of interest, must be separated from the

much larger incoherent fifth-order response. Below, we discuss issues particular to this aspect of the data analysis.

Table 7.2. Parameters of Model Based on Empirical Fit of Spontaneous Raman Signals

[a]Parameter	Value
$\omega_{eg}/2\pi c$	23250 cm^{-1}
ω_{AP} & ω_{RP}	set equal to ω_{eg}
[b] ϖ_1	220 cm^{-1}
[b] ϖ_2	370 cm^{-1}
[b] ϖ_3	674 cm^{-1}
[b] ϖ_4	1356 cm^{-1}
[c] d_1	0.47
[c] d_2	0.20
[c] d_3	0.26
[c] d_4	0.34
Γ_{vib}/c	10 cm^{-1}
Γ_{eg}/c	750 cm^{-1}
μ_{eg}	8.8 D

[a] The number density (N), refractive index ($n(\omega_t)$), and path length (l) do not affect these results because normalized intensities are displayed (see Equation D.20 in Appendix D).
[b] The parameter, ϖ_j, is the wavenumber for mode j, $\varpi_j = \omega_j/2\pi c$.
[c] The parameter, d_j, is the dimensionless potential energy minimum displacement for mode j.

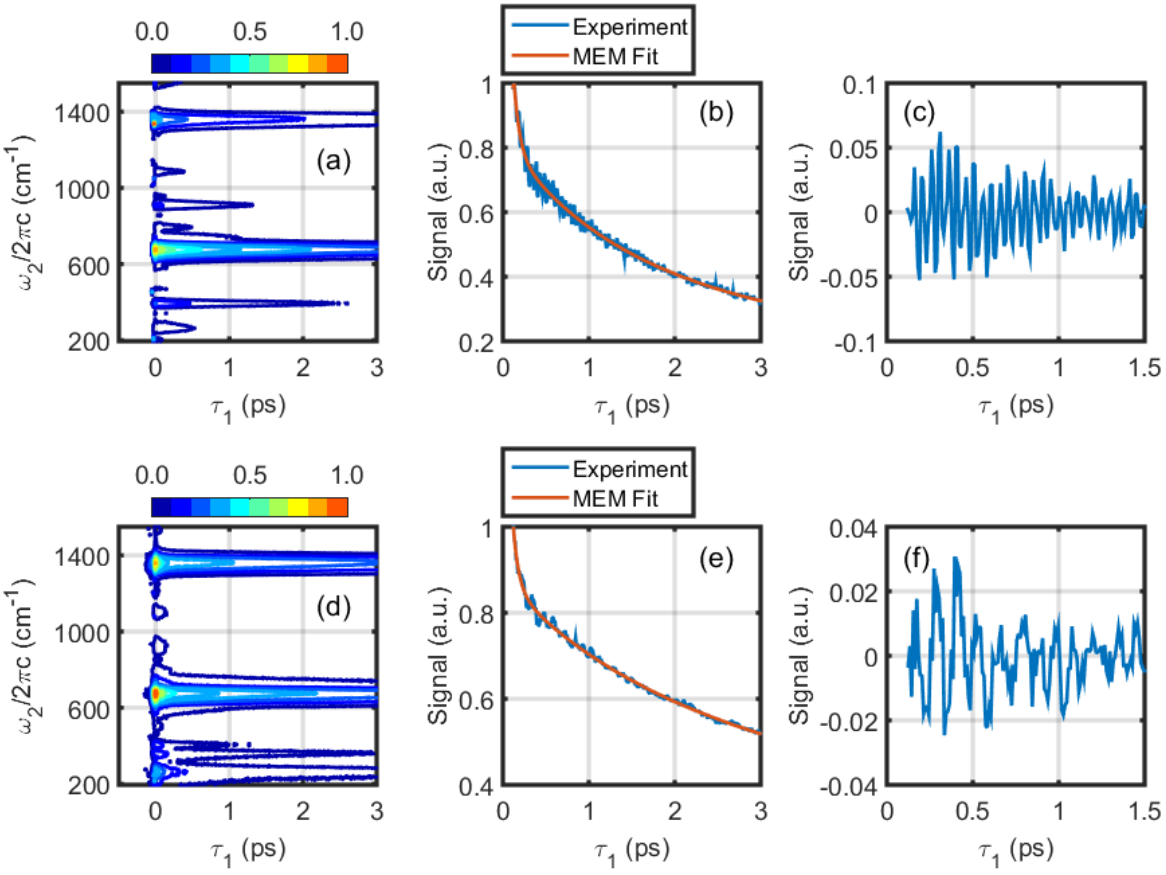

Figure 7.7. Signals obtained for (a) metMb and (d) MbO_2 in a FSRS-like representation. At each point in ω_2, the incoherent baseline is generated using the maximum entropy method. Shown here are slices of the signals for (b) the 670-cm^{-1} mode of metMb and (e) the 370-cm^{-1} mode of MbO_2. Coherent residuals are obtained by subtracting incoherent MEM baselines from the total signals for (b) metMb and (e) MbO_2. The coherent residuals are presented for (c) metMb and (f) MbO_2.

To illustrate the method of data analysis, we begin by examining time-dependent Raman spectra obtained for both metMb and MbO_2 in Figure 7.7. In both cases, peaks are observed near 220 cm^{-1}, 370 cm^{-1}, 675 cm^{-1}, and 1356 cm^{-1}. The in-plane bond stretching mode is a particularly useful marker for the oxidation state of the heme. The vibrational wavenumber is 1356 cm^{-1} in MbO_2 and 1373 cm^{-1} in metMB.[59] The 220 cm^{-1} resonance corresponds to the iron-histidine stretch on the proximal side of the heme group. The 370 cm^{-1} mode represents a

bending motion between the porphyrin and propionic substituents originating from double bond (methylene) stretching (deformation) near the propionic acid side chains (see Figure 7.8). Finally, the 670 and 1356 cm^{-1} (or 1373 cm^{-1}) modes correspond to deformation and bond-stretching motions localized on the tetrapyrrole moiety, respectively. The intensity of the 220 cm^{-1} mode varies significantly between systems, because photodissociation is initiated only in MbO_2. That is, there is a significant excited state potential energy gradient for the iron-histidine stretch in MbO_2, because the iron moves out of plane following photodissociation.

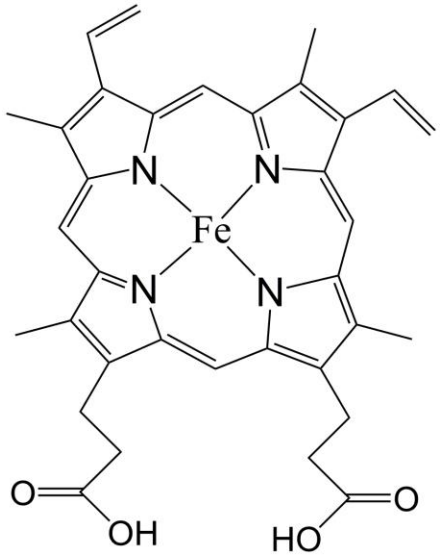

Figure 7.8. Molecular structure of iron protoporphyrin-IX.

Oscillatory signal components in τ_1 are isolated by subtracting incoherent baselines generated using the maximum entropy method (MEM), which suppresses low-frequency artifacts that may arise when baselines are produced using a small number of exponential functions.[68] In Figures 7.7b and 7.7e, we overlay example MEM fits with signals obtained for both metMb and MbO_2; residuals are plotted in Figures 7.7c and 7.7f. The analysis is carried out beginning at a delay time of 0.1 ps in τ_1 to remove contributions from the region of pulse overlap. The 2DRR

spectra shown in Figure 7.9 are obtained by repeating this procedure at every point in ω_2 (i.e. every pixel on the CCD array), then carrying out a Fourier transformation with respect to τ_1

$$S(\omega_1,\omega_2)=\int S(\tau_1,\omega_2)\exp(i\omega_1\tau_1-\alpha\tau_1)d\tau_1 \tag{7.3}$$

where $S(\tau_1,\omega_2)$ is the baseline-subtracted signal, $S(\omega_1,\omega_2)$ is the 2DRR spectrum, and α is a rate constant used to suppress contributions from delay times at which the oscillations have decayed below the noise level. In the present work we set α equal to 1.4 ps^{-1}.

The 2DRR spectra of both systems shown in Figure 7.9 exhibit diagonal peaks near 220 cm^{-1}, 370 cm^{-1}, 674 cm^{-1}, and 1356 cm^{-1} (close to 1373 cm^{-1} in metMb).[59,67] The peaks near 1356 cm^{-1} are relatively weak, because the 24 fs period of this mode is only slightly larger than the 19 fs instrument response width at this particular value of the Raman shift. Two cross peaks are located above the diagonal. The cross peaks at $\omega_1/2\pi c$=50 cm^{-1} and $\omega_2/2\pi c$=674 cm^{-1} reflect motion along the doming coordinate in τ_1. Cross peaks are also located near $\omega_1/2\pi c$=370 cm^{-1} and $\omega_2/2\pi c$=1356 cm^{-1}. It is interesting that only one cross peak is found in the slices of the 2D spectra near $\omega_2/2\pi c$=1356 cm^{-1}; cross peaks near $\omega_1/2\pi c$=674 cm^{-1} and $\omega_2/2\pi c$=1356 cm^{-1} are below the detection threshold despite the significant intensity of the diagonal peak at 674 cm^{-1}. This aspect of the spectra is consistent with the simulation in Figure 7.6. In this calculation, an intense cross peak is generated above the diagonal near $\omega_1/2\pi c$=220 cm^{-1} and $\omega_2/2\pi c$=1356 cm^{-1}, but not at $\omega_1/2\pi c$=674 cm^{-1} and $\omega_2/2\pi c$=1356 cm^{-1}. The measurement in Figure 7.9 differs from Figure 7.6 in that off-diagonal peaks are not detected below diagonal peaks in ω_2 (e.g. at $\omega_1/2\pi c$=674 cm^{-1} and $\omega_2/2\pi c$=454 cm^{-1}). The key issue is

that the iron-histidine stretch is less intense than the prediction based on a fit to the spontaneous Raman excitation profile.[67]

Cross peaks are detected below the diagonal near $\omega_1 / 2\pi c$ =990 cm^{-1} and $\omega_2 / 2\pi c$ =674 cm^{-1}. We tentatively suggest that a Franck-Condon active vinyl wagging mode is responsible for the 990 cm^{-1}location of this peak in the first dimension.[59] The absence of a diagonal peak at $\omega_1 / 2\pi c = \omega_2 / 2\pi c$ =990 cm^{-1} could be explained by the weaker Franck-Condon activity of this mode. It is unclear why a cross peak is not also detected at $\omega_1 / 2\pi c$ =674 cm^{-1} and $\omega_2 / 2\pi c$ =990 cm^{-1}. One possibility is that anharmonicity redistributes intensities among cross peaks as demonstrated in Figure 7.5. The calculation presented in Figure 7.6 captures many aspects of the measured 2DRR spectra in Figure 7.9; however, knowledge of the anharmonic couplings may be the key to precisely reproducing peak intensities. The calculations presented in Figure 7.5 suggest that intensity borrowing effects may be observed with relatively modest anharmonic couplings.

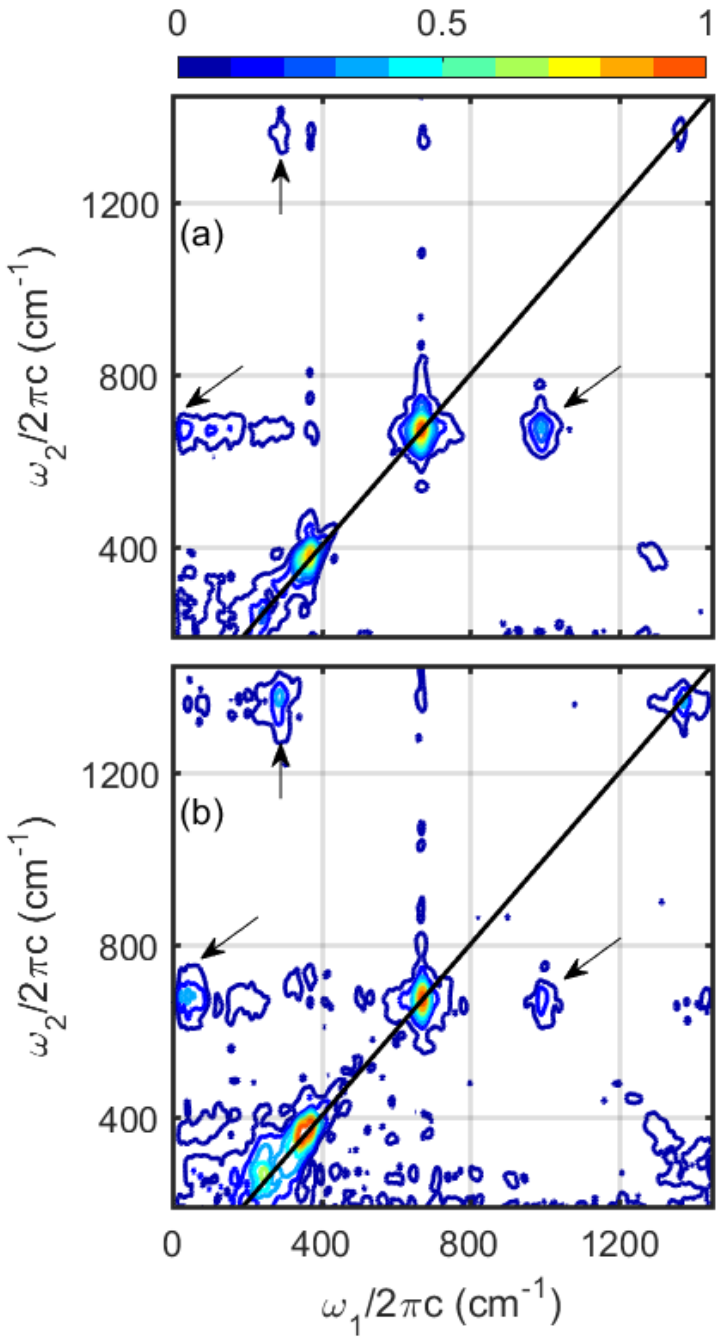

Figure 7.9. Experimental 2DRR spectra for (a) metMb and (b) MbO_2 are generated by Fourier transforming the coherent residuals with respect to τ_1 at each point in ω_2 (i.e. at each pixel on the CCD detector). For both systems, diagonal peaks are detected near 220, 370, 674, and 1356 cm^{-1} (close to 1373 cm^{-1} in metMb). Arrows are used to identify cross peaks.

7.4.2. Analysis of Spectral Line Shapes

The ability to distinguish inhomogeneous and homogeneous line broadening mechanisms motivated the first multidimensional Raman experiments.[18,21] As in 2D infrared spectroscopy, information about the line broadening mechanism can be read directly from the line shape. Inhomogenous broadening will cause peaks to elongate on the diagonal of the 2DRR spectrum; the diagonal width will then be greater than the anti-diagonal width. Correlated line shapes may be observed when spectral diffusion of a vibrational resonance frequency is much slower than the time-scale of the inverse line width (roughly 1 ps). In this section, we characterize the 2DRR line shapes shown in Figure 7.9. The present analysis is limited to the region of the spectrum between 200 and 800 cm^{-1} in both dimensions, because we find no evidence of inhomogeneous line broadening elsewhere.

In Figure 7.10, all peaks are fit to two-dimensional Gaussian line shapes of the form given in Equation 7.2. The correlation parameter, ρ, generally ranges from the fully anti-correlated (ρ=-1) to fully correlated (ρ=+1) limits. However, ρ should not be less than zero for diagonal peaks. This form of the 2D Gaussian function takes into account the difference in frequency resolution associated with the two dimensions. The correlation parameters must be equal to zero if the line broadening mechanisms are fully homogeneous. With inspiration from 2D infrared spectroscopy, slopes obtained with a linear regression analysis are overlaid on various peaks in Figures 7.10c and 7.10f. The slopes are useful for inspection of the data but are less rigorous than the 2D Gaussian fits, because they are affected by frequency resolution.

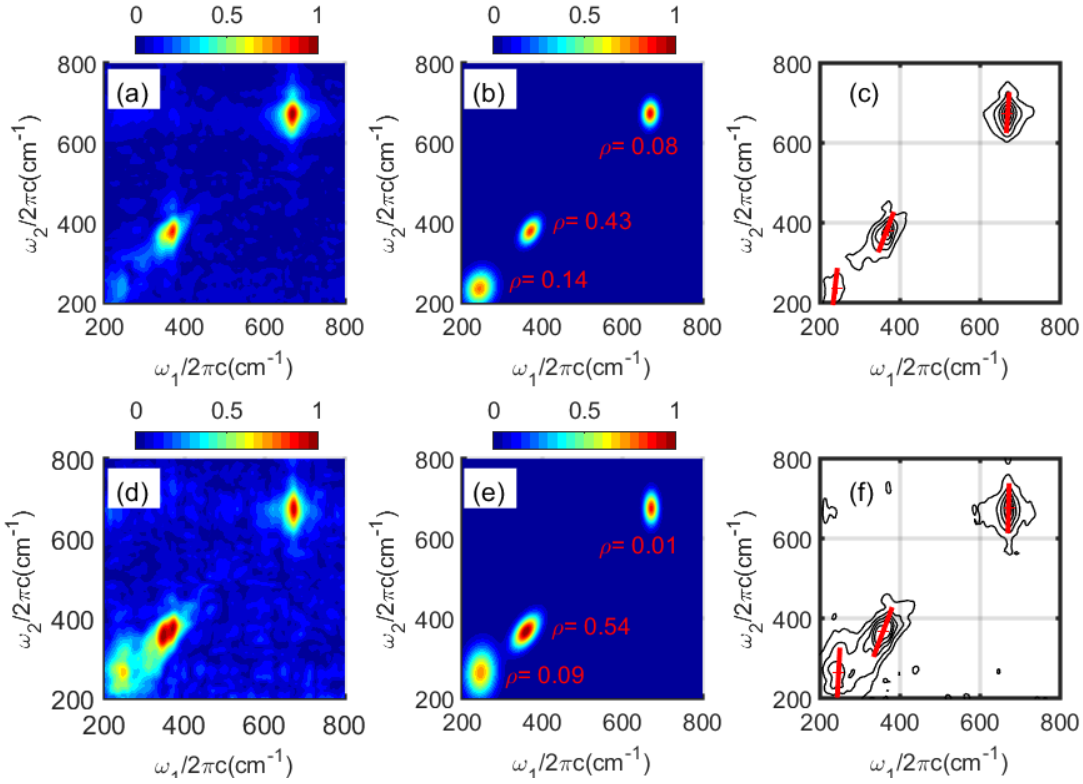

Figure 7.10. Line shapes of diagonal peaks are examined in lower-frequency regions of 2DRR spectra obtained for (a) metMb and (b) MbO_2. Peaks are fit to two-dimensional Gaussians with correlation parameters in panels **(c)** and **(d)** (see Equation 7.2). The parameter, ρ, ranges between the uncorrelated (ρ=0) and fully correlated (ρ=1) limits for diagonal peaks. A correlation parameter greater than 0 is a signature of inhomogeneous line broadening. In panels (e) and (f), the slope consistent with each correlation parameter is overlaid on the experimental data to offer an additional perspective. For both systems, the 370-cm^{-1} methylene deformation mode local to the propionic acid side chains exhibits the greatest amount of heterogeneity (wavenumber near 370 cm^{-1}).

The iron-histidine stretching mode near 220-cm^{-1} exhibits a smaller amount of heterogeneity; the correlation parameter is 0.14 in metMb and 0.09 in MbO_2. For both systems, the greatest amount of heterogeneity is associated with the 370-cm^{-1} methylene deformation mode local to the propionic acid groups. The correlation parameter for this mode is 0.43 in metMb and 0.54 in MbO_2. We hypothesize that this heterogeneity originates in fluctuations of

the "floppy" propionic acid side chains. That is, the 2DRR data suggest that rigidity of the macrocycle suppresses heterogeneity in higher frequency modes such as the in-plane deformation mode near 674 cm^{-1}.

7.4.3. Computational Analysis of Line Broadening Mechanism

In this section, computational models are used to explore the effects that motions of the propionic acid side chains have on the vibrational frequency of the 370-cm^{-1} methylene deformation mode. In particular, we are interested in how the magnitudes of the fluctuations compare to the characteristic frequencies in the spectral densities (i.e. spectra of vibrational freqeuncy fluctuations). These comparisons will provide further insights into the line broadening mechanisms. It is relatively straightforward to model fluctuations in the geometries of the proteins with classical molecular dynamics (MD) simulations; however, the vibrational frequencies should be calculated at a higher level of theory. Therefore, we use *ab initio* maps to parameterize the vibrational frequencies associated with geometries extracted from classical molecular dynamics simulations. Similar approaches have been used to interpret 2D infrared experiments conducted on proteins and pure liquids.[69-72]

Fluctuations in the geometries of the proteins are modeled with MD simulations as implemented in the GROMACS96 force field[73-75] To prepare the systems, heavy atoms in the proteins were restrained and an energy minimization (steepest descent method) was implemented to relax the solvent around the protein. This was followed by two equilibration steps in the isothermal-isochoric and isothermal-isobaric ensembles for a total of 400 ps. Simulations were run for 1 ns with 2 fs steps. The *ab initio* maps are constructed by first optimizing the geometries of the isolated hemes at the B3LYP/6-311G(2d,3p) level.[76] The equilibrium dihedral

angles associated with the propionic acid side chains (see Figure 7.11) are Φ_L =81.3° and Φ_R =81.1° for metMb and Φ_L =94.4° and Φ_R =109° for MbO_2. The *ab initio* maps are produced by varying these dihedral angles (in steps of 5°) over the ranges covered by the MD simulations while holding all other coordinates fixed at the values corresponding to the equilibrium geometries (it is assumed that the frequency of the methylene deformation mode local to the propionic acid side chains is primarily affected by these "floppy" coordinates). The vibrational modes are computed at each geometry, and the methylene deformation mode is identified by (i) large-amplitude motion of the methylene bonds near the propionic acid side chains and (ii) the scalar product with the normal mode calculated at the equilibrium geometry. The resulting maps of vibrational frequencies are presented in Figures 7.11b and 7.11d. With these maps, the vibrational frequencies are readily generated at each step in the MD trajectory by extracting the two dihedral angles. Segments of the trajectories are presented in Figures 7.11c and 7.11f. Scatter plots of the dihedral angles suggest that the fluctuations in these coordinates are fairly evenly distributed about the equilibrium geometry (see Appendix D).

MD trajectories of vibrational frequencies for metMb and MbO_2 yield standard deviations of 5.9 and 7.0 cm^{-1}, respectively. These standard deviations correspond to FWHM line widths of 13.9 and 16.5 cm^{-1} under the assumption of Gaussian line shapes. These line widths are smaller than those found in the 2DRR measurements shown in Figure 7.9 because of finite spectral resolution. In order to obtain further insight into the line broadening mechanism, time-correlation functions associated with the MD trajectories are Fourier transformed to produce the spectral densities shown in Figure 7.12.[77,78] The spectral densities show how the fluctuation amplitudes are distributed in the frequency domain. The simulations suggest that the fluctuations

are dominated by thermal motion below 10 cm^{-1}; however, broad components with magnitudes up to 10% of the maximum value are found in both systems.

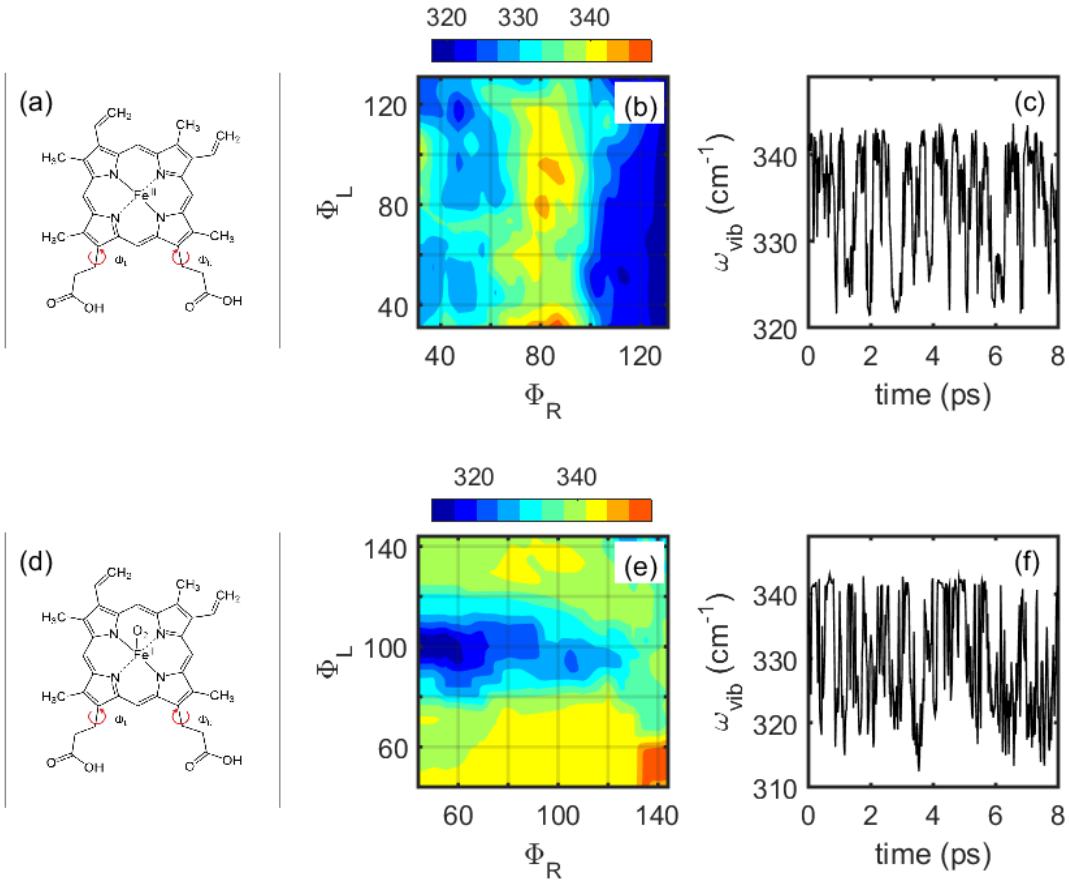

Figure 7.11. Dihedral angles associated with the propionic acid chains are defined for the heme in (a) metMb and (d) MbO_2. The vibrational frequency of the methylene deformation mode local to the propionic acid side chains is computed as a function of the two dihedral angles for (b) metMb and (e) MbO_2. These ab initio maps are used to parameterize the vibrational frequencies in a molecular dynamics simulation. Segments of the trajectories of vibrational frequencies are shown for **(c)** metMb and (f) MbO_2.

The line broadening mechanism can be interpreted by comparing the fluctuation amplitudes (5.9 cm^{-1} in metMb and 7.0 cm^{-1} in MbO_2) to the characteristic frequencies of thermal motion (i.e. dominant part of spectral density). In the homogeneous limit, the fluctuation amplitude must be small compared to the characteristic frequency, whereas the opposite applies

in the inhomogeneous limit. The spectral densities computed with MD simulations are roughly 50% of their maximum values at frequencies corresponding to the 5.9 and 7.0-cm^{-1} fluctuation amplitudes computed for metMb and MbO_2, respectively. Thus, the calculations suggest that line broadening in both systems resides in the intermediate regime. The correlation parameters of 0.43 and 0.54 determined from experimental data for metMb and MbO_2 (see Figure 7.10) are consistent with the line broadening regime predicted by the MD simulations.

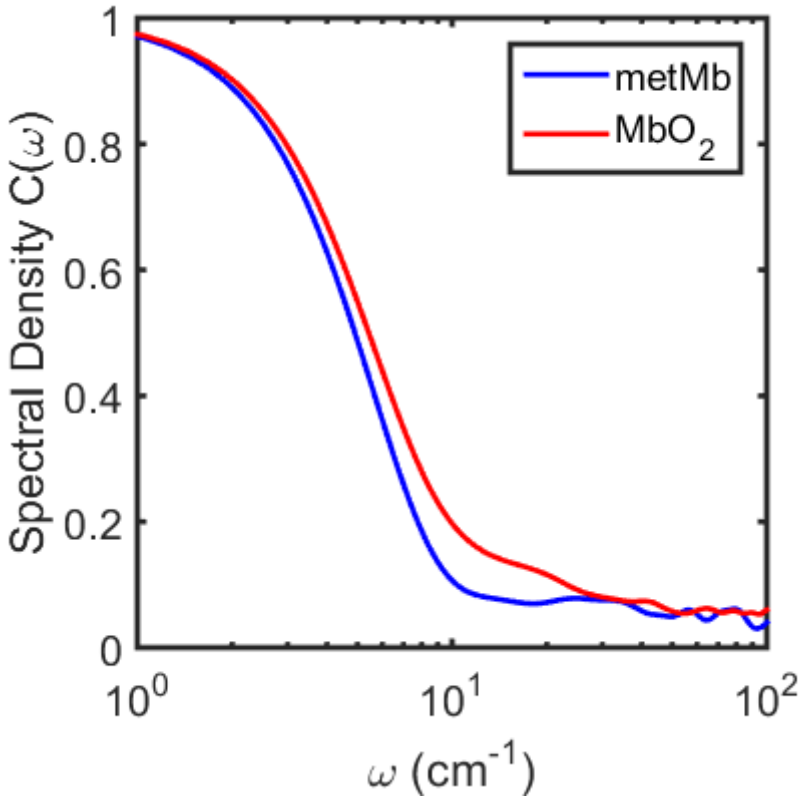

Figure 7.12. Spectral densities of the methylene deformation modes obtained from molecular dynamics simulations. The spectral densities decay to less than 50% of the maximum amplitude at frequencies corresponding to the fluctuation amplitudes (5.9 and 7.0 cm^{-1} for metMb and MbO_2). These calculations are consistent with an intermediate line broadening regime. The line broadening mechanism would become more homogeneous as the spectral density shifts to higher frequencies.

7.4.4. Implications for the Vibrational Cooling Mechanism

The propionic acid groups are known to dominate vibrational energy exchange of the heme with its surrounding environment. Hochstrasser first proposed this mechanism in 1994, and MD simulations contributed further support for this idea several years later.[49-51] In 2006, the role of the propionic acid groups was finally confirmed by a direct experimental test in which vibrational cooling rates were compared for the native protein and a mutant.[52] These earlier works suggest that the propionic acid side chains are an effective gateway for vibrational energy transfer, because they hydrogen bond with the aqueous solvent. In contrast, the porphyrin is enclosed in a hydrophobic pocket devoid of solvent. The surrounding protein matrix is less effective than the solvent in exchanging vibrational energy with the porphyrin despite close to 90 van der Waals contacts.[79] This behavior underscores the important role of hydrogen bonds in accelerating solute-to-solvent vibrational energy transfer.[80]

The experimental data and computational simulations presented in Figures 7.10-7.12 suggest that the 2DRR line shapes of the methylene deformation modes reflect heterogeneity in the geometries of the side chains. It is interesting to consider whether or not heterogeneity in the structure translates into heterogeneity in the vibrational cooling rate. This issue cannot be directly addressed with 2DRR spectroscopy. However, Berg and co-workers have shown that such information about incoherent dynamics can be derived from six-wave mixing experiments.[81,82] We are presently using a related approach to examine heterogeneity in vibrational cooling rates in heme proteins.

7.5. Concluding Remarks

In summary, we have conducted quasi-degenerate (one-color) 2DRR spectroscopy experiments on oxygen- and water-ligated myoglobin. The experimental technique developed in Reference [41] has been leveraged to produce 2D resonance Raman spectra. For both systems, we find that the greatest amount of heterogeneity is associated with the methylene deformation mode local to the propionic acid side chains. The computational model presented in Section 6.4.3 yields distributions with standard deviations of 5.9 and 7.0 cm^{-1} for metMb and MbO_2, respectively. The model suggests that the dihedral angles associated with the side chains vary over roughly a 60° range (see Appendix D). It is interesting to consider whether or not the vibrational cooling rate of the heme varies as a consequence of heterogeneity in the propionic acid groups. This issue will be addressed in future work using pump-repump-probe spectroscopy.

Model calculations suggest that two key points must be considered when interpreting 2DRR signals. First, 2DRR experiments do not necessarily yield information about anharmonic mode couplings, because the signal is allowed for harmonic systems. The absence of a signal for harmonic systems is one of the primary motivations for conducting electronically off-resonant 2D Raman experiments.[19,27,28,55,56] Thus, a tradeoff between information content and susceptibility to experimental artifacts is made in 2DRR spectroscopy. A two-color implementation of 2DRR spectroscopy may expand the range of scientific questions that can be addressed, but does not change this essential aspect of the signal generation mechanism.[54] Second, 2DRR experiments can be used to characterize vibrational line broadening mechanisms in a straightforward way. As in 2D infrared experiments, inhomogeneous line broadening is made clear by inspection of the 2DRR signal. Notably, the line broadening mechanism cannot

be directly determined from traditional (third-order) coherent Raman or spontaneous Raman spectroscopies.[18]

7.6. REFERENCES

(1) Asplund, M. C.; Zanni, M. T.; Hochstrasser, R. M. *Proc. Natl. Acad. Sci.* **2000**, *97*, 8219.

(2) Golonzka, O.; Khalil, M.; Demirdöven, N.; Tokmakoff, A. *Phys. Rev. Lett.* **2000**, *86*, 2154.

(3) Jonas, D. M. *Annu. Rev. Phys. Chem.* **2003**, *54*, 425.

(4) Brixner, T.; Mancal, T.; Stiopkin, I. V.; Fleming, G. R. *J. Chem. Phys.* **2004**, *121*, 4221.

(5) Cowan, M. L.; Ogilvie, J. P.; Miller, R. J. D. *Chem. Phys. Lett.* **2004**, *386*, 184.

(6) Ogilvie, J. P.; Kubarych, K. J. *Adv. At. Mol. Opt. Phys.* **2009**, *57*, 249.

(7) Pakoulev, A. V.; Block, S. B.; Yurs, L. A.; Mathew, N. A.; Kornau, K. M.; Wright, J. C. *J. Phys. Chem. Lett.* **2010**, *1*, 822.

(8) Hamm, P.; Zanni, M. T. *Concepts and Methods of 2D Infrared Spectroscopy*; Cambridge University Press: Cambridge, 2011.

(9) Wright, J. C. *Annu. Rev. Phys. Chem.* **2011**, *62*, 209.

(10) Slenkamp, K. M.; Lynch, M. S.; Van Kuiken, B. E.; Brookes, J. F.; Bannan, C. C.; Daifuku, S. L.; Khalil, M. *J. Chem. Phys.* **2014**, *140*, 084505.

(11) Laubereau, A.; Kaiser, W. *Rev. Mod. Phys.* **1978**, *50*, 607.

(12) Hesp, B. H.; Wiersma, D. A. *Chem. Phys. Lett.* **1980**, *75*, 423.

(13) Velsko, S.; Trout, J.; Hochstrasser, R. M. *J. Chem. Phys.* **1983**, *79*, 2114.

(14) Schosser, C. L.; Dlott, D. D. *J. Chem. Phys.* **1984**, *80*, 1394.

(15) Laubereau, A.; Wochner, G.; Kaiser, W. *Phys. Rev. A* **1976**, *13*, 2212.

(16) Oxtoby, D. W. *J. Chem. Phys.* **1981**, *74*, 5371.

(17) George, S. M.; Harris, A. L.; Berg, M.; Harris, C. B. *J. Chem. Phys.* **1984**, *80*, 83.

(18) Loring, R. F.; Mukamel, S. *J. Chem. Phys.* **1985**, *83*, 2116.

(19) Tanimura, Y.; Mukamel, S. *J. Chem. Phys.* **1993**, *99*, 9496.

(20) Jansen, T. I. C.; Snijders, J. G.; Duppen, K. *J. Chem. Phys.* **2001**, *114*, 109210.

(21) Berg, M.; Vanden Bout, D. A. *Acc. Chem. Res.* **1997**, *30*, 65.

(22) Ivanecky III, J. E.; Wright, J. C. *Chem. Phys. Lett.* **1993**, *206*, 437.

(23) Tominaga, K.; Yoshihara, K. *J. Chem. Phys.* **1996**, *104*, 4419.

(24) Steffen, T.; Duppen, K. *J. Chem. Phys.* **1997**, *106*, 3854.

(25) Tokmakoff, A.; Lang, M. J.; Larsen, D. S.; Fleming, G. R.; Chernyak, V.; Mukamel, S. *Phys. Rev. Lett.* **1997**, *79*, 2702.

(26) Blank, D. A.; Kaufman, L. J.; Fleming, G. R. *J. Chem. Phys.* **1999**, *111*, 3105.

(27) Kubarych, K. J.; Milne, C. J.; Lin, S.; Astinov, V.; Miller, R. J. D. *J. Chem. Phys.* **2002**, *116*, 2016.

(28) Kaufman, L. J.; Heo, J.; Ziegler, L. D.; Fleming, G. R. *Phys. Rev. Lett.* **2002**, *88*, 207402:1.

(29) Fujiyoshi, S.; Takeuchi, S.; Tahara, T. *J. Phys. Chem. A* **2003**, *107*, 494.

(30) McCamant, D. W.; Kukura, P.; Yoon, S.; Mathies, R. A. *Rev. Sci. Instrum.* **2004**, *75*, 4971.

(31) Underwood, D. F.; Blank, D. A. *J. Phys. Chem. A* **2005**, *109*, 3295.

(32) Kukura, P.; McCamant, D. W.; Mathies, R. A. *Annu. Rev. Phys. Chem.* **2007**, *58*, 461.

(33) Moran, A. M.; Nome, R. A.; Scherer, N. F. *J. Chem. Phys.* **2007**, *127*, 184505:1.

(34) Marek, M. S.; Buckup, T.; Motzkus, M. *J. Phys. Chem. B* **2011**, *115*, 8328.

(35) Kraack, J. P.; Wand, A.; Buckup, T.; Motzkus, M.; Ruhman, S. *Phys. Chem. Chem. Phys.* **2013**, *15*, 14487.

(36) Weigel, A.; Dobryakov, A.; Klaumünzer, B.; Sajadi, M.; Saalfrank, P.; Ernsting, N. P. *J. Phys. Chem. B* **2011**, *115*, 3656.

(37) Yu, W.; Zhou, J.; Bragg, A. E. *J. Phys. Chem. Lett.* **2012**, *3*, 1321.

(38) Park, S.; Kim, J.; Scherer, N. F. *Phys. Chem. Chem. Phys.* **2012**, *14*, 8116.

(39) Grumstrup, E. M.; Chen, Z.; Vary, R. P.; Moran, A. M.; Schanze, K. S.; Papanikolas, J. P. *J. Phys. Chem. B* **2013**, *117*, 8245.

(40) Silva, W. R.; Frontiera, R. R. *Phys. Chem. Chem. Phys.* **2016**, DOI: 10.1039/C5CP06195D.

(41) Molesky, B. M.; Guo, Z.; Moran, A. M. *J. Chem. Phys.* **2015**, *142*, 212405.

(42) Petrich, J. W.; Poyart, C.; Martin, J.-L. *Biochemistry* **1988**, *27*, 4049.

(43) Franzen, S.; Kiger, L.; Poyart, C.; Martin, J.-L. *Biophys. J.* **2001**, *80*, 2372.

(44) Ye, X.; Demidov, A.; Rosca, F.; Wang, W.; Kumar, A.; Ionascu, D.; Zhu, L.; Barrick, D.; Wharton, D.; Champion, P. M. *J. Phys. Chem. A* **2003**, *107*, 8156.

(45) Martin, J.-L.; Vos, M. H. *Annu. Rev. Biophys. Biomol. Struct.* **2006**, *21*, 199.

(46) Vos, M. H. *Biochim. Biophys. Acta* **2008**, *1777*, 15.

(47) Consani, C.; Auböck, G.; Bräm, O.; van Mourik, F.; Chergui, M. *J. Chem. Phys.* **2014**, *140*, 025103.

(48) Champion, P. M.; Rosca, F.; Ionascu, D.; Cao, W.; Ye, X. *Faraday. Discuss.* **2004**, *127*, 123.

(49) Tian, T.; Locke, B.; Kholodenko, Y.; Hochstrasser, R. M. *J. Phys. Chem.* **1994**, *98*, 11648.

(50) Sagnella, D. E.; Straub, J. E. *J. Phys. Chem. B* **2001**, *105*, 7057.

(51) Bu, L.; Straub, J. E. *J. Phys. Chem. B* **2003**, *107*, 10634.

(52) Gao, Y.; Koyama, M.; El-Mashtoly, S.; Hayashi, T.; Harada, K.; Mizutani, Y.; Kitagawa, T. *Chem. Phys. Lett.* **2006**, *429*, 239.

(53) Molesky, B. P.; Giokas, P. G.; Guo, Z.; Moran, A. M. *J. Chem. Phys.* **2014**, *114*, 114202.

(54) Guo, Z.; Molesky, B. M.; Cheshire, T. P.; Moran, A. M. *J. Chem. Phys.* **2015**, *143*, 124202.

(55) Wilson, K. C.; Lyons, B.; Mehlenbacher, R.; Sabatini, R.; McCamant, D. W. *J. Chem. Phys.* **2009**, *131*, 214502.

(56) Mehlenbacher, R.; Lyons, B.; Wilson, K. C.; Du, Y.; McCamant, D. W. *J. Chem. Phys.* **2009**, *131*, 244512.

(57) Ye, X.; Demidov, A.; Champion, P. M. *J. Am. Chem. Soc.* **2002**, *124*, 5914.

(58) Morikis, D.; Sage, J. T.; Rizos, A. K.; Champion, P. M. *J. Am. Chem. Soc.* **1988**, *110*, 6341.

(59) Hu, S.; Smith, K. M.; Spiro, T. G. *J. Am. Chem. Soc.* **1996**, *118*, 12638.

(60) Tauber, M. J.; Mathies, R. A.; Chen, X.; Bradforth, S. E. *Rev. Sci. Instrum.* **2003**, *74*, 4958.

(61) Cho, M. *Chem. Rev.* **2008**, *108*, 1331.

(62) Fayer, M. D. *Annu. Rev. Phys. Chem.* **2009**, *60*, 21.

(63) Demirdöven, N.; Khalil, M.; Golonzka, O.; Tokmakoff, A. *J. Phys. Chem. A* **2001**, *105*, 8025.

(64) Venkatramani, R.; Mukamel, S. *J. Chem. Phys.* **2002**, *117*, 11089.

(65) Valley, D. T.; Hoffman, D. P.; Mathies, R. A. *Phys. Chem. Chem. Phys.* **2015**, *17*, 9231.

(66) Wang, Y.; Liu, W.; Tang, L.; Oscar, B.; Han, F.; Fang, C. *J. Phys. Chem. A* **2013**, *117*, 6024.

(67) Bangcharoenpaurpong, O.; Schomacker, K. T.; Champion, P. M. *J. Am. Chem. Soc.* **1984**, *106*, 5688.

(68) Kumar, A. T. N.; Zhu, L.; Christian, J. F.; Demidov, A.; Champion, P. M. *J. Phys. Chem. B* **2001**, *105*, 7847.

(69) Corcelli, S. A.; Lawrence, C. P.; Skinner, J. L. *J. Chem. Phys.* **2004**, *120*, 8107.

(70) Hayashi, T.; Jansen, T. I. C.; Zhuang, W.; Mukamel, S. *J. Phys. Chem. A* **2005**, *109*, 64.

(71) Jansen, T. I. C.; Knoester, J. *J. Chem. Phys.* **2006**, *124*, 044502.

(72) Wang, J.; Zhuang, W.; Mukamel, S.; Hochstrasser, R. M. *J. Phys. Chem. B* **2008**, *112*, 5930.

(73) van der Spoel, D.; Lindahl, E.; Hess, B.; Groenhof, G.; Mark, A. E.; Berendsen, H. J. C. *J. Comp. Chem.* **2005**, *26*, 1701.

(74) Pronk, S.; Pall, S.; Schulz, R.; Larsson, P.; Bjelkmar, P.; Apostolov, R.; Shirts, M. R.; Smith, J. C.; Kasson, P. M.; van der Spoel, D.; Hess, B.; Lindahl, E. *Bioinformatics* **2013**, *29*, 845.

(75) Vanommeslaeghe, K.; Hatcher, E.; Acharya, C.; Kundu, S.; Zhong, S.; Shim, J.; Darian, E.; Guvench, O.; Lopes, P.; Vorobyov, I.; MacKerell, A. D. *J. Comp. Chem.* **2010**, *31*, 671.

(76) Frisch, M. J.; Trucks, G. W.; Schlegel, H. B.; Scuseria, G. E.; Robb, M. A.; Cheeseman, J. R.; Scalmani, G.; Barone, V.; Mennucci, B.; Petersson, G. A.; Nakatsuji, H.; Caricato, M.; Li, X.; Hratchian, H. P.; Izmaylov, A. F.; Bloino, J.; Zheng, G.; Sonnenberg, J. L.; Hada, M.; Ehara, M.; Toyota, K.; Fukuda, R.; Hasegawa, J.; Ishida, M.; Nakajima, T.; Honda, Y.; Kitao, O.; Nakai, H.; Vreven, T.; Montgomery, J. A., Jr.; Peralta, J. E.; Ogliaro, F.; Bearpark, M.; Heyd, J. J.; Brothers, E.; Kudin, K. N.; Staroverov, V. N.; Kobayashi, R.; Normand, J.; Raghavachari, K.; Rendell, A.; Burant, J. C.; Iyengar, S. S.; Tomasi, J.; Cossi, M.; Rega, N.; Millam, J. M.; Klene, M.; Knox, J. E.; Cross, J. B.; Bakken, V.; Adamo, C.; Jaramillo, J.; Gomperts, R.; Stratmann, R. E.; Yazyev, O.; Austin, A. J.; Cammi, R.; Pomelli, C.; Ochterski, J. W.; Martin, R. L.; Morokuma, K.; Zakrzewski, V. G.; Voth, G. A.; Salvador, P.; Dannenberg, J. J.; Dapprich, S.; Daniels, A. D.; Farkas, Ö.; Foresman, J. B.; Ortiz, J. V.; Cioslowski, J.; Fox, D. J. Gaussian 09 Wallingford,CT, 2009.

(77) Mukamel, S. *Principles of Nonlinear Optical Spectroscopy*; Oxford University Press: New York, 1995.

(78) Nitzan, A. *Chemical Dynamics in Condensed Phases*; Oxford University Press: Oxford, 2006.

(79) Miller, R. J. D. *Annu. Rev. Phys. Chem.* **1991**, *42*, 581.

(80) Middleton, C. T.; Cohen, B.; Kohler, B. *J. Phys. Chem. A* **2007**, *111*, 10460.

(81) van Veldhoven, E.; Khurmi, C.; Zhang, X.; Berg, M. A. *ChemPhysChem* **2007**, *8*, 1761.

(82) Khurmi, C.; Berg, M. A. *J. Chem. Phys.* **2008**, *129*, 064504.

CHAPTER 8: CONCLUDING REMARKS

8.1. Concluding Remarks

The work in this dissertation has developed two-dimensional resonance Raman (2DRR) spectroscopy as a powerful tool for providing new insights into fast chemical reactions of both simple and complex molecules in condensed phases. Specifically, this work has investigated reactant to product vibrational coherence transfer and heterogeneity in molecular structures responsible for energy transfer with the surroundings. In addition, rigorous tests have been conducted to ensure that 2DRR is not susceptible to the technical challenges that plagued off-resonant multidimensional Raman techniques. Chapter 1 introduced the scientific background and context motivating the experimental studies in this dissertation. Chapter 2 laid out the basic theoretical framework that underpins the more complex descriptions in later chapters. Chapter 3 detailed the nonlinear spectroscopic techniques and unconventional pulse generation mechanisms developed and/or utilized in the rest of the work.

The initial development and implementation of 2DRR was contained in Chapter 4. Ground state vibrations of triiodide were probed using femtosecond UV laser pulses generated by filamentation in high pressure Ne gas. The findings of this study were shown to match the predictions of a theoretical model constructed from parameters in the literature.[1,2] A battery of scrupulous experimental tests was performed verifying that the desired 2DRR response dominates the signal. A publication containing the work in Chapter 4 was an Editor's Choice in the *Journal of Chemical Physics* for the year 2014.[3]

After proving the viability of 2DRR in Chapter 4, Chapter 5 set out to measure correlations between nuclear motions of the reactant and product in the photodissociation reaction of triiodide. 2DRR experiments showed, for the first time, exactly how displacements in the nonequilibrium bond length of triiodide determine the vibrational coherence frequency of diiodide. A theoretical model treating the reaction as a 'coherence transfer transition' made predictions matching the experimentally measured signals.

In Chapter 6, focus was shifted to myoglobin in order to move toward more complex systems possessing many active vibrational coordinates. A second variant of 2DRR was developed where one dimension is gathered in the time domain and one in the frequency domain (rather than both in the time domain), drastically reducing data acquisition times and improving sensitivity. The evolution of vibrations of the heme, occurring simultaneously with electronic processes, was detected throughout the fingerprint region. The time scales of vibrational relaxation were in agreement with the electronic relaxation time scales measured by Chergui and coworkers.[4] Similar to the triiodide studies, rigorous tests based on experiment and theory indicated that the 2DRR signal from myoglobin was not contaminated by technical issues that had affected off-resonant multidimensional Raman spectroscopies. A publication containing the work in Chapter 6 was an Editor's Choice in the *Journal of Chemistry Physics* for the year 2015.[5]

The next step in the myoglobin study was completed in Chapter 7. Signatures of inhomogeneous line broadening and anharmonicity in 2DRR spectra were illustrated through model calculations, and it was shown that the primary information to be had corresponds to line broadening mechanisms. 2DRR data and computational simulations suggested that the greatest amount of inhomogeneous line broadening is found for a vibrational mode local to the heme

group's propionic acid chains, reflecting significant heterogeneity in their equilibrium geometries. Since the propionic acid side chains are known to act as a gateway for the fast exchange of thermal energy between the heme and solvent[6-10], it was suggested that structural heterogeneity may play a critical role in this process.

In the next step of this work, the connection between structural heterogeneity in the heme group's propionic acid chains and the rate of heme-to-solvent energy transfer is being investigated. 2DRR experiments have been conducted on both deoxygenated myoglobin (deoxyMb) and carbonmonoxide-ligated mylogbin (MbCO) in order to characterize heterogeneity in the rates of vibrational energy exchange between the heme and solvent. Both systems are well suited for comparison because they both undergo ground state recovery on the 100 fs time scale. However, upon excitation, MbCO experiences ligand dissociation, causing a transition from a planar to a nonplanar geometry, whereas deoxyMb does not relax by way of out-of-plane distortions. These properties provide a distinct difference between the two species.[11-16]

At the current stage in analysis it appears that deoxyMb exhibits a greater amount of heterogeneity in its vibrational energy transfer dynamics than does MbCO. Since the propionic acid chains (which extend into the solvent) are common to both systems, this difference most likely involves nuclear motions within the hydrophobic pocket that encloses the porphyrin. It is hypothesized that the large out-of-plane reorganization of the heme that follows ligand dissociation in MbCO limits heterogeneity in the rates of energy exchange with the solvent, while the amount of heterogeneity for deoxyMb is greater in relation because its geometry remains much more constant throughout the relaxation process. Further analysis is still underway.

In addition to photodissociation in triiodide and myoglobin, 2DRR should be sensitive to other interesting mechanisms in important systems where a non-radiative transition impulsively initiates vibrational coherence. New insights could be generated for processes such as energy transfer in photosynthetic complexes[17-22], charge transfer at molecular-semiconductor interfaces[23,24] and bulk heterojunctions[25], and even the chemistry comprising the initial steps of vision![26-28] The primary information content of these insights should relate to correlations between reactant and product nuclear motions and structural/dynamic heterogeneity involved with the process of interest.

It has been suggested that 2DRR spectra should also provide clear information regarding anharmonic couplings between nuclear modes.[29] Rigorous modeling and experimental work conducted in this dissertation suggests that it is actually quite difficult, or impossible, to tease knowledge of anharmonic couplings out of a 2DRR spectrum. It is important to note that both the harmonic and anharmonic character of vibrational modes contribute to the signal under resonant conditions (i.e. when the sample absorbs the perturbative laser light). Of course, the contribution from harmonic character is much stronger than the contribution from anharmonicity, complicating acquisition of information about anharmonic couplings.

8.2. REFERENCES

(1) Banin, U.; Kosloff, R.; Ruhman, S. *Chem. Phys.* **1994**, *183*, 289.

(2) Johnson, A. E.; Myers, A. B. *J. Chem. Phys.* **1995**, *102*, 3519.

(3) Molesky, B. P.; Giokas, P. G.; Guo, Z.; Moran, A. M. *J. Chem. Phys.* **2014**, *141*, 114202.

(4) Consani, C.; Auböck, G.; Bräm, O.; Mourik, F. V.; Chergui, M. *J. Chem. Phys.* **2014**, *140*, 025103.

(5) Molesky, B. P.; Guo, Z.; Moran, A. M. *J. Chem. Phys.* **2015**, *142*, 212405.

(6) Lian, T.; Locke, B.; Kholodenko, Y.; Hochstrasser, R. M. *J. Phys. Chem.* **1994**, *98*, 11648.

(7) Sagnella, D. E.; Straub, J. E. *J. Phys. Chem. B* **2001**, *105*, 7057.

(8) Bu, L.; Straub, J. E. *J. Phys. Chem. B* **2003**, *107*, 10634.

(9) Gao, Y.; Koyama, M.; El-Mashtoly, S. F.; Hayashi, T.; Harada, K.; Mizutani, Y.; Kitagawa, T. *Chem. Phys. Lett.* **2006**, *429*, 239.

(10) Koyama, M.; Neya, S.; Mizutani, Y. *Chem. Phys. Lett.* **2006**, *430*, 404.

(11) Li, P.; Sage, J. T.; Champion, P. M. *J. Chem. Phys.* **1992**, *97*, 3214.

(12) Lim, M.; Jackson, T. A.; Anfinrud, P. A. *J. Phys. Chem.* **1996**, *100*, 12043.

(13) Ye, X.; Demidov, A.; Rosca, F.; Wang, W.; Kumar, A.; Ionaseu, D.; Zhu, L.; Barrick, D.; Wharton, D.; Champion, P. M. *J. Phys. Chem. A* **2003**, *107*, 8156.

(14) Martin, J.-L.; Vos, M. H. *Annu. Rev. Biophys. Biomol. Struct.* **1992**, *21*, 199.

(15) Vos, M. H. *Biochim. Biophys. Acta* **2008**, *1777*, 15.

(16) Consani, C.; Auböck, G.; Mourik, F. V.; Chergui, M. *Science* **2013**, *339*, 1586.

(17) Fuller, F. D.; Pan, J.; Gelzinis, A.; Butkus, V.; Senlik, S. S.; Wilcox, D. E.; Yocum, C. F.; Valkunas, L.; Abramavicius, D.; Ogilvie, J. P. *Nat. Chem.* **2014**, *6*, 706.

(18) Womick, J. M.; Moran, A. M. *J. Phys. Chem. B* **2011**, *115*, 1347.

(19) Christensson, N.; Kauffmann, H. F.; Pullerits, T.; Mančal, T. *J. Phys. Chem. B* **2012**, *116*, 7449.

(20) Kolli, A.; O'Reilly, E. J.; Scholes, G. D.; Olaya-Castro, A. *J. Chem. Phys.* **2012**, *137*, 174109.

(21) Chin, A. W.; Prior, J.; Rosenbach, R.; Caycedo-Soler, F.; Huelga, S. F.; Plenio, M. B. *Nat. Phys.* **2013**, *9*, 113.

(22) Fujihashi, Y.; Fleming, G. R.; Ishizaki, A. *J. Chem. Phys.* **2015**, *142*, 212403.

(23) Tisdale, W. A.; Williams, K. J.; Timp, B. A.; Norris, D. J.; Aydil, E. S.; Zhu, X.-Y. *Science* **2010**, *328*, 1543.

(24) Zimmermann, C.; Willig, F.; Ramakrishna, S.; Burfeindt, B.; Pettinger, B.; Eichberger, R.; Storck, W. *J. Phys. Chem. B* **2001**, *105*, 9245.

(25) Song, Y.; Clafton, S. N.; Pensack, R. D.; Kee, T. W.; Scholes, G. D. *Nat. Commun.* **2014**, *5*, 4933.

(26) Polli, D.; Altoé, P.; Weingart, O.; Spillane, K. M.; Manzoni, C.; Brida, D.; Tomasello, G.; Orlandi, G.; Kukura, P.; Mathies, R. A.; Garavelli, M.; Cerullo, G. *Nature* **2010**, *467*, 440.

(27) Wang, Q.; Schoenlein, R. W.; Peteanu, L. A.; Mathies, R. A.; Shank, C. V. *Science* **1994**, *266*, 422.

(28) Johnson, P. J. M.; Halpin, A.; Morizumi, T.; Prokhorenko, V. I.; Ernst, O. P.; Miller, R. J. D. *Nat. Chem.* **2015**, *7*, 980.

(29) Hoffman, D. P.; Mathies, R. A. *Acc. Chem. Res.* **2016**, *49*, 616.

APPENDIX A: SUPPLEMENT TO "MULTIDIMENSIONAL RESONANCE RAMAN SPECTROSCOPY BY SIX-WAVE MIXING IN THE DEEP UV"

A.1. Auxiliary Response Functions

This section summarizes the auxiliary response functions used to compute the relative magnitudes of cascaded third-order and direct fifth-order nonlinearities in Section 4.5.2. The full derivation of these formulas are presented in Section A.8. The present analytical approach is motivated by two key issues: (i) its manageable computational expense facilitates the "bird's eye view" of the dependence of the ratio on the displacement parameter in Figure 4.14; (ii) it avoids errors in precision that may be introduced through numerical integration. With respect to point (ii), we remark that confidence in the relative precisions of $E_{cas}(t)$ and $E^{(5)}(t)$ is essential, because the magnitudes of two signal fields must be compared on the same footing.

In Equation 4.22, the ratio between the cascaded third-order and direct fifth-order signal fields is expressed in terms of the following products of auxiliary response functions,

$$\eta_{seq}^{(3)}(\tau_1,\tau_2)=\sum_{\alpha=1}^{2}\sum_{\beta=1}^{2}\left\{\phi_{\alpha}^{(3)}(\tau_1)\mathrm{f}_{seq1}\left(\Delta k_{seq1}l\right)+\left[\phi_{\alpha}^{(3)}(\tau_1,t)\right]^{*}\mathrm{f}_{seq2}\left(\Delta k_{seq2}l\right)\right\}\phi_{\beta}^{(3)}(\tau_2), \tag{A.1}$$

$$\eta_{par}^{(3)}(\tau_1,\tau_2)=\sum_{\alpha=1}^{2}\sum_{\beta=1}^{2}\left\{\phi_{\alpha}^{(3)}(\tau_2)\mathrm{f}_{par1}\left(\Delta k_{par1}l\right)+\phi_{\alpha}^{(3)}(\tau_2,t)\mathrm{f}_{par2}\left(\Delta k_{par2}l\right)\right\}\phi_{\beta}^{(3)}(\tau_1+\tau_2)\right\}, \tag{A.2}$$

and

$$\eta_{direct}^{(5)}(\tau_1,\tau_2)=\mathrm{f}_{direct}\left(\Delta k_{direct}l\right)\sum_{\alpha=1}^{4}\phi_{\alpha}^{(5)}\left(\tau_1,\tau_2\right). \tag{A.3}$$

Auxiliary response functions associated with the third-order polarization are

$$\phi_1^{(3)}(\tau) = i\sum_{mnkl} B_m \langle n|m\rangle\langle n|k\rangle\langle l|k\rangle\langle l|m\rangle I_{en,gm}(\omega_L) I_{gk,gm}(\tau) I_{el,gm}(\omega_L) \tag{A.4}$$

and

$$\phi_2^{(3)}(\tau) = i\sum_{mnkl} B_m \langle n|m\rangle\langle n|k\rangle\langle l|m\rangle\langle l|k\rangle I_{gm,en}(-\omega_L) I_{gm,gk}(\tau) I_{el,gk}(\omega_L). \tag{A.5}$$

Each auxiliary response function involves a sum over dummy indices associated with vibrational energy levels of the ground (m, k, u) and excited electronic states (n, l, v). Each term is also weighted by a Boltzmann population, B_m, and a product of vibrational overlap integrals, $\langle n|m\rangle$. The (frequency-domain) line shapes associated with electronic coherences are written as

$$I_{en,gm}(\omega_L) = \frac{1}{\omega_L - \omega_{eg} - \omega_{nm} + i\Gamma_{eg}} \tag{A.6}$$

whereas the (time-domain) vibrational coherence is given by

$$I_{gk,gm}(\tau) = \theta(\tau)\exp(-i\omega_{km}\tau - \Gamma_{vib}\tau) \tag{A.7}$$

The auxiliary response functions associated with the fifth-order polarization are

$$\begin{aligned}\phi_1^{(5)}(\tau_1,\tau_2) = \sum_{mnkluv} & B_m \langle n|m\rangle\langle n|k\rangle\langle l|k\rangle\langle l|u\rangle\langle v|u\rangle\langle v|m\rangle I_{en,gm}(\omega_L) \\ & \times I_{gk,gm}(\tau_1) I_{el,gm}(\omega_L) I_{gu,gm}(\tau_2) I_{ev,gm}(\omega_L)\end{aligned}, \tag{A.8}$$

$$\begin{aligned}\phi_2^{(5)}(\tau_1,\tau_2) = \sum_{mnkluv} & B_m \langle n|m\rangle\langle n|k\rangle\langle l|m\rangle\langle l|u\rangle\langle v|k\rangle\langle v|u\rangle I_{en,gm}(\omega_L) \\ & \times I_{gk,gm}(\tau_1) I_{gk,el}(-\omega_L) I_{gk,gu}(\tau_2) I_{ev,gu}(\omega_L)\end{aligned}, \tag{A.9}$$

$$\begin{aligned}\phi_3^{(5)}(\tau_1,\tau_2) = \sum_{mnkluv} & B_m \langle n|m\rangle\langle n|k\rangle\langle l|k\rangle\langle l|u\rangle\langle v|m\rangle\langle v|u\rangle I_{gm,en}(-\omega_L) \\ & \times I_{gm,gk}(\tau_1) I_{gm,el}(-\omega_L) I_{gm,gu}(\tau_2) I_{ev,gu}(\omega_L)\end{aligned}, \tag{A.10}$$

and

$$\phi_4^{(5)}(\tau_1,\tau_2) = \sum_{mnkluv} B_m \langle n|m\rangle\langle n|k\rangle\langle l|m\rangle\langle l|u\rangle\langle v|u\rangle\langle v|k\rangle I_{gm,en}(-\omega_L) \times I_{gm,gk}(\tau_1) I_{el,gk}(\omega_L) I_{gu,gk}(\tau_2) I_{ev,gk}(\omega_L) \quad \text{(A.11)}$$

A.2. Anharmonic Excited State Potential Energy Surface

The auxiliary response functions summarized in Section A.1 are parameterized using the empirical excited state potential energy surface developed by Ruhman[1] (with parameters for I_3^- in ethanol determined by Myers).[2] The excited state potential energy surface is generated using surface C and Equation (5) in Reference[2]. Anharmonic vibrational wavefunctions for the symmetric stretching coordinate are generated by computing derivatives of the excited state potential energy surface (along the slice with equal bond lengths) up to fourth-order and substituting them into the following vibrational Hamiltonian[3]

$$H = \frac{\hbar\omega}{2}\left(2a^\dagger a + 1\right) + U_3\left[a^\dagger a^\dagger a^\dagger + 3a^\dagger a^\dagger a + 3a^\dagger aa + aaa + 3a^\dagger + 3a\right] + U_4\left[a^\dagger a^\dagger a^\dagger a^\dagger + 4a^\dagger a^\dagger a^\dagger a + 6a^\dagger a^\dagger aa + 4a^\dagger aaa + aaaa + 6a^\dagger a^\dagger + 12a^\dagger a + 6aa + 3\right] \quad \text{(A.12)}$$

where

$$U_j = \frac{1}{j!\sqrt{2^j m^j \omega^j \hbar^{-j}}}\left(\frac{d^j V}{dq^j}\right)_0 . \quad \text{(A.13)}$$

We find that the excited state potential energy surface possesses lower curvature than the ground state (ω=95 cm^{-1}) and is also modestly anharmonic (U_3=-1.5 cm^{-1} and U_4=0.1 cm^{-1}). Anharmonic vibrational wavefunctions are obtained by diagonalizing the Hamiltonian in a basis of harmonic oscillators (up to the 20 vibrational quanta).[4]

The vibrational overlap integrals needed to evaluate the response functions are obtained using

$$\langle n|m\rangle = \sum_k \varphi_{nk} \langle k|m\rangle \tag{A.14}$$

where φ_{nk} is the expansion coefficient for basis vector k and excited state vibrational wavefunction, n. The ground state potential energy surface is taken to be harmonic with a fundamental frequency of 112 cm^{-1}. We obtain a dimensionless potential energy displacement of 8.8 based on the 63.5-amu reduced mass[5] and 0.66-angstrom increase in each I-I bond length in the excited state.[1] Myers found that a dimensionless displacement near 7.0 produces a best-fit to the total emission spectrum using a modified harmonic model.[2] These estimations define the region of parameter space relevant to the present model.

A.3. Modeling Concentration Dependence of Direct and Cascaded Responses

In the present experiments, attenuation of the incoming laser beams and absorption of the signal field must be accounted for in order to establish how the direct fifth-order and cascaded signal intensities vary with concentration. In this section, we obtain formulas that describe general behaviors in order to interpret the measured signals. The direct fifth-order signal intensity at position x in the sample is subject to the relation,

$$I^{(5)}(x,C) \propto C^2 \left|\chi^{(5)}\right|^2 I_L^5(x,C) \tag{A.15}$$

where C is concentration, $\chi^{(5)}$ is the susceptibility, and $I_L(x,C)$ is the laser intensity. The direct fifth-order signal intensity accumulated at the exit of the sample is obtained by integrating over x

$$I^{(5)}(C) \propto C^2 \int_0^a dx \exp[-5\sigma C x] \exp\left[\sigma C (x-a)\right] \tag{A.16}$$

where a is the path length, σ is the linear absorption coefficient (product of $\ln(10)$ and the molar extinction coefficient), and the first and second exponentials respectively represent attenuation of the incident laser beams and (exiting) signal beam. The susceptibility can be removed from the proportionality in Equation A.16 because it is independent of x.

Treatment of the cascaded signal field must take into account accumulation of both the primary and secondary third-order signal intensities. The primary four-wave mixing signal intensity scales according to $I_L^3(x,C)$. However, the intensity of the secondary four-wave mixing process depends on the product of $I_L^2(x,C)$, which decreases exponential with x, and the intensity of the primary four-wave mixing signal (denoted as $I_{primary}^{(3)}(x,C)$), which increases in a (slightly) sub-quadratic fashion with x at modest optical densities. With consideration of these factors, the cascaded signal intensity is written as

$$I_{cas}(C) \propto C^2 \int_0^a dx \exp[-2\sigma C x] \exp\left[\sigma C (x-a)\right] I_{primary}^{(3)}(x,C) \tag{A.17}$$

where the primary four-wave mixing signal intensity at position x is given by

$$I_{primary}^{(3)}(x,C) \propto C^2 \int_0^x dx' \exp[-3\sigma C x'] \exp\left[\sigma C (x'-a)\right]. \tag{A.18}$$

A.4. Third-Harmonic Generation via Filamentation in Neon at High Pressures

The cell used for third-harmonic generation is constructed from stainless steel 2.75" ConFlat (CF) and ¼" Swagelok components, chosen for their abilities to sustain high pressure differentials and the secure nature of the seals between parts. A 5" long CF full nipple (Kurt J. Lesker: FN-0275) is affixed to one end of a 5" long CF tee (Kurt J. Lesker: T-0275). CF viewport flanges containing 5-mm thick, uncoated fused silica windows (Thorlabs: VPCH412) are installed in the ends of the nipples and tees to allow passage of the laser beam through the cell. The nipples provide distance for the laser beams to focus and defocus inside the cell, thereby avoiding damage of the entrance and exit windows. A 2.75" CF to ¼" Swagelok tube fitting adaptor (Kurt J. Lesker: F0275X4SWG) is attached to the third port of the CF tee for gas to enter and exit the cell via ¼" nylon hose (McMaster Carr: 9685T3) secured to the Swagelok tube fitting. Nylon hose is used because of its relatively high pressure rating (54.5 atm at 24°C). CF components are joined with high-purity, oxygen free Cu gaskets (Kurt J. Lesker: GA-0275) and stainless steel ¼"-28, 12-point socket cap screws bolted into nuts and washers (Kurt J. Lesker: TBS25028212). The cell has a small leak rate (<0.1 atm/hour at 35 atm) despite employing parts that are not specified for operation at positive pressures.

Pulses generated in filaments may exhibit undesired temporal structure, particularly at higher plasma densities. In earlier work, we found that suitable pulses can be obtained in argon only at fairly low pressures (below 2 atm).[6,7] Higher neon pressures may be employed because the ionization potential of neon (21.6 eV) is lower than that of argon (15.8 eV). Therefore, multi-photon ionization processes associated with plasma formation are less problematic in neon. The pulse generation mechanism is quite complicated.[8] We developed a procedure to

characterize the third-harmonic pulses inside the high-pressure cell in order to better understand the capabilities of the setup.

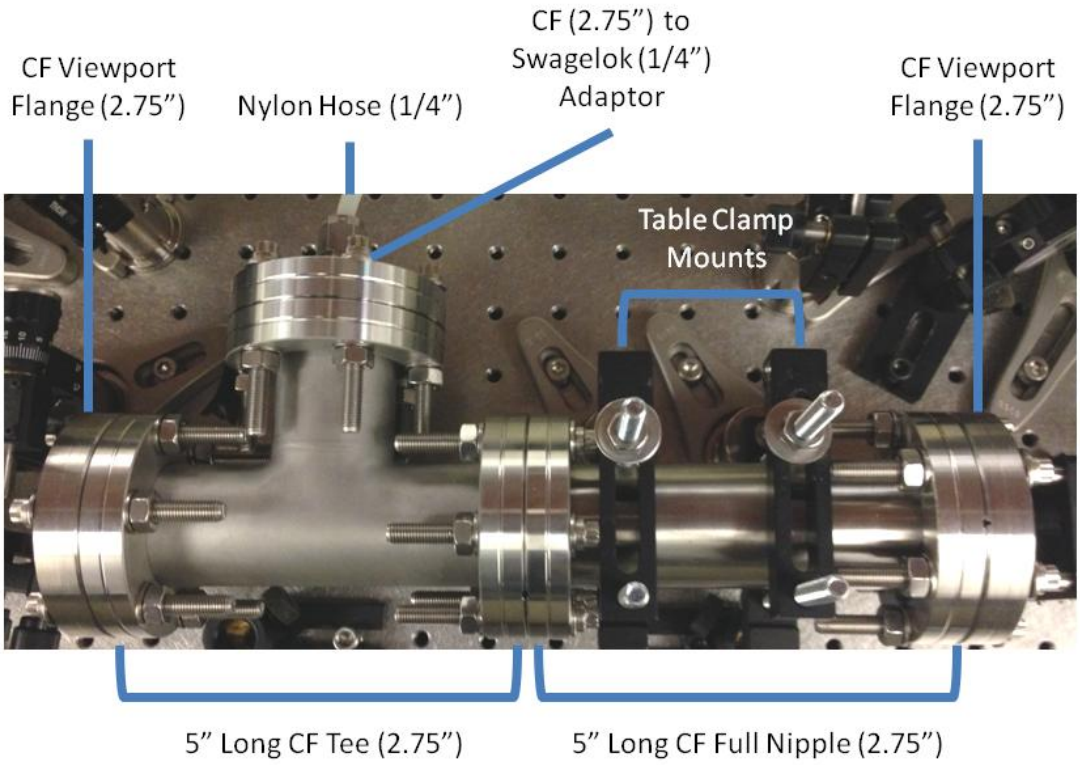

Figure A.1. Cell used for third-harmonic generation via filamentation in neon.

Third-harmonic pulses generated in the cell were directed into a transient grating frequency resolved optical gating (TG-FROG) apparatus without compression; bypassing a compressor makes it more straightforward to compare measurements conducted at a wide variety of pressures (and bandwidths). TG-FROG measurements were conducted using a 0.25-mm-thick fused silica window as a nonlinear medium, and the spectrograms were analyzed with commercial software (Femtosoft FROG 3.2). The software yielded the intensity and spectral phase of the laser pulse at the sample position. The spectral phase of the pulse before it exits the

cell (i.e. inside the filament) was obtained by subtracting the second and third-order dispersion coefficients associated with all transmissive optics encountered after the filament.

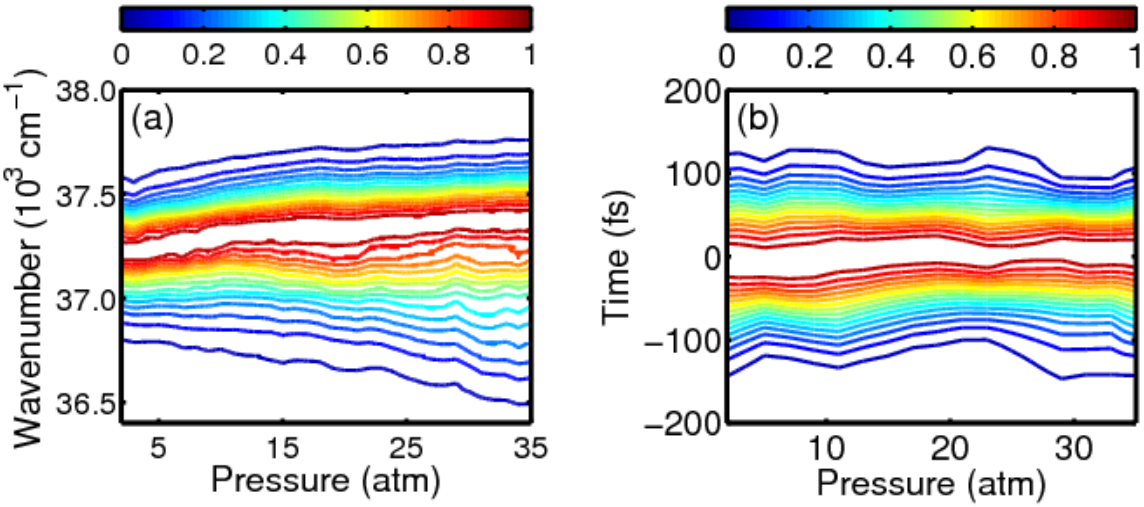

Figure A.2. (a) Spectrum of third-harmonic measured as a function of neon pressure. (b) Intensity of third-harmonic field inside the high-pressure cell determined using the TG-FROG measurements described in the text.

The results presented in Figure A.2 demonstrate that the temporal profile of the third-harmonic varies little as the neon pressure (and plasma density) increases. Notably, the spectral width of the laser pulse expands as the pressure increases, whereas the temporal width remains fairly constant. Of course, the temporal width should decrease as the bandwidth increases if the pulses are transform-limited. Thus, our data indicate that dispersion is accumulated as the pressure increases. Figure A.2b is understood by considering that the growth in the spectral width originates in the nonlinearity of the refractive index, which modulates the phase of the electric field. The bandwidth expands because of both self-phase modulation (a single-beam effect) and cross-phase modulation (effect related to a pair of beams) due to the multi-color nature of the filament.[8] Such phase modulation of the electric field is accompanied by positive

group delay dispersion (GDD) in which the lower-frequency portion of the pulse precedes the higher-frequency portion. Such an increase in the GDD at higher pressures is consistent with the insensitivity of the temporal profile to pressure observed in Figure A.2b.

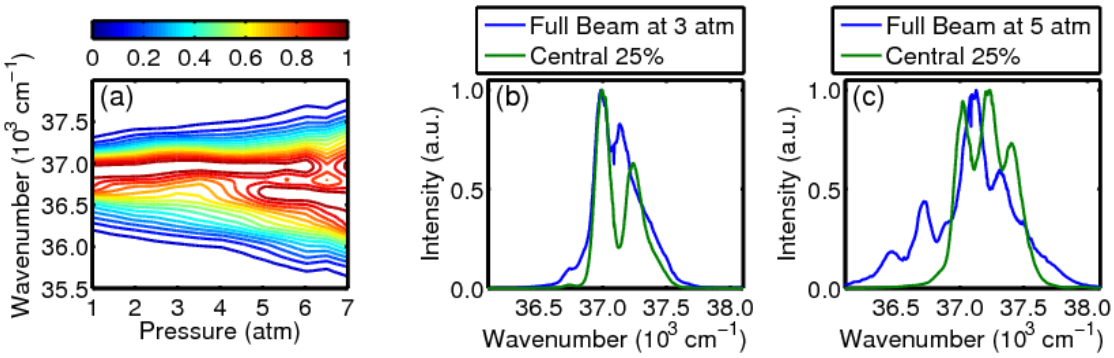

Figure A.3. (a) Spectrum of third-harmonic measured as a function of argon pressure. Compared to pulses generated in neon, the spectrum of the third-harmonic varies significantly between the full beam and the central 25%. Examples are shown for (b) 3 atm and (c) 5 atm.

In Figure A.3, we present data acquired for third-harmonic pulses produced in argon gas. The spectral width increases more steeply with pressure in argon than it does in neon because of the larger nonlinearity in the refractive index. However, the third-harmonic pulses produced in argon are not suitable for experiments because the spectrum of the laser pulse is far from spatially uniform, particularly at higher pressures. Figures A.3b and A.3c show spectra measured for the full beam and central 25% (defined as 25% of the intensity). This spatial heterogeneity in the beam makes it impossible to compress the pulses to short durations. Attempts were made to conduct experiments by filtering the central portion of the beam at 5 atm. This approach was ineffective because of instability in the spatio-temporal properties of the laser beam (e.g. the bandwidth and spatial profile fluctuated significantly).

A.5. Fifth-Order Cumulant Expansion

We begin by considering the general six-point correlation function for the dipole operator, V_{ge}

$$F\left(\hat{\tau}_1,\hat{\tau}_2,\hat{\tau}_3,\hat{\tau}_4,\hat{\tau}_5,\hat{\tau}_6\right)=\left\langle V_{ge}\left(\hat{\tau}_1\right)V_{eg}\left(\hat{\tau}_2\right)V_{ge}\left(\hat{\tau}_3\right)V_{eg}\left(\hat{\tau}_4\right)V_{ge}\left(\hat{\tau}_5\right)V_{eg}\left(\hat{\tau}_6\right)\right\rangle. \tag{A.19}$$

Response functions are obtained by carrying out a cumulant expansion on the six-point correlation function

$$\begin{aligned}\left\langle V_{ge}\left(\hat{\tau}_1\right)V_{eg}\left(\hat{\tau}_2\right)V_{ge}\left(\hat{\tau}_3\right)V_{eg}\left(\hat{\tau}_4\right)V_{ge}\left(\hat{\tau}_5\right)V_{eg}\left(\hat{\tau}_6\right)\right\rangle &= \left|\mu_{eg}\right|^6\exp\left[-i\omega_{eg}\left(\hat{\tau}_1-\hat{\tau}_2+\hat{\tau}_3-\hat{\tau}_4+\hat{\tau}_5-\hat{\tau}_6\right)\right]\\ &\times\left\langle \exp_+\left[-i\int_0^{\hat{\tau}_1}d\hat{\tau}_1'U\left(\hat{\tau}_1'\right)\right]\exp_-\left[i\int_0^{\hat{\tau}_2}d\hat{\tau}_2'U\left(\hat{\tau}_2'\right)\right]\exp_+\left[-i\int_0^{\hat{\tau}_3}d\tau_3'U\left(\tau_3'\right)\right]\right.\\ &\left.\times\exp_-\left[i\int_0^{\hat{\tau}_4}d\hat{\tau}_4'U\left(\hat{\tau}_4'\right)\right]\exp_+\left[-i\int_0^{\hat{\tau}_5}d\hat{\tau}_5'U\left(\hat{\tau}_5'\right)\right]\exp_-\left[i\int_0^{\hat{\tau}_6}d\hat{\tau}_6'U\left(\hat{\tau}_6'\right)\right]\right\rangle\end{aligned} \tag{A.20}$$

where ω_{eg} is the mean energy gap at the equilibrium geometry of the ground state. Here, the points in time at which field-matter interactions occur are denoted as $\hat{\tau}_j'$; this notation is used to distinguish these times from experimentally controlled delays, τ_1 and τ_2. For a harmonic bath, cumulants higher than second order vanish and the correlation function is given by

$$\begin{aligned}&\left\langle V_{ge}\left(\hat{\tau}_1\right)V_{eg}\left(\hat{\tau}_2\right)V_{ge}\left(\hat{\tau}_3\right)V_{eg}\left(\hat{\tau}_4\right)V_{ge}\left(\hat{\tau}_5\right)V_{eg}\left(\hat{\tau}_6\right)\right\rangle\\ &=\left|\mu_{eg}\right|^6\exp\left[-i\omega_{eg}\left(\hat{\tau}_1-\hat{\tau}_2+\hat{\tau}_3-\hat{\tau}_4+\hat{\tau}_5-\hat{\tau}_6\right)\right]\\ &\times\exp\left[-g\left(\hat{\tau}_1-\hat{\tau}_2\right)+g\left(\hat{\tau}_1-\hat{\tau}_3\right)-g\left(\hat{\tau}_1-\hat{\tau}_4\right)+g\left(\hat{\tau}_1-\hat{\tau}_5\right)-g\left(\hat{\tau}_1-\hat{\tau}_6\right)\right.\\ &-g\left(\hat{\tau}_2-\hat{\tau}_3\right)+g\left(\hat{\tau}_2-\hat{\tau}_4\right)-g\left(\hat{\tau}_2-\hat{\tau}_5\right)+g\left(\hat{\tau}_2-\hat{\tau}_6\right)\\ &-g\left(\hat{\tau}_3-\hat{\tau}_4\right)+g\left(\hat{\tau}_3-\hat{\tau}_5\right)-g\left(\hat{\tau}_3-\hat{\tau}_6\right)\\ &-g\left(\hat{\tau}_4-\hat{\tau}_5\right)+g\left(\hat{\tau}_4-\hat{\tau}_6\right)\\ &\left.-g\left(\hat{\tau}_5-\hat{\tau}_6\right)\right]\end{aligned}. \tag{A.21}$$

Each of the Feynman diagrams in Figure A.4 correspond to different time-ordering of the field-matter interactions. Written in terms of the time intervals, t_i, we have the following terms.

$$\begin{aligned}
&R_1(t_5,t_4,t_3,t_2,t_1) = F(t_1+t_2+t_3+t_4+t_5, t_1+t_2+t_3+t_4, t_1+t_2+t_3, t_1+t_2, t_1, 0) \\
&= |\mu_{eg}|^6 \exp\left[-i\omega_{eg}(t_1+t_3+t_5)\right] \exp\left[-g(t_5)+g(t_4+t_5)\right. \\
&-g(t_3+t_4+t_5)+g(t_2+t_3+t_4+t_5)-g(t_1+t_2+t_3+t_4+t_5)-g(t_4) \\
&+g(t_3+t_4)-g(t_2+t_3+t_4)+g(t_1+t_2+t_3+t_4)-g(t_3)+g(t_2+t_3) \\
&\left.-g(t_1+t_2+t_3)-g(t_2)+g(t_1+t_2)-g(t_1)\right]
\end{aligned} \tag{A.22}$$

$$\begin{aligned}
&R_2(t_5,t_4,t_3,t_2,t_1) = F(t_1+t_2, t_1+t_2+t_3, t_1+t_2+t_3+t_4+t_5, t_1+t_2+t_3+t_4, t_1, 0) \\
&= |\mu_{eg}|^6 \exp\left[-i\omega_{eg}(t_1-t_3+t_5)\right] \exp\left[-g^*(t_3)+g^*(t_3+t_4+t_5)\right. \\
&-g^*(t_3+t_4)+g(t_2)-g(t_1+t_2)-g^*(t_4+t_5)+g^*(t_4)-g(t_2+t_3) \\
&+g(t_1+t_2+t_3)-g(t_5)+g(t_2+t_3+t_4+t_5)-g(t_1+t_2+t_3+t_4+t_5) \\
&\left.-g(t_2+t_3+t_4)+g(t_1+t_2+t_3+t_4)-g(t_1)\right]
\end{aligned} \tag{A.23}$$

$$\begin{aligned}
&R_3(t_5,t_4,t_3,t_2,t_1) = F(0, t_1, t_1+t_2, t_1+t_2+t_3, t_1+t_2+t_3+t_4+t_5, t_1+t_2+t_3+t_4) \\
&= |\mu_{eg}|^6 \exp\left[-i\omega_{eg}(-t_1-t_3+t_5)\right] \exp\left[-g^*(t_1)+g^*(t_1+t_2)\right. \\
&-g^*(t_1+t_2+t_3)+g^*(t_1+t_2+t_3+t_4+t_5)-g^*(t_1+t_2+t_3+t_4)-g^*(t_2) \\
&+g^*(t_2+t_3)-g^*(t_2+t_3+t_4+t_5)+g^*(t_2+t_3+t_4)-g^*(t_3)+g^*(t_3+t_4+t_5) \\
&\left.-g^*(t_3+t_4)-g^*(t_4+t_5)+g^*(t_4)-g(t_5)\right]
\end{aligned} \tag{A.24}$$

$$\begin{aligned}
&R_4(t_5,t_4,t_3,t_2,t_1) = F(0, t_1, t_1+t_2+t_3+t_4+t_5, t_1+t_2+t_3+t_4, t_1+t_2+t_3, t_1+t_2) \\
&= |\mu_{eg}|^6 \exp\left[-i\omega_{eg}(-t_1+t_3+t_5)\right] \exp\left[-g^*(t_1)+g^*(t_1+t_2+t_3+t_4+t_5)\right. \\
&-g^*(t_1+t_2+t_3+t_4)+g^*(t_1+t_2+t_3)-g^*(t_1+t_2)-g^*(t_2+t_3+t_4+t_5) \\
&+g^*(t_2+t_3+t_4)-g^*(t_2+t_3)+g^*(t_2)-g(t_5)+g(t_4+t_5)-g(t_3+t_4+t_5) \\
&\left.-g(t_4)+g(t_3+t_4)-g(t_3)\right]
\end{aligned} \tag{A.25}$$

$$
\begin{aligned}
&R_5(t_5,t_4,t_3,t_2,t_1)=F(t_1,t_1+t_2+t_3+t_4,t_1+t_2+t_3+t_4+t_5,t_1+t_2+t_3,t_1+t_2,0)\\
&=|\mu_{eg}|^6\exp\left[-i\omega_{eg}(t_1-t_3+t_5)\right]\exp\left[-g^*(t_2+t_3+t_4)+g^*(t_2+t_3+t_4+t_5)\right.\\
&-g^*(t_2+t_3)+g^*(t_2)-g\ (t_1)-g^*(t_5)+g\ (t_4)-g\ (t_3+t_4)\\
&+g\ (t_1+t_2+t_3+t_4)-g\ (t_4+t_5)+g\ (t_3+t_4+t_5)-g\ (t_1+t_2+t_3+t_4+t_5)\\
&\left.-g\ (t_3)+g\ (t_1+t_2+t_3)-g\ (t_1+t_2)\right]
\end{aligned}
\tag{A.26}
$$

$$
\begin{aligned}
&R_6(t_5,t_4,t_3,t_2,t_1)=F(t_1,t_1+t_2,t_1+t_2+t_3,t_1+t_2+t_3+t_4,t_1+t_2+t_3+t_4+t_5,0)\\
&=|\mu_{eg}|^6\exp\left[-i\omega_{eg}(t_1+t_3+t_5)\right]\exp\left[-g^*(t_2)+g^*(t_2+t_3)-g^*(t_2+t_3+t_4)\right.\\
&+g^*(t_2+t_3+t_4+t_5)-g\ (t_1)-g^*(t_3)+g^*(t_3+t_4)-g^*(t_3+t_4+t_5)\\
&+g\ (t_1+t_2)-g^*(t_4)+g^*(t_4+t_5)-g\ (t_1+t_2+t_3)-g^*(t_5)\\
&\left.+g\ (t_1+t_2+t_3+t_4)-g\ (t_1+t_2+t_3+t_4+t_5)\right]
\end{aligned}
\tag{A.27}
$$

$$
\begin{aligned}
&R_7(t_5,t_4,t_3,t_2,t_1)=F(\tau_1,t_1+t_2+t_3+t_4,t_1+t_2+t_3+t_4+t_5,t_1+t_2+t_3,t_1+t_2,\tau_6)\\
&=|\mu_{eg}|^6\exp\left[-i\omega_{eg}(-t_1-t_3+t_5)\right]\exp\left[-g^*(t_1+t_2+t_3+t_4)\right.\\
&+g^*(t_1+t_2+t_3+t_4+t_5)-g^*(t_1+t_2+t_3)+g^*(t_1+t_2)-g^*(t_1)-g^*(t_5)+g\ (t_4)\\
&-g\ (t_3+t_4)+g\ (t_2+t_3+t_4)-g\ (t_4+t_5)+g\ (t_3+t_4+t_5)-g\ (t_2+t_3+t_4+t_5)\\
&\left.-g\ (t_3)+g\ (t_2+t_3)-g\ (t_2)\right]
\end{aligned}
\tag{A.28}
$$

$$
\begin{aligned}
&R_8(t_5,t_4,t_3,t_2,t_1)=F(\tau_1,t_1+t_2,t_1+t_2+t_3,t_1+t_2+t_3+t_4,t_1+t_2+t_3+t_4+t_5,t_1)\\
&=|\mu_{eg}|^6\exp\left[-i\omega_{eg}(-t_1+t_3+t_5)\right]\exp\left[-g^*(t_1+t_2)+g^*(t_1+t_2+t_3)\right.\\
&-g^*(t_1+t_2+t_3+t_4)+g^*(t_1+t_2+t_3+t_4+t_5)-g^*(t_1)-g^*(t_3)+g^*(t_3+t_4)\\
&-g^*(t_3+t_4+t_5)+g\ (t_2)-g^*(t_4)+g^*(t_4+t_5)-g\ (t_2+t_3)-g^*(t_5)\\
&\left.+g\ (t_2+t_3+t_4)-g\ (t_2+t_3+t_4+t_5)\right]
\end{aligned}
\tag{A.29}
$$

$$
\begin{aligned}
&R_9(t_5,t_4,t_3,t_2,t_1)=F(t_1+t_2+t_3,t_1+t_2+t_3+t_4,t_1+t_2+t_3+t_4+t_5,t_1+t_2,t_1,0)\\
&=|\mu_{eg}|^6\exp\left[-i\omega_{eg}(t_1+t_3+t_5)\right]\exp\left[-g^*(t_4)+g^*(t_4+t_5)-g\ (t_3)\right.\\
&+g\ (t_2+t_3)-g\ (t_1+t_2+t_3)-g^*(t_5)+g\ (t_3+t_4)-g\ (t_2+t_3+t_4)\\
&+g\ (t_1+t_2+t_3+t_4)-g\ (t_3+t_4+t_5)+g\ (t_2+t_3+t_4+t_5)\\
&\left.-g\ (t_1+t_2+t_3+t_4+t_5)-g\ (t_2)+g\ (t_1+t_2)-g\ (t_1)\right]
\end{aligned}
\tag{A.30}
$$

$$
\begin{aligned}
&R_{10}\left(t_5,t_4,t_3,t_2,t_1\right)=F\left(t_1+t_2,t_1+t_2+t_3+t_4,t_1+t_2+t_3+t_4+t_5,t_1+t_2+t_3,t_1,0\right)\\
&=\left|\mu_{eg}\right|^6\exp\left[-i\omega_{eg}\left(t_1-t_3+t_5\right)\right]\exp\left[-g^*\left(t_3+t_4\right)+g^*\left(t_3+t_4+t_5\right)-g^*\left(t_3\right)\right.\\
&+g\ \left(t_2\right)-g\ \left(t_1+t_2\right)-g^*\left(t_5\right)+g\ \left(t_4\right)-g\ \left(t_2+t_3+t_4\right)+g\ \left(t_1+t_2+t_3+t_4\right)\\
&-g\ \left(t_4+t_5\right)+g\ \left(t_2+t_3+t_4+t_5\right)-g\ \left(t_1+t_2+t_3+t_4+t_5\right)-g\ \left(t_2+t_3\right)\\
&\left.+g\ \left(t_1+t_2+t_3\right)-g\ \left(t_1\right)\right]
\end{aligned}
\tag{A.31}
$$

$$
\begin{aligned}
&R_{11}\left(t_5,t_4,t_3,t_2,t_1\right)=F\left(0,t_1,t_1+t_2+t_3,t_1+t_2+t_3+t_4,t_1+t_2+t_3+t_4+t_5,t_1+t_2\right)\\
&=\left|\mu_{eg}\right|^6\exp\left[-i\omega_{eg}\left(-t_1+t_3+t_5\right)\right]\exp\left[-g^*\left(t_1\right)+g^*\left(t_1+t_2+t_3\right)\right.\\
&-g^*\left(t_1+t_2+t_3+t_4\right)+g^*\left(t_1+t_2+t_3+t_4+t_5\right)-g^*\left(t_1+t_2\right)-g^*\left(t_2+t_3\right)\\
&+g^*\left(t_2+t_3+t_4\right)-g^*\left(t_2+t_3+t_4+t_5\right)+g^*\left(t_2\right)-g^*\left(t_4\right)+g^*\left(t_4+t_5\right)-g\ \left(t_3\right)\\
&\left.-g^*\left(t_5\right)+g\ \left(t_3+t_4\right)-g\ \left(t_3+t_4+t_5\right)\right]
\end{aligned}
\tag{A.32}
$$

$$
\begin{aligned}
&R_{12}\left(t_5,t_4,t_3,t_2,t_1\right)=F\left(0,t_1,t_1+t_2,t_1+t_2+t_3+t_4,t_1+t_2+t_3+t_4+t_5,t_1+t_2+t_3\right)\\
&=\left|\mu_{eg}\right|^6\exp\left[-i\omega_{eg}\left(-t_1-t_3+t_5\right)\right]\exp\left[-g^*\left(t_1\right)+g^*\left(t_1+t_2\right)\right.\\
&-g^*\left(t_1+t_2+t_3+t_4\right)+g^*\left(t_1+t_2+t_3+t_4+t_5\right)-g^*\left(t_1+t_2+t_3\right)-g^*\left(t_2\right)\\
&+g^*\left(t_2+t_3+t_4\right)-g^*\left(t_2+t_3+t_4+t_5\right)+g^*\left(t_2+t_3\right)-g^*\left(t_3+t_4\right)\\
&\left.+g^*\left(t_3+t_4+t_5\right)-g^*\left(t_3\right)-g^*\left(t_5\right)+g\ \left(t_4\right)-g\ \left(t_4+t_5\right)\right]
\end{aligned}
\tag{A.33}
$$

$$
\begin{aligned}
&R_{13}\left(t_5,t_4,t_3,t_2,t_1\right)=F\left(t_1,t_1+t_2+t_3,t_1+t_2+t_3+t_4+t_5,t_1+t_2+t_3+t_4,t_1+t_2,0\right)\\
&=\left|\mu_{eg}\right|^6\exp\left[-i\omega_{eg}\left(t_1-t_3+t_5\right)\right]\exp\left[-g^*\left(t_2+t_3\right)+g^*\left(t_2+t_3+t_4+t_5\right)\right.\\
&-g^*\left(t_2+t_3+t_4\right)+g^*\left(t_2\right)-g\ \left(t_1\right)-g^*\left(t_4+t_5\right)+g^*\left(t_4\right)-g\left(t_3\right)\\
&+g\ \left(t_1+t_2+t_3\right)-g\ \left(t_5\right)+g\ \left(t_3+t_4+t_5\right)-g\ \left(t_1+t_2+t_3+t_4+t_5\right)\\
&\left.-g\ \left(t_3+t_4\right)+g\ \left(t_1+t_2+t_3+t_4\right)-g\ \left(t_1+t_2\right)\right]
\end{aligned}
\tag{A.34}
$$

$$
\begin{aligned}
&R_{14}\left(t_5,t_4,t_3,t_2,t_1\right)=F\left(t_1,t_1+t_2,t_1+t_2+t_3+t_4+t_5,t_1+t_2+t_3+t_4,t_1+t_2+t_3,0\right)\\
&=\left|\mu_{eg}\right|^6\exp\left[-i\omega_{eg}\left(t_1+t_3+t_5\right)\right]\exp\left[-g^*\left(t_2\right)+g^*\left(t_2+t_3+t_4+t_5\right)-g^*\left(t_2+t_3+t_4\right)\right.\\
&+g^*\left(t_2+t_3\right)-g\ \left(t_1\right)-g^*\left(t_3+t_4+t_5\right)+g^*\left(t_3+t_4\right)-g^*\left(t_3\right)+g\ \left(t_1+t_2\right)-g\ \left(t_5\right)\\
&\left.+g\ \left(t_4+t_5\right)-g\ \left(t_1+t_2+t_3+t_4+t_5\right)-g\ \left(t_4\right)+g\ \left(t_1+t_2+t_3+t_4\right)-g\ \left(t_1+t_2+t_3\right)\right]
\end{aligned}
\tag{A.35}
$$

$$
\begin{aligned}
&R_{15}\left(t_5,t_4,t_3,t_2,t_1\right)=F\left(0,t_1+t_2+t_3,t_1+t_2+t_3+t_4+t_5,t_1+t_2+t_3+t_4,t_1+t_2,t_1\right)\\
&=\left|\mu_{eg}\right|^6\exp\left[-i\omega_{eg}\left(-t_1-t_3+t_5\right)\right]\exp\left[-g^*\left(t_1+t_2+t_3\right)+g^*\left(t_1+t_2+t_3+t_4+t_5\right)\right.\\
&-g^*\left(t_1+t_2+t_3+t_4\right)+g^*\left(t_1+t_2\right)-g^*\left(t_1\right)-g^*\left(t_4+t_5\right)+g^*\left(t_4\right)-g\ \left(t_3\right)\\
&+g\ \left(t_2+t_3\right)-g\ \left(t_5\right)+g\ \left(t_3+t_4+t_5\right)-g\ \left(t_2+t_3+t_4+t_5\right)\\
&\left.-g\ \left(t_3+t_4\right)+g\ \left(t_2+t_3+t_4\right)-g\ \left(t_2\right)\right]
\end{aligned}
\tag{A.36}
$$

$$
\begin{aligned}
&R_{16}\left(t_5,t_4,t_3,t_2,t_1\right)=F\left(0,t_1+t_2,t_1+t_2+t_3+t_4+t_5,t_1+t_2+t_3+t_4,t_1+t_2+t_3,t_1\right)\\
&=\left|\mu_{eg}\right|^6\exp\left[-i\omega_{eg}\left(-t_1+t_3+t_5\right)\right]\exp\left[-g^*\left(t_1+t_2\right)+g^*\left(t_1+t_2+t_3+t_4+t_5\right)\right.\\
&-g^*\left(t_1+t_2+t_3+t_4\right)+g^*\left(t_1+t_2+t_3\right)-g^*\left(t_1\right)-g^*\left(t_3+t_4+t_5\right)+g^*\left(t_3+t_4\right)\\
&-g^*\left(t_3\right)+g\ \left(t_2\right)-g\ \left(t_5\right)+g\ \left(t_4+t_5\right)-g\ \left(t_2+t_3+t_4+t_5\right)\\
&\left.-g\ \left(t_4\right)+g\ \left(t_2+t_3+t_4\right)-g\ \left(t_2+t_3\right)\right]
\end{aligned}
\tag{A.37}
$$

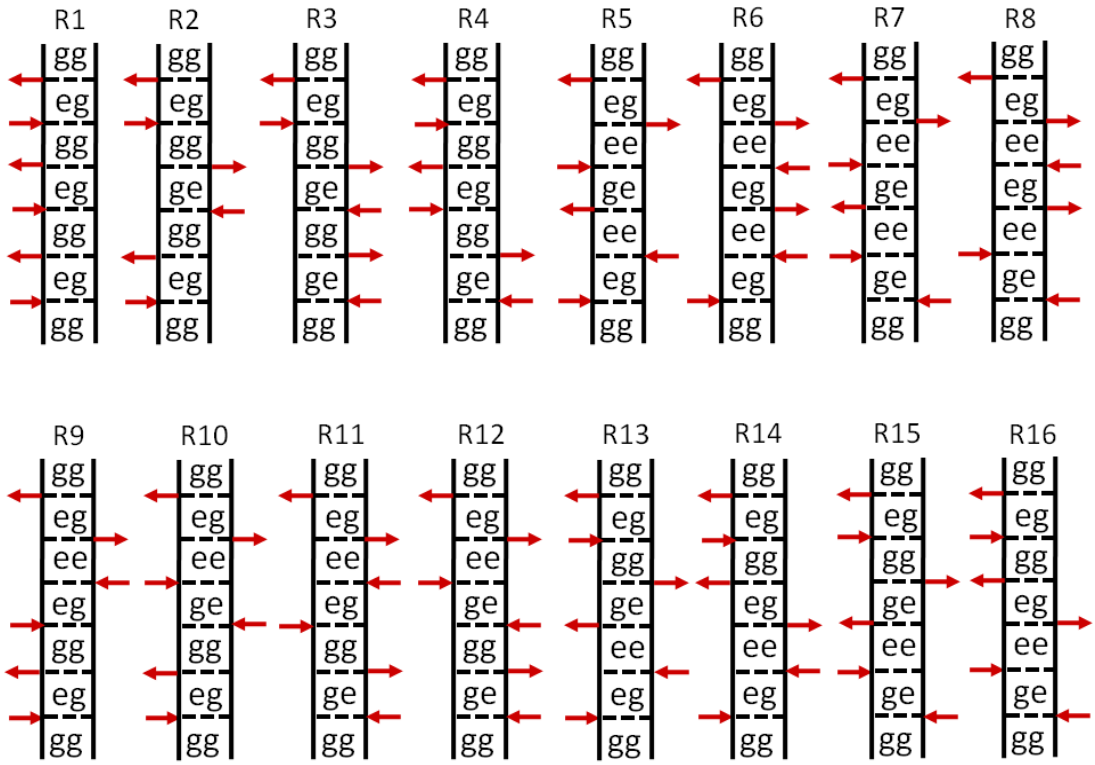

Figure A.4. Double-sided Feynman diagrams for all 16 terms in the fifth-order response function for a two-level system. Terms R_1-R_4 dominate the response in the present application to I_3^-.

A.6. Reproducibility of Real and Imaginary Signal Components

As discussed in Section 4.4.2, the real and imaginary parts of the signal are separated based on (i) dominance of vibrational oscillations in the real signal component and (ii) dominance of an undesired four-wave mixing signal at τ_1>0.1 ps in the imaginary signal component. Notably, the choice of which part of the signal is real and imaginary is arbitrary, because the two components can be reversed along with their associated information content (i.e. a shift in the signal phase of +/-π/2 is arbitrary). This section presents additional data sets (in addition to Figure 4.8) to demonstrate that the procedure used to separate the signal components is robust.

Figure A.5 compares the real and imaginary signal components for a different set of data than that shown in Chapter 4. A coherence spike dominates the imaginary part of the signal when all pulses are overlapped in the sample, whereas the vibrational recurrences are readily apparent in the real component. Two-dimensional Fourier transformation of the imaginary part of the signal yields a low-quality Raman spectrum, because the amplitudes of the vibrational recurrences are so small in this signal component. In all cases, Fourier transforms are carried out on the data at τ_1>0.1 ps to eliminate undesired effects associated with pulse overlap. Figures A.6 and A.7 present additional data sets in which these aspects of the signal persist.

Vibrational amplitude must dominate the absorptive signal component because the mode frequency is much smaller than the absorbance line width. Figure A.8 shows that this general insight is consistent with our model. For this reason, we suggest that the real signal component is primarily absorptive. The dominance of the coherence spike in the imaginary signal component is also consistent with this interpretation. Notably, this phasing procedure is

implemented only to reduce noise in the 2D spectrum. This phasing is not implemented with the goal of suppressing third-order cascades. Third-order cascades are 180º out-of-phase with the direct fifth-order signal under resonant conditions (not 90º as in off-resonant 2D Raman spectroscopy).

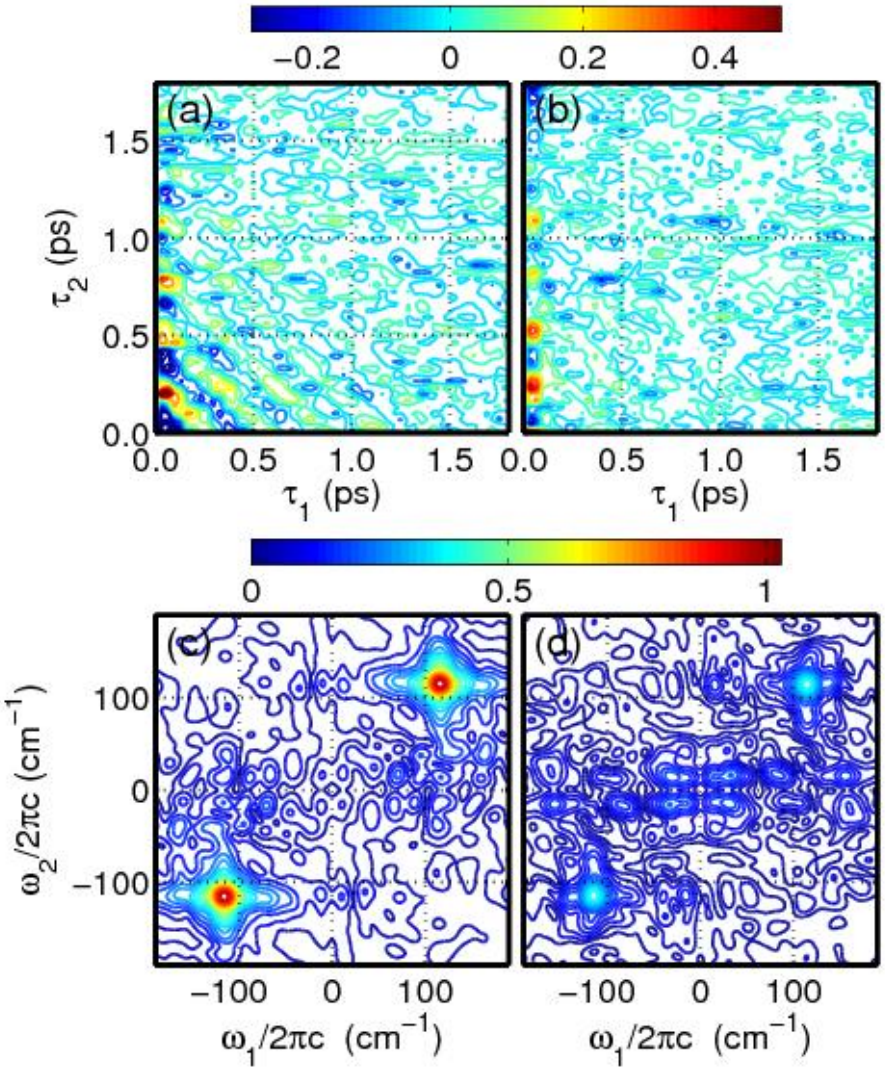

Figure A.5. (a) Real and (b) imaginary parts of signal field. Absorptive and dispersive responses dominate the real and imaginary signal components, respectively. Vibrational recurrences with large amplitudes are found in the real signal component shown in panel (a). Absolute values of Fourier transforms for (c) real and (d) imaginary signal components are shown below the respective time-domain data. The non-oscillatory part of the signal has been subtracted from panels (a) and (b), so that the Raman response can be more clearly visualized.

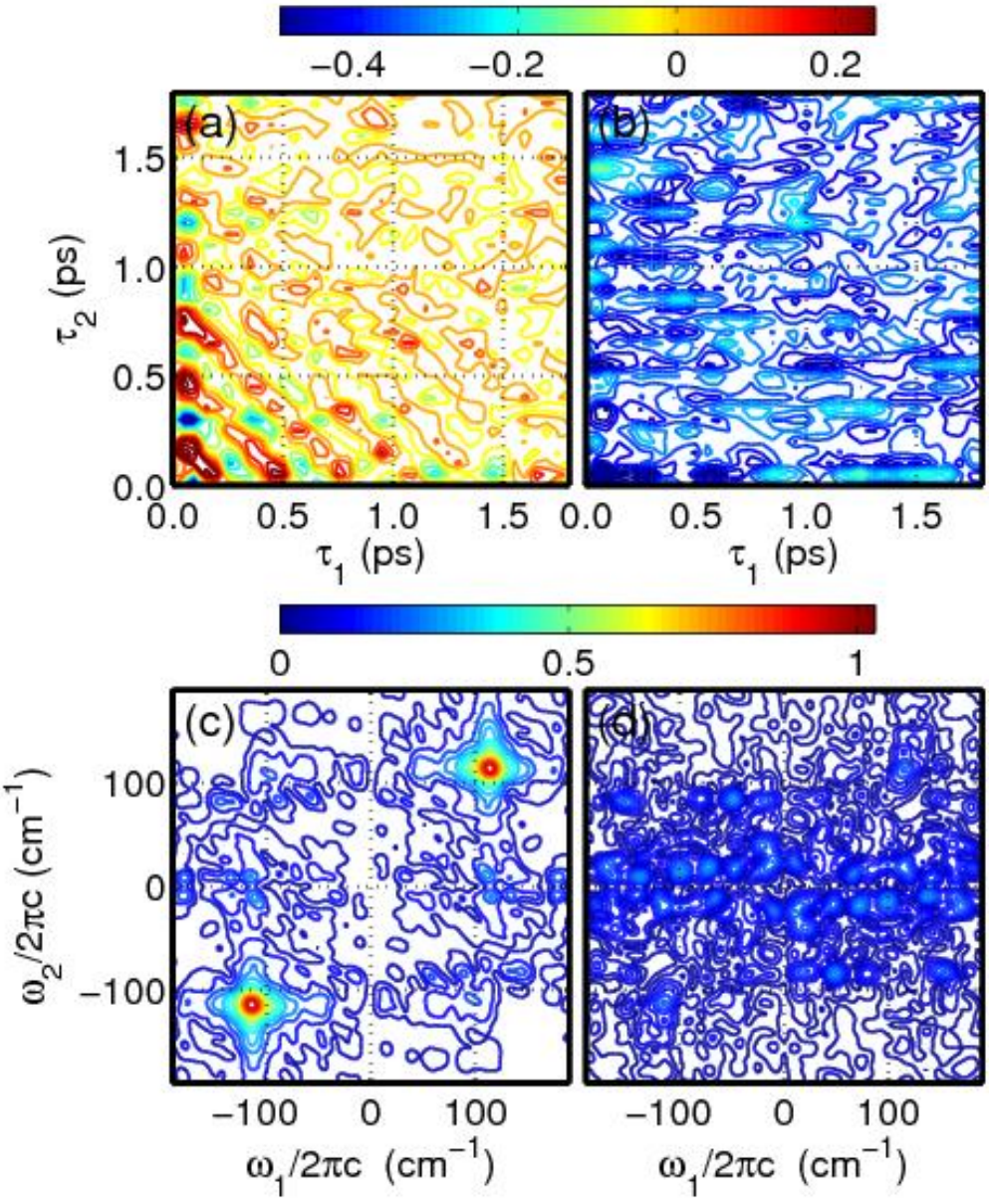

Figure A.6. Same as Figure A.5 for an experiment conducted on a different day.

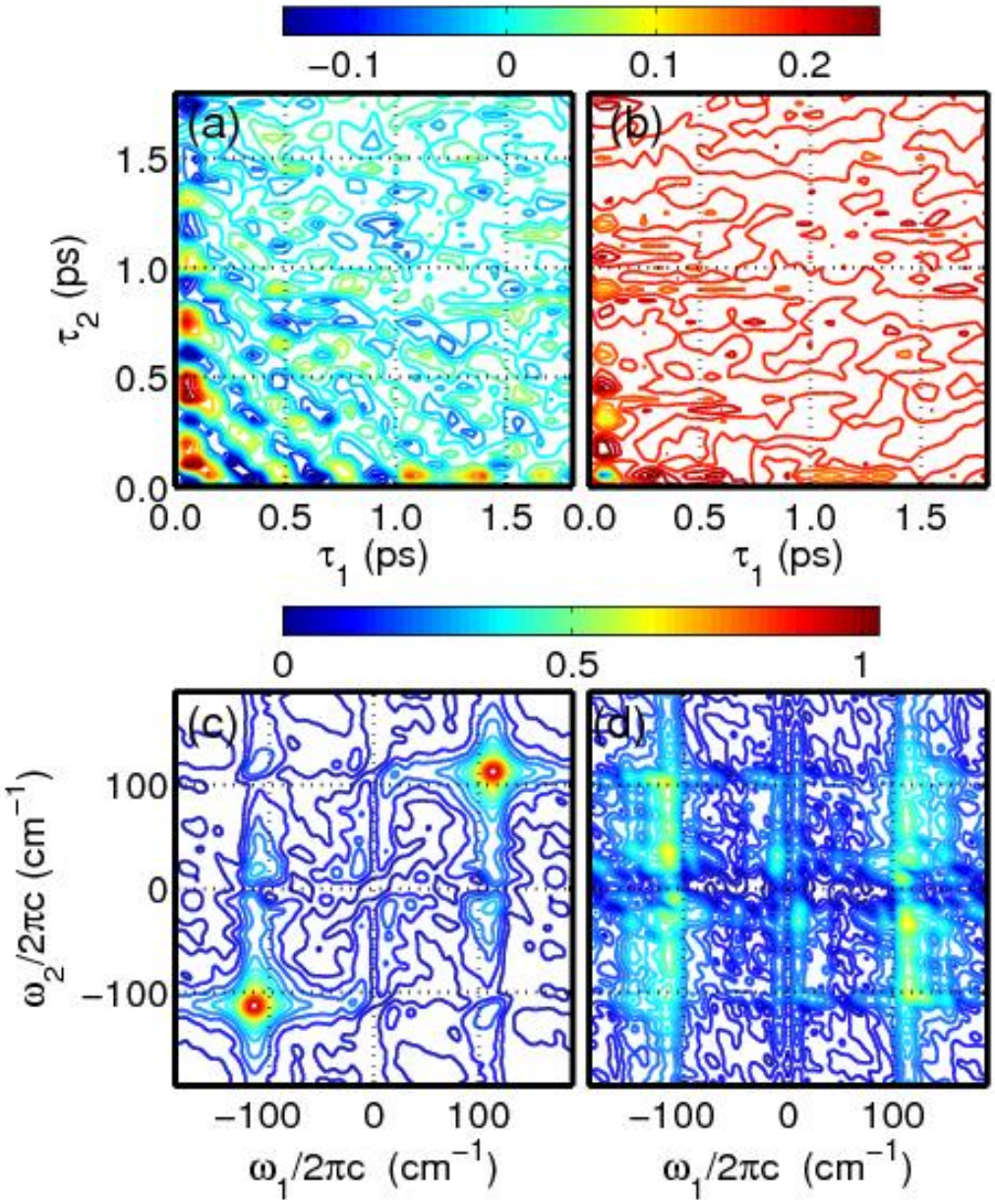

Figure A.7. Same as Figure A.5 for an experiment conducted on a different day.

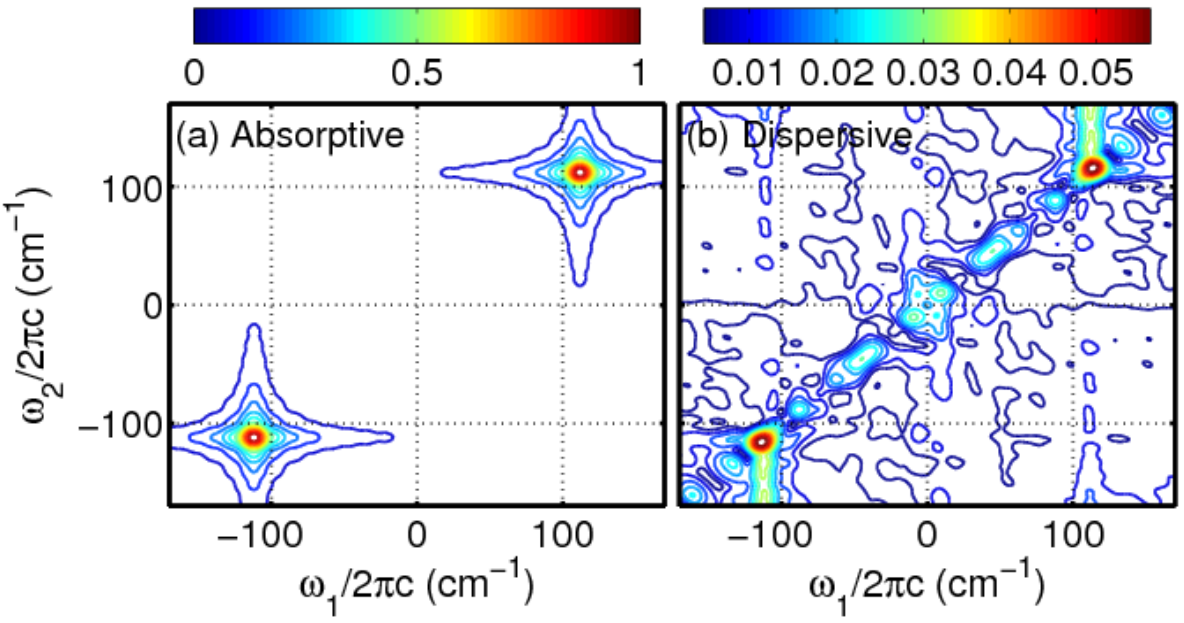

Figure A.8. Absolute values of 2D Raman spectra computed for (a) absorptive and (b) dispersive signal components using the parameters in Table 4.1 and the model described in Section 4.3 of Chapter 4. Vibrational amplitude is dominant in the absorptive signal component because the 112-cm^{-1} mode frequency is small compared to the 4000-cm^{-1} absorbance line width. These calculations suggest that the real signal component defined in Figures A.5-A.7 is primarily absorptive. The large (non-resonant) coherence spike observed in the imaginary signal component is also consistent with this interpretation of the signal phase.

A.7. Four-Wave Mixing Response in Region of Pulse Overlap

A four-wave mixing signal is radiated in the direction of the fifth-order signal when τ_1 < 100 fs and τ_2 < 100 fs (i.e. when the laser pulses are overlapped in the sample). This section discusses why these nonlinearities do not contribute at greater delay times. Figure A.9 defines the relevant BOXCARS geometry and presents diagrams associated with four sequences of field-matter interactions. Of course, additional diagrams that evolve in excited state populations in the interval between the second and third field-matter interactions may contribute at short delay times because it cannot be assumed that solvation, internal conversion, and/or photodissociation

shift the response to lower frequencies on this time scale. Such nonlinearities will also vanish when τ_1 > 100 fs and τ_2 > 100 fs, so this is not relevant to the present discussion.

The undesired four-wave mixing responses vanish at τ_1 < 100 fs and τ_2 < 100 fs because the pulses that induce the transient grating (first two field-matter interactions) are not members of the same pulse pair. The four-wave mixing signal contributes only when either pulse 2 or pulse 3 is overlapped with pulse 5 because electronic dephasing in the first time interval between field-matter interactions is much shorter than the pulse duration (the response of the medium can be regarded as quasi-instantaneous because of the broad absorbance line width). Straightforward experimental tests can be used to confirm this understanding of the four-wave mixing response. At τ_1=0 fs and τ_2 = 0 fs, we observe less than 5% change in the overall signal strength when pulses 1 and/or 4 are blocked. At τ_1>100 fs and τ_2 >100 fs, the signal completely vanishes when pulses 1 and/or 4 are blocked.

Contributions from the four-wave mixing response at τ_1<100 fs and τ_2 <100 fs can be eliminated by chopping either pulse 1 or pulse 4. Notably, several other successful fifth-order spectroscopies modulate incoming beams to remove direct third-order contributions (e.g. FSRS, RAPTORS, PORS).[9-12] An elegant aspect of Berg's laser beam geometry[13] is that the undesired four-wave mixing response contributes only in an uninteresting delay range, which is dominated by a "coherence spike".[14-16] We do not modulate the beams because we are not interested in the response during the region of pulse overlap.

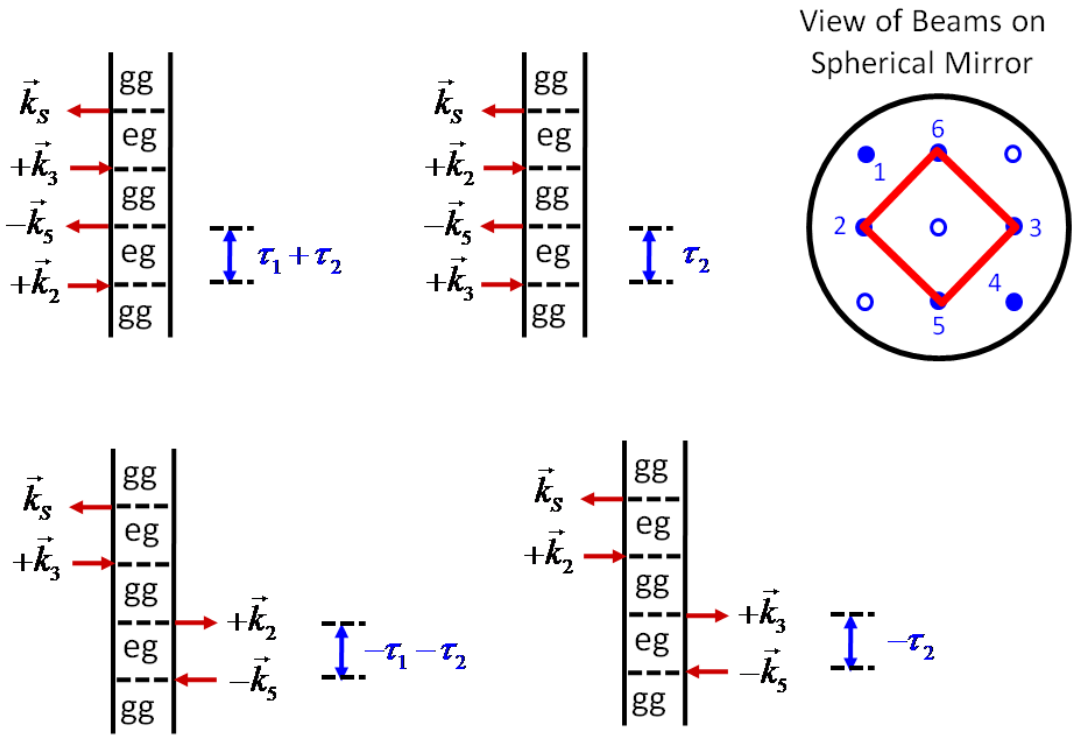

Figure A.9. Feynman diagrams associated with four field-matter interaction sequences that contribute to the four-wave mixing response when τ_1 < 100 fs and τ_2 < 100 fs. For each of the four Feynman diagrams, the transient grating induced by the first two field-matter interactions does not involve members of the same pulse pair.

A.8. Derivation of Response Functions Used to Compute Ratio in Cascaded Third-Order and Direct Fifth-Order Signal Strengths

A.8.1. Third- and Fifth-Order Response Functions

In this section, we present third and fifth order response functions that support an analytical approach to computing cascaded third-order and direct fifth-order signal fields. The Feynman diagrams in Figure A.10 include dummy indices for vibrational levels (m, n, k, l, u, and v) in addition to indices for the ground and excited electronic states (g and e). The indices (m, k, u) belong to the ground state, whereas (n, l, v) are associated with the excited

state. As explained in Section 4.3.4, it is assumed that ground state wavepacket motions dominate the response of I_3^- in the deep UV.[1,2] Response functions are written in the Condon approximation, where the integral over electronic and nuclear degrees of freedom in the transition dipole is separated into a product. For example, an interaction that couples vibrational level m on the ground electronic state and vibrational level n on the excited electronic state contributes the product $\mu_{eg}\langle n|m\rangle$ to the response function, where μ_{eg} is the electronic transition dipole and $\langle n|m\rangle$ is a vibrational overlap integral. With Lorentzian line shapes, the response functions corresponding to the fifth-order diagrams in the first row of Figure A.10 are written below.

$$R_1(t_5,t_4,t_3,t_2,t_1) = |\mu_{eg}|^6 \sum_{mnkluv} B_m \langle n|m\rangle\langle n|k\rangle\langle l|k\rangle\langle l|u\rangle\langle v|u\rangle\langle v|m\rangle I_{en,gm}(t_1) \times I_{gk,gm}(t_2) I_{el,gm}(t_3) I_{gu,gm}(t_4) I_{ev,gm}(t_5) \quad \text{(A.38)}$$

$$R_2(t_5,t_4,t_3,t_2,t_1) = |\mu_{eg}|^6 \sum_{mnkluv} B_m \langle n|m\rangle\langle n|k\rangle\langle l|m\rangle\langle l|u\rangle\langle v|k\rangle\langle v|u\rangle I_{en,gm}(t_1) \times I_{gk,gm}(t_2) I_{gk,el}(t_3) I_{gk,gu}(t_4) I_{ev,gu}(t_5) \quad \text{(A.39)}$$

$$R_3(t_5,t_4,t_3,t_2,t_1) = |\mu_{eg}|^6 \sum_{mnkluv} B_m \langle n|m\rangle\langle n|k\rangle\langle l|k\rangle\langle l|u\rangle\langle v|m\rangle\langle v|u\rangle I_{gm,en}(t_1) \times I_{gm,gk}(t_2) I_{gm,el}(t_3) I_{gm,gu}(t_4) I_{ev,gu}(t_5) \quad \text{(A.40)}$$

$$R_4(t_5,t_4,t_3,t_2,t_1) = |\mu_{eg}|^6 \sum_{mnkluv} B_m \langle n|m\rangle\langle n|k\rangle\langle l|m\rangle\langle l|u\rangle\langle v|u\rangle\langle v|k\rangle I_{gm,en}(t_1) \times I_{gm,gk}(t_2) I_{el,gk}(t_3) I_{gu,gk}(t_4) I_{ev,gk}(t_5) \quad \text{(A.41)}$$

The propagation functions corresponding to vibronic (in t_1, t_3, or t_5) and purely vibrational coherences (in t_2 or t_4) are respectively given by[17]

$$I_{em,gn}(t) = \theta(t)\exp\left[-i\omega_{eg}t - i\omega_{mn}t - \Gamma_{eg}t\right] \tag{A.42}$$

and

$$I_{gm,gn}(t) = \theta(t)\exp\left(-i\omega_{mn}t - \Gamma_{vib}t\right) \tag{A.43}$$

where $\theta(t)$ is a Heaviside step function. Equation A.42 assumes that electronic dephasing is fast compared to vibrational dephasing (i.e. $\Gamma_{eg} >> \Gamma_{vib}$).

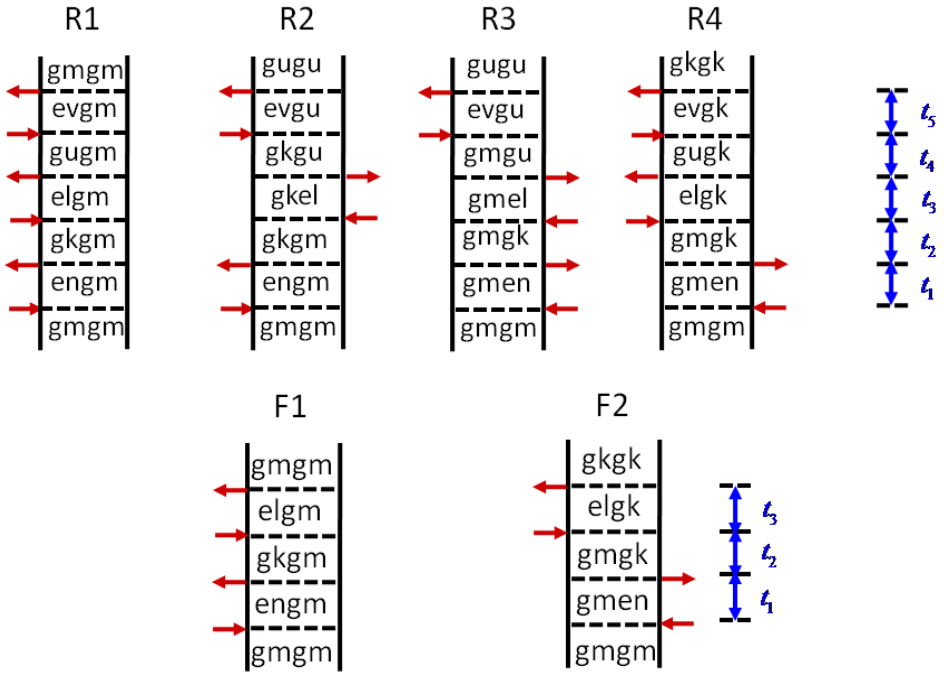

Figure A.10. Feynman diagrams associated with response functions written in a sum-over-states representation. The indices g and e refer to the ground and excited electronic states. Each term involves a sum over dummy indices associated with vibrational energy levels of the ground (m, k, u) and excited electronic states (n, l, v). Diagrams in the first and second rows correspond to ground state wavepacket motions at fifth and third-order in perturbation theory, respectively.

We convolute the response functions and electric fields to obtain the four components of the fifth-order polarization. For the R_1 term, the dominant component of the fifth-order polarization is given by

$$P_1^{(5)}(t) = N\left(\frac{i}{\hbar}\right)^5 \int_0^\infty dt_5 \int_0^\infty dt_4 \int_0^\infty dt_3 \int_0^\infty dt_2 \int_0^\infty dt_1 R_1^{(5)}(t_5,t_4,t_3,t_2,t_1) E_5(t-t_5) E_4^*(t-t_5-t_4) \times E_3(t-t_5-t_4-t_3) E_2^*(t-t_5-t_4-t_3-t_2) E_1(t-t_5-t_4-t_3-t_2-t_1) \quad \text{(A.44)}$$

where N is the number density. Integral evaluation is facilitated by recognizing that our experimental conditions are consistent with Mukamel's "snapshot limit" in which the pulse durations are long compared to electronic dephasing but short compared to the vibrational period. Under these conditions we write the electric field function as

$$E_j(t) = \xi_L \exp(-i\omega_L t) \quad \text{(A.45)}$$

where it is assumed that all five pulses (j =1-5) have the same (real) electric field amplitude, ξ_L, and carrier frequency, ω_L. The polarization component, $P_1^{(5)}(t)$, can now be rewritten as

$$P_1^{(5)}(t) = N\left(\frac{i\xi_L}{\hbar}\right)^5 \exp(-i\omega_L t) \int_0^\infty dt_5 \int_0^\infty dt_4 \int_0^\infty dt_3 \int_0^\infty dt_2 \int_0^\infty dt_1 R_1^{(5)}(t_5,t_4,t_3,t_2,t_1) \times \exp(i\omega_L t_1 + i\omega_L t_3 + i\omega_L t_5) . \quad \text{(A.46)}$$

The time intervals, t_2 and t_4, can be replaced with the experimentally controlled delay times, τ_1 and τ_2, when the pulse duration is short compared to the vibrational period.[17] We then have

$$P_1^{(5)}(\tau_1,\tau_2,t) = N\left(\frac{i\xi_L}{\hbar}\right)^5 \left|\mu_{eg}\right|^6 \exp(-i\omega_L t) \sum_{mnkluv} B_m \langle n|m\rangle\langle n|k\rangle\langle l|k\rangle\langle l|u\rangle\langle v|u\rangle\langle v|m\rangle$$
$$\times\int_0^\infty dt_5 \int_0^\infty dt_3 \int_0^\infty dt_1 I_{en,gm}(t_1) I_{gk,gm}(\tau_1) I_{el,gm}(t_3) I_{gu,gm}(\tau_2) \quad .(A.47)$$
$$\times I_{ev,gm}(t_5) \exp(i\omega_L t_1 + i\omega_L t_3 + i\omega_L t_5)$$

Evaluation of the three remaining integrals yields

$$P_1^{(5)}(\tau_1,\tau_2,t) = N\left(\frac{\xi_L}{\hbar}\right)^5 \left|\mu_{eg}\right|^6 \exp(-i\omega_L t) \sum_{mnkluv} B_m \langle n|m\rangle\langle n|k\rangle\langle l|k\rangle\langle l|u\rangle\langle v|u\rangle\langle v|m\rangle \quad (A.48)$$
$$\times I_{en,gm}(\omega_L) I_{gk,gm}(\tau_1) I_{el,gm}(\omega_L) I_{gu,gm}(\tau_2) I_{ev,gm}(\omega_L)$$

where the frequency domain line shape corresponding to the vibronic coherences is given by[17]

$$I_{en,gm}(\omega_L) = \frac{1}{\omega_L - \omega_{eg} - \omega_{nm} + i\Gamma_{eg}} . \quad (A.49)$$

Under the same approximations, expressions for the three remaining fifth-order polarization components are written as

$$P_2^{(5)}(\tau_1,\tau_2,t) = N\left(\frac{\xi_L}{\hbar}\right)^5 \left|\mu_{eg}\right|^6 \exp(-i\omega_L t) \sum_{mnkluv} B_m \langle n|m\rangle\langle n|k\rangle\langle l|m\rangle\langle l|u\rangle\langle v|k\rangle\langle v|u\rangle \quad , (A.50)$$
$$\times I_{en,gm}(\omega_L) I_{gk,gm}(\tau_1) I_{gk,el}(-\omega_L) I_{gk,gu}(\tau_2) I_{ev,gu}(\omega_L)$$

$$P_3^{(5)}(\tau_1,\tau_2,t) = N\left(\frac{\xi_L}{\hbar}\right)^5 \left|\mu_{eg}\right|^6 \exp(-i\omega_L t) \sum_{mnkluv} B_m \langle n|m\rangle\langle n|k\rangle\langle l|k\rangle\langle l|u\rangle\langle v|m\rangle\langle v|u\rangle \quad , (A.51)$$
$$\times I_{gm,en}(-\omega_L) I_{gm,gk}(\tau_1) I_{gm,el}(-\omega_L) I_{gm,gu}(\tau_2) I_{ev,gu}(\omega_L)$$

and

$$P_4^{(5)}(\tau_1,\tau_2,t) = N\left(\frac{\xi_L}{\hbar}\right)^5 \left|\mu_{eg}\right|^6 \exp(-i\omega_L t) \sum_{mnkluv} B_m \langle n|m\rangle\langle n|k\rangle\langle l|m\rangle\langle l|u\rangle\langle v|u\rangle\langle v|k\rangle \times I_{gm,en}(-\omega_L) I_{gm,gk}(\tau_1) I_{el,gk}(\omega_L) I_{gu,gk}(\tau_2) I_{ev,gk}(\omega_L) \quad \text{(A.52)}$$

The third-order response functions needed to compute the cascaded nonlinearities can be obtained in a similar way. Third-order diagrams associated with ground state wavepacket motions are presented in the second row of Figure A.10. Response functions corresponding to these diagrams can be written as

$$F_1(t_3,t_2,t_1) = \left|\mu_{eg}\right|^4 \sum_{mnkl} B_m \langle n|m\rangle\langle n|k\rangle\langle l|k\rangle\langle l|m\rangle I_{en,gm}(t_1) I_{gk,gm}(t_2) I_{el,gm}(t_3) \quad \text{(A.53)}$$

and

$$F_2(t_3,t_2,t_1) = \left|\mu_{eg}\right|^4 \sum_{mnkl} B_m \langle n|m\rangle\langle n|k\rangle\langle l|m\rangle\langle l|k\rangle I_{gm,en}(t_1) I_{gm,gk}(t_2) I_{el,gk}(t_3). \quad \text{(A.54)}$$

The polarization component associated with term, $F_1(t_3,t_2,t_1)$, is given by

$$P_1^{(3)}(t) = N\left(\frac{i}{\hbar}\right)^3 \int_0^\infty dt_3 \int_0^\infty dt_2 \int_0^\infty dt_1 F_1(t_3,t_2,t_1) E_3(t-t_3) E_2^*(t-t_3-t_2) E_1(t-t_3-t_2-t_1). \quad \text{(A.55)}$$

Substitution of Equations A.45 and A.53 in Equation A.55 yields

$$P_1^{(3)}(\tau_1,t) = N\left(\frac{i\xi_L}{\hbar}\right)^3 \left|\mu_{eg}\right|^4 \exp(-i\omega_L t) \sum_{mnkl} B_m \langle n|m\rangle\langle n|k\rangle\langle l|k\rangle\langle l|m\rangle \times \int_0^\infty dt_3 \int_0^\infty dt_1 I_{en,gm}(t_1) I_{gk,gm}(\tau_1) I_{el,gm}(t_3) \exp(i\omega_L t_1 + i\omega_L t_3 + i\omega_L t_5) \quad \text{(A.56)}$$

where (as above) the integral over t_2 has been eliminated under the approximation that the pulse duration is short compared to the vibrational period.[17] Equation A.56 can be rewritten as

$$P_1^{(3)}(\tau_1,t)=iN\left(\frac{\xi_L}{\hbar}\right)^3\left|\mu_{eg}\right|^4\exp\left(-i\omega_L t\right)\sum_{mnkl}B_m\left\langle n\middle|m\right\rangle\left\langle n\middle|k\right\rangle\left\langle l\middle|k\right\rangle\left\langle l\middle|m\right\rangle \\ \times I_{en,gm}\left(\omega_L\right)I_{gk,gm}\left(\tau_1\right)I_{el,gm}\left(\omega_L\right) \tag{A.57}$$

Using the same procedure, the polarization component associated with $F_2\left(t_3,t_2,t_1\right)$ is given by

$$P_2^{(3)}(\tau_1,t)=iN\left(\frac{\xi_L}{\hbar}\right)^3\left|\mu_{eg}\right|^4\exp\left(-i\omega_L t\right)\sum_{mnkl}B_m\left\langle n\middle|m\right\rangle\left\langle n\middle|k\right\rangle\left\langle l\middle|m\right\rangle\left\langle l\middle|k\right\rangle \\ \times I_{gm,en}\left(-\omega_L\right)I_{gm,gk}\left(\tau_1\right)I_{el,gk}\left(\omega_L\right) \tag{A.58}$$

Note that the factor of i appears in $P_1^{(3)}(\tau_1,t)$ and $P_2^{(3)}(\tau_1,t)$ because

$$I_{en,gm}\left(\omega_L\right)=-i\int_0^\infty dtI_{en,gm}\left(t\right)\exp\left(i\omega t\right). \tag{A.59}$$

A.8.2. Third and Fifth-Order Auxiliary Response Functions

Formulas for the signal strengths can be made more transparent if auxiliary response functions are employed. The general auxiliary response function for the j-th fifth-order polarization component is written as

$$\phi_j^{(5)}\left(\tau_1,\tau_2,t\right)=\frac{P_j^{(5)}\left(\tau_1,\tau_2,t\right)}{N\exp\left(-i\omega_L t\right)\left|\mu_{eg}\right|^6\left(\frac{\xi_L}{\hbar}\right)^5} \tag{A.60}$$

For completeness, we write the four auxiliary response functions explicitly.

$$\phi_1^{(5)}\left(\tau_1,\tau_2\right)=\sum_{mnkluv}B_m\left\langle n\middle|m\right\rangle\left\langle n\middle|k\right\rangle\left\langle l\middle|k\right\rangle\left\langle l\middle|u\right\rangle\left\langle v\middle|u\right\rangle\left\langle v\middle|m\right\rangle I_{en,gm}\left(\omega_L\right) \\ \times I_{gk,gm}\left(\tau_1\right)I_{el,gm}\left(\omega_L\right)I_{gu,gm}\left(\tau_2\right)I_{ev,gm}\left(\omega_L\right) \tag{A.61}$$

$$\phi_2^{(5)}(\tau_1,\tau_2) = \sum_{mnkluv} B_m \langle n|m\rangle\langle n|k\rangle\langle l|m\rangle\langle l|u\rangle\langle v|k\rangle\langle v|u\rangle I_{en,gm}(\omega_L) \times I_{gk,gm}(\tau_1) I_{gk,el}(-\omega_L) I_{gk,gu}(\tau_2) I_{ev,gu}(\omega_L) \tag{A.62}$$

$$\phi_3^{(5)}(\tau_1,\tau_2) = \sum_{mnkluv} B_m \langle n|m\rangle\langle n|k\rangle\langle l|k\rangle\langle l|u\rangle\langle v|m\rangle\langle v|u\rangle I_{gm,en}(-\omega_L) \times I_{gm,gk}(\tau_1) I_{gm,el}(-\omega_L) I_{gm,gu}(\tau_2) I_{ev,gu}(\omega_L) \tag{A.63}$$

$$\phi_4^{(5)}(\tau_1,\tau_2) = \sum_{mnkluv} B_m \langle n|m\rangle\langle n|k\rangle\langle l|m\rangle\langle l|u\rangle\langle v|u\rangle\langle v|k\rangle I_{gm,en}(-\omega_L) \times I_{gm,gk}(\tau_1) I_{el,gk}(\omega_L) I_{gu,gk}(\tau_2) I_{ev,gk}(\omega_L) \tag{A.64}$$

Similarly, the auxiliary response functions associated with the third-order polarization components are given by

$$\phi_j^{(3)}(\tau) = \frac{P_j^{(3)}(\tau,t)}{N\exp(-i\omega_L t)|\mu_{eg}|^4\left(\frac{\xi_L}{\hbar}\right)^3}. \tag{A.65}$$

For completeness, we write the third-order auxiliary response functions explicitly as

$$\phi_1^{(3)}(\tau) = i\sum_{mnkl} B_m \langle n|m\rangle\langle n|k\rangle\langle l|k\rangle\langle l|m\rangle I_{en,gm}(\omega_L) I_{gk,gm}(\tau) I_{el,gm}(\omega_L) \tag{A.66}$$

and

$$\phi_2^{(3)}(\tau) = i\sum_{mnkl} B_m \langle n|m\rangle\langle n|k\rangle\langle l|m\rangle\langle l|k\rangle I_{gm,en}(-\omega_L) I_{gm,gk}(\tau) I_{el,gk}(\omega_L). \tag{A.67}$$

A.8.3. Computing Relative Cascaded and Direct Signal Magnitudes

In this section we derive Equation 4.22 in Chapter 4. The fifth-order signal field is given by

$$E^{(5)}(t) = \frac{i2\pi l\omega_t}{n(\omega_t)c} P^{(5)}(t) \mathrm{f}_{direct}\left(\Delta k_{direct} l\right) \tag{A.68}$$

which simply adds the phase mismatch function, $\mathrm{f}_j\left(\Delta k_j l\right) = \mathrm{sinc}\left(\Delta k_j l/2\right)$, to Equation 4.6 in Chapter 4. We consider only the phase matching efficiency in this work and do not treat the phase accumulated in the medium because phase is not leveraged to achieve contrast between the direct fifth-order signal and the third-order cascade. We next consider fields radiated by the two types of cascades. Figures A.11 and A.12 present Feynman diagrams for the two classes of sequential cascades (i.e. total of 4 types of diagrams in each class). The field radiated by the sequential cascades can be written as

$$\begin{aligned} E_{seq}(\tau_1,\tau_2,t) = \left(\frac{i2\pi l\omega_t}{n(\omega_t)c}\right)^2 \sum_{\alpha=1}^{2}\sum_{\beta=1}^{2}\Big\{ & \exp(i\omega_L t) P_\alpha^{(3)}(\tau_1,t) \mathrm{f}_{seq1}\left(\Delta k_{seq1} l\right) \\ & + \left[\exp(i\omega_L t) P_\alpha^{(3)}(\tau_1,t)\right]^* \mathrm{f}_{seq2}\left(\Delta k_{seq2} l\right)\Big\} P_\beta^{(3)}(\tau_2,t) \end{aligned} \tag{A.69}$$

where the prefactor is squared to account for the fields radiated by molecules A and B (see Figures A.11 and A.12). Complex exponential functions, $\exp(i\omega_L t)$, appear in Equation A.69, because the field is radiated near ω_L (not at the second harmonic). Similarly, Figures A.13 and A14 present Feynman diagrams for the two classes of parallel cascades (i.e. total of 4 types of diagrams for each class). The total field radiated by parallel cascades can be written as

$$\begin{aligned} E_{par}(\tau_1,\tau_2,t) = \left(\frac{i2\pi l\omega_t}{n(\omega_t)c}\right)^2 & \exp(i\omega_L t) \sum_{\alpha=1}^{2}\sum_{\beta=1}^{2} P_\alpha^{(3)}(\tau_1+\tau_2,t) P_\beta^{(3)}(\tau_2,t) \\ & \times\left[\mathrm{f}_{par1}\left(\Delta k_{par1} l\right) + \mathrm{f}_{par2}\left(\Delta k_{par2} l\right)\right] \end{aligned} \tag{A.70}$$

where the prefactor is again squared to account for the fields radiated by molecules A and B (see Figures A.13 and A.14). Finally, the total field radiated by cascaded nonlinearities is given by the sum

$$E_{cas}(t) = E_{seq}(t) + E_{par}(t). \tag{A.71}$$

The ratio between $E_{cas}(t)$ and $E^{(5)}(t)$ is the key quantity governing the feasibility of the present experiment.

$$\frac{E_{cas}(t)}{E^{(5)}(t)} = \left(\frac{7}{25}\right)\frac{E_{par}(\tau_1,\tau_2,t) + E_{seq}(\tau_1,\tau_2,t)}{E^{(5)}(t)} \tag{A.72}$$

Here the factor of 7/25 comes from the orientational average for isotropic systems with all-parallel electric field polarizations.[18] Substitution of the auxiliary response functions into Equation A.72 yields

$$\frac{E_{cas}(t)}{E^{(5)}(t)} = \left(\frac{7}{25}\right)\frac{2\pi l N \omega_t \left|\mu_{eg}\right|^2}{n(\omega_t)\hbar c}\frac{\eta^{(3)}_{seq}(\tau_1,\tau_2) + \eta^{(5)}_{seq}(\tau_1,\tau_2)}{\eta^{(5)}_{direct}(\tau_1,\tau_2)}. \tag{A.73}$$

As in the work of Zanni and co-workers,[18] multiplication of Equation A.73 by Coulomb's constant produces the unitless ratio

$$\frac{E_{cas}(t)}{E^{(5)}(t)} = \left(\frac{7}{25}\right)\frac{l N \omega_t \left|\mu_{eg}\right|^2}{2n(\omega_t)\varepsilon_0\hbar c}\frac{\eta^{(3)}_{seq}(\tau_1,\tau_2) + \eta^{(3)}_{par}(\tau_1,\tau_2)}{\eta^{(5)}_{direct}(\tau_1,\tau_2)} \tag{A.74}$$

where

$$\eta^{(3)}_{seq}(\tau_1,\tau_2) = \sum_{\alpha=1}^{2}\sum_{\beta=1}^{2}\left\{\phi^{(3)}_{\alpha}(\tau_1,t)\mathrm{f}_{seq1}\left(\Delta k_{seq1} l\right) + \left[\phi^{(3)}_{\alpha}(\tau_1,t)\right]^{*}\mathrm{f}_{seq2}\left(\Delta k_{seq2} l\right)\right\}\phi^{(3)}_{\beta}(\tau_2,t), \tag{A.75}$$

$$\eta_{par}^{(3)}(\tau_1,\tau_2)=\sum_{\alpha=1}^{2}\sum_{\beta=1}^{2}\left\{\phi_{\alpha}^{(3)}(\tau_2,t)\mathrm{f}_{par1}\left(\Delta k_{par1}l\right)+\phi_{\alpha}^{(3)}(\tau_2,t)\mathrm{f}_{par2}\left(\Delta k_{par2}l\right)\right\}\phi_{\beta}^{(3)}(\tau_1+\tau_2,t)\Big\},\quad\text{(A.76)}$$

and

$$\eta_{direct}^{(5)}(\tau_1,\tau_2)=\mathrm{f}_{direct}\left(\Delta k_{direct}l\right)\sum_{\alpha=1}^{4}\phi_{\alpha}^{(5)}\left(\tau_1,\tau_2\right).\qquad\text{(A.77)}$$

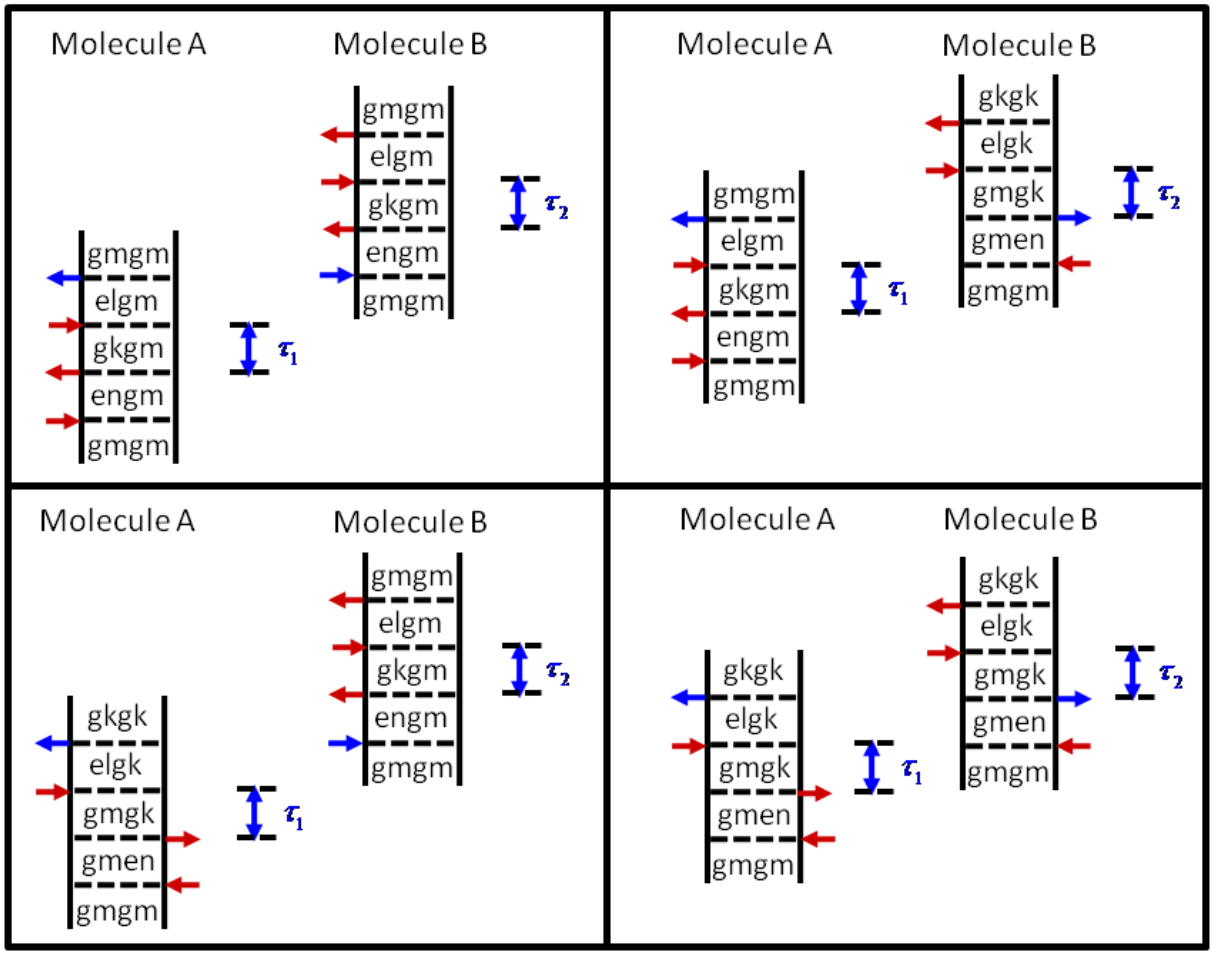

Figure A.11. Summary of four sequential cascades with the intermediate phase matching condition $k_1-k_2+k_3$ on molecule A. The field radiated by molecule A (blue arrow) induces one of the first two field-matter interactions on molecule B (blue arrow). Feynman diagrams for molecules A and B involve sums over independent dummy indices for vibrational levels (m, n, k, l).

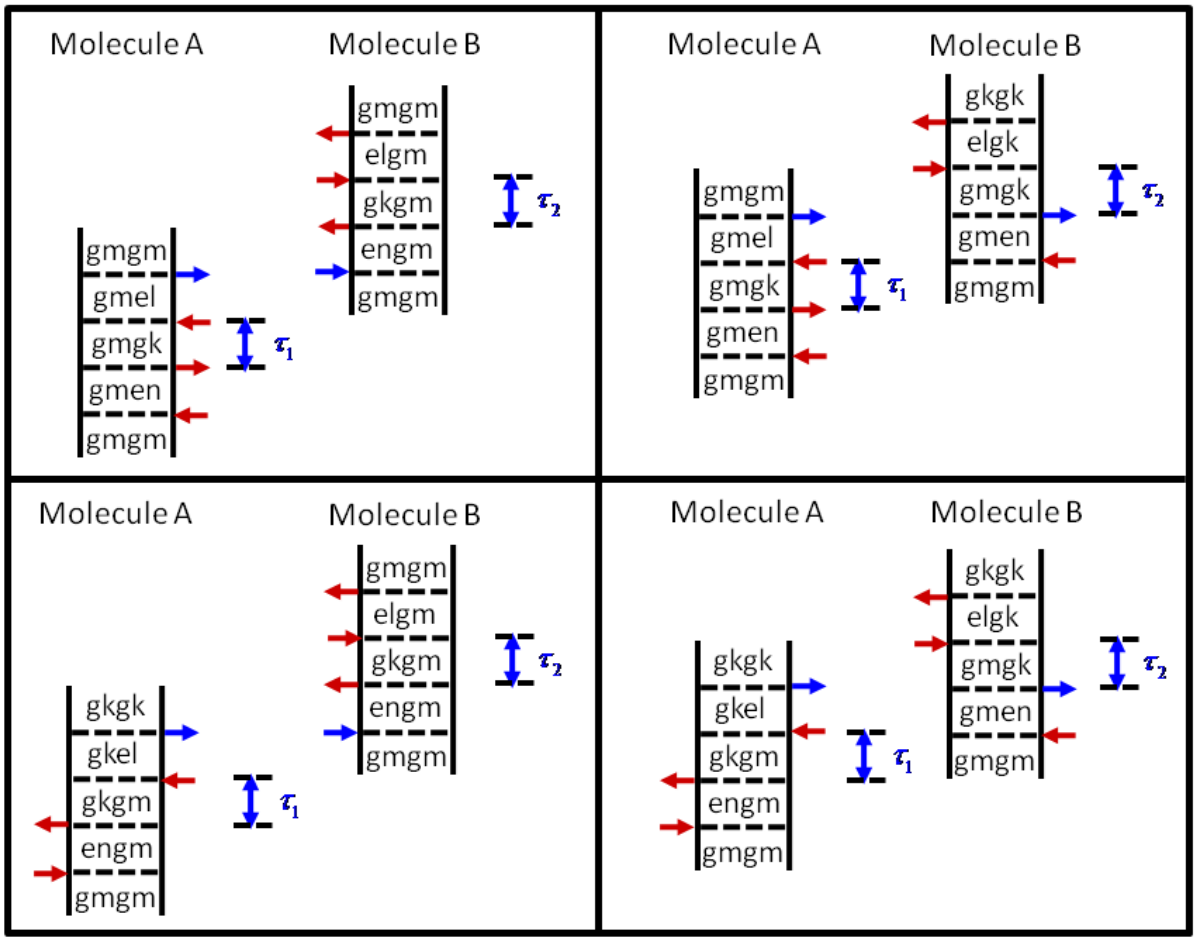

Figure A.12. Summary of four sequential cascades with the intermediate phase matching condition, $-k_1+k_2+k_4$. The field radiated by molecule A (blue arrow) induces one of the first two field-matter interactions on molecule B (blue arrow). Changing the signs of the wavevectors for pulses 1, 2, and 4 translates into complex conjugation of the term in the response function associated with molecule A. Feynman diagrams for molecules A and B involve sums over independent dummy indices for vibrational levels (m, n, k, l).

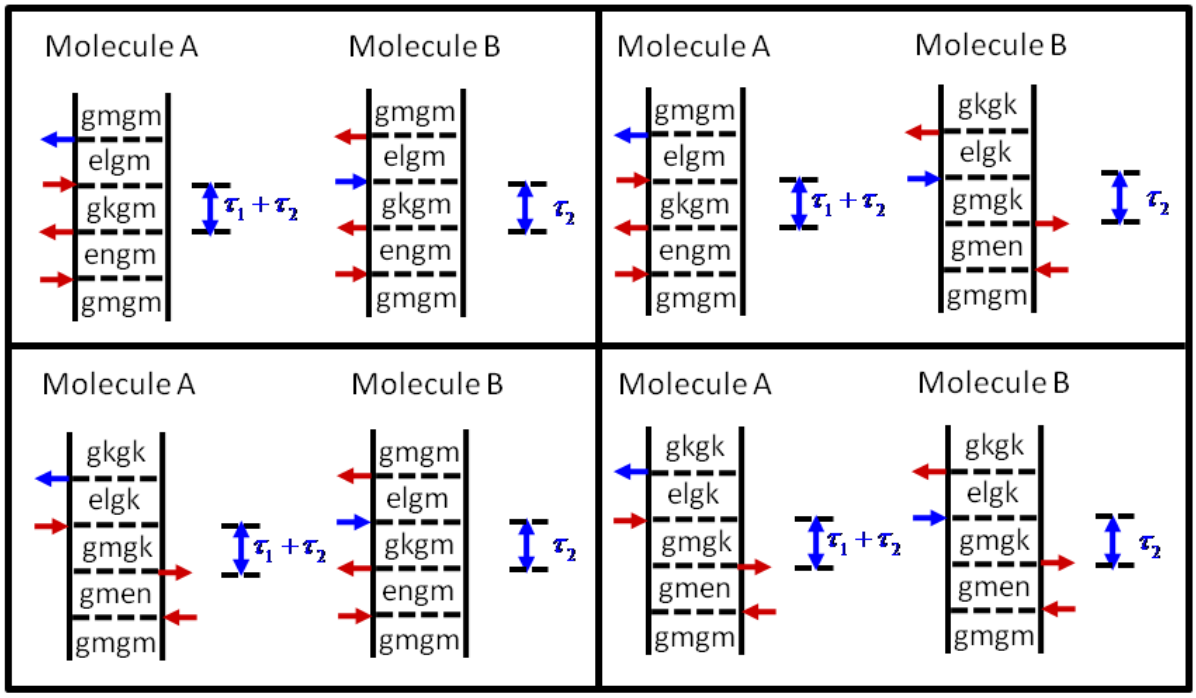

Figure A.13. Summary of parallel cascades with the intermediate phase matching condition $k_1 - k_2 + k_5$ on molecule A. The field radiated by molecule A (blue arrow) induces the third field-matter interaction on molecule B (blue arrow). Feynman diagrams for molecules A and B involve sums over independent dummy indices for vibrational levels (m, n, k, l).

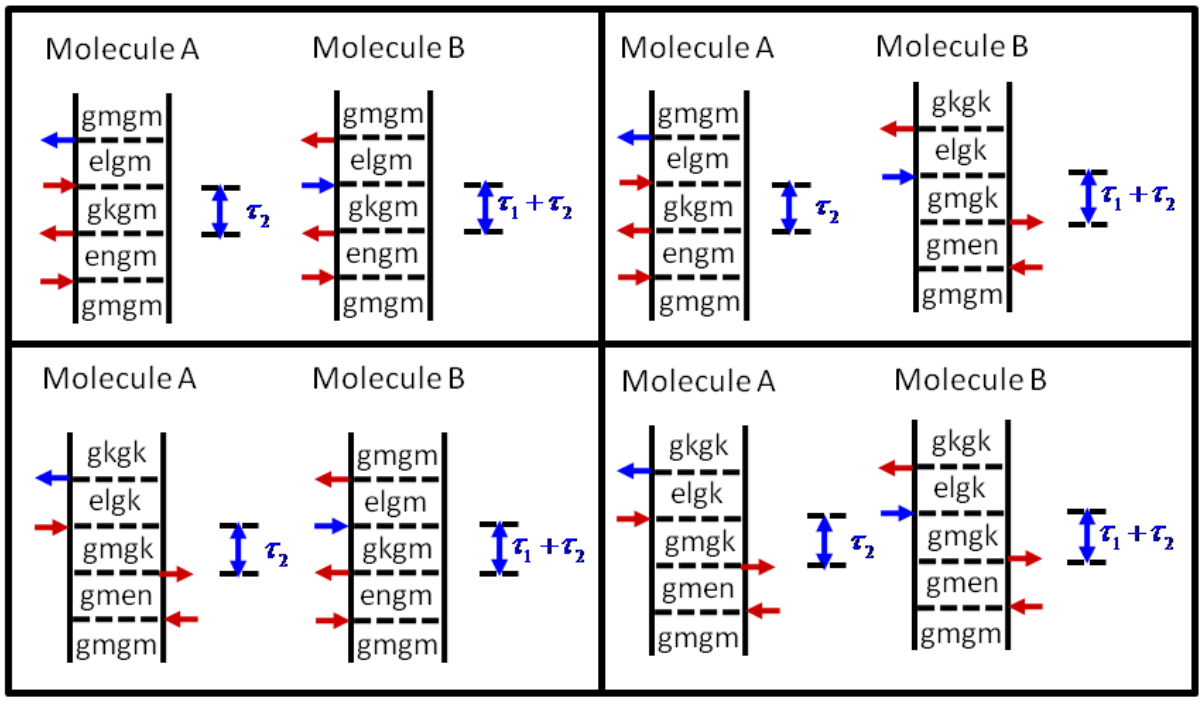

Figure A.14. Summary of parallel cascades with the intermediate phase matching condition $k_3 - k_4 + k_5$ on molecule A. The field radiated by molecule A (blue arrow) induces the third field-matter interaction on molecule B (blue arrow). Feynman diagrams for molecules A and B involve sums over independent dummy indices for vibrational levels (m, n, k, l).

A.8.4. Magnitude of Prefactor

This section explicitly outlines the calculation of the prefactor for Equation 4.22 in Chapter 4. For clarity, we show all unit conversion explicitly and break the calculation into several steps. First, we compute the product of experimentally controlled parameters in the numerator and divide by the speed of light to simplify the units.

$$\frac{lN\omega_t}{n(\omega_t)c} = \frac{\left(1\times10^{-3}\,\text{mole}\cdot\text{L}^{-1}\right)\left(10^{3}\,\text{L}\cdot\text{m}^{-3}\right)\left(6.022\times10^{23}\,\text{mole}^{-1}\right)\left(0.3\,\text{mm}\right)\left(7.014\,\text{cycles}\cdot\text{fs}^{-1}\right)}{1.4\cdot\left(2.998\times10^{-4}\,\text{mm}\cdot\text{fs}^{-1}\right)} \quad \text{(A.78)}$$
$$= 3.0153\times10^{27}\,\text{m}^{-3}$$

The product of constants in the denominator is

$$\frac{\left|\mu_{eg}\right|^2}{2\varepsilon_0\hbar} = \frac{\left|\mu_{eg}\right|^2}{2\left(8.8542\times10^{-12}\,\mathrm{s^4\cdot A^2\cdot m^{-3}\cdot kg^{-1}}\right)\left(1.0546\times10^{-34}\,\mathrm{kg\cdot m^2\cdot s^{-1}}\right)} = \frac{\left|\mu_{eg}\right|^2}{\left(9.3374\times10^{-46}\,\mathrm{s^3\cdot A^2\cdot m^{-1}}\right)} \quad \text{(A.79)}$$

For convenience, we use units of Debye for the transition dipole

$$\frac{\left|\mu_{eg}\right|^2}{2\varepsilon_0\hbar} = \frac{\left(8.8\,\mathrm{D}\right)^2}{2\left(9.3374\times10^{-46}\,\mathrm{s^3\cdot A^2\cdot m^{-1}}\right)}\left(\frac{3.3356\times10^{-30}\,\mathrm{s\cdot A\cdot m}}{1\,\mathrm{D}}\right)^2 = 4.6139\times10^{-13}\ \mathrm{m^3\cdot s^{-1}} \quad \text{(A.80)}$$

where the 8.8-D magnitude of the transition dipole is taken from the fit of Johnson and Myers.[19]

Finally, we combine all parts of the prefactor to obtain

$$\left(\frac{7}{25}\right)\left(\frac{lN\omega_t}{n(\omega_t)c}\right)\left(\frac{\left|\mu_{eg}\right|^2}{2\varepsilon_0\hbar}\right) = \left(\frac{7}{25}\right)\left(3.0153\times10^{27}\ \mathrm{m^{-3}}\right)\left(4.6139\times10^{-13}\ \mathrm{m^3\cdot s^{-1}}\right) = \left(3.8954\times10^{14}\ \mathrm{s^{-1}}\right) \quad \text{(A.81)}$$

A.9. 2D Spectra for Sequential Cascades Simulated Using Measured Third-Order Signals

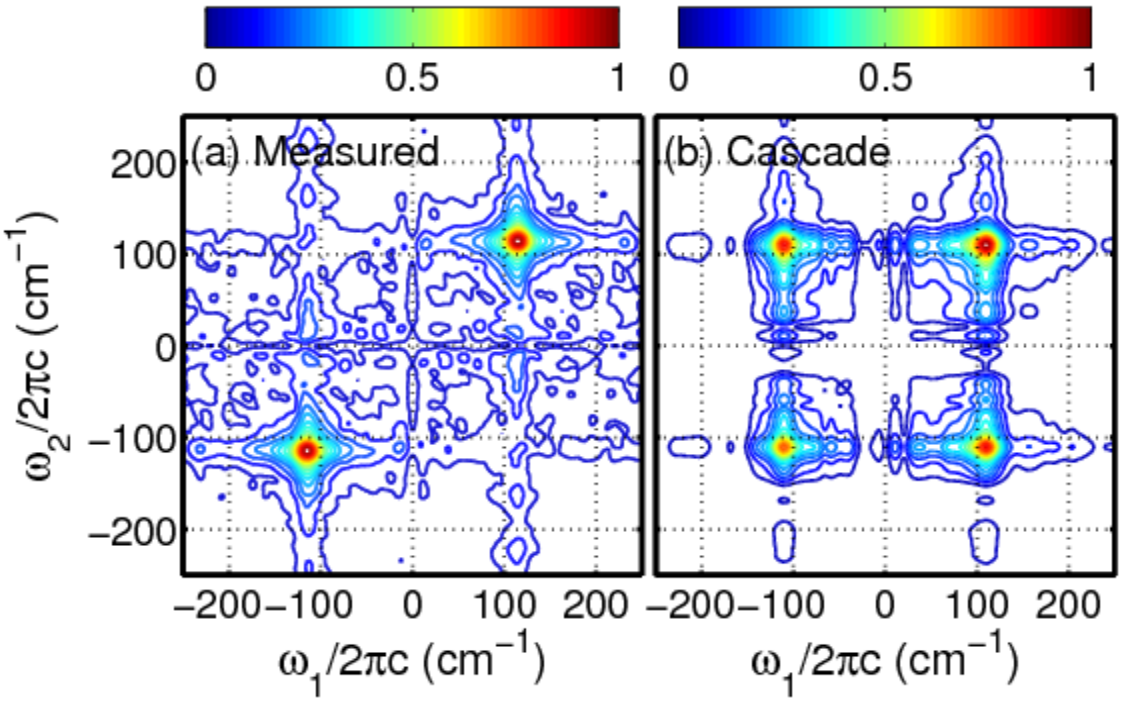

Figure A.15. Absolute values of two-dimensional Raman spectra (a) measured by six-wave mixing and (b) the sequential cascade computed using an experimental third-order transient grating measurement. The 2D spectrum associated with the parallel cascade is generated by two-dimensional Fourier transformation of the product, $S^{(3)}(\tau_1)\,S^{(3)}(\tau_2)$, where $S^{(3)}(\tau)$ is an experimental transient grating signal field.

A.10. Tables of Phase-Matching Efficiencies for Three and Four-Beam Geometries

Table A.1. Calculated Wavevector Mismatches for Direct and Cascaded Nonlinearities in Geometry Shown in Figure 4.17a

Wavevector of Intermediate Nonlinearity	Δk_A (cm^{-1})	Δk_B (cm^{-1})	[(a),(b)] $f_j\left(\Delta k_j l\right)$
$k_1 - k_2 + k_3 - k_4 + k_5$ (Direct 5th-Order Signal)	-470	----------	-0.008
$k_1 - k_2 + k_3$ (Sequential Cascade #1)	-235	-470	0.4×10^{-3}
$k_2 - k_1 + k_4$ (Sequential Cascade #2)	-235	-470	0.7×10^{-3}
$k_1 - k_2 + k_5$ (Parallel Cascade #1)	-470	-470	0.6×10^{-4}
$k_3 - k_4 + k_5$ (Parallel Cascade #2)	-470	-470	0.7×10^{-4}

[(a)] The path length is 300 μm.

[(b)] Direct and cascaded signal generation efficiencies are computed using $\mathrm{sinc}\left(\Delta k_A l/2\right)$ and $\mathrm{sinc}\left(\Delta k_A l/2\right)\mathrm{sinc}\left(\Delta k_B l/2\right)$, respectively.

Table A.2. Calculated Wavevector Mismatches for Direct and Cascaded Nonlinearities in Geometry Shown in Figure 4.17b

Wavevector of Intermediate Nonlinearity	Δk_A (cm^{-1})	Δk_B (cm^{-1})	[(a),(b)] $f_j\left(\Delta k_j l\right)$
$k_1 - k_2 + k_3 - k_4 + k_5$ (Direct 5^{th}-Order Signal)	-245	----------	-0.070
$k_1 - k_2 + k_3$ (Sequential Cascade #1)	-470	-245	0.001
$k_2 - k_1 + k_4$ (Sequential Cascade #2)	-695	-245	-0.002
$k_1 - k_2 + k_5$ (Parallel Cascade #1)	-470	-245	0.0006
$k_3 - k_4 + k_5$ (Parallel Cascade #2)	-245	-690	-0.002

[(a)] The path length is 300 μm.

[(b)] Direct and cascaded signal generation efficiencies are computed using $\mathrm{sinc}\left(\Delta k_A l/2\right)$ and $\mathrm{sinc}\left(\Delta k_A l/2\right)\mathrm{sinc}\left(\Delta k_B l/2\right)$, respectively.

Table A.3. Calculated Wavevector Mismatches for Direct and Cascaded Nonlinearities in Geometry Shown in Figure 4.17c

Wavevector of Intermediate Nonlinearity	Δk_A (cm^{-1})	Δk_B (cm^{-1})	[(a),(b)] $f_j\left(\Delta k_j l\right)$
$k_1 - k_2 + k_3 - k_4 + k_5$ (Direct 5^{th}-Order Signal)	-10	----------	0.96
$k_1 - k_2 + k_3$ (Sequential Cascade #1)	-470	-10	-0.007
$k_2 - k_1 + k_4$ (Sequential Cascade #2)	-695	-10	0.029
$k_1 - k_2 + k_5$ (Parallel Cascade #1)	-235	-10	-0.086
$k_3 - k_4 + k_5$ (Parallel Cascade #2)	-10	-270	-0.017

[(a)] The path length is 300 μm.

[(b)] Direct and cascaded signal generation efficiencies are computed using $\mathrm{sinc}\left(\Delta k_A l/2\right)$ and $\mathrm{sinc}\left(\Delta k_A l/2\right)\mathrm{sinc}\left(\Delta k_B l/2\right)$, respectively.

Table A.4. Calculated Wavevector Mismatches for Direct and Cascaded Nonlinearities in the Three-Beam Pump-Repump-Probe Geometry (Data in Figure 4.19)

Wavevector of Intermediate Nonlinearity	Δk_A (cm^{-1})	Δk_B (cm^{-1})	[(a),(b)] $f_j\left(\Delta k_j l\right)$
$k_1 - k_2 + k_3 - k_4 + k_5$ (Direct 5^{th}-Order Signal)	0	----------	1
$k_1 - k_2 + k_3$ (Sequential Cascade #1)	-235	0	-0.090
$k_2 - k_1 + k_4$ (Sequential Cascade #2)	-235	0	-0.090
$k_1 - k_2 + k_5$ (Parallel Cascade #1)	0	0	1
$k_3 - k_4 + k_5$ (Parallel Cascade #2)	0	0	1

[(a)]The path length is 300 μm.

[(b)] Direct and cascaded signal generation efficiencies are computed using $\mathrm{sinc}\left(\Delta k_A l/2\right)$ and $\mathrm{sinc}\left(\Delta k_A l/2\right)\mathrm{sinc}\left(\Delta k_B l/2\right)$, respectively.

A.11. REFERENCES

(1) Benjamin, I.; Banin, U.; Ruhman, S. *J. Chem. Phys.* **1993**, *98*, 8337.

(2) Johnson, A. E.; Myers, A. B. *J. Chem. Phys.* **1996**, *104*, 2497.

(3) Moran, A. M.; Dreyer, J.; Mukamel, S. *J. Chem. Phys.* **2003**, *118*, 1347.

(4) West, B. A.; Womick, J. M.; Moran, A. M. *J. Phys. Chem. A* **2013**, *117*, 5865.

(5) Choi, H.; Bise, R. T.; Hoops, A. A.; Neumark, D. M. *J. Chem. Phys.* **2000**, *113*, 2255.

(6) West, B. A.; Molesky, B. P.; Giokas, P. G.; Moran, A. M. *Chem. Phys.* **2013**, *423*, 92.

(7) West, B. A.; Giokas, P. G.; Molesky, B. P.; Ross, A. D.; Moran, A. M. *Opt. Express* **2013**, *21*, 2118.

(8) Fuji, T.; Suzuki, T.; Serebryannikov, E. E.; Zheltikov, A. *Phys. Rev. A* **2009**, *80*, 063822.

(9) Schmidtke, S. J.; Underwood, D. F.; Blank, D. A. *J. Phys. Chem. A* **2005**, *109*, 7033.

(10) Moran, A. M.; Nome, R. A.; Scherer, N. F. *J. Chem. Phys.* **2007**, *127*, 184505:1.

(11) Park, S.; Kim, J.; Scherer, N. F. *Phys. Chem. Chem. Phys.* **2012**, *14*, 8116.

(12) Kukura, P.; McCamant, D. W.; Mathies, R. A. *Annu. Rev. Phys. Chem.* **2007**, *58*, 461.

(13) van Veldhoven, E.; Khurmi, C.; Zhang, X.; Berg, M. A. *ChemPhysChem* **2007**, *8*, 1761.

(14) Zimdars, D.; Francis, R. S.; Ferrante, C.; Fayer, M. D. *J. Chem. Phys.* **1997**, *106*, 7498.

(15) Ajdarzadeh Oskouei, A.; Bräm, O.; Cannizzo, A.; van Mourik, F.; Tortschanoff, A.; Chergui, M. *J. Mol. Liq.* **2008**, *141*, 118.

(16) West, B. A.; Moran, A. M. *J. Phys. Chem. Lett.* **2012**, *3*, 2575.

(17) Mukamel, S. *Principles of Nonlinear Optical Spectroscopy*; Oxford University Press: New York, 1995.

(18) Ding, F.; Fulmer, E. C.; Zanni, M. T. *J. Chem. Phys.* **2005**, *123*, 094502.

(19) Johnson, A. E.; Myers, A. B. *J. Chem. Phys.* **1995**, *104*, 3519.

APPENDIX B: SUPPLEMENT TO "ELUCIDATION OF REACTIVE WAVEPACKETS BY TWO-DIMENSIONAL RESONANCE RAMAN SPECTROSCOPY"

B.1. Vibrational Hamiltonian

The present model assumes that both triiodide and diiodide possess two electronic levels and one nuclear coordinate whose potential energy minimum is displaced between the ground and excited electronic states. The rationale behind the model is discussed in Section 5.2.1. The anharmonic vibrational wavefunctions for the Franck-Condon active bond stretching mode of diiodide and the symmetric stretching coordinate of triiodide are generated using a Hamiltonian with the following form[1]

$$H_\alpha = \frac{\hbar\omega_{\alpha,vib}}{2}\left(2a^\dagger a + 1\right) + U_{3,\alpha}\left[a^\dagger a^\dagger a^\dagger + 3a^\dagger a^\dagger a + 3a^\dagger aa + aaa + 3a^\dagger + 3a\right] \tag{B.1}$$

where

$$U_{3,\alpha} = \frac{1}{3!\sqrt{2^3 m^3 \omega^3 \hbar^{-3}}}\left(\frac{d^3V}{dq^3}\right)_0 . \tag{B.2}$$

The wavefunctions are obtained by diagonalizing this Hamiltonian in a basis set of harmonic oscillators that includes states with up to the 40 vibrational quanta. Parameters of the vibrational Hamiltonian are given in Table 5.1. We use a notation in which α represents the molecule (r for triiodide or p for diiodide) and an asterisk indicates an electronically excited state.

The vibrational overlap integrals used to evaluate the response functions of diiodide are obtained using

$$\langle n|m\rangle = \sum_{jk} \varphi_{nk}\varphi_{mj}\langle k|j\rangle \tag{B.3}$$

where φ_{nk} is the expansion coefficient for harmonic basis vector, k, and the anharmonic excited state vibrational wavefunction, n. Vibrational overlap integrals of triiodide are given by a different formula

$$\langle n|m\rangle = \sum_k \varphi_{nk} \langle k|m\rangle \tag{B.4}$$

because the ground and excited states are taken to be harmonic and anharmonic, respectively (see discussion in Section 5.2). In order to evaluate the overlap integrals, we assume a dimensionless displacement of 7.0 based on spontaneous Raman measurements for triiodide[2] and our earlier 2DRR study.[3] A displacement of 7.0 also produces an excited state potential energy gradient of 225 eV/pm in diiodide which is identical to that associated with a previously employed exponential surface at a displacement of only 9 pm from the Franck-Condon geometry.[4,5] As discussed in Section 5.2.1, this gradient is the key quantity that must be reproduced by the present model, because electronic dephasing is fast compared to the vibrational period.[6] For this reason, the spectroscopic signals investigated in this work are insensitive to features of the excited state potential energy surface that are displaced from the Franck-Condon geometry.

B.2. Two-Dimensional Resonance Raman Signal Components

The Feynman diagrams presented in Figure 5.2 include dummy indices for vibrational levels (m, n, j, k, l, u, v, w) associated with the ground and excited electronic states (r and $r*$ for triiodide, p and $p*$ for diiodide). Response functions are written in the Condon approximation, where the integral over electronic and nuclear degrees of freedom in the transition dipole is separated into a product of two integrals. For example, an interaction that

couples vibrational level m in the ground electronic state of the reactant and vibrational level n in the excited electronic state of the reactant contributes the product, $\mu_{r^*r}\langle n|m\rangle$, to the response function, where μ_{r^*r} is the electronic transition dipole and $\langle n|m\rangle$ is a vibrational overlap integral. We use a notation in which the excited state vibrational energy level is always written in the bra.[7]

The first polarization component is given in Equation 5.3. The remaining 11 polarization components, which are derived in Section B.3, are given by

$$P_2^{(5)}(\omega_1,\omega_2) = -\frac{N\xi_{UV}^5|\mu_{r^*r}|^6}{\hbar^5}\sum_{mnjklu} B_m \langle n|m\rangle\langle n|j\rangle\langle k|m\rangle\langle k|l\rangle\langle u|j\rangle\langle u|l\rangle \times L_{r^*n,rm}(\omega_{UV}) D_{rj,rm}(\omega_1) L_{rj,r^*k}(-\omega_{UV}) D_{rj,rl}(\omega_2) L_{r^*u,rl}(\omega_t), \quad \text{(B.5)}$$

$$P_3^{(5)}(\omega_1,\omega_2) = -\frac{N\xi_{UV}^5|\mu_{r^*r}|^6}{\hbar^5}\sum_{mnjklu} B_m \langle n|m\rangle\langle n|j\rangle\langle k|j\rangle\langle k|l\rangle\langle u|m\rangle\langle u|l\rangle \times L_{rm,r^*n}(-\omega_{UV}) D_{rm,rj}(\omega_1) L_{rm,r^*k}(-\omega_{UV}) D_{rm,rl}(\omega_2) L_{r^*u,rl}(\omega_t), \quad \text{(B.6)}$$

$$P_4^{(5)}(\omega_1,\omega_2) = -\frac{N\xi_{UV}^5|\mu_{r^*r}|^6}{\hbar^5}\sum_{mnjklu} B_m \langle n|m\rangle\langle n|j\rangle\langle k|m\rangle\langle k|l\rangle\langle u|l\rangle\langle u|j\rangle \times L_{rm,r^*n}(-\omega_{UV}) D_{rm,rj}(\omega_1) L_{r^*k,rj}(\omega_{UV}) D_{rl,rj}(\omega_2) L_{r^*u,rj}(\omega_t), \quad \text{(B.7)}$$

$$P_5^{(5)}(\omega_1,\omega_2) = -\frac{N\xi_{UV}^2\xi_{VIS}^3|\mu_{r^*r}|^2|\mu_{p^*p}|^4}{\hbar^5}\sum_{mnjkluvw} B_m \langle n|m\rangle\langle j|m\rangle\langle u|k\rangle\langle u|v\rangle\langle w|v\rangle\langle w|l\rangle \times L_{r^*n,rm}(\omega_{UV}) D_{pk,pl}(\omega_1) L_{p^*u,pl}(\omega_{VIS}) D_{pv,pl}(\omega_2) L_{p^*w,pl}(\omega_t), \quad \text{(B.8)}$$

$$P_6^{(5)}(\omega_1,\omega_2) = -\frac{N\xi_{UV}^2\xi_{VIS}^3|\mu_{r^*r}|^2|\mu_{p^*p}|^4}{\hbar^5}\sum_{mnjkluvw} B_m \langle n|m\rangle\langle j|m\rangle\langle u|k\rangle\langle u|v\rangle\langle w|v\rangle\langle w|l\rangle \times L_{rm,r^*n}(-\omega_{UV}) D_{pk,pl}(\omega_1) L_{p^*u,pl}(\omega_{VIS}) D_{pv,pl}(\omega_2) L_{p^*w,pl}(\omega_t), \quad \text{(B.9)}$$

$$P_7^{(5)}(\omega_1,\omega_2) = -\frac{N\xi_{UV}^2\xi_{VIS}^3\left|\mu_{r^*r}\right|^2\left|\mu_{p^*p}\right|^4}{\hbar^5}\sum_{mnjkluvw} B_m\langle n|m\rangle\langle j|m\rangle\langle u|l\rangle\langle u|v\rangle\langle w|k\rangle\langle w|v\rangle, \quad \text{(B.10)}$$
$$\times L_{r^*n,rm}(\omega_{UV})D_{pk,pl}(\omega_1)L_{pk,p^*u}(-\omega_{VIS})D_{pk,pv}(\omega_2)L_{p^*w,pv}(\omega_t)$$

$$P_8^{(5)}(\omega_1,\omega_2) = -\frac{N\xi_{UV}^2\xi_{VIS}^3\left|\mu_{r^*r}\right|^2\left|\mu_{p^*p}\right|^4}{\hbar^5}\sum_{mnjkluvw} B_m\langle n|m\rangle\langle j|m\rangle\langle u|l\rangle\langle u|v\rangle\langle w|k\rangle\langle w|v\rangle, \quad \text{(B.11)}$$
$$\times L_{rm,r^*n}(-\omega_{UV})D_{pk,pl}(\omega_1)L_{pk,p^*u}(-\omega_{VIS})D_{pk,pv}(\omega_2)L_{p^*w,pv}(\omega_t)$$

$$P_9^{(5)}(\omega_1,\omega_2) = -\frac{N\xi_{UV}^4\xi_{VIS}\left|\mu_{r^*r}\right|^4\left|\mu_{p^*p}\right|^2}{\hbar^5}\sum_{mnjkluvw} B_m\langle n|m\rangle\langle n|j\rangle\langle k|j\rangle\langle l|m\rangle\langle w|u\rangle\langle w|v\rangle, \quad \text{(B.12)}$$
$$\times L_{r^*n,rm}(\omega_{UV})D_{rj,rm}(\omega_1)L_{r^*k,rm}(\omega_{UV})D_{pu,pv}(\omega_2)L_{p^*w,pv}(\omega_t)$$

$$P_{10}^{(5)}(\omega_1,\omega_2) = -\frac{N\xi_{UV}^4\xi_{VIS}\left|\mu_{r^*r}\right|^4\left|\mu_{p^*p}\right|^2}{\hbar^5}\sum_{mnjkluvw} B_m\langle n|m\rangle\langle n|j\rangle\langle k|m\rangle\langle l|j\rangle\langle w|u\rangle\langle w|v\rangle, \quad \text{(B.13)}$$
$$\times L_{rm,r^*n}(-\omega_{UV})D_{rm,rj}(\omega_1)L_{r^*k,rj}(\omega_{UV})D_{pu,pv}(\omega_2)L_{p^*w,pv}(\omega_t)$$

$$P_{11}^{(5)}(\omega_1,\omega_2) = -\frac{N\xi_{UV}^4\xi_{VIS}\left|\mu_{r^*r}\right|^4\left|\mu_{p^*p}\right|^2}{\hbar^5}\sum_{mnjkluvw} B_m\langle n|m\rangle\langle n|j\rangle\langle k|m\rangle\langle l|j\rangle\langle w|u\rangle\langle w|v\rangle, \quad \text{(B.14)}$$
$$\times L_{r^*n,rm}(\omega_{UV})D_{rj,rm}(\omega_1)L_{rj,r^*k}(-\omega_{UV})D_{pu,pv}(\omega_2)L_{p^*w,pv}(\omega_t)$$

and

$$P_{12}^{(5)}(\omega_1,\omega_2) = -\frac{N\xi_{UV}^4\xi_{VIS}\left|\mu_{r^*r}\right|^4\left|\mu_{p^*p}\right|^2}{\hbar^5}\sum_{mnjkluvw} B_m\langle n|m\rangle\langle n|j\rangle\langle k|j\rangle\langle l|m\rangle\langle w|u\rangle\langle w|v\rangle. \quad \text{(B.15)}$$
$$\times L_{rm,r^*n}(-\omega_{UV})D_{rm,rj}(\omega_1)L_{rm,r^*k}(-\omega_{UV})D_{pu,pv}(\omega_2)L_{p^*w,pv}(\omega_t)$$

In the above polarization components, laser pulses with the subscripts *UV* and *VIS* are taken to interact with triiodide and diiodide, respectively.

For convenience, we further group the terms into three classes of signal fields under the assumption of perfect phase-matching conditions

$$E_{r,r}^{(5)}(\omega_1,\omega_2)=\left(\frac{i\omega_t l}{2\varepsilon_0 n(\omega_t)c}\right)\sum_{m=1}^{4}P_m^{(5)}(\omega_1,\omega_2), \tag{B.16}$$

$$E_{p,p}^{(5)}(\omega_1,\omega_2)=\left(\frac{i\omega_t l}{2\varepsilon_0 n(\omega_t)c}\right)\sum_{m=5}^{8}P_m^{(5)}(\omega_1,\omega_2)\ , \tag{B.17}$$

and

$$E_{r,p}^{(5)}(\omega_1,\omega_2)=\left(\frac{i\omega_t l}{2\varepsilon_0 n(\omega_t)c}\right)\sum_{m=9}^{12}P_m^{(5)}(\omega_1,\omega_2)\ . \tag{B.18}$$

Here, the two subscripts of the signal fields represent sensitivity to the triiodide reactant (subscript r) and diiodide product (subscript p) in the two frequency dimensions, ω_1 and ω_2.

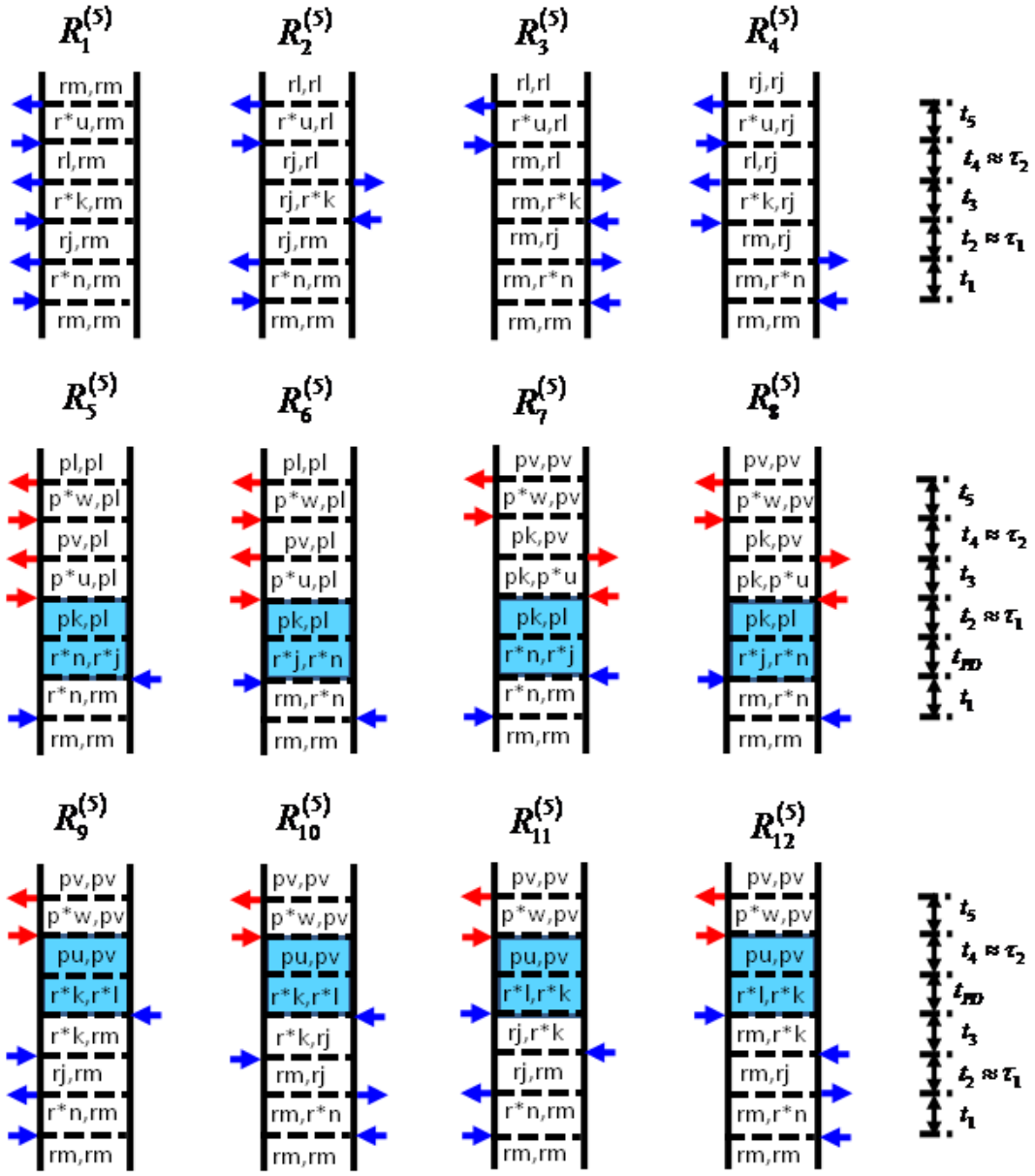

Figure B.1. Fenyman diagrams associated with dominant 2DRR nonlinearities. Blue and red arrows represent pulses resonant with triiodide and diiodide, respectively. The indices r and $r*$ represent the ground and excited electronic states of the triiodide reactant, whereas p and $p*$ correspond to the diiodide photoproduct. Vibrational levels associated with these electronic states are specified by dummy indices (m, n, j, k, l, u, v, w). Each row represents a different class of terms: (i) both dimensions correspond to triiodide in terms 1-4; (ii) both dimensions correspond to diiodide in terms 5-8; (iii) vibrational resonances of triiodide and diiodide appear in separate dimensions in terms 9-12. The intervals shaded in blue represent a non-radiative transfer of vibronic coherence from triiodide to diiodide.

B.3. Derivation of Formula for the Direct Fifth-Order Signal Field

The Feynman diagrams presented in Figure B.1 include dummy indices for vibrational levels (m, n, j, k, l, u, v, w) associated with the ground and excited electronic states of the reactant (r and $r*$) and product (p and $p*$). Response functions are written in the Condon approximation, where the integral over electronic and nuclear degrees of freedom in the transition dipole is separated into a product of integrals. For example, an interaction that couples vibrational level m in the ground electronic state of the reactant and vibrational level n in the excited electronic state contributes the product, $\mu_{r*r}\langle n|m\rangle$, to the response function, where μ_{r*r} is the electronic transition dipole of the reactant and $\langle n|m\rangle$ is a vibrational overlap integral. We use a notation in which the index for the excited state vibrational energy level is always written in the bra.[7]

Under the assumption that the photodissociation time scale is short compared to the vibrational period, the time interval, t_{PD}, can be eliminated from consideration. The response functions corresponding to the fifth-order diagrams in Figure B.1 can then be written as

$$R_1^{(5)}(t_1,t_2,t_3,t_4,t_5) = |\mu_{r*r}|^6 \sum_{mnjklu} B_m \langle n|m\rangle\langle n|j\rangle\langle k|j\rangle\langle k|l\rangle\langle u|l\rangle\langle u|m\rangle L_{r*n,rm}(t_1) \times L_{rj,rm}(t_2) L_{r*k,rm}(t_3) L_{rl,rm}(t_4) L_{r*u,rm}(t_5), \quad \text{(B.19)}$$

$$R_2^{(5)}(t_1,t_2,t_3,t_4,t_5) = |\mu_{r*r}|^6 \sum_{mnjklu} B_m \langle n|m\rangle\langle n|j\rangle\langle k|m\rangle\langle k|l\rangle\langle u|j\rangle\langle u|l\rangle L_{r*n,rm}(t_1) \times L_{rj,rm}(t_2) L_{rj,r*k}(t_3) L_{rj,rl}(t_4) L_{r*u,rl}(t_5), \quad \text{(B.20)}$$

$$R_3^{(5)}(t_1,t_2,t_3,t_4,t_5) = |\mu_{r*r}|^6 \sum_{mnjklu} B_m \langle n|m\rangle\langle n|j\rangle\langle k|j\rangle\langle k|l\rangle\langle u|m\rangle\langle u|l\rangle L_{rm,r*n}(t_1) \times L_{rm,rj}(t_2) L_{rm,r*k}(t_3) L_{rm,rl}(t_4) L_{r*u,rl}(t_5), \quad \text{(B.21)}$$

$$R_4^{(5)}(t_1,t_2,t_3,t_4,t_5) = |\mu_{r^*r}|^6 \sum_{mnjklu} B_m \langle n|m\rangle\langle n|j\rangle\langle k|m\rangle\langle k|l\rangle\langle u|l\rangle\langle u|j\rangle L_{rm,r^*n}(t_1) \times L_{rm,rj}(t_2) L_{r^*k,rj}(t_3) L_{rl,rj}(t_4) L_{r^*u,rj}(t_5), \quad \text{(B.22)}$$

$$R_5^{(5)}(t_1,t_2,t_3,t_4,t_5) = |\mu_{r^*r}|^2 |\mu_{p^*p}|^4 \sum_{mnjkluvw} B_m \langle n|m\rangle\langle j|m\rangle\langle u|k\rangle\langle u|v\rangle\langle w|v\rangle\langle w|l\rangle \times L_{r^*n,rm}(t_1) L_{pk,pl}(t_2) L_{p^*u,pl}(t_3) L_{pv,pl}(t_4) L_{p^*w,pl}(t_5), \quad \text{(B.23)}$$

$$R_6^{(5)}(t_1,t_2,t_3,t_4,t_5) = |\mu_{r^*r}|^2 |\mu_{p^*p}|^4 \sum_{mnjkluvw} B_m \langle n|m\rangle\langle j|m\rangle\langle u|k\rangle\langle u|v\rangle\langle w|v\rangle\langle w|l\rangle \times L_{rm,r^*n}(t_1) L_{pk,pl}(t_2) L_{p^*u,pl}(t_3) L_{pv,pl}(t_4) L_{p^*w,pl}(t_5), \quad \text{(B.24)}$$

$$R_7^{(5)}(t_1,t_2,t_3,t_4,t_5) = |\mu_{r^*r}|^2 |\mu_{p^*p}|^4 \sum_{mnjkluvw} B_m \langle n|m\rangle\langle j|m\rangle\langle u|l\rangle\langle u|v\rangle\langle w|k\rangle\langle w|v\rangle \times L_{r^*n,rm}(t_1) L_{pk,pl}(t_2) L_{pk,p^*u}(t_3) L_{pk,pv}(t_4) L_{p^*w,pv}(t_5), \quad \text{(B.25)}$$

$$R_8^{(5)}(t_1,t_2,t_3,t_4,t_5) = |\mu_{r^*r}|^2 |\mu_{p^*p}|^4 \sum_{mnjkluvw} B_m \langle n|m\rangle\langle j|m\rangle\langle u|l\rangle\langle u|v\rangle\langle w|k\rangle\langle w|v\rangle \times L_{rm,r^*n}(t_1) L_{pk,pl}(t_2) L_{pk,p^*u}(t_3) L_{pk,pv}(t_4) L_{p^*w,pv}(t_5), \quad \text{(B.26)}$$

$$R_9^{(5)}(t_1,t_2,t_3,t_4,t_5) = |\mu_{r^*r}|^2 |\mu_{p^*p}|^2 \sum_{mnjkluvw} B_m \langle n|m\rangle\langle n|j\rangle\langle k|j\rangle\langle l|m\rangle\langle w|u\rangle\langle w|v\rangle \times L_{r^*n,rm}(t_1) L_{rj,rm}(t_2) L_{r^*k,rm}(t_3) L_{pu,pv}(t_4) L_{p^*w,pv}(t_5), \quad \text{(B.27)}$$

$$R_{10}^{(5)}(t_1,t_2,t_3,t_4,t_5) = |\mu_{r^*r}|^4 |\mu_{p^*p}|^2 \sum_{mnjkluvw} B_m \langle n|m\rangle\langle n|j\rangle\langle k|m\rangle\langle l|j\rangle\langle w|u\rangle\langle w|v\rangle \times L_{rm,r^*n}(t_1) L_{rm,rj}(t_2) L_{r^*k,rj}(t_3) L_{pu,pv}(t_4) L_{p^*w,pv}(t_5), \quad \text{(B.28)}$$

$$R_{11}^{(5)}(t_1,t_2,t_3,t_4,t_5) = |\mu_{r^*r}|^4 |\mu_{p^*p}|^2 \sum_{mnjkluvw} B_m \langle n|m\rangle\langle n|j\rangle\langle k|m\rangle\langle l|j\rangle\langle w|u\rangle\langle w|v\rangle \times L_{r^*n,rm}(t_1) L_{rj,rm}(t_2) L_{rj,r^*k}(t_3) L_{pu,pv}(t_4) L_{p^*w,pv}(t_5), \quad \text{(B.29)}$$

and

$$R_{12}^{(5)}(t_1,t_2,t_3,t_4,t_5) = |\mu_{r^*r}|^4 |\mu_{p^*p}|^2 \sum_{mnjkluvw} B_m \langle n|m\rangle\langle n|j\rangle\langle k|j\rangle\langle l|m\rangle\langle w|u\rangle\langle w|v\rangle \times L_{rm,r^*n}(t_1) L_{rm,rj}(t_2) L_{rm,r^*k}(t_3) L_{pu,pv}(t_4) L_{p^*w,pv}(t_5) \quad \text{(B.30)}$$

In the above equations, the propagation functions corresponding to vibronic (in t_1, t_3, or t_5) and purely vibrational (in t_2 or t_4) coherences are respectively given by[8]

$$L_{r^*m,rn}(t) = \theta(t)\exp(-i\omega_{r^*r}t - i\omega_{mn}t - \Gamma_{r^*r}t) \quad \text{(B.31)}$$

and

$$L_{rm,rn}(t) = \theta(t)\exp(-i\omega_{mn}t - \Gamma_{vib}t) \quad \text{(B.32)}$$

where $\theta(t)$ is a Heaviside step function. It is assumed in Equation B.31 that electronic dephasing is much faster than vibrational dephasing (i.e. $\Gamma_{r^*r} >> \Gamma_{vib}$).

We next obtain the 12 components of the fifth-order polarization by convoluting the response functions with the external electric fields. The component of the fifth-order polarization corresponding to the R_1 term is given by

$$P_1^{(5)}(t) = N\left(\frac{i}{\hbar}\right)^5 \int_0^\infty dt_5 \int_0^\infty dt_4 \int_0^\infty dt_3 \int_0^\infty dt_2 \int_0^\infty dt_1 R_1^{(5)}(t_1,t_2,t_3,t_4,t_5) E_{UV}(t-t_5) E_{UV}^*(t+\tau_2-t_5-t_4) E_{UV}(t+\tau_2-t_5-t_4-t_3) E_{UV}^*(t+\tau_1+\tau_2-t_5-t_4-t_3-t_2) E_{UV}(t+\tau_1+\tau_2-t_5-t_4-t_3-t_2-t_1) \quad \text{(B.33)}$$

where N is the number density and τ_j are the pulse delay times defined in Chapter 5. Pulses with the subscripts *UV* and *VIS* are taken to interact with triiodide and diiodide, respectively. Attainment of analytic expressions is facilitated by use of double-sided exponential electric field envelopes

$$E_j(t) = \xi_j \exp\left(-i\omega_j t - \Lambda_j |t|\right) \tag{B.34}$$

where ξ_j is the (real) electric field amplitude, Λ_j is the HWHM spectral width, and ω_j is the carrier frequency of the laser pulse (the index, j, signifies either the "pump" or "probe"), which we take to be resonant with the triiodide reactant. The polarization component, $P_1^{(5)}(t)$, can now be rewritten as

$$\begin{aligned} P_1^{(5)}(t) = N\xi_{UV}^5 \exp\left(-i\omega_{UV}t\right)\left(\frac{i}{\hbar}\right)^5 \int_0^\infty dt_5 \int_0^\infty dt_4 \int_0^\infty dt_3 \int_0^\infty dt_2 \int_0^\infty dt_1 R_1^{(5)}\left(t_1,t_2,t_3,t_4,t_5\right) \\ \times \exp\left[i\omega_{UV}t_1 + i\omega_{UV}t_3 + i\omega_{UV}t_5\right] \\ \times \exp\left[-\Lambda_{UV}\left|t-t_5\right| - \Lambda_{UV}\left|t+\tau_2-t_5-t_4\right| - \Lambda_{UV}\left|t+\tau_2-t_5-t_4-t_3\right|\right] \\ \times \exp\left[-\Lambda_{UV}\left|t+\tau_1+\tau_2-t_5-t_4-t_3-t_2\right| - \Lambda_{UV}\left|t+\tau_1+\tau_2-t_5-t_4-t_3-t_2-t_1\right|\right] \end{aligned} \tag{B.35}$$

We use a "doorway wavepacket" to filter vibrational coherences with frequencies that exceed the bandwidth of the pump pulse.[8] To this end, we introduce the change of variables, $t' = t + \tau_1 - t_2$ and $t'' = t + \tau_2 - t_4$. The polarization component is then rewritten as

$$\begin{aligned} P_1^{(5)}(t) = N\xi_{UV}^5 \left(\frac{i}{\hbar}\right)^5 \int_0^\infty dt_5 \int_{-\infty}^\infty dt'' \int_0^\infty dt_3 \int_{-\infty}^\infty dt' \int_0^\infty dt_1 R_1^{(5)}\left(t_1, t+\tau_1-t', t_3, t+\tau_2-t'', t_5\right) \\ \times \exp\left[i\omega_{UV}t_1 + i\omega_{UV}t_3 + i\omega_{UV}t_5 - i\omega_{UV}t\right] \\ \times \exp\left[-2\Lambda_{UV}\left|t''\right| - 2\Lambda_{UV}\left|t'\right|\right] \end{aligned} \tag{B.36}$$

Here, we have assumed that (i) $t_2 \approx \tau_1$ in order to carry out the integral over t' and (ii) the pulse durations are short compared to the delay times to make the upper limits of the integrals over t' and t'' infinite. The time intervals, t_1 , t_3, and t_5, have also been removed from the arguments of

the laser pulses under the assumption that the pulse durations are long compared to the electronic dephasing time. We next introduce the approximation, $t = t_5$,

$$P_1^{(5)}(\omega_1,\omega_2) = N\xi_{UV}^5\left(\frac{i}{\hbar}\right)^5\int_0^\infty dt\int_0^\infty d\tau_2\int_0^\infty d\tau_1\int_{-\infty}^\infty dt''\int_0^\infty dt_3\int_{-\infty}^\infty dt'\int_0^\infty dt_1 R_1^{(5)}\left(t_1,\tau_1-t',t_3,\tau_2-t'',t\right) \\ \times\exp\left[i\omega_{UV}t_1+i\omega_{UV}t_3+i\omega_1\tau_1+i\omega_2\tau_2+i\omega_t t-2\Lambda_{UV}\left|t''\right|-2\Lambda_{UV}\left|t'\right|\right] \tag{B.37}$$

and Fourier transform the expression with respect to τ_1, τ_2, and t. Evaluation of the seven integrals in Equation B.37 yields

$$P_1^{(5)}(\omega_1,\omega_2) = -\frac{N\xi_{UV}^5\left|\mu_{r^*r}\right|^6}{\hbar^5}\sum_{mnjklu}B_m\langle n|m\rangle\langle n|j\rangle\langle k|j\rangle\langle k|l\rangle\langle u|l\rangle\langle u|m\rangle \\ \times L_{r^*n,rm}\left(\omega_{UV}\right)D_{rj,rm}\left(\omega_1\right)L_{r^*k,rm}\left(\omega_{UV}\right)D_{rl,rm}\left(\omega_2\right)L_{r^*u,rm}\left(\omega_t\right) \tag{B.38}$$

where the line shape of the electronic resonance is given by

$$L_{r^*n,rm}\left(\omega\right) = -i\int_0^\infty L_{r^*n,rm}\left(t\right)\exp\left(i\omega t\right)dt = \frac{1}{\omega-\omega_{r^*r}-\omega_{nm}+i\Gamma_{r^*r}}. \tag{B.39}$$

The spectroscopic line shape associated with the doorway wavepacket is written as

$$D_{rk,rm}\left(\omega\right) = -i\int_{-\infty}^\infty dt\exp\left(i\omega_{km}t-\Gamma_{vib}\left|t\right|-2\Lambda_{UV}\left|t\right|\right)\int_0^\infty dt L_{rk,rm}\left(\tau\right)\exp\left(i\omega\tau\right) \\ = \frac{2\Gamma_{vib}+4\Lambda_{UV}}{\omega_{km}^2+\left(\Gamma_{vib}+2\Lambda_{UV}\right)^2}\left(\frac{1}{\omega-\omega_{km}+i\Gamma_{vib}}\right) \tag{B.40}$$

We obtain the remaining 11 polarization components, given in Section B.2, by following the same procedure.

B.4. Dominance of the Direct 2DRR Response Over Third-Order Cascades

Fifth-order coherent Raman spectroscopies conducted under off-resonant conditions are susceptible to artifacts known as cascades.[9-13] A cascade is a sequence in which the four-wave mixing signal field generated by one molecule induces a four-wave mixing response on a second molecule. The second molecule then radiates a signal field in the same direction as the fifth-order signal of interest. Cascades are problematic under off-resonant conditions, because they can be many orders of magnitude more intense than the direct fifth-order response. It is thought that selection rules primarily govern this mismatch in signal intensities.[3,13,14] That is, two-quantum transitions involved in the direct fifth-order process are forbidden in harmonic systems when the polarizability scales linearly in the vibrational coordinate. In contrast, third-order cascades are allowed in harmonic systems, which gives them a significant advantage over the fifth-order process. Cascades require this difference in selection rules to dominate over the direct fifth-order response, because they are higher-order in the sense that they involve two more field-matter interactions than the direct process (i.e. this extra factor of the polarizability operator suppresses the relative intensity of the cascaded response).

Cascades were ruled out in our previous all-UV 2DRR study of triiodide using control experiments based on the signal phase, concentration dependence of the signal intensity, and the relative phases of the vibrations detected in four and six-wave mixing signals.[3] The direct 2DRR response should be even more dominant in the present study because lower-frequency laser beams are employed. Moreover, the direct response is favored in the present experiments for the same reasons discussed at length in Chapter 4. In pump-repump-probe experiments, inspection of the signal phase is a particularly convenient way to check for cascades, because third and fifth-order signals possess a readily detected sign difference (i.e. a 90º phase-shift is found under

electronically off-resonant conditions).[10,11] In contrast, cascades have the same sign as the direct third-order response. To illustrate this point, we present (third-order) pump-probe and (fifth-order) pump-repump-probe signals acquired for triiodide in Figure B.2. The two signals have opposite signs as expected for the direct response. Compared to the all-UV approach taken in Chapter 4, the phase difference for vibrational motion is not straightforward to predict in the present two-color experiments because of sensitivity to the complex photodissociation process. Nonetheless, in Figure B.2b, we compare the third-order signal to a slice of the fifth-order signal in τ_2 (at τ_1=0) at a signal detection wavenumber of 20,000 cm^{-1}. The analysis carried out in Chapter 4 suggests that a phase shift near 180º is expected for the direct fifth-order response under these conditions. This prediction is consistent with the measurement shown in Figure B.2b.

Our work suggests that contributions from cascades will generally be negligible in systems such as triiodide, where the potential energy surface displacement is extremely large.[3] Franck-Condon activity eliminates the problematic selection rules found under off-resonant conditions (see Figure 4.14 in Chapter 4). We emphasize that the direct response is not necessarily predicted to dominate in systems with modest mode displacements (i.e. dimensionless displacements below 1), which are typically found in larger molecules. However, in our study of metmyoglobin (see Chapter 6), we still found that the direct fifth-order nonlinearity is at least 10 times larger than the cascaded response in dilute solution.[15] It is worth noting that experiments in which the final four field-matter interactions are off-resonant with the equilibrium system are much less susceptible to cascades than our earlier all-resonant approaches.[3,15] In such a two-color configuration, the fifth-order response will be fully (electronically) resonant, whereas one of the four-wave mixing responses involved in a cascade

must be (electronically) off-resonant (cf., Figure 5.7 or terms 5-8 in Figure 5.3). Pulse sequences in which the final four field-matter interactions are off-resonant with the equilibrium system are often used in other types of optical pump-Raman probe experiments.[16-21]

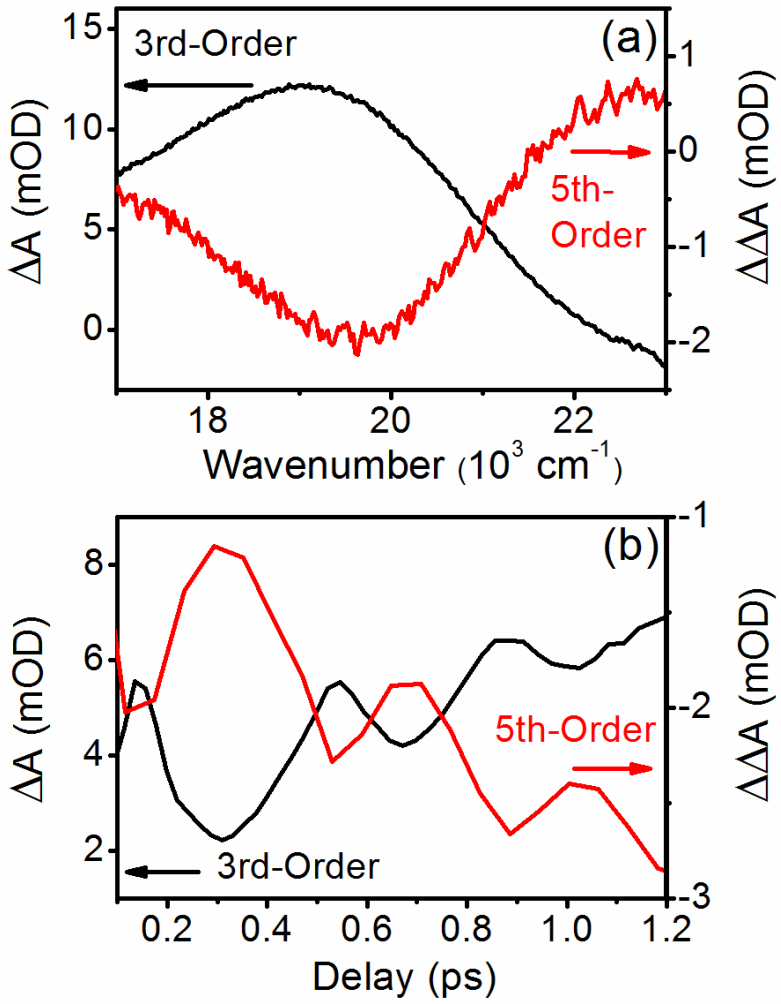

Figure B.2. Comparison of signal phases obtained for third-order (pump-probe) and fifth-order (pump-repump-probe) signals. (a) Pump-probe (delay of 0.5 ps) and pump-repump-probe ($\tau_1 = \tau_2$ =0.5 ps) signals have similar line shapes but opposite signs. This sign-difference suggests that the pump-repump-probe signal is dominated by the desired fifth-order nonlinearity (i.e. not third-order cascades). (b) Oscillations in pump-probe and pump-repump-probe signals are compared via signal detection at 20,000 cm^{-1}. This is a slice of the pump-repump-probe signal in τ_2 with the delay, τ_1, fixed at 0 ps. A relative phase-shift near 180° suggests that the oscillatory component of the pump-repump-probe signal is dominated by the direct fifth order nonlinearity.

B.5. REFERENCES

(1) Moran, A. M.; Dreyer, J.; Mukamel, S. *J. Chem. Phys.* **2003**, *118*, 1347.

(2) Johnson, A. E.; Myers, A. B. *J. Chem. Phys.* **1995**, *104*, 3519.

(3) Molesky, B. P.; Giokas, P. G.; Guo, Z.; Moran, A. M. *J. Chem. Phys.* **2014**, *114*, 114202.

(4) Baratz, A.; Ruhman, S. *Chem. Phys. Lett.* **2008**, *461*, 211.

(5) Nishiyama, Y.; Terazima, M.; Kimura, Y. *J. Phys. Chem. B* **2012**, *116*, 9023.

(6) Myers, A. B. Excited Electronic State Properties From Ground-State Resonance Raman Intensities. In *Laser Techniques in Chemistry*; Myers, A. B., Rizzo, T. R., Eds.; John Wiley & Sons: New York, 1995; Vol. 23; pp 325.

(7) Myers, A. B.; Mathies, R. A.; Tannor, D. J.; Heller, E. J. *J. Chem. Phys.* **1982**, *77*, 3857.

(8) Mukamel, S. *Principles of Nonlinear Optical Spectroscopy*; Oxford University Press: New York, 1995.

(9) Ivanecky III, J. E.; Wright, J. C. *Chem. Phys. Lett.* **1993**, *206*, 437.

(10) Blank, D. A.; Kaufman, L. J.; Fleming, G. R. *J. Chem. Phys.* **1999**, *111*, 3105.

(11) Kubarych, K. J.; Milne, C. J.; Lin, S.; Astinov, V.; Miller, R. J. D. *J. Chem. Phys.* **2002**, *116*, 2016.

(12) Wilson, K. C.; Lyons, B.; Mehlenbacher, R.; Sabatini, R.; McCamant, D. W. *J. Chem. Phys.* **2009**, *131*, 214502.

(13) Ulness, D. J.; Kirkwood, J. C.; Albrecht, A. C. *J. Chem. Phys.* **1998**, *108*, 3897.

(14) Garret-Roe, S.; Hamm, P. *J. Chem. Phys.* **2009**, *130*, 164510.

(15) Molesky, B. P.; Guo, Z.; Moran, A. M. *J. Chem. Phys.* **2015**, *142*, 212405.

(16) Underwood, D. F.; Blank, D. A. *J. Phys. Chem. A* **2005**, *109*, 3295.

(17) Moran, A. M.; Nome, R. A.; Scherer, N. F. *J. Chem. Phys.* **2007**, *127*, 184505:1.

(18) Marek, M. S.; Buckup, T.; Motzkus, M. *J. Phys. Chem. B* **2011**, *115*, 8328.

(19) Rhinehart, J. M.; Challa, J. R.; McCamant, D. W. *J. Phys. Chem. B* **2012**, *116*, 10522.

(20) Wang, Y.; Liu, W.; Tang, L.; Oscar, B.; Han, F.; Fang, C. *J. Phys. Chem. A* **2013**, *117*, 6024.

(21) Valley, D. T.; Hoffman, D. P.; Mathies, R. A. *Phys. Chem. Chem. Phys.* **2015**, *17*, 9231.

APPENDIX C: SUPPLEMENT TO "FEMTOSECOND STIMULATED RAMAN SPECTROSCOPY BY SIX-WAVE MIXING"

C.1. Distinguishing the Broadband and FSRS Responses

The present experiments must contend with an intense broadband (pump-repump-probe) response because all laser pulses are electronically resonant with the Soret band. We suppress this broadband response by introducing a delay between the two Raman pump pulses. This enforces the desired order of field-matter interactions; the final interaction occurs with the Raman pump and Stokes pulses in the FSRS and pump-repump-probe nonlinearities, respectively.

Figure C.1 compares FSRS signals acquired with τ_2 = 0 and 290 fs. The types of terms in the response function responsible for both signal components are also presented. The FSRS resonances are not visible when τ_2 = 0 fs because of the dominant pump-repump-probe response. Notably, such a delay between Raman pump interactions cannot be achieved in a traditional three-beam geometry. The measurement obtained with τ_2 = 0 fs reflects the ratio between the FSRS and broadband responses that would be observed in a three-beam geometry with the same laser pulses.

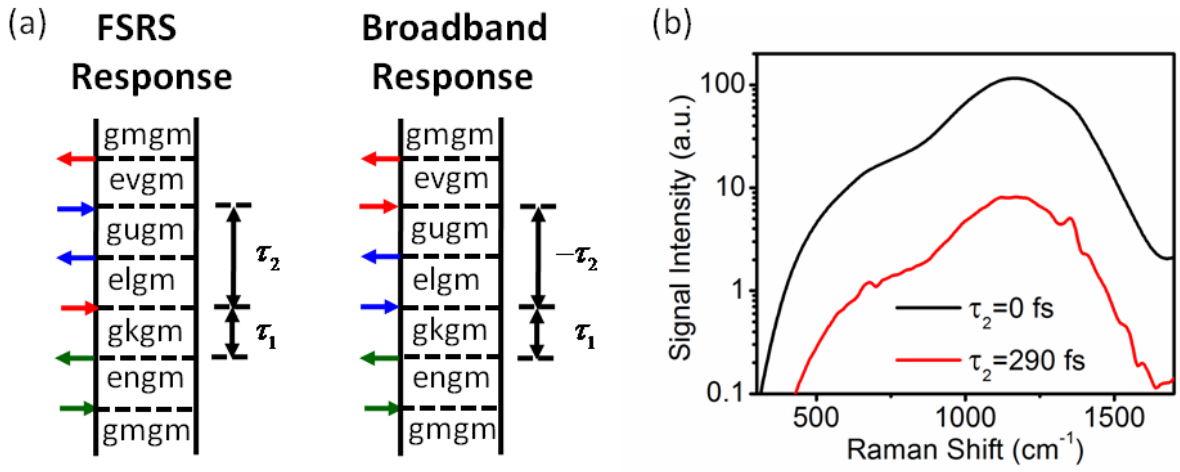

Figure C.1. (a) Examples of Feynman diagrams associated with the (desired) FSRS and (undesired) broadband responses. The indices, g and e, represent the ground and excited electronic states, whereas dummy indices (m, n, k, l, u, and v) denote vibrational levels. Green, blue, and red arrows represent the actinic pump, Raman pump, and Stokes pulses, respectively. (b) The relative contribution from the FSRS signal component increases as the delay, τ_2, increases (the delay, τ_1, is 0.5 ps here). This effect can be understood by inspection of the Feynman diagrams, which suggest that the FSRS response will be preferred over the broadband pump-repump-probe response as the delay, τ_2, increases.

C.2. Derivation of Formula for Direct Fifth-Order Signal Field

Here, we obtain formulas that can be used to compute the relative magnitudes of cascaded third-order and direct fifth-order signal fields. The Feynman diagrams presented in Figure C.2 include dummy indices for vibrational levels (m, n, k, l, u, and v) associated with the ground and excited electronic states (g and e). Response functions are written in the Condon approximation, where the integral over electronic and nuclear degrees of freedom in the transition dipole is separated into a product of integrals. For example, an interaction that couples vibrational level m in the ground electronic state and vibrational level n in the excited electronic state contributes the product $\mu_{eg}\langle n|m\rangle$ to the response function, where μ_{eg} is the

electronic transition dipole and $\langle n|m\rangle$ is a vibrational overlap integral. We use a notation in which the excited state vibrational energy level is always written in the bra.[1]

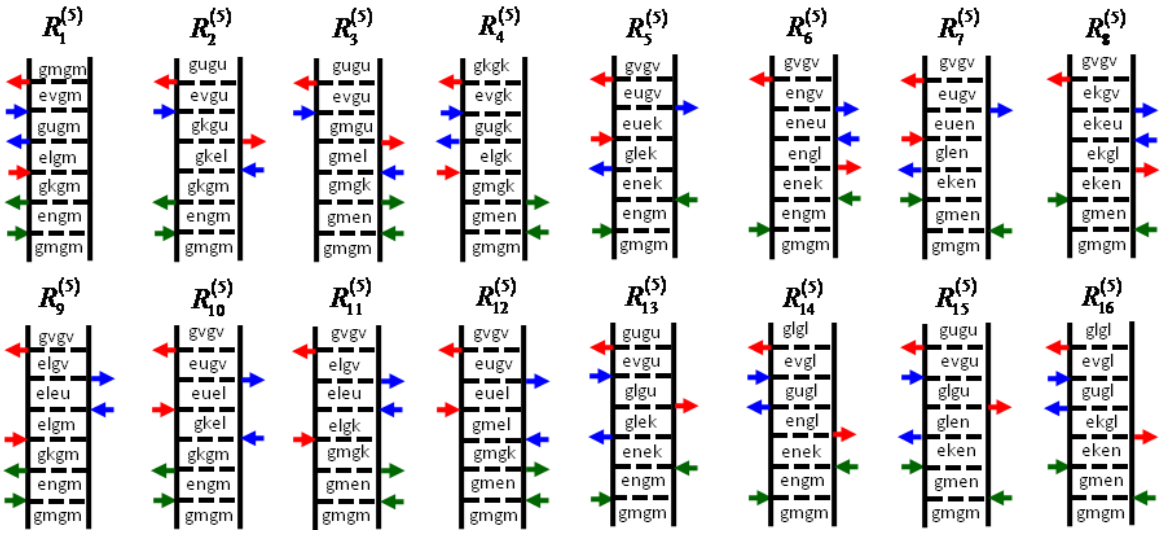

Figure C.2. Feynman diagrams associated with the direct fifth-order response. The indices, g and e, represent the ground and excited electronic states, whereas dummy indices (m, n, k, l, u, and v) denote vibrational levels. Green, blue, and red arrows represent the actinic pump, Raman pump, and Stokes pulses, respectively. We restrict the response function to these 16 terms under the assumption that the signal is primarily resonance-enhanced by the Soret band.

The response functions corresponding to the fifth-order diagrams in Figure C.2 can be written as

$$R_1^{(5)}(t_1,t_2,t_3,t_4,t_5) = |\mu_{eg}|^6 \sum_{mnkluv} B_m \langle n|m\rangle\langle n|k\rangle\langle l|k\rangle\langle l|u\rangle\langle v|u\rangle\langle v|m\rangle \times L_{en,gm}(t_1) L_{gk,gm}(t_2) L_{el,gm}(t_3) L_{gu,gm}(t_4) L_{ev,gm}(t_5), \quad \text{(C.1)}$$

$$R_2^{(5)}(t_1,t_2,t_3,t_4,t_5) = |\mu_{eg}|^6 \sum_{mnkluv} B_m \langle n|m\rangle\langle n|k\rangle\langle l|m\rangle\langle l|u\rangle\langle v|k\rangle\langle v|u\rangle \times L_{en,gm}(t_1) L_{gk,gm}(t_2) L_{gk,el}(t_3) L_{gk,gu}(t_4) L_{ev,gu}(t_5), \quad \text{(C.2)}$$

$$R_3^{(5)}(t_1,t_2,t_3,t_4,t_5) = |\mu_{eg}|^6 \sum_{mnkluv} B_m \langle n|m\rangle\langle n|k\rangle\langle l|k\rangle\langle l|u\rangle\langle v|m\rangle\langle v|u\rangle \times L_{gm,en}(t_1) L_{gm,gk}(t_2) L_{gm,el}(t_3) L_{gm,gu}(t_4) L_{ev,gu}(t_5), \quad \text{(C.3)}$$

$$R_4^{(5)}(t_1,t_2,t_3,t_4,t_5) = |\mu_{eg}|^6 \sum_{mnkluv} B_m \langle n|m\rangle\langle n|k\rangle\langle l|m\rangle\langle l|u\rangle\langle v|u\rangle\langle v|k\rangle \times L_{gm,en}(t_1) L_{gm,gk}(t_2) L_{el,gk}(t_3) L_{gu,gk}(t_4) L_{ev,gk}(t_5), \quad \text{(C.4)}$$

$$R_5^{(5)}(t_1,t_2,t_3,t_4,t_5) = |\mu_{eg}|^6 \sum_{mnkluv} B_m \langle n|m\rangle\langle k|m\rangle\langle n|l\rangle\langle u|l\rangle\langle k|v\rangle\langle u|v\rangle \times L_{en,gm}(t_1) L_{en,ek}(t_2) L_{gl,ek}(t_3) L_{eu,ek}(t_4) L_{eu,gv}(t_5), \quad \text{(C.5)}$$

$$R_6^{(5)}(t_1,t_2,t_3,t_4,t_5) = |\mu_{eg}|^6 \sum_{mnkluv} B_m \langle n|m\rangle\langle k|m\rangle\langle k|l\rangle\langle u|l\rangle\langle u|v\rangle\langle n|v\rangle \times L_{en,gm}(t_1) L_{en,ek}(t_2) L_{en,gl}(t_3) L_{en,eu}(t_4) L_{en,gv}(t_5), \quad \text{(C.6)}$$

$$R_7^{(5)}(t_1,t_2,t_3,t_4,t_5) = |\mu_{eg}|^6 \sum_{mnkluv} B_m \langle n|m\rangle\langle k|m\rangle\langle k|l\rangle\langle u|l\rangle\langle n|v\rangle\langle u|v\rangle \times L_{gm,en}(t_1) L_{ek,en}(t_2) L_{gl,en}(t_3) L_{eu,en}(t_4) L_{eu,gv}(t_5), \quad \text{(C.7)}$$

$$R_8^{(5)}(t_1,t_2,t_3,t_4,t_5) = |\mu_{eg}|^6 \sum_{mnkluv} B_m \langle n|m\rangle\langle k|m\rangle\langle n|l\rangle\langle u|l\rangle\langle u|v\rangle\langle k|v\rangle \times L_{gm,en}(t_1) L_{ek,en}(t_2) L_{ek,gl}(t_3) L_{ek,eu}(t_4) L_{ek,gv}(t_5), \quad \text{(C.8)}$$

$$R_9^{(5)}(t_1,t_2,t_3,t_4,t_5) = |\mu_{eg}|^6 \sum_{mnkluv} B_m \langle n|m\rangle\langle n|k\rangle\langle l|k\rangle\langle u|m\rangle\langle u|v\rangle\langle l|v\rangle \times L_{en,gm}(t_1) L_{gk,gm}(t_2) L_{el,gm}(t_3) L_{el,eu}(t_4) L_{el,gv}(t_5), \quad \text{(C.9)}$$

$$R_{10}^{(5)}(t_1,t_2,t_3,t_4,t_5) = |\mu_{eg}|^6 \sum_{mnkluv} B_m \langle n|m\rangle\langle n|k\rangle\langle l|m\rangle\langle u|k\rangle\langle l|v\rangle\langle u|v\rangle \times L_{en,gm}(t_1) L_{gk,gm}(t_2) L_{gk,el}(t_3) L_{eu,el}(t_4) L_{eu,gv}(t_5), \quad \text{(C.10)}$$

$$R_{11}^{(5)}(t_1,t_2,t_3,t_4,t_5) = |\mu_{eg}|^6 \sum_{mnkluv} B_m \langle n|m\rangle\langle n|k\rangle\langle l|m\rangle\langle u|k\rangle\langle u|v\rangle\langle l|v\rangle \times L_{gm,en}(t_1) L_{gm,gk}(t_2) L_{el,gk}(t_3) L_{el,eu}(t_4) L_{el,gv}(t_5), \quad \text{(C.11)}$$

$$R_{12}^{(5)}(t_1,t_2,t_3,t_4,t_5) = |\mu_{eg}|^6 \sum_{mnkluv} B_m \langle n|m\rangle\langle n|k\rangle\langle l|k\rangle\langle u|m\rangle\langle l|v\rangle\langle u|v\rangle \times L_{gm,en}(t_1) L_{gm,gk}(t_2) L_{gm,el}(t_3) L_{eu,el}(t_4) L_{eu,gv}(t_5), \quad \text{(C.12)}$$

$$R_{13}^{(5)}(t_1,t_2,t_3,t_4,t_5) = |\mu_{eg}|^6 \sum_{mnkluv} B_m \langle n|m\rangle\langle k|m\rangle\langle n|l\rangle\langle k|u\rangle\langle v|l\rangle\langle v|u\rangle \times L_{en,gm}(t_1) L_{en,ek}(t_2) L_{gl,ek}(t_3) L_{gl,gu}(t_4) L_{ev,gu}(t_5), \quad \text{(C.13)}$$

$$R_{14}^{(5)}(t_1,t_2,t_3,t_4,t_5) = |\mu_{eg}|^6 \sum_{mnkluv} B_m \langle n|m\rangle\langle k|m\rangle\langle k|l\rangle\langle n|u\rangle\langle v|u\rangle\langle v|l\rangle \times L_{en,gm}(t_1) L_{en,ek}(t_2) L_{en,gl}(t_3) L_{gu,gl}(t_4) L_{ev,gl}(t_5), \quad \text{(C.14)}$$

$$R_{15}^{(5)}(t_1,t_2,t_3,t_4,t_5) = |\mu_{eg}|^6 \sum_{mnkluv} B_m \langle n|m\rangle\langle k|m\rangle\langle k|l\rangle\langle n|u\rangle\langle v|l\rangle\langle v|u\rangle \times L_{gm,en}(t_1) L_{ek,en}(t_2) L_{gl,en}(t_3) L_{gl,gu}(t_4) L_{ev,gu}(t_5), \quad \text{(C.15)}$$

and

$$R_{16}^{(5)}(t_1,t_2,t_3,t_4,t_5) = |\mu_{eg}|^6 \sum_{mnkluv} B_m \langle n|m\rangle\langle k|m\rangle\langle n|l\rangle\langle k|u\rangle\langle v|u\rangle\langle v|l\rangle \times L_{gm,en}(t_1) L_{ek,en}(t_2) L_{ek,gl}(t_3) L_{gu,gl}(t_4) L_{ev,gl}(t_5). \quad \text{(C.16)}$$

In the above equations, the propagation functions corresponding to vibronic (in t_1, t_3, or t_5) and purely vibrational (in t_2 or t_4) coherences are respectively given by[2]

$$L_{em,gn}(t) = \theta(t)\exp\left(-i\omega_{eg}t - i\omega_{mn}t - \Gamma_{eg}t\right) \quad \text{(C.17)}$$

and

$$L_{gm,gn}(t) = \theta(t)\exp(-i\omega_{mn}t - \Gamma_{vib}t) \tag{C.18}$$

where $\theta(t)$ is a Heaviside step function. Equation C.17 assumes that electronic dephasing is fast compared to vibrational dephasing (i.e. $\Gamma_{eg} >> \Gamma_{vib}$).

We next convolute the response functions and electric fields to obtain the 16 components of the fifth-order polarization. The component of the fifth-order polarization corresponding to the R_1 term is given by

$$\begin{aligned} P_1^{(5)}(t) = N\left(\frac{i}{\hbar}\right)^5 \int_0^\infty dt_5 \int_0^\infty dt_4 \int_0^\infty dt_3 \int_0^\infty dt_2 \int_0^\infty dt_1 R_1^{(5)}(t_1,t_2,t_3,t_4,t_5) E_{RP}(t-t_5) \\ \times E_{RP}^*(t+\tau_2-t_5-t_4) E_{St}(t+\tau_2-t_5-t_4-t_3) \\ \times E_{AP}^*(t+\tau_1+\tau_2-t_5-t_4-t_3-t_2) E_{AP}(t+\tau_1+\tau_2-t_5-t_4-t_3-t_2-t_1) \end{aligned} \tag{C.19}$$

where N is the number density, τ_j are the pulse delay times defined in Chapter 6, and subscripts are used to specify the three types of laser pulses (actinic pump, Raman pump, and Stokes pulses). Attainment of analytic expressions is facilitated by use of double-sided exponential electric field envelopes

$$E_j(t) = \xi_j \exp(-i\omega_j t - \Lambda_j |t|) \tag{C.20}$$

where ξ_j is the (real) electric field amplitude, Λ_j is the HWHM spectral width, and ω_j is the carrier frequency. The polarization component, $P_1^{(5)}(t)$, can now be rewritten as

$$P_1^{(5)}(t) = N\xi_{AP}^2\xi_{RP}^2\xi_{St}\exp\left(-i\omega_{St}t\right)\left(\frac{i}{\hbar}\right)^5\int_0^\infty dt_5\int_0^\infty dt_4\int_0^\infty dt_3\int_0^\infty dt_2\int_0^\infty dt_1 R_1^{(5)}\left(t_1,t_2,t_3,t_4,t_5\right)$$
$$\times\exp\left[i\omega_{AP}t_1 + i\omega_{St}t_3 + i\left(\omega_{St}-\omega_{RP}\right)t_4 + i\omega_{St}t_5\right]$$
$$\times\exp\left[-\Lambda_{RP}\left|t-t_5\right| - \Lambda_{RP}\left|t+\tau_2-t_5-t_4\right| - \Lambda_{St}\left|t+\tau_2-t_5-t_4-t_3\right|\right]$$
$$\times\exp\left[-\Lambda_{AP}\left|t+\tau_1+\tau_2-t_5-t_4-t_3-t_2\right| - \Lambda_{AP}\left|t+\tau_1+\tau_2-t_5-t_4-t_3-t_2-t_1\right|\right] \quad \text{. (C.21)}$$

The 65 fs actinic pump pulse employed in this work cannot initiate vibrational coherences in the high-frequency, bond-stretching modes in the delay, τ_1. Therefore, we use a "doorway wavepacket" to filter vibrational coherences with frequencies that exceed the bandwidth of the actinic pump pulse (i.e. this assumption is valid in the limit of non-overlapping actinic pump and Stokes pulses).[2] We introduce the change of variables, $t_2 = \tau_1 + t'$, to obtain

$$P_1^{(5)}(t) = N\xi_{AP}^2\xi_{RP}^2\xi_{St}\exp\left(-i\omega_{St}t\right)\left(\frac{i}{\hbar}\right)^5\int_0^\infty dt_5\int_0^\infty dt_4\int_0^\infty dt_3\int_{-\infty}^\infty dt'\int_0^\infty dt_1 R_1^{(5)}\left(t_1,\tau_1+t',t_3,t_4,t_5\right)$$
$$\times\exp\left[i\omega_{AP}t_1 + i\omega_{St}t_3 + i\left(\omega_{St}-\omega_{RP}\right)t_4 + i\omega_{St}t_5\right]$$
$$\times\exp\left[-\Lambda_{RP}\left|t\right| - \Lambda_{RP}\left|t+\tau_2-t_4\right| - \Lambda_{St}\left|t+\tau_2-t_4\right|\right] \quad \text{(C.22)}$$
$$\times\exp\left[-2\Lambda_{AP}\left|t'\right|\right]$$

where we have eliminated t_1 , t_3, and t_5 from the arguments of the pulse envelopes under the assumption that the pulse durations are long compared to the electronic dephasing time. Since we must carefully bookkeep on the phase-angle of the polarization, it should be noted that the infinite limits of the integral over t' yield a *real* Lorentzian function. We next introduce the approximation $t_4 \approx t + \tau_2$

$$P_1^{(5)}(t) = N\xi_{AP}^2\xi_{RP}^2\xi_{St}\theta\left(t+\tau_2\right)\left(\frac{i}{\hbar}\right)^5\int_0^\infty dt_5\int_0^\infty dt_3\int_{-\infty}^\infty dt'\int_0^\infty dt_1 R_1^{(5)}\left(t_1,\tau_1+t',t_3,t+\tau_2,t_5\right) \quad \text{(C.23)}$$
$$\times\exp\left[i\omega_{AP}t_1 + i\omega_{St}t_3 + i\left(\omega_{St}-\omega_{RP}\right)\tau_2 - i\omega_{RP}t + i\omega_{St}t_5 - \Lambda_{RP}\left|t\right| - 2\Lambda_{AP}\left|t'\right|\right]$$

under the assumption that $\Gamma_{eg} >> \Gamma_{vib}$. Evaluation of the four integrals in Equation C.23 yields

$$\begin{aligned} P_1^{(5)}(t) = & \frac{N\xi_{AP}^2\xi_{RP}^2\xi_{St}\left|\mu_{eg}\right|^6}{\hbar^5}\theta(t+\tau_2)\sum_{mnkluv} B_m \langle n|m\rangle\langle n|k\rangle\langle l|k\rangle\langle l|u\rangle\langle v|u\rangle\langle v|m\rangle \\ & \times L_{en,gm}(\omega_{AP}) D_{gk,gm}(\tau_1) L_{el,gm}(\omega_{St}) L_{ev,gm}(\omega_{St}) \\ & \times \exp\left[i(\omega_{St} - \omega_{RP} - \omega_{um})\tau_2 - i(\omega_{RP} + \omega_{um})t - \Gamma_{vib}(t+\tau_2) - \Lambda_{RP}|t| \right] \end{aligned} \quad \text{(C.24)}$$

where the line shape of the electronic resonance is given by

$$L_{en,gm}(\omega) = -i\int_0^\infty L_{en,gm}(t)\exp(i\omega t)\,dt = \frac{1}{\omega - \omega_{eg} - \omega_{nm} + i\Gamma_{eg}} \quad \text{(C.25)}$$

and the doorway wavepacket induced by the actinic pump pulse is written as

$$D_{gk,gm}(\tau_1) = L_{gk,gm}(\tau_1)\int_{-\infty}^{\infty} dt' \exp\left(-i\omega_{km}t' - \Gamma_{vib}|t'| - \Lambda_{AP}|t'|\right) = L_{gk,gm}(\tau_1)\frac{2\Lambda_{AP}}{\omega_{km}^2 + \Lambda_{AP}^2}. \quad \text{(C.26)}$$

The polarization component, $P_1^{(5)}(t)$, must be Fourier transformed to the frequency domain to account for dispersed detection. To this end, it is useful to consider the following integral

$$\begin{aligned} & i\int_{-\tau_2}^{\infty} dt\,\theta(t+\tau_2)\exp\left[i(\omega_t - \omega_{RP} - \omega_{um})t - \Gamma_{vib}t - \Lambda_{RP}|t| \right] \\ & = -i\int_0^{\tau_2} dt \exp\left[-i(\omega_t - \omega_{RP} - \omega_{um})t + \Gamma_{vib}t - \Lambda_{RP}t \right] \\ & \quad + i\int_0^{\infty} dt \exp\left[i(\omega_t - \omega_{RP} - \omega_{um})t - \Gamma_{vib}t - \Lambda_{RP}t \right] \end{aligned} \quad \text{(C.27)}$$

where ω_t is the frequency of light emission observed on the array detector. Evaluation of the sum of integrals in Equation C.27 yields

$$
\begin{aligned}
& i\int_{-\tau_2}^{\infty} dt\theta\left(t+\tau_2\right)\exp\left[i\left(\omega_t-\omega_{RP}-\omega_{um}\right)t-\Gamma_{vib}t-\Lambda_{RP}\left|t\right|\right] \\
&= i\frac{1-\exp\left[-i\left(\omega_t-\omega_{RP}-\omega_{um}\right)\tau_2+\Gamma_{vib}\tau_2-\Lambda_{RP}\tau_2\right]}{i\left(\omega_t-\omega_{RP}-\omega_{um}\right)-\Gamma_{vib}+\Lambda_{RP}} \\
&\quad -i\frac{1}{i\left(\omega_t-\omega_{RP}-\omega_{um}\right)-\Gamma_{vib}-\Lambda_{RP}}
\end{aligned}
\tag{C.28}
$$

where $\omega_t-\omega_{RP}$ is the Raman shift. The first and third terms in Equation C.28 cancel each other when $\Gamma_{vib}<<\Lambda_{RP}$ (i.e. a reasonable approximation for the present experimental conditions) and we obtain

$$
\begin{aligned}
& i\int_{-\tau_2}^{\infty} dt\theta\left(t+\tau_2\right)\exp\left[i\left(\omega_t-\omega_{RP}-\omega_{um}\right)t-\Gamma_{vib}t-\Lambda_{RP}\left|t\right|\right] \\
&\approx -\frac{\exp\left[-i\left(\omega_t-\omega_{RP}-\omega_{um}\right)\tau_2-\left(\Lambda_{RP}-\Gamma_{vib}\right)\tau_2\right]}{\left(\omega_t-\omega_{RP}-\omega_{um}\right)+i\left(\Gamma_{vib}-\Lambda_{RP}\right)} \quad .
\end{aligned}
\tag{C.29}
$$

Equation C.29 reveals a desirable line narrowing effect that originates in the difference between Γ_{vib} and Λ_{RP} in the denominator (i.e. the line widths of the vibrational resonances can be narrower than the bandwidth of the Raman pump). The above equations can be combined to obtain

$$
\begin{aligned}
P_1^{(5)}(\omega_t) = i\frac{N\xi_{AP}^2\xi_{RP}^2\xi_{St}\left|\mu_{eg}\right|^6}{\hbar^5}\sum_{mnkluv} B_m\left\langle n\middle|m\right\rangle\left\langle n\middle|k\right\rangle\left\langle l\middle|k\right\rangle\left\langle l\middle|u\right\rangle\left\langle v\middle|u\right\rangle\left\langle v\middle|m\right\rangle \\
\times L_{en,gm}\left(\omega_{AP}\right)D_{gk,gm}\left(\tau_1\right)L_{el,gm}\left(\omega_t\right)J_{gu,gm}\left(\omega_t-\omega_{RP}\right)L_{ev,gm}\left(\omega_t\right)
\end{aligned}
\tag{C.30}
$$

where

$$
D_{gk,gm}\left(\tau_1\right)=\frac{2\Lambda_{AP}}{\omega_{km}^2+\Lambda_{AP}^2}\theta\left(\tau_1\right)\exp\left(-i\omega_{km}\tau_1-\Gamma_{vib}\tau_1\right), \tag{C.31}
$$

$$L_{en,gm}(\omega)=\frac{1}{\omega-\omega_{eg}-\omega_{nm}+i\Gamma_{eg}}, \tag{C.32}$$

and

$$J_{gu,gm}(\omega_t-\omega_{RP})=\frac{\exp(-\Lambda_{RP}\tau_2)}{(\omega_t-\omega_{RP}-\omega_{um})+i(\Gamma_{vib}-\Lambda_{RP})}. \tag{C.33}$$

This expression sets ω_{St} equal to ω_t under the assumption of vibrationally resonant conditions, $\omega_{St}-\omega_{RP}\approx\omega_{um}$ and $\omega_t-\omega_{RP}\approx\omega_{um}$. We obtain the following 15 polarization components by following the same procedure

$$\begin{aligned}P_2^{(5)}(\omega_t)=i\frac{N\xi_{AP}^2\xi_{RP}^2\xi_{St}\left|\mu_{eg}\right|^6}{\hbar^5}\sum_{mnkluv}B_m\langle n|m\rangle\langle n|k\rangle\langle l|m\rangle\langle l|u\rangle\langle v|k\rangle\langle v|u\rangle \\ \times L_{en,gm}(\omega_{AP})D_{gk,gm}(\tau_1)L_{gk,el}(-\omega_{RP})J_{gk,gu}(\omega_t-\omega_{RP})L_{ev,gu}(\omega_t)\end{aligned}, \tag{C.34}$$

$$\begin{aligned}P_3^{(5)}(\omega_t)=i\frac{N\xi_{AP}^2\xi_{RP}^2\xi_{St}\left|\mu_{eg}\right|^6}{\hbar^5}\sum_{mnkluv}B_m\langle n|m\rangle\langle n|k\rangle\langle l|k\rangle\langle l|u\rangle\langle v|m\rangle\langle v|u\rangle \\ \times L_{gm,en}(-\omega_{AP})D_{gm,gk}(\tau_1)L_{gm,el}(-\omega_{RP})J_{gm,gu}(\omega_t-\omega_{RP})L_{ev,gu}(\omega_t)\end{aligned}, \tag{C.35}$$

$$\begin{aligned}P_4^{(5)}(\omega_t)=i\frac{N\xi_{AP}^2\xi_{RP}^2\xi_{St}\left|\mu_{eg}\right|^6}{\hbar^5}\sum_{mnkluv}B_m\langle n|m\rangle\langle n|k\rangle\langle l|m\rangle\langle l|u\rangle\langle v|u\rangle\langle v|k\rangle \\ \times L_{gm,en}(-\omega_{AP})D_{gm,gk}(\tau_1)L_{el,gk}(\omega_t)J_{gu,gk}(\omega_t-\omega_{RP})L_{ev,gk}(\omega_t)\end{aligned}, \tag{C.36}$$

$$\begin{aligned}P_5^{(5)}(\omega_t)=i\frac{N\xi_{AP}^2\xi_{RP}^2\xi_{St}\left|\mu_{eg}\right|^6}{\hbar^5}\sum_{mnkluv}B_m\langle n|m\rangle\langle k|m\rangle\langle n|l\rangle\langle u|l\rangle\langle k|v\rangle\langle u|v\rangle \\ \times L_{en,gm}(\omega_{AP})D_{en,ek}(\tau_1)L_{gl,ek}(-\omega_{RP})J_{eu,ek}(\omega_t-\omega_{RP})L_{eu,gv}(\omega_t)\end{aligned}, \tag{C.37}$$

$$P_6^{(5)}(\omega_t) = i\frac{N\xi_{AP}^2\xi_{RP}^2\xi_{St}\left|\mu_{eg}\right|^6}{\hbar^5}\sum_{mnkluv} B_m \langle n|m\rangle\langle k|m\rangle\langle k|l\rangle\langle u|l\rangle\langle u|v\rangle\langle n|v\rangle, \\ \times L_{en,gm}(\omega_{AP}) D_{en,ek}(\tau_1) L_{en,gl}(\omega_t) J_{en,eu}(\omega_t - \omega_{RP}) L_{en,gv}(\omega_t) \tag{C.38}$$

$$P_7^{(5)}(\omega_t) = i\frac{N\xi_{AP}^2\xi_{RP}^2\xi_{St}\left|\mu_{eg}\right|^6}{\hbar^5}\sum_{mnkluv} B_m \langle n|m\rangle\langle k|m\rangle\langle k|l\rangle\langle u|l\rangle\langle n|v\rangle\langle u|v\rangle, \\ \times L_{gm,en}(-\omega_{AP}) D_{ek,en}(\tau_1) L_{gl,en}(-\omega_{RP}) J_{eu,en}(\omega_t - \omega_{RP}) L_{eu,gv}(\omega_t) \tag{C.39}$$

$$P_8^{(5)}(\omega_t) = i\frac{N\xi_{AP}^2\xi_{RP}^2\xi_{St}\left|\mu_{eg}\right|^6}{\hbar^5}\sum_{mnkluv} B_m \langle n|m\rangle\langle k|m\rangle\langle n|l\rangle\langle u|l\rangle\langle u|v\rangle\langle k|v\rangle, \\ \times L_{gm,en}(-\omega_{AP}) D_{ek,en}(\tau_1) L_{ek,gl}(\omega_t) J_{ek,eu}(\omega_t - \omega_{RP}) L_{ek,gv}(\omega_t) \tag{C.40}$$

$$P_9^{(5)}(\omega_t) = i\frac{N\xi_{AP}^2\xi_{RP}^2\xi_{St}\left|\mu_{eg}\right|^6}{\hbar^5}\sum_{mnkluv} B_m \langle n|m\rangle\langle n|k\rangle\langle l|k\rangle\langle u|m\rangle\langle u|v\rangle\langle l|v\rangle, \\ \times L_{en,gm}(\omega_{AP}) D_{gk,gm}(\tau_1) L_{el,gm}(\omega_t) J_{el,eu}(\omega_t - \omega_{RP}) L_{el,gv}(\omega_t) \tag{C.41}$$

$$P_{10}^{(5)}(\omega_t) = i\frac{N\xi_{AP}^2\xi_{RP}^2\xi_{St}\left|\mu_{eg}\right|^6}{\hbar^5}\sum_{mnkluv} B_m \langle n|m\rangle\langle n|k\rangle\langle l|m\rangle\langle u|k\rangle\langle l|v\rangle\langle u|v\rangle, \\ \times L_{en,gm}(\omega_{AP}) D_{gk,gm}(\tau_1) L_{gk,el}(-\omega_{RP}) J_{eu,el}(\omega_t - \omega_{RP}) L_{eu,gv}(\omega_t) \tag{C.42}$$

$$P_{11}^{(5)}(\omega_t) = i\frac{N\xi_{AP}^2\xi_{RP}^2\xi_{St}\left|\mu_{eg}\right|^6}{\hbar^5}\sum_{mnkluv} B_m \langle n|m\rangle\langle n|k\rangle\langle l|m\rangle\langle u|k\rangle\langle u|v\rangle\langle l|v\rangle, \\ \times L_{gm,en}(-\omega_{AP}) D_{gm,gk}(\tau_1) L_{el,gk}(\omega_t) J_{el,eu}(\omega_t - \omega_{RP}) L_{el,gv}(\omega_t) \tag{C.43}$$

$$P_{12}^{(5)}(\omega_t) = i\frac{N\xi_{AP}^2\xi_{RP}^2\xi_{St}\left|\mu_{eg}\right|^6}{\hbar^5}\sum_{mnkluv} B_m \langle n|m\rangle\langle n|k\rangle\langle l|k\rangle\langle u|m\rangle\langle l|v\rangle\langle u|v\rangle, \\ \times L_{gm,en}(-\omega_{AP}) D_{gm,gk}(\tau_1) L_{gm,el}(-\omega_{RP}) J_{eu,el}(\omega_t - \omega_{RP}) L_{eu,gv}(\omega_t) \tag{C.44}$$

$$P_{13}^{(5)}(\omega_t) = i\frac{N\xi_{AP}^2\xi_{RP}^2\xi_{St}\left|\mu_{eg}\right|^6}{\hbar^5}\sum_{mnkluv} B_m \langle n|m\rangle\langle k|m\rangle\langle n|l\rangle\langle k|u\rangle\langle v|l\rangle\langle v|u\rangle, \\ \times L_{en,gm}(\omega_{AP}) D_{en,ek}(\tau_1) L_{gl,ek}(-\omega_{RP}) J_{gl,gu}(\omega_t - \omega_{RP}) L_{ev,gu}(\omega_t) \tag{C.45}$$

$$P_{14}^{(5)}(\omega_t) = i\frac{N\xi_{AP}^2\xi_{RP}^2\xi_{St}\left|\mu_{eg}\right|^6}{\hbar^5}\sum_{mnkluv} B_m \langle n|m\rangle\langle k|m\rangle\langle k|l\rangle\langle n|u\rangle\langle v|u\rangle\langle v|l\rangle, \\ \times L_{en,gm}(\omega_{AP}) D_{en,ek}(\tau_1) L_{en,gl}(\omega_t) J_{gu,gl}(\omega_t - \omega_{RP}) L_{ev,gl}(\omega_t) \tag{C.46}$$

$$P_{15}^{(5)}(\omega_t) = i\frac{N\xi_{AP}^2\xi_{RP}^2\xi_{St}\left|\mu_{eg}\right|^6}{\hbar^5}\sum_{mnkluv} B_m \langle n|m\rangle\langle k|m\rangle\langle k|l\rangle\langle n|u\rangle\langle v|l\rangle\langle v|u\rangle, \\ \times L_{gm,en}(-\omega_{AP}) D_{ek,en}(\tau_1) L_{gl,en}(-\omega_{RP}) J_{gl,gu}(\omega_t - \omega_{RP}) L_{ev,gu}(\omega_t) \tag{C.47}$$

and

$$P_{16}^{(5)}(\omega_t) = i\frac{N\xi_{AP}^2\xi_{RP}^2\xi_{St}\left|\mu_{eg}\right|^6}{\hbar^5}\sum_{mnkluv} B_m \langle n|m\rangle\langle k|m\rangle\langle n|l\rangle\langle k|u\rangle\langle v|u\rangle\langle v|l\rangle. \\ \times L_{gm,en}(-\omega_{AP}) D_{ek,en}(\tau_1) L_{ek,gl}(\omega_t) J_{gu,gl}(\omega_t - \omega_{RP}) L_{ev,gl}(\omega_t) \tag{C.48}$$

The direct fifth-order signal field is expressed in terms of these polarization components as

$$E_{direct}^{(5)}(\omega_t) = \frac{1}{7}\left(\frac{i\omega_t l}{2\varepsilon_0 n(\omega_t) c}\right)\sum_{m=1}^{16} P_m^{(5)}(\omega_t)\,\mathrm{sinc}\left(\frac{\Delta k_{direct}^{(5)} l}{2}\right)\exp\left(i\frac{\Delta k_{direct}^{(5)} l}{2}\right) \tag{C.49}$$

where the factor of 1/7 represents the orientational average for all-parallel electric field polarizations[3]; and the wavevector mismatch, $\Delta k_{direct}^{(5)}$, is given for the five and four beam geometries in Tables C.1 and C.2.

C.3. Derivation of Formula for Third-Order Cascaded Signal Field

The third-order response functions needed to compute cascaded nonlinearities can be derived under the same approximations outlined above. Feynman diagrams for third-order nonlinearities are presented in Figure C.3. Response functions corresponding to these diagrams can be written as

$$R_1^{(3)}(t_1,t_2,t_3) = |\mu_{eg}|^4 \sum_{mnkl} B_m \langle n|m\rangle\langle k|m\rangle\langle k|l\rangle\langle n|l\rangle L_{en,gm}(t_1) L_{en,ek}(t_2) L_{en,gl}(t_3), \quad \text{(C.50)}$$

$$R_2^{(3)}(t_1,t_2,t_3) = |\mu_{eg}|^4 \sum_{mnkl} B_m \langle n|m\rangle\langle k|m\rangle\langle n|l\rangle\langle k|l\rangle L_{gm,en}(t_1) L_{ek,en}(t_2) L_{ek,gl}(t_3), \quad \text{(C.51)}$$

$$R_3^{(3)}(t_1,t_2,t_3) = |\mu_{eg}|^4 \sum_{mnkl} B_m \langle n|m\rangle\langle n|k\rangle\langle l|k\rangle\langle l|m\rangle L_{en,gm}(t_1) L_{gk,gm}(t_2) L_{el,gm}(t_3), \quad \text{(C.52)}$$

and

$$R_4^{(3)}(t_1,t_2,t_3) = |\mu_{eg}|^4 \sum_{mnkl} B_m \langle n|m\rangle\langle n|k\rangle\langle l|m\rangle\langle l|k\rangle L_{gm,en}(t_1) L_{gm,gk}(t_2) L_{el,gk}(t_3). \quad \text{(C.53)}$$

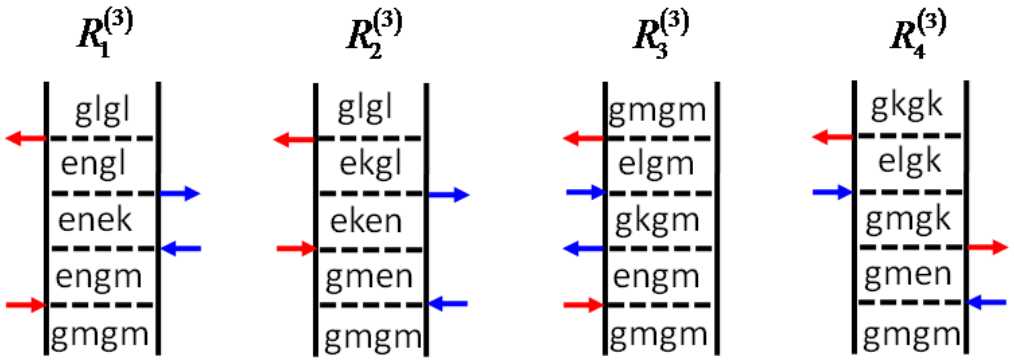

Figure C.3. Feynman diagrams associated with the direct third-order CSRS response. The indices, g and e, represent the ground and excited electronic states whereas dummy indices

(m, n, k, and l) denote vibrational levels. Blue and red arrows represent the Raman pump and Stokes pulses, respectively.

C.3.1 Direct Coherent Stokes Raman Scattering (CSRS) Signal Field Obtained with the Phase Matching Condition $k_3 - k_4 + k_5$

We first consider the direct third-order CSRS signal field, which is compared to the direct fifth-order signal field in the four-beam geometry in Section 6.3.4 of Chapter 6. The CSRS polarization component associated with the term, $F_1\left(t_1,t_2,t_3\right)$, is given by

$$P_{1,CSRS}^{(3)}(t)=N\left(\frac{i}{\hbar}\right)^3\int_0^\infty dt_3\int_0^\infty dt_2\int_0^\infty dt_1 R_1^{(3)}\left(t_1,t_2,t_3\right)E_{RP}(t-t_5)E_{RP}^*(t+\tau_2-t_3-t_2)\cdot \\ \times E_{St}(t+\tau_2-t_3-t_2-t_1) \tag{C.54}$$

Application of the approximations and procedure outlined above yields

$$P_{1,CSRS}^{(3)}(\omega_t)=-\frac{N\xi_{RP}^2\xi_{St}\left|\mu_{eg}\right|^4}{\hbar^3}\sum_{mnkl}B_m\left\langle n\middle|m\right\rangle\left\langle k\middle|m\right\rangle\left\langle k\middle|l\right\rangle\left\langle n\middle|l\right\rangle\cdot \\ \times L_{en,gm}\left(\omega_t\right)J_{en,ek}\left(\omega_t-\omega_{RP}\right)L_{en,gl}\left(\omega_t\right) \tag{C.55}$$

The polarization components for the three remaining terms are

$$P_{2,CSRS}^{(3)}(\omega_t)=-\frac{N\xi_{RP}^2\xi_{St}\left|\mu_{eg}\right|^4}{\hbar^3}\sum_{mnkl}B_m\left\langle n\middle|m\right\rangle\left\langle k\middle|m\right\rangle\left\langle n\middle|l\right\rangle\left\langle k\middle|l\right\rangle, \\ \times L_{gm,en}\left(-\omega_{RP}\right)J_{ek,en}\left(\omega_t-\omega_{RP}\right)L_{ek,gl}\left(\omega_t\right) \tag{C.56}$$

$$P_{3,CSRS}^{(3)}(\omega_t)=-\frac{N\xi_{RP}^2\xi_{St}\left|\mu_{eg}\right|^4}{\hbar^3}\sum_{mnkl}B_m\left\langle n\middle|m\right\rangle\left\langle n\middle|k\right\rangle\left\langle l\middle|k\right\rangle\left\langle l\middle|m\right\rangle, \\ \times L_{en,gm}\left(\omega_t\right)J_{gk,gm}\left(\omega_t-\omega_{RP}\right)L_{el,gm}\left(\omega_t\right) \tag{C.57}$$

and

$$P_{4,CSRS}^{(3)}(\omega_t) = -\frac{N\xi_{RP}^2\xi_{St}\left|\mu_{eg}\right|^4}{\hbar^3}\sum_{mnkl} B_m \langle n|m\rangle\langle n|k\rangle\langle l|m\rangle\langle l|k\rangle \cdot \times L_{gm,en}(-\omega_{RP}) J_{gm,gk}(\omega_t - \omega_{RP}) L_{el,gk}(\omega_t) \quad \text{(C.58)}$$

The third-order CSRS signal field is given by

$$E_{CSRS}^{(3)}(\omega_t) = \frac{1}{5}\left(\frac{i\omega_t l}{2\varepsilon_0 n(\omega_t)c}\right)\sum_{m=1}^{4} P_{m,CSRS}^{(3)}(\omega_t)\,\mathrm{sinc}\left(\frac{\Delta k_{direct}^{(3)} l}{2}\right)\exp\left(i\frac{\Delta k_{direct}^{(3)} l}{2}\right) \quad \text{(C.59)}$$

where the factor of 1/5 represents the orientational average for all-parallel electric field polarizations at third-order in perturbation theory.[4]

C.3.2. Cascades with Intermediate Phase-Matching Conditions $k_1 - k_2 + k_5$ and $k_3 - k_4 + k_5$

In this section, we obtain an expression for the signal field generated by third-order cascades with intermediate phase-matching conditions $k_1 - k_2 + k_5$ and $k_3 - k_4 + k_5$, which we refer to as cascades 1 and 2, respectively. Figures C.4 and C.5 display all terms in the response functions associated with these types of cascades. The two processes essentially permute the type of nonlinearity that occurs on each molecule. A pump-probe-like response precedes a CSRS process in cascade 1, whereas the opposite is true for cascade 2. The polarization components for the CSRS process are given in Equations C.55-C.58. Therefore, we must first derive equations related to the pump-probe response (actinic pump and Stokes probe).

The pump-probe-like polarization component associated with the term, $F_1(t_1, t_2, t_3)$, is given by

$$P_{1,PP}^{(3)}(t) = N\left(\frac{i}{\hbar}\right)^3 \int_0^\infty dt_3 \int_0^\infty dt_2 \int_0^\infty dt_1 F_1\ (t_1,t_2,t_3)\, E_{St}(t-t_5) \times E_{AP}^*(t+\tau_2-t_3-t_2) E_{AP}(t+\tau_2-t_3-t_2-t_1) \quad \text{(C.60)}$$

Application of the procedure used to derive the fifth-order polarization components in Section C.2 yields

$$P_{1,PP}^{(3)}(\omega_t) = i\frac{N\xi_{AP}^2\xi_{St}\left|\mu_{eg}\right|^4}{\hbar^3}\sum_{mnkl} B_m \langle n|m\rangle\langle k|m\rangle\langle k|l\rangle\langle n|l\rangle \times L_{en,gm}(\omega_{AP}) D_{en,ek}(\tau_1) L_{en,gl}(\omega_t) \quad \text{(C.61)}$$

Under the same approximations, the polarization components for the three remaining terms are

$$P_{2,PP}^{(3)}(\omega_t) = i\frac{N\xi_{AP}^2\xi_{St}\left|\mu_{eg}\right|^4}{\hbar^3}\sum_{mnkl} B_m \langle n|m\rangle\langle k|m\rangle\langle n|l\rangle\langle k|l\rangle \times L_{gm,en}(-\omega_{AP}) D_{ek,en}(\tau_1) L_{ek,gl}(\omega_t) \quad \text{(C.62)}$$

$$P_{3,PP}^{(3)}(\omega_t) = i\frac{N\xi_{AP}^2\xi_{St}\left|\mu_{eg}\right|^4}{\hbar^3}\sum_{mnkl} B_m \langle n|m\rangle\langle n|k\rangle\langle l|k\rangle\langle l|m\rangle \times L_{en,gm}(\omega_{AP}) D_{gk,gm}(\tau_1) L_{el,gm}(\omega_t) \quad \text{(C.63)}$$

and

$$P_{4,PP}^{(3)}(\omega_t) = i\frac{N\xi_{AP}^2\xi_{St}\left|\mu_{eg}\right|^4}{\hbar^3}\sum_{mnkl} B_m \langle n|m\rangle\langle n|k\rangle\langle l|m\rangle\langle l|k\rangle \times L_{gm,en}(-\omega_{AP}) D_{gm,gk}(\tau_1) L_{el,gk}(\omega_t) \quad \text{(C.64)}$$

The total signal field generated by the two cascades can be written as

$$E_{cas}(\omega_t) = \frac{1}{25}\left(\frac{i\omega_t l}{2\varepsilon_0 n(\omega_t) c}\right)^2 \sum_{m=1}^{4}\sum_{n=1}^{4} \xi_{St}^{-1} P_{m,PP}^{(3)}(\omega_t) P_{n,CSRS}^{(3)}(\omega_t) f_{cas}(\Delta k_1, \Delta k_2) \quad \text{(C.65)}$$

where the phase matching function is given by

$$f_{cas}\left(\Delta k_1, \Delta k_2\right) = \sum_{j=1}^{2} \operatorname{sinc}\left(\frac{\Delta k_{jA} l}{2}\right) \operatorname{sinc}\left(\frac{\Delta k_{jB} l}{2}\right) \exp\left[i \frac{\left(\Delta k_{jA} + \Delta k_{jB}\right) l}{2}\right] \tag{C.66}$$

where the factor of 1/25 represents the product of orientational averages for all-parallel electric field polarizations at third-order in perturbation theory.[4] Wavevector mismatches, Δk_{jA} and Δk_{jB}, associated with all direct and cascaded processes are given in Tables C.2-C.4. In Tables C.2 and C.3 we consider the four and five-beam geometries employed in Chapter 6. In Table C.4, calculations are also carried out for a hypothetical three-beam geometry in which the actinic and Raman pump pulses cross at 6.9º and are bisected by the Stokes beam (i.e., traditional FSRS).

Table C.1. Parameters of Theoretical Model

Parameter	Value
$\left(\omega_{AP}-\omega_{eg}\right)/2\pi c$	varied
ω_{RP}	ω_{AP}
d	varied
Γ_{vib}/c	10 cm^{-1}
Γ_{eg}/c	750 cm^{-1}
μ_{eg}	8.8 D
N	1.2×10^{23} m^{-3}
$\omega_t/2\pi c$	23250 cm^{-1}
$n\left(\omega_t\right)$	1.39
l	0.22 mm

Table C.2. Wavevector Mismatch in the Five-Beam Geometry

Nonlinearity	$\Delta k_{direct}^{(n)}$ (cm^{-1})	Δk_A (cm^{-1})	Δk_B (cm^{-1})	[a],[b]Efficiency
Direct Fifth-Order (FSRS)	-215	------	------	0.123
Direct Third-Order (CSRS)	-430	------	------	0.050
Cascade #1 ($k_1 - k_2 + k_5$ intermediate)	------	-18	-197	0.069
Cascade #2 ($k_3 - k_4 + k_5$ intermediate)	------	-412	196	0.005

[a] The efficiency is computed using $\mathrm{sinc}\left(\frac{\Delta k_{direct}^{(n)} l}{2}\right)$ and $\mathrm{sinc}\left(\frac{\Delta k_A l}{2}\right)\mathrm{sinc}\left(\frac{\Delta k_B l}{2}\right)$ for direct and cascaded processes, respectively.
[b] Path length, l, is 0.022 cm.

Table C.3. Wavevector Mismatch in the Four-Beam Geometry

Nonlinearity	$\Delta k_{direct}^{(n)}$ (cm^{-1})	Δk_A (cm^{-1})	Δk_B (cm^{-1})	[a],[b]Efficiency
Direct Fifth-Order (FSRS)	-198	----------	----------	0.123
Direct Third-Order (CSRS)	-225	----------	----------	0.128
Cascade #1 ($k_1 - k_2 + k_5$ intermediate)	----------	-215	-215	0.015
Cascade #2 ($k_3 - k_4 + k_5$ intermediate)	----------	-215	-180	-0.002

[a] The efficiency is computed using $\mathrm{sinc}\left(\frac{\Delta k_{direct}^{(n)} l}{2}\right)$ and $\mathrm{sinc}\left(\frac{\Delta k_A l}{2}\right)\mathrm{sinc}\left(\frac{\Delta k_B l}{2}\right)$ for direct and cascaded processes, respectively.
[b] Path length, l, is 0.022 cm.

Table C.4. Wavevector Mismatch in a (Hypothetical) Three-Beam Geometry

Nonlinearity	$\Delta k_{direct}^{(n)}$ (cm^{-1})	Δk_A (cm^{-1})	Δk_B (cm^{-1})	[(a),(b)]Efficiency
Direct Fifth-Order (FSRS)	0	------	------	1.000
Direct Third-Order (CSRS)	0	------	------	1.000
Cascade #1 ($k_1 - k_2 + k_5$ intermediate)	------	0	0	1.000
Cascade #2 ($k_3 - k_4 + k_5$ intermediate)	------	0	0	1.000

[(a)] The efficiency is computed using $\mathrm{sinc}\left(\frac{\Delta k_{direct}^{(n)} l}{2}\right)$ and $\mathrm{sinc}\left(\frac{\Delta k_A l}{2}\right)\mathrm{sinc}\left(\frac{\Delta k_B l}{2}\right)$ for direct and cascaded processes, respectively.
[(b)] Path length, l, is 0.022 cm.

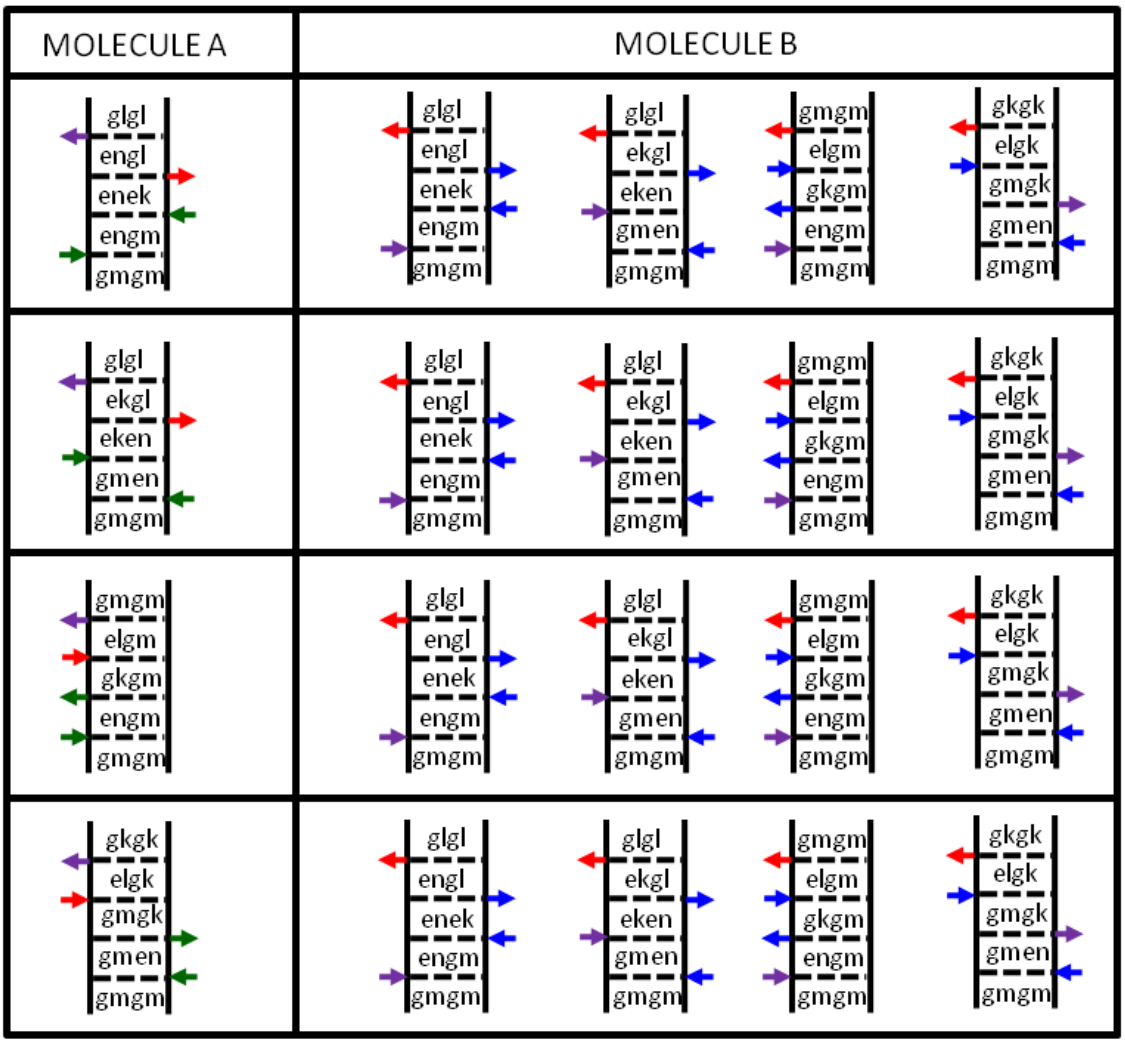

Figure C.4. Feynman diagrams associated with third-order cascades with the intermediate phase-matching condition $k_1 - k_2 + k_5$ (referred to as cascade #1 in text). The indices, g and e, represent the ground and excited electronic states, whereas dummy indices (m, n, k, l, u, and v) denote vibrational levels. Field-matter interactions are color-coded as follows: actinic pump is green; Raman pump is blue; Stokes is red; radiated signal field is red; the field radiated at the intermediate step in the cascade is purple. We restrict the response function to these terms (total of 16 products) under the assumption that the signal is primarily resonance-enhanced by the Soret band.

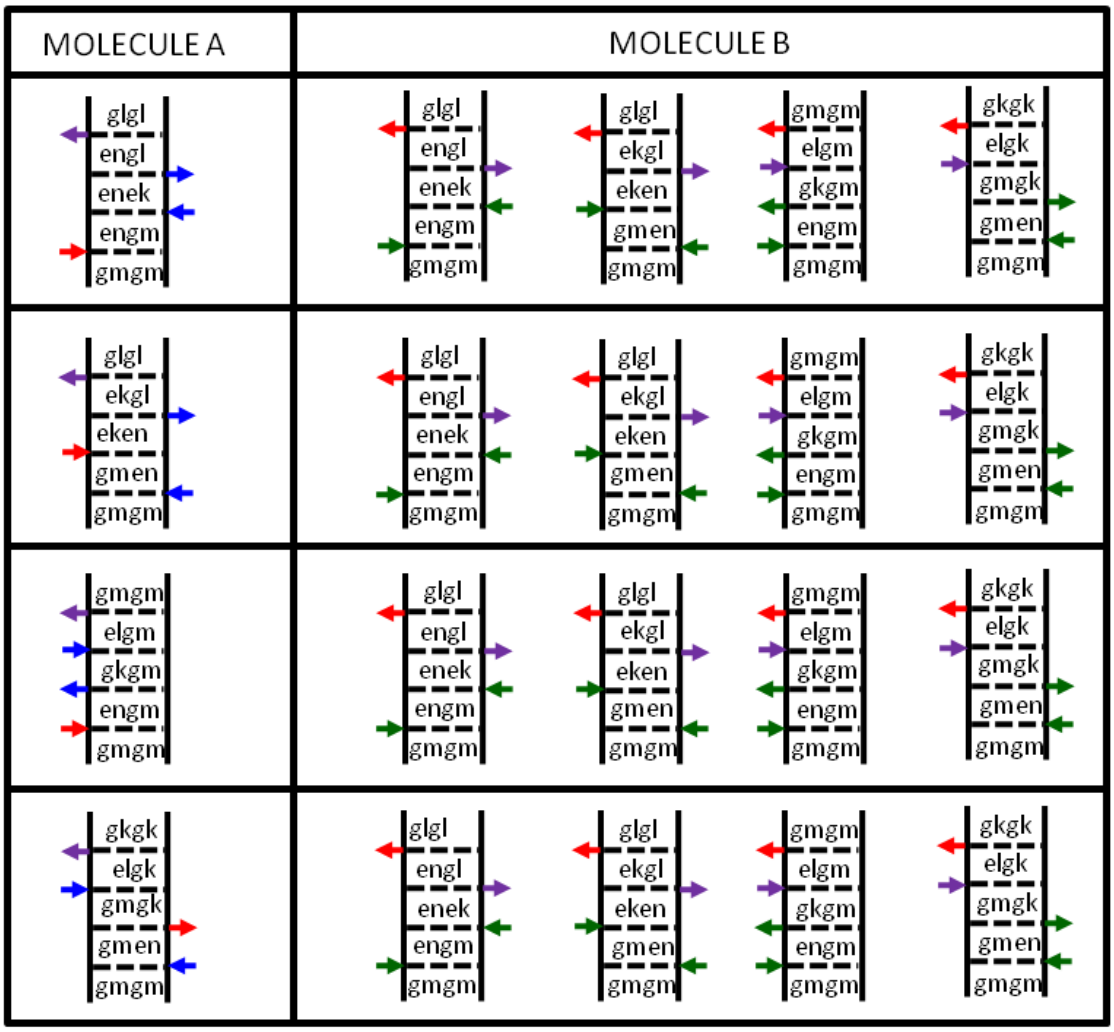

Figure C.5. Feynman diagrams associated with third-order cascades with the intermediate phase-matching condition $k_3 - k_4 + k_5$ (referred to as cascade #2 in text). The indices, g and e, represent the ground and excited electronic states, whereas dummy indices (m, n, k, l, u, and v) denote vibrational levels. Field-matter interactions are color-coded as follows: actinic pump is green; Raman pump is blue; Stokes is red; radiated signal field is red; the field radiated at the intermediate step in the cascade is purple. We restrict the response function to these terms (total of 16 products) under the assumption that the signal is primarily resonance-enhanced by the Soret band.

C.4. REFERENCES

(1) Myers, A. B.; Mathies, R. A.; Tannor, D. J.; Heller, E. J. *J. Chem. Phys.* **1982**, *77*, 3857.

(2) Mukamel, S. *Principles of Nonlinear Optical Spectroscopy*; Oxford University Press: New York, 1995.

(3) Ding, F.; Fulmer, E. C.; Zanni, M. T. *J. Chem. Phys.* **2005**, *123*, 094502.

(4) Hochstrasser, R. M. *Chem. Phys.* **2001**, *266*, 273.

APPENDIX D: SUPPLEMENT TO "TWO-DIMENSIONAL RESONANCE RAMAN SPECTROSCOPY OF WATER- AND OXYGEN- LIGATED MYOGLOBIN"

D.1. Response Functions

The fifth-order polarization possesses 16 components when a single electronic resonance dominates the optical response.[1] The 2DRR spectra in this work are calculated by Fourier transforming the polarization components presented in Reference [1] with respect to the delay time, τ_1. The frequency dimension, ω_2, is equal to the difference between the detection frequency, ω_t, and the frequency of the narrowband Raman pump, ω_{RP}. The summations below are restricted to eliminate population terms from the dimensions, ω_1 and ω_2. The 16 polarization components are

$$P_1^{(5)}(\omega_1,\omega_2) = -\frac{N\xi_{AP}^2\xi_{RP}^2\xi_{St}\left|\mu_{eg}\right|^6}{\hbar^5}\sum_{\substack{mnkluv \\ k\neq m,u\neq m}} B_m \langle n|m\rangle\langle n|k\rangle\langle l|k\rangle\langle l|u\rangle\langle v|u\rangle\langle v|m\rangle \times L_{en,gm}(\omega_{AP}) D_{gk,gm}(\omega_1) L_{el,gm}(\omega_t) J_{gu,gm}(\omega_2) L_{ev,gm}(\omega_t), \quad \text{(D.1)}$$

$$P_2^{(5)}(\omega_1,\omega_2) = -\frac{N\xi_{AP}^2\xi_{RP}^2\xi_{St}\left|\mu_{eg}\right|^6}{\hbar^5}\sum_{\substack{mnkluv \\ k\neq m,u\neq k}} B_m \langle n|m\rangle\langle n|k\rangle\langle l|m\rangle\langle l|u\rangle\langle v|k\rangle\langle v|u\rangle \times L_{en,gm}(\omega_{AP}) D_{gk,gm}(\omega_1) L_{gk,el}(-\omega_{RP}) J_{gk,gu}(\omega_2) L_{ev,gu}(\omega_t), \quad \text{(D.2)}$$

$$P_3^{(5)}(\omega_1,\omega_2) = -\frac{N\xi_{AP}^2\xi_{RP}^2\xi_{St}\left|\mu_{eg}\right|^6}{\hbar^5}\sum_{\substack{mnkluv \\ k\neq m,u\neq m}} B_m \langle n|m\rangle\langle n|k\rangle\langle l|k\rangle\langle l|u\rangle\langle v|m\rangle\langle v|u\rangle \times L_{gm,en}(-\omega_{AP}) D_{gm,gk}(\omega_1) L_{gm,el}(-\omega_{RP}) J_{gm,gu}(\omega_2) L_{ev,gu}(\omega_t), \quad \text{(D.3)}$$

$$P_4^{(5)}(\omega_1,\omega_2) = -\frac{N\xi_{AP}^2\xi_{RP}^2\xi_{St}\left|\mu_{eg}\right|^6}{\hbar^5}\sum_{\substack{mnkluv\\ k\neq m,u\neq k}} B_m\langle n|m\rangle\langle n|k\rangle\langle l|m\rangle\langle l|u\rangle\langle v|u\rangle\langle v|k\rangle, \quad \text{(D.4)}$$
$$\times L_{gm,en}(-\omega_{AP})D_{gm,gk}(\omega_1)L_{el,gk}(\omega_t)J_{gu,gk}(\omega_2)L_{ev,gk}(\omega_t)$$

$$P_5^{(5)}(\omega_1,\omega_2) = -\frac{N\xi_{AP}^2\xi_{RP}^2\xi_{St}\left|\mu_{eg}\right|^6}{\hbar^5}\sum_{\substack{mnkluv\\ k\neq n,u\neq k}} B_m\langle n|m\rangle\langle k|m\rangle\langle n|l\rangle\langle u|l\rangle\langle k|v\rangle\langle u|v\rangle, \quad \text{(D.5)}$$
$$\times L_{en,gm}(\omega_{AP})D_{en,ek}(\omega_1)L_{gl,ek}(-\omega_{RP})J_{eu,ek}(\omega_2)L_{eu,gv}(\omega_t)$$

$$P_6^{(5)}(\omega_1,\omega_2) = -\frac{N\xi_{AP}^2\xi_{RP}^2\xi_{St}\left|\mu_{eg}\right|^6}{\hbar^5}\sum_{\substack{mnkluv\\ k\neq n,u\neq n}} B_m\langle n|m\rangle\langle k|m\rangle\langle k|l\rangle\langle u|l\rangle\langle u|v\rangle\langle n|v\rangle, \quad \text{(D.6)}$$
$$\times L_{en,gm}(\omega_{AP})D_{en,ek}(\omega_1)L_{en,gl}(\omega_t)J_{en,eu}(\omega_2)L_{en,gv}(\omega_t)$$

$$P_7^{(5)}(\omega_1,\omega_2) = -\frac{N\xi_{AP}^2\xi_{RP}^2\xi_{St}\left|\mu_{eg}\right|^6}{\hbar^5}\sum_{\substack{mnkluv\\ k\neq n,u\neq n}} B_m\langle n|m\rangle\langle k|m\rangle\langle k|l\rangle\langle u|l\rangle\langle n|v\rangle\langle u|v\rangle, \quad \text{(D.7)}$$
$$\times L_{gm,en}(-\omega_{AP})D_{ek,en}(\omega_1)L_{gl,en}(-\omega_{RP})J_{eu,en}(\omega_2)L_{eu,gv}(\omega_t)$$

$$P_8^{(5)}(\omega_1,\omega_2) = -\frac{N\xi_{AP}^2\xi_{RP}^2\xi_{St}\left|\mu_{eg}\right|^6}{\hbar^5}\sum_{\substack{mnkluv\\ k\neq n,u\neq k}} B_m\langle n|m\rangle\langle k|m\rangle\langle n|l\rangle\langle u|l\rangle\langle u|v\rangle\langle k|v\rangle, \quad \text{(D.8)}$$
$$\times L_{gm,en}(-\omega_{AP})D_{ek,en}(\omega_1)L_{ek,gl}(\omega_t)J_{ek,eu}(\omega_2)L_{ek,gv}(\omega_t)$$

$$P_9^{(5)}(\omega_1,\omega_2) = -\frac{N\xi_{AP}^2\xi_{RP}^2\xi_{St}\left|\mu_{eg}\right|^6}{\hbar^5}\sum_{\substack{mnkluv\\ k\neq m,u\neq l}} B_m\langle n|m\rangle\langle n|k\rangle\langle l|k\rangle\langle u|m\rangle\langle u|v\rangle\langle l|v\rangle, \quad \text{(D.9)}$$
$$\times L_{en,gm}(\omega_{AP})D_{gk,gm}(\omega_1)L_{el,gm}(\omega_t)J_{el,eu}(\omega_2)L_{el,gv}(\omega_t)$$

$$P_{10}^{(5)}(\omega_1,\omega_2) = -\frac{N\xi_{AP}^2\xi_{RP}^2\xi_{St}\left|\mu_{eg}\right|^6}{\hbar^5}\sum_{\substack{mnkluv\\ k\neq m,u\neq l}} B_m\langle n|m\rangle\langle n|k\rangle\langle l|m\rangle\langle u|k\rangle\langle l|v\rangle\langle u|v\rangle, \quad \text{(D.10)}$$
$$\times L_{en,gm}(\omega_{AP})D_{gk,gm}(\omega_1)L_{gk,el}(-\omega_{RP})J_{eu,el}(\omega_2)L_{eu,gv}(\omega_t)$$

$$P_{11}^{(5)}(\omega_1,\omega_2) = -\frac{N\xi_{AP}^2\xi_{RP}^2\xi_{St}\left|\mu_{eg}\right|^6}{\hbar^5}\sum_{\substack{mnkluv\\ k\neq m,u\neq l}} B_m \langle n|m\rangle\langle n|k\rangle\langle l|m\rangle\langle u|k\rangle\langle u|v\rangle\langle l|v\rangle, \quad \text{(D.11)}$$
$$\times L_{gm,en}(-\omega_{AP}) D_{gm,gk}(\omega_1) L_{el,gk}(\omega_t) J_{el,eu}(\omega_2) L_{el,gv}(\omega_t)$$

$$P_{12}^{(5)}(\omega_1,\omega_2) = -\frac{N\xi_{AP}^2\xi_{RP}^2\xi_{St}\left|\mu_{eg}\right|^6}{\hbar^5}\sum_{\substack{mnkluv\\ k\neq m,u\neq l}} B_m \langle n|m\rangle\langle n|k\rangle\langle l|k\rangle\langle u|m\rangle\langle l|v\rangle\langle u|v\rangle, \quad \text{(D.12)}$$
$$\times L_{gm,en}(-\omega_{AP}) D_{gm,gk}(\omega_1) L_{gm,el}(-\omega_{RP}) J_{eu,el}(\omega_2) L_{eu,gv}(\omega_t)$$

$$P_{13}^{(5)}(\omega_1,\omega_2) = -\frac{N\xi_{AP}^2\xi_{RP}^2\xi_{St}\left|\mu_{eg}\right|^6}{\hbar^5}\sum_{\substack{mnkluv\\ k\neq n,u\neq l}} B_m \langle n|m\rangle\langle k|m\rangle\langle n|l\rangle\langle k|u\rangle\langle v|l\rangle\langle v|u\rangle, \quad \text{(D.13)}$$
$$\times L_{en,gm}(\omega_{AP}) D_{en,ek}(\omega_1) L_{gl,ek}(-\omega_{RP}) J_{gl,gu}(\omega_2) L_{ev,gu}(\omega_t)$$

$$P_{14}^{(5)}(\omega_1,\omega_2) = -\frac{N\xi_{AP}^2\xi_{RP}^2\xi_{St}\left|\mu_{eg}\right|^6}{\hbar^5}\sum_{\substack{mnkluv\\ k\neq n,u\neq l}} B_m \langle n|m\rangle\langle k|m\rangle\langle k|l\rangle\langle n|u\rangle\langle v|u\rangle\langle v|l\rangle, \quad \text{(D.14)}$$
$$\times L_{en,gm}(\omega_{AP}) D_{en,ek}(\omega_1) L_{en,gl}(\omega_t) J_{gu,gl}(\omega_2) L_{ev,gl}(\omega_t)$$

$$P_{15}^{(5)}(\omega_1,\omega_2) = -\frac{N\xi_{AP}^2\xi_{RP}^2\xi_{St}\left|\mu_{eg}\right|^6}{\hbar^5}\sum_{\substack{mnkluv\\ k\neq n,u\neq l}} B_m \langle n|m\rangle\langle k|m\rangle\langle k|l\rangle\langle n|u\rangle\langle v|l\rangle\langle v|u\rangle, \quad \text{(D.15)}$$
$$\times L_{gm,en}(-\omega_{AP}) D_{ek,en}(\omega_1) L_{gl,en}(-\omega_{RP}) J_{gl,gu}(\omega_2) L_{ev,gu}(\omega_t)$$

and

$$P_{16}^{(5)}(\omega_1,\omega_2) = -\frac{N\xi_{AP}^2\xi_{RP}^2\xi_{St}\left|\mu_{eg}\right|^6}{\hbar^5}\sum_{\substack{mnkluv\\ k\neq n,u\neq l}} B_m \langle n|m\rangle\langle k|m\rangle\langle n|l\rangle\langle k|u\rangle\langle v|u\rangle\langle v|l\rangle. \quad \text{(D.16)}$$
$$\times L_{gm,en}(-\omega_{AP}) D_{ek,en}(\omega_1) L_{ek,gl}(\omega_t) J_{gu,gl}(\omega_2) L_{ev,gl}(\omega_t)$$

The electronic line shape function, $L_{en,gm}(\omega)$, is written as

$$L_{en,gm}(\omega) = \frac{1}{\omega - \omega_{eg} - \omega_{nm} + i\Gamma_{eg}}. \tag{D.17}$$

The vibrational line shape functions, $D_{gk,gm}(\omega_1)$ and $J_{gu,gm}(\omega_2)$, are given by

$$D_{gk,gm}(\omega_1) = \frac{2\Lambda_{AP}}{\omega_{km}^2 + \Lambda_{AP}^2} \cdot \frac{1}{(\omega_1 - \omega_{km}) + i\Gamma_{vib}} \tag{D.18}$$

and

$$J_{gu,gm}(\omega_2) = \frac{\exp[i\omega\tau_2 - \Lambda_{RP}\tau_2]}{(\omega_2 - \omega_{um}) + i(\Gamma_{vib} - \Lambda_{RP})}. \tag{D.19}$$

The fifth-order 2DRR signal field is expressed in terms of these polarization components as

$$E_{2DRR}^{(5)}(\omega_1, \omega_2) = \frac{1}{7}\left(\frac{i\omega_t l}{2\varepsilon_0 n(\omega_t) c}\right)\sum_{j=1}^{16} P_j^{(5)}(\omega_1, \omega_2) \tag{D.20}$$

where perfect phase-matching has been assumed and the factor of 1/7 represents the orientational average for all-parallel electric field polarizations.[2]

D.2. Anharmonic Vibrational Hamiltonian

All calculations conducted in this work are based on the following vibrational Hamiltonian[3]

$$\begin{aligned} H = \sum_j \left[\frac{\hbar\omega_j}{2}\left(2a_j^\dagger a_j + 1\right) + U_{jjj}\left(3a_j^\dagger + 3a_j\right)\right] + \sum_{jkl} U_{jkl}\left(a_j^\dagger a_k^\dagger a_l^\dagger + 3a_j^\dagger a_k^\dagger a_l\right. \\ \left. + 3a_j^\dagger a_k a_l + a_j a_k a_l\right) \end{aligned} \tag{D.21}$$

where the cubic expansion coefficients are given by

$$U_{jkl} = \frac{1}{3!\sqrt{2^3 m^3 \omega^3 \hbar^{-3}}} \left(\frac{\partial^3 V}{\partial q_j \partial q_k \partial q_l} \right)_0 . \tag{D.22}$$

The basis set is taken to be uncoupled at second-order for this Hamiltonian. Therefore, normal modes are recovered if the cubic expansion coefficients are set equal to zero. This is the most natural basis set for the present study, because the calculations in Section 6.3 make use of fitting parameters obtained in a basis of normal modes.[4] Vibrational wavefunctions are obtained by diagonalizing the Hamiltonian in a basis of harmonic oscillators (up to 20 vibrational quanta in each mode results in good convergence).

The vibrational overlap integrals needed to evaluate the response functions are written as

$$\langle n | m \rangle = \sum_{\alpha\beta} \varphi_{n\alpha} \varphi_{m\beta} \langle \alpha | \beta \rangle \tag{D.23}$$

where $\varphi_{n\alpha}$ is the expansion coefficient for harmonic basis function α and the anharmonic vibrational wavefunction, n.

D.3. Signatures of Anarhmonicity

As discussed in the main text, anharmonic coupling between modes may cause the vibrational resonance frequencies in ω_2 to oscillate with respect to τ_1 for FSRS signals represented in the traditional way (τ_1 and ω_2 in our notation). Here, we examine this representation in our calculated signals. The first dimension may be expressed in the time domain by inverse Fourier transforming $E^{(5)}(\omega_1, \omega_2)$ with respect to τ_1. Analytic expressions for this representation, which we denote as $E^{(5)}(\tau_1, \omega_2)$, were given in Chapter 6.[1] The mean vibrational frequencies in ω_2 are then Fourier transformed with respect to τ_1

$$\sigma(\omega_1) = \int_{-\infty}^{\infty} \left[\frac{\int_{\alpha}^{\beta} \left| E^{(5)}(\tau_1, \omega_2) \right| \omega_2 d\omega_2}{\int_{\alpha}^{\beta} \left| E^{(5)}(\tau_1, \omega_2) \right| d\omega_2} \right] \exp(i\omega_1 \tau_1) d\tau_1 \qquad \text{(D.24)}$$

in order to produce a vibrational spectrum associated with the quantum beats in the resonance frequencies. The lower, α, and upper, β, limits of the integral over ω_2 are respectively set equal to 250 and 550 cm^{-1} for the 400-cm^{-1} mode. Limits of 950 and 1250 cm^{-1} are used for the 1100-cm^{-1} resonance in ω_2.

In Figure D.1 we present vibrational spectra associated with quantum beats in the resonance frequencies. The harmonic system in Figure D.1e exhibits the most intense oscillations at the frequency corresponding to a coherence between the two modes (i.e. 700 cm^{-1} is the difference in wavenumbers). As in Chapter 4[5], we find that oscillations in the mean vibrational resonance frequencies are observed even for a harmonic system (see Figure 4.10 in Chapter 4). Anharmonicity causes the relative amplitude of the quantum beat at 400 cm^{-1} to increase; the effect is most pronounced in panels D.1a, D.1c, D.1g, and D.1i (i.e. the parameters with the greatest amount of anharmonicity). These results suggest that the relative amplitudes of various spectral components carry the key information about anharmonicity in this representation. Quantum beats at difference frequencies occur even in the harmonic system. This conclusion is still valid if the real or imaginary parts of the fifth-order signal field enter Equation D.24. We process the absolute value of the signal field, $E^{(5)}(\tau_1, \omega_2)$, because the time evolution (in τ_1) between absorptive and dispersive line shapes (in ω_2) gives rise to artificially large oscillations in the mean resonance frequencies (in ω_2).

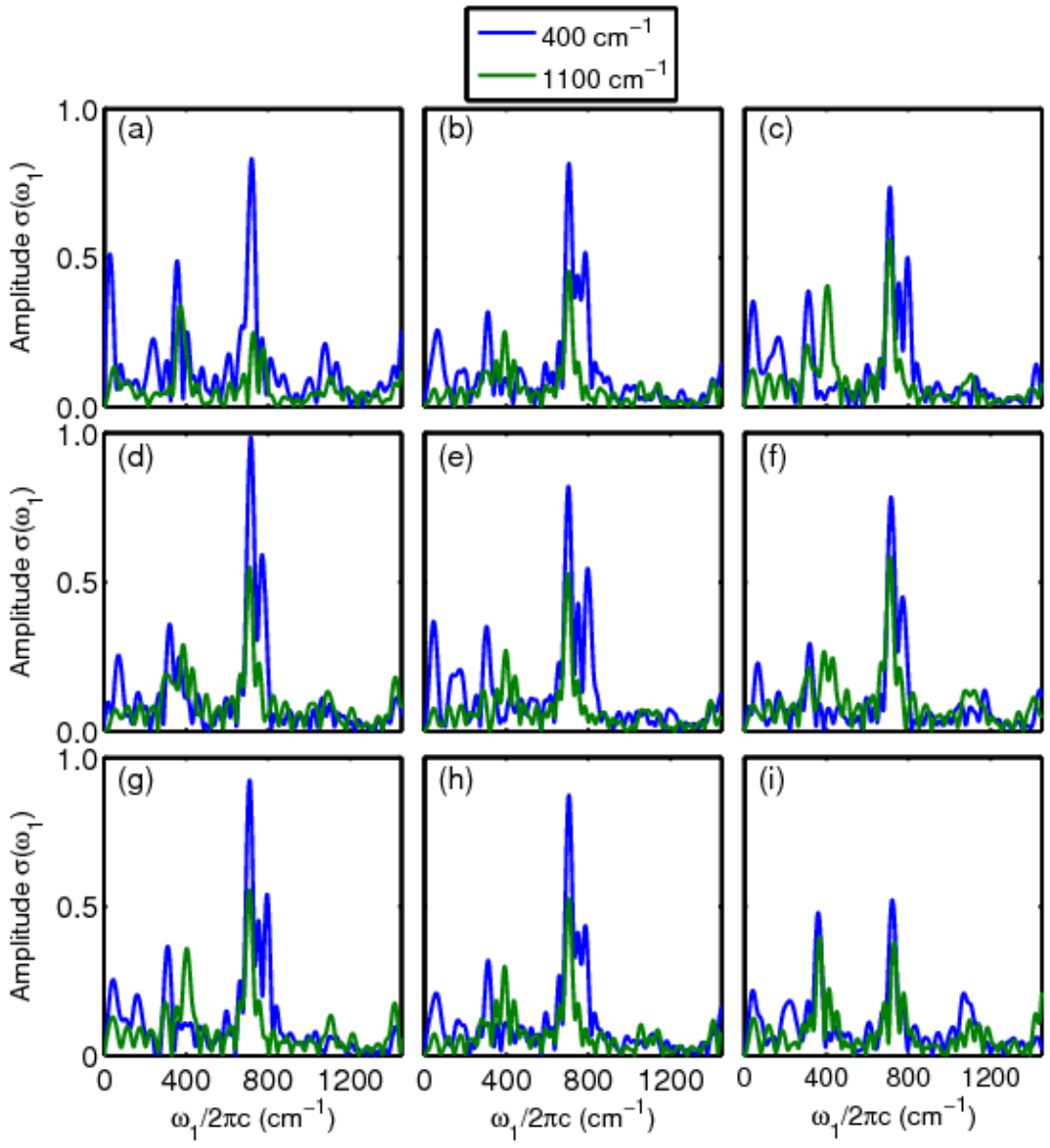

Figure D.1. Spectral components associated with oscillations of the mean vibrational resonance frequencies computed with an anharmonic vibrational Hamiltonian. The diagonal expansion coefficients are set equal to -5 (first row), 0 (second row), and 5 cm^{-1} (third row). The off-diagonal expansion coefficients are set equal to -5 (first row), 0 (second row), and 5 cm^{-1} (third row). All amplitudes are normalized to the maximum found for the 400-cm^{-1} mode in the second row and first column. These calculations show that oscillations in the mean vibrational resonance frequencies occur primarily at the difference frequency in the harmonic system (see panel (e)). Anharmonicity increases the amplitude of oscillations at the fundamental frequencies of the vibrations.

D.4. Fluctuations in the Geometries of the Propionic Acid Side Chains

In this section, we present scatter plots for 5000 steps in the molecular dynamics trajectories of metMb and MbO_2, respectively. The structures fluctuate in a fairly symmetric manner with respect to the equilibrium geometries.

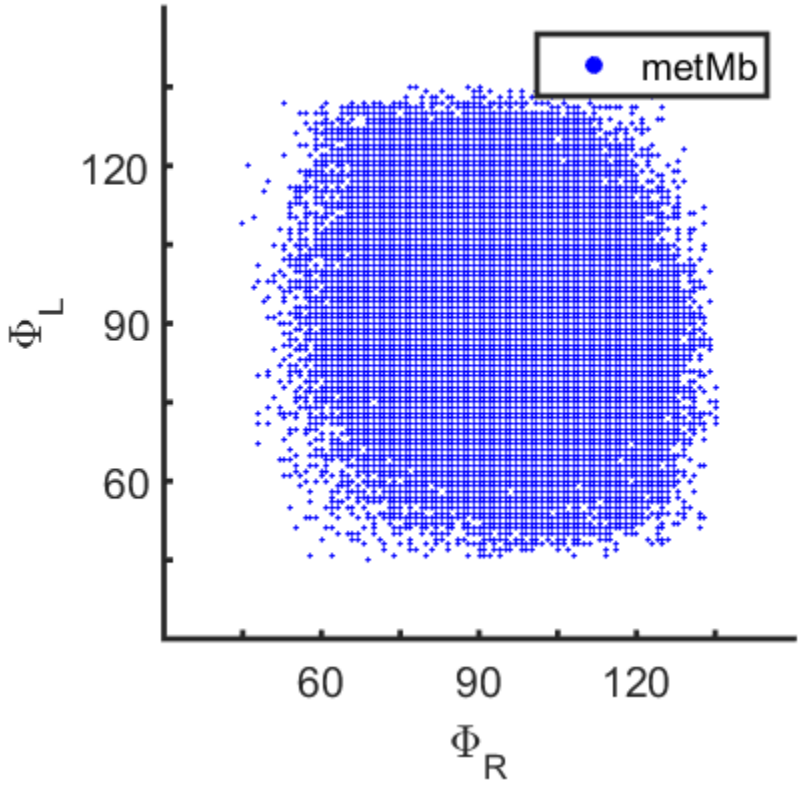

Figure D.2. Distribution of dihedral angles for 5000 steps of the molecular dynamics trajectory simulated for metMb. The equilibrium dihedral angles associated with the propionic acid side chains (see Figure 7.11) are Φ_L =81.3° and Φ_R =81.1°.

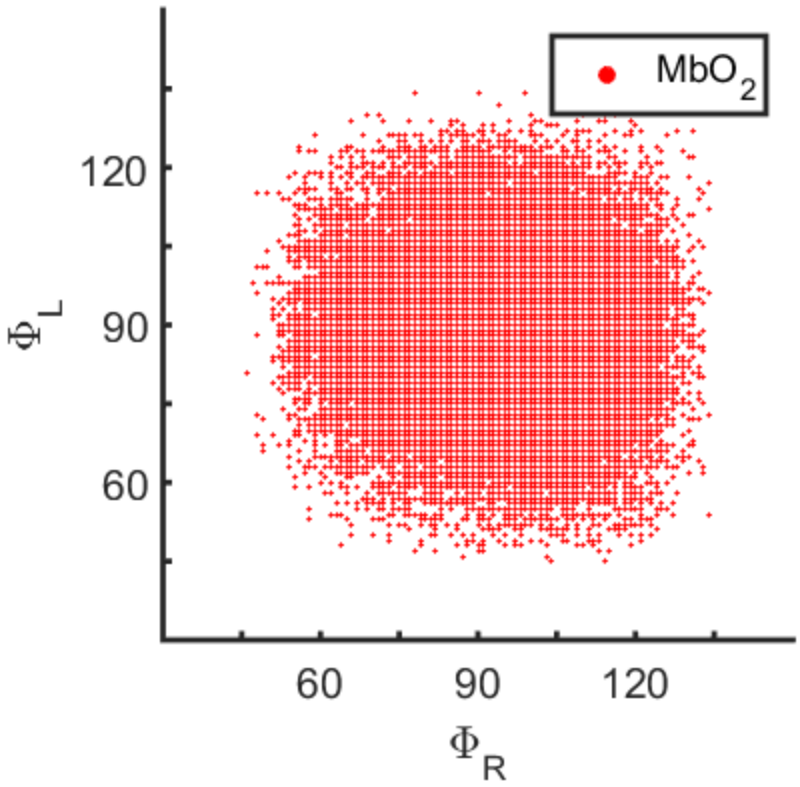

Figure D.3. Distribution of dihedral angles for 5000 steps of the molecular dynamics trajectory simulated for MbO_2. The equilibrium dihedral angles associated with the propionic acid side chains (see Figure 7.11) are Φ_L =94.4° and Φ_R =109°.

D.5. REFERENCES

(1) Molesky, B. M.; Guo, Z.; Moran, A. M. *J. Chem. Phys.* **2015**, *142*, 212405.

(2) Ding, F.; Fulmer, E. C.; Zanni, M. T. *J. Chem. Phys.* **2005**, *123*, 094502.

(3) Moran, A. M.; Dreyer, J.; Mukamel, S. *J. Chem. Phys.* **2003**, *118*, 1347.

(4) Bangcharoenpaurpong, O.; Schomacker, K. T.; Champion, P. M. *J. Am. Chem. Soc.* **1984**, *106*, 5688.

(5) Molesky, B. P.; Giokas, P. G.; Guo, Z.; Moran, A. M. *J. Chem. Phys.* **2014**, *114*, 114202.